

EXPERIMENTAL EVALUATION OF MULTISCALE BEHAVIOR
OF HUMAN BONE

A Dissertation
Submitted to the Graduate Faculty
of the
North Dakota State University
of Agriculture and Applied Science

By

Chunju Gu

In Partial Fulfillment of the Requirements
for the Degree of
DOCTOR OF PHILOSOPHY

Major Program:
Materials and Nanotechnology

December 2014

Fargo, North Dakota

North Dakota State University
Graduate School

Title

EXPERIMENTAL EVALUATION OF MULTISCALE BEHAVIOR OF
HUMAN BONE

By

Chunju Gu

The Supervisory Committee certifies that this *disquisition* complies with North Dakota State
University's regulations and meets the accepted standards for the degree of

DOCTOR OF PHILOSOPHY

SUPERVISORY COMMITTEE:

Kalpana S Katti

Co-Chair

Dinesh R Katti

Co-Chair

Xuefeng Chu

Sangita Sinha

Approved:

9/10/2015

Date

Erik Hobbie

Department Chair

ABSTRACT

Bone is the most important structural member of the human body. It has a unique hierarchical structure and its primary constituents, collagen molecules and hydroxyapatite, are arranged in a staggered pattern at nanometer scale. Osteogenesis imperfecta (OI) is an inheritable disease characterized by the fragility of bones and other tissues rich in the type I collagen. OI provides an interesting platform for investigating how alterations of collagen at the molecular level cause changes in the structure of bone. In this dissertation, multi-scale-, particularly nanometer and sub-micro scale-, behaviors of both normal and OI (putative type I) human bones have been evaluated experimentally. Since chemical treatment influences collagen or mineral structure, we have used “undisturbed bone samples” that are not subjected to any chemicals as previously done in literature. Photoacoustic-Fourier transform infrared spectroscopy (PA-FTIR) experiments reveal orientational differences in stoichiometry of hydroxyapatite. FTIR, electron microscopy, scanning probe microscopy, and nanomechanical tests also show that the OI disease results in a distorted microstructure in bone and that the mineralization of hydroxyapatite in OI is also altered. Modulus mapping test displays the distribution of mineralized fibril and extrafibrillar mineral according to the spatial variation of elastic properties. Dynamic nanomechanical behaviors of OI bone and normal bone indicates that the viscoelasticity of intact bone is mostly determined by the mineral. Also investigated are molecular composition and nanomechanical properties of different anatomical positions in the diaphysis of an OI human tibia. Our study on OI bone describes unique differences in collagen as previously described but also elaborates on unique influence of the non-collagenous proteins on mineralization of bone in OI. The fundamental premise of this work is investigation of the molecular basis of this highly debilitating bone disease.

ACKNOWLEDGMENTS

“Strength and growth come only through continuous effort and struggle” (Napoleon Hill). After six years’ effort and struggle toward completing this dissertation, I gained strength and growth as a researcher. But I would have not completed it without many helping hands. I take this opportunity to express my gratitude for those who are generous and made their contributions to this work.

First of all, I would like to gratefully and sincerely thank my advisor, Dr. Kalpana S. Katti, for her continuous guidance, understanding, encouragement, and patience. Without her support, I would not have reached this stage of getting a doctoral degree. Next, I would like to sincerely thank my co-advisor, Dr. Dinesh Katti, for his invaluable suggestions and candid feedback on the progress of my doctoral work.

My sincere thanks to esteemed committee members Dr. Xuefeng (Michael) Chu and Dr. Sangita Sinha for generously serving in my committee and helping my doctoral work as well.

I am also grateful to the NDSU graduate school for awarding me “Doctoral Dissertation Fellowship”, NSF MRI and IMR grants for providing the instruments for the experiments, as well as Civil and Environmental department for hiring me as a grader and giving me financial support.

I owe special thanks to the bone donors and their families. Without them, the research work could not have been done.

In addition, I thank Jan Lofberg and Milka Singha as well as Civil and Environmental department for being helpful to me in many aspects during my graduate studies.

Further, I would like to thank all of my group members for instrument operation training (Nanoindentation and AFM: Bedabibhas Mohanty, NanoDMA: Rohit Khanna, FTIR: Avinash

Ambre, SEM and FE-SEM: Scott Payne, and Polisher: Kristin N. Alstadt), cooperations (bone sample preparation: Amanda Grosz and Ashley Roder) and helpful discussions (Shashindra M. Pradhan, Anurag Sharma, Him Upadhyay, Md. Molla, Mohammad Reza Parsa, Keshab Thapa, etc.) throughout my graduate study.

Finally, I owe special thanks to my parents (Xingchang Bao and Shanrong Gu), my parents-in-law (Heling Bu and Baoyun Li), my sister (Hanzhen Bao), my brother-in-law (Yinming Zhu), and my husband (Honggang Bu) for their love and support.

DEDICATION

This dissertation is dedicated to my dear husband (Honggang Bu) and my lovely daughters (Gu and Laura).

TABLE OF CONTENTS

ABSTRACT.....	iii
ACKNOWLEDGMENTS.....	iv
DEDICATION.....	vi
LIST OF TABLES.....	xiii
LIST OF FIGURES.....	xv
LIST OF ABBREVIATIONS.....	xix
LIST OF APPENDIX FIGURES.....	xxii
CHAPTER 1. INTRODUCTION.....	1
1.1. Bone.....	1
1.2. Structure of bone.....	3
1.2.1. Level 1: Collagen fibrils and minerals (molecular and nanometer scales).....	5
1.2.2. Level 2: Mineralized fibril (sub-micro scale).....	6
1.2.3. Level 3: Fibrillar arrays (micro- scale).....	8
1.2.4. Level 4: Fibrillar array pattens (micro-scale).....	9
1.2.5. Level 5: Osteon (micro-scale).....	10
1.2.6. Level 6: Cortical (compact) and cancellous (spongy or trabecular) bone (meso-scale).....	10
1.3. Bone mechanics.....	11
1.3.1. Macro-scale mechanical properties of bone.....	12
1.3.2. Meso-scale mechanical properties of bone.....	15
1.3.3. Micro-scale mechanical properties of bone.....	16
1.3.4. Sub-micro-scale mechanical properties of bone.....	17
1.3.5. Nano-scale mechanical properties of bone.....	20
1.4. Bone diseases and bone quality characterization.....	21

1.4.1. Osteogenesis imperfecta	23
1.4.2. Characterization methods of bone quality	26
1.5. Scope of this dissertation	27
1.6. References	29
CHAPTER 2. PHOTOACOUSTIC FTIR SPECTROSCOPIC STUDY OF UNDISTURBED HUMAN CORTICAL BONE.....	45
2.1. Introduction.....	45
2.2. Materials and Methodology	50
2.2.1. Materials	50
2.2.2. Methods.....	51
2.3. Results.....	51
2.3.1. Microstructures of human bone in transverse and longitudinal planes.....	51
2.3.2. Comparison of PA-FTIR and TS-FTIR spectra.....	54
2.3.3. Comparison of PA spectra from transverse and longitudinal sections	55
2.3.4. Comparison of three smaller sections in the transverse and longitudinal planes	63
2.3.5. Depth profiling.....	65
2.3.6. Discussion.....	69
2.4. Conclusion	75
2.5. Acknowledgements.....	76
2.6. References.....	76
CHAPTER 3. MICROSTRUCTURAL AND INFRARED SPECTROSCOPIC STUDIES OF HUMAN CORTICAL BONE WITH OSTEOGENESIS IMPERFECTA.....	89
3.1. Introduction.....	89
3.2. Methods and Materials.....	96
3.2.1. Materials	96

3.2.2. Experiments	97
3.3. Results.....	98
3.3.1. Microstructure of OI human cortical bone.....	98
3.3.2. Comparison of PA-FTIR spectra of normal and OI bones	101
3.3.3. Comparison of PA-FTIR spectra of OI bone in transverse and longitudinal planes	106
3.3.4. XRD and EDS results	108
3.4. Discussion	113
3.5. Conclusion	121
3.6. Acknowledgements.....	122
3.7. References.....	122
CHAPTER 4. NANOMECHANICAL PROPERTIES OF UNDISTURBED HUMAN NORMAL AND OSTEOGENESIS IMPERFECTA CORTICAL BONES.....	135
4.1. Introduction.....	135
4.2. Materials and Methods.....	138
4.2.1. Materials	138
4.2.2. Methods.....	139
4.3. Results.....	142
4.3.1. Modulus mapping	142
4.3.2. In situ HR-SEM nanoindentation.....	147
4.4. Discussion	151
4.5. Conclusion	157
4.6. References.....	158
CHAPTER 5. DYNAMIC NANOMECHANICAL BEHAVIOR OF HEALTHY AND OI HUMAN CORTICAL BONES.....	170
5.1. Introduction.....	170

5.2. Materials and Methods.....	173
5.2.1. Materials	173
5.2.2. FTIR and AFM characterizations	175
5.2.3. Dynamic nanoindentation tests.....	176
5.3. Results and Discussion	177
5.3.1. Dynamic nanomechanical behaviour of intact normal human cortical bone.....	177
5.3.2. Demineralization of normal human cortical bone	179
5.3.3. Dynamic nanomechanical behaviour of demineralized normal human cortical bone.....	182
5.3.4. Dynamic nanomechanical behaviour of OI human cortical bone.....	186
5.3.5. Effects of frequency, orientation and composition on viscoelasticity of bone	188
5.4. Conclusion	190
5.5. Acknowledgement	191
5.6. References.....	191
CHAPTER 6. ANISOTROPIC PROPERTIES OF HUMAN CORTICAL BONE WITH OSTEOGENESIS IMPERFECTA.....	198
6.1. Introduction.....	198
6.2. Methods and Materials.....	202
6.2.1. Materials	202
6.2.2. Experiment.....	203
6.3. Results.....	205
6.3.1. Microstructure of OI human cortical bone.....	205
6.3.2. Photoacoustic-FTIR (PA-FTIR) spectra	208
6.3.3. In situ FE-SEM nanoindentation.....	211
6.4. Discussion	216

6.5. Conclusion	219
6.6. Acknowledgements.....	220
6.7. References.....	221
CHAPTER 7. SUMMARY AND CONCLUSIONS.....	228
CHAPTER 8. MAJOR CONTRIBUTIONS.....	232
CHAPTER 9. FUTURE WORK.....	234
APPENDIX A. INFORMATION SHEETS FOR HUMAN BONE SAMPLES.....	235
A.1. Healthy human femur.....	235
A.2. Osteogenesis imperfecta human tibia	236
APPENDIX B. SEM IMAGES OF HEALTHY HUMAN FEMUR.....	237
B.1. Anterior section	237
B.1.1. Transverse section	237
B.1.2. Longitudinal section.....	243
B.2. Medial section	249
B.2.1. Transverse section	249
B.2.2. Longitudinal section.....	251
B.3. Lateral section	253
B.3.1. Transverse section	253
B.3.2. Longitudinal section.....	255
B.4. Posterior section	257
B.4.1. Transverse section	257
B.4.2. Longitudinal section.....	259
APPENDIX C. SEM IMAGES OF OI HUMAN TIBIA.....	262
C.1. Anterior section, fixed with a series of chemicals and fractured in liquid N ₂	262

C.1.1. Transverse section	262
C.1.2. Longitudinal section.....	268
C.2. Medial section, fixed with a series of chemicals and fractured in liquid N ₂	278
C.2.1. Transverse section (acquired on 2/6/2014)	278
C.2.2. Longitudinal section (acquired on 2/5/2014)	285
C.3. Lateral section, fixed with a series of chemicals and fractured in liquid N ₂	288
C.3.1. Transverse section (acquired on 2/6/2014)	288
C.3.2. Longitudinal section (acquired on 2/6/2014)	295
C.4. Posterior section, fixed with a series of chemicals and fractured in liquid N ₂	297
C.4.1. Transverse section (acquired on 2/6/2014)	297
C.4.2. Longitudinal section (acquired on 2/6/2014)	306
APPENDIX D. AFM IMAGES OF HEALTHY AND OI HUMAN BONES	311
D.1. Healthy human femur (left image: height, right image: phase)	311
D.1.1. No treatment, not polished.....	311
D.1.2. No treatment, polished	312
D.1.3. Demineralized for 5 minutes in EDTA (left image: height, right image: phase)	313
D.1.4. Demineralized for 4 hours in EDTA.....	314
D.2. OI human tibia	316
D.2.1. No treatment, not polished.....	316
D.2.2. No treatment, polished	317
D.2.3. Demineralized for 5 minutes.....	320

LIST OF TABLES

<u>Table</u>	<u>Page</u>
1.1. Composition of human cortical bone (7).....	3
1.2. Elastic properties of human femoral cortical bone (39).	14
1.3. Ultimate stresses of human femoral cortical bone (39).....	14
1.4. AFM mechanical measurement at mineralized fibril level of bone tissue (96).....	21
1.5. Nanoindentation measurements at lamellar level and micronanoindentation measurements at osteonal level (96).	22
1.6. OI Nosology (118).....	24
2.1. Band assignments of PA-FTIR spectra from human bone.	56
2.2. Major components of the ν_1 , ν_3 PO_4^{3-} bands in bone (27, 87, 88).....	61
2.3. Thermal diffusion depths of bone varying with Phase Modulation (PM) frequencies.....	66
3.1. Band assignments of PA-FTIR spectra from OI bone.....	102
3.2. Major components of the ν_1 , ν_3 PO_4^{3-} bands (75, 77, 78).....	110
3.3. Crystal size along c-axis direction of bone mineral (nm).....	112
3.4. Ca/P molar ratio of bone specimens (\pm STD).....	113
4.1 Statistics of elastic moduli from all modulus maps (Figure 4.4 and Figure 4.5) ^a	147
4.2. Elastic moduli and hardness of normal and OI bones for the transverse sections.....	149
4.3. Elastic moduli and hardness of normal and OI bones for the longitudinal sections.....	150
5.1. Roughness R_q of the bone specimens of intact and demineralized bone samples (average \pm STDEV).....	182
5.2. $\text{Tan } \delta$, E' , and maximum displacement values of intact and demineralized normal bone specimens at frequencies of 25, 50 and 100Hz (average \pm STDEV).....	185
5.3. $\text{Tan } \delta$, E' , and maximum displacement values of normal and OI bone specimens at frequencies of 25, 50 and 100Hz (average \pm STDEV).....	188
6.1. Band assignments of PA-FTIR spectra from OI bone.....	210

6.2. Elastic moduli and hardness of anterior and posterior sections of human OI cortical bone for the transverse sections.....	214
6.3. Elastic moduli and hardness of anterior and posterior sections of human OI cortical bone for the longitudinal sections.	216

LIST OF FIGURES

<u>Figure</u>	<u>Page</u>
1.1. Hierarchical organization of a human femur bone from macro- to nanoscale. (a) Macroscale organ level—human femur bone. (b) Macroscale tissue level—osteon. (c) Microscopic level—bone lamellae (adapted from (15, 16)). (d) Mesoscopic level—fiber bundle. (e) Nanoscale level—mineralized fibril. (f) Molecular level—collagen molecule and mineral particle (adapted from(14)).	4
1.2. Collagen molecules and intermolecular cross-linking (a) Triple-helical structural motif of collagen molecules (adapted from (15)). (b) Lysyl oxidase cross-linking (adapted from (17)).	6
1.3. SEM image of staggered arrangement of mineralized fibrils.	7
1.4. Schematic illustration of the arrangement of mineralized collagen fibrils aligned both with respect to crystal layers and fibril axes. (a) Orthotropic symmetry arrangement. (b) Transversal isotropic arrangement (adapted from (4)).	8
1.5. Four most common fibril array patterns with SEM images of fractured surfaces and schematic illustrations (not drawn to scale) of the basic organizational motifs. (a) Parallel fibrils array. (b) Woven fibrils array. (c) Plywood-like structure present in lamellar. (d) Radial fibril arrays (adapted from (4)).	9
1.6. SEM micrograph of an osteon.	10
1.7. Different types of loads that can be applied on bone.	13
1.8. A schematic representation of load versus indenter displacement data for an indentation experiment. The quantities shown are P_{max} : the peak indentation load; h_{max} : the indenter displacement at peak load; h_f : the final depth of the contact impression after unloading and S : the initial unloading stiffness.	19
2.1. Schematic diagram of PA-FTIR instrument.	49
2.2. (a) Location of the tested sample from the human femur; and (b) Schematic representation of bone showing from where the sample were cut, 1 represents inner side, 2 middle, and 3 outer side of the bone piece.	50
2.3. SEM micrographs of human bone (a and b) Transverse section; and (c and d) Longitudinal section.	52
2.4. HAP in bone. (a) Staggered arrangement if mineralized fibrils. (b) Relationship between collagen molecules and intra-fibrillar HAP crystal. (c) HAP structure projected on the (001) plane and (100) plane (adapted from (71)).	53
2.5. LS-PA-FTIR spectra of human bone in the 4000-400 cm^{-1} region, velocity of mirror: 0.158 cm/s : (a) Transverse; and (b) Longitudinal sections.	54

2.6. (a) PA-FTIR spectra of human bone (transverse and longitudinal) in the 4000-2000 cm^{-1} region; and (b) Inverted second-derivative curves in the energy range of 3900-2400 cm^{-1}	57
2.7. Photoacoustic infrared spectra of human bone (transverse and longitudinal) in the energy range of 2000-1180 cm^{-1}	59
2.8. Photoacoustic infrared spectra of human bone (transverse and longitudinal) in the energy range of 1180-400 cm^{-1}	60
2.9. (a) Inverted second-derivative curves in the energy range of 1180-927 cm^{-1} ; curve fitting analysis of the ν_1 , ν_3 phosphate band (1180–927 cm^{-1}) of (b) Transverse section, and (c) Longitudinal section.....	62
2.10. PA-LS-FTIR spectra of human bone in the 4000-400 cm^{-1} region, velocity of mirror: 0.158 cm/s. (a) Transverse section, 4000-400 cm^{-1} region; (b) Longitudinal section, 4000-400 cm^{-1} region.....	65
2.11. SS-PA-FTIR spectra of human bone: (a) Transverse section (4000-830 cm^{-1}); (b) Longitudinal section (4000-830 cm^{-1}); (c) Transverse section (2000-830 cm^{-1}); and (d) Longitudinal section (2000-830 cm^{-1}).....	67
3.1. Schematic representation of bone showing from where the samples were cut; transverse section and longitudinal section are both from the anterior area of OI bone specimen.....	97
3.2. (a-j) SEM micrographs of OI bone specimens.....	100
3.3. PA-FTIR spectra of human OI cortical bone and healthy cortical bone (longitudinal and transverse sections, respectively) in the 4000-400 cm^{-1} region, velocity of mirror: 0.158 cm/s.....	101
3.4. PA-FTIR spectra of human OI cortical bone and healthy cortical bone (longitudinal and transverse sections, respectively) in the 2400-1180 cm^{-1} region.....	104
3.5. Inverted second-derivative curves in the energy range of 2400-3900 cm^{-1}	105
3.6. PA-FTIR spectra of human OI cortical bone and healthy cortical bone (longitudinal and transverse sections, respectively) in the 1180-420 cm^{-1} region.....	106
3.7. Inverted second-derivative curves of OI longitudinal and transverse sections in the 1720-1590 cm^{-1} region.....	107
3.8. (a) Curve fitting analysis of the ν_1 , ν_3 phosphate band (1180–927 cm^{-1}) of (a) Transverse section, and (b) Longitudinal section.....	109
3.9. X-ray diffractogram of bone specimens: Healthy bone (T-transverse section and L-longitudinal section) and OI bone specimens.....	112

3.10. Structure of an HAP nanocrystal.	118
4.1. Schematic of cutting bone.....	139
4.2. Modulus mapping instrument	140
4.3. In situ HR-SEM nanoindentation were performed on (a) Transverse surface; (b) Longitudinal surface.	141
4.4. Modulus map images and corresponding data of normal human bone. (a) Modulus map image for the longitudinal section, area: $2\mu\text{m}\times 2\mu\text{m}$; (b) Modulus data of the black line in Figure a; (c) Modulus map image for the transverse section, area: $5\mu\text{m}\times 5\mu\text{m}$; (d) The square subset in Figure c.	143
4.5. Modulus map images and corresponding data of OI human bone. (a) Modulus map image for the transverse section, area: $3\mu\text{m}\times 3\mu\text{m}$; (b) The square subset in Figure a; (c) Modulus data of the black line in Figure a; (d) Modulus map image for the longitudinal section, area: $3\mu\text{m}\times 3\mu\text{m}$; (e) The square subset in Figure c; (f) Modulus data of the black line in Figure d.	145
4.6. Elastic modulus results produced by modulus mapping on the longitudinal and transverse sections of both normal and OI bones. Bars show the median with 25th (Q1) and 75th (Q3) percentiles. The lines perpendicular to the box are whiskers. Upper limit of whisker = $Q3 + 1.5(Q3 - Q1)$; lower limit of whisker = $Q1 - 1.5(Q3 - Q1)$. *outliers of the whisker. (N=35840).	146
4.7. Representative load-displacement (L~D) curve for bone sample at peak load of $50\mu\text{N}$..	148
4.8. Elastic modulus values of human bone in the transverse section.	149
4.9. Schematic illustration of the mineralized collagen fibril (not drawn to scale). Plate-like mineral crystals are sandwiched between layers of collagen molecules. P, T, L refer to the periosteal, transverse and longitudinal planes, respectively, perpendicular to the corresponding arrows. Transverse plane is normal to the bone long axis and periosteal plane is parallel to the natural outer surface of the bone (adapted from (77)).	152
4.10. Arrangement of collagen and mineral, black lines represent collagen molecules; green squares represent mineral particles (not drawn to scale).....	153
5.1. Bone samples (Specimens for testing are from the mid-diaphysis part as shown in squares).....	174
5.2. Schematic of bone specimen positions and indentation directions.....	174
5.3. Schematic plot of load versus time for a variable dynamic load test.	177
5.4. The mean loss tangent with 95% confidence intervals of normal bone specimens with variable static force (a) Longitudinal section; (b) Transverse section.	178

5.5. Representative storage modulus, loss modulus and loss tangent values of the human bone during one dynamic nanoindentation (Longitudinal section, frequency: 50Hz) (a) E' and E'' ; (b) $\text{Tan}\delta$	179
5.6. Photoacoustic infrared spectra of undisturbed and demineralized human bone in the energy range of $4000\text{-}400\text{cm}^{-1}$ (a) Transverse section, time of demineralization: 5 minutes, 4, 8, 24, and 72hours; (b) Transverse and longitudinal sections, time of demineralization: 5 minutes, and 4hours.....	181
5.7. The mean loss tangent with 95% confidence intervals of demineralized normal bone specimens with variable static force (a) Longitudinal section, demineralized for 5 minutes; (b) Longitudinal section, demineralized for 4hours; (c) Transverse section, demineralized for 5 minutes; (d) Transverse section, demineralized for 4 hours.	183
5.8. The mean loss tangent with 95% confidence intervals of OI bone specimens with variable static force (a) Longitudinal section (b) Transverse section.	187
6.1. Schematic representation of bone showing from where the samples were cut, transverse section and longitudinal section are both from the anterior, medial, posterior, and lateral areas of OI bone specimen.	203
6.2. In situ FE-SEM nanoindention performed on the surface of (a)(b) Trans-anterior section; (c)(d) Longi-anterior section.....	205
6.3. SEM images of human OI cortical bone (a, b) Anterior section; (c, d, e) Medial section; (f, g, h) Posterior section; (i, j) Lateral section (Thin arrows indicate secondary osteon (SO) regions and arrowheads bone powder region probably created from cutting procedure).....	207
6.4. PA-FTIR spectra of human OI cortical bone (anterior, medial, posterior, and lateral sections for the longitudinal and transverse sections, respectively). Velocity of mirror: 0.158 cm/s . (a) $4000\text{-}450\text{ cm}^{-1}$ region; (b) $2300\text{-}450\text{ cm}^{-1}$ region.....	209
6.5. Representative load-displacement curve taken during a single nanoindentation test of the OI bone specimen with peak load of $50\text{ }\mu\text{N}$: (a) Trans-anterior section; (b) Trans-posterior section.	212
6.6. Nanomechanical properties of normal and OI bones (anterior and posterior sections) in the transverse plane. OL refers to osteonal lamellae, and IL refers to interstitial lamellae. (a) Elastic modulus; (b) Hardness.....	213
6.7. Nanomechanical properties of normal and OI bones (anterior and posterior sections) in the longitudinal plane. OL is osteonal lamellae, and IL is interstitial lamellae. (a) Elastic modulus; (b) Hardness.....	215

LIST OF ABBREVIATIONS

AD.....	Autosomal dominant
AR.....	Autosomal recessive
AFM.....	Atomic force microscopy
BMD.....	Bone mineral density
CT.....	Computerized tomography
Demi.....	Demineralized
DI.....	Deionized
DMA.....	Dynamic mechanical analyzer
DXA.....	Dual-energy X-ray absorptiometry
EDS.....	Energy-dispersive X-ray spectroscopy
EDTA.....	Ethylenediaminetetraacetic acid
FEA.....	Finite element analysis
FE-SEM.....	Field emission-scanning electron microscope
FTIR.....	Fourier transform infrared spectroscopy
FTIRI.....	Fourier transform infrared imaging
FWHM.....	Full width at half maximum ()
GMA.....	Glycolmethacrylate
HAP.....	Hydroxyapatite
HPLC.....	High-performance liquid chromatography
Longi.....	Longitudinal
LS.....	Linear-scan
μCT.....	Micro-computed tomography

MMModulus mapping

MR.....Microradiography

MRI.....Magnetic resonance imaging

NCPsNon-collagenous proteins

NI.....Nanoindentation

NMR.....Nuclear magnetic resonance

OI.....Osteogenesis imperfecta

PA-FTIR.....Photo acoustic Fourier transform infrared spectroscopy

PBS.....Phosphate buffered saline

PMMA.....Poly(methyl methacrylate)

qBEI.....Quantitative backscattered electron imaging

RANKL.....Receptor activator of nuclear factor- κ B ligand

RMS.....Root mean squared

SAMScanning acoustic microscopy

SEM.....Scanning electron microscope

SAXS.....Small angle X-ray scattering

SR μ CT.....Synchrotron radiation micro computed tomography

SS.....Step-scan

STDEV.....Standard Deviation

TEMTransmission electron microscopy

TGF.....Transforming growth factor beta

Trans.....Transverse

TS-FTIR.....Transmission Fourier transform infrared spectroscopy

WAXSWide-angle X-ray scattering

XRD.....X-ray Diffraction

LIST OF APPENDIX FIGURES

<u>Figure</u>	<u>Page</u>
A.1. Information sheet of healthy human femur from NDRI.....	235
A.2. Information sheet of OI human tibia from NDRI.....	236
B.1. SEM image of healthy human femur (transverse, anterior section) ×85..	237
B.2. SEM image of healthy human femur (transverse, anterior section) ×100	237
B.3. SEM image of healthy human femur (transverse, anterior section) ×550	237
B.4. SEM image of healthy human femur (transverse, anterior section) ×1,000	237
B.5. SEM image of healthy human femur (transverse, anterior section) ×5,000	238
B.6. SEM image of healthy human femur (transverse, anterior section) ×13,000	238
B.7. SEM image of healthy human femur (transverse, anterior section) ×15,000	238
B.8. SEM image of healthy human femur (transverse, anterior section) ×40,000	238
B.9. SEM image of healthy human femur (transverse, anterior section) ×70,000	238
B.10. SEM image of healthy human femur (transverse, anterior section) ×37,000	238
B.11. SEM image of healthy human femur (transverse, anterior section) ×400	239
B.12. SEM image of healthy human femur (transverse, anterior section) ×1,400	239
B.13. SEM image of healthy human femur (transverse, anterior section) ×60	239
B.14. SEM image of healthy human femur (transverse, anterior section) ×450	239
B.15. SEM image of healthy human femur (transverse, anterior section) ×60	239
B.16. SEM image of healthy human femur (transverse, anterior section) ×500	239
B.17. SEM image of healthy human femur (transverse, anterior section) ×1,500	240
B.18. SEM image of healthy human femur (transverse, anterior section) ×85	240
B.19. SEM image of healthy human femur (transverse, anterior section) ×100	240
B.20. SEM image of healthy human femur (transverse, anterior section) ×550.....	240
B.21. SEM image of healthy human femur (transverse, anterior section) ×1,000	240

B.22. SEM image of healthy human femur (transverse, anterior section) ×15,000	241
B.23. SEM image of healthy human femur (transverse, anterior section) ×40,000	241
B.24. SEM image of healthy human femur (transverse, anterior section) ×70,000	241
B.25. SEM image of healthy human femur (transverse, anterior section) ×40,000	241
B.26. SEM image of healthy human femur (transverse, anterior section) ×100	241
B.27. SEM image of healthy human femur (transverse, anterior section) ×220	241
B.28. SEM image of healthy human femur (transverse, anterior section) ×180	242
B.29. SEM image of healthy human femur (transverse, anterior section) ×350	242
B.30. SEM image of healthy human femur (transverse, anterior section) ×750	242
B.31. SEM image of healthy human femur (transverse, anterior section) ×900	242
B.32. SEM image of healthy human femur (transverse, anterior section) ×5,000	242
B.33. SEM image of healthy human femur (transverse, anterior section) ×2,000	242
B.34. SEM image of healthy human femur (longi., anterior section) ×30,000	243
B.35. SEM image of healthy human femur (longi., anterior section) ×75,000	243
B.36. SEM image of healthy human femur (longi., anterior section) ×7,000	243
B.37. SEM image of healthy human femur (longi., anterior section) ×20,000	243
B.38. SEM image of healthy human femur (longi., anterior section) ×13,000	244
B.39. SEM image of healthy human femur (longi., anterior section) ×3,000	244
B.40. SEM image of healthy human femur (longi., anterior section) ×10,000	244
B.41. SEM image of healthy human femur (longi., anterior section) ×30,000	244
B.42. SEM image of healthy human femur (longi., anterior section) ×80,000	244
B.43. SEM image of healthy human femur (longi., anterior section) ×15,000	244
B.44. SEM image of healthy human femur (longi., anterior section) ×25,000	245
B.45. SEM image of healthy human femur (longi., anterior section) ×40,000	245
B.46. SEM image of healthy human femur (longi., anterior section) ×40	245
B.47. SEM image of healthy human femur (longi., anterior section) ×150	245

B.48. SEM image of healthy human femur (longi., anterior section) ×700	245
B.49. SEM image of healthy human femur (longi., anterior section) ×3,500	245
B.50. SEM image of healthy human femur (longi., anterior section) ×10,000	246
B.51. SEM image of healthy human femur (longi., anterior section) ×20,000	246
B.52. SEM image of healthy human femur (longi., anterior section) ×60,000	246
B.53. SEM image of healthy human femur (longi., anterior section) ×120,000	246
B.54. SEM image of healthy human femur (longi., anterior section) ×40,000	246
B.55. SEM image of healthy human femur (longi., anterior section) ×15,000	246
B.56. SEM image of healthy human femur (longi., anterior section) ×35,000	247
B.57. SEM image of healthy human femur (longi., anterior section) ×40,000	247
B.58. SEM image of healthy human femur (longi., anterior section) ×60,000	247
B.59. SEM image of healthy human femur (longi., anterior section) ×60,000	247
B.60. SEM image of healthy human femur (longi., anterior section) ×15,000	247
B.61. SEM image of healthy human femur (longi., anterior section) ×40,000	247
B.62. SEM image of healthy human femur (longi., anterior section) ×40,000	248
B.63. SEM image of healthy human femur (longi., anterior section) ×15,000	248
B.64. SEM image of healthy human femur (longi., anterior section) ×50	248
B.65. SEM image of healthy human femur (longi., anterior section) ×20,000	248
B.66. SEM image of healthy human femur (longi., anterior section) ×50,000	248
B.67. SEM image of healthy human femur (longi., anterior section) ×35,000	249
B.68. SEM image of healthy human femur (longi., anterior section) ×23,000	249
B.69. SEM image of healthy human femur (longi., anterior section) ×80,000	249
B.70. SEM image of healthy human femur (transverse, medial section) ×25	249
B.71. SEM image of healthy human femur (transverse, medial section) ×50.....	249
B.72. SEM image of healthy human femur (transverse, medial section) ×30	250
B.73. SEM image of healthy human femur (transverse, medial section) ×100.....	250

B.74. SEM image of healthy human femur (transverse, medial section) ×300	250
B.75. SEM image of healthy human femur (transverse, medial section) ×1,000.....	250
B.76. SEM image of healthy human femur (transverse, medial section) ×100	250
B.77. SEM image of healthy human femur (transverse, medial section) ×95.....	250
B.78. SEM image of healthy human femur (longi., medial section) ×25	251
B.79. SEM image of healthy human femur (longi., medial section) ×50.....	251
B.80. SEM image of healthy human femur (longi., medial section) ×150	251
B.81. SEM image of healthy human femur (longi., medial section) ×1,000.....	251
B.82. SEM image of healthy human femur (longi., medial section) ×20,000	251
B.83. SEM image of healthy human femur (longi., medial section) ×80,000.....	251
B.84. SEM image of healthy human femur (longi., medial section) ×100	252
B.85. SEM image of healthy human femur (longi., medial section) ×1,000.....	252
B.86. SEM image of healthy human femur (longi., medial section) ×10,000	252
B.87. SEM image of healthy human femur (longi., medial section) ×40,000.....	252
B.88. SEM image of healthy human femur (longi., medial section) ×80,000	252
B.89. SEM image of healthy human femur (longi., medial section) ×80,000.....	252
B.90. SEM image of healthy human femur (longi., medial section) ×80,000.....	253
B.91. SEM image of healthy human femur (transverse, lateral section) ×25.....	253
B.92. SEM image of healthy human femur (longi., medial section) ×25.....	253
B.93. SEM image of healthy human femur (transverse, lateral section) ×100	254
B.94. SEM image of healthy human femur (transverse, lateral section) ×500.....	254
B.95. SEM image of healthy human femur (transverse, lateral section) ×3,000.....	254
B.96. SEM image of healthy human femur (transverse, lateral section) ×20,000.....	254
B.97. SEM image of healthy human femur (transverse, lateral section) ×80,000.....	254
B.98. SEM image of healthy human femur (transverse, lateral section) ×80,000.....	254
B.99. SEM image of healthy human femur (transverse, lateral section) ×10,000	255

B.100. SEM image of healthy human femur (transverse, lateral section) ×7,000.....	255
B.101. SEM image of healthy human femur (transverse, lateral section) ×40,000	255
B.102. SEM image of healthy human femur (transverse, lateral section) ×10,000.....	255
B.103. SEM image of healthy human femur (longi., lateral section) ×25	255
B.104. SEM image of healthy human femur (longi., lateral section) ×100.....	255
B.105. SEM image of healthy human femur (longi., lateral section) ×100	256
B.106. SEM image of healthy human femur (longi., lateral section) ×100.....	256
B.107. SEM image of healthy human femur (longi., lateral section) ×500	256
B.108. SEM image of healthy human femur (longi., lateral section) ×1,000.....	256
B.109. SEM image of healthy human femur (longi., lateral section) ×7,000	256
B.110. SEM image of healthy human femur (longi., lateral section) ×80,000.....	256
B.111. SEM image of healthy human femur (longi., lateral section) ×40,000.....	257
B.112. SEM image of healthy human femur (transverse, posterior section) ×25	257
B.113. SEM image of healthy human femur (transverse, posterior section) ×25.....	257
B.114. SEM image of healthy human femur (transverse, posterior section) ×25	258
B.115. SEM image of healthy human femur (transverse, posterior section) ×100.....	258
B.116. SEM image of healthy human femur (transverse, posterior section) ×1,000	258
B.117. SEM image of healthy human femur (transverse, posterior section) ×4,500.....	258
B.118. SEM image of healthy human femur (transverse, posterior section) ×200	258
B.119. SEM image of healthy human femur (transverse, posterior section) ×20,000.....	258
B.120. SEM image of healthy human femur (transverse, posterior section) ×30,000	259
B.121. SEM image of healthy human femur (transverse, posterior section) ×40,000.....	259
B.122. SEM image of healthy human femur (longi., posterior section) ×25	259
B.123. SEM image of healthy human femur (longi., posterior section) ×100.....	259
B.124. SEM image of healthy human femur (longi., posterior section) ×550	260
B.125. SEM image of healthy human femur (longi., posterior section) ×3,000.....	260

B.126. SEM image of healthy human femur (longi., posterior section) ×10,000	260
B.127. SEM image of healthy human femur (longi., posterior section) ×45,000.....	260
B.128. SEM image of healthy human femur (longi., posterior section) ×100	260
B.129. SEM image of healthy human femur (longi., posterior section) ×100.....	260
B.130. SEM image of healthy human femur (longi., posterior section) ×43	261
B.131. SEM image of healthy human femur (longi., posterior section) ×25.....	261
B.132. SEM image of healthy human femur (longi., posterior section) ×100.....	261
B.133. SEM image of healthy human femur (longi., posterior section) ×150.....	261
B.134. SEM image of healthy human femur (longi., posterior section) ×180	261
B.135. SEM image of healthy human femur (longi., posterior section) ×180.....	261
C.1. SEM image of OI human tibia (transverse, anterior section) ×37	262
C.2. SEM image of OI human tibia (transverse, anterior section) ×100	262
C.3. SEM image of OI human tibia (transverse, anterior section) ×150	262
C.4. SEM image of OI human tibia (transverse, anterior section) ×250	262
C.5. SEM image of OI human tibia (transverse, anterior section) ×650	263
C.6. SEM image of OI human tibia (transverse, anterior section) ×40,000	263
C.7. SEM image of OI human tibia (transverse, anterior section) ×80,000	263
C.8. SEM image of OI human tibia (transverse, anterior section) ×3,000	263
C.9. SEM image of OI human tibia (transverse, anterior section) ×10,000	263
C.10. SEM image of OI human tibia (transverse, anterior section) ×40,000	263
C.11. SEM image of OI human tibia (transverse, anterior section) ×40,000	264
C.12. SEM image of OI human tibia (transverse, anterior section) ×3,000	264
C.13. SEM image of OI human tibia (transverse, anterior section) ×3,000	264
C.14. SEM image of OI human tibia (transverse, anterior section) ×7,000	264
C.15. SEM image of OI human tibia (transverse, anterior section) ×35,000	264
C.16. SEM image of OI human tibia (transverse, anterior section) ×40,000	264

C.17. SEM image of OI human tibia (transverse, anterior section) ×25	265
C.18. SEM image of OI human tibia (transverse, anterior section) ×50	265
C.19. SEM image of OI human tibia (transverse, anterior section) ×100	265
C.20. SEM image of OI human tibia (transverse, anterior section) ×1,000	265
C.21. SEM image of OI human tibia (transverse, anterior section) ×5,000	265
C.22. SEM image of OI human tibia (transverse, anterior section) ×10,000	265
C.23. SEM image of OI human tibia (transverse, anterior section) ×20,000	266
C.24. SEM image of OI human tibia (transverse, anterior section) ×250	266
C.25. SEM image of OI human tibia (transverse, anterior section) ×1,000	266
C.26. SEM image of OI human tibia (transverse, anterior section) ×100	266
C.27. SEM image of OI human tibia (transverse, anterior section) ×750	266
C.28. SEM image of OI human tibia (transverse, anterior section) ×500	266
C.29. SEM image of OI human tibia (transverse, anterior section) ×1,000	267
C.30. SEM image of OI human tibia (transverse, anterior section) ×500	267
C.31. SEM image of OI human tibia (transverse, anterior section) ×100	267
C.32. SEM image of OI human tibia (transverse, anterior section) ×500	267
C.33. SEM image of OI human tibia (transverse, anterior section) ×700	267
C.34. SEM image of OI human tibia (transverse, anterior section) ×3,000	267
C.35. SEM image of OI human tibia (transverse, anterior section) ×10,000	268
C.36. SEM image of OI human tibia (longi., anterior section) ×100	268
C.37. SEM image of OI human tibia (longi., anterior section) ×1,500	268
C.38. SEM image of OI human tibia (longi., anterior section) ×6,000	269
C.39. SEM image of OI human tibia (longi., anterior section) ×15,000	269
C.40. SEM image of OI human tibia (longi., anterior section) ×35	269
C.41. SEM image of OI human tibia (longi., anterior section) ×150	269
C.42. SEM image of OI human tibia (longi., anterior section) ×50	269

C.43. SEM image of OI human tibia (longi., anterior section) ×250	269
C.44. SEM image of OI human tibia (longi., anterior section) ×100	270
C.45. SEM image of OI human tibia (longi., anterior section) ×50	270
C.46. SEM image of OI human tibia (longi., anterior section) ×150	270
C.47. SEM image of OI human tibia (longi., anterior section) ×3,000	270
C.48. SEM image of OI human tibia (longi., anterior section) ×6,000	270
C.49. SEM image of OI human tibia (longi., anterior section) ×7,000	270
C.50. SEM image of OI human tibia (longi., anterior section) ×3,000	271
C.51. SEM image of OI human tibia (longi., anterior section) ×7,000	271
C.52. SEM image of OI human tibia (longi., anterior section) ×30,000	271
C.53. SEM image of OI human tibia (longi., anterior section) ×100	271
C.54. SEM image of OI human tibia (longi., anterior section) ×3,000	271
C.55. SEM image of OI human tibia (longi., anterior section) ×7,000	271
C.56. SEM image of OI human tibia (longi., anterior section) ×3,000	272
C.57. SEM image of OI human tibia (longi., anterior section) ×7,000	272
C.58. SEM image of OI human tibia (longi., anterior section) ×14,000	272
C.59. SEM image of OI human tibia (longi., anterior section) ×18,000	272
C.60. SEM image of OI human tibia (longi., anterior section) ×3,000	272
C.61. SEM image of OI human tibia (longi., anterior section) ×7,000	272
C.62. SEM image of OI human tibia (longi., anterior section) ×14,000	273
C.63. SEM image of OI human tibia (longi., anterior section) ×18,000	273
C.64. SEM image of OI human tibia (longi., anterior section) ×3,000	273
C.65. SEM image of OI human tibia (longi., anterior section) ×7,000	273
C.66. SEM image of OI human tibia (longi., anterior section) ×3,300	273
C.67. SEM image of OI human tibia (longi., anterior section) ×3,000	273
C.68. SEM image of OI human tibia (longi., anterior section) ×7,000	274

C.69. SEM image of OI human tibia (longi., anterior section) ×14,000	274
C.70. SEM image of OI human tibia (longi., anterior section) ×18,000	274
C.71. SEM image of OI human tibia (longi., anterior section) ×700	274
C.72. SEM image of OI human tibia (longi., anterior section) ×7,000	274
C.73. SEM image of OI human tibia (longi., anterior section) ×3,000	274
C.74. SEM image of OI human tibia (longi., anterior section) ×100	275
C.75. SEM image of OI human tibia (longi., anterior section) ×100	275
C.76. SEM image of OI human tibia (longi., anterior section) ×3,300	275
C.77. SEM image of OI human tibia (longi., anterior section) ×7,000	275
C.78. SEM image of OI human tibia (longi., anterior section) ×18,000	275
C.79. SEM image of OI human tibia (longi., anterior section) ×18,000	275
C.80. SEM image of OI human tibia (longi., anterior section) ×3,000	276
C.81. SEM image of OI human tibia (longi., anterior section) ×300	276
C.82. SEM image of OI human tibia (longi., anterior section) ×300	276
C.83. SEM image of OI human tibia (longi., anterior section) ×3,000	276
C.84. SEM image of OI human tibia (longi., anterior section) ×3,000	276
C.85. SEM image of OI human tibia (longi., anterior section) ×7,000	276
C.86. SEM image of OI human tibia (longi., anterior section) ×25	277
C.87. SEM image of OI human tibia (longi., anterior section) ×50	277
C.88. SEM image of OI human tibia (longi., anterior section) ×250	277
C.89. SEM image of OI human tibia (longi., anterior section) ×500	277
C.90. SEM image of OI human tibia (longi., anterior section) ×1,000.....	277
C.91. SEM image of OI human tibia (longi., anterior section) ×3,000	277
C.92. SEM image of OI human tibia (longi., anterior section) ×10,000	278
C.93. SEM image of OI human tibia (longi., anterior section) ×7,000	278
C.94. SEM image of OI human tibia (transverse, medial section) ×25	278

C.95. SEM image of OI human tibia (transverse, medial section) ×50.....	278
C.96. SEM image of OI human tibia (transverse, medial section) ×500	279
C.97. SEM image of OI human tibia (transverse, medial section) ×1,000.....	279
C.98. SEM image of OI human tibia (transverse, medial section) ×3,000.....	279
C.99. SEM image of OI human tibia (transverse, medial section) ×10,000.....	279
C.100. SEM image of OI human tibia (transverse, medial section) ×3,000.....	279
C.101. SEM image of OI human tibia (transverse, medial section) ×10,000.....	279
C.102. SEM image of OI human tibia (transverse, medial section) ×250.....	280
C.103. SEM image of OI human tibia (transverse, medial section) ×500.....	280
C.104. SEM image of OI human tibia (transverse, medial section) ×1,000.....	280
C.105. SEM image of OI human tibia (transverse, medial section) ×3,000.....	280
C.106. SEM image of OI human tibia (transverse, medial section) ×10,000.....	280
C.107. SEM image of OI human tibia (transverse, medial section) ×70.....	280
C.108. SEM image of OI human tibia (transverse, medial section) ×25.....	281
C.109. SEM image of OI human tibia (transverse, medial section) ×50.....	281
C.110. SEM image of OI human tibia (transverse, medial section) ×100.....	281
C.111. SEM image of OI human tibia (transverse, medial section) ×3,000.....	281
C.112. SEM image of OI human tibia (transverse, medial section) ×100.....	281
C.113. SEM image of OI human tibia (transverse, medial section) ×250.....	281
C.114. SEM image of OI human tibia (transverse, medial section) ×1,000	282
C.115. SEM image of OI human tibia (transverse, medial section) ×3,000.....	282
C.116. SEM image of OI human tibia (transverse, medial section) ×250.....	282
C.117. SEM image of OI human tibia (transverse, medial section) ×3,000.....	282
C.118. SEM image of OI human tibia (transverse, medial section) ×500.....	282
C.119. SEM image of OI human tibia (transverse, medial section) ×1,000.....	282
C.120. SEM image of OI human tibia (transverse, medial section) ×3,000.....	283

C.121. SEM image of OI human tibia (transverse, medial section) ×10,000.....	283
C.122. SEM image of OI human tibia (transverse, medial section) ×500.....	283
C.123. SEM image of OI human tibia (transverse, medial section) ×1,000.....	283
C.124. SEM image of OI human tibia (transverse, medial section) ×3,000.....	283
C.125. SEM image of OI human tibia (transverse, medial section) ×2,000.....	283
C.126. SEM image of OI human tibia (transverse, medial section) ×10,000.....	284
C.127. SEM image of OI human tibia (transverse, medial section) ×500.....	284
C.128. SEM image of OI human tibia (transverse, medial section) ×1,000	284
C.129. SEM image of OI human tibia (transverse, medial section) ×250.....	284
C.130. SEM image of OI human tibia (transverse, medial section) ×250.....	284
C.131. SEM image of OI human tibia (transverse, medial section) ×1,000.....	284
C.132. SEM image of OI human tibia (transverse, medial section) ×3,000	285
C.133. SEM image of OI human tibia (transverse, medial section) ×500.....	285
C.134. SEM image of OI human tibia (longi., medial section) ×50.....	285
C.135. SEM image of OI human tibia (longi., medial section) ×3,000.....	285
C.136. SEM image of OI human tibia (longi., medial section) ×10,000.....	285
C.137. SEM image of OI human tibia (longi., medial section) ×40,000.....	285
C.138. SEM image of OI human tibia (longi., medial section) ×80,000.....	286
C.139. SEM image of OI human tibia (longi., medial section) ×20,000.....	286
C.140. SEM image of OI human tibia (longi., medial section) ×30,000.....	286
C.141. SEM image of OI human tibia (longi., medial section) ×20,000.....	286
C.142 SEM image of OI human tibia (longi., medial section) ×10,000.....	286
C.143. SEM image of OI human tibia (longi., medial section) ×3,700.....	286
C.144. SEM image of OI human tibia (longi., medial section) ×10,000.....	287
C.145. SEM image of OI human tibia (longi., medial section) ×40,000.....	287
C.146. SEM image of OI human tibia (longi., medial section) ×2,500.....	287

C.147. SEM image of OI human tibia (longi., medial section) ×5,000.....	287
C.148. SEM image of OI human tibia (longi., medial section) ×27,000.....	287
C.149. SEM image of OI human tibia (longi., medial section) ×10,000.....	287
C.150. SEM image of OI human tibia (longi., medial section) ×40,000.....	288
C.151. SEM image of OI human tibia (longi., medial section) ×5,000.....	288
C.152. SEM image of OI human tibia (transverse, lateral section) ×25	288
C.153. SEM image of OI human tibia (transverse, lateral section) ×50.....	288
C.154. SEM image of OI human tibia (transverse, lateral section) ×100	289
C.155. SEM image of OI human tibia (transverse, lateral section) ×500.....	289
C.156. SEM image of OI human tibia (transverse, lateral section) ×1,000.....	289
C.157. SEM image of OI human tibia (transverse, lateral section) ×500.....	289
C.158. SEM image of OI human tibia (transverse, lateral section) ×100.....	289
C.159. SEM image of OI human tibia (transverse, lateral section) ×1,000.....	289
C.160. SEM image of OI human tibia (transverse, lateral section) ×3,000.....	290
C.161. SEM image of OI human tibia (transverse, lateral section) ×10,000.....	290
C.162. SEM image of OI human tibia (transverse, lateral section) ×500	290
C.163. SEM image of OI human tibia (transverse, lateral section) ×3,000.....	290
C.164. SEM image of OI human tibia (transverse, lateral section) ×1,000	290
C.165. SEM image of OI human tibia (transverse, lateral section) ×5,000.....	290
C.166. SEM image of OI human tibia (transverse, lateral section) ×500.....	291
C.167. SEM image of OI human tibia (transverse, lateral section) ×1,000.....	291
C.168. SEM image of OI human tibia (transverse, lateral section) ×5,000	291
C.169. SEM image of OI human tibia (transverse, lateral section) ×500.....	291
C.170. SEM image of OI human tibia (transverse, lateral section) ×1,000	291
C.171. SEM image of OI human tibia (transverse, lateral section) ×3,000.....	291
C.172. SEM image of OI human tibia (transverse, lateral section) ×10,000.....	292

C.173. SEM image of OI human tibia (transverse, lateral section) ×25.....	292
C.174. SEM image of OI human tibia (transverse, lateral section) ×50	292
C.175. SEM image of OI human tibia (transverse, lateral section) ×100.....	292
C.176. SEM image of OI human tibia (transverse, lateral section) ×250.....	292
C.177. SEM image of OI human tibia (transverse, lateral section) ×500.....	292
C.178. SEM image of OI human tibia (transverse, lateral section) ×1,000.....	293
C.179. SEM image of OI human tibia (transverse, lateral section) ×3,000.....	293
C.180. SEM image of OI human tibia (transverse, lateral section) ×10,000	293
C.181. SEM image of OI human tibia (transverse, lateral section) ×100.....	293
C.182. SEM image of OI human tibia (transverse, lateral section) ×500.....	293
C.183. SEM image of OI human tibia (transverse, lateral section) ×250.....	293
C.184. SEM image of OI human tibia (transverse, lateral section) ×500	294
C.185. SEM image of OI human tibia (transverse, lateral section) ×1,000.....	294
C.186. SEM image of OI human tibia (transverse, lateral section) ×3,000	294
C.187. SEM image of OI human tibia (transverse, lateral section) ×10,000.....	294
C.188. SEM image of OI human tibia (transverse, lateral section) ×250	294
C.189. SEM image of OI human tibia (transverse, lateral section) ×1,000.....	294
C.190. SEM image of OI human tibia (transverse, lateral section) ×3,000.....	295
C.191. SEM image of OI human tibia (transverse, lateral section) ×10,000.....	295
C.192. SEM image of OI human tibia (longi., lateral section) ×50	295
C.193. SEM image of OI human tibia (longi., lateral section) ×100.....	295
C.194. SEM image of OI human tibia (longi., lateral section) ×250	296
C.195. SEM image of OI human tibia (longi., lateral section) ×500.....	296
C.196. SEM image of OI human tibia (longi., lateral section) ×50	296
C.197. SEM image of OI human tibia (longi., lateral section) ×100.....	296
C.198. SEM image of OI human tibia (longi., lateral section) ×250	296

C.199. SEM image of OI human tibia (longi., lateral section) ×550.....	296
C.200. SEM image of OI human tibia (transverse, posterior section) ×25	297
C.201. SEM image of OI human tibia (transverse, posterior section) ×50.....	297
C.202. SEM image of OI human tibia (transverse, posterior section) ×100	297
C.203. SEM image of OI human tibia (transverse, posterior section) ×100.....	297
C.204. SEM image of OI human tibia (transverse, posterior section) ×250.....	298
C.205. SEM image of OI human tibia (transverse, posterior section) ×1,000.....	298
C.206. SEM image of OI human tibia (transverse, posterior section) ×3,000	298
C.207. SEM image of OI human tibia (transverse, posterior section) ×10,000.....	298
C.208. SEM image of OI human tibia (transverse, posterior section) ×250	298
C.209. SEM image of OI human tibia (transverse, posterior section) ×500.....	298
C.210. SEM image of OI human tibia (transverse, posterior section) ×1,000	299
C.211. SEM image of OI human tibia (transverse, posterior section) ×3,000.....	299
C.212. SEM image of OI human tibia (transverse, posterior section) ×10,000	299
C.213. SEM image of OI human tibia (transverse, posterior section) ×100.....	299
C.214. SEM image of OI human tibia (transverse, posterior section) ×250	299
C.215. SEM image of OI human tibia (transverse, posterior section) ×500.....	299
C.216. SEM image of OI human tibia (transverse, posterior section) ×1,000	300
C.217. SEM image of OI human tibia (transverse, posterior section) ×3,000.....	300
C.218. SEM image of OI human tibia (transverse, posterior section) ×5,000	300
C.219. SEM image of OI human tibia (transverse, posterior section) ×10,000.....	300
C.220. SEM image of OI human tibia (transverse, posterior section) ×250.....	300
C.221. SEM image of OI human tibia (transverse, posterior section) ×500.....	300
C.222. SEM image of OI human tibia (transverse, posterior section) ×1,000.....	301
C.223. SEM image of OI human tibia (transverse, posterior section) ×4,300.....	301
C.224. SEM image of OI human tibia (transverse, posterior section) ×10,000.....	301

C.225. SEM image of OI human tibia (transverse, posterior section) ×50.....	301
C.226. SEM image of OI human tibia (transverse, posterior section) ×100.....	301
C.227. SEM image of OI human tibia (transverse, posterior section) ×500.....	301
C.228. SEM image of OI human tibia (transverse, posterior section) ×1,000	302
C.229. SEM image of OI human tibia (transverse, posterior section) ×3,000.....	302
C.230. SEM image of OI human tibia (transverse, posterior section) ×10,000	302
C.231. SEM image of OI human tibia (transverse, posterior section) ×20.....	302
C.232. SEM image of OI human tibia (transverse, posterior section) ×50	302
C.233. SEM image of OI human tibia (transverse, posterior section) ×250.....	302
C.234. SEM image of OI human tibia (transverse, posterior section) ×100	303
C.235. SEM image of OI human tibia (transverse, posterior section) ×250.....	303
C.236. SEM image of OI human tibia (transverse, posterior section) ×500.....	303
C.237. SEM image of OI human tibia (transverse, posterior section) ×1,000.....	303
C.238. SEM image of OI human tibia (transverse, posterior section) ×3,000.....	303
C.239. SEM image of OI human tibia (transverse, posterior section) ×1,000.....	303
C.240. SEM image of OI human tibia (transverse, posterior section) ×500	304
C.241. SEM image of OI human tibia (transverse, posterior section) ×3,000.....	304
C.242. SEM image of OI human tibia (transverse, posterior section) ×5,000	304
C.243. SEM image of OI human tibia (transverse, posterior section) ×10,000.....	304
C.244. SEM image of OI human tibia (transverse, posterior section) ×500.....	304
C.245. SEM image of OI human tibia (transverse, posterior section) ×100.....	304
C.246. SEM image of OI human tibia (transverse, posterior section) ×250.....	305
C.247. SEM image of OI human tibia (transverse, posterior section) ×250.....	305
C.248. SEM image of OI human tibia (transverse, posterior section) ×100.....	305
C.249. SEM image of OI human tibia (transverse, posterior section) ×1,000.....	305
C.250. SEM image of OI human tibia (transverse, posterior section) ×1,000.....	305

C.251. SEM image of OI human tibia (transverse, posterior section) ×3,000.....	305
C.252. SEM image of OI human tibia (transverse, posterior section) ×3,000	306
C.253. SEM image of OI human tibia (transverse, posterior section) ×5,000.....	306
C.254. SEM image of OI human tibia (longi., posterior section) ×50	306
C.255. SEM image of OI human tibia (longi., posterior section) ×100.....	306
C.256. SEM image of OI human tibia (longi., posterior section) ×250	306
C.257. SEM image of OI human tibia (longi., posterior section) ×550.....	306
C.258. SEM image of OI human tibia (longi., posterior section) ×1,000	307
C.259. SEM image of OI human tibia (longi., posterior section) ×3,000.....	307
C.260. SEM image of OI human tibia (longi., posterior section) ×7,500	307
C.261. SEM image of OI human tibia (longi., posterior section) ×19,000.....	307
C.262. SEM image of OI human tibia (longi., posterior section) ×3,500	307
C.263. SEM image of OI human tibia (longi., posterior section) ×6,000.....	307
C.264. SEM image of OI human tibia (longi., posterior section) ×40,000	308
C.265. SEM image of OI human tibia (longi., posterior section) ×40,000.....	308
C.266. SEM image of OI human tibia (longi., posterior section) ×12,000	308
C.267. SEM image of OI human tibia (longi., posterior section) ×10,000.....	308
C.268. SEM image of OI human tibia (longi., posterior section) ×10,000	308
C.269. SEM image of OI human tibia (longi., posterior section) ×40,000.....	308
C.270. SEM image of OI human tibia (longi., posterior section) ×40,000	309
C.271. SEM image of OI human tibia (longi., posterior section) ×5,000.....	309
C.272. SEM image of OI human tibia (longi., posterior section) ×35,000	309
C.273. SEM image of OI human tibia (longi., posterior section) ×10,000.....	309
C.274. SEM image of OI human tibia (longi., posterior section) ×40,000.....	309
C.275. SEM image of OI human tibia (longi., posterior section) ×10,000.....	309
C.276. SEM image of OI human tibia (longi., posterior section) ×5,000.....	310

C.277. SEM image of OI human tibia (longi., posterior section) ×2,000.....	310
C.278. SEM image of OI human tibia (longi., posterior section) ×10,000	310
C.279. SEM image of OI human tibia (longi., posterior section) ×40,000.....	310
D.1. AFM image of healthy human femur (longi., anterior section, no treatment, not polished), 5µm×5µm	311
D.2. AFM image of healthy human femur (longi., anterior section, no treatment, not polished), 2µm×2µm	311
D.3. AFM image of healthy human femur (longi., anterior section, no treatment, polished), 2µm×2µm.....	312
D.4. AFM image of healthy human femur (longi., anterior section, no treatment, polished), 2µm×2µm.....	312
D.5. AFM image of healthy human femur (longi., anterior section, demineralized for 5 minutes), 2.66µm×2.66µm.....	313
D.6. AFM image of healthy human femur (longi., anterior section, demineralized for 5 minutes), 2µm×2µm.....	313
D.7. AFM image of healthy human femur (longi., anterior section, demineralized for 5 minutes), 1µm×1µm.....	314
D.8. AFM image of healthy human femur (longi., anterior section, demineralized for 4 hours), 1µm×1µm.....	314
D.9. AFM image of healthy human femur (longi., anterior section, demineralized for 4 hours), 2µm×2µm.....	315
D.10. AFM image of healthy human femur (longi., anterior section, demineralized for 4 hours), 1µm×1µm.....	315
D.11. AFM image of OI human femur (longi., anterior section, no treatment, not polished), 1µm×1µm.....	316
D.12. AFM image of OI human femur (longi., anterior section, no treatment, not polished), 5µm×5µm.....	316
D.13. AFM image of OI human femur (longi., anterior section, no treatment, not polished), 1µm×1µm.....	317
D.14. AFM image of OI human femur (transverse, anterior section, no treatment, polished), 5µm×5µm.....	317
D.15. AFM image of OI human femur (transverse, anterior section, no treatment, polished), 2µm×2µm.....	318

D.16. AFM image of OI human femur (transverse, anterior section, no treatment, polished), 1 μm \times 1 μm	318
D.17. AFM image of OI human femur (transverse, anterior section, no treatment, polished), 1 μm \times 1 μm	319
D.18. AFM image of OI human femur (longi., anterior section, no treatment, polished), 2 μm \times 2 μm	319
D.19. AFM image of OI human femur (longi., anterior section, demineralized for 5 minutes), 5 μm \times 5 μm	320
D.20. AFM image of OI human femur (longi., anterior section, demineralized for 5 minutes), 2 μm \times 2 μm	320
D.21. AFM image of OI human femur (longi., anterior section, demineralized for 5 minutes), 1 μm \times 1 μm	321
D.22. AFM image of OI human femur (longi., anterior section, demineralized for 5 minutes), 2 μm \times 2 μm	321
D.23. AFM image of OI human femur (longi., anterior section, demineralized for 5 minutes), 1 μm \times 1 μm	322

CHAPTER 1. INTRODUCTION¹

Section 1.2 is adapted from a book chapter, Chapter 2: Biomimetics: Inspiration from the Structural Organization of Biological Systems, Kalpana S. Katti, Chunju Gu and Dinesh R. Katti, Natural Polymers: Volume 1: Composites, 2012, 1, 8-36.

1.1. Bone

The natural world provides us with a multitude of examples of materials that are perfectly adapted to fulfil a specific functional role with durability, strength, and mechanisms of programmed self-assembly and biodegradability. Bone is a representative of these materials. Bone can be regarded as a tissue or material with a particular capacity for growth, a distinctive chemical composition, and unique properties as a substance. Meanwhile, as an organ, with its distinctive structure and function, bone provides support and movement throughout a lifetime. All mammals share the same mechanisms for bone growth, repair, and nourishment as well as identical microscopic components of bone. The arrangement and shape of bones reflect the evolutionary heritage of organisms.

Three types of bone cells are responsible for bone metabolism (1). One is osteoblasts, which secrete new bone, and one is osteoclasts, which break bone down. After osteoclast-mediated resorption of the existing bone, osteoblasts lay down new bone matrix to be entrapped and become osteocytes inside. The cellular activities of bone modeling and remodeling determine the composition and structure of bone. Bone modeling refers to the deposition of new

¹ Section 1.2 in this chapter was co-authored by Chunju Gu, Kalpana Katti, and Dinesh Katti. Chunju Gu had primary responsibility for collecting references and drafting this section. Kalpana Katti and Dinesh Katti revised this section.

bone, while bone remodeling refers to the resorption of old bone followed by the formation of new Haversian system. Bone remodeling usually occurs to maintain bone strength by removal of microdamage. After completion of growth, bone modeling continues in adulthood modestly to increase bone size further, whereas bone remodeling occurs lifelong to reshape the bone in response to functional demands. Osteocytes serve as a detector of microdamage, and their death by apoptosis may activate or signal osteoclasts to start the remodeling process (2). The metabolic balance regulated by the bone cells form the assembly of collagen molecules and mineral phase in a unique hierarchical structure, which impart both stiffness and toughness to bone. This rather unusual combination of material properties provides both rigidity and resistance against fracture (3). In this way, bone provides skeletal stability, support and protection of vital organs and also heals itself through remodeling process. The unique structure and mechanical properties of bone have drawn much attention.

Bone refers to a family of materials having in common, mineralized collagen fibril, a basic building block; however, the structural organization of the fibril is different in different bone types. For example, dentin, cementum, and mineralized tendon are also included in the family of bone, and the composition and organization of their mineralized collagen fibrils are different (4). Each healthy adult possesses in total 206 pieces of bones with different shapes, including long bones, such as humerus, radius, ulna, femur, tibia, fibula, metacarpals and metatarsals, and flat bones, such as pelvis, scapula and skull (Curry 2002 p195). Disregarding the different shapes, bone is generally mechanically divided by compact bone and cancellous bone (5).

The chemical analysis of bone shows that there are three chief components in bone: collagen, mineral, and water. Collagen accounts for nearly 1/3 and mineral accounts for nearly

2/3 of the dry weight of bone matrix (1). The water component is on average 10-12wt% of cortical bone and 20% of the bone matrix (6). The crystals of mineral secrete and grow in the triple helical collagen fibers, and replace some of the water while mineralization takes place. The typical composition of human cortical bone is listed in Table 1.1.

Table 1.1. Composition of human cortical bone (7).

Components	Weight percentage (%)
Hydroxyapatite (HAP)	60
Type I collagen	20
Water	9
Ions and Non-collagenous proteins	11

1.2. Structure of bone

Research on the structure of bone dates back to the early 17th century when the compound microscope was invented. Clopton Havers is generally credited with the first description of the porous nature of bone in 1691, but due to the poor quality of the magnifying lenses, the initial descriptions dealt primarily with the canal system and the “laminar” structure of bone without the presence of osteonal bone. In the 18th and 19th century, some observations were described and defined in detail such as the Haversian system of lamellae, and the orientation and disposition of lacunae and canaliculi (8). By utilizing polarized light microscopy, Schmidt found that the *c* crystallographic axis is well aligned with the collagen fibrils (9). The greater detailed work came after the invention of scanning electron microscopy (SEM) and transmission electron microscopy (TEM) in 1930, which gave people the ability to examine structures on the nanometer scale. With the help of these high resolution instruments and other techniques such as X-ray diffraction, polarized optical microscopy, sonic velocity, as well as mechanical tests, the hierarchical structure of bone was discovered and depicted. Atomic force

microscopy (AFM), which appeared in 1980, makes it possible to investigate the structure of bone in the ambient environment on the nanometer scale (10-12). Although the overall structure from nano to macro scales of bone has been extensively studied, it is still far from ending.

Bone components are assembled in a unique hierarchical structure. Hierarchical materials contain structural elements which themselves have recognizable structure. At each level of the structural hierarchy, one may model the material as a continuum for the purpose of analysis (13). Bone has been described in terms of up to 6 or 7 hierarchical levels of organization from nanoscale collagen and mineral to macroscale femur bone (4, 14), as shown in Figure 1.1.

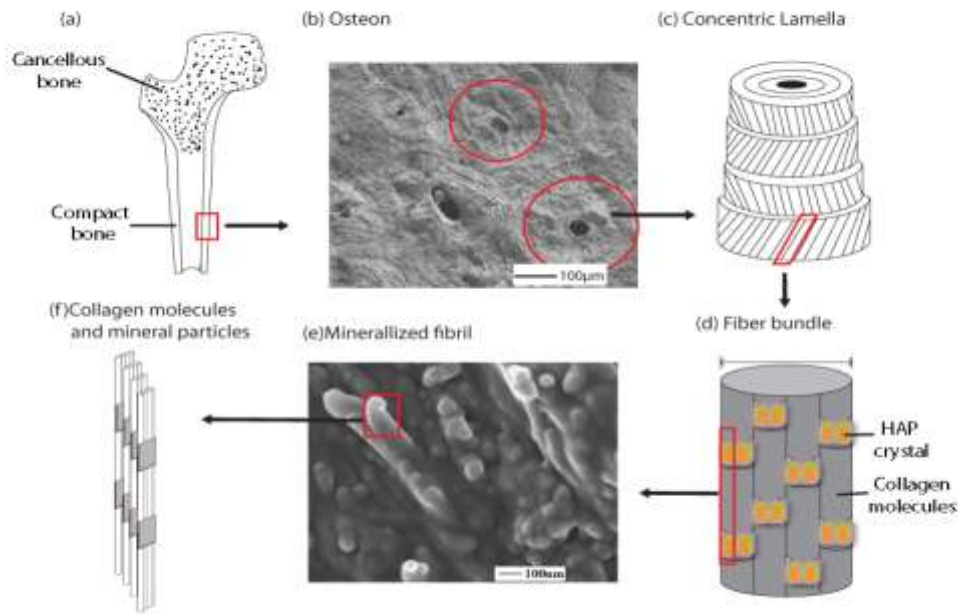


Figure 1.1. Hierarchical organization of a human femur bone from macro- to nanoscale. (a) Macroscale organ level—human femur bone. (b) Macroscale tissue level—osteon. (c) Microscopic level—bone lamellae (adapted from (15, 16)). (d) Mesoscopic level—fiber bundle. (e) Nanoscale level—mineralized fibril. (f) Molecular level—collagen molecule and mineral particle (adapted from(14)).

1.2.1. Level 1: Collagen fibrils and minerals (molecular and nanometer scales)

Collagen type I accounts for nearly 90% of its total organic content. Type I collagen molecules, also called triple helices (Figure 1.2a), are supercoiled assemblies of three polypeptide chains-- two identical $\alpha 1$ - chains and one $\alpha 2$ -chain, each with over 1000 amino acid residues. The main part of a collagen chain consists of Gly-X-Y repeats, in which X and Y can be any amino acid, but are frequently the amino acids proline and hydroxyproline. A triple-helical molecule is cylindrically shaped, with an average diameter of about 1.5nm, and lengths of 300nm. (Figure 1.2a) (15). Besides the main helical part, collagen triple helices are also comprised of short nonhelical end sequences called telopeptides with both N and C terminal ends. Telopeptides account for 2% of the molecule and are critical for fibril formation in the self-assembly process (17) .

During the formation of a fibril, the collagen spontaneously self-assembles into cross-striated fibrils that occur in the extracellular matrix of connective tissues. The fibrils are stabilized by covalent cross-linking (Figure 1.2b), which is initiated by oxidative deamination of specific lysine and hydroxylysine residues in collagen by lysyl oxidase (17). The intermolecular cross-linking provides the fibrillar matrices with various mechanical properties such as tensile strength and viscoelasticity. Both high-performance liquid chromatography (HPLC) and Fourier Transform Infrared (FTIR) have been frequently adopted to cross-link analysis (18).

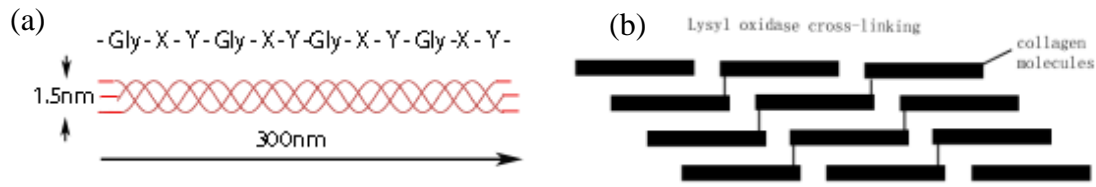


Figure 1.2. Collagen molecules and intermolecular cross-linking (a) Triple-helical structural motif of collagen molecules (adapted from (15)). (b) Lysyl oxidase cross-linking (adapted from (17)).

Mineral primarily consists of poorly crystalline nonstoichiometric carbonated hydroxyapatite (dahllite) which has a plate-shaped hexagonal crystal structure. Bone crystallites are probably the smallest biogenic crystals. They are only 1.5-4 nm thick, 25 nm wide, and 50 nm long on average (4), but we still know very little about the atomic structure. The size of the mineral crystallites is smaller than the “Griffith length” necessary for cracks to spread (19). The *c*-axis of the unit cells of these crystallites in bone is usually aligned parallel with the long axis of the adjacent collagen fibers (20); but the main orientation changes a small angle to the long axis over a few micrometers (21). By AFM, many of these mineral plates appear to be aligned, forming larger aggregates (475–600 nm long \times 75–90 nm thick) that also retain collagen periodicity along their exposed edges (12). The precision with which they can be laid down allows exquisite adaptations to the loads falling on the skeletons. The factors preventing crystal growth beyond the favorable thickness of 3 nm are suggested to be citrate ions that bound to the apatite surface (22).

1.2.2. Level 2: Mineralized fibril (sub-micro scale)

The triple-helical collagen molecules assemble into the fibril in a staggered arrangement. Within the fibril there is a linear shift of ~ 67 nm (D-period) between neighboring molecules. D-period is divided by overlap and gap, where overlap is around 27 nm and gap is 40 nm (shown in

Figure 1.2a). Robinson and Watson (20, 23) pioneered TEM study and reported the 68-nm banding pattern in collagen fibrils. The assembly of collagen molecules into fibrils is an entropy-driven process, driven by the loss of solvent molecules from the surface of protein molecules, resulting in assemblies with a circular cross section, which minimizes the surface area/volume ratio of the final assembly (17).

Mineralized fibrils are the basic building blocks of bone. As shown in the Figure 1.1f, minerals are intimately associated with the collagen framework in which they form, resulting in a highly complex but ordered mineral-organic composite material. Studies of crystal growth show that crystals are first formed in the gap, and then they continue to grow and penetrate into the overlap zone, thus pushing aside the triple-helical collagen molecules, and even breaking cross-linking and other bonds (24). Because the density of crystals is higher in the gap region, a periodic mineral density profile with around 67nm spacing is easily observed by electron microscopy, as shown in Figure 1.3. Figure 1.3 also shows that the width of a mineralized fibril is about 100nm.

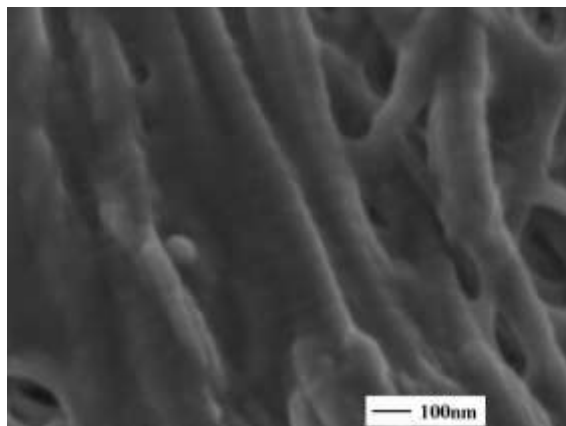


Figure 1.3. SEM image of staggered arrangement of mineralized fibrils.

It is also important to mention that the spaces between mineralized collagen fibrils (extrafibrillar) are filled with noncollagenous macromolecules and minerals. The extrafibrillar volume is at least 60% of the total, while the fibrils are no more than 40%. More of the mineral appears to be extrafibrillar than within the fibrils, and cemented together by noncollagenous organic matter (25, 26).

1.2.3. Level 3: Fibrillar arrays (micro- scale)

The mineralized fibrils are self-organized into fiber bundles along their length and the bundles may fuse with neighboring bundles. How the mineralized fibrils are aligned is of great interest, which leads to a great difference of mechanical properties. As shown in Figure 1.4, two arrangements are suggested. One has an arrangement of mineralized collagen fibrils aligned both with respect to crystal layers and fibril axes. The other arrangement of mineralized collagen fibrils is with only the fibril axes aligned (4). Sonic velocity measurements in three orthogonal directions of macroscopic specimens show significant differences (27), implying that orthotropic order at the fibril level may well extend to millimeter distances.

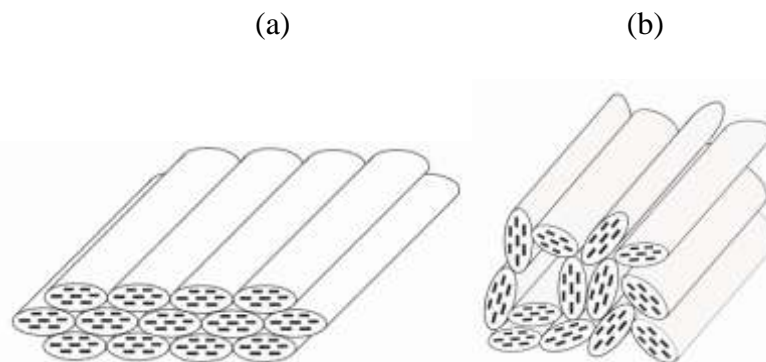


Figure 1.4. Schematic illustration of the arrangement of mineralized collagen fibrils aligned both with respect to crystal layers and fibril axes. (a) Orthotropic symmetry arrangement. (b) Transversal isotropic arrangement (adapted from (4)).

1.2.4. Level 4: Fibrillar array patterns (micro-scale)

The fibril bundles continue to be organized into layers or lamellae with a few microns thickness, and there in turn are arranged in a variety of ways into higher-order structures depending on the bone type. Four of the most common patterns are presented in Figure 1.5. In a parallel array pattern (Figure 1.5a), all the fibrils are parallel to each other. In a woven array pattern (Figure 1.5b), individual fibrils or fibril bundles are randomly organized. A radial fibril array (Figure 1.5d) is characteristic of the bulk of dentin, which also belongs to bone family (4).

Plywood-like structures (Figure 1.5c) are common in nature, which is believed to have a structure-function relationship (15). SEM and TEM studies showed that lamellar bone is made up of alternating collagen-rich and collagen –poor layers, all having an interwoven arrangement of fibers (28). The successive layers in a thin/thick lamellar unit proceeded by an angle of roughly 30° from one layer to the next (29).

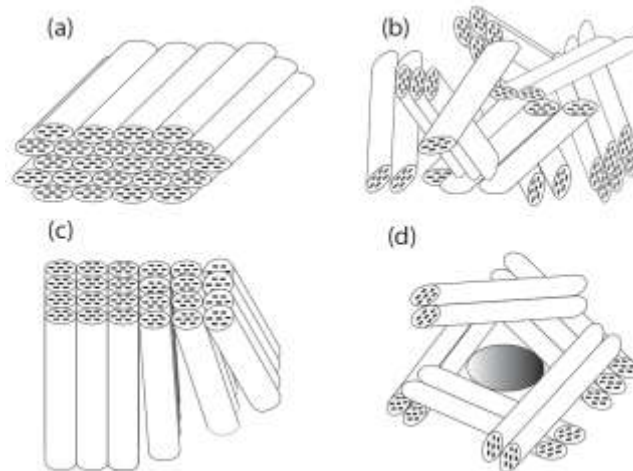


Figure 1.5. Four most common fibril array patterns with SEM images of fractured surfaces and schematic illustrations (not drawn to scale) of the basic organizational motifs. (a) Parallel fibrils array. (b) Woven fibrils array. (c) Plywood-like structure present in lamellar. (d) Radial fibril arrays (adapted from (4)).

1.2.5. Level 5: Osteon (micro-scale)

The osteon, as shown in Figure 1.6, also called Haversian system, is the fundamental structural unit of compact bone. Each osteon consists of concentric layers, or lamellae that surround a central canal, the Haversian canal. The Haversian canal, parallel to the long axis of the bone, contains the bone's nerve and blood supplies. Between adjoining osteons there are angular intervals that are occupied by interstitial lamellae. These lamellae are remnants of osteons, the greater parts of which have been destroyed (1). The osteon takes part in the remodeling process, whereby tunnels are eroded and then filled in again with cylinders of bone.

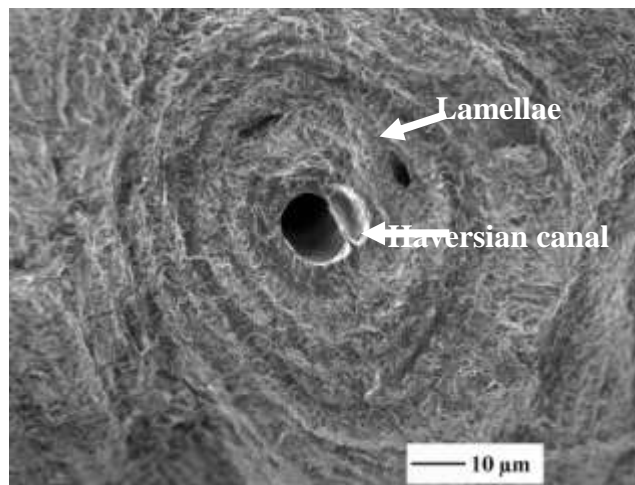


Figure 1.6. SEM micrograph of an osteon.

1.2.6. Level 6: Cortical (compact) and cancellous (spongy or trabecular) bone (meso-scale)

Cortical bone, synonymous with compact bone, is solid, with the only porosity for canaliculi, osteocyte lacunae, blood channels and erosion cavities. Cancellous bone, synonymous with spongy or trabecular bone, has porosity that is easily visible to the naked eye, as shown in Figure 1.1 (a). Usually, the bone material that has a porosity of about 25% or more is considered to be cancellous, and if less is cortical (30). Bone serves a protective function by the construction

of two cortical plates separated by intervening cancellous bone. This construction is beneficial for the maximum absorption of energy with minimum trauma to bone itself. Microstructurally, there is no difference between normal cortical and cancellous bones (8).

1.3. Bone mechanics

The structure of bone is modulated by genetic, mechanical, nutritional, and hormonal patterning throughout a lifetime (31). According to Wolff's law, bone adapts itself to be stronger in positions subjected to higher loads (32). Due to the remodeling process, bone is a highly mechanically anisotropic material at both the macroscopic (organ) and microscopic (material) level. The field of bone mechanics has been at a very sophisticated level where mechanical properties of various bone specimens are available for many anatomic sites. Bone properties are usually thought to be influenced by many factors, such as tissue composition, amount of secondary mineralization, collagen crosslinking, and the presence of microdamage (33).

As mentioned earlier, bone consists of nano-sized mineral platelets and collagen proteins. These components have extremely different mechanical properties: the mineral is stiff and brittle, while the protein is softer but also tougher than the mineral. However, the composite combines the optimal properties of both components. This rather unusual combination of material properties provides both rigidity and resistance against fracture (3). In addition, the arrangement of the constituents leads to anisotropic property and heterogeneity of bone tissue as well. The mechanical properties of bone tissue varies from type to type. Although the cortical bone was reported having similar nanomechanical properties as trabecular bone (34), the nanostructure of bone tissue differ substantially among lamellar type, anatomical sites and individuals (35). As pointed out by Gao et al. (19), bone is much less sensitive to flaws because

of its hierarchical structure. The hierarchical design distributes stresses throughout the levels of structure, thereby minimizing dangerous stress concentrations that could precipitate failure and fracture. The hierarchical feature of bone controls the fracture properties, particularly the toughness (5). Because the collagen fibers in neighboring lamellae are oriented at an angle to each other, fracture surfaces show considerable roughness. The work of driving a crack across the interfaces consisting of the plates, sheets, and Haversian systems of bone is much greater than it would be if the material were homogeneous (36). Therefore, besides the hierarchical structure, the mechanical properties of bone at different length scales and their relationship with structure are of great interest. Although the study of bone mechanics advanced in the 1970s, it was not until the beginning of the 1980s that its study really started off and it has been driven by advances in techniques(30). In addition to experimental work, simulation has also been conducted through different length scales to investigate the bone mechanics.

1.3.1. Macro-scale mechanical properties of bone

There have been a great amount of studies on mechanical properties of bone in the last 50 years (5). The early researches are focused on macro-scale mechanical properties of bone, where bulk bone pieces are applied to different load forms (Figure 1.7). The mechanical properties at the macro level are mainly: elastic properties (mainly Young's modulus), strength (in tension, compression, shear, and torsion), fatigue, fracture mechanics as well as dynamic mechanical properties (creep and stress-relaxation).

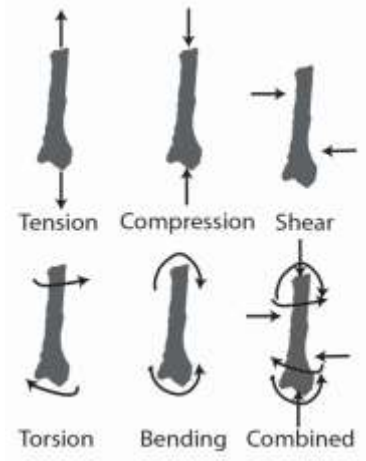


Figure 1.7. Different types of loads that can be applied on bone.

The elastic properties of bone can be measured by two main methods: (1) applying a load to a specimen and calculating the elastic properties from the resulting deformation (mechanical testing) and (2) measuring the velocity of sound waves in bone (ultrasonic testing). Mechanical testing is more straightforward and can investigate the effect of strain rate on mechanical properties. Ultrasonic testing is less straightforward and has some difficulties in testing wet specimens, but it is a nondestructive technique (37). Both mechanical testing and ultrasonic methods can conduct multiscale assessment of bone elastic properties. Ultrasound method has the scalability of the acoustic wavelength from 6mm at 500 kHz down to 0.5 μm at 2 GHz. The low frequency methods (500 kHz to 10 MHz) are widely used in clinical devices to assess bone quality at the macro-scale, while the higher frequency method (50 MHz to 2 GHz), scanning acoustic microscopy (SAM), is used to investigate bone microarchitecture (38).

The elastic strength of human cortical bone is anisotropic because of its microstructure. Cortical bone is both stronger and stiffer when subjected to a load longitudinally along its long axis (Table 1.2) (39). This property results from its evolutionary adaptation to most efficiently

resist the largely uniaxial stresses. Human femoral cortical bone also shows both anisotropic and asymmetrical ultimate stresses that it is stronger in the longitudinal direction and also stiffer in compression than in tension (Table 1.3). In addition, it is weak in shear and loaded transversely in tension (Table 1.3).

Table 1.2. Elastic properties of human femoral cortical bone (39).

Modulus (GPa)	Longitudinal	17.9 (3.9)*
	Transverse	10.1(2.4)
	Shear modulus	3.3 (0.4)
Poisson's ratio	Longitudinal	0.4 (0.16)
	Transverse	0.62 (0.26)

*Standard deviations are given in parentheses.

Table 1.3. Ultimate stresses of human femoral cortical bone (39).

Longitudinal stress (MPa)	Tension	135 (15.6)*
	Compression	205 (17.3)
Transverse stress (MPa)	Tension	53 (10.7)
	Compression	131 (20.7)
Shear stress (MPa)		65 (4.0)

*Standard deviations are given in parentheses.

Meanwhile, bone has extremely poor fatigue resistance. Fully reversed cyclic loading to one half of the yield strain causes fatigue fracture in 1000 cycles (40). Cyclic loading can induce modulus reductions accompanied by structural damage such as microcracks very early in the loading history (41). Bone specimens exhibit an almost immediate loss of stiffness and an increase in stress/strain hysteresis (40). Fracture mechanics has been applied to bone as a measure of the inherent resistance to crack initiation and propagation. Fracture toughness can be

evaluated from a precracked specimen, assuming linear elastic fracture mechanics, in terms of critical stress intensity factor, K_{Ic} , and critical strain energy release rate G_c (42). The fracture toughness is influenced by strain rate: the fracture toughness decreases by about 33% as the strain rate increases (by about four orders of magnitude) (43). The crack deflection at the osteonal interfaces adds an extrinsic toughness to bone at low strain rate (43).

Bone is also considered as a viscoelastic material, though the effect of loading rate on modulus and strength is only moderate (44). The strain-rate sensitivity, creep and relaxation behavior, are usually investigated as its viscoelastic behavior (45). At macro-scale, this viscoelastic response is measured by some designed-systems (46-48) or a dynamic mechanical analyzer (DMA) (45, 49-53).

1.3.2. Meso-scale mechanical properties of bone

Currey JD (30) classified cancellous and cortical bones as meso-scale features of bone. However, there is no specific technique for this length scale. Turner CH et al.(34) used acoustic microscopy and nanoindentation methods and found that: the Young's modulus of cortical bone in the longitudinal direction is about 40% greater than the Young's modulus in the transverse direction; the Young's modulus of cancellous bone tissue is slightly higher than the transverse Young's modulus of cortical bone, but significantly lower than the longitudinal Young's modulus of cortical bone. At the end of long bones, the cancellous bone distributes loads away from the joint and into the cortical bone, which has a much smaller cross-sectional area than the joint cartilage surfaces. Thus, the transitional cancellous bone protects the delicate cartilage from larger impact stresses from the cortical bone (30).

1.3.3. Micro-scale mechanical properties of bone

The macro-scale mechanical properties are on average features for bulk bone tissue. It is often appropriate to assume average mechanical properties from cortical bone; however, in some cases it may be necessary to consider the heterogeneity that can arise from variations in microstructure. Microindentation hardness testing, more commonly called microhardness testing, is widely used to study fine scale changes in hardness of materials. Hardness values are generally calculated as the peak force divided by the area of contact (as shown in Equation 1.1), the contact area differs between the test techniques.

$$\text{Hardness} = (\text{Peak Force}) / (\text{Contact Area}) \quad (1.1)$$

The hardness values usually decrease as the peak force increases; therefore, the peak force is always mentioned in the test. With hardness values, modulus can be derived with the following equation (54):

$$E^d = 0.58 + 0.36H_v \quad (1.2)$$

The most commonly used indenter points are Vickers and Knoop. The Vickers indenter is a regular pyramid with equal diagonals, while the Knoop indenter has diagonals of two different lengths. Knoop indenter is more sensitive to elastic anisotropy than the Vickers, and Knoop indenter is also more applicable to very thin materials (55). The typical residual impression long diagonal of Knoop indenter can be about 200 μm while that of Vickers is about 70 μm (55). Microindentation has been extensively used to measure the micro-scale mechanical properties of different anatomical positions of bone tissue (56-60), and it has the ability to discriminate between damaged and intact human bone tissue (61). Recently, a reference point indentation (RPI) instrument, which can perform bone microindentation testing, has even been developed for

measuring bone tissue mechanical properties in vivo and is expected for clinical application (62-64). This instrument can assess bone quality with little harm to the body.

As mentioned earlier, SAM can be used to evaluate the elastic properties of bone at micro-scale level. Turner CH et al. (34) compared SAM (30-60 μm resolution) and nanoindentation (NI) (1-5 μm resolution) methods and obtained consistent results from these two methods (34).

Experimental testing can give straight forward mechanical properties of bone specimens; however, in many instances, experimental testing on humans and cadavers is not always feasible. In comparison, different modeling and simulation methods provide alternatives for studying mechanical properties of bone. Among these methods, finite element analysis (FEA) has become a popular and powerful tool used by biomechanics and orthopedics researchers over the last 30 years (65). Finite element analysis can mimic the bone system in CT or μCT datasets and integrates density and geometry information to predict the response of bone under a variety of loading conditions and estimate bone strength parameters (66-81). The work done by FEA combined with experimental work contributes to the studies of damage mechanism, fracture, bone disease, and bone mechanics.

1.3.4. Sub-micro-scale mechanical properties of bone

In recent years, considerable progress has been possible in the understanding of bone properties, mainly due to new methodology in micromechanics: nanoindentation (NI), in situ electron scanning microscopy (SEM) nanoindentation, and atomic force microscopy (AFM). It becomes possible that micro-scale and nano-scale stiffness and hardness of bone can be measured excluding the artifacts from higher levels of hierarchy (3). Nanoindentation usually probes materials into less than 1 micron to several microns, therefore, it is usually regarded as a

technique acquiring sub-micro-scale mechanical properties. The micro-scale measurements correspond to osteonal level of bone structure, while the sub-micro-scale measurements correspond to lamellar level. Nanoindentation and micro-hardness testing differ in a couple of ways, but the results are comparable when tip geometries used are similar so that similar strains are provided in the material when testing, such as the Vickers and Berkovich shaped tips (both are pyramidal-shaped).

Nanoindentation emerged in the early 1980s from improving microindentation methods by enhancing force and depth sensing capabilities (82). Later, NI technique combined the AFM imaging so that it provides more accurate position selection on the sample. It was originally developed to investigate coatings, and it was over a decade before the first work on bone NI was published (83). In 1992, Oliver and Pharr established a comparatively mature method to determine hardness and elastic modulus from indentation load-displacement data of NI (84). The indentation load-displacement data are shown schematically in Figure 1.8, and then are analyzed according to the equation (1.3)

$$S = \frac{dP}{dh} = \frac{2}{\sqrt{\pi}} E_r \sqrt{A} \quad (1.3)$$

where $S = dP/dh$ is the experimentally measured stiffness of linear portion of the unloading data. P , h , E_r , and A are force, displacement, reduced modulus, and the projected area of the elastic contact, respectively. A relates to h and the indenter geometry. Then, elastic modulus of the sample can be calculated according to the equation (1.4)

$$\frac{1}{E_r} = \frac{(1 - \nu^2)}{E} + \frac{(1 - \nu_i^2)}{E_i} \quad (1.4)$$

where E_i and ν_i are Young's modulus and Poisson's ratio for the nanoindenter and E and ν are for the specimen. The hardness can be computed from its normal definition:

$$H = \frac{P_{max}}{A} \quad (1.5)$$

where P_{max} is the peak indentation load.

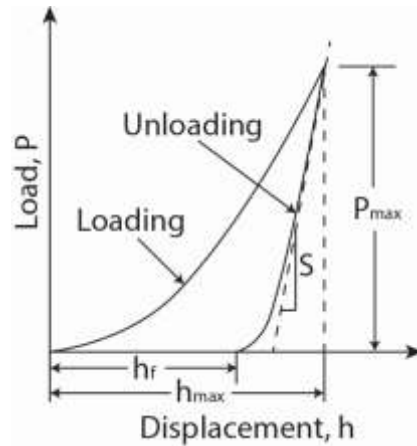


Figure 1.8. A schematic representation of load versus indenter displacement data for an indentation experiment. The quantities shown are P_{max} : the peak indentation load; h_{max} : the indenter displacement at peak load; h_f : the final depth of the contact impression after unloading and S : the initial unloading stiffness.

Nowadays, nanoindentation is probably the most important tool for the assessment of the elastic modulus and hardness of bone tissue (66, 85-91). Up to now, hundreds of papers have been published using nanoindentation to study bone mechanical properties. It enables an improved understanding of the mechanical properties correlation with microstructure of bone tissue. For example, significant modulus variations were found on opposing sides of the osteonal canal for the same lamella (88). However, there are variations in reported values for elastic modulus and hardness according to different sample conditions (wet or dry), different sample sources, and different experimental conditions, such as different tips and different loads are used.

The variation can also arise from the heterogeneity of bone, resulting in local difference in composition and multiscale organization of the bone volume element tested. Hence, it is essential to carefully design the experimental protocol as well as being aware of the limitations of the technique during interpretation of acquired data (92).

Besides traditional NI, in situ SEM nanoindentation also emerged to perform nanoindentation while capture high-resolution images simultaneously to watch the deformation behavior of materials closely. The use of in situ SEM nanoindentation will be introduced in Chapter 4 in detail.

1.3.5. Nano-scale mechanical properties of bone

Atomic force microscope (AFM) is well known for probing surface images of materials in ambient environment or even in buffered saline liquids that is very close to its physiological state. In addition, AFM can also be conducted to study the mechanical properties of materials at nano scale. Using contact mode, AFM cantilevers have been used for indentation experiments on isolated collagen fibrils in a dried state and reported values for the elastic modulus of 3.7 to 11.5 GPa (93). Recently, AFM stiffness mapping has been developed for bone study (94, 95).

Besides AFM, modulus mapping (MM) have also been proposed, combining a nanoindenter with an AFM x-y stage to map material properties over a surface. The introduction and experiments about MM will be discussed in Chapter 4 in detail.

These techniques are sometimes utilized together to investigate the mechanical properties at different length scales: (1) the mineralized fibril level (~100 nm); (2) the lamellar level (~6 μm); and (3) the osteon level (up to ~30 μm). AFM, NI, and microindentation are applied as techniques to these three levels, respectively (96). The mechanical properties tested are also related to the conditions of the bone samples. The mechanical properties under dry conditions are

higher by 30-50% compared to wet conditions (96, 97). Table 1.4 and Table 1.5 list the mechanical properties of both wet and dry metacarpal horse bone specimens acquired using AFM, NI, and microindentation.

Table 1.4. AFM mechanical measurement at mineralized fibril level of bone tissue (96).

	Dry conditions	Wet conditions
Stiffness (N/m) Transverse plane	534 ± 69	291 ± 124
Stiffness (N/m) Longitudinal plane	513 ± 86	334 ± 88
p-Value (t-test between two planes)	0.01	0.04

Besides experimental work, numerous modeling studies such as molecular dynamics have been performed on the deformation mechanisms of collagen fibril (98-106) and collagen-HAP interactions in bone (103, 107, 108). Molecular dynamics studies addressed that: (1) the importance of crosslinks to the mechanical properties of collagen fibril (98, 100); (2) the shape of mineral crystals can be a strong determinant of the nanoscale strength of bone (109); and (3) the nanomechanics of collagen fibril has its own hierarchy (101, 102). These studies can help to understand bone mechanics at nano-scale and atomic-scale levels.

1.4. Bone diseases and bone quality characterization

The quality of bone refers to its ability to perform its functions. The quality contains important determinants such as intrinsic properties of bone matrix, bone architecture, turnover, and bone disease. Bone metabolic disease refers to the medical conditions that damage the skeleton and make bone weak and prone to fracture. Studies of bone diseases help to understand the relative importance of each constituent of the bone composition and its interactions with

other constituents as well as bone structure. Bone diseases can be caused by disorders of collagen (osteogenesis imperfecta and Paget’s disease of bone), mineral content, composition and distribution (fluorosis and osteomalacia); diseases of high remodeling (postmenopausal osteoporosis, hyperparathyroidism, and hyperthyroidism) and low remodeling (osteopetrosis, pycnodysotosis); and other reasons (idiopathic male osteoporosis, corticosteroid-induced osteoporosis) (110).

Table 1.5. Nanoindentation measurements at lamellar level and micronanoindentation measurements at osteonal level (96).

		Dry conditions		Wet conditions	
		E(GPa)	H(GPa)	E(GPa)	H(GPa)
Nanoindentation	Transverse plane	20.8 ± 2.1	0.61 ± 0.12	12.4 ± 2.5	0.28 ± 0.08
	Longitudinal plane	17.6 ± 2.1	0.54 ± 0.12	12.8 ± 1.9	0.35 ± 0.07
	<i>p</i> -Value (t-test between two planes)	6×10^{-12}	0.004	0.4	2×10^{-5}
Microindentation*	Transverse plane	18.6 ± 1.7	50.5 ± 5	14.6 ± 1.2	39 ± 3
	Longitudinal plane	17.0 ± 1.4	46 ± 4	13.8 ± 1.2	37 ± 3
	<i>p</i> -Value (t-test between two planes)		0.02		0.09

* For microindentation, E is derived modulus ($E_d=0.58+0.36H_v$)(54) and H is Vickers hardness under 10 gr loading (Hv10).

The most common bone disease is osteoporosis, which is characterized by progressive loss of bone mass and by deterioration of bone microarchitecture and quality, resulting in a reduction in bone strength. This combination increases bone fragility, leading to a greater propensity for fracture. This bone disease is particularly endemic in postmenopausal osteoporotic women. The cause of this disease is the imbalance in the skeletal turnover that bone resorption exceeds bone formation (111). Bisphosphonate has been proven beneficial for improving bone

mineral density and decreasing incidence of new vertebral fractures by inhibiting bone resorption and lowering bone turnover (112, 113). Adequate calcium and vitamin D intake is also suggested to be crucial for developing optimal peak bone mass and preserving bone mass throughout life (114).

Paget's disease of bone is a chronic disorder that can disrupt bone remodeling process and result in enlarged and misshapen bones. Paget's disease of bone most commonly occurs in the pelvis, skull, spine and legs. Typically, Paget's disease is localized, affecting only one or a few bones, as opposed to osteoporosis, which usually affects all the bones in the body. The risk of Paget's disease of bone increases with age. The risk also increases if family members have the disorder. Complications of Paget's disease of bone can include broken bones, hearing loss and pinched nerves in the spine. Bisphosphonate is also the mainstay of treatment for this disease (115).

1.4.1. Osteogenesis imperfecta

Among all of the bone diseases, osteogenesis imperfect (OI) is our greatest interest since it is a disease with direct defects in collagen molecules and this disease provides an interesting platform for investigating how alterations of collagen at the molecular level cause changes in the structure of bone. Osteogenesis Imperfecta is a genetic disorder characterized by substantial bone fragility and osteopenia. It affects about 1:5000-10000 individuals and is a rare and potentially incapacitating disease (116). In 1979, Sillence classified OI into 4 types according to a system based on mode of inheritance, clinical picture, and information from X-rays: type I (mild OI with bone fragility and blue sclerae), type II (perinatal lethal), type III (progressive deforming), and type IV (normal sclerae and mild deformity) (117). These four types are entirely designated for mutations in COL1A1 or COL1A2, causing autosomal dominant OI (118, 119). Because of

specific clinical/radiological and/or histological features and the discovery of rare recessive genetic causes of OI, this classification was expanded into 7 by Rauch et al. in 2004 (120), and then it was further expanded into 11 by Forlino et al. in 2011, as shown in Table 1.6 (118).

Table 1.6. OI Nosology (118).

	OI type	Inheritance*	Phenotype	Gene Defect
Classical Sillence Types	I	AD	Mild	Null <i>COL1A1</i> allele
	II	AD	Lethal	<i>COL1A1/ COL1A2</i>
	III	AD	Progressive Deforming	<i>COL1A1/ COL1A2</i>
	IV	AD	Moderate	<i>COL1A1/ COL1A2</i>
Unknown Etiology	V	AD	Distinctive Histology	Unknown
	VI	AR?	Mineralization Defect	Unknown
3-Hydroxylation Defects	VII	AR	Severe (Hypomorphic) Lethal (Null)	<i>CRTAP</i>
	VIII	AR	Severe to Lethal	<i>LEPRE1 (P3H1)</i>
	IX	AR	Moderate to Severe	<i>PPIB (CyPB)</i>
Defects	X	AR	Severe to Lethal	<i>SERPINH1 (HSP47)</i>
	XI	AR	Progressive Deforming Bruck Syndrome?	<i>FKBP10 (FKBP65)</i>

*Inheritance: AD- autosomal dominant; AR- autosomal recessive

The detailed description of OI disease will be discussed in Chapter 3, while the diagnosis and treatment of this disease are briefly discussed here. The typical OI features can be identified using ultrasound clinically; however, if the clinical examination is not definitive, then laboratory tests for OI are appropriate. Laboratory diagnosis of OI relies on two approaches that cultured fibroblasts make either less or abnormal type I procollagen molecules or identification of a mutation in *COL1A1* or *COL1A2* (121). For primary OI cases, the tests are categorized as: (1) Collagen Biochemical Test, also referred to as a “skin biopsy”, examines collagen proteins made

by skin cells (fibroblasts); (2) Collagen Molecular Testing, also known as “DNA analysis”, examines the mutation in collagen by sequencing at the gene level. It requires a blood sample (116). Both tests can use a skin sample. The method of cultured dermal fibroblasts now has been supplanted by direct DNA sequence analysis which takes 10-30 days to complete (122). Collagen screening and DNA-based testing can be performed at the University of Washington (www.pathology.washington.edu/clinical/collagen) and National Institutes of Health, Bethesda, MD (<http://www.oiprogram.nichd.nih.gov/>), DNA-based testing is available at the Tulane University MatrixDNADiagnostic Lab, and Athena Diagnostics.

The treatment of OI disease has been studied for many years. However, there is still no cure for this genetic disease. Bisphosphonate pamidronate is reported to have a beneficial effect in children and adolescents with severe OI (123, 124). The mechanism is suggested to be that in remodeling, bone resorption and formation are coupled and consequently both processes are inhibited by bisphosphonate pamidronate. However, during modeling of cortical bone, osteoclasts and osteoblasts are uncoupled, and continuing bone formation can increase cortical width, whereas the resorption is selectively targeted (125). Therefore, studies have also raised concerns about high cumulative doses impairing bone modelling and healing, decreasing bone material quality and mineralization heterogeneity and impairing bone cells (126-129). Recently, a study on OI mice found excessive activity of transforming growth factor beta (TGF), which is responsible for coordinating the shaping and reshaping of bone, is. They also found that using an antibody, which can block TGF, improves whole bone and tissue strength (130). In another study, a new class of agents targeting the receptor activator of nuclear factor- κ B ligand (RANKL) was also evaluated to improve the density and some geometric and biomechanical properties of *oim/oim* bone (131).

Besides bone diseases, aging also affects the composition and mechanical properties of bone. Aging increases the concentration of mature (pyridinium and deoxypyridinium) crosslinks. Bone mineral density (BMD) declines with age in both women and men. Tensile ultimate stress of human cortical bone decreases at a rate of about 2% per decade while tensile ultimate strain decreases at a rate of approximately 10% per decade (132, 133).

1.4.2. Characterization methods of bone quality

Bone quality includes microarchitecture, mineralization, and quality of organic matrix (maturity and crosslinking). Microradiography (MR) was the first technique to quantify the mineral content within cortices and trabeculae (134). MR is very fast, accurate, and simple. However, a disadvantage of MR is that it can only acquire two dimensional images. Then, Computerized tomography (CT), micro-computed tomography (μ CT), and quantitative computed tomography (QCT) were developed permitting both 3D (and 2D) reconstructions and volumetric measurements. From clinical perspective, both QCT and Dual-energy X-ray absorptiometry (DXA) can measure bone mineral density. More advanced and sensitive techniques include quantitative backscattered electron imaging (qBEI) (135) and synchrotron radiation micro computed tomography (SR μ CT) (136). Both qBEI and SR μ CT methods require bone samples to be transiliac bone biopsies. Complimentary information on the bone matrix at identical topographic locations is obtained with other techniques such as small angle and wide-angle X-ray scattering (SAXS/WAXS), NI, scanning acoustic microscopy (SAM), Raman microspectroscopy (RAMAN) and Fourier transform infrared imaging (FTIRI). For clinical use, the characterization of bone quality usually includes CT scan and Magnetic resonance imaging (MRI), which can measure the geometry and microstructure of bone. Finite-element analysis, which is an image-based method, can also calculate bone strength (137).

1.5. Scope of this dissertation

Given the trends of bone structure and mechanics studies, it is evident that with various emerging techniques, the studies of bone are forwarding to a more nano-scale, atomic-scale, and hierarchical aspect to discover the anatomical position-specific structure and mechanical properties and help to understand bone and bone diseases. However, bone research is still far from the end. Firstly, bone mineral, although many studies have given the formula of bone mineral which is similar to hydroxyapatite and possesses vacancies and ion substitutes, the problem still hovers about the structural OH and its presence in the crystal structure. Besides the molecular structure of bone mineral, some debates are also aroused concerning the crystal structure and heterogeneity of bone mineral, as well as the details of extrafibrillar mineral due to sample preparation problems and instrumentation limits. Secondly, although the collagen sequence is well-understood, the interactions between mineral and collagen is still under study. Thirdly, what is the significance of collagen mutations for initial mineral nucleation and biomineralization? Fourthly, the role of different noncollagenous proteins in the initial nucleation and growth of bone mineral is not well-understood, especially in diseased bones. Therefore, in this doctoral dissertation, Field emission-Scanning probe microscopy (FE-SEM), modulus mapping, in situ FE-SEM nanoindentation, and nanoDMA techniques are utilized to explore the structure and nanomechanical properties and of bone at multi-scales, particularly, nanometer and sub-micro scales. In addition, our group's multiscale modeling work has also demonstrated the influence of the interactions among different constituents on the mechanics of collagen; the interaction is of our specific interest and studied by using Fourier transform infrared spectroscopy (FTIR). Further, X-ray diffraction (XRD) is used to study the crystal structure of bone mineral as a supplement. Overall, this doctoral dissertation focuses on the study of

molecular bases of bone constituents, bone crystal structure, nanomechanical properties of bone, and OI diseased bone.

This dissertation is organized in the following manner:

- Chapter 1: Introduction
- Chapter 2: This chapter presents SEM images, photoacoustic FTIR spectroscopic study of undisturbed human cortical bone.
- Chapter 3: This chapter presents microstructural (SEM images) and infrared spectroscopic of human cortical bone (anterior region) with osteogenesis imperfect.
- Chapter 4: This chapter presents nanomechanical properties of undisturbed human normal and OI cortical bones (anterior region) measured by modulus mapping and in situ FE-SEM nanoindentation.
- Chapter 5: This chapter presents dynamic nanomechanical behavior of both healthy and OI human cortical bone (anterior regions) using nanoDMA technique
- Chapter 6: This chapter presents SEM images, FTIR studies of four sections (anterior, medial, posterior, and lateral) of OI human cortical bone and nanomechanical properties of anterior and posterior sections obtained using in situ FE-SEM nanoindentation technique.
- Chapter 7: This chapter summarizes our research work and major conclusions.
- Chapter 8: This chapter describes the major contributions of this work.
- Chapter 9: This chapter discusses some future directions for the research in this field.

1.6. References

1. Bourne GH. The Biochemistry and Physiology of Bone. 2 ed: Academic Press; 1972.
2. Verborgt O, Gibson GJ, Schaffler MB. Loss of osteocyte integrity in association with microdamage and bone remodeling after fatigue in vivo. *Journal of Bone and Mineral Research*. 2000;15(1):60-7.
3. Fratzl P, Gupta HS, Paschalis EP, Roschger P. Structure and mechanical quality of the collagen-mineral nano-composite in bone. *Journal of Materials Chemistry*. 2004;14(14):2115-23.
4. Weiner S, Wagner HD. The material bone: Structure mechanical function relations. *Annual Review of Materials Science*. 1998;28:271-98.
5. Currey J. The mechanical adaptations of bones. Princeton: Princeton University Press; 1984.
6. Utku FS, Klein E, Saybasili H, Yucesoy CA, Weiner S. Probing the role of water in lamellar bone by dehydration in the environmental scanning electron microscope. *Journal of Structural Biology*. 2008;162(3):361-7.
7. Murugan R, Ramakrishna S. Development of nanocomposites for bone grafting. *Composites Science and Technology*. 2005;65(15-16):2385-406.
8. Martin RB, Burr DB. Structure, Function, and Adaptation of Compact Bone. New York: Raven Press; 1989.
9. Schmidt WI. Über die Orientierung der Kristallite im Zahnschmelz. *Die Naturwissenschaften*. 1936;24(23).
10. Baranauskas V, Vidal BC, Parizotto NA. Observation of geometric structure of collagen molecules by atomic force microscopy. *Applied Biochemistry and Biotechnology*. 1998;69(2):91-7.

11. Baselt DR, Revel JP, Baldeschwieler JD. Subfibrillar structure of type-I collagen observed by atomic-force microscopy. *Biophysical Journal*. 1993;65(6):2644-55.
12. Siperko LM, Landis WJ. Aspects of mineral structure in normally calcifying avian tendon. *Journal of Structural Biology*. 2001;135(3):313-20.
13. Lakes R. Materials with structural hierarchy. *Nature*. 1993;361(6412):511-5.
14. Fratzl P. Bone fracture - When the cracks begin to show. *Nature Materials*. 2008;7(8):610-2.
15. Giraud-Guille MM. Plywood structures in nature. *Current Opinion in Solid State & Materials Science*. 1998;3(3):221-7.
16. Giraudguille MM. Twisted plywood architecture of collagen fibrils in human compact-bone osteons. *Calcified Tissue International*. 1988;42(3):167-80.
17. Kadler KE, Holmes DF, Trotter JA, Chapman JA. Collagen fibril formation. *Biochemical Journal*. 1996;316:1-11.
18. Paschalis EP, Verdelis K, Doty SB, Boskey AL, Mendelsohn R, Yamauchi M. Spectroscopic characterization of collagen cross-links in bone. *Journal of Bone and Mineral Research*. 2001;16(10):1821-8.
19. Gao HJ, Ji BH, Jager IL, Arzt E, Fratzl P. Materials become insensitive to flaws at nanoscale: Lessons from nature. *Proceedings of the National Academy of Sciences of the United States of America*. 2003;100(10):5597-600.
20. Watson ML, Robinson RA. Collagen-crystal relationships in bone. 2. Electron microscope study of basic calcium phosphate crystals. *American Journal of Anatomy*. 1953;93(1):25-59.

21. Currey JD. Materials science - Hierarchies in biomineral structures. *Science*. 2005;309(5732):253-4.
22. Hu YY, Rawal A, Schmidt-Rohr K. Strongly bound citrate stabilizes the apatite nanocrystals in bone. *Proceedings of the National Academy of Sciences of the United States of America*. 2010;107(52):22425-9.
23. Robinson RA, Watson ML. Collagen-crystal relationships in bone as seen in the electron microscope. *Anatomical Record*. 1952;114(3):383-&.
24. Landis WJ, Hodgens KJ, Arena J, Song MJ, McEwen BF. Structural relations between collagen and mineral in bone as determined by high voltage electron microscopic tomography. *Microscopy Research and Technique*. 1996;33(2):192-202.
25. Lees S, Probst KS, Ingle VK, Kjoller K. The loci of mineral in turkey leg tendon as seen by atomic-force microscope and electron-microscopy. *Calcified Tissue International*. 1994;55(3):180-9.
26. Sasaki N, Tagami A, Goto T, Taniguchi M, Nakata M, Hikichi K. Atomic force microscopic studies on the structure of bovine femoral cortical bone at the collagen fibril-mineral level. *Journal of Materials Science-Materials in Medicine*. 2002;13(3):333-7.
27. Lees S, Page EA. A study of some properties of mineralized turkey leg tendon. *Connective Tissue Research*. 1992;28(4):263-87.
28. Marotti G, Lees, Reeve. A new theory of bone lamellation. *Calcified Tissue International*. 1993;53:S47-S56.
29. Ziv V, Sabanay I, Arad T, Traub W, Weiner S. Transitional structures in lamellar bone. *Microscopy Research and Technique*. 1996;33(2):203-13.

30. Currey JD. The structure and mechanics of bone. *Journal of Materials Science*. 2012;47(1):41-54.
31. Bass SL, Saxon L, Daly RM, Turner CH, Robling AG, Seeman E, et al. The effect of mechanical loading on the size and shape of bone in pre-, peri-, and postpubertal girls: A study in tennis players. *Journal of Bone and Mineral Research*. 2002;17(12):2274-80.
32. Frost HM. Wolff law and bones structural adaptations to mechanical usage-an overview for clinician. *Angle Orthodontist*. 1994;64(3):175-88.
33. Boskey AL, Myers ER. Is bone mineral crystal size a significant contributor to "bone quality"? *BoneKEy-Osteovision*. 2004;1:4-7.
34. Turner CH, Rho J, Takano Y, Tsui TY, Pharr GM. The elastic properties of trabecular and cortical bone tissues are similar: results from two microscopic measurement techniques. *Journal of Biomechanics*. 1999;32(4):437-41.
35. Zysset PK, Guo XE, Hoffler CE, Moore KE, Goldstein SA. Elastic modulus and hardness of cortical and trabecular bone lamellae measured by nanoindentation in the human femur. *Journal of Biomechanics*. 1999;32(10):1005-12.
36. Board NMA. *Hierarchical Structures in Biology as a Guide for New Materials Technology*: National Academy of Science; 1994.
37. Rho JY. An ultrasonic method for measuring the elastic properties of human tibial cortical and cancellous bone. *Ultrasonics*. 1996;34(8):777-83.
38. Laugier P, Saied A, Granke M, Raum K. Quantitative Scanning Acoustic Microscopy of Bone. In: Maev RG, editor. *Advances in Acoustic Microscopy and High Resolution Imaging*. Boschstr. 12, 69469 Weinheim, Germany: Wiley-VCH Verlag & Co. KGaA; 2013.

39. Reilly DTB, Albert H. The Elastic and Ultimate Properties of Compact Bone Tissue. *Journal of Biomechanics*. 1975;8(6):393-6, IN9-IN11, 7-405.
40. Carter DR, Caler WE, Spengler DM, Frankel VH. Fatigue behavior of adult cortical bone - the influence of mean strain and strain range. *Acta Orthopaedica Scandinavica*. 1981;52(5):481-90.
41. Zioupos P, Currey JD, Sedman AJ. An examination of the micromechanics of failure of bone and antler by acoustic-emission tests and laser scanning-confocal-microscopy. *Medical Engineering & Physics*. 1994;16(3):203-12.
42. Vashishth D, Behiri JC, Bonfield W. Crack growth resistance in cortical bone: Concept of microcrack toughening. *Journal of Biomechanics*. 1997;30(8):763-9.
43. Zimmermann EA, Gludovatz B, Schaible E, Busse B, Ritchie RO. Fracture resistance of human cortical bone across multiple length-scales at physiological strain rates. *Biomaterials*. 2014;35(21):5472-81.
44. Keaveny TM, Morgan EF, Yeh OC. Bone Mechanics. In: Kutz M, editor. *Standard Handbook of Biomedical Engineering & Design*. 1 ed: McGraw-Hill Professional; 2002.
45. Abdel-Wahab AA, Alam K, Silberschmidt VV. Analysis of anisotropic viscoelastoplastic properties of cortical bone tissues. *Journal of the Mechanical Behavior of Biomedical Materials*. 2011;4(5):807-20.
46. Iyo T, Maki Y, Sasaki N, Nakata M. Anisotropic viscoelastic properties of cortical bone. *Journal of Biomechanics*. 2004;37(9):1433-7.
47. Deymier-Black AC, Yuan F, Singhal A, Almer JD, Brinson LC, Dunand DC. Evolution of load transfer between hydroxyapatite and collagen during creep deformation of bone. *Acta Biomaterialia*. 2012;8(1):253-61.

48. Lakes RS, Katz JL, Sternstein SS. Viscoelastic properties of wet cortical bone. 1. torsional and biaxial studies. *Journal of Biomechanics*. 1979;12(9):657-&.
49. Yamashita J, Furman BR, Rawls HR, Wang XD, Agrawal CM. The use of dynamic mechanical analysis to assess the viscoelastic properties of human cortical bone. *Journal of Biomedical Materials Research*. 2001;58(1):47-53.
50. Yamashita J, Li XO, Furman BR, Rawls HR, Wang XD, Agrawal CM. Collagen and bone viscoelasticity: A dynamic mechanical analysis. *Journal of Biomedical Materials Research*. 2002;63(1):31-6.
51. Wang T, Feng Z. Dynamic mechanical properties of cortical bone: The effect of mineral content. *Materials Letters*. 2005;59(18):2277-80.
52. Les CM, Vance JL, Christopherson GT, Turner AS, Divine GW, Fyhrie DP. Long-term ovariectomy decreases ovine compact bone viscoelasticity. *Journal of Orthopaedic Research*. 2005;23(4):869-76.
53. Chang YT, Chen CM, Tu MY, Chen HL, Chang SY, Tsai TC, et al. Effects of osteoporosis and nutrition supplements on structures and nanomechanical properties of bone tissue. *Journal of the Mechanical Behavior of Biomedical Materials*. 2011;4(7):1412-20.
54. Currey JD, Brear K. Hardness, Young modulus and yield stress in mammalian mineralized tissues. *Journal of Materials Science-Materials in Medicine*. 1990;1(1):14-20.
55. Johnson WM, Rapoff AJ. Microindentation in bone: Hardness variation with five independent variables. *Journal of Materials Science-Materials in Medicine*. 2007;18(4):591-7.
56. Oehman C, Zwierzak I, Baleani M, Viceconti M. Human bone hardness seems to depend on tissue type but not on anatomical site in the long bones of an old subject. *Proceedings of the*

Institution of Mechanical Engineers Part H-Journal of Engineering in Medicine.

2013;227(H2):200-6.

57. Gardner-Morse MG, Tacy NJ, Beynon BD, Roemhildt ML. In Situ Microindentation for Determining Local Subchondral Bone Compressive Modulus. *Journal of Biomechanical Engineering-Transactions of the Asme.* 2010;132(9).

58. Dall'Ara E, Karl C, Mazza G, Franzoso G, Vena P, Pretterklieber M, et al. Tissue properties of the human vertebral body sub-structures evaluated by means of microindentation. *Journal of the Mechanical Behavior of Biomedical Materials.* 2013;25:23-32.

59. Yin L, Venkatesan S, Kalyanasundaram S, Qin Q-H. Effect of microstructure on micromechanical performance of dry cortical bone tissues. *Materials Characterization.* 2009;60(12):1424-31.

60. Daegling DJ, Hotzman JL, McGraw WS, Rapoff AJ. Material Property Variation of Mandibular Symphyseal Bone in Colobine Monkeys. *Journal of Morphology.* 2009;270(2):194-204.

61. Dall'Ara E, Schmidt R, Zysset P. Microindentation can discriminate between damaged and intact human bone tissue. *Bone.* 2012;50(4):925-9.

62. Diez-Perez A, Guerri R, Nogues X, Caceres E, Pena MJ, Mellibovsky L, et al. Microindentation for in vivo measurement of bone tissue mechanical properties in humans. *J Bone Miner Res.* 2010;25(8):1877-85.

63. Gueerri-Fernandez RC, Nogues X, Quesada Gomez JM, Torres del Pliego E, Puig L, Garcia-Giralt N, et al. Microindentation for In Vivo Measurement of Bone Tissue Material Properties in Atypical Femoral Fracture Patients and Controls. *Journal of Bone and Mineral Research.* 2013;28(1):162-8.

64. Gallant MA, Brown DM, Organ JM, Allen MR, Burr DB. Reference-point indentation correlates with bone toughness assessed using whole-bone traditional mechanical testing. *Bone*. 2013;53(1):301-5.
65. Erdemira A, Guess TM, Halloran J, Tadepalli SC, Morrison TM. Considerations for reporting finite element analysis studies in biomechanics. *Journal of Biomechanics*. 2012;45(4):625-33.
66. Lucchini R, Carnelli D, Ponzoni M, Bertarelli E, Gastaldi D, Vena P. Role of damage mechanics in nanoindentation of lamellar bone at multiple sizes: Experiments and numerical modeling. *Journal of the Mechanical Behavior of Biomedical Materials*. 2011;4(8):1852-63.
67. Schwen LO, Wolfram U. Validation of composite finite elements efficiently simulating elasticity of trabecular bone. *Computer methods in biomechanics and biomedical engineering*. 2014;17(6):652-60.
68. Mueller R, Kampschulte M, El Khassawna T, Schlewitz G, Huerter B, Boecker W, et al. Change of mechanical vertebrae properties due to progressive osteoporosis: combined biomechanical and finite-element analysis within a rat model. *Medical & Biological Engineering & Computing*. 2014;52(4):405-14.
69. Carriero A, Doube M, Vogt M, Busse B, Zustin J, Levchuk A, et al. Altered lacunar and vascular porosity in osteogenesis imperfecta mouse bone as revealed by synchrotron tomography contributes to bone fragility. *Bone*. 2014;61:116-24.
70. Ali AA, Cristofolini L, Schileo E, Hu H, Taddei F, Kim RH, et al. Specimen-specific modeling of hip fracture pattern and repair. *Journal of Biomechanics*. 2014;47(2):536-43.

71. Ho K-Y, Keyak JH, Powers CM. Comparison of patella bone strain between females with and without patellofemoral pain: A finite element analysis study. *Journal of Biomechanics*. 2014;47(1):230-6.
72. Robson Brown K, Tarsuslugil S, Wijayathunga VN, Wilcox RK. Comparative finite-element analysis: a single computational modelling method can estimate the mechanical properties of porcine and human vertebrae. *Journal of the Royal Society, Interface / the Royal Society*. 2014;11(95):20140186-.
73. Christen D, Zwahlen A, Mueller R. Reproducibility for linear and nonlinear micro-finite element simulations with density derived material properties of the human radius. *Journal of the Mechanical Behavior of Biomedical Materials*. 2014;29:500-7.
74. Oshkour AA, Abu Osman NA, Davoodi MM, Yau YH, Tarlochan F, Abas WABW, et al. Finite element analysis on longitudinal and radial functionally graded femoral prosthesis. *International Journal for Numerical Methods in Biomedical Engineering*. 2013;29(12):1412-27.
75. Hamed E, Jasiuk I. Multiscale damage and strength of lamellar bone modeled by cohesive finite elements. *Journal of the Mechanical Behavior of Biomedical Materials*. 2013;28:94-110.
76. Ruegsegger P, Koller B, Muller R. A microtomographic system for the nondestructive evaluation of bone architecture. *Calcified Tissue International*. 1996;58(1):24-9.
77. Vanrietbergen B, Weinans H, Huiskes R, Odgaard A. A new method to determine trabecular bone elastic properties and loading using micromechanical finite-element models. *Journal of Biomechanics*. 1995;28(1):69-&.
78. Ulrich D, Van Rietbergen B, Laib A, Ruegsegger P. The ability of three-dimensional structural indices to reflect mechanical aspects of trabecular bone. *Bone*. 1999;25(1):55-60.

79. Morgan EF, Bayraktar HH, Keaveny TM. Trabecular bone modulus-density relationships depend on anatomic site. *Journal of Biomechanics*. 2003;36(7):897-904.
80. Carter DR, Orr TE, Fyhrie DP. Relationships between loading history and femoral cancellous bone architecture. *Journal of Biomechanics*. 1989;22(3):231-44.
81. Keyak JH, Meagher JM, Skinner HB, Mote CD. Automated 3-dimensional finite-element modeling of bone - a new method. *Journal of Biomedical Engineering*. 1990;12(5):389-97.
82. Newey D, Wilkins MA, Pollock HM. An ultra-low-load penetration hardness tester. *Journal of Physics E-Scientific Instruments*. 1982;15(1):119-22.
83. Rho JY, Tsui TY, Pharr GM. Elastic properties of human cortical and trabecular lamellar bone measured by nanoindentation. *Biomaterials*. 1997;18(20):1325-30.
84. Oliver WC, Pharr GM. An improved technique for determining hardness and elastic-modulus using load and displacement sensing indentation experiments. *Journal of Materials Research*. 1992;7(6):1564-83.
85. Sui T, Sandholzer MA, Le Bourhis E, Baimpas N, Landini G, Korsunsky AM. Structure-mechanical function relations at nano-scale in heat-affected human dental tissue. *Journal of the Mechanical Behavior of Biomedical Materials*. 2014;32:113-24.
86. Lee K-L, Sobieraj M, Baldassarri M, Gupta N, Pinisetty D, Janal MN, et al. The effects of loading conditions and specimen environment on the nanomechanical response of canine cortical bone. *Materials Science & Engineering C-Materials for Biological Applications*. 2013;33(8):4582-6.
87. Lau M-l, Lau K-t, Ku H, Cardona F, Lee J-H. Analysis of heat-treated bovine cortical bone by thermal gravimetric and nanoindentation. *Composites Part B-Engineering*. 2013;55:447-52.

88. Faingold A, Cohen SR, Reznikov N, Wagner HD. Osteonal lamellae elementary units: Lamellar microstructure, curvature and mechanical properties. *Acta Biomaterialia*. 2013;9(4):5956-62.
89. Giambini H, Wang H-J, Zhao C, Chen Q, Nassr A, An K-N. Anterior and posterior variations in mechanical properties of human vertebrae measured by nanoindentation. *Journal of Biomechanics*. 2013;46(3):456-61.
90. Albert C, Jameson J, Toth JM, Smith P, Harris G. Bone properties by nanoindentation in mild and severe osteogenesis imperfecta. *Clinical Biomechanics*. 2013;28(1):110-6.
91. Chen X, Goh JCH, Teoh SH, Das De S, Soong R, Lee T. Localized sclerotic bone response demonstrated reduced nanomechanical creep properties. *Journal of the Mechanical Behavior of Biomedical Materials*. 2013;17:198-208.
92. Thurner PJ. Atomic force microscopy and indentation force measurement of bone. *Wiley Interdisciplinary Reviews-Nanomedicine and Nanobiotechnology*. 2009;1(6):624-49.
93. Wenger MPE, Bozec L, Horton MA, Mesquida P. Mechanical properties of collagen fibrils. *Biophysical Journal*. 2007;93(4):1255-63.
94. McLeod MA, Wilusz RE, Guilak F. Depth-dependent anisotropy of the micromechanical properties of the extracellular and pericellular matrices of articular cartilage evaluated via atomic force microscopy. *Journal of Biomechanics*. 2013;46(3):586-92.
95. Wilusz RE, DeFrate LE, Guilak F. Immunofluorescence-guided atomic force microscopy to measure the micromechanical properties of the pericellular matrix of porcine articular cartilage. *Journal of the Royal Society Interface*. 2012;9(76):2997-3007.

96. Faingold A, Cohen SR, Shahar R, Weiner S, Rapoport L, Wagner HD. The effect of hydration on mechanical anisotropy, topography and fibril organization of the osteonal lamellae. *Journal of Biomechanics*. 2014;47(2):367-72.
97. Rho JY, Pharr GM. Effects of drying on the mechanical properties of bovine femur measured by nanoindentation. *Journal of Materials Science-Materials in Medicine*. 1999;10(8):485-8.
98. Buehler MJ. Nanomechanics of collagen fibrils under varying cross-link densities: Atomistic and continuum studies. *Journal of the Mechanical Behavior of Biomedical Materials*. 2008;1(1):59-67.
99. Pradhan SM, Katti KS, Katti DR. Multiscale Model of Collagen Fibril in Bone: Elastic Response. *Journal of Engineering Mechanics*. 2014;140(3):454-61.
100. Uzel SGM, Buehler MJ. Molecular structure, mechanical behavior and failure mechanism of the C-terminal cross-link domain in type I collagen. *Journal of the Mechanical Behavior of Biomedical Materials*. 2011;4(2):153-61.
101. Gautieri A, Vesentini S, Redaelli A, Buehler MJ. Hierarchical Structure and Nanomechanics of Collagen Microfibrils from the Atomistic Scale Up. *Nano Letters*. 2011;11(2):757-66.
102. Pradhan S, Katti K, Katti D. Structural Hierarchy Controls Deformation Behavior of Collagen. *Biomacromolecules*, accepted. 2012.
103. Pradhan SM, Katti DR, Katti KS. Steered Molecular Dynamics Study of Mechanical Response of Full Length and Short Collagen Molecules. *Journal of nanomechanics and micromechanics*. 2011;1(3):104-10.

104. Buehler MJ, Keten S, Ackbarow T. Theoretical and computational hierarchical nanomechanics of protein materials: Deformation and fracture. *Progress in Materials Science*. 2008;53(8):1101-241.
105. Buehler MJ. Nature designs tough collagen: Explaining the nanostructure of collagen fibrils. *Proceedings of the National Academy of Sciences of the United States of America*. 2006;103(33):12285-90.
106. Tang Y, Ballarini R, Buehler MJ, Eppell SJ. Deformation micromechanisms of collagen fibrils under uniaxial tension. *Journal of the Royal Society Interface*. 2010;7(46):839-50.
107. Dubey DK, Tomar V. Role of Molecular Level Interfacial Forces in Hard Biomaterial Mechanics: A Review. *Annals of Biomedical Engineering*. 2010;38(6):2040-55.
108. Bhowmik R, Katti KS, Katti DR. Mechanics of molecular collagen is influenced by hydroxyapatite in natural bone. *Journal of Materials Science*. 2007;42(21):8795-803.
109. Dubey DK, Tomar V. Role of hydroxyapatite crystal shape in nanoscale mechanical behavior of model tropocollagen-hydroxyapatite hard biomaterials. *Materials Science & Engineering C-Materials for Biological Applications*. 2009;29(7):2133-40.
110. Chavassieux P, Seeman E, Delmas PD. Insights into material and structural basis of bone fragility from diseases associated with fractures: How determinants of the biomechanical properties of bone are compromised by disease. *Endocrine Reviews*. 2007;28(2):151-64.
111. Teitelbaum SL. Bone resorption by osteoclasts. *Science*. 2000;289(5484):1504-8.
112. Bala Y, Kohles J, Recker RR, Boivin G. Oral Ibandronate in Postmenopausal Osteoporotic Women Alters Micromechanical Properties Independently of Changes in Mineralization. *Calcified Tissue International*. 2013;92(1):6-14.

113. Liberman UA, Weiss SR, Broll J, Minne HW, Quan H, Bell NH, et al. Effect of oral alendronate on bone-mineral density and the incidence of fractures in postmenopausal osteoporosis. *New England Journal of Medicine*. 1995;333(22):1437-43.
114. Klibanski A, Adams-Campbell L, Bassford T, Blair SN, Boden SD, Dickersin K, et al. Osteoporosis prevention, diagnosis, and therapy. *Jama-Journal of the American Medical Association*. 2001;285(6):785-95.
115. <http://www.mayoclinic.org/>.
116. <http://www.oif.org>.
117. Silience DO, Senn A, Danks DM. Genetic-heterogeneity in osteogenesis imperfecta. *Journal of Medical Genetics*. 1979;16(2):101-16.
118. Forlino A, Cabral WA, Barnes AM, Marini JC. New perspectives on osteogenesis imperfecta. *Nature Reviews Endocrinology*. 2011;7(9):540-57.
119. Bishop N. Characterising and treating osteogenesis imperfecta. *Early Human Development*. 2010;86(11):743-6.
120. Rauch F, Glorieux FH. Osteogenesis imperfecta. *Lancet*. 2004;363(9418):1377-85.
121. Byers PH, Krakow D, Nunes ME, Pepin M. Genetic evaluation of suspected osteogenesis imperfecta (OI). *Genetics in Medicine*. 2006;8(6):383-8.
122. van Dijk FS, Byers PH, Dagleish R, Malfait F, Mauerer A, Rohrbach M, et al. EMQN best practice guidelines for the laboratory diagnosis of osteogenesis imperfecta. *European Journal of Human Genetics*. 2012;20(1):11-9.
123. Rauch F, Plotkin H, Zeitlin L, Glorieux FH. Bone mass, size, and density in children and adolescents with osteogenesis imperfecta: Effect of intravenous pamidronate therapy. *Journal of Bone and Mineral Research*. 2003;18(4):610-4.

124. Astrom E, Soderhall S. Beneficial effect of bisphosphonate during five years of treatment of severe osteogenesis imperfecta. *Acta Paediatrica*. 1998;87(1):64-8.
125. Rauch F, Travers R, Plotkin H, Glorieux FH. The effects of intravenous pamidronate on the bone tissue of children and adolescents with osteogenesis imperfecta. *Journal of Clinical Investigation*. 2002;110(9):1293-9.
126. Uveges TE, Kozloff KM, Ty JM, Ledgard F, Raggio CL, Gronowicz G, et al. Alendronate Treatment of the Brl Osteogenesis Imperfecta Mouse Improves Femoral Geometry and Load Response Before Fracture but Decreases Predicted Material Properties and Has Detrimental Effects on Osteoblasts and Bone Formation. *Journal of Bone and Mineral Research*. 2009;24(5):849-59.
127. Rao SH, Evans KD, Oberbauer AM, Martin RB. Bisphosphonate treatment in the oim mouse model alters bone modeling during growth. *Journal of Biomechanics*. 2008;41(16):3371-6.
128. Gourion-Arsiquaud S, Allen MR, Burr DB, Vashishth D, Tang SY, Boskey AL. Bisphosphonate treatment modifies canine bone mineral and matrix properties and their heterogeneity. *Bone*. 2010;46(3):666-72.
129. Marini JC. BONE Use of bisphosphonates in children-proceed with caution. *Nature Reviews Endocrinology*. 2009;5(5):241-3.
130. Grafe I, Yang T, Alexander S, Homan EP, Lietman C, Jiang MM, et al. Excessive transforming growth factor-[beta] signaling is a common mechanism in osteogenesis imperfecta. *Nature Medicine*. 2014.

131. Bargman R, Huang A, Boskey AL, Raggio C, Pleshko N. RANKL Inhibition Improves Bone Properties in a Mouse Model of Osteogenesis Imperfecta. *Connective Tissue Research*. 2010;51(2):123-31.
132. Burstein AH, Reilly DT, Martens M. AGING OF BONE TISSUE - MECHANICAL-PROPERTIES. *Journal of Bone and Joint Surgery-American Volume*. 1976;58(1):82-6.
133. McCalden RW, McGeough JA, Barker MB, Courtbrown CM. Age-related-changes in the tensile properties of cortical bone - the relative importance of changes in porosity, mineralization, and microstructure. *Journal of Bone and Joint Surgery-American Volume*. 1993;75A(8):1193-205.
134. Amprino R, Engstrom A. Studies on X-ray absorption and diffraction of bone tissue. *Acta Anatomica*. 1952;15(1-2):1-22.
135. Boyde A, Jones SJ. Backscattered electron imaging of skeletal tissues. *Metabolic Bone Disease & Related Research*. 1984;5(3):145-50.
136. Nuzzo S, Lafage-Proust MH, Martin-Badosa E, Boivin G, Thomas T, Alexandre C, et al. Synchrotron radiation microtomography allows the analysis of three-dimensional microarchitecture and degree of mineralization of human iliac crest biopsy specimens: Effects of etidronate treatment. *Journal of Bone and Mineral Research*. 2002;17(8):1372-82.
137. Torres-del-Piiego E, Vilaplana L, Gueerri-Fernandez R, Diez-Perez A. Measuring Bone Quality. *Current Rheumatology Reports*. 2013;15(11).

CHAPTER 2. PHOTOACOUSTIC FTIR SPECTROSCOPIC STUDY OF UNDISTURBED HUMAN CORTICAL BONE²

This chapter presents SEM images and photoacoustic FTIR spectroscopic study of undisturbed healthy human cortical bone. Here we find that the stoichiometry of bone mineral is influenced by the interactions between collagen and mineral. The content of this chapter has been published in Gu, C.; Katti, D. R.; Katti, K. S.; Photoacoustic FTIR spectroscopic study of undisturbed human cortical bone. *Spectrochimica acta Part A*. 2013, 103, 25-37.

2.1. Introduction

Bone tissue is composed of collagen fibers, crystals of a calcium-phosphate mineral, hydroxyapatite or cement containing mucopolysaccharides etc., among which collagen, mineral and water are three primary components. Collagen accounts for nearly 1/3 of the dry weight of bone and the mineral accounts for nearly 2/3 of the dry weight of bone matrix (1). The water component is on average 10-12wt.% of cortical bone (2). As all structural materials in biology, bone exhibits a detailed hierarchical organization (3-5) that spans length scales from nm to mm (6, 7). The collagen found in bone (type I), forms a fibrillar structure consisting of staggered arrangement of collagen molecules with a periodicity of 67 nm (6, 7). The hydroxyapatite crystals are present in the hole-zone between collagen molecules (3-5). The collagen mineral interactions as well as collagen structural behavior have been extensively studied through modeling efforts (8-15). The principle orientation of bone mineral is along the long axis of the

² This chapter was co-authored by Chunju Gu, Kalpana Katti, and Dinesh Katti. Chunju Gu had primary responsibility for preparing samples, conducting all tests, and drafting this chapter. Kalpana Katti and Dinesh Katti directed the research orientation and revised this chapter.

bone, whereas bone collagen fibers are aligned with alternating fiber orientation in successive lamellae (16).

The human bone mineral is composed of a poorly crystallized apatite, with similar composition to synthetic hydroxyapatite $\text{Ca}_{10}(\text{OH})_2(\text{PO}_4)_6$. Hydroxyapatite has a hexagonal crystal structure (space group $\text{P6}_3/\text{M}$) (17). However, in contrast to synthetic hydroxyapatite, bone mineral is structurally disordered, and compositionally nonstoichiometric. Synthetic hydroxyapatite prepared in a laboratory is often stoichiometric but hydroxyapatite present in bone is known to be nonstoichiometric (18). In the hydroxyapatite structure, some ions can be replaced, leading to the presence of vacancies. For example, CO_3^{2-} can substitute for either PO_4^{3-} or OH^- ions. The bone crystal structure is primarily maintained by electrostatic cohesion such that bone crystals are more soluble as compared to stoichiometric apatite (19).

Mechanical properties of bone have orientation dependence resulting from preferential orientation of collagen and mineral. It was found that two orders of magnitude change in the fracture energy can be observed depending on the orientation of collagen (20, 21). Using Raman spectral mapping, bone osteonal tissues were studied indicating that, the PO_4^{3-} v1 and amide I vibrations are sensitive to the orientation and the polarization direction of the incident light. This is in accordance with the mineral c-axis and the position of carbonyl in collagen chains, while amide III, v2 and v4 PO_4^{3-} vibrations are observed to be less sensitive to orientation effects (22). It was also shown that the v1 PO_4^{3-} to amide I ratio is indicative of the lamellar bone orientation, and v2 PO_4^{3-} to amide III and CO_3^{2-} to v2 PO_4^{3-} ratios are suggestive of variation in bone composition (23).

As a nondestructive technique, Fourier transform infrared (FTIR) spectroscopy has been extensively used to study the composition and structure of bone tissue by calculating the

lipid/protein ratio, Ca/P ratio, protein/mineral ratio, the crystallinity of the mineral phase (24), crystallinity index (25) as well as collagen cross-link ratio (26). The most widely used mode for FTIR experiments on bone is transmission (TS). TS-FTIR combined with microscopy (27-29) and imaging have been extensively used to study the correlation between the image, spectra and the structure of bone (29-33) as well as different ages (26, 34) and diseases such as osteoporosis (35), osteopetrosis (36), osteomalacia (37), and osteogenesis imperfect (38), etc. TS-FTIR has the highest signal-to-noise ratio, and is useful for quantitative measurements (39). Transmission is the most frequently used mode for infrared spectroscopy and one of the common methods for sample preparation involves fixation, dehydration of bone tissue followed by embedding of the sample in resin that is sectioned using a microtome (25, 26, 33, 34, 40, 41) or directly mixing the sample with Potassium bromide (KBr) powder in a mortar and pestle (24, 42-45). Both sample preparation methods have the potential to influence the water content and interactions between mineral and collagen. Further, fixation of bone specimens prevents bacterial growth and degradation of the specimen before data are collected. However, it was found that formalin fixation had little effect on the collagen, but a significant effect on the mineral structure, while ethanol fixation had the opposite effect (46).

Thus, chemical pretreatment may potentially influence the organic matrix and mineral interaction. For example, literature prior to 2003 indicated that there are almost no hydroxyl groups in bone mineral crystals (47-52). Most of the specimens reported underwent chemical pretreatments and were characterized by FTIR, Raman, Nuclear magnetic resonance (NMR) and inelastic neutron-scattering. However, for samples with no pretreatment other than cryogenic grinding it was found that hydroxyl ions could be detected by solid-state NMR spectroscopy and the OH⁻ content of human cortical bone was roughly 20% of the amount expected in

stoichiometric hydroxyapatite (53). Therefore, techniques of sample preparation are crucial for spectroscopic investigations of bone.

Photoacoustic (PA-) FTIR spectroscopy is commonly used technique due to minimal sample preparation requirements and ability to examine specimen in situ. Recently, this has been particularly useful while investigating nanocomposites of biological origin such as seashells (54) and geological origin such as oil shales (55). In the photoacoustic technique (Figure 2.1), the infrared beam incidents on the sample and excites vibrational motion of molecules which causes the perturbation of coupling gas, thereby generating compression waves in the inert gas in the proximity of the sample which can be detected by a sensitive microphone (56). PA-FTIR is insensitive to surface morphology and capable of measuring spectra of all types of solids without exposure to air or moisture, and also applicable to liquids and gases (57). Therefore, sample preparation of PA mode is faster and easier as compared to that for transmission mode. In addition, as shown in Figure 2.1, the coupling inert gas, helium, has shown to inhibits bacteria growth in bone by displacing oxygen (58). Two modes of data collection are used in PA-FTIR, linear-scan (LS, also called continuous scan or rapid scan), and step-scan (SS). The primary distinction between these methods is the varied or constant modulation frequency for a given wavelength. The expression for the modulation frequency at a certain wavenumber is given by (57).

$$f = 2v \bar{\nu} \quad (2.1)$$

where v is the velocity of the interferometer mirror (cm/s), and $\bar{\nu}$ is the wavenumber (cm^{-1}). Step-scan (SS-PA-FTIR) spectroscopy measures samples' absorbance spectrum directly with a controllable sampling depth by keeping the beam modulation frequency constant. The thermal

waves decay to 37% (1/e) of their original amplitude over a distance L, which is called the thermal diffusion depth or the thermal wave decay length, given by the following equation:

$$L = (D/\pi f)^{1/2} \quad (2.2)$$

where D and f refer to the sample's thermal diffusivity and the infrared beam phase modulation frequency, respectively (59).

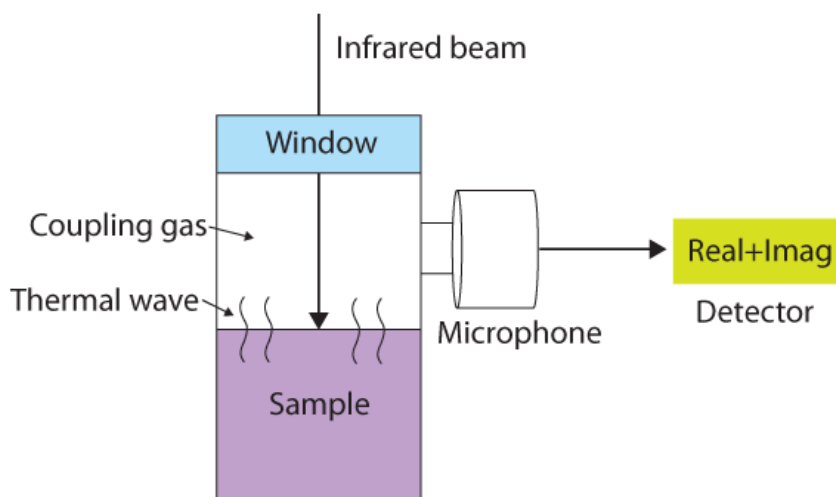


Figure 2.1. Schematic diagram of PA-FTIR instrument.

PA-FTIR technique has already been utilized to study heterogeneous polymer (60, 61) and polymer clay nanocomposites (62, 63), seashells (54, 64), and enamel of an intact human tooth (65, 66). Thermal damages by lasers on the tibia of rabbits was investigated by Linear scan (LS-PA-FTIR) spectroscopy (67). Heated deer antler (group I) and whale tympanic bulla were also investigated by LS-PA-FTIR spectroscopy recently (68).

In the present study, PA-FTIR has been utilized to study undisturbed human cortical bone from both transverse and longitudinal planes. We have also conducted depth profiling experiments, utilizing SS-PA-FTIR to study human bone at several penetration depths.

2.2. Materials and Methodology

2.2.1. Materials

The human femur was obtained from National Disease Research Interchange, PA (from 27 years old, female donor with no apparent metabolic bone disease record) and was stored in a freezer at -70°C . The femur was cut into small pieces with a saw and cleaned thoroughly using deionized water at room temperature in a very short time. A diamond-wafering blade (Buehler, Isomet, Lake Bluff, IL) was used to cut the pieces into smaller samples ($\sim 8\text{mm}$, 6mm , 1mm) in both longitudinal and transverse planes to get longitudinal section and transverse section correspondingly for FTIR experiments. Another set of samples with the same preparation methods as above were further cut into three sections for additional FTIR experiments (Figure 2.2).

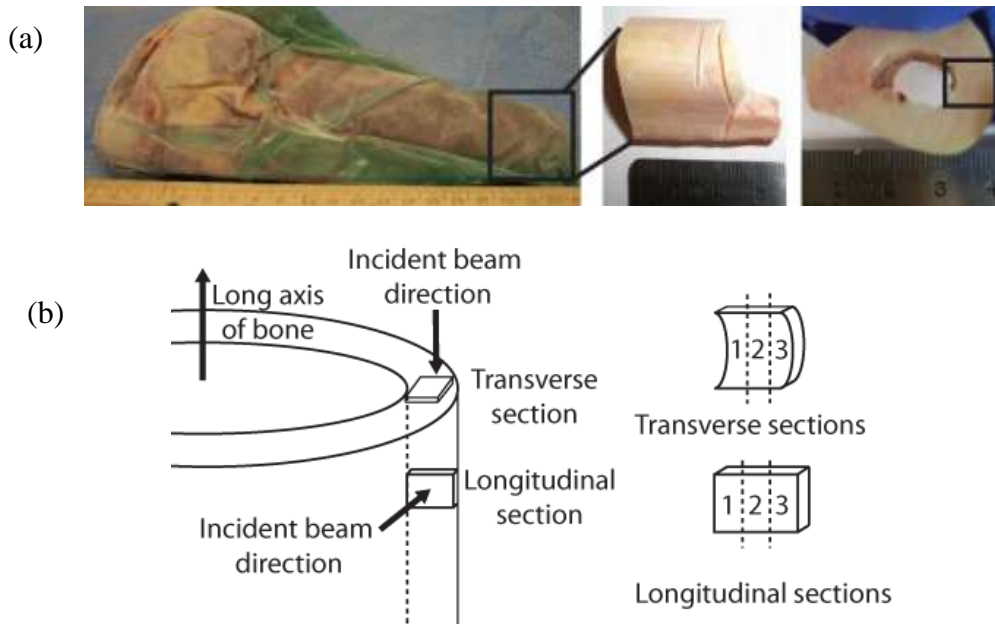


Figure 2.2. (a) Location of the tested sample from the human femur; and (b) Schematic representation of bone showing from where the sample were cut, 1 represents inner side, 2 middle, and 3 outer side of the bone piece.

For SEM imaging, the samples in both longitudinal and transverse planes were further fixed in 2.5% Glutaraldehyde (Tousimis) overnight. Further, the resulting specimens were rinsed twice with sodium phosphate buffer (0.1M PH 7.35, Tousimis), followed by post-fixation in 1% Osmium-tetroxide (Electron Microscopy Sciences) for 2 h. The samples were then rinsed twice again as before, followed by dehydration through a graded series of ethanol (30%, 50%, 70%, 90%, 100%, 100%, 100%, 100%, from Aaper Alcohol and Chemical Co.). After being critical point-dried in liquid CO₂ (Autosamdri-810, Tousimis) and fractured in liquid nitrogen, the specimens were coated with carbon (Carbon coater: Cressington 208 carbon) and examined using a Field Emission Scanning Electron Microscope (JEOL JSM-7600F).

2.2.2. Methods

FTIR spectra were collected using Thermo Electron, Nexus 870 spectrometer equipped with MTEC Model 300 photoacoustic accessory. Before each data collection, the PA chamber was purged with dry helium for 15 min. All spectra were collected in the range of 4000-400 cm⁻¹, at a spectral resolution of 4 cm⁻¹ and SS-PA experiments were done at frequencies ranging from 50Hz to 1000Hz. GRAMS/32 software was used for spectra analysis. The center positions for each sub-band in curve-fitting were determined by second-derivative analysis and the shapes of the underlying bands were chosen by Gaussian algorithm.

2.3. Results

2.3.1. Microstructures of human bone in transverse and longitudinal planes

The human bone exhibits a hierarchical structure with the osteon as an important structural element. Figure 2.3 shows microstructure of bone sample in transverse and longitudinal planes. Figure 2. 3a shows an osteon with a haversian canal at the center which is

surrounded by concentric lamellae of collagen fibers. Lamellae are made up of fiber bundles with normally plywood-like array pattern (69). The fiber bundles are further composed of mineralized fibrils which consist of nanoscale collagen and minerals. In mineralized fibrils, collagen and mineral have a staggered arrangement with periodicity of 67nm, as shown in Figure 2.3d. Bone collagen is assembled in an orderly manner with hole-zones of neighboring molecules being adjacent to one another to form channels or grooves in the packed assemblage (schematically shown in Figure 2.4a and b). Platelet-shaped hydroxyapatite (HAP) crystals are positioned in channels or grooves and crystal sizes may exceed the dimensions of hole-zones (4, 9, 70).

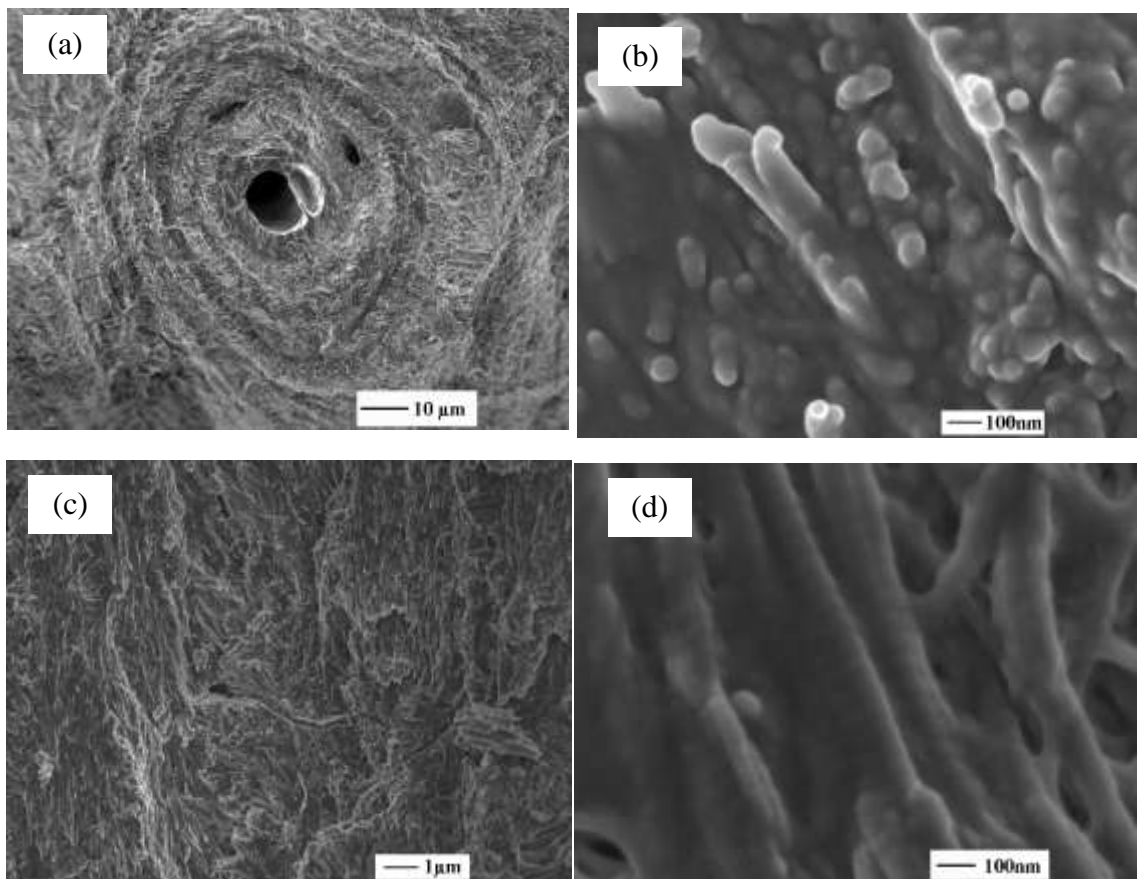


Figure 2.3. SEM micrographs of human bone (a and b) Transverse section; and (c and d) Longitudinal section.

Collagen and mineral have preferential orientations. In the transverse plane, round osteons can be seen on the section, and the mineralized fibrils are protruding out of lamellae as shown in Figure 2.3b. In the longitudinal plane, the fibrils are aligned parallel or at an angles to the long axis, as shown in Figure 2.3c, and the mineral crystals are roughly along the long axis of the bone (16). Figure 2.4c shows a model of the mineral structure in the (001) plane and the (100) plane. Details of model construction are reported elsewhere (71). As seen from the model for (100) plane (from Figure 2.4c), each of the two OH ions is surrounded by a Ca triangle, and the OH ions are relatively isolated from the other structural units such as PO_4 tetrahedral and CaO_6 octahedra.

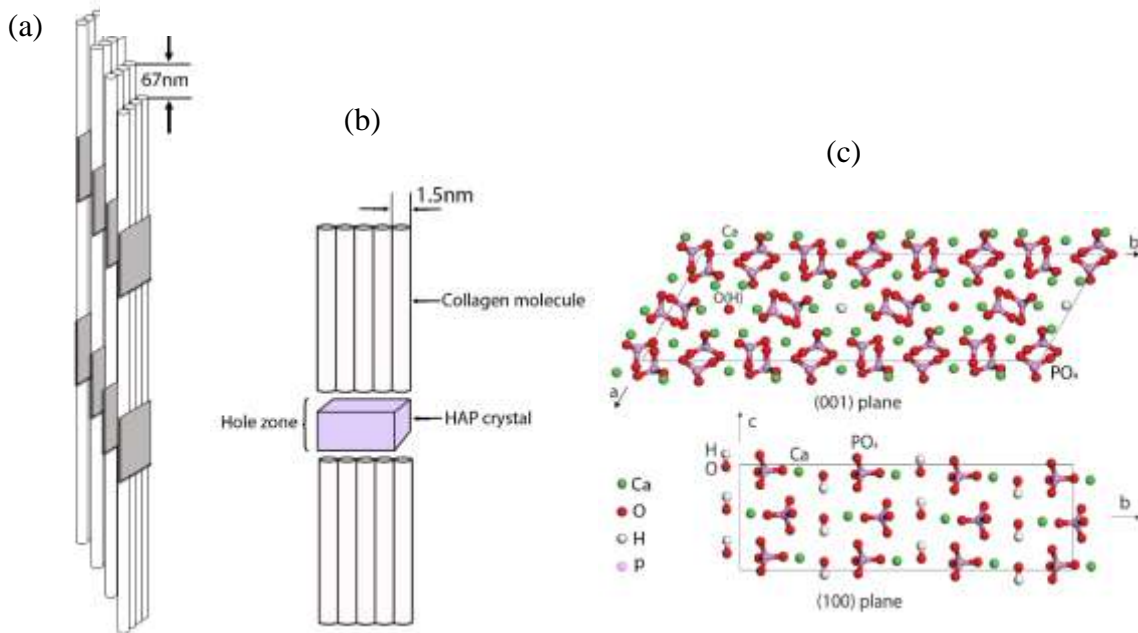


Figure 2.4. HAP in bone. (a) Staggered arrangement of mineralized fibrils. (b) Relationship between collagen molecules and intra-fibrillar HAP crystal. (c) HAP structure projected on the (001) plane and (100) plane (adapted from (71)).

2.3.2. Comparison of PA-FTIR and TS-FTIR spectra

A typical PA-FTIR spectrum (linear-scan) from bone sample is shown in Figure 2.5. On comparing the PA spectra to TS-FTIR spectra such as that obtained from rat tibia (obtained from powder in a KBr pellet) in the range of 4000-400 cm^{-1} (24) or healthy human cortical bone in the range of 1800-800 cm^{-1} (26), band positions appear similar, but some band-shapes such as the phosphate ν_3 band and the carbonate ν_2 band are observed to be different. Further, the intensity of the phosphate ν_3 band in transmission mode is the strongest while in PA mode it is much weaker; For PA-FTIR spectra, the OH band at 2262-3732 cm^{-1} is the strongest.

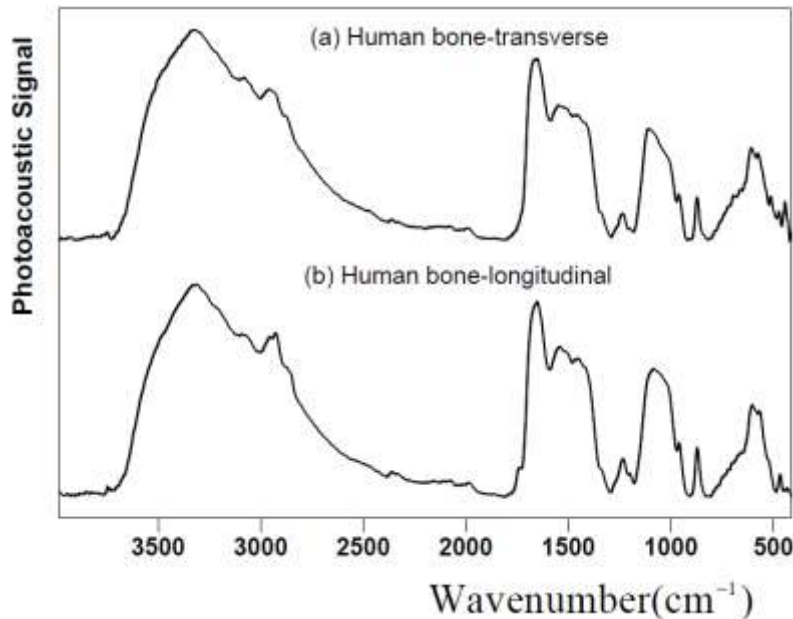


Figure 2.5. LS-PA-FTIR spectra of human bone in the 4000-400 cm^{-1} region, velocity of mirror: 0.158 cm/s : (a) Transverse; and (b) Longitudinal sections.

TS-FTIR experiments evaluate the bulk sample, whereas PA-FTIR measures the near-surface ($\sim 35\mu\text{m}$) molecular structures. In addition, magnitude of the PA-FTIR signal is proportional to absorptivity, concentration or sampling depth (59). All of these factors influence the intensity of bands. In PA mode, the detector is replaced by a photoacoustic sample cell which

has a KBr window for transmitting mid-infrared radiation and a microphone for photoacoustic signal detection. The carbonate ν_2 vibration shows a sharp band which indicates that PA-FTIR is more sensitive to carbonate ν_2 . In a previous work, PA-FTIR appears more sensitive than TS-FTIR in observing some cross-linking reactions (72). The appearance of amide III as a distinct band as seen in Figure 2.5 also indicates that PA-FTIR is more sensitive to this band.

Additionally, ν_1 PO_4^{3-} vibration at 960cm^{-1} and ν_4 PO_4^{3-} at $\sim 476\text{cm}^{-1}$ are also distinctly observed in the PA-FTIR spectrum while being very weak in transmission mode (26). Phosphate exhibits four fundamental modes of vibrations: ν_1 the symmetric stretching at $\sim 962\text{cm}^{-1}$, ν_2 symmetric bending at ~ 470 , ν_3 antisymmetric stretching at $900\text{-}1200\text{cm}^{-1}$, and ν_4 antisymmetric bending at $564\text{-}603\text{cm}^{-1}$. Only the triply degenerate vibration species of the tetrahedral molecules are infrared active, so only ν_3 and ν_4 should be observed in the FTIR spectra. However, when the geometrical parameters shift to lower molecular symmetry, ν_1 and ν_2 become observable(43). As observed in the data, in the transmission mode, these two bands are very weak, but very prominent in the photoacoustic mode. Therefore, it appears that phosphate ion geometry is less symmetric in its undisturbed state as detected by the PA-FTIR, with all phosphate vibrations detected.

2.3.3. Comparison of PA spectra from transverse and longitudinal sections

Figure 2.5 shows LS-PA-FTIR spectra for solid bone samples from the transverse and the longitudinal sections in the energy range of $4000\text{-}400\text{cm}^{-1}$. The spectra were normalized with the O-H peak (3322cm^{-1}). The assignments of the bands are given in Table 2.1. The spectral analyses from these data were performed in three spectral ranges corresponding to $3700\text{-}2500$, $2000\text{-}1180$, and $1180\text{-}450\text{cm}^{-1}$.

Table 2.1. Band assignments of PA-FTIR spectra from human bone.

Wavenumber (cm ⁻¹) transverse	Wavenumber (cm ⁻¹) longitudinal	Band assignment	Ref.
3564	3570	Structural OH	(73)
3322	3328	OH stretching vibration from embedded water	(43)
2959	2961	CH ₃ asymmetric stretch: mainly lipids	(24)
2926	2926	CH ₂ asymmetric stretch: mainly lipids, with the little contribution from proteins, carbohydrates, nucleic acids	(24)
2884	2885	CH ₃ symmetric stretch: mainly proteins, with the little contribution from lipids, carbohydrates, nucleic acids	(24)
2855	2853	CH ₂ symmetric stretch: mainly lipids, with the little contribution from proteins, carbohydrates, nucleic acids	(24)
	1747	C=O stretch: lipids, cholesterol esters, triglycerides	(74)
1652	1654	Amide 1 (protein C=O stretch)	(74)
1549-1505	1546-1506	Amide 2 (Protein N-H bend, C-N stretch)	(74)
1449,1415	1447,1415	carbonyl and carbonate ν_3 vibration	(24)
1342	1340	CH ₂ wagging	(43)
1236	1236	Amide 3(C-N stretch, N-H bend, C-C stretch)	(43)
1180-1000	1180-1100	ν_3 PO ₄ ³⁻	(43)
962	963	ν_1 PO ₄ ³⁻	(43)
874	875	ν_2 CO ₃ ²⁻	(43)
609,576	606,567	ν_4 PO ₄ ³⁻	(43)
476	470	ν_2 PO ₄ ³⁻	(43)

As seen in Figure 2.6a in the energy range of 4000-2000cm⁻¹, a broad band in the region around 3322cm⁻¹ is observed, that is attributed to the O-H stretching vibration from water

combined with N-H stretching (amide A) (43). This indicates that there is a large amount of water present in both bone samples. Figure 2.6b shows the second-derivative spectral curves for this region. The bands at 3564cm^{-1} and 3570cm^{-1} are assigned to the stretching vibration of the structural hydroxyl group from hydroxyapatite (73). Although the presence of hydroxyl ions in the bone mineral has been debated (52, 53), from the appearance of a shoulder to the broad O-H band and the resulting features in second-derivative (Figure 2.6b), we believe that there are a small amount of structural OH ions in the bone mineral. The band at around 3074cm^{-1} is attributed to amide B which is Fermi resonance band of the first overtone of the amide II band powered by the N-H stretching vibration (75). The O-H bending band from water is overlapped by amide I. The band around 2100cm^{-1} is assigned to OH stretching vibrations from P-OH. These bands lie in 2100cm^{-1} region and have been previously observed in hydroxyapatite spectra (76-78). They were attributed to PO_4^{3-} (76) and P-OH vibrational modes (79). In the present spectra, the shapes of these bands are more like those obtained from hydroxyapatite.

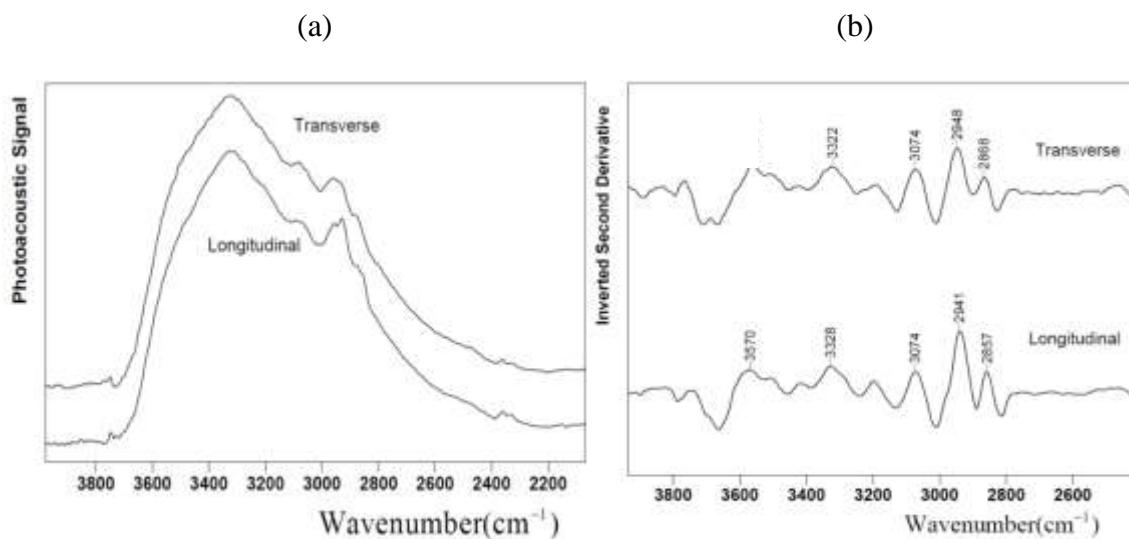


Figure 2.6. (a) PA-FTIR spectra of human bone (transverse and longitudinal) in the $4000\text{-}2000\text{cm}^{-1}$ region; and (b) Inverted second-derivative curves in the energy range of $3900\text{-}2400\text{cm}^{-1}$.

In the second-derivative curves, the sharp C-H stretching bands from organic matrix are smoothed out. It is observed in the spectra that CH₃, and CH₂ asymmetric and symmetric stretching vibrations are present at 2960, 2926, 2884 and 2854cm⁻¹ in both sample sections (see Table 2.1). The CH₂ asymmetric band (~2926cm⁻¹) arises primarily from lipids, with the little contribution from proteins, carbohydrates, and nucleic acids in the longitudinal section, this band is observed to be comparatively stronger than that in the transverse section. This may result from structure difference between longitudinal and transverse sections. In the longitudinal section, the cross-section of arteries is probed as compared to only cross-section of osteons observed in the transverse section.

The energy range of 2000-1180cm⁻¹ (Figure 2.7) is attributed primarily to the organic matrix of bone. The band at around 1654cm⁻¹ arises from amide I, which corresponds to C=O stretching of protein. In the longitudinal section, the band at 1747cm⁻¹ is attributed to C=O stretching of lipids, cholesterol esters, and triglycerides from the arteries (74). The bands in the range of 1555-1500cm⁻¹ are attributed to amide II, which corresponds to the N-H bending and C-N stretching of protein. The bands at around 1454, 1413 cm⁻¹ are attributed to CH₃ and carbonate v₃ asymmetric stretching (80). The band at 1236 cm⁻¹ is attributed to amide III. No significant differences are observed between the two sections of these bands, which indicate that these bands are not orientation dependent. Kazanci et al. found that v₁ PO₄³⁻ and amide I vibrations are sensitive to the orientation and the polarization direction of the incident light in Raman spectra (22). However, because of overlapping O-H bending vibration, amide I in PA-FTIR spectra does not show orientation dependence.

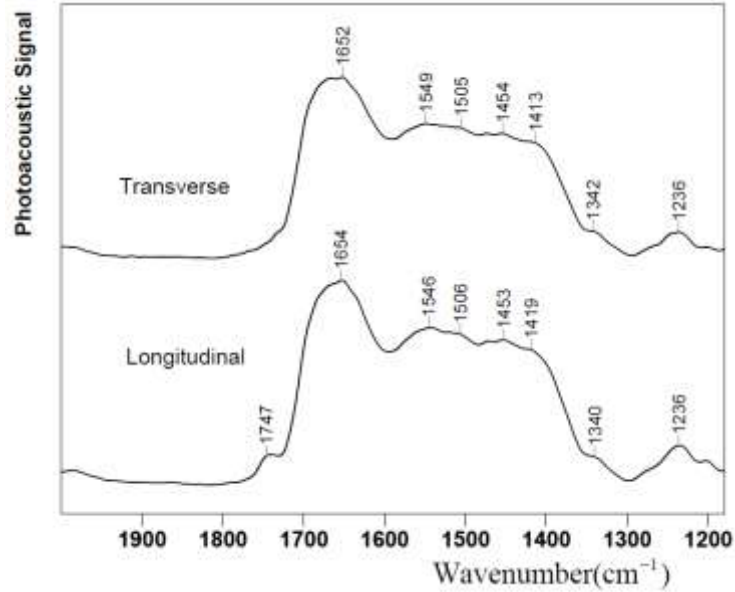


Figure 2.7. Photoacoustic infrared spectra of human bone (transverse and longitudinal) in the energy range of 2000-1180 cm^{-1} .

In the energy range of 1180-400 cm^{-1} , as seen in Figure 2.8, spectra intensity rises primarily from mineral vibrations. The broad and strong absorption band in the region 1180-900 cm^{-1} is typically assigned to ν_1 and ν_3 PO_4^{3-} , and the band at 609-576 cm^{-1} is assigned to ν_4 PO_4^{3-} vibrations. The band at 874 cm^{-1} is assigned to ν_2 out-of-plane bending of CO_3^{2-} . In the energy range of 1180-900 cm^{-1} , there is a small amount of contribution from collagen around 1030 cm^{-1} and 1080 cm^{-1} (81). In Paschalis's and Magne's studies, a subtraction procedure was developed using spectra from decalcified bone to remove those contributions (27, 82). However, those contributions are very small, and the decalcification procedure also includes some change to the organic matrix structure, and therefore, in recent papers, the subtraction step is not performed (41, 83). It is widely accepted that PO_4^{3-} vibrations have orientation dependence (22, 84). In Raman spectra, the band at 1059 cm^{-1} displayed a strong intensity dependence on the scattering configuration of the parallel polarization. In the regions of ν_4 and ν_2 PO_4^{3-} modes,

bands showing orientation dependent intensity are observed (84). In the present study, we also see the orientation-dependent changes of ν_3 and ν_2 PO_4^{3-} , but ν_1 and ν_4 vibration modes exhibit little change in the different planes.

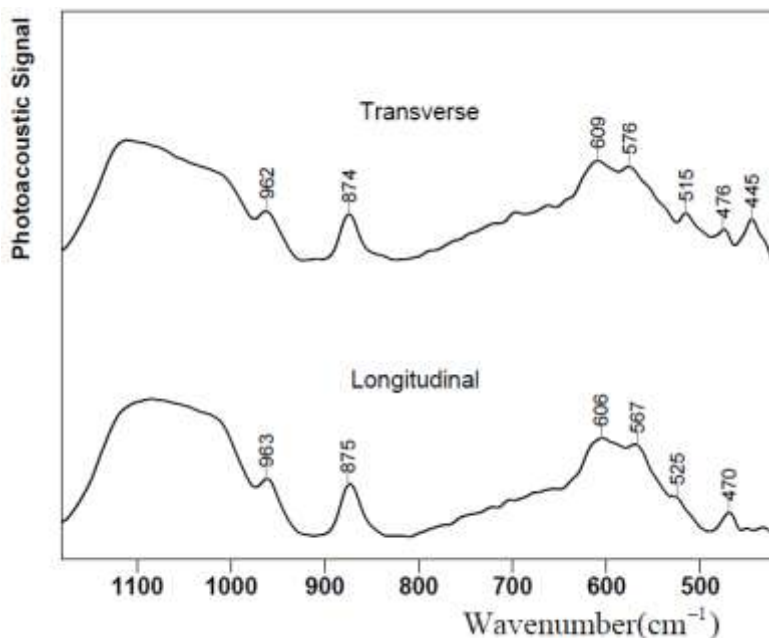


Figure 2.8. Photoacoustic infrared spectra of human bone (transverse and longitudinal) in the energy range of 1180-400 cm^{-1} .

The inverted second-derivative curve in the energy range of 1180-927 cm^{-1} is shown in Figure 2.9a, exhibiting a broad band from mineral. This broad mineral band arises from 12 sub-bands (Table 2.2). These ν_1 , ν_3 PO_4^{3-} sub-bands were previously observed using X-ray and FTIR studies (27, 85, 86). Curve-fitting in this region is shown in Figure 2.9b and c after normalization. The ratio of the 1023/1038 cm^{-1} bands (often used to describe stoichiometry) (35) in the transverse section is 0.51, while in the longitudinal section it is 0.29. Further, at around 1090 cm^{-1} the sub-band area in the longitudinal section is larger than that in the transverse section. Therefore, bone appears to be more stoichiometric in longitudinal section surface.

Table 2.2. Major components of the ν_1 , ν_3 PO_4^{3-} bands in bone (27, 87, 88).

Position Transverse	Area Transverse	Position Longitudinal	Area Longitudinal	Band assignment
1150	23	1140	60	HPO_4^{2-} containing apatites
1122	211	1121	95	ν_3 PO_4^{3-} in Poorly crystalline apatites
1110	125	1105	217	ν_3 PO_4^{3-} in Poorly crystalline apatites
1091	48	1086	52	ν_3 PO_4^{3-} in stoichiometric HA
1077	0.16	1071	60	ν_3 PO_4^{3-} in Poorly crystalline apatites
1067	262	1059	120	ν_3 PO_4^{3-} in Poorly crystalline apatites
1050	41	1047	139	HPO_4^{2-} containing apatites and type B carbonate-containing apatites
1038	53	1038	58	PO_4^{3-} in stoichiometric HA
1023	27	1023	17	Nonstoichiometric apatites containing HPO_4^{2-} and/or CO_3^{2-}
1007	163	1010	144	ν_3 PO_4^{3-} in apatitic environment
993	19	988	80	ν_3 PO_4^{3-} in apatitic environment
959	73	959	62	ν_1 PO_4^{3-}

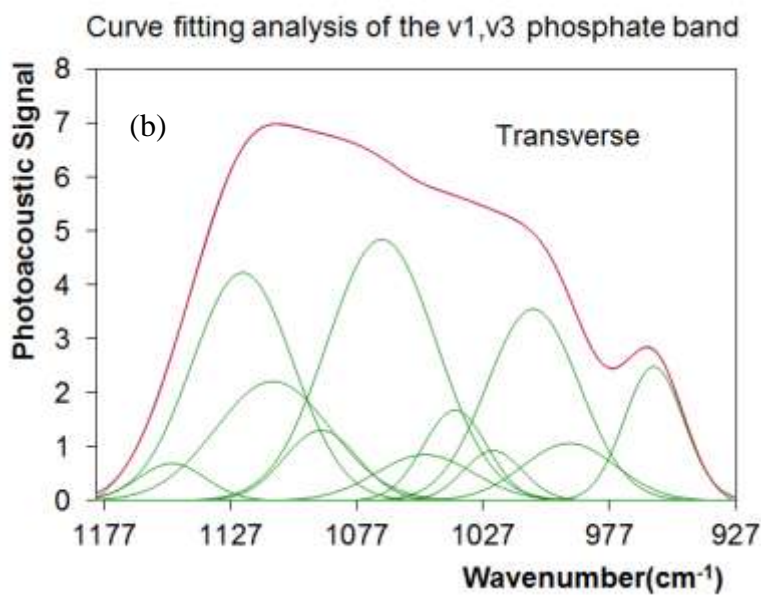
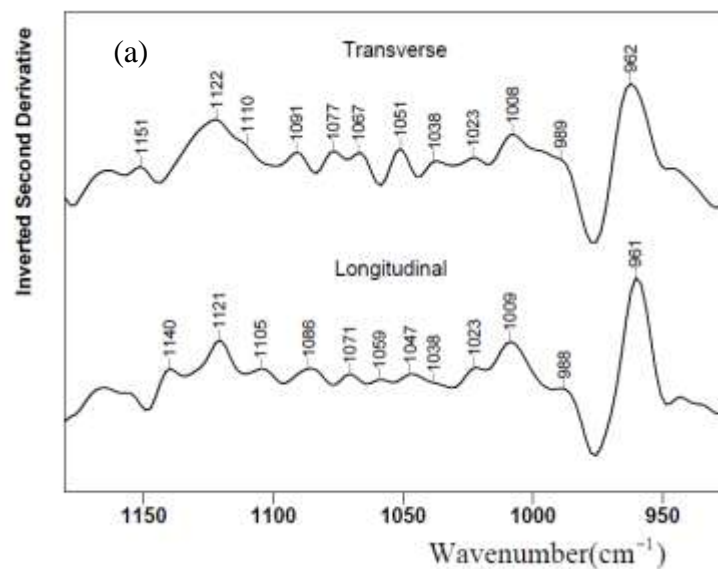


Figure 2.9. (a) Inverted second-derivative curves in the energy range of 1180-927 cm^{-1} ; curve fitting analysis of the ν_1, ν_3 phosphate band (1180–927 cm^{-1}) of (b) Transverse section, and (c) Longitudinal section.

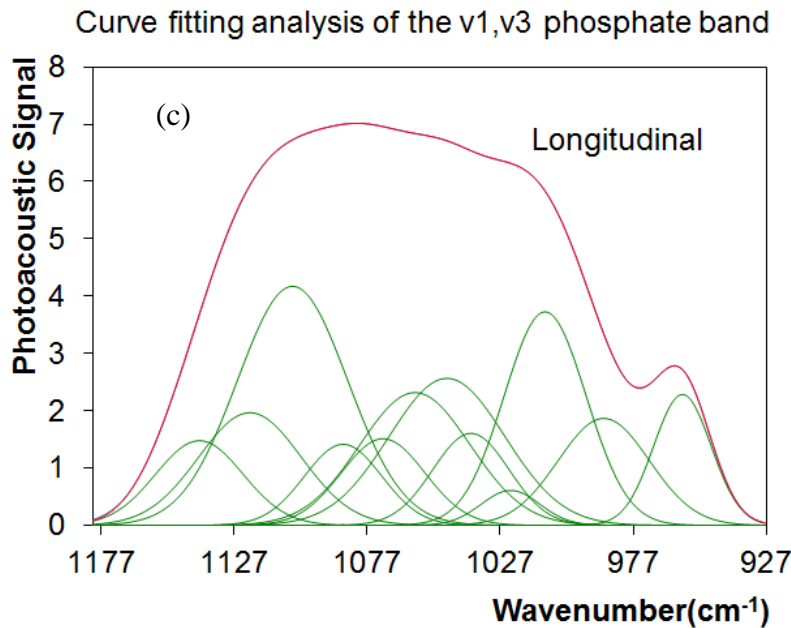


Figure 2.9. (a) Inverted second-derivative curves in the energy range of $1180\text{--}927\text{ cm}^{-1}$; curve fitting analysis of the ν_1, ν_3 phosphate band ($1180\text{--}927\text{ cm}^{-1}$) of (b) transverse section, and (c) longitudinal section (continued).

2.3.4. Comparison of three smaller sections in the transverse and longitudinal planes

Further, similar positioned bone pieces are cut into three smaller sections in both transverse and longitudinal planes respectively (Figure 2.2b), and the spectra collected are shown in Figure 2.10. It is to be noted that the outer section includes periosteum and the inner section includes endosteum in the vicinity of the medullary cavity.

From the spectrum of the transverse sections, it is clearly seen that when closer to the inner side, the shoulder around 3550 cm^{-1} appears stronger indicating that more structural O-H appears towards the medullary cavity. However, this band does not show any obvious change in the longitudinal sections. Both two planes exhibit similar characteristics, when approaching the inner side, C-H stretching bands arising from lipids, proteins etc. appear stronger, the C=O stretching band at 1747 cm^{-1} appears sharper on the inner side of both planes. Nevertheless, the

C=O stretching band shows small peaks on the outer and middle sides of the longitudinal sections, while being significantly reduced on these sides of the transverse sections. It is known that the major intra-cortical arteries (mainly Haversian canal and Volkman's canal) carry the longitudinal blood supply (89). On the longitudinal section surface, some canals are crosscut so that the materials from arteries appear on the surface which make this C=O stretching band more intense in the longitudinal section rather than in the transverse section. Moreover, a great number of arterioles in the endosteal membrane were seen so that the inner sides along both planes also exhibit this sharp band. This phenomenon can also be confirmed by the stronger signs of C-H band at around 2900 cm^{-1} in the corresponding spectra. In addition, $\nu_3\text{ PO}_4^{3-}$ broad band profile is varying in these sections.

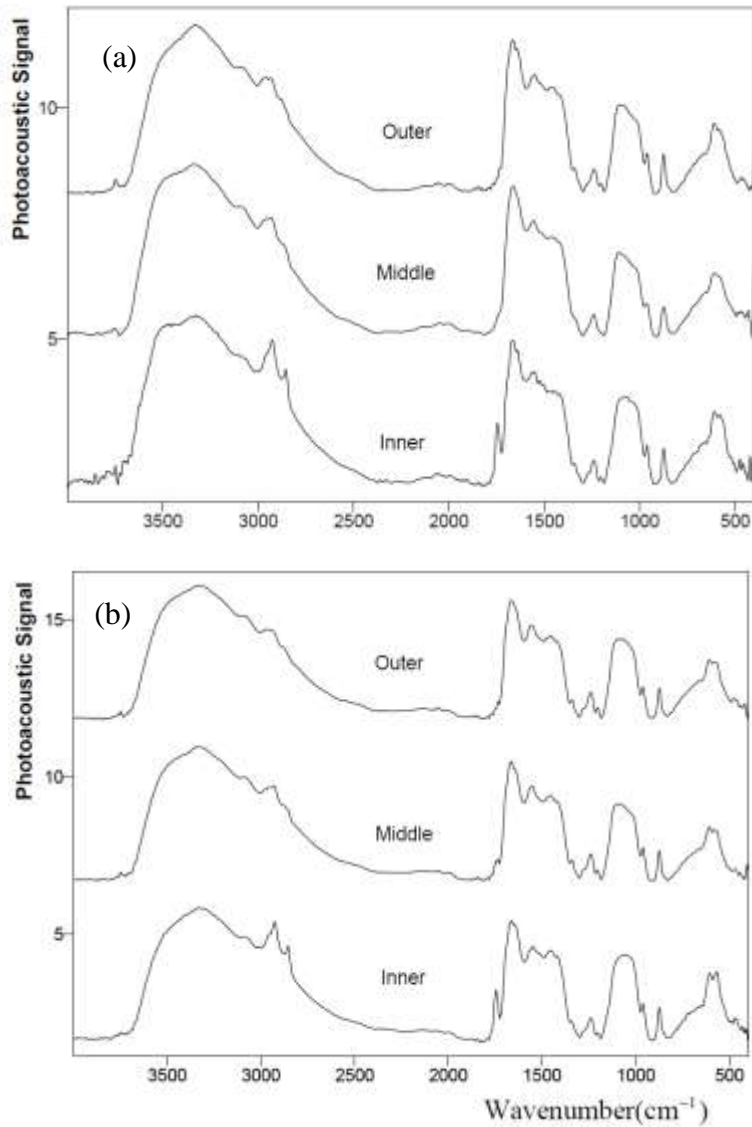


Figure 2.10. PA-LS-FTIR spectra of human bone in the 4000-400 cm^{-1} region, velocity of mirror: 0.158 cm/s . (a) Transverse section, 4000-400 cm^{-1} region; (b) Longitudinal section, 4000-400 cm^{-1} region.

2.3.5. Depth profiling

For cortical bone, thermal diffusivity D equals $5.5 \times 10^{-3} \text{ cm}^2/\text{s}$ in the transverse section and $4.4 \times 10^{-3} \text{ cm}^2/\text{s}$ in the longitudinal section (90). L is calculated using Eq. (2.2). In our experiments, we used the frequencies of 50, 100, 200, 500, and 1000Hz, resulting in values of L

to be 59.2, 41.8, 29.6, 18.7, 13.2 μm in the transverse section and 52.9, 37.4, 26.5, 16.7, 11.8 μm respectively in the longitudinal section (Table 2.3).

Table 2.3. Thermal diffusion depths of bone varying with Phase Modulation (PM) frequencies.

PM frequency(Hz)	50	100	200	500	1000
$L_{\text{transverse}}(\mu\text{m})$	59.2	41.8	29.6	18.7	13.2
$L_{\text{longitudinal}}(\mu\text{m})$	52.9	37.4	26.5	16.7	11.8

Figure 2.11a and Figure 2.11b show the SS-PA-FTIR spectra obtained at the five penetration depths in the transverse and longitudinal sections in the energy range of 4000-830 cm^{-1} . The spectra were normalized with the O-H peak (3323 cm^{-1}). In both sections, the O-H broad band (3732-2262 cm^{-1}) appears sharper and the intensity of this band appears lower as compared to the matrix band or mineral band. This is primarily due to the loss of water during cutting of bone. Interestingly it is found that the structural O-H shoulder appears increasingly reduced on approaching the surface of the sample. The bands at 2926 cm^{-1} (stretching from lipids) in Figure 2.11a appear stronger at 200hz and 500hz compared to other frequencies which indicates that through different penetration depths, the component of lipids may vary due to the plywood-like array pattern of lamellae. Comparing the different penetration depths, it is apparent that when closer to the surface, the variation becomes stronger.

Figure 2.11c and d shows the SS-PA-FTIR spectra in the energy range of 2000-830 cm^{-1} . In both sections, the broad amide I band appears sharper as the thermal diffusion depth L decreases. Amide II and amide III appear similar at different penetration depths. Usually bands in the amide III region are more resolved in the original protein spectrum than they are in the amide I spectrum. This results from reduced OH vibrations in the amide III region due to reduced water interfering with spectrum as compared to amide I region (91). Hence, the variation

of amide I also reflects the loss of water when approaching the surface. Thus significant change of the organic matrix in the spectra is not observed.

The most significant variation at different depths arises from the mineral bands including CO_3^{2-} stretching and PO_4^{3-} bands. The intensity of $\nu_3 \text{PO}_4^{3-}$ band appears stronger and sharper close to the surface which probably can result from loss of water near surface. Water forms hydrogen bonds between water and collagen, and also water and mineral, which broaden the ν_3 phosphate and amide I bands. Additionally, it is interesting to note that all of the changes are gradual, but from 500Hz to 1000 Hz the change is particularly abrupt. This may imply that the material system is significantly altered around $12\mu\text{m}$ because of the surface structure distortion and the loss of surface water.

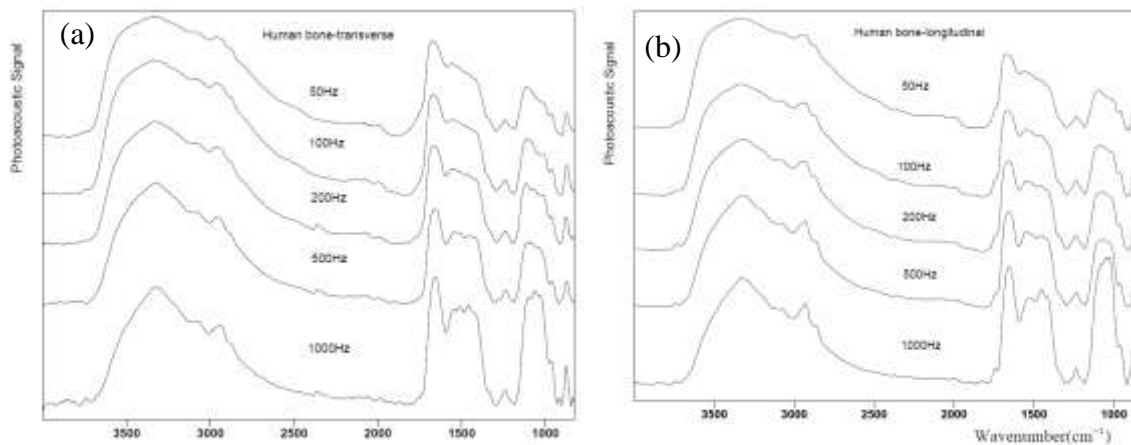


Figure 2.11. SS-PA-FTIR spectra of human bone: (a) Transverse section ($4000\text{--}830\text{ cm}^{-1}$); (b) Longitudinal section ($4000\text{--}830\text{ cm}^{-1}$); (c) Transverse section ($2000\text{--}830\text{ cm}^{-1}$); and (d) Longitudinal section ($2000\text{--}830\text{ cm}^{-1}$).

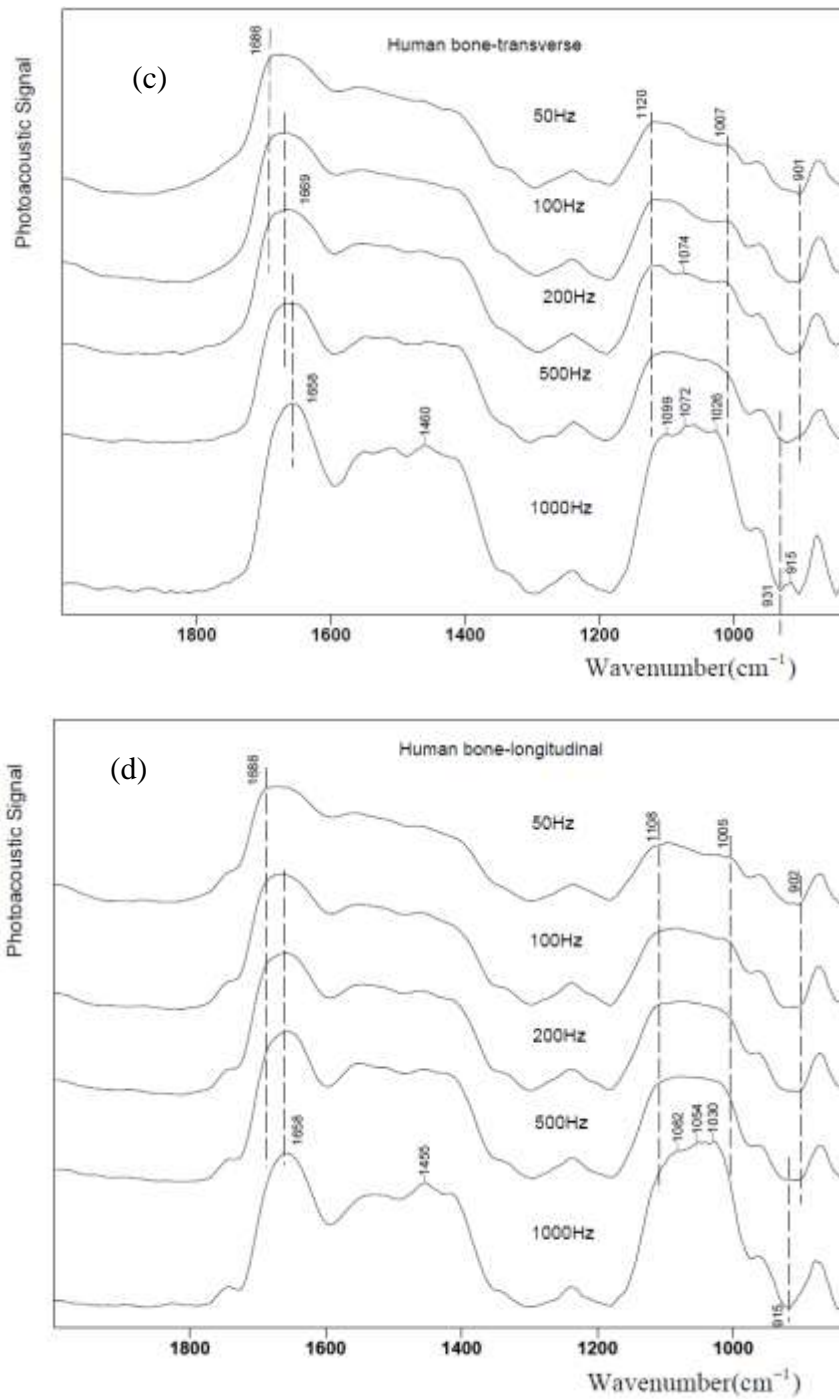


Figure 2.11. SS-PA-FTIR spectra of human bone (continued): (a) Transverse section (4000-830 cm^{-1}); (b) Longitudinal section (4000-830 cm^{-1}); (c) Transverse section (2000-830 cm^{-1}); and (d) Longitudinal section (2000-830 cm^{-1}).

2.3.6. Discussion

PA-FTIR is shown to be a useful technique for investigation of bone since it enables samples to be tested as-received and also the coupling gas helium (He) protects the material from bacterial growth. Comparison of the FTIR spectra obtained using transmission and photoacoustic modes, indicated differences: (1) Sample in photoacoustic mode indicates a broad O-H band due to presence of water in the as-received PA sample. In addition, the OH band and the band from organic matrix band at around 1500 cm^{-1} are both stronger than those in the transmission mode. (2) Changes to ν_3 phosphate band: in PA-FTIR, the band shows higher intensity at higher energy side while in TS-FTIR the reverse is observed. We found that the ν_3 phosphate band not only depends on the orientation of bone sample, but also depends on the position of the sample. However, overall the composition is the most crucial factor. By inspecting the spectrum obtained by PA-FTIR from our group's study on synthetic HAP (92), we saw that the shape of ν_3 phosphate band of synthetic HAP was quite similar to that of healthy human cortical bone obtained by transmission mode which underwent a series of treatments (26). Therefore, we believe that the difference between the shapes of $\nu_3\text{ PO}_4^{3-}$ band from both modes is primarily due to the sample condition. Further, the undisturbed healthy cortical human sample exhibits nonstoichiometric HAP based on the study of PA-FTIR spectra. (3) Both amide III and $\nu_2\text{ CO}_3^{2-}$ bands are more prominent in PA-FTIR than those in TS-FTIR (26). Amide III region from FTIR is quite promising for studying protein secondary structure because it has more resolved differences and has no water interference (93). However, this region was not sufficiently investigated due to low signal in TS-FTIR. The $\nu_2\text{ CO}_3^{2-}$ bands could be related to Ca/P ratio and mineral structure(94).

The presence of hydroxyl groups in bone mineral crystals has been long debated. The absence of the OH infrared spectral band in bone was first reported by Biltz and Pellegrino (47) and was later confirmed by extensive studies of undisturbed and deproteinated isolated crystals of bone (48-52). Furthermore, free and unbounded OH appeared after the bone was heated to above 600°C which was explained by the decomposition of carbonate ions with the presence of water to form O-H apatite (47). Blumenthal and Posner attributed the failure to detect OH group in IR spectrum to distortions in the lattice of the bone crystals and hydrogen bonding with water especially that on the surfaces of the crystals (48). We know that, the formation of hydrogen bonds usually leads to lowering of the frequency of vibration, broadening of the O-H stretching vibrations, as well as skewing of the band profile. Rey et al. (50) utilized FTIR, magic angle spinning and proton nuclear magnetic resonance spectroscopy to confirm that there was no detectable O-H in bone mineral. And they also found that the decomposition of carbonate ions were eliminated by CO₂ environment at elevated temperature which confirmed the conclusion of Biltz and Pellegrino (47). Inelastic neutron-scattering study (51) showed the absence of structural OH group but only very small amount of OH ions belonging to HPO₄⁻ like species. Raman spectra also showed that there was no OH ions in bone mineral while they exist in dentin and enamel to some degree (52). However, almost all of the above studies have done chemical pretreatments on bone to make it anorganic and the pretreatments may eliminate interference from the organic matrix to the mineral. A two-dimensional solid-state nuclear magnetic resonance (NMR) spectroscopy technique that detects the proton spectrum of bone crystals while suppressing the interfering matrix signals was utilized to eliminate the need for specimen pretreatment other than cryogenic grinding show that the bone crystal OH⁻ is readily detectable (53). The OH⁻ content of human cortical bone is roughly 20% of the amount expected in

stoichiometric hydroxyapatite (53). Later C. Rey concluded that “the biological bone apatites contain only a very small percentage of the total number of hydroxyl groups present stoichiometric hydroxyapatites” (95). However, due to the lack of accurate chemical analytic techniques and the presence of numerous trace elements and a hydrated surface layer, it is still very difficult to correctly describe the chemical composition of bone apatites such as the amounts of HPO_4^{2-} and OH^- ions (95).

Based on the PA-FTIR spectra, from the shoulder of the broad OH band and second-derivative of undisturbed bone spectra in both longitudinal and transverse sections, we believe that there is a small amount of structural OH ions existing in bone mineral. By inspecting the PO_4^{3-} broad band of three small sections, it is observed that in the transverse section structural OH is more prominent in the inner side of bone sample. This phenomenon is consistent with results from Paschalis et al. (28) which indicate that the mineral lying in the vicinity of the medullary cavity is more crystalline/mature, and has more hydroxyapatite-like stoichiometry. Therefore in the vicinity of the medullary cavity there is more structural OH, and more stoichiometric phosphate.

In collagen molecules, C=O bonds are perpendicular to the backbone of the collagen molecule and the mineral *c*-axis, so amide I has preferential orientation. In polarized Raman experiments, amide I stretching vibration is the strongest when the beam is perpendicular to *c*-axis (22, 96). However, in our PA-FTIR experiments, orientation effect of amide I band is not observed since the band is severely overlapped by O-H bending vibration.

In our present study, it is interesting to note a band at 1747 cm^{-1} is observed which is quite prominent in the vicinity of the medullary cavity in the both sections. In previous studies, this band was absent in most cases after subtraction by Poly(methyl methacrylate) (PMMA) (26,

34, 97, 98) or glycolmethacrylate (GMA) in which the tissue was fixed (99). The C=O band from PMMA or GMA is centered at around 1730cm^{-1} , and is strong and broad and may overlap the weak C=O band from bone. In the current experiments, no pretreatment of bone is performed hence this band cannot be attributed to PMMA or GMA. In some other studies, the presence of carbonates at the channel sites in the structure may also generate a small band at 1745cm^{-1} (44, 84). In the apatite structure, the channel site is defined by triads of Ca ions. The Ca ions are bonded not only to oxygen (of the phosphate groups), but also to hydroxyls that make them distinguishable (52). However, in the vicinity of the medullary cavity, the 1747cm^{-1} band appears very intense and may have contributions from sources other than Ca ions. According to the literature, the total lipid content of bone is less than 3% (100), but content is high in arteries(74) or other tissues (101). After comparison of the spectra in different planes and different sites, we infer that this band can be attributed to the C=O stretching of lipids, cholesterol esters, triglycerides (74) from the arteries.

In polarized Raman experiments, $\nu_1 \text{PO}_4^{3-}$ stretching vibration is the strongest parallel to the axis of the fiber (22, 102) and exhibits orientation effect. But in infrared spectrum, only those modes accompanying dipole moment changes during vibration are active, hence $\nu_3 \text{PO}_4^{3-}$ stretching vibration has the strongest signal. This broad band shows different sub-bands according to orientations and sites of bone. Although compositionally and structurally similar to synthetic calcium hydroxyapatite $\text{Ca}_{10}(\text{OH})_2(\text{PO}_4)_6$, human bone mineral is composed of a poorly crystallized apatite which is calcium (Ca)-deficient and contains hydrogen phosphate (HPO_4^{2-}), carbonate (CO_3^{2-}), and other ions. The hydroxyapatite crystal in bone has a hexagonal structure with space group $\text{P6}_3/\text{m}$; however, many vacancies and substitutes exist in the structure that cause distortions. Considerations of site group symmetry and factor group symmetry would

result in six phosphate bands to be active in the ν_3 domain of stoichiometric hydroxyapatite (103). Additionally, due to the vacancies and substitutes, C. Rey found more sub-bands based on the deconvoluted spectra in this domain (88). Boskey's group (27, 28, 86) assigned 11 or 12 peaks in the $\nu_1\nu_3$ domain based on second-derivative of the spectra. Their work also presented a "crystallinity/maturity index" as the ratio of $1020/1030\text{cm}^{-1}$ and the more crystalline/mature, the more hydroxyapatite-like stoichiometry, the bigger the crystalline size, the less the ion substitution by ions such as CO_3^{2-} (28, 88). Magne et al. followed these assignments (based on Fourier Self-Deconvolution treatment of spectra) in studying dentin and confirmed that the two sub-bands at around 1030cm^{-1} and 1090cm^{-1} can be attributed to $\nu_3 \text{PO}_4^{3-}$ in stoichiometric apatites whereas other sub-bands were all from $\nu_3\text{PO}_4^{3-}$ in poor crystalline or from HPO_4^{2-} , except $\nu_1\text{PO}_4^{3-}$ (82, 87). Magne et al. also agreed that when the apatite gets increasingly mature, probably through the loss of HPO_4^{2-} and vacancies, the stoichiometric apatite would tend to increase. But the evolution of carbonate ions is controversial in these studies. Farlay et al. questioned the denotation of "crystallinity/ maturity index" and suggested that it should be only "maturity index" because an increase in $1030/1020$ ratio is not necessarily related to an increase of crystal size in human bone (25). Additionally, Farlay et al. suggested using $1030/1100 \text{cm}^{-1}$ ratio instead as the "maturity index" and the trend of which is in accordance with that of $1030/1020\text{cm}^{-1}$ ratio by peak curve-fitting.

The data presented here thus indicates that based on the ratio of $1023/1038\text{cm}^{-1}$ bands, human bone shows more stoichiometric characteristics in the longitudinal surface. As shown in Figure 2.3a, intrafibrillar mineral is positioned in the hole-zone and the shape of the mineral is regulated by the collagen around it. The surface of the longitudinal section being launched by incident infrared beam contains the interface between the mineral and the three chains of

collagen, while the surface of the transverse section contains mainly the interface between the mineral and the collagen telopeptide. On the mineral surface, there is a hydrated layer containing loosely bound ions which are easily exchangeable with charged groups of proteins present in collagen and non-collagenous protein. The collagen molecules are mainly composed of uncharged amino acids including glycine, proline, alanine, hydroxyproline, etc. which account for about 68% of the total collagen composition (104). The charged amino acids such as glutamic and aspartic acid, lysine, arginine, hydroxylysine and histidine may form ion bindings with mineral ions (105). On the other hand, collagen molecules have a partial positive charge at the N-telopeptide and a partial negative charge at the C-telopeptide. An interface formed from the interactions of these telopeptides and HAP has been found to significantly influence the load-deformation behavior of collagen (8, 10). Additionally, it was found that the positive net charge close to the C-telopeptide of the collagen molecules is the most favorable for interaction with negative charges and promotes the infiltration of the fibrils with amorphous calcium phosphate to induce mineral nucleation and organization (106). Therefore, we suggest that the strong interaction between exchangeable ions-contained-mineral surface and the charged collagen telopeptides leads to higher non-stoichiometry in the transverse surface rather than in the longitudinal surface.

Hence in our opinion, by scrutinizing the assignments of the $\nu_1 \nu_3 \text{PO}_4^{3-}$ contour suggested by Paschalis and Magne (27, 28, 82, 87), the positions of the bands have some differences because for different samples the mineral structures may vary to a certain degree. Therefore based on second-derivative treatment of the raw spectra, we come up with 12 sub-bands by peak curve-fitting. The ratio of 1023/1038 cm^{-1} bands in the longitudinal section is much larger than that in the transverse section. At around 1090 cm^{-1} the sub-band area in the

longitudinal section is larger than that in the transverse section. Therefore, the bone in the longitudinal section appears more stoichiometric.

2.4. Conclusion

In the present study, PA-FTIR experiments were performed on undisturbed human cortical bone. Specifically, the directionality of molecular interactions is probed by testing the samples in longitudinal and transverse modes. The spectra obtained demonstrate that this technique has similar results as compared to traditionally used transmission mode, and it is more sensitive to amide amide III and ν_2 carbonate bands. PA-FTIR spectra of bone shows a C=O band at 1747 cm^{-1} in undisturbed human bone that can result from C=O stretching of lipids, cholesterol esters, and triglycerides from the arteries. The comparison of the spectra in the transverse and longitudinal sections indicates that the mineral in the longitudinal surface is more stoichiometric. This may result from reduced interaction between exchangeable ions contained within mineral surface and collagen molecules than that between mineral surface and collagen termini on the transverse surface. In the vicinity of the medullary cavity, bone also has more organic matrix, and the mineral is more stoichiometric as compared to that in the middle or near periosteum. The depth profiling results of PA-FTIR demonstrate that the presence of hydroxyl group in FTIR may relate to the water content of bone, and the organic matrix and mineral structure are both affected by surface cutting. These studies describe the spectroscopic evidence of role of mineral protein interactions on mineral structure and stoichiometry.

2.5. Acknowledgements

Instrumentation obtained from National Science Foundation MRI grants is acknowledged for enabling experiments conducted in this work. I would also like to acknowledge assistance in electron microscopy laboratory from Mr. Scott Payne.

2.6. References

1. Bourne GH. *The Biochemistry and Physiology of Bone*. 2 ed: Academic Press; 1972.
2. Utku FS, Klein E, Saybasili H, Yucesoy CA, Weiner S. Probing the role of water in lamellar bone by dehydration in the environmental scanning electron microscope. *Journal of Structural Biology*. 2008;162(3):361-7.
3. Landis WJ, Hodgens KJ, Song MJ, Arena J, Kiyonaga S, Marko M, et al. Mineralization of collagen may occur on fibril surfaces: Evidence from conventional and high-voltage electron microscopy and three-dimensional imaging. *Journal of Structural Biology*. 1996;117(1):24-35.
4. Landis WJ, Hodgens KJ, Arena J, Song MJ, McEwen BF. Structural relations between collagen and mineral in bone as determined by high voltage electron microscopic tomography. *Microscopy Research and Technique*. 1996;33(2):192-202.
5. Weiner S, Traub W, Wagner HD. Lamellar bone: Structure-function relations. *Journal of Structural Biology*. 1999;126(3):241-55.
6. Fratzl P, Weinkamer R. Nature's hierarchical materials. *Progress in Materials Science*. 2007;52(8):1263-334.
7. Hodge AJ, Petruska JA, editors. Recent studies with the electron microscope on ordered aggregates of the tropocollagen macromolecule. *Aspects Of Protein Structure Proceedings Of A Symposium*; 1963.

8. Bhowmik R, Katti KS, Katti DR. Mechanics of molecular collagen is influenced by hydroxyapatite in natural bone. *Journal of Materials Science*. 2007;42(21):8795-803.
9. Bhowmik R, Katti KS, Katti DR. Mechanisms of Load-Deformation Behavior of Molecular Collagen in Hydroxyapatite-Tropocollagen Molecular System: Steered Molecular Dynamics Study. *Journal of Engineering Mechanics-Asce*. 2009;135(5):413-21.
10. Katti DR, Pradhan SM, Katti KS. Directional dependence of hydroxyapatite-collagen interactions on mechanics of collagen. *Journal of Biomechanics*. 2010;43(9):1723-30.
11. Pradhan SM, Katti DR, Katti KS. Steered Molecular Dynamics Study of Mechanical Response of Full Length and Short Collagen Molecules. *Journal of nanomechanics and micromechanics*. 2011;1(3):104-10.
12. Dubey DK, Tomar V. Effect of changes in tropocollagen residue sequence and hydroxyapatite mineral texture on the strength of ideal nanoscale tropocollagen-hydroxyapatite biomaterials. *Journal of Materials Science-Materials in Medicine*. 2010;21(1):161-71.
13. Almora-Barrios N, de Leeuw NH. A Density Functional Theory Study of the Interaction of Collagen Peptides with Hydroxyapatite Surfaces. *Langmuir*. 2010;26(18):14535-42.
14. Streeter I, de Leeuw NH. Atomistic Modeling of Collagen Proteins in Their Fibrillar Environment. *Journal of Physical Chemistry B*. 2010;114(41):13263-70.
15. Pradhan SM, Katti KS, Katti DR. A multiscale model of collagen fibril in bone: elastic response. *Journal of engineering mechanics*. 2012.
16. Skedros JG, Sorenson SM, Takano Y, Turner CH. Dissociation of mineral and collagen orientations may differentially adapt compact bone for regional loading environments: Results from acoustic velocity measurements in deer calcanei. *Bone*. 2006;39(1):143-51.

17. Posner AS, Perloff A, Diorio AF. Refinement of the hydroxyapatite structure. *Acta Crystallographica*. 1958;11(4):308-9.
18. Sobczak A, Kowalski Z, Wzorek Z. Preparation of hydroxyapatite from animal bones. *Acta of Bioengineering and Biomechanics*. 2009;11(4):23-8.
19. Barry AB, Baig AA, Miller SC, Higuchi WI. Effect of age on rat bone solubility and crystallinity. *Calcified Tissue International*. 2002;71(2):167-71.
20. Peterlik H, Roschger P, Klaushofer K, Fratzl P. From brittle to ductile fracture of bone. *Nature Materials*. 2006;5(1):52-5.
21. Peterlik H, Roschger P, Klaushofer K, Fratzl P. Orientation dependent fracture toughness of lamellar bone. *International Journal of Fracture*. 2006;139(3-4):395-405.
22. Kazanci M, Roschger P, Paschalis EP, Klaushofer K, Fratzl P. Bone osteonal tissues by Raman spectral mapping: Orientation-composition. *Journal of Structural Biology*. 2006;156(3):489-96.
23. Kazanci M, Roschger P, Paschalis EP, Klaushofer K, Fratzl P. Raman spectral mapping of bone osteonal tissues. *Bone*. 2006;39(5):S16-S.
24. Garip S, Severcan F. Determination of simvastatin-induced changes in bone composition and structure by Fourier transform infrared spectroscopy in rat animal model. *Journal of Pharmaceutical and Biomedical Analysis*. 2010;52(4):580-8.
25. Farlay D, Panczer G, Rey C, Delmas PD, Boivin G. Mineral maturity and crystallinity index are distinct characteristics of bone mineral. *Journal of Bone and Mineral Metabolism*. 2010;28(4):433-45.
26. Boskey AL, Spevak L, Weinstein RS. Spectroscopic markers of bone quality in alendronate-treated postmenopausal women. *Osteoporosis International*. 2009;20(5):793-800.

27. Paschalis EP, DiCarlo E, Betts F, Sherman P, Mendelsohn R, Boskey AL. FTIR microspectroscopic analysis of human osteonal bone. *Calcified Tissue International*. 1996;59(6):480-7.
28. Paschalis EP, Betts F, DiCarlo E, Mendelsohn R, Boskey AL. FTIR microspectroscopic analysis of normal human cortical and trabecular bone. *Calcified Tissue International*. 1997;61(6):480-6.
29. Paschalis EP, Recker R, DiCarlo E, Doty S, Atti E, Boskey AL. Distribution of collagen cross-links in normal human trabecular bone. *Journal of Bone and Mineral Research*. 2003;18(11):1942-6.
30. Ou-Yang H, Paschalis EP, Boskey AL, Mendelsohn R. Chemical structure-based three-dimensional reconstruction of human cortical bone from two-dimensional infrared images. *Applied Spectroscopy*. 2002;56(4):419-22.
31. Ou-Yang H, Paschalis EP, Mayo WE, Boskey AL, Mendelsohn R. Infrared microscopic imaging of bone: Spatial distribution of CO₃²⁻. *Journal of Bone and Mineral Research*. 2001;16(5):893-900.
32. Miller L, Vairavamurthy V, Chance M, Mendelsohn R, Paschalis E, Betts F, et al. In situ analysis of mineral content and crystallinity in bone using infrared micro-spectroscopy of the ν_4 PO₄(³⁻) vibration. *Biochim Biophys Acta*. 2001;1527(1-2):11-9.
33. Donnelly E, Chen DX, Boskey AL, Baker SP, van der Meulen MCH. Contribution of Mineral to Bone Structural Behavior and Tissue Mechanical Properties. *Calcified Tissue International*. 2010;87(5):450-60.

34. Gourion-Arsiquaud S, Burket JC, Havill LM, DiCarlo E, Doty SB, Mendelsohn R, et al. Spatial Variation in Osteonal Bone Properties Relative to Tissue and Animal Age. *Journal of Bone and Mineral Research*. 2009;24(7):1271-81.
35. Paschalis EP, Betts F, DiCarlo E, Mendelsohn R, Boskey AL. FTIR microspectroscopic analysis of human iliac crest biopsies from untreated osteoporotic bone. *Calcified Tissue International*. 1997;61(6):487-92.
36. Boskey A. Mineral changes in osteopetrosis. *Critical Reviews in Eukaryotic Gene Expression*. 2003;13(2-4):109-16.
37. Faibish D, Gomes A, Boivin G, Binderman I, Boskey A. Infrared imaging of calcified tissue in bone biopsies from adults with osteomalacia. *Bone*. 2005;36(1):6-12.
38. Boskey A, Pleshko Camacho N. FT-IR imaging of native and tissue-engineered bone and cartilage. *Biomaterials*. 2007;28(15):2465-78.
39. Koenig JL. *Spectroscopy of polymers*. 2nd ed. New York: Elsevier science Inc.; 1999.
40. Nakada H, Numata Y, Sakae T, Kimura-Suda H, Tanimoto Y, Saeki H, et al. Changes in Bone Quality Associated with the Mineralization of New Bone Formed Around Implants - Using XPS, Polarized Microscopy, and FTIR imaging. *Journal of Hard Tissue Biology*. 2010;19(2):101-9.
41. Gourion-Arsiquaud S, Allen MR, Burr DB, Vashishth D, Tang SY, Boskey AL. Bisphosphonate treatment modifies canine bone mineral and matrix properties and their heterogeneity. *Bone*. 2010;46(3):666-72.
42. Kourkoumelis N, Tzaphlidou M. Multivariate statistical evaluation of bone site and sex as parameters for the Fourier transform infrared spectroscopic study of normal bone. *Spectroscopy-an International Journal*. 2010;24(1-2):99-104.

43. Kourkoumelis N, Tzaphlidou M. Spectroscopic Assessment of Normal Cortical Bone: Differences in Relation to Bone Site and Sex. *TheScientificWorldJournal*. 2010;10:402-12.
44. Trujillo S, Martinez-Torres P, Quintana P, Alvarado-Gil J. Photothermal Radiometry and Diffuse Reflectance Analysis of Thermally Treated Bones. *International Journal of Thermophysics*. 2010;31(4-5):805-15.
45. Trueman CN, Privat K, Field J. Why do crystallinity values fail to predict the extent of diagenetic alteration of bone mineral? *Palaeogeography Palaeoclimatology Palaeoecology*. 2008;266(3-4):160-7.
46. Carden A, Morris M. Application of vibrational spectroscopy to the study of mineralized tissues (review). *J Biomed Opt*. 2000;5(3):259-68.
47. Biltz RM, Pellegrini Ed. Hydroxyl content of calcified tissue mineral - letter to editors and readers of *Calcified Tissue Research*. *Calcified Tissue Research*. 1971;7(3):259-&.
48. Blumenthal NC, Posner AS. Hydroxyapatite - mechanism of formation and properties. *Calcified Tissue Research*. 1973;13(3):235-43.
49. Biltz RM, Pellegrini ED. The composition of recrystallized bone-mineral. *Journal of Dental Research*. 1983;62(12):1190-5.
50. Rey C, Miquel JL, Facchini L, Legrand AP, Glimcher MJ. Hydroxyl-groups in bone-mineral. *Bone*. 1995;16(5):583-6.
51. Loong CK, Rey C, Kuhn LT, Combes C, Wu Y, Chen SH, et al. Evidence of hydroxyl-ion deficiency in bone apatites: An inelastic neutron-scattering study. *Bone*. 2000;26(6):599-602.
52. Pasteris JD, Wopenka B, Freeman JJ, Rogers K, Valsami-Jones E, van der Houwen JAM, et al. Lack of OH in nanocrystalline apatite as a function of degree of atomic order: implications for bone and biomaterials. *Biomaterials*. 2004;25(2):229-38.

53. Cho GY, Wu YT, Ackerman JL. Detection of hydroxyl ions in bone mineral by solid-state NMR spectroscopy. *Science*. 2003;300(5622):1123-7.
54. Verma D, Katti K, Katti D. Photoacoustic FTIR spectroscopic study of undisturbed nacre from red abalone. *Spectrochimica Acta Part a-Molecular and Biomolecular Spectroscopy*. 2006;64(4):1051-7.
55. Alstadt KN, Katti DR, Katti KS. An in situ FTIR step-scan photoacoustic investigation of kerogen and minerals in oil shale. *Spectrochimica Acta Part a-Molecular and Biomolecular Spectroscopy*. 2012;89:105-13.
56. Rosencwaig A, Gersho A. Theory of photoacoustic effect with solids. *Journal of Applied Physics*. 1976;47(1):64-9.
57. Michaelian KH. *Photoacoustic IR Spectroscopy: Instrumentation, Applications and Data Analysis*: Wiley-VCH Verlag GmbH & Co. KGaA, Weinheim; 2010. 408 p.
58. Chai XS, Dong CX, Deng YL. In situ determination of bacterial growth by multiple headspace extraction gas chromatography. *Analytical Chemistry*. 2008;80(20):7820-5.
59. Chalmers JM, Griffiths PR. *Handbook of vibrational spectroscopy* 2002.
60. Katti KS, Urban MW. Conductivity model and photoacoustic FT-IR surface depth profiling of heterogeneous polymers. *Polymer*. 2003;44(11):3319-25.
61. Katti KS, Urban MW. Effect of inclusions in polymeric coatings on quantitative surface depth profiling: Modeling and step-scan photoacoustic FT-IR spectroscopy. *Abstracts of Papers of the American Chemical Society*. 2001;222:65-PMSE.
62. Katti KS, Sikdar D, Katti DR, Ghosh P, Verma D. Molecular interactions in intercalated organically modified clay and clay-polycaprolactam nanocomposites: Experiments and modeling. *Polymer*. 2006;47(1):403-14.

63. Verma D, Katti K, Katti D. Experimental investigation of interfaces in hydroxyapatite/polyacrylic acid/polycaprolactone composites using photoacoustic FTIR spectroscopy. *Journal of Biomedical Materials Research Part A*. 2006;77A(1):59-66.
64. Verma D, Katti K, Katti D. Nature of water in nacre: A 2D Fourier transform infrared spectroscopic study. *Spectrochimica Acta Part a-Molecular and Biomolecular Spectroscopy*. 2007;67(3-4):784-8.
65. Sowa MG, Mantsch HH. FT-IR photoacoustic depth profiling spectroscopy of enamel . *Calcified Tissue International*. 1994;54(6):481-5.
66. Sowa MG, Mantsch HH. FT-IR Step-scan photoacoustic phase-analysis and depth profiling of calcified tissue. *Applied Spectroscopy*. 1994;48(3):316-9.
67. Spencer P, Payne JM, Cobb CM, Reinisch L, Peavy GM, Drummer DD, et al. Effective laser ablation of bone based on the absorption characteristics of water and proteins. *Journal of Periodontology*. 1999;70(1):68-74.
68. Mkukuma LD, Skakle JMS, Gibson IR, Imrie CT, Aspden RM, Hukins DWL. Effect of the proportion of organic material in bone on thermal decomposition of bone mineral: An investigation of a variety of bones from different species using thermogravimetric analysis coupled to mass spectrometry, high-temperature X-ray diffraction, and Fourier transform infrared spectroscopy. *Calcified Tissue International*. 2004;75(4):321-8.
69. Giraud-Guille MM. Plywood structures in nature. *Current Opinion in Solid State & Materials Science*. 1998;3(3):221-7.
70. Khanna R, Katti KS, Katti DR. Bone nodules on chitosan-polygalacturonic acid-hydroxyapatite nanocomposite films mimic hierarchy of natural bone. *Acta Biomaterialia*. 2011;7(3):1173-83.

71. Bhowmik R, Katti KS, Katti D. Molecular dynamics simulation of hydroxyapatite-polyacrylic acid interfaces. *Polymer*. 2007;48(2):664-74.
72. Urban MW, Gaboury SR. On the sensitivity of photoacoustic Fourier-transform infrared-spectroscopy to cross-linking reactions. *Macromolecules*. 1989;22(3):1486-7.
73. Reyes-Gasga J, Garcia-Garcia R, Arellano-Jimenez MJ, Sanchez-Pastenes E, Tiznado-Orozco GE, Gil-Chavarria IM, et al. Structural and thermal behaviour of human tooth and three synthetic hydroxyapatites from 20 to 600 degrees C. *Journal of Physics D-Applied Physics*. 2008;41(22).
74. Singh K, Lee KS, Lee D, Kim YK, Kim KC. Spectroscopic techniques as a diagnostic tool for early detection of osteoporosis. *Journal of Mechanical Science and Technology*. 2010;24(8):1661-8.
75. Moore WH, Krimm S. Vibrational analysis of peptides, polypeptides, and proteins. 1. Polyglycine I. *Biopolymers*. 1976;15(12):2439-64.
76. Cheng ZH, Yasukawa A, Kandori K, Ishikawa T. FTIR study of adsorption of CO₂ on nonstoichiometric calcium hydroxyapatite. *Langmuir*. 1998;14(23):6681-6.
77. Bertoni E, Bigi A, Cojazzi G, Gandolfi M, Panzavolta S, Roveri N. Nanocrystals of magnesium and fluoride substituted hydroxyapatite. *Journal of Inorganic Biochemistry*. 1998;72(1-2):29-35.
78. Kumar R, Prakash KH, Cheang P, Gower L, Khor KA. Chitosan-mediated crystallization and assembly of hydroxyapatite nanoparticles into hybrid nanostructured films. *Journal of the Royal Society Interface*. 2008;5(21):427-39.

79. Maeda Y, Kitano H. The structure of water in polymer systems as revealed by Raman spectroscopy. *Spectrochimica Acta Part a-Molecular and Biomolecular Spectroscopy*. 1995;51(14):2433-46.
80. Fleet ME, Liu X. Coupled substitution of type A and B carbonate in sodium-bearing apatite. *Biomaterials*. 2007;28(6):916-26.
81. Liu KZ, Dixon IMC, Mantsch HH. Distribution of collagen deposition in cardiomyopathic hamster hearts determined by infrared microscopy. *Cardiovascular Pathology*. 1999;8(1):41-7.
82. Magne D, Pilet P, Weiss P, Daculsi G. Fourier transform infrared microspectroscopic investigation of the maturation of nonstoichiometric apatites in mineralized tissues: A horse dentin study. *Bone*. 2001;29(6):547-52.
83. Boskey AL, Gelb BD, Pourmand E, Kudrashov V, Doty SB, Spevak L, et al. Ablation of Cathepsin K Activity in the Young Mouse Causes Hypermineralization of Long Bone and Growth Plates. *Calcified Tissue International*. 2009;84(3):229-39.
84. Antonakos A, Liarokapis E, Leventouri T. Micro-Raman and FTIR studies of synthetic and natural apatites. *Biomaterials*. 2007;28(19):3043-54.
85. Pleshko N, Boskey A, Mendelsohn R. Novel infrared spectroscopic method for the determination of crystallinity of hydroxyapatite minerals. *Biophysical Journal*. 1991;60(4):786-93.
86. Gadaleta SJ, Paschalis EP, Betts F, Mendelsohn R, Boskey AL. Fourier transform infrared spectroscopy of the solution-mediated conversion of amorphous calcium phosphate to hydroxyapatite: New correlations between X-ray diffraction and infrared data. *Calcified Tissue International*. 1996;58(1):9-16.

87. Magne D, Weiss P, Bouler JM, Laboux O, Daculsi G. Study of the maturation of the organic (type I collagen) and mineral (nonstoichiometric apatite) constituents of a calcified tissue (dentin) as a function of location: A Fourier transform infrared microspectroscopic investigation. *Journal of Bone and Mineral Research*. 2001;16(4):750-7.
88. Rey C, Shimizu M, Collins B, Glimcher MJ. Resolution-enhanced Fourier-transform infrared spectroscopy study of the environment of phosphate ion in the early deposits of a solid-phase of calcium-phosphate in bone and enamel and their evolution with age .2. investigations in the NU-3 PO₄ domain. *Calcified Tissue International*. 1991;49(6):383-8.
89. The biochemistry and physiology of bone volume 1: structure. 2 ed. New York and London: Academic press; 1972.
90. Rodriguez GP, Arenas AC, Hernandez RAM, Stolik S, Orea AC, Sinencio FS. Measurement of thermal diffusivity of bone, hydroxyapatite and metals for biomedical application. *Analytical Sciences*. 2001;17:S357-S60.
91. Singh BR. Infrared analysis of peptides and proteins: principles and applications: American chemical society; 2000.
92. Verma D, Katti KS, Katti DR. Effect of biopolymers on structure of hydroxyapatite and interfacial interactions in biomimetically synthesized hydroxyapatite/biopolymer nanocomposites. *Annals of Biomedical Engineering*. 2008;36(6):1024-32.
93. Cai SW, Singh BR. A distinct utility of the amide III infrared band for secondary structure estimation of aqueous protein solutions using partial least squares methods. *Biochemistry*. 2004;43(9):2541-9.

94. Rey C, Renugopalakrishnan V, Collins B, Glimcher MJ. Fourier-transform infrared spectroscopic study of the carbonate ions in bone-mineral during aging. *Calcified Tissue International*. 1991;49(4):251-8.
95. Rey C, Combes C, Drouet C, Glimcher MJ. Bone mineral: update on chemical composition and structure. *Osteoporosis International*. 2009;20(6):1013-21.
96. Rousseau ME, Lefevre T, Beaulieu L, Asakura T, Pezolet M. Study of protein conformation and orientation in silkworm and spider silk fibers using Raman microspectroscopy. *Biomacromolecules*. 2004;5(6):2247-57.
97. Boskey A, Mendelsohn R. Infrared analysis of bone in health and disease. *J Biomed Opt*. 2005;10(3):031102.
98. Aparicio S, Doty SB, Camacho NP, Paschalis EP, Spevak L, Mendelsohn R, et al. Optimal methods for processing mineralized tissues for Fourier transform infrared microspectroscopy. *Calcified Tissue International*. 2002;70(5):422-9.
99. Boskey A, Goldberg M, Kulkarni A, Gomez S. Infrared imaging microscopy of bone: illustrations from a mouse model of Fabry disease. *Biochim Biophys Acta*. 2006;1758(7):942-7.
100. Bartlett JD, Ganss B, Goldberg M, Moradian-Oldak J, Paine ML, Snead ML, et al. Protein-protein interactions of the developing enamel matrix. *Current Topics in Developmental Biology*, Vol 74. *Current Topics in Developmental Biology*. 74. San Diego: Elsevier Academic Press Inc; 2006. p. 57-+.
101. Wetzel DL, Slatkin DN, Levine SM. FT-IR microspectroscopic detection of metabolically deuterated compounds in the rat cerebellum: A novel approach for the study of brain metabolism. *Cellular and Molecular Biology*. 1998;44(1):15-27.

102. Leroy G, Penel G, Leroy N, Bres E. Human tooth enamel: A Raman polarized approach. *Applied Spectroscopy*. 2002;56(8):1030-4.
103. Fowler BO. Infrared studies of apatites .1. Vibrational assignments for calcium, strontium, and barium hydroxyapatites utilizing isotopic-substitution. *Inorganic Chemistry*. 1974;13(1):194-207.
104. Eastoe JE. The amino acid composition of mammalian collagen and gelatin. *Biochemical Journal*. 1955;61:589-600.
105. Landis WJ, Silver FH. Mineral Deposition in the Extracellular Matrices of Vertebrate Tissues: Identification of Possible Apatite Nucleation Sites on Type I Collagen. *Cells Tissues Organs*. 2009;189(1-4):20-4.
106. Nudelman F, Pieterse K, George A, Bomans PHH, Friedrich H, Brylka LJ, et al. The role of collagen in bone apatite formation in the presence of hydroxyapatite nucleation inhibitors. *Nature Materials*. 2010;9(12):1004-9.

CHAPTER 3. MICROSTRUCTURAL AND INFRARED SPECTROSCOPIC STUDIES OF HUMAN CORTICAL BONE WITH OSTEOGENESIS IMPERFECTA

This chapter presents microstructural (SEM images), FTIR spectral, and XRD studies of normal and osteogenesis imperfecta (OI) human cortical bones.

3.1. Introduction

Osteogenesis imperfecta (OI) is an inheritable disease characterized by the fragility of bones and other tissues rich in the type I collagen. About 90% of OI cases result from a causative variant in one of the two structural genes (COL1A1 or COL1A2) for the type I procollagens. OI provides an interesting platform for investigating how alterations of collagen at the molecular level cause changes in the structure of bone. Severity of the disease varies ranging from very mild forms without fractures to intrauterine fractures and perinatal lethality. This disease is associated with all tissues containing type I collagen and also manifests itself to include dentinogenesis imperfecta, blue sclera, hyperlaxicity of ligaments and tendons, hearing impairment and the presence of wormian bones on skull radiographs (1). Usually, the collagen from OI bone has reduced tensile strength; it breaks more easily than normal bone when deformed because fatigue damage accumulates much faster on repetitive loading. It was found that 90% or more of probands with OI have a mutation in one of the two structural genes for type I procollagens (2), with the remaining 10% due to causative recessive variants in the 8 genes known so far, or in other currently unknown genes (3). The two structural genes, COL1A1 and COL1A2, which encode the pro α 1(I) and pro α 2(I) chains of type I procollagen, have 1277 (776 in COL1A1, 501 in COL1A2) distinct mutations in the event of osteogenesis imperfecta (R Dalglish: Osteogenesis Imperfecta Variant Database, <http://oi.gene.le.ac.uk>, accessed 7 July,

2014) (4). These mutations range in complexity from simple deletions, insertions, and single base substitutions that convert a codon for glycine to a codon for a bulkier amino acid preventing proper folding of the triple helix of collagen. Among the 1277 mutations found, over 85% are substitutions. These mutations may affect the primary structure of a procollagen by preventing the zipper-like folding of the triple helix and causing degradation of normal and abnormal pro α chains through procollagen suicide, or producing a kink in the triple helix and causing assembly of abnormally branched or dendritic collagen fibrils (5).

Classically, four types of OI were first described by Sillence et al. in 1979 based on clinical features of the severity of the skeletal phenotype: type I (mild OI with bone fragility and blue sclerae), type II (perinatal lethal), type III (progressive deforming), and type IV (normal sclerae and mild deformity) (6). These four types are entirely designated for mutations in *COL1A1* or *COL1A2*, causing autosomal dominant OI (7, 8). Because of specific clinical/radiological and/or histological features and the discovery of rare recessive genetic causes of OI, this classification was expanded into 11 (7). Among all of the OI phenotypes, OI type I is the mildest form. Patients usually have normal or slightly short stature. They have slender shafts of tubular bones with thin cortex and poorly trabeculated spingiosa as well as vertebral compression fractures (3). In the vast majority of instances, this classic non-deforming OI results from mutations in one *COL1A1* allele (frameshift, nonsense and splice-site alteration) that cause mRNA instability and haploinsufficiency. In a small number of individuals with OI type I, substitutions for glycine were found by small amino acids (cysteine, alanine and serine) near the amino terminal ends of the triple-helical domains of either *COL1A1* or *COL1A2* (9). Recently, Forlino et al. proposed that type I OI should be limited to cases with type I collagen

haploinsufficiency and the occasional individual with a collagen mutation and a very mild phenotype should be designated type IV OI (7).

Many studies have attempted to find a relation between phenotype and genotypes with phenotypic severity (10-13) . As a general rule, the phenotypic severity depends on the affected alpha chain, the position of the mutation, the substituting amino acid, or the combination of these three variables. For example, OI severity increases with an amino to carboxyl terminal orientation and substitution by large and charged amino acids (10-12). When the substituting amino acid in the alpha 1 chain is charged or branched and affects a glycine at the amino acid position that is C-terminal of position 200, these substitutions are more likely to have a lethal outcome. No such relationship was found for the alpha 2 chain (14). Researchers have also conducted some related modeling work to investigate this genotype-phenotype relationship. For example, seven types of single point glycine mutations are investigated, and a reduction of the mechanical stiffness of individual tropocollagen molecules is observed (15). It is also shown that the mutations that lead to the most severe OI phenotype correlate with the strongest effects, leading to weakened intermolecular adhesion, increased intermolecular spacing, reduced stiffness, as well as reduced failure strength of collagen fibrils (16). A more recent work demonstrates that the free energy changes as a function of OI point mutations in model collagen molecules which agrees with the trend in the severity of OI from statistical analysis in collagen Type I (17).

In other studies, researchers have conducted various experiments to examine the influences of collagen defects on different constituents of bone, different structural characteristics of bone, and cell activities as well. The findings evaluate the mechanisms of OI

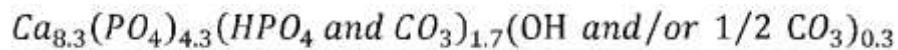
disease. Bone samples are usually from OI patients or OI mouse models. As a direct effect from the mutations in the procollagen, it is found that the amount of collagen from OI bone is less than that from age-matched normal controls (18), collagen aggregation is abnormal (19), stabilizing intermolecular cross-links are reduced (20), and the diameter of type I collagen fibrils in OI bone is larger (21) or smaller (22) as compared with normal bone, and the distribution of D-periodic spacing values was distinctive between WT and *Brl/+* mouse phenotypes (23, 24). As an indirect effect from the mutations in the procollagens, other organic matrix proteins might have an abnormal expression pattern (25-27). Osteonectin is found to be reduced in the bone of all OI patients, with the lowest levels from severely affected type III OI patients (18, 28). The reduction of three proteoglycans (a large chondroitin sulfate proteoglycan, biglycan, and decorin) are also observed from OI bone (18). In another work, an elevated amount of bone sialoprotein and similar decorin level are observed in the bones of OI patients as compared with normal controls (28). Further, higher steady-state levels of fibronectin, thrombospondin, and matrix hyaluronan are observed from bone cells produced by OI patients compared with age-matched controls, exhibiting deficient osteoblastic matrix synthesis (18, 25). Mineral phase from OI models are also found with defects including higher average mineralization density (29-32), smaller, less well aligned, and highly packed mineral crystals with decreased crystallinity (33-37). In addition, higher mineral/matrix ratio and lower carbonate: mineral ratio are usually seen in the mouse model of osteogenesis imperfect (34, 38, 39). Lower Ca/P ratio is also seen in OI human patients (40). There is a contradiction about the heterogeneity of OI bone mineralization in literature: increased heterogeneity in high bone mineralization density (BMD) OI (41) and reduced heterogeneity in OI-I patients (32). Moreover, other structural characteristics are reported with defects due to the procollagen mutations, such as a decrease in the stabilizing enzymatic cross-

links (42), thinner and more disrupted lamellae (1, 43), lower bone mass, and decreased size and amounts of cortical and cancellous bone (32, 44) are seen in OI models. Increased bone turnover is also observed in children and mice with OI (44-46), whereas reduced bone turnover is seen in some OI (type I, and IV) adults and children (47, 48). Immature woven bone is also seen in most clinically, severely affected patients (43). Further, cell activities are influenced by the defective procollagen as an increase in the number of vascular channels (1, 43) and increased osteoclasts and osteocytes are seen in OI bone (49). Meanwhile, deposition of new bone at the single osteoblast level is reduced, and is not compensated by the increased osteoblast cell number (32, 44, 50). Synchrotron radiation-based computed tomography shows that *oim* bone has more numerous and more branched canals ($p < 0.001$) and more osteocyte lacunae per unit volume compared to WT ($p < 0.001$), although total cortical porosity is comparable between *oim* and WT bone (51). A similar technique reveals drastically increased cortical porosity, canal diameter, and connectivity of OI bone as compared to pediatric controls (52). The contradictory findings discussed above such as diameter of collagen fibrils, amount of some proteoglycans, and heterogeneity of mineralization are due to large variations of OI phenotypes.

With these findings, the mechanisms of OI disease have been explored. It is suggested that the increased remodeling in OI (increased number of osteoclast and osteocyte) might be due to increased microdamage in the bone matrix (44), and the occurrence of the microdamage might be caused by higher mineralization (53). The higher mineralization density is created by increased nucleation centers in OI bone matrix (32). Therefore, Roschger et al. attributes the OI phenotype to a failure in the osteoblast differentiation pathway and concomitant synthesis of noncollagenous matrix protein which disturbs bone matrix stoichiometry, and this failure causes similar bone mineralization conditions in different OI types (32). In other studies, it is also

suggested that the low ultimate strength observed in *oim/oim* bone despite its high mineralization content is because the defective quality of mineral present in *oim/oim* bone might prohibit normal fusion of crystals into an end-to-end fusion of contiguous structure (42). In addition, the structural changes in the mineral also result from abnormal collagen fibril scaffold for mineral deposition (42).

In nature, the most common biominerals are calcium carbonates and calcium phosphates. Their extraordinary ability to accept substitutions and vacancies made the latter occur as a crystalline apatite structure in vertebrates (54). This ability imparts its adaptability to the biological function of different tissues. For example, bone crystals are found to contain significant and varying amounts of CO_3^{2-} and HPO_4^{2-} ions. The suggested formula for bone mineral is (55):



In literature, four items have been usually selected as standards to describe the composition and mineral crystal of OI bone: (1) mineral/matrix ratio (calculated from the integrated areas of phosphate (916-1180 cm^{-1}) to amide I (1592–1712 cm^{-1})), (2) collagen cross-linking network maturity (XLR, the peak intensity ratio of amide I subbands at 1660 and 1690 cm^{-1}), (3) carbonate/phosphate ratio (calculated as the integrated area of the ν_2 carbonate peak (840–892 cm^{-1}) to that of the phosphate), and (4) crystallinity (XST, calculated as the phosphate subband 1030/1020 cm^{-1} peak intensity ratio 1030/1020 cm^{-1}). These studies on human beings with osteogenesis imperfecta include that: (1) significantly increased mineral/matrix ratio in both cortical and trabecular bone of two high BMD OI patients is observed as compared with normal or classical OI bone (41). In this work, increased collagen maturity in trabecular bone is

also seen and the heterogeneity of both mineral and crystallinity distribution is increased in the two patients relative to both classic OI and the controls (41). (2) FTIR is conducted on different clinical types (I, IB, and IVA) of OI patients; however, there is no conclusion drawn from FTIR spectra (40). FTIR studies of OI mouse models include: (1) *Fro/fro* and *oim/oim* genotypes exhibit abnormal collagen crosslinking as determined by FTIRI (39); (2) Higher mineral/matrix ratio and lower carbonate/phosphate ratio for *oim/oim* as compared with normal controls are observed (34, 38, 42, 56); (3) In the *oim/oim* mouse model, the bisphosphonate treatment results in increased metaphyseal bone mineralization, but does not improve mineral maturity (57). In addition to the four items mentioned above, acid phosphate content HPO_4^{2-} ($1128/1096\text{ cm}^{-1}$) has also been utilized to estimate the amount of acid phosphate substitution in the mineral lattice in recent publications and increased acid phosphate content was noted in *Brtl/+teeth* (58, 59). Almost all of these studies focus on these specific bands without considering the wavenumber beyond 2000 cm^{-1} or below 800 cm^{-1} . In the present study, we attempt to inspect the FTIR spectra carefully throughout the $4000\text{-}400\text{ cm}^{-1}$ range.

In addition, since bone is an orthotropic material, orientational difference in stoichiometry of hydroxyapatite was investigated using FTIR in our previous study (60). This orientational difference was found to be influenced by the interactions between the collagen molecules and mineral. In the present study, the stoichiometry of hydroxyapatite from both transverse and longitudinal planes is also examined using FTIR. XRD and EDS would help to understand the mineral phase of the OI and healthy bone samples in the transverse and longitudinal planes. We found that the OI bone shows similar viscoelastic response as the normal bone in Chapter 5 (61). In this work, the ultrastructure, molecular differences, and mineral

crystal structure as well as Ca/P ratio were studied with the techniques of FE-SEM, FTIR, XRD and EDS.

3.2. Methods and Materials

3.2.1. Materials

Human normal cortical bone (femur, no apparent metabolic bone disease record, 27 years old, female) and OI cortical bone (tibia, no apparent metabolic bone disease record, 22 years old, female with pregnancy experience) were both obtained from National Disease Research Interchange, PA, and were stored in a freezer at -70°C . The OI type is putative type I, the mildest type, since the person had a height of 67 inches and weight of 180lb. The microstructure and spectroscopic studies of the normal cortical bone have been reported in a published work (60). One 20-mm-thick transverse section was cut from the mid-diaphysis of the cortical bone with a diamond saw. Marrow and flesh were removed by scraping with a ceramic knife and then the bone was washed with deionized (DI) water at room temperature for approximately 10min to avoid deterioration of bone. Then, it was further trimmed down using a low-speed diamond-wafering blade (Buehler, Isomet, Lake Bluff, IL) to obtain specimens with thickness of about 1 mm from both transverse and longitudinal planes (Figure 3.1). These specimens were ready for photoacoustic-FTIR (PA-FTIR) and X-ray diffraction (XRD) characterizations.

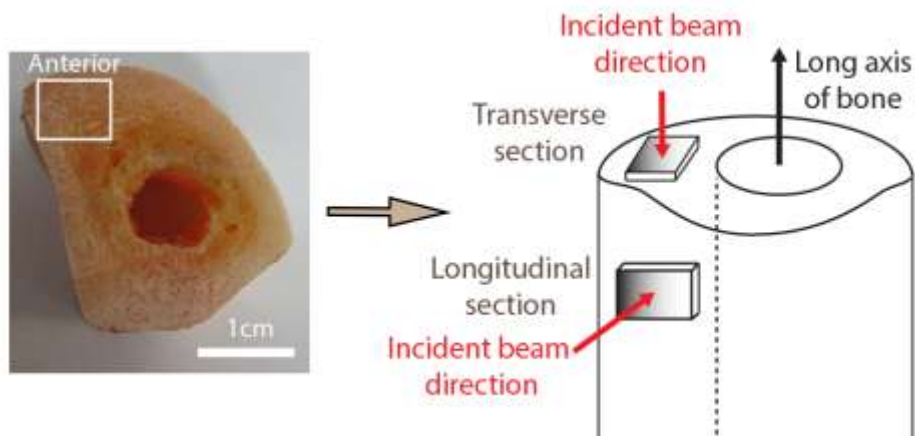


Figure 3.1. Schematic representation of bone showing from where the samples were cut; transverse section and longitudinal section are both from the anterior area of OI bone specimen.

3.2.2. Experiments

3.2.2.1. Scanning electron microscopy

Microstructure of the bone specimens was examined using a JEOL JSM-7600F analytical high resolution field-emission scanning electron microscope. Sample preparation for the scanning electron microscope (SEM) imaging involved fixing in 2.5% Glutaraldehyde (Tousimis) overnight followed by rinsing twice with sodium phosphate buffer (0.1M PH 7.35, Tousimis). These samples were further fixed in 1% Osmium-tetroxide (Electron Microscopy Sciences) for 2 hours. Details of the sample preparation for imaging are reported earlier (60).

3.2.2.2. FTIR

FTIR spectra were obtained with a Thermo Electron, Nexus 870 spectrometer which is equipped with MTEC Model 300 photoacoustic (PA) accessory. Before collecting data for each sample, the PA chamber was purged with dry helium for 15 minutes. All spectra were obtained in the range of $4000\text{-}400\text{ cm}^{-1}$, with a spectral resolution of 4 cm^{-1} . GRAMS/32 software was used for spectra analysis. The center positions for each sub-band in the curve-fitting were

determined by second-derivative analysis. The shapes of the underlying bands were chosen by Gaussian algorithm.

3.2.2.3. XRD method

XRD characterization was performed using X-ray diffractometer (Philips Analytical X'pert MPD, Almelo, Netherlands) with a secondary monochromator and Cu-tube by $\text{CuK}\alpha$ radiation wavelength of 1.5406\AA . XRD was conducted at a scan rate of $0.05^\circ/\text{s}$ with the scan range of $2\theta = 20\text{-}60^\circ$. Samples for XRD characterization are transverse and longitudinal sections for healthy and OI bone. The widths of the 002 profiles from all the samples were measured to obtain information on the size and/or internal perfection of the crystals along their c-axis. Assuming the changes in crystallinity are due to size rather than strain effects, the crystal size of bone mineral can be obtained by using Scherrer equation, $D = \lambda/\beta\cos\theta$, where D is the mean crystallite size, λ is the X-ray wavelength, θ is the Bragg angle, and β is the full width at half maximum (FWHM) of 002 profile expressed in radians (36).

3.3. Results

3.3.1. Microstructure of OI human cortical bone

It has been shown that healthy bone has a comparatively homogenous structure with well attached mineralized fibrils (62). In contrast, the structure of OI bone is quite different. Figure 3.2 (a-j) shows the SEM images of the surfaces of OI bone specimen fractured in liquid N_2 . OI bone surface shows loosely bound fibers and particles (Figure 3.2a and b, see arrows), indicating a weaker interaction between the constituents of OI bone than those in healthy bone. Figures 3.2a and 2b also show some osteons with good lamellae shapes; however, some osteons are irregular with big Haversian canal channels (Figure 3.2c and d, see arrows) which can arise from

abnormal remodeling processes. These significant porous structures exacerbate the fragility of OI bone. In addition, OI bone has abnormal collagen fiber areas within crevices (Figure 3.2e and f). No banding pattern was observed on these abnormal collagen fibers using a low angle backscattered electron (LAGE) detector. In contrast, a regular banding pattern was detected by the LAGE detector on the normal areas of OI bone specimen (Figure 3.2h). However, the periodicity for the OI samples was measured to be about 62.0 nm on average which is smaller than healthy bone periodicity of 67.0 nm. Traub et al. compared the ultrastructure of healthy and different types of OI bones and found that the OI type I bone has a similar texture to healthy cortical bone, which has a relatively homogenous coherent appearance, while type II, III and IV bones have abnormal deposition of mineral regions and loose fibers (62). Our OI bone specimen also shows the abnormal deposition of the mineral region with the size of about $485\ \mu\text{m} \times 629\ \mu\text{m}$ as a separate cluster (Figure 3.2i). The image at higher magnification (Figure 3.2j) reveals that this area is over mineralized with globules of several microns.

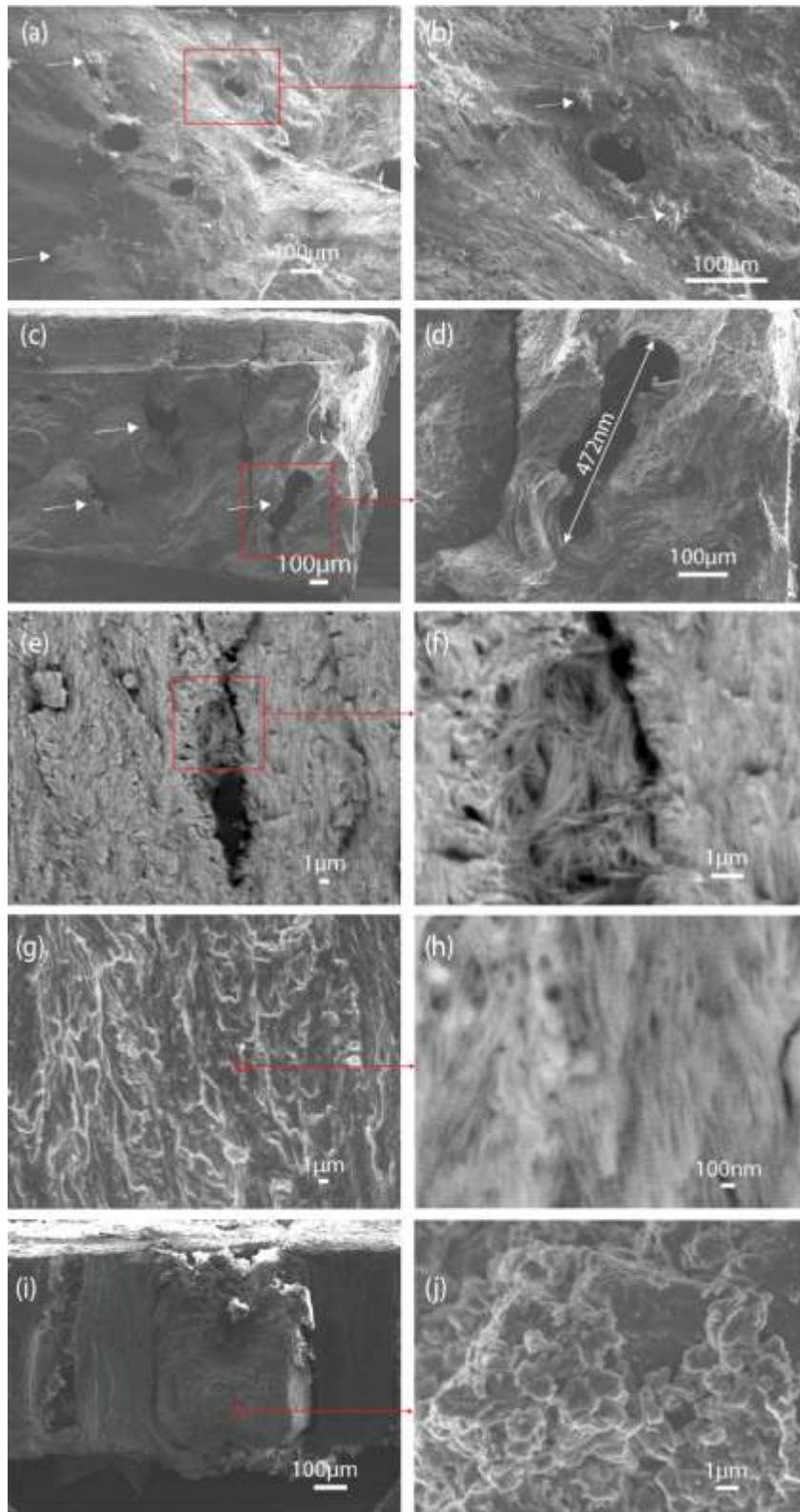


Figure 3.2. (a-j) SEM micrographs of OI bone specimens.

3.3.2. Comparison of PA-FTIR Spectra of Normal and OI bones

Infrared microscopy and Fourier transform infrared (FTIR) spectroscopy have been utilized to investigate healthy and diseased bones (63). These spectroscopic techniques can reveal molecular information of materials regarding both composition and conformation. Due to the genetic mutants of procollagen molecules, an abnormal molecular structure of protein in OI is expected. Figure 3.3 depicts PA-FTIR spectra for healthy and OI solid bone samples from the transverse and longitudinal sections in the energy range of $4000\text{--}400\text{ cm}^{-1}$. The spectra were normalized with respect to the O–H band (3322 cm^{-1}). The assignments of the bands are shown in Table 3.1.

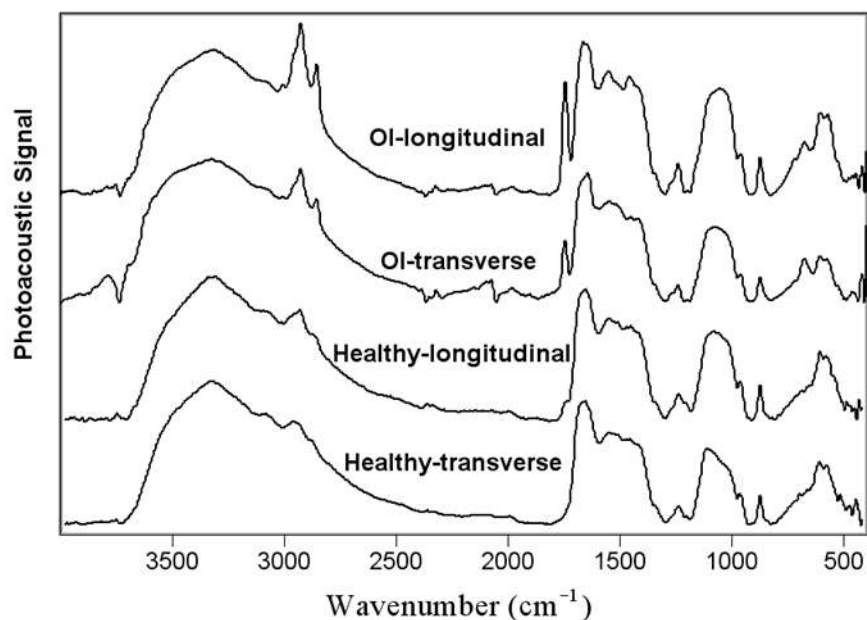


Figure 3.3. PA-FTIR spectra of human OI cortical bone and healthy cortical bone (longitudinal and transverse sections, respectively) in the $4000\text{--}400\text{ cm}^{-1}$ region, velocity of mirror: 0.158 cm/s .

Table 3.1. Band assignments of PA-FTIR spectra from OI bone.

Wavenumber (cm ⁻¹) Transverse	Wavenumber (cm ⁻¹) Longi.	Band Assignment	Ref.
3588	3588	Structural OH	(64)
3322	3322	OH stretching vibration from water and combination of Amide A with N-H stretching	(65)
3072	3074	Amide B Fermi resonance band of the first overtone of the Amide II band powered by N-H stretching vibration	(66)
2967	2965	CH ₃ asymmetric stretch: mainly lipids	(67)
2925	2925	CH ₂ asymmetric stretch: mainly lipids, with the little contribution from proteins, carbohydrates, nucleic acids	(67)
2856	2856	CH ₂ symmetric stretch: mainly lipids, with the little contribution from proteins, carbohydrates, nucleic acids	(67)
2074, 1984	2076, 1983	OH stretching vibrations from P-OH	(68-70)
1746	1747	C=O stretch: lipids, cholesterol esters, triglycerides	(71)
~1652	~1652	Amide I (protein C=O stretch)	(71)
1551-1505	1550-1506	Amide II (Protein N-H bend, C-N stretch)	(71)
1455,1414	1457,1413	CH ₃ and carbonate ν_3 vibration	(67)
1342	1342	CH ₂ wagging	(65)
~1241	~1241	Amide 3(C-N stretch, N-H bend, C-C stretch)	(65)
1180-927	1180-927	$\nu_3 \nu_1 \text{PO}_4^{3-}$	(65)
875	875	$\nu_2 \text{CO}_3^{2-}$	(65)
640-710	640-710	C-S stretching vibration	(72)
607,573	608,570	$\nu_4 \text{PO}_4^{3-}$	(65)

Significant differences between healthy and OI bone specimens can be observed in Figure 3.3. For the organic component, C-H stretching bands around 2854 cm^{-1} and 2926 cm^{-1} of OI bone exhibit much higher and sharper peaks than those of healthy bone. The appearance of these bands are from organic components such as lipids, proteins, carbohydrates, and nucleic acids (67). Likewise, C=O stretching band at 1747 cm^{-1} of OI bone also has much higher intensity than that of healthy bone. The C=O stretching band is attributed to lipids, cholesterol esters, and triglycerides (71). These intensity differences indicate that this OI bone specimen contains relatively more non-collagenous organic components (as compared to collagen) than the healthy bone specimen, whereas the band positions remain the same, which suggests that their compositions are not noticeably abnormal. In addition, a new prominent broad band appears at around $640\text{-}710\text{ cm}^{-1}$ in OI bone spectra, which is probably attributed to C-S stretching vibration (72). In some cases of type I OI, glycine can be replaced by small amino acids, such as alanine, serine, and cysteine, near the amino terminal ends of the triple-helical domains of either COL1A1 or COL1A2 (9). The appearance of a C-S vibration band indicates that the collagen molecules or other organics in the OI tibia may contain more cysteine. Since collagen molecules occupy 90% of all organic components in bone, the relatively high intensity of this new band is likely from the type I collagen molecules. Therefore, the structure of collagen molecules may possess more cysteine replacement for glycine. However, another possibility cannot be ruled out that relatively higher concentration of osteonectin, a cysteine-rich phosphorylated glycoprotein, is present in the OI tibia.

The amide I, II, and III bands are major bands of collagen molecules. As seen from Figure 3.4, Amide I (protein C=O stretch, at around 1652 cm^{-1}) bands of the two sections from healthy bone are similar; however, they are different from those of OI bone. Although

overlapped with OH bending vibration, the amide I band profiles of OI bone are still different, exhibiting significant altered collagen structures. The bands of amide II (Protein N–H bend, C–N stretch) at around 1546-1506 cm^{-1} , CH_3 and carbonate ν_3 vibrations at around 1457 and 1413 cm^{-1} , respectively, are not prominent; therefore, they do not show apparent difference between healthy and OI bone specimens. In contrast, the amide III (C–N stretch, N–H bend, C–C stretch) band of healthy bone is apparently different from that of OI bone: a small band at 1275 cm^{-1} arises in the OI bone spectra; the peak of amide III in the OI spectra is at 1241 cm^{-1} , 5 cm^{-1} upshifting from that peak in the healthy bone spectra; a band at around 1200 cm^{-1} in the healthy bone spectra almost disappears in the OI bone spectra. The band of amide III provides both composition and secondary structure information of proteins. Therefore, it is too complex to analyze, but still reflects the significant alteration of the organic component of OI bone from healthy one.

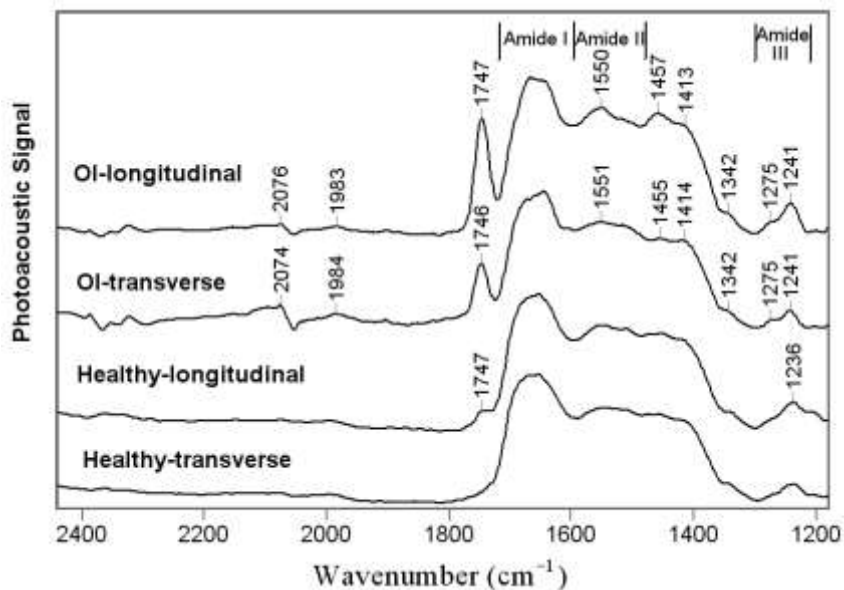


Figure 3.4. PA-FTIR spectra of human OI cortical bone and healthy cortical bone (longitudinal and transverse sections, respectively) in the 2400-1180 cm^{-1} region.

For the mineral component part, the bands at 3073 cm^{-1} and 3628 cm^{-1} from the OI second-derivative spectral curve (Figure 3.5) are assigned to OH asymmetric stretching mode (ν_3), and symmetric stretching mode (ν_1) for water associated with HAP (64). The appearances of these new bands in the OI bone spectra implies that the water interacts more closely with HAP in OI bone specimen. The band at 3588 cm^{-1} is attributed to the stretching vibration of the structural hydroxyl group from HAP (64); however, it shifts to higher energy as compared to that band at 3570 cm^{-1} in healthy bone spectra, implying that the molecular structure of OI HAP is slightly different from healthy bone. The bands at around 2100 cm^{-1} , OH stretching vibrations from P–OH (60), are more prominent in OI bone than in healthy bone. Unlike synthetic HAP, the HAP present in human bone is calcium (Ca)-deficient and contains specific lattice substitutions such as labile and stable CO_3^{2-} and HPO_4^{2-} species, and ion vacancies in the apatitic crystals as well (73). Since P-OH originates from HPO_4^{2-} , the stronger intensity of OH stretching vibrations from P-OH band of OI bone indicates that OI bone contains more HPO_4^{2-} than healthy bone.

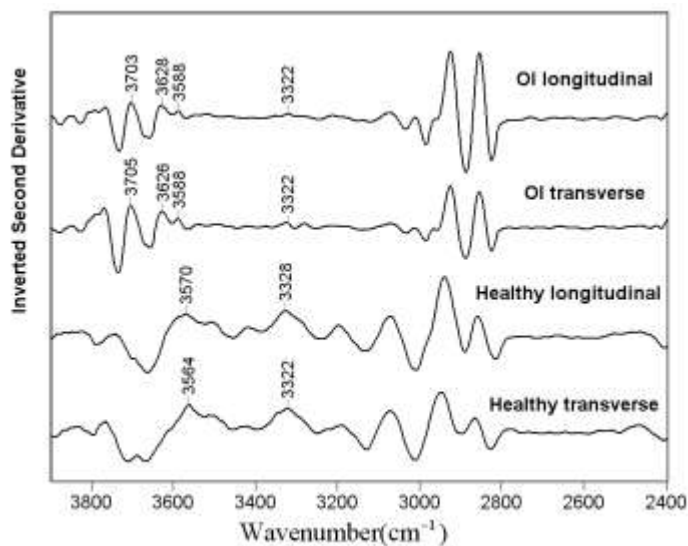


Figure 3.5. Inverted second-derivative curves in the energy range of $2400\text{--}3900\text{ cm}^{-1}$.

The ν_4 PO_4^{3-} band at $572\text{-}610\text{ cm}^{-1}$ of these two bone specimen appears similar, as shown in Figure 3.6. However, the broad profiles of $\nu_3\nu_1$ PO_4^{3-} band at $1180\text{-}927\text{ cm}^{-1}$ all vary from one another due to orientational effect and the difference of bone species as well. Detailed analysis using curve fitting is described in a subsequent section. The ν_2 out-of-plane bending vibration of CO_3^{2-} at 873 cm^{-1} almost remains in the same band position and shape. However, the ratio of its intensity over $\nu_3\nu_1$ PO_4^{3-} band is lower in OI bone than in healthy bone, indicating that CO_3^{2-} ions present in the OI mineral are less than those in the healthy mineral.

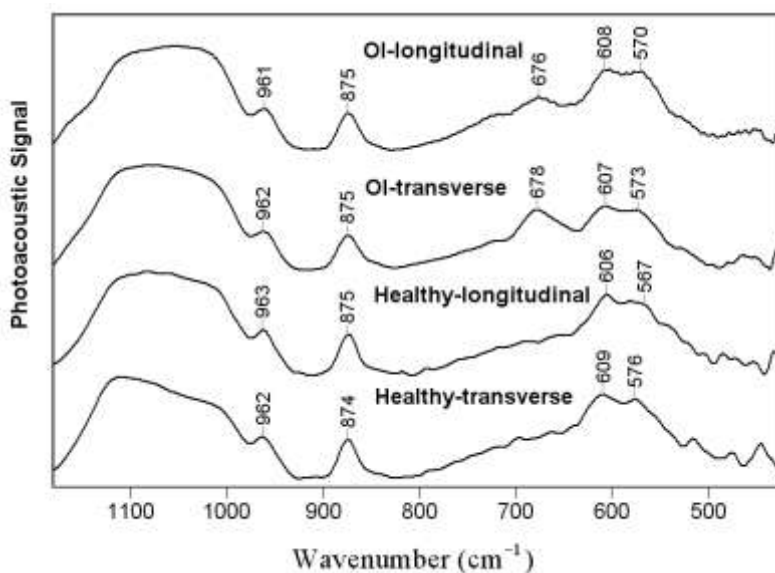


Figure 3.6. PA-FTIR spectra of human OI cortical bone and healthy cortical bone (longitudinal and transverse sections, respectively) in the $1180\text{-}420\text{ cm}^{-1}$ region.

3.3.3. Comparison of PA-FTIR spectra of OI bone in transverse and longitudinal planes

The PA-FTIR spectra of the transverse and longitudinal sections of OI bone are also compared. As for the organic part, as seen in Figure 3.3, the C-H stretching vibrations at around 2855 cm^{-1} and 2926 cm^{-1} , and C=O stretching vibration at around 1747 cm^{-1} of the longitudinal section are more intense than those of the transverse section. This phenomenon is also seen in

healthy bone, probably due to more canals crosscut and exposed on the longitudinal section surface (60). As mentioned before, the amide I (protein C=O stretch, at around 1652 cm^{-1}) band of OI bone differs from healthy bone. Raman spectral mapping of bone osteonal tissues shows that amide I bands are more intense in the perpendicular direction to the fiber axis since C=O bonds are perpendicular to the collagen backbone, while amide III, ν_2 and $\nu_4\text{PO}_4^{3-}$ vibrations are observed to be less sensitive to orientation effects (74). Unlike Raman spectroscopy, in FTIR studies, the amide I band is overlapped by O-H bending band from water. Therefore, the orientational difference of the amide I band is not easily seen. However, in OI, the amide I band of the longitudinal section differs from that of the transverse section as can be seen in Figure 3.7. The bands of amide II (Protein N-H bend, C-N stretch) at around $1546\text{-}1506\text{ cm}^{-1}$, and CH_3 and carbonate ν_3 vibrations at around 1457 and 1413 cm^{-1} , respectively, are all more intense in the longitudinal section than in the transverse section. These effects have also been observed in the amide III band.

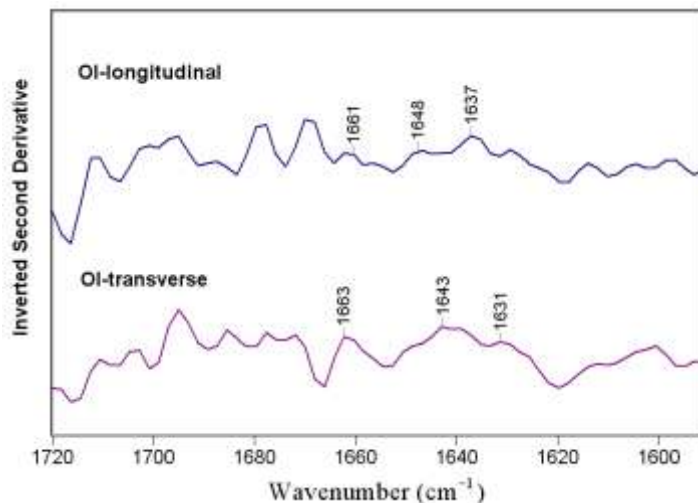


Figure 3.7. Inverted second-derivative curves of OI longitudinal and transverse sections in the $1720\text{-}1590\text{ cm}^{-1}$ region.

For the mineral part, the O-H stretching bands from P-OH at around 2000 cm^{-1} from the transverse section is stronger than that of the longitudinal section, indicating that the transverse section contains more HPO_4^{2-} than the longitudinal section. From Figure 3.3, more CO_3^{2-} ion content and less HPO_4^{2-} ion in the longitudinal sections than in the transverse sections are also noticed. The broad profile of $\nu_3 \nu_1 \text{ PO}_4^{3-}$ band at $1180\text{-}927\text{ cm}^{-1}$ arises from 12 sub-bands (Table 3.2). Curve fitting in this region is performed based on the second derivative of the curves with the normalization depicted in Figure 3.8 (a) and (b). The ratio of the $1023/1038\text{ cm}^{-1}$ bands (often used to describe the relative amount of crystal perfection or amount of non-stoichiometric apatite in the lattice) (58, 75, 76) in the transverse section is 0.45, while, in the longitudinal section, it is 0.21. Further, the sub-band area at around 1090 cm^{-1} (often used to describe the amount of stoichiometric apatite in the lattice) (58, 75, 76) in the longitudinal section is larger than that in the transverse section. Therefore, OI bone appears to be more stoichiometric in the longitudinal section surface. This phenomenon is the same as in healthy bone (60).

3.3.4. XRD and EDS results

Usually a sample of bone tissue contains crystals of very different ages and stages of maturation. The ages and the stages of maturation are attributed to the length of time the individual crystals remain in the tissue and the remodeling proceeds heterogeneously throughout the life (79). In this XRD experiment, a piece of copper filter with a $10\text{ mm} \times 1\text{ mm}$ window was used to focus that size of the beam on the samples. The mineral information acquired by XRD reflects an average from that size of bone tissue. XRD is sensitive to the long-range crystalline structure of the material (80).

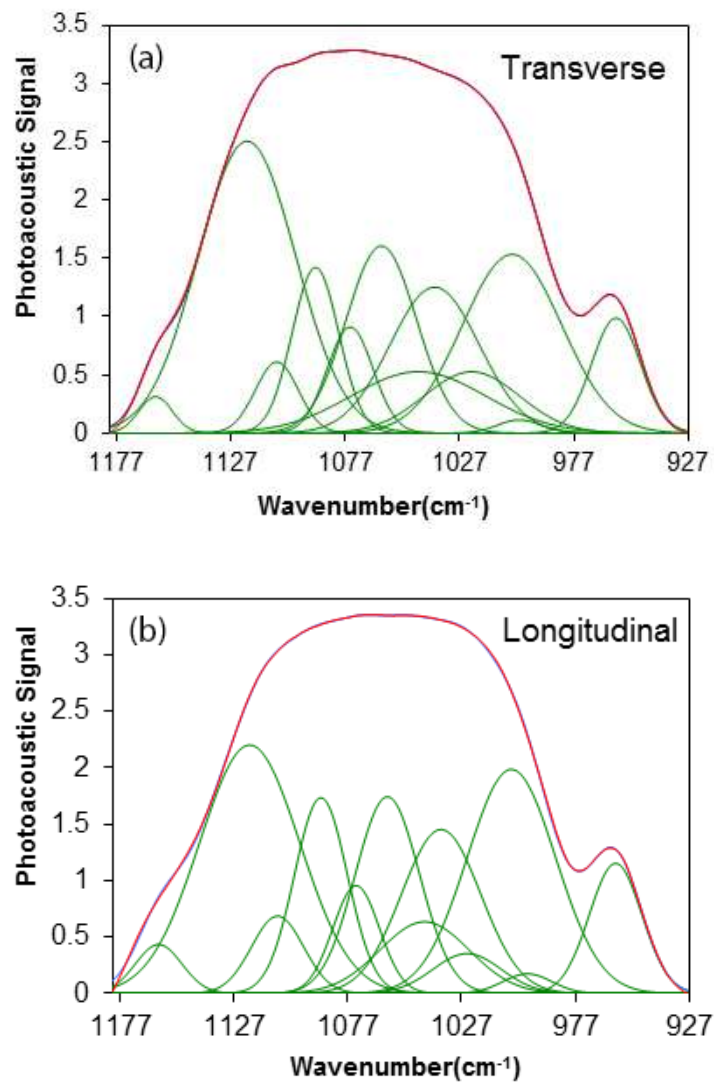


Figure 3.8. (a) Curve fitting analysis of the ν_1, ν_3 phosphate band (1180–927 cm^{-1}) of (a) Transverse section, and (b) Longitudinal section.

Table 3.2. Major components of the ν_1 , ν_3 PO_4^{3-} bands (75, 77, 78).

Position Transverse	Area Transverse	Position Longitudinal	Area Longitudinal	Band assignment
1160	6	1160	11	HPO_4^{2-} containing apatites
1120	134	1120	121	ν_3 PO_4^{3-} in Poorly crystalline apatites
1107	14	1108	20	ν_3 PO_4^{3-} in Poorly crystalline apatites
1090	36	1089	51	ν_3 PO_4^{3-} in stoichiometric HA
1075	23	1073	24	ν_3 PO_4^{3-} in Poorly crystalline apatites
1061	62	1060	62	ν_3 PO_4^{3-} in Poorly crystalline apatites
1045	39	1043	31	HPO_4^{2-} containing apatites and type B carbonate-containing apatites
1038	61	1036	63	PO_4^{3-} in stoichiometric HA
1022	28	1025	13	Nonstoichiometric apatites containing HPO_4^{2-} and/or CO_3^{2-}
1004	83	1005	97	ν_3 PO_4^{3-} in apatitic environment
1001	3	998	5	ν_3 PO_4^{3-} in apatitic environment
959	26	959	33	ν_1 PO_4^{3-}

Figure 3.9 shows the X-ray diffraction profiles of healthy and OI bone specimens, with their transverse section and longitudinal section, respectively. The profiles show obvious intensity peaks of (002), (211), (202), (310), (203), (213), and (004) planes. All the profiles are normalized at the strongest peak of (211) reflection. As compared to the well-crystallized HAP (81), all X-ray lines of bone specimens are broadened except (002) reflection. The X-ray

line broadening is mainly due to smaller crystallite size (<200nm) and lattice strain or crystal distortions resulting from atomic substitutions within the crystal lattice. The (211) broad profile is overlapped with (112), (300), and (202) reflections (82). The (002) reflection is the only one free of any overlapping adjacent lines. This (002) reflection reflects the length axis of the bone crystal with minimal strain influence. The average crystallite size in the *c*-axis direction was found to increase with age under 20 years old, and reach a constant average domain size above 20 years old. Microstrain has the opposite trend and decreases to a constant small average strain value above 20 years old (see the figures in (82)). In this study, the healthy bone sample is 27 years old; the OI bone sample is 22 years old. Therefore, we can ignore the aging effects and only consider disease as affecting crystal size. Scherrer equation has been employed to calculate the crystal size in other bone studies (30, 36, 83). The present study also uses Scherrer equation, and the crystal sizes along *c*-axis direction of healthy and OI bone specimen are listed in Table 3.3. The crystal sizes along *c*-axis direction of healthy bone in the transverse and longitudinal sections are calculated as 28.35 and 25.82 nm, whereas the crystal sizes of OI bone in the transverse and longitudinal sections are 28.42 and 20.80 nm, respectively. It seems that the direction of specimens affects the results. The crystal sizes from the two transverse sections are the greatest among all the specimens, and they are very close. The biggest difference is from the two longitudinal sections. These differences are still under investigation with orientational effect. Since the *c*-axis is perpendicular to the transverse section plane, the signals from the transverse sections are much stronger than the longitudinal section. The (002) plane also shows apparent orientational difference: the transverse section is more intense in both healthy and OI bone specimens than the longitudinal section. In addition, the experimental error due to the weak signal in the longitudinal section cannot be ignored.

Overall, the crystal size along the *c*-axis direction of OI bone is close to healthy bone, implying that OI and healthy bone have almost identical mineral crystals.

To further investigate the elemental ratios in bone specimens, Energy-dispersive X-ray spectroscopy (EDS) in SEM was used to examine Ca/P molar ratio. As seen in Table 3.4, for the same kind of samples, the Ca/P molar ratio of healthy and OI bone specimens are similar.

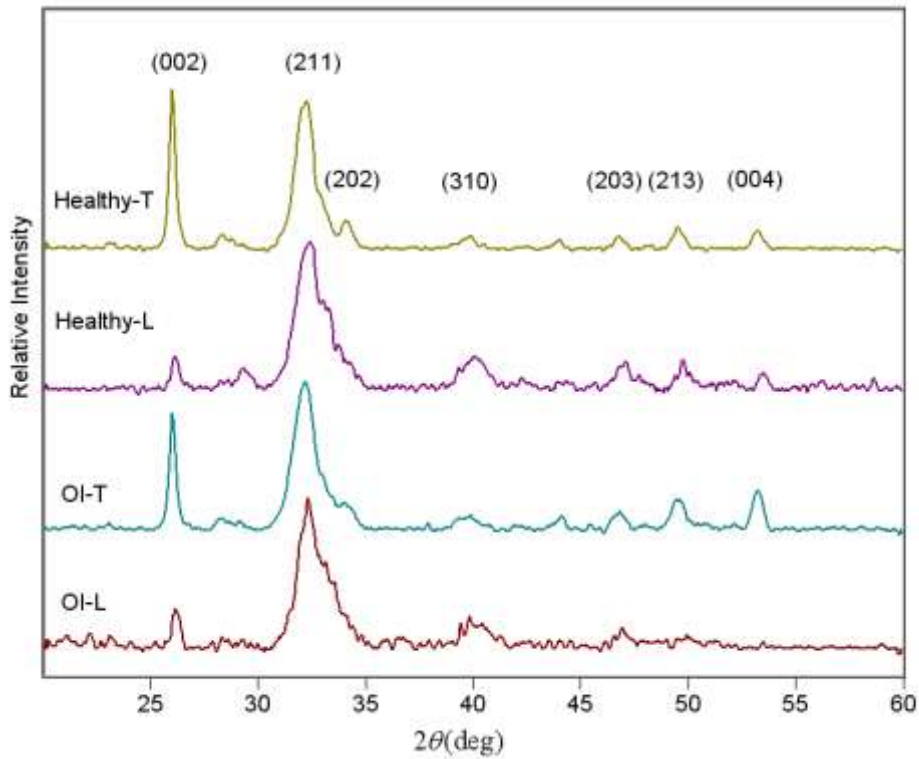


Figure 3.9. X-ray diffractogram of bone specimens: Healthy bone (T-transverse section and L-longitudinal section) and OI bone specimens.

Table 3.3. Crystal size along *c*-axis direction of bone mineral (nm).

Bone sample	Transverse section	Longitudinal section
Healthy bone	28.35	25.82
OI bone	28.42	20.80

Table 3.4. Ca/P molar ratio of bone specimens (\pm STD).

Bone sample	Transverse section	Longitudinal section
Healthy bone	1.53 \pm 0.06	1.41 \pm 0.09
OI bone	1.46 \pm 0.02	1.42 \pm 0.02

3.4. Discussion

The classic non-deforming OI cases either result from mutations in one COL1A1 allele or substitutions for glycine by a small amino acid (cysteine, alanine and serine). As the mutations are heterozygous, some of the gene products still should be normal. Even in severe OI, there are normal lamellar bone structures composed of normally mineralized fibrils (62). In the present study, FE-SEM images show some normal lamellae. Meanwhile, these images also reveal significant altered structures of OI bone from healthy bone on all scales, e.g.: OI bone is more porous and fibrous; OI bone contains abnormal collagen fibril areas and over mineralized deposits; and an abnormal banding pattern of mineralized fibrils. The changes in bone porosity at the tissue level indicate changes in bone metabolism and altered bone mechanical integrity. The loosely attached fibrils and condensed mineral areas are the signs of weakened intermolecular adhesion and interaction between collagen molecules and mineral phase. The abnormal banding pattern of mineralized fibrils demonstrates the influence of the poor collagen matrix, which serves as a framework for biomineralization. It seems that the whole bone structure as seen in SEM images is significantly altered due to the collagen defects and secondary changes caused by the collagen defects.

PA-FTIR spectra display aberrant structures of collagen molecules and slightly altered minerals. According to FTIR analysis of the organic components: (1) The C-H stretching bands and C=O stretching bands from the non-collagenous organic components exhibit similar shape

and position in the OI spectra as in the healthy bone spectra, implying that the main compositions of the non-collagenous organic components are not noticeably abnormal. However, the volume of the non-collagenous organic components is relatively greater because of their higher intensity. This phenomenon can result from the porous feature of OI bone which can accommodate more non-collagenous proteins (NCPs). In a previous study, the amount of total protein synthesized by osteoblasts from patients with mild to moderately severe forms of OI was found normal when compared to that of an age-matched control (18). It is generally regarded that increased levels of NCPs in OI bone reflect a reduced collagen content, leaving space that is passively filled by deposition of some NCPs (28). This viewpoint accords with the present FTIR results; (2) The collagen molecules of OI bone have altered structures due to the apparently altered amide I and amide III bands; and (3) The appearance of a new band at $705\text{-}640\text{ cm}^{-1}$ implies that more cysteine may be contained in the collagen molecules as substitutions or/and higher concentration of osteonectin (a cysteine-rich phosphorylated glycoprotein) is present in OI tibia. Osteonectin was found reduced in bones from OI patients as compared with age-matched normal controls (18, 28). However, as seen from the figure in (18), the amount of collagen from OI type I is about 20% of age-matched normal controls while the amount of osteonectin from OI type I is about 60% of age-matched normal controls. Therefore, in comparison with collagen, osteonectin is highly increased in OI type I bone. The source of this C-S band requires further study through either collagen analysis or NCPs analysis.

The mineral component shows three different kinds of OH stretching bands between OI and healthy bones: (1) The first kind of OH stretching bands shows two new bands at 3703 and 3628cm^{-1} , and their appearance indicates that water interacts more closely with HAP in OI bone specimens; (2) The upshifting 12 cm^{-1} of the stretching vibration of the structural hydroxyl group

from hydroxyapatite implies that the molecular structure of OI hydroxyapatite is slightly different from healthy bone; (3) Around 2000 cm^{-1} , bands of OH stretching vibrations from P–OH of OI bone are more prominent than in healthy bone, indicating that OI bone may contain more HPO_4^{2-} ions. This agrees with a previous study which demonstrates increased acid phosphate content in Brtl/+ teeth (59). In contrast to the OH stretching bands, the intensity ratio of $\nu_2\text{ CO}_3^{2-}$ over $\nu_3\nu_1\text{ PO}_4^{3-}$ band in OI is lower than in healthy bone, indicating less CO_3^{2-} ions in OI mineral. This lower $\text{CO}_3^{2-}/\text{PO}_4^{3-}$ ratio has also been found in several OI bone studies (34, 38). However, PO_4^{3-} and CO_3^{2-} bands of OI bone do not display significant differences as compared to healthy bone. Therefore, in OI, the mineral component does not have significant molecular alterations. Our XRD and EDS results on both healthy and OI bone specimens also support that the mineral crystals in OI are not significantly altered. Studies of phosphorus-31 solid state nuclear magnetic resonance ($^{31}\text{P-NMR}$) spectra also suggest that the bulk of the phosphorus in both healthy and OI samples is present in the same phase (40). No detectable defect of matrix mineralization was found in OI patients by histomorphometric study (44). For the type I OI, crystal size is reduced in children only and returns to normal in adolescence (36). As mentioned before, the bone samples investigated in the present study are both from post adolescence. Therefore, it is reasonable that our samples do not show significant alterations. In another study, it is reported that the monovalent ion OH^- within the apatite tunnels can be easily exchanged at high temperatures without any crystal alteration, whereas the trivalent ion PO_4^{3-} and bivalent ion Ca^{2+} that constitute the apatite frame can be substituted, but with structure reorganization (84). Therefore, in OI, there are alterations of OH^- groups, but these alterations do not remarkably influence the whole crystal structure. Instead, they change the mineral ion environment, making it more attachable to water and elevating the number of HPO_4^{2-} ions in the

hydrated layer of the mineral crystal. The improved attachability of OI bone mineral to water and the nonstoichiometry of the mineral favor the resorption of bone by osteoclasts.

^{31}P -NMR spin-spin relaxation studies (85) show that a substantial fraction of the protonated phosphates (HPO_4^{2-}) are situated on the surfaces of the bone mineral crystals and the concentration of unprotonated phosphates (PO_4^{3-}) within the apatitic lattice increases toward the center of the crystal. The studies also demonstrate that the younger, less mature biological crystals contain a higher concentration of the surface HPO_4^{2-} groups. C. Rey et al. (79) find that maturation of bone mineral is accompanied by an increase of CO_3^{2-} ion content and a decrease of HPO_4^{2-} ion content. When bone is more mature, the mineral also becomes more stoichiometric (75). Our FTIR spectra exhibit increased CO_3^{2-} ion content and reduced HPO_4^{2-} ion content in healthy bone than in OI bone, implying that healthy bone is more mature than OI bone, which also suggests that healthy bone is more stoichiometric. The piece of healthy bone in the present study is 5 years older than the OI bone. The difference in maturation between OI and healthy bone mineral may originate from both the age difference and the OI disease. In our previous paper (60), we discussed that the longitudinal section is more stoichiometric than the transverse section. This phenomenon is attributed to the reduced interaction between exchangeable ions contained within the mineral surface and collagen molecules in the longitudinal section rather than the interaction between the mineral surface and collagen termini in the transverse section. Therefore, the nonstoichiometry of OI bone mineral might also be influenced by the interactions between the collagen and mineral.

It is noteworthy that $1020/1030\text{cm}^{-1}$ has long been regarded as the measure of “crystallinity/maturity index” of bone mineral, and the more crystalline/mature, the more

hydroxyapatite-like stoichiometry, the bigger the crystalline size, and the less the ion substitution by ions such as CO_3^{2-} (76, 86). However, Farley et al. argued that an increase in 1030/1020 ratio is not necessarily related to an increase of crystal size in human bone and therefore this ratio should only be maturity index (73). A more recent work agrees with Farley et al.'s point when the crystal size is measured by XRD (39). Regardless of crystallinity and maturity, 1030cm^{-1} and 1020cm^{-1} are assigned to stoichiometric and nonstoichiometric apatite; therefore, in the present study, stoichiometry is used as a description of the mineral phase instead of crystallinity or maturity.

Our FTIR spectra also exhibit the trend of more CO_3^{2-} ion content and less HPO_4^{2-} ion content in the longitudinal section of OI bone than in the transverse section, implying that the longitudinal section is more stoichiometric for the same reason as previously discussed. This conclusion, which concurs with our curve-fitting analysis in the results section, is also in accordance with the prior spectral study on healthy bone (60). Since the crystalline HAP core is stoichiometric, the nonstoichiometric ions and vacancies are located on the mineral surface as the hydrated layer. The transverse section is more nonstoichiometric, implying that the hydrated layer in the transverse plane has a greater volume than it does in the longitudinal plane. This schematic nanocrystal of bone mineral is illustrated in Figure 3.10. This structure is similar to what Jager et al. suggests based on solid-state NMR studies (87).

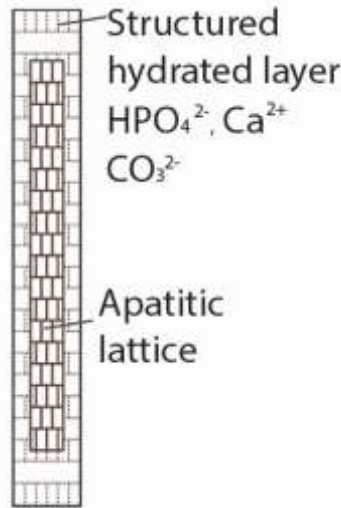


Figure 3.10. Structure of an HAP nanocrystal.

It appears that collagen type I abnormalities lead to secondary changes in the mineral phase of the bone material due to the poor collagen framework and the interactions between collagen molecules and mineral surfaces. However, Roschger et al. suggest that the tissue- and materials- abnormalities found in OI-I seem to be independent of the collagen mutations because no differences of mineralization (measured by quantitative backscattered electron imaging (qBEI)) are found between two different OI mutation types (qualitative and quantitative) (32). Roschger et al. prefers a failure in the osteoblast differentiation pathway and concomitant synthesis of noncollagenous matrix proteins as the cause of OI phenotype (32). Likewise, Jones et al. claims that the increased mineral content, which seems to be the hallmark for all types of OI, is due to impaired osteoblastic function rather than to the altered structure of the collagen matrix, since increased cellularity, increased osteocyte lacunar density and abnormal areas of woven bone have been observed in different types of OI (88). Impaired osteoblast differentiation, abnormal metabolism and altered secretion of non-collagenous proteins are common features in

OI (18). The proliferative capacity and growth rate of OI cells are reduced relatively to normal cells (89). Striking abnormalities in the differentiation pathway of bone marrow progenitor cells towards osteoblasts have been recently demonstrated in an OI mouse model (90). It is also believed that altered osteoblastic differentiation may arise from altered extracellular matrix feedback into cellular metabolism, since the pattern of expression and fine structure of the proteoglycans (PGs) were consistent with OI-derived osteoblasts, failing to follow a developmental differentiation pattern (27). Bone histomorphometry also reveals that osteoblasts from affected patients produce only half the amount of collagen matrix; however, the adaptation of skeleton to the increasing mechanical needs during growth is improved by increased recruitment of remodeling units, yet this improvement cannot compensate for the bone loss (44). The increased remodeling process is reflected by elevated osteoclast formation; meanwhile, decreased osteoblast function is also seen in OI mice models (91, 92). Besides impaired osteoblast and osteoclast functions, increased numbers of osteocytes and multiple osteocytes in some lacunae of OI are observed in human bone (49). In bone homeostasis, osteoblasts sense osteocyte apoptosis via gap junctions; and then osteoblasts trigger osteoclast maturation and recruitment (93). Therefore, in OI bone, cellular interactions with abnormal matrix and compromised osteoblast development influence signaling between osteoblasts and osteoclasts, increasing bone remodeling and exacerbating the bone weakness caused by the primary collagen change. All in all, secreted mutant collagen from OI bone affects fibril structure, interactions of NCPs with matrix, matrix mineralization, osteoblast development, and cell-cell and cell-matrix cross-talk (7).

It has long been debated whether or not collagen or non-collagenous proteins (NCPs) initiate intrafibrillar mineralization. In addition, the debate extends to the mechanisms producing

intrafibrillar mineralization at the molecular level (94). Many believe that the biomineralization process is controlled by bone cells and interactive noncollagenous phosphorylated proteins, and is also influenced by collagen (95). Osteoblast cells derived from OI patients are found to have reduced levels of collagen, osteonectin, three proteoglycans (a large chondroitin sulfate proteoglycan, biglycan, and decorin), and elevated amounts of thrombospondin and fibronectin when compared with levels found in age-matched control bone cell cultures (18, 96). In another study, osteonectin is found to be reduced in the bone of all OI patients, with the lowest levels from severely affected type III OI patients (28). These alterations in NCPs give rise to an extracellular matrix with an aberrant stoichiometry (18). In the present study, osteonectin is probably the source of the C-S band at around $640\text{-}710\text{ cm}^{-1}$ from OI bone. Osteonectin is found in highest concentrations in developing bone and thereby regarded as related to mineral nucleation and mineral crystal formation with the ability to bind Ca^{2+} ions (97, 98). The relative higher amount of osteonectin as compared to collagen (18) might be the cause of the high mineralization of OI bone. Except for the probable abnormal amount of osteonectin, the overall composition of NCPs in OI do not show remarkable change as compared to healthy bone in IR spectra, and the crystal structure and Ca/P ratio as investigated by XRD and EDS do not have significant differences between OI and healthy bones. Conversely, collagen molecules are significantly altered. Therefore, we also claim that the biomineralization process is more controlled by NCPs than collagen.

It should be noted that there are several limitations in this study: (1) Sample size is obviously insufficient to address many important questions. For statistical reasons, more OI samples and more controlled samples are required; (2) Collagen analysis or NCPs analysis of the

OI bone is required to confirm the source of the C-S band at around 640-710 cm^{-1} on FTIR spectra.

3.5. Conclusion

With OI disease, the mutations in procollagen molecules cause aberrant collagen molecules and secondary changes in mineral, NCPs, and cell activities due to their interactions and cross-talks with collagen matrix. In the present study, FE-SEM, PA-FTIR, XRD and EDS are utilized to characterize the OI human cortical bone (putative type I) and healthy human cortical bone. The study demonstrates that OI bone structure is significantly altered due to collagen defects. FE-SEM images show more porous, fibrous features, abnormal collagen fibrils, overmineralized deposits, as well as an altered banding pattern of mineralized fibrils of OI bone. PA-FTIR spectra demonstrate altered OI collagen molecules with a markedly different amide III band and the appearance of a new C-S band which might be caused by a collagen defect (cysteine replacement of glycine) or/and an increased amount of osteonectin (a cysteine-rich phosphorylated glycoprotein). The slightly altered mineral structure in the OH^- group and more HPO_4^{2-} in OI is also seen in the spectra. However, NCPs in OI do not show significant alteration in shape or position in spectra except for their higher intensity. These phenomena indicate that the biomineralization process is more controlled by the bone cells and non-collagenous phosphorylated proteins as suggested by other studies. However, the biomineralization process is also significantly influenced by the collagen, in addition to the interactions between the collagen molecules and mineral phase. PA-FTIR spectra also show that OI bone mineral is more attachable to water and is more nonstoichiometric than healthy bone, which can result from the altered mineral ion environment. The loosely attached fibrils and condensed mineral areas are the

results of weakened intermolecular adhesions and poor collagen frameworks. Also, the banding pattern of mineralized fibrils is slightly altered in OI because of the altered collagen framework. OI bone has the same orientational stoichiometry of hydroxyapatite as healthy cortical bone; that is; the longitudinal section is more stoichiometric than the transverse section. This orientational stoichiometry results from the interaction between the mineral surface and the different parts of collagen molecules as discussed in our previous study (290). The larger volume of the hydrated layer in the transverse plane of bone mineral nanocrystal is also suggested. It should be stressed that further study involving collagen analysis or NCPs analysis of the OI bone is needed.

3.6. Acknowledgements

Instrumentation obtained from National Science Foundation MRI grants is acknowledged for enabling experiments conducted in this work. I would like to acknowledge the assistance in electron microscopy laboratory from Mr. Scott Payne. I would also like to acknowledge the support from Doctoral Dissertation Award of NDSU graduate school.

3.7. References

1. Rauch F, Glorieux FH. Osteogenesis imperfecta. *Lancet*. 2004;363(9418):1377-85.
2. Sykes B, Ogilvie D, Wordsworth P, Wallis G, Mathew C, Beighton P, et al. Consistent linkage of dominantly inherited osteogenesis-imperfecta to the type-I collagen loci - COLIA1 AND COLIA2. *American Journal of Human Genetics*. 1990;46(2):293-307.
3. Dijk FSv, Cobben JM, A. K, Maugeri A, Nikkels PGJ, Rijn RRv, et al. Osteogenesis Imperfecta: A Review with Clinical Examples. *Molecular Syndromology*. 2011;2:1-20.

4. Dalglish R. The Human Collagen Mutation Database 1998. *Nucleic Acids Research*. 1998;26(1):253-5.
5. Kuivaniemi H, Tromp G, Prockop DJ. Mutations in collagen genes - causes of rare and some common diseases in humans. *Faseb Journal*. 1991;5(7):2052-60.
6. Silience DO, Senn A, Danks DM. Genetic-heterogeneity in osteogenesis imperfecta. *Journal of Medical Genetics*. 1979;16(2):101-16.
7. Forlino A, Cabral WA, Barnes AM, Marini JC. New perspectives on osteogenesis imperfecta. *Nature Reviews Endocrinology*. 2011;7(9):540-57.
8. Bishop N. Characterising and treating osteogenesis imperfecta. *Early Human Development*. 2010;86(11):743-6.
9. van Dijk FS, Byers PH, Dalglish R, Malfait F, Maugeri A, Rohrbach M, et al. EMQN best practice guidelines for the laboratory diagnosis of osteogenesis imperfecta. *European Journal of Human Genetics*. 2012;20(1):11-9.
10. Yang W, Battineni ML, Brodsky B. Amino acid sequence environment modulates the disruption by osteogenesis imperfecta glycine substitutions in collagen-like peptides. *Biochemistry*. 1997;36(23):6930-5.
11. Beck K, Chan VC, Shenoy N, Kirkpatrick A, Ramshaw JAM, Brodsky B. Destabilization of osteogenesis imperfecta collagen-like model peptides correlates with the identity of the residue replacing glycine. *Proceedings of the National Academy of Sciences of the United States of America*. 2000;97(8):4273-8.
12. Byers PH. Folding defects in fibrillar collagens. *Philosophical Transactions of the Royal Society of London Series B-Biological Sciences*. 2001;356(1406):151-7.

13. Marini JC, Forlino A, Cabral WA, Barnes AM, San Antonio JD, Milgrom S, et al. Consortium for osteogenesis imperfecta mutations in the helical domain of type I collagen: Regions rich in lethal mutations align with collagen binding sites for integrins and proteoglycans. *Human Mutation*. 2007;28(3):209-21.
14. Amor IMB, Glorieux FH, Rauch F. Genotype-phenotype correlations in autosomal dominant osteogenesis imperfecta. *Journal of Osteoporosis* [Internet]. 2011; 2011:[1-9 pp.].
15. Gautieri A, Vesentini S, Redaelli A, Buehler MJ. Single molecule effects of osteogenesis imperfecta mutations in tropocollagen protein domains. *Protein Science*. 2009;18(1):161-8.
16. Gautieri A, Uzel S, Vesentini S, Redaelli A, Buehler MJ. Molecular and Mesoscale Mechanisms of Osteogenesis Imperfecta Disease in Collagen Fibrils. *Biophysical Journal*. 2009;97(3):857-65.
17. Lee KH, Kuczera K, Holl MMB. The Severity of Osteogenesis Imperfecta: A Comparison to the Relative Free Energy Differences of Collagen Model Peptides. *Biopolymers*. 2011;95(3):182-93.
18. Fedarko N, Vetter U, Robey P. The bone cell biology of osteogenesis imperfecta. *Connective Tissue Research*. 1995;31(4):269-73.
19. Teitelbaum SL, Kraft WJ, Lang R, Avioli LV. Bone collagen aggregation abnormalities in osteogenesis imperfecta. *Calcified Tissue Research*. 1974;17(1):75-9.
20. Sims TJ, Miles CA, Bailey AJ, Camacho NP. Properties of collagen in OIM mouse tissues. *Connective Tissue Research*. 2003;44:202-5.
21. Cassella JP, Barber P, Catterall AC, Ali SY. A morphometric analysis of osteoid collagen fibril diameter in osteogenesis imperfecta. *Bone*. 1994;15(3):329-34.

22. Sarathchandra P, Pope FM, Ali SY. Morphometric analysis of type I collagen fibrils in the osteoid of osteogenesis imperfecta. *Calcified Tissue International*. 1999;65(5):390-5.
23. Wallace JM, Orr BG, Marini JC, Holl MMB. Nanoscale morphology of Type I collagen is altered in the Brl mouse model of Osteogenesis Imperfecta. *Journal of Structural Biology*. 2011;173(1):146-52.
24. Kemp AD, Harding CC, Cabral WA, Marini JC, Wallace JM. Effects of tissue hydration on nanoscale structural morphology and mechanics of individual Type I collagen fibrils in the Brl mouse model of Osteogenesis Imperfecta. *Journal of Structural Biology*. 2012;180(3):428-38.
25. Fedarko NS, Robey PG, Vetter UK. Extracellular-matrix stoichiometry in osteoblasts from patients with osteogenesis imperfecta. *Journal of Bone and Mineral Research*. 1995;10(7):1122-9.
26. Fedarko NS, Sponseller PD, Shapiro JR. Long-term extracellular matrix metabolism by cultured human osteogenesis imperfecta osteoblasts. *Journal of Bone and Mineral Research*. 1996;11(6):800-5.
27. Grzesik WJ, Frazier CR, Shapiro JR, Sponseller PD, Robey PG, Fedarko NS. Age-related changes in human bone proteoglycan structure - Impact of osteogenesis imperfecta. *Journal of Biological Chemistry*. 2002;277(46):43638-47.
28. Vetter U, Fisher LW, Mintz KP, Kopp JB, Tuross N, Termine JD, et al. Osteogenesis imperfecta - changes in noncollagenous proteins in bone. *Journal of Bone and Mineral Research*. 1991;6(5):501-5.

29. Boyde A, Travers R, Glorieux FH, Jones SJ. The mineralization density of iliac crest bone from children with osteogenesis imperfecta. *Calcified Tissue International*. 1999;64(3):185-90.
30. Fratzl-Zelman N, Schmidt I, Roschger P, Glorieux FH, Klaushofer K, Fratzl P, et al. Mineral particle size in children with osteogenesis imperfecta type I is not increased independently of specific collagen mutations. *Bone*. 2014;60:122-8.
31. Fratzl-Zelman N, Morello R, Lee B, Rauch F, Glorieux FH, Misof BM, et al. CRTAP deficiency leads to abnormally high bone matrix mineralization in a murine model and in children with osteogenesis imperfecta type VII. *Bone*. 2010;46(3):820-6.
32. Roschger P, Fratzl-Zelman N, Misof BM, Glorieux FH, Klaushofer K, Rauch F. Evidence that abnormal high bone mineralization in growing children with osteogenesis imperfecta is not associated with specific collagen mutations. *Calcified Tissue International*. 2008;82(4):263-70.
33. Fratzl P, Paris O, Klaushofer K, Landis WJ. Bone mineralization in an osteogenesis imperfecta mouse model studied by small-angle x-ray scattering. *Journal of Clinical Investigation*. 1996;97(2):396-402.
34. Camacho NP, Landis WJ, Boskey AL. Mineral changes in a mouse model of osteogenesis imperfecta detected by Fourier transform infrared microscopy. *Connective Tissue Research*. 1996;35(1-4):259-65.
35. Vanleene M, Porter A, Guillot PV, Boyde A, Oyen M, Shefelbine S. Ultra-structural defects cause low bone matrix stiffness despite high mineralization in osteogenesis imperfecta mice. *Bone*. 2012;50(6):1317-23.

36. Vetter U, Eanes ED, Kopp JB, Termine JD, Robey PG. Changes in apatite crystal size in bones of patients with osteogenesis imperfecta. *Calcified Tissue International*. 1991;49(4):248-50.
37. Vetter U, Weis MA, Morike M, Eanes ED, Eyre DR. Collagen cross-links and mineral crystallinity in bone of patients with osteogenesis imperfecta. *Journal of Bone and Mineral Research*. 1993;8(2):133-7.
38. Camacho NP, Hou L, Toledano TR, Ilg WA, Brayton CF, Raggio CL, et al. The material basis for reduced mechanical properties in oim mice bones. *Journal of Bone and Mineral Research*. 1999;14(2):264-72.
39. Coleman RM, Aguilera L, Quinones L, Lukashoya L, Poirier C, Boskey A. Comparison of bone tissue properties in mouse models with collagenous and non-collagenous genetic mutations using FTIRI. *Bone*. 2012;51(5):920-8.
40. Cassella JP, Barrie PJ, Garrington N, Ali SY. A Fourier transform infrared spectroscopic and solid-state NMR study of bone mineral in osteogenesis imperfecta. *Journal of Bone and Mineral Metabolism*. 2000;18(5):291-6.
41. Lindahl K, Barnes AM, Fratzl-Zelman N, Whyte MP, Hefferan TE, Makareeva E, et al. COL1 C-Propeptide Cleavage Site Mutations Cause High Bone Mass Osteogenesis Imperfecta. *Human Mutation*. 2011;32(6):598-609.
42. Carriero A, Zimmermann EA, Paluszny A, Tang SY, Bale H, Busse B, et al. How tough is brittle bone? Investigating osteogenesis imperfecta in mouse bone. *Journal of bone and mineral research : the official journal of the American Society for Bone and Mineral Research*. 2014;29(6):1392-401.

43. Cassella JP, Stamp TCB, Ali SY. A morphological and ultrastructural study of bone in osteogenesis imperfecta. *Calcified Tissue International*. 1996;58(3):155-65.
44. Rauch F, Travers R, Parfitt AM, Glorieux FH. Static and dynamic bone histomorphometry in children with osteogenesis imperfecta. *Bone*. 2000;26(6):581-9.
45. Baron R, Gertner JM, Lang R, Vignery A. Increased bone turnover with decreased bone-formation by osteoblasts in children with osteogenesis imperfecta tarda. *Pediatric Research*. 1983;17(3):204-7.
46. Kalajzic I, Terzic J, Rumboldt Z, Mack K, Naprta A, Ledgard F, et al. Osteoblastic response to the defective matrix in the osteogenesis imperfecta murine (oim) mouse. *Endocrinology*. 2002;143(5):1594-601.
47. McCarthy EF, Earnest K, Rossiter K, Shapiro J. Bone histomorphometry in adults with type IA osteogenesis imperfecta. *Clinical Orthopaedics and Related Research*. 1997(336):254-62.
48. Lund AM, Hansen M, Kollerup G, Juul A, Teisner B, Skovby F. Collagen-derived markers of bone metabolism in osteogenesis imperfecta. *Acta Paediatrica*. 1998;87(11):1131-7.
49. Sarathchandra P, Pope FM, Kayser MV, Ali SY. A light and electron microscopic study of osteogenesis imperfecta bone samples, with reference to collagen chemistry and clinical phenotype. *Journal of Pathology*. 2000;192(3):385-95.
50. Rauch F, Lalic L, Roughley P, Glorieux FH. Relationship Between Genotype and Skeletal Phenotype in Children and Adolescents with Osteogenesis Imperfecta. *Journal of Bone and Mineral Research*. 2010;25(6):1367-74.

51. Carriero A, Doube M, Vogt M, Busse B, Zustin J, Levchuk A, et al. Altered lacunar and vascular porosity in osteogenesis imperfecta mouse bone as revealed by synchrotron tomography contributes to bone fragility. *Bone*. 2014;61:116-24.
52. Jameson JR, Albert CI, Busse B, Smith PA, Harris GF, editors. 3D micron-scale imaging of the cortical bone canal network in human osteogenesis imperfecta (OI). Conference on Medical Imaging - Biomedical Applications in Molecular, Structural, and Functional Imaging; 2013 Feb 10-13; Lake Buena Vista, FL2013.
53. Wasserman N, Yerramshetty J, Akkus O. Microcracks colocalize within highly mineralized regions of cortical bone tissue. *European Journal of Morphology*. 2005;42(1-2):43-51.
54. Elliott JC. Structure and Chemistry of the Apatites and Other Calcium Orthophosphates. Amsterdam, Netherlands: Elsevier Science BV; 1994.
55. Legros R, Balmain N, Bonel G. Structure and composition of the mineral phase of periosteal bone. *Journal of Chemical Research-S*. 1986(1):8-9.
56. Bogan R, Riddle RC, Li Z, Kumar S, Nandal A, Faugere M-C, et al. A Mouse Model for Human Osteogenesis Imperfecta Type VI. *Journal of Bone and Mineral Research*. 2013;28(7):1531-6.
57. Camacho NP, Carroll P, Raggio CL. Fourier transform infrared imaging spectroscopy (FT-IRIS) of mineralization in bisphosphonate-treated oim/oim mice. *Calcified Tissue International*. 2003;72(5):604-9.
58. Spevak L, Flach CR, Hunter T, Mendelsohn R, Boskey A. Fourier Transform Infrared Spectroscopic Imaging Parameters Describing Acid Phosphate Substitution in Biologic Hydroxyapatite. *Calcified Tissue International*. 2013;92(5):418-28.

59. Boskey AL, Verdelis K, Spevak L, Lukashova L, Beniash E, Yang X, et al. Mineral and matrix changes in Brtl/+ teeth provide insights into mineralization mechanisms. *BioMed research international*. 2013;2013:295812-.
60. Gu C, Katti DR, Katti KS. Photoacoustic FTIR spectroscopic study of undisturbed human cortical bone. *Spectrochimica acta Part A*. 2013;103:25-37.
61. Gu C, Katti DR, Katti KS. Dynamic mechanical behavior of undisturbed and demineralized human cortical bone measured by nanoindentation. *Bioinspired, Biomimetic and Nanobiomaterials*. 2014;3:1-11.
62. Traub W, Arad T, Vetter U, Weiner S. Ultrastructural studies of bones from patients with osteogenesis imperfecta. *Matrix Biology*. 1994;14(4):337-45.
63. Boskey A, Mendelsohn R. Infrared analysis of bone in health and disease. *J Biomed Opt*. 2005;10(3):031102.
64. Reyes-Gasga J, Garcia-Garcia R, Arellano-Jimenez MJ, Sanchez-Pastenes E, Tiznado-Orozco GE, Gil-Chavarria IM, et al. Structural and thermal behaviour of human tooth and three synthetic hydroxyapatites from 20 to 600 degrees C. *Journal of Physics D-Applied Physics*. 2008;41(22).
65. Kourkoumelis N, Tzaphlidou M. Spectroscopic Assessment of Normal Cortical Bone: Differences in Relation to Bone Site and Sex. *TheScientificWorldJournal*. 2010;10:402-12.
66. Moore WH, Krimm S. Vibrational analysis of peptides, polypeptides, and proteins.1. polyglycine I. *Biopolymers*. 1976;15(12):2439-64.
67. Garip S, Severcan F. Determination of simvastatin-induced changes in bone composition and structure by Fourier transform infrared spectroscopy in rat animal model. *Journal of Pharmaceutical and Biomedical Analysis*. 2010;52(4):580-8.

68. Cheng ZH, Yasukawa A, Kandori K, Ishikawa T. FTIR study of adsorption of CO₂ on nonstoichiometric calcium hydroxyapatite. *Langmuir*. 1998;14(23):6681-6.
69. Bertoni E, Bigi A, Cojazzi G, Gandolfi M, Panzavolta S, Roveri N. Nanocrystals of magnesium and fluoride substituted hydroxyapatite. *Journal of Inorganic Biochemistry*. 1998;72(1-2):29-35.
70. Kumar R, Prakash KH, Cheang P, Gower L, Khor KA. Chitosan-mediated crystallization and assembly of hydroxyapatite nanoparticles into hybrid nanostructured films. *Journal of the Royal Society Interface*. 2008;5(21):427-39.
71. Singh K, Lee KS, Lee D, Kim YK, Kim KC. Spectroscopic techniques as a diagnostic tool for early detection of osteoporosis. *Journal of Mechanical Science and Technology*. 2010;24(8):1661-8.
72. Socrates G. *Infrared and Raman Characteristic group frequencies: tables and charts*. 3rd ed. Chichester: John Wiley & Sons; 2004.
73. Farlay D, Panczer G, Rey C, Delmas PD, Boivin G. Mineral maturity and crystallinity index are distinct characteristics of bone mineral. *Journal of Bone and Mineral Metabolism*. 2010;28(4):433-45.
74. Kazanci M, Roschger P, Paschalis EP, Klaushofer K, Fratzl P. Bone osteonal tissues by Raman spectral mapping: Orientation-composition. *Journal of Structural Biology*. 2006;156(3):489-96.
75. Paschalis EP, DiCarlo E, Betts F, Sherman P, Mendelsohn R, Boskey AL. FTIR microspectroscopic analysis of human osteonal bone. *Calcified Tissue International*. 1996;59(6):480-7.

76. Paschalis EP, Betts F, DiCarlo E, Mendelsohn R, Boskey AL. FTIR microspectroscopic analysis of normal human cortical and trabecular bone. *Calcified Tissue International*. 1997;61(6):480-6.
77. Magne D, Weiss P, Bouler JM, Laboux O, Daculsi G. Study of the maturation of the organic (type I collagen) and mineral (nonstoichiometric apatite) constituents of a calcified tissue (dentin) as a function of location: A Fourier transform infrared microspectroscopic investigation. *Journal of Bone and Mineral Research*. 2001;16(4):750-7.
78. Rey C, Shimizu M, Collins B, Glimcher MJ. Resolution-enhanced Fourier-transform infrared-spectroscopy study of the environment of phosphate ion in the early deposits of a solid-phase of calcium-phosphate in bone and enamel and their evolution with age.2. investigations in the NU-3 PO₄ domain. *Calcified Tissue International*. 1991;49(6):383-8.
79. Rey C, Hina A, Tofighi A, Glimcher MJ. Maturation of poorly crystalline apatites: Chemical and structural aspects in vivo and in vitro. *Cells and Materials*. 1995;5(4):345-56.
80. Wopenka B, Pasteris JD. A mineralogical perspective on the apatite in bone. *Materials Science & Engineering C-Biomimetic and Supramolecular Systems*. 2005;25(2):131-43.
81. Harper RA, Posner AS. Measurement of non-crystalline calcium phosphate in bone mineral. *Proceedings of the Society for Experimental Biology and Medicine*. 1966;122(1):137-&.
82. Handschin RG, Stern WB. X-ray -diffraction studies on the lattice perfection of human bone apatite (crista-iliaca). *Bone*. 1995;16(4):S355-S63.
83. Bonar LC, Roufosse AH, Sabine WK, Grynepas MD, Glimcher MJ. X-ray -diffraction studies of the crystallinity of bone-mineral in newly synthesized and density fractionated bone. *Calcified Tissue International*. 1983;35(2):202-9.

84. Cazalbou S, Combes C, Eichert D, Rey C. Adaptive physico-chemistry of bio-related calcium phosphates. *Journal of Materials Chemistry*. 2004;14(14):2148-53.
85. Wu YT, Ackerman JL, Kim HM, Rey C, Barroug A, Glimcher MJ. Nuclear magnetic resonance spin-spin relaxation of the crystals of bone, dental enamel, and synthetic hydroxyapatites. *Journal of Bone and Mineral Research*. 2002;17(3):472-80.
86. Rey C, Shimizu M, Collins B, Glimcher MJ. Resolution-enhanced Fourier-transform infrared-spectroscopy study of the environment of phosphate ion in the early deposits of a solid-phase of calcium-phosphate in bone and enamel and their evolution with age.2. investigations in the NU-3 PO₄ domain. *Calcified Tissue International*. 1991;49(6):383-8.
87. Jager C, Welzel T, Meyer-Zaika W, Epple M. A solid-state NMR investigation of the structure of nanocrystalline hydroxyapatite. *Magnetic Resonance in Chemistry*. 2006;44(6):573-80.
88. Jones SJ, Glorieux FH, Travers R, Boyde A. The microscopic structure of bone in normal children and patients with osteogenesis imperfecta: A survey using backscattered electron imaging. *Calcified Tissue International*. 1999;64(1):8-17.
89. Fedarko NS, Davis P, Frazier CR, Burrill MJ, Fergusson V, Tayback M, et al. Cell-proliferation of human fibroblasts and osteoblasts in osteogenesis imperfecta - influence of age. *Journal of Bone and Mineral Research*. 1995;10(11):1705-12.
90. Gioia R, Panaroni C, Besio R, Palladini G, Merlini G, Giansanti V, et al. Impaired Osteoblastogenesis in a Murine Model of Dominant Osteogenesis Imperfecta: A New Target for Osteogenesis Imperfecta Pharmacological Therapy. *Stem Cells*. 2012;30(7):1465-76.
91. Uveges TE, Collin-Osdoby P, Cabral WA, Ledgard F, Goldberg L, Bergwitz C, et al. Cellular Mechanism of Decreased Bone in Brl Mouse Model of OI: Imbalance of Decreased

Osteoblast Function and Increased Osteoclasts and Their Precursors. *Journal of Bone and Mineral Research*. 2008;23(12):1983-94.

92. Li H, XiDelaney, JohnFranceschetti, TizianaBilic-Curcic, InesKalinovsky, JudyLorenzo, Joseph A.Grcevic, DankaRowe, David W.Kalajzic, Ivo. Immature Osteoblast Lineage Cells Increase Osteoclastogenesis in Osteogenesis Imperfecta Murine. *American Journal of Pathology*. 2010;176(5):2405-13.

93. Nakahama K-i. Cellular communications in bone homeostasis and repair. *Cellular and Molecular Life Sciences*. 2010;67(23):4001-9.

94. Gomez-Morales J, Iafisco M, Delgado-Lopez JM, Sarda S, Drouet C. Progress on the preparation of nanocrystalline apatites and surface characterization: Overview of fundamental and applied aspects. *Progress in Crystal Growth and Characterization of Materials*. 2013;59(1):1-46.

95. George A, Veis A. Phosphorylated Proteins and Control over Apatite Nucleation, Crystal Growth, and Inhibition. *Chemical Reviews*. 2008;108(11):4670-93.

96. Fedarko NS, Moerike M, Brenner R, Robey PG, Vetter U. Extracellular-matrix formation by osteoblasts from patients with osteogenesis imperfecta. *Journal of Bone and Mineral Research*. 1992;7(8):921-30.

97. Gehron Robey P. The biochemistry of bone. *Endocrinology and metabolism clinics of North America*. 1989;18(4):858-902.

98. Termine JD, Kleinman HK, Whitson SW, Conn KM, McGarvey ML, Martin GR. Osteonectin, a bone-specific protein linking mineral to collagen. *Cell*. 1981;26(1):99-105.

CHAPTER 4. NANOMECHANICAL PROPERTIES OF UNDISTURBED HUMAN NORMAL AND OSTEOGENESIS IMPERFECTA CORTICAL BONES

This chapter presents nanomechanical properties of undisturbed healthy and OI human cortical bones measured by modulus mapping and in situ FE-SEM nanoindentation.

4.1. Introduction

Nanoindentation has been widely utilized to examine elastic modulus and hardness of bone (1-7). The reported nanoindentation values for human femur vary from 16.58 to 26.6 GPa for elastic modulus, and ranging from 234 to 840 MPa for hardness (4, 5, 8-11). The nanoindentation depth in these studies is at least 150 nm. Over that last 15 years, modulus mapping technique, is utilized to study the surface modulus of materials for small areas with high spatial resolution. Modulus mapping measures the elastic properties of a material surface by applying extremely shallow displacements (2 to 3 nm). Detailed descriptions of the principle of modulus mapping can be found in the literature (12, 13). This technique has been utilized to measure mechanical properties of trabecular bone of osteoporotic rats (14), bone matrix of mice (15), trabecular bone of glucocorticoid-treated mice (14-16), bone nodules (17), and human trabecular bone extracted from proximal femur (18). Bone is anisotropic and heterogeneous, so the local variations in mechanical properties detectable with this technique play an important role in controlling the mechanical behavior at macroscopic length scales. Hence, in this work, modulus mapping technique is used to examine the surface mechanical property variation of human cortical bones in longitudinal and transverse planes. We also attempt to reveal the relationship between structure and mechanical properties at the nanometer level.

Other than examining surface properties, nanoindentation generally measures the bulk properties of material. The structure and mechanical properties of bone vary markedly at different sites due to the complex constituents and heterogeneity. In order to investigate mechanical properties of bone, typically hundreds of indents are required. Also, the scanning process using a traditional triboscope instrument is time consuming. In contrast, in situ field emission-scanning electron microscopy (FE-SEM) nanoindentation provides a new tool to investigate the mechanical properties of materials with simultaneous imaging and precise positioning of the indenter. A quantitative nanoindentation system integrated into a high-resolution SEM was developed recently (19) and the real-time observation of the nanoindentation test also allows for visualization of certain material deformation behaviors such as pileup, sink-in and delamination. The in situ FE-SEM nanoindentation technique has been utilized to study the mechanical behavior of several metallic and semiconductive materials (19-29), and nacre (30) as well. Here we use SEM nanoindentation to investigate the nanomechanical properties of human cortical bones.

Bone with Osteogenesis imperfecta (OI) disease is characterized by the fragility, primarily due to a causative variant in one of the two structural genes (COL1A1 or COL1A2) for the type I procollagens. The amount of collagen from OI bone is observed to be less than that from age-matched normal controls (31). The distribution of D-periodic spacing values was found to be distinctive between *Brtl/+* (a kind of OI type) mouse phenotype and normal one (32, 33). In addition, smaller, less well aligned, highly packed mineral crystals with decreased crystallinity, and higher mineral/matrix ratio are found in OI bone (34-40). The heterogeneity of OI bone mineralization in literature show different trends: increased heterogeneity in high bone mineralization density (BMD) OI (41) and reduced heterogeneity in OI-I patients (42). However,

the details of extrafibrillar mineral of bone and the nanomechanical properties of OI bone are not well understood. Here, in order to have a better understanding of the extrafibrillar mineral and the arrangements of mineral and collagen in the near-surface area, both modulus mapping and in situ FE-SEM nanoindentation techniques have been utilized to observe the nanomechanical properties of undisturbed normal and OI bone.

Mechanical properties of bone are orders of magnitude better than a simple sum of the individual components of bone (43) due to the interactions among the organic phase, mineral phase, and noncollagenous proteins(44, 45). Research shows that collagen alone fails to bind calcium or phosphate ions of mineral. However, the stereochemical configurations and charges provided by specific amino acid residues of collagen can bind calcium and phosphate ions and likely provide sufficient closeness to induce ion interaction (46). In addition, the interaction between collagen and mineral is mediated by noncollagenous acidic proteins which are bound to the triple helices of collagen (47). Our group's modeling work demonstrated that the mechanical behavior of collagen is significantly influenced by collagen-mineral interaction as well as collagen-water-mineral interactions (45, 48, 49). Nevertheless, the commonly used pretreatment on bone samples such as dehydration affects the interactions and mechanical properties of bone (50, 51). Furthermore, The indentation moduli of bone specimens were reported to increase from 11% to 28% after dehydration (6, 50, 52, 53), with additional increase after embedding (53). Therefore, in the present work, "undisturbed" bone specimens are used to study their nanomechanical properties.

4.2. Materials and Methods

4.2.1. Materials

The normal human femur (no apparent metabolic bone disease record, 27 years old, female) and OI human tibia (no apparent metabolic bone disease record, 22 years old, female with pregnancy experience) were both obtained from National Disease Research Interchange, PA and stored in a freezer at -70°C . The OI type is putative type I, the mildest type, because the person had a height of 67 inches and weight of 180lb. One 20-mm-thick transverse section was cut from the mid-diaphysis of the femur with a low-speed diamond saw. Then, it was further cut with a low-speed diamond-wafering blade (Buehler, Isomet, Lake Bluff, IL) to obtain specimens with thickness of about 1 mm in both transverse and longitudinal directions (Figure 4.1). Marrow and flesh were removed by scraping with a ceramic knife and then the bone was washed with deionized (DI) water at room temperature in approximately 10 minutes to avoid deterioration of bone.

In order to perform modulus mapping and nanoindentation, the specimens were ground with silicon carbide paper (Buehler, 600, 800 and 1200 grit) and polished using a series of diamond compound paste (Buehler, 3 μm , 1 μm , 0.25 μm) on cloth and finished by polishing with 0.02 μm non-crystallizing colloidal silica polishing suspension. After each polishing step, the specimens were ultrasonically cleaned in DI water for 30 seconds (the total rinsing time was limited about 3.5 minutes to avoid demineralization (54)).

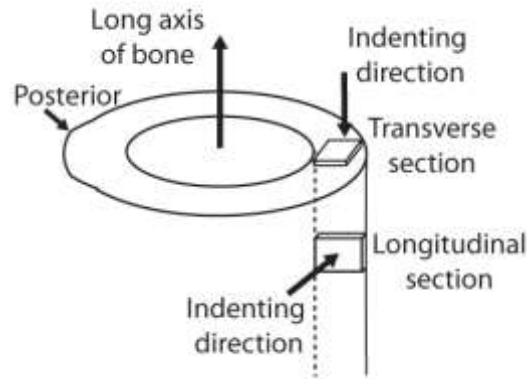


Figure 4.1. Schematic of cutting bone.

In order to perform modulus mapping and nanoindentation, the specimens were ground with silicon carbide paper (Buehler, 600, 800 and 1200 grit) and polished using a series of diamond compound paste (Buehler, 3 μm , 1 μm , 0.25 μm) on cloth and finished by polishing with 0.02 μm non-crystallizing colloidal silica polishing suspension. After each polishing step, the specimens were ultrasonically cleaned in DI water for 30 seconds (the total rinsing time was limited about 3.5 minutes to avoid demineralization (54)).

4.2.2. Methods

Modulus mapping experiments were conducted on a Hysitron triboscope nanomechanical instrument (Minneapolis, MN), equipped with a Nanoscope IIIa controller (Veeco Metrology, Santa Barbara, CA) with a Berkovich (three-sided pyramid, 100–200 nm tip radius) diamond indenter tip. Modulus maps of the surface of bone specimens were acquired by applying a quasi-static force of 3 μN with a superimposed 1–2 μN sinusoidal force at a frequency of 200 Hz. The sinusoidal dynamic force was adjusted while scanning to get AC displacement amplitude of approximately 1nm. Each of the images created have a pixel resolution of 256 \times 256, meaning 65,536 individual modulus values are acquired. Tip shape calibration was performed using a

standard fused quartz sample of known elastic modulus. During the performance of experiments, dry helium was kept flowing into the experimental chamber (Figure 4.2) to prevent bacteria growth as much as possible (55). Although carefully polished, many holes still existed in the bone specimens such as canals, lacunae, and canaliculi; the maps with these holes were excluded from the results.



Figure 4.2. Modulus mapping instrument

Nanoindentation tests were performed with a Hysitron PI-85 nanomechanical instrument with a Berkovich tip made of boron-through-doped diamond (Minneapolis, MN), which was installed in a high-resolution Field Emission Scanning Electron Microscope (FE-SEM, mode: Jeol JSM-7600F). Detailed descriptions of the principle of this instrument can be found in the literature (19). The probe was also calibrated on fused quartz. Lower secondary electron images (LEI) were obtained by FE-SEM while nanoindentation was performed.

The elastic modulus and hardness of bone are determined by using the common method developed by Oliver and Pharr (56). The Young's modulus is calculated using the following equation (4.1):

$$\frac{1}{E_r} = \frac{(1 - \nu^2)}{E} + \frac{(1 - \nu_i^2)}{E_i} \quad (4.1)$$

where E is the elastic modulus, ν is Poisson's ratio, s and i refer to sample and indenter tip material, respectively. E_r is the reduced modulus which can be obtained from indentation curve; ν_s of bone is set to 0.3; E_i and ν_i are the same quantities for the diamond indenter: $E_i = 1141$ GPa, $\nu_i = 0.07$.

In situ FE-SEM nanoindentation was performed with static load control; $50 \mu\text{N}$ was applied as the load for the samples on the transverse section plane (Figure 4.3a). An interlamellar cement band is obviously seen in the figure and separates the osteon and interstitial lamellae. Thirty indents were performed inside the osteon, and ten indents outside the osteon. For the samples on the longitudinal plane (Figure 4.3b), $15 \mu\text{N}$, $50 \mu\text{N}$, and $100 \mu\text{N}$ were applied with thirty indents for each load. To avoid pile-up effect, indent spacing was set about $0.8 \mu\text{m}$. Some surface defects were observed (e.g., pitch, cracks, pop-outs) and excluded from the nanoindentation.

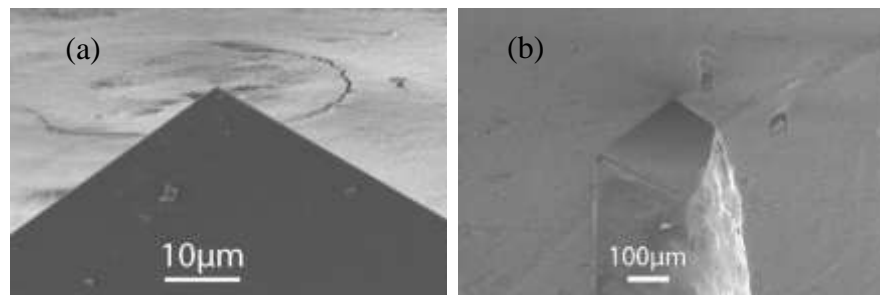


Figure 4.3. In situ HR-SEM nanoindentation were performed on (a) Transverse surface; (b) Longitudinal surface.

4.3. Results

4.3.1. Modulus mapping

The representative modulus maps of normal bone for the longitudinal and transverse sections are shown in Figure 4.4a and Figure 4.4c, respectively. These two figures display the nanomechanical properties from the areas of $2\mu\text{m}\times 2\mu\text{m}$ and $5\mu\text{m}\times 5\mu\text{m}$, respectively. The corresponding elastic modulus values in the longitudinal section are marked as black lines in Figure 4.4b. Figure 4.4d is the square subset of Figure 4.4c. Figure 4.4b shows a periodicity of elastic modulus along the marked line. Every peak spans about 140-167 nm on average in Figure 4.4b. Scale bars in Figure 4.4a and Figure 4.4c display the range of the modulus values in these two maps: 10.86-45.37 GPa and 6.2-120.9 GPa, respectively. The scale bars exhibit large variation among different areas of bone specimens. The bright areas in these figures correspond to the materials with higher modulus values than those dark areas. In Figure 4.4a and Figure 4.4c, the mineralized collagen fibers can also be clearly seen. In Figure 4.4d, the short white line “a” passes through 4 mineralized collagen fibers and the diameter of each mineralized collagen fiber is measured as about 122.42nm. Bright plates and dots are observed in Figure 4.4c. Since they possess greater modulus, they are likely arising from mineral crystals or mineral crystal agglomerates. Several bright plates shown in Figure 4.4d are measured and noted as “b”, “c”, and “d”. The area noted as “b” contains 6 plates. The white line perpendicular to these plates is measured with each periodicity at about 61.98nm. The bright plate noted as “c” has a length of 93.50nm and a width of 40.00nm, while the “d” plate has a length of 100.23nm and a width of 26.98nm. It is also clearly seen that the size of other bright plates or dots are similar or smaller to “c” and “d” plates.

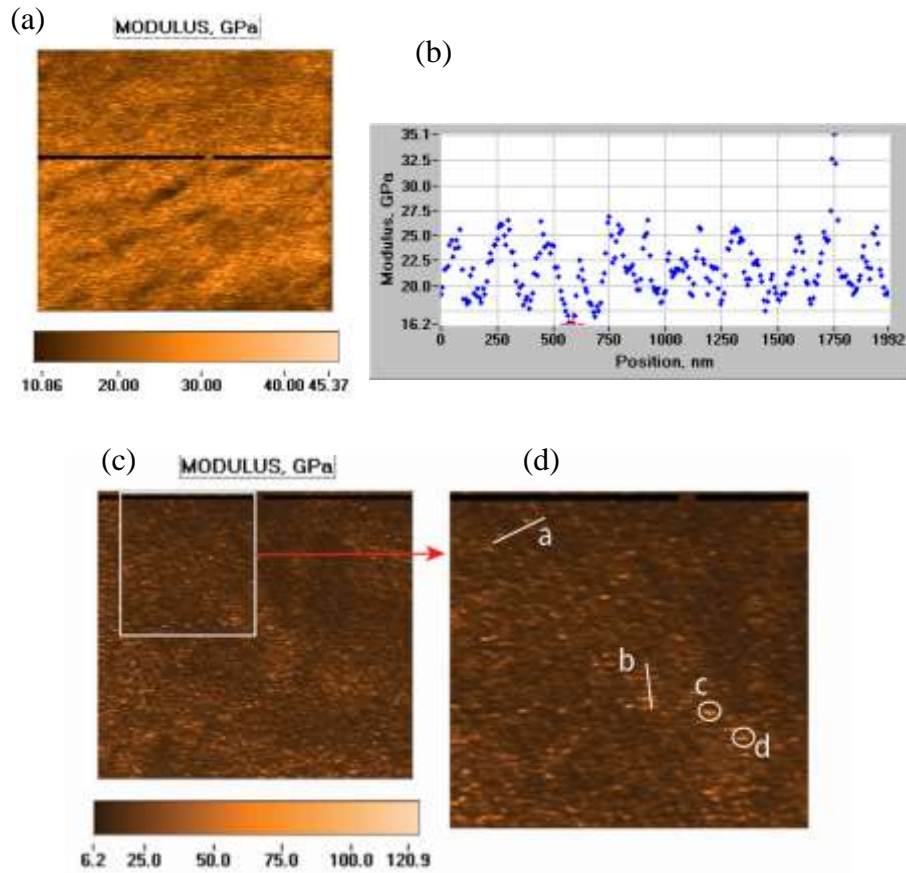


Figure 4.4. Modulus map images and corresponding data of normal human bone. (a) Modulus map image for the longitudinal section, area: $2\mu\text{m}\times 2\mu\text{m}$; (b) Modulus data of the black line in Figure a; (c) Modulus map image for the transverse section, area: $5\mu\text{m}\times 5\mu\text{m}$; (d) The square subset in Figure c.

The representative modulus maps of OI bone for the transverse and longitudinal sections are shown in Figure 4.5a and Figure 4.5d, respectively. Both figures display the nanomechanical properties from $3\mu\text{m}\times 3\mu\text{m}$ areas. Scale bars in Figure 4.5a and Figure 4.5d display the range of the modulus values in these two maps: 20.5-99.8 GPa and 3.0-199.1 GPa, respectively. The scale bars also exhibit great variation among different areas of OI bone specimens. The square subsets of Figure 4.5a and Figure 4.5d are shown in Figure 4.5b and Figure 4.5e. In Figure 5b, the white line crosses 3 mineralized collagen fibers, and the diameter of each fiber is about 78.75 nm.

Similar to the normal bone, Figure 4.5c also shows a periodicity of elastic modulus along the black line from Figure 4.5a. Each peak spans about 176 nm on average, which corresponds to collagen fiber bundles. In Figure 4.5d, many bright dots are distributed and are attributed to bone mineral crystals. The magnified square is shown in Figure 4.5e. The bright dot “a” has a length of 40.19nm and a width of 28.05nm, while the bright dot “b” has a length of 32.10nm and a width of 24.00nm. Plate “C” has a length of 64.19nm and a width of 24.00nm. As compared to normal bone shown in Figure 4.4d, it appears that the mineral crystals in OI bone exhibit more “dot” style instead of “plate” form and the length/width ratio is lower than that of normal bone. Figure 4.5f does not show as obvious periodicity as Figure 4.5c or Figure 4.4b since the black line in Figure 4.5d goes through observable dark lines (observed in Figure 4.5e), which represent pure collagen fibrils or noncollagenous organic matrix areas. As seen in Figure 4.5f, the dots exhibit pit-like appearance in “a” and “b” areas and are consistently about 5.1 GPa.

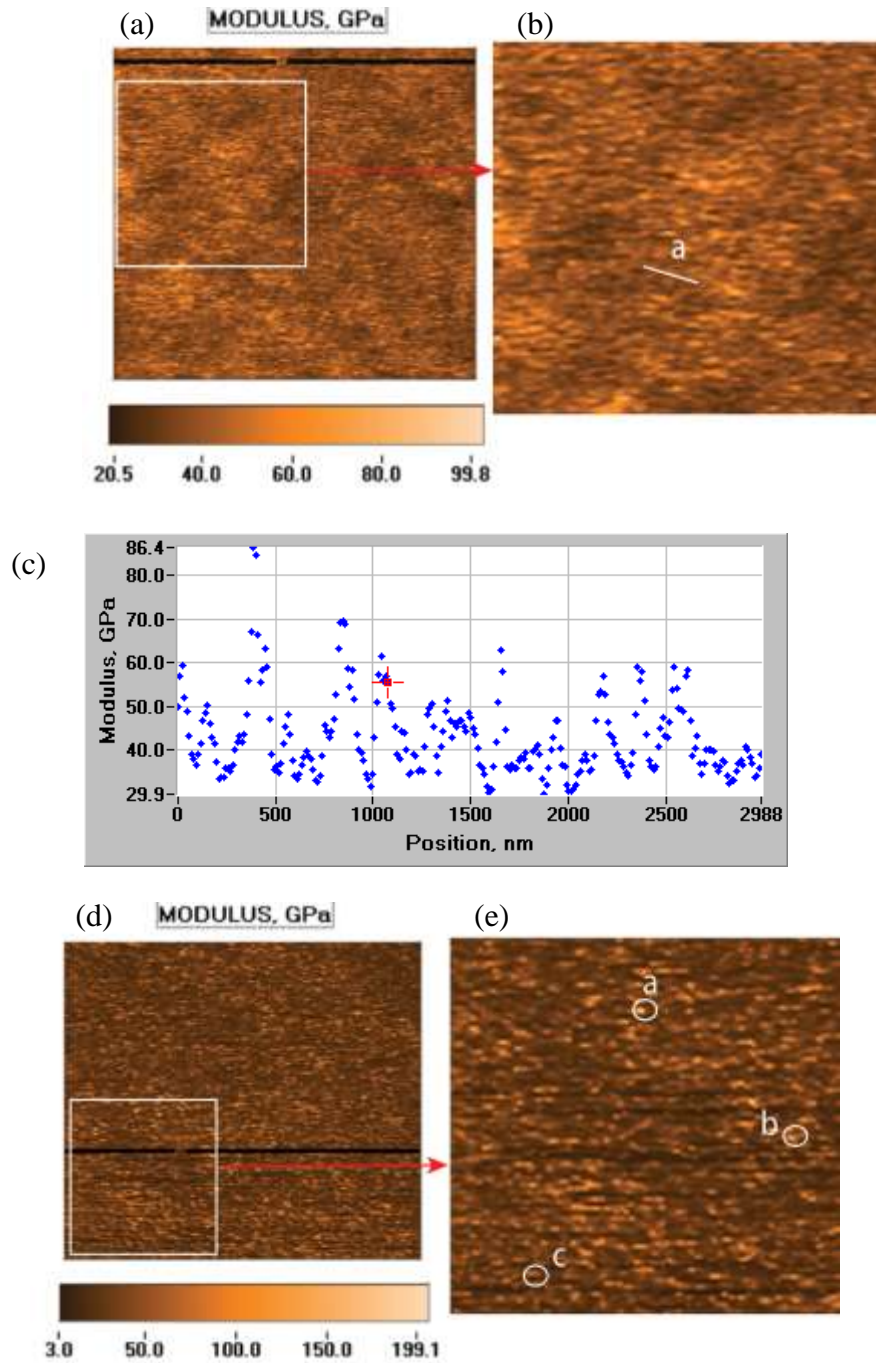


Figure 4.5. Modulus map images and corresponding data of OI human bone. (a) Modulus map image for the transverse section, area: $3\mu\text{m}\times 3\mu\text{m}$; (b) The square subset in Figure a; (c) Modulus data of the black line in Figure a; (d) Modulus map image for the longitudinal section, area: $3\mu\text{m}\times 3\mu\text{m}$; (e) The square subset in Figure c; (f) Modulus data of the black line in Figure d.

The elastic moduli data drawn from all modulus maps (data are from 10 black lines from each modulus map) are shown in Figure 4.6, and the corresponding statistical results are listed in Table 4.1. It is seen that the highest elastic modulus values are in the range of 12.86-22.52 GPa (Q1-Q3) for normal bone, which is in agreement with those data of mineralized collagen fibrils obtained from other techniques such as nanoindentation or acoustic method (57). The median moduli for the longitudinal and transverse sections are 18.69 and 16.79 GPa, respectively. It is also observed in Table 4.1 that the minimum elastic modulus is 2.42 GPa, which is quite similar to that of pure collagen (totally demineralized bone) observed experimentally (58) and through steered molecular dynamics (59, 60). This minimum elastic modulus can be attributed to that from near-pure collagen. The highest elastic modulus is observed to be 189.85 GPa, which can arise from near-pure mineral because the elastic modulus of hydroxyapatite is from 135 GPa (61) to 150 GPa (62-64) and acquired using nanoindentation method. However, values of high elastic moduli above 100 GPa are only present in very few points of all maps.

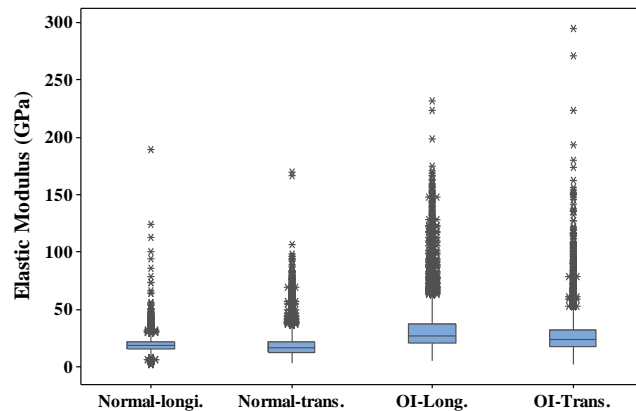


Figure 4.6. Elastic modulus results produced by modulus mapping on the longitudinal and transverse sections of both normal and OI bones. Bars show the median with 25th (Q1) and 75th (Q3) percentiles. The lines perpendicular to the box are whiskers. Upper limit of whisker = $Q3 + 1.5(Q3 - Q1)$; lower limit of whisker = $Q1 - 1.5(Q3 - Q1)$. *outliers of the whisker. (N=35840).

Table 4.1 Statistics of elastic moduli from all modulus maps (Figure 4.4 and Figure 4.5)^a.

Sample		Q1 (GPa)	Median (GPa)	Q3 (GPa)	Whisker (GPa)	Max. (GPa)	Min. (GPa)
Normal	Longitudinal	15.83	18.69	21.57	7.21-30.19	189.85	2.42
	Transverse	12.86	16.79	22.52	3.10-37.00	169.31	3.10
OI	Longitudinal	20.80	27.63	37.78	5.93-63.22	231.65	5.93
	Transverse	18.16	23.68	32.05	2.85-52.85	294.69	2.85

^a N = 35840 for both sections.

From Figure 4.6 and Table 4.1, it is also seen that, as compared to normal bone, OI bone exhibits higher median moduli for the longitudinal and transverse sections at 27.63 and 23.68 GPa, respectively. OI bone also exhibits greater variation of moduli from 18.16 to 37.78 GPa (Q1-Q3) than normal bone. The minimum modulus for OI bone is 2.85 GPa, while the maximum modulus is 294.69 GPa. This maximum modulus of OI bone is much greater than that of normal bone. Therefore, the maximum modulus of OI bone is suspected to be from polishing residues. However, the elastic modulus of one possible polishing residue silicon carbide is 450 GPa, and another possible polishing residue colloidal silica has lower elastic modulus depending on the size (65) than bulk silica, which possesses the elastic modulus of 66.3-74.8 GPa. Therefore, the observed moduli higher than 200 GPa do not originate from the residues from polishing. In addition, after each polishing step, bone specimens were washed using ultrasound. Hence, the moduli over 200 GPa are also suggested to be from bone mineral crystals in OI bone. Overall, the data points above 200 GPa are very rare.

4.3.2. In situ HR-SEM nanoindentation

In order to investigate the nanomechanical properties of bone in the near-surface area, in situ FE-SEM nanoindentation has also been performed on normal and OI bone samples in the

two directions. The representative load displacement curve is shown in Figure 4.7, from which we can see that the loading curve is nonlinear.

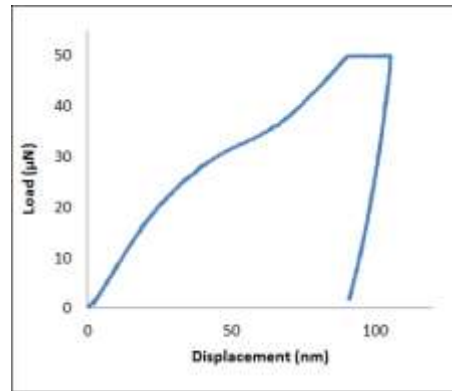


Figure 4.7. Representative load-displacement (L~D) curve for bone sample at peak load of 50 μ N.

In the transverse plane, in addition to the Haversian canal, bone has other holes like lacunae. With SEM imaging, we can effectively avoid indenting those holes. The resulting elastic modulus and hardness from the transverse sections of normal and OI bones are shown in Table 4.2. Each test was performed horizontally with around 1 μ m between neighboring indents. Figure 4.8 shows elastic modulus of normal bone from the vicinity of the Haversian canal toward the interstitial lamellae. Figure 4.8 contains about 8 periodic modulations of properties, and each modulation covers around 5 indents wide (5 μ m). This is in accordance with the thickness of a lamella which is 3-7 μ m (66). From Figure 4.8, it is interestingly found that the lowest values in the osteon are located in the vicinity of the Haversian canal, whereas the highest values are also beside the central area and close to the lowest values. Then the values gradually decrease toward the periphery of the osteon. Table 4.2 also show that, for normal bone, the elastic modulus and hardness of interstitial lamellae are 27.92 and 3.29 GPa, respectively; elastic modulus and hardness of osteonal lamellae are 18.5 and 2.86GPa, respectively. The interstitial lamellae have

higher median elastic modulus and hardness than osteonal lamellae. The reason is that the interstitial lamellae are more mature than the osteonal lamellae. For OI bone, this trend is the same: the elastic modulus and hardness of interstitial lamellae are 30.77 and 1.65 GPa, respectively; elastic modulus and hardness of osteonal lamellae are 25.18 and 1.39 GPa, respectively. The interstitial lamellae also have higher median elastic modulus and hardness than osteonal lamellae. We also observe that the OI bone has higher elastic modulus than normal bone. This phenomenon can be attributed to the higher mineral/matrix ratio of OI bone (67). Nevertheless, regardless of greater elastic moduli, median hardness values of OI bone are lower for the transverse sections than the corresponding normal bone. In addition, it is also observed that the range of elastic moduli of OI bone is greater than that of normal bone.

Table 4.2. Elastic moduli and hardness of normal and OI bones for the transverse sections.

Bone sample		Elastic moduli(GPa)			Hardness(GPa)		
		Min	Median	Max	Min	Median	Max
Normal	Osteonal lamellae	6.78	18.35	54.28	0.34	2.86	18.26
	Interstitial lamellae	15.47	27.92	72.38	2.40	3.29	16.90
OI	Osteonal lamellae	6.51	25.18	138.99	0.21	1.39	13.46
	Interstitial lamellae	1.13	30.77	123.51	0.04	1.65	9.40

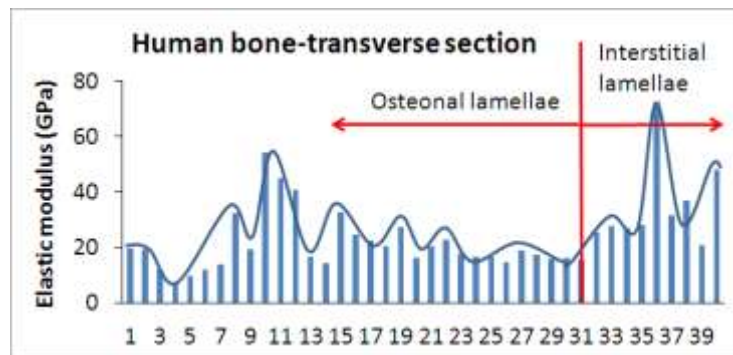


Figure 4.8. Elastic modulus values of human bone in the transverse section.

Table 4.3 shows maximum, minimum, and median values of elastic modulus and hardness of normal and OI bones in the longitudinal section. As seen from the table, for normal bone, the variation of mechanical values with the lower load is greater than that with higher load. This phenomenon has been observed previously in other bio-nanocomposites such as nacre (68). Lower load corresponds to shallow indents reflecting more individual constituent properties rather than bulk properties at deeper indents. As compared to elastic moduli of individual collagen and hydroxyapatite, which is obtained by the modulus mapping technique, the values shown in Table 4.3 are intermediate between the two. At a displacement of around 20 nm at 15 μN loads, all properties detected are from bulk; however, the fraction of the constituents varies greater than that at deeper displacements. For OI bone, the longitudinal section does not have the same trend of a greater elastic modulus at lower load, possibly arising from a more heterogeneous feature of OI bone which makes elastic moduli of the longitudinal section of OI bone more dependent on the indentation site.

Table 4.3. Elastic moduli and hardness of normal and OI bones for the longitudinal sections.

Bone Sample		Elastic modulus (GPa)			Hardness (GPa)		
		Min	Median	Max	Min	Median	Max
Normal	15 μN	10.13	32.87	60.90	0.30	2.14	4.22
	50 μN	8.00	17.57	40.20	0.21	0.88	3.42
	100 μN	8.12	10.86	18.82	0.22	0.36	1.02
OI	15 μN	2.96	15.86	172.17	0.02	1.47	16.92
	50 μN	2.57	15.87	34.04	0.06	1.07	2.37
	100 μN	11.55	27.92	69.72	0.33	1.36	4.27

4.4. Discussion

At the nanometer scale, bone is composed of mineralized collagen fibrils which consist of three tiered triple-helical collagen molecules and mineral particles. They are arranged in a staggered pattern as shown in Figure 4.9 and Figure 4.10. The diameter of a collagen molecule is approximately 1.23 nm, and the length is about 300 nm (46). The diameter of collagen fibers are 50-70 nm, and collagen fiber bundles are 150-250 nm (69). The typical size of a bone mineral crystal is about 50*25*3 nm (69). This size is determined from TEM imaging experiments (70). The size of the bright plates or dots shown in Figure 4.4c are on the same length scale as this size. Therefore, it is reasonable to suggest that these bright plates or dots are bone mineral crystals or mineral crystal aggregates. Since the displacement in modulus mapping is only 2-3 nm, the material under the tip is probed within the elastic region. Due to this small scale, the properties of pure collagen molecules and mineral crystal are possibly detected with this technique. However, according to the modulus maps, very few points have values exceeding 100 GPa. This indicates that, although there is a large amount of mineral in bone (e.g., in bone, the mineral component accounts for nearly 2/3 of the dry weight and about half volume of bone matrix (71); 70-75% of the mineral might be extrafibrillar (72)), in these two directions pure mineral is hardly detected. This phenomenon may arise from the following reasons: (1) Intrafibrillar mineral crystal is aligned as shown in Figure 3.9. From both longitudinal and transverse surfaces only the edge of mineral crystal appears, which is about 3nm thick and hardly detected with the indenter with the radius of hundreds of nanometer; however, since the mineralized collagen fibrils are not accurately aligned along the c-axis of bone, some of the mineral crystals are still seen. Sasaki et al. (73) proposed a model for the arrangement of extrafibrillar mineral as a crust around collagen fibrils based on AFM study. The crust was said

to be usually divided into a few pieces by intercalation of collagen microfibrils. The extrafibrillar mineral volume is also found to be at least 60% of the total and cemented together by noncollagenous organic matter (73, 74). In addition, bone mineral is nonstoichiometric overall, and the mineral crystals are found to contain significant and varying amounts of CO_3^{2-} and HPO_4^{2-} ions (75). There is a substantial fraction of the protonated phosphates (HPO_4^{2-}) situated on the surfaces of the bone mineral crystals and the concentration of unprotonated phosphates (PO_4^{3-}) within the apatitic lattice increases toward the center of the crystal as shown by ^{31}P -NMR spin-spin relaxation studies (76). Therefore, because of the significant difference of the moduli between collagen fibrils and mineral crystals, the modulus maps can reveal the arrangement of near-pure organic matrix (collagen or non-collagenous proteins), mineralized collagen fiber bundles which combines collagen fibrils with intrafibrillar mineral, and mineral crystals with nonstoichiometric parts. Figure 4.4a, 4c, 5a, and Figure 5d, clearly display these arrangements.

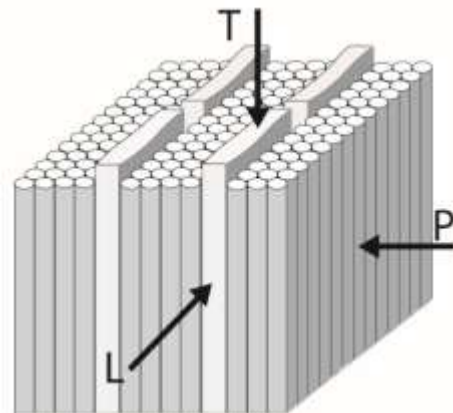


Figure 4.9. Schematic illustration of the mineralized collagen fibril (not drawn to scale). Plate-like mineral crystals are sandwiched between layers of collagen molecules. P, T, L refer to the periosteal, transverse and longitudinal planes, respectively, perpendicular to the corresponding arrows. Transverse plane is normal to the bone long axis and periosteal plane is parallel to the natural outer surface of the bone (adapted from (77)).

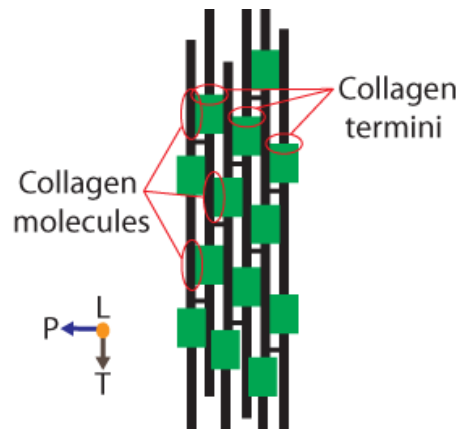


Figure 4.10. Arrangement of collagen and mineral, black lines represent collagen molecules; green squares represent mineral particles (not drawn to scale).

Figure 4.4 and Figure 4.5 display the same trends of normal and OI bones: (1) the great variation of modulus, which originates from the different composition and their arrangement of bone at different sites; (2) the median modulus of the longitudinal sections are greater than the transverse sections. The differences between normal and OI bones include: (1) normal bone appears more compact than OI bone since OI bone modulus map consists of black lines indicating low moduli as displayed in Figure 4.5d; (2) the diameter of a collagen fiber in normal (122.42 nm) is greater than that in OI bone (78.75 nm), but the size of the collagen fiber bundles are similar in these two bones (140-167 nm in normal bone and around 176nm in OI bone); (3) OI mineral crystals are smaller than normal mineral crystals, and OI mineral crystal is less heterogeneous. This conclusion is in accordance with another study which shows reduced heterogeneity of bone mineral in OI-I patients (42). In our previous work (Chapter 3), XRD data of mineral crystal of normal and OI bones are observed to be not significantly different. However, in this work, the plates or dots in modulus maps reflect varying mechanical properties. Therefore, the OI bone mineral crystal may contain some mineral with low nanomechanical

properties outside of the surface; (4) OI bone has higher median elastic modulus than normal bone, probably due to higher mineral/matrix ratio (35, 39, 40) and higher elastic modulus of mineral crystal of OI bone as seen in Figure 4.5.

In the modulus mapping experiments, as mentioned earlier, the median elastic moduli of the longitudinal sections are greater than those of the transverse sections for both normal and OI bones. However, in the in situ FE-SEM nanoindentation experiments, when applying the same load as $50\mu\text{N}$, the elastic moduli of the longitudinal sections are smaller than either those of osteonal lamellae or interstitial lamellae for normal and OI bones. The latter result is quite reasonable since much of the nanoindentation and microindentation studies in literature indicate that bone has generally a higher elastic modulus in its longitudinal compared to its transverse direction (6, 77-80). As shown in Figure 4.9, in both directions, the indenter encounters the mineral crystal layers edge-on, but because the Young's modulus of unmineralized collagen fibrils is 1.43 times greater than that perpendicular to the fibril axes (81), the elastic modulus of bone in the longitudinal direction is generally greater than that in the transverse direction, as explained in the literature (77). In the modulus mapping experiments, the result is the opposite possibly because at the modulus mapping scale which only probes 2-3 nm depth, the composition of collagen and mineral as well as their interactions should be taken into account. In our previous work (82), we have discussed that the longitudinal section surface contains extensive interactions between collagen molecules and mineral surface while the transverse section surface contains extensive interactions between collagen termini and mineral surface (Figure 3.10). Since collagen molecules are comprised of about 68% uncharged amino acid, and collagen termini are both charged groups which possess stronger interactions with exchangeable ions contained within mineral surface, the mineral in the longitudinal section surface appears to

be more stoichiometric than that in the transverse section surface, as suggested by FTIR spectra. Therefore, the elastic modulus of the longitudinal section surface might also be greater than that of the transverse section surface. In a previous modeling study, the collagen pulled parallel to the mineral (100) surface (periosteal plane) is found to have a higher elastic modulus than that when the collagen pulled perpendicular to (001) mineral surface (transverse plane) in the proximity of mineral (49). This is different from the results on microindentation on bone (77), indicating that, at nanoscale, the interaction between collagen and mineral plays a more important role than at larger scales. Another modeling study (83) also reflects this scale issue by suggesting that: the nonbonded interactions have a far more important role than hydrogen bonds in the mechanics of full-length collagen; however, for short-length collagen models, interchain hydrogen bonds dominate the conformation.

A periodicity of about $5\mu\text{m}$ in accordance with the width of lamella is seen in Figure 3.7. This periodic modulation was also found in the literature (84) and was understood to arise from a variable fiber orientation and mineral content which helps prevent incipient microcracks in osteons from developing into catastrophic failures. Interstitial lamellae is made of the remnants of the remodeled old osteons or primary bone tissue, so in general, osteons are less mineralized and less stiff than interstitial lamellae. Therefore, the elastic modulus of interstitial lamellae is significantly greater than that of osteonal lamellae (5, 6). Our results agree with this phenomenon. There are different mechanical trends when increasing the distance from the center of osteon toward the periphery. A decreasing trend was obtained from osteons in human femur samples (5). Meanwhile, decreasing osteonal mineralization was observed with distance from the central Haversian canal from microradiographic imaging (85) and backscattered electron imaging (86). Though the work from Gupta's group did not show significant variation between

osteonal lamellae, from the diagrams shown in the paper (84), it can be observed that the largest indentation modulus is at the location near the Haversian canal, just as seen in Figure 4.8. This highly mineralized inner ring (also called a calcification “halo”) adjacent to the Haversian canal present in old completed osteons was reported as having high mineral density (87) and great hardness (88) since it contains more amorphous calcium phosphate. On the other hand, the opposite trend was observed with FTIRM from human iliac crest biopsies (89, 90) and with Raman from baboon femur samples (91). Both of the spectra showed an increase in the mineral:organic ratio with increasing distance from the Haversian canal. Increasing elastic modulus with distance from the osteonal center toward the periphery was also found as probed by nanoindentation (91). Therefore, further study is needed to clarify the debate.

The comparison of nanomechanical properties between OI and normal bones is mixed for the longitudinal sections (Table 4.3) because of more site-specific feature of OI bone. In contrast, the comparison of the nanomechanical properties of the normal and OI cortical bones for the transverse sections have more applicable indications, because nanoindentation force applied on the transverse section is parallel to the long axis of bone (see Figure 4.1), which is the direction of physiological loading. Table 4.2 shows that the median elastic moduli of OI bone are higher than those of normal bone, however, the trend for median hardness values is the opposite. Elastic modulus is an intrinsic material property and fundamentally related to atomic bonding. Hardness is the resistance of a material to deformation due to a constant compression load, and also is a good indication of the underlying microstructure. Elastic modulus is generally considered to be related to hardness from statistical trend, but there are exceptions depending on the microstructure (92). The lower hardness values explain the fragility of OI bone despite its higher

elastic modulus, which also reflects the influence of the porous microstructure and altered molecular structure on the mechanical properties of materials.

Modulus mapping technique provides the capability to quantitatively map both the contact stiffness and elastic modulus of a material surface with nanometer resolution. Unlike the bone specimens embedded in resins, the undisturbed bone specimens still possess many holes such as canals, lacunae, and canaliculi. Therefore, the maps with these holes are excluded from the results. In situ SEM nanoindentation has the advantage of high resolution images and precise positioning of the indenter compared to the traditional triboscope instrument, especially for metals and semiconductors; however, bone specimens, without gold or carbon covering, which can affect mechanical tests, don't produce high-resolution images. In addition, the nanoindentation accessory needs to be tilted to a specified degree so that the sample can be detected by SEM; the tilt degree is too small for the specimens to be detected by Energy Dispersive X-ray Spectral (EDS or EDX) detector which is commonly used for elemental analysis. Future instrumentation models are expected to overcome these limitations.

4.5. Conclusion

Modulus mapping and in situ FE-SEM nanoindentation were both performed for the first time on “undisturbed” human normal and OI cortical bones. Modulus mapping, which is able to map the surface elastic moduli of materials, reveals elastic moduli of near-pure hydroxyapatite and collagen, and the distribution of mineralized fibrils and extrafibrillar minerals. In situ FE-SEM nanoindentation, on the other hand, reveals the bulk properties of bone. With this technique, the elastic modulus of interstitial lamellae and osteonal lamellae were compared; the largest indentation modulus was also observed at the location near the Haversian canal which is

due to the highly mineralized inner ring adjacent to the Haversian canal present in older osteons. Both techniques demonstrate that nanomechanical properties of bone specimens are structure specific due to the periodic modulations for mineralized fibers and lamellae.

The comparison of the results from these two techniques showed the opposite trends about the median elastic modulus of transverse and longitudinal sections. This indicates that at the shallow depth of about 2-3nm, the interactions between collagen and mineral should be taken into account, whereas at the deeper depths, the orientation and arrangement of mineral and collagen play more important roles. Therefore, the nanomechanical behaviors should be analyzed with the knowledge of the structure of bone at nanoscale as well as the interactions between different constituents of bone. Normal and OI bones are also compared by these two techniques and smaller collagen fiber bundles, smaller and less heterogeneous mineral crystals, greater median and maximum elastic modulus of OI bone are found. The transverse section of OI bone shows greater elastic moduli for both interstitial and osteonal lamellae, but lower hardness than that of normal bone.

4.6. References

1. Thurner PJ. Atomic force microscopy and indentation force measurement of bone. Wiley Interdisciplinary Reviews-Nanomedicine and Nanobiotechnology. 2009;1(6):624-49.
2. Rho JY, Tsui TY, Pharr GM. Elastic properties of human cortical and trabecular lamellar bone measured by nanoindentation. Biomaterials. 1997;18(20):1325-30.
3. Rho JY, Kuhn-Spearing L, Zioupos P. Mechanical properties and the hierarchical structure of bone. Medical engineering & physics. 1998;20(2):92-102.

4. Turner CH, Rho J, Takano Y, Tsui TY, Pharr GM. The elastic properties of trabecular and cortical bone tissues are similar: results from two microscopic measurement techniques. *Journal of Biomechanics*. 1999;32(4):437-41.
5. Rho JY, Zioupos P, Currey JD, Pharr GM. Variations in the individual thick lamellar properties within osteons by nanoindentation. *Bone*. 1999;25(3):295-300.
6. Rho JY, Roy ME, Tsui TY, Pharr GM. Elastic properties of microstructural components of human bone tissue as measured by nanoindentation. *Journal of Biomedical Materials Research*. 1999;45(1):48-54.
7. Rho JY, Currey JD, Zioupos P, Pharr GM. The anisotropic Young's modulus of equine secondary osteons and interstitial bone determined by nanoindentation. *The Journal of experimental biology*. 2001;204(Pt 10):1775-81.
8. Zysset PK, Guo XE, Hoffler CE, Moore KE, Goldstein SA. Elastic modulus and hardness of cortical and trabecular bone lamellae measured by nanoindentation in the human femur. *Journal of Biomechanics*. 1999;32(10):1005-12.
9. Hoffler CE, Moore KE, Kozloff K, Zysset PK, Brown MB, Goldstein SA. Heterogeneity of bone lamellar-level elastic moduli. *Bone*. 2000;26(6):603-9.
10. Xu J, Rho JY, Mishra SR, Fan Z. Atomic force microscopy and nanoindentation characterization of human lamellar bone prepared by microtome sectioning and mechanical polishing technique. *Journal of Biomedical Materials Research Part A*. 2003;67A(3):719-26.
11. Hofmann T, Heyroth F, Meinhard H, Franzel W, Raum K. Assessment of composition and anisotropic elastic properties of secondary osteon lamellae. *Journal of Biomechanics*. 2006;39(12):2282-94.

12. Asif SAS, Wahl KJ, Colton RJ, Warren OL. Quantitative imaging of nanoscale mechanical properties using hybrid nanoindentation and force modulation. *Journal of Applied Physics*. 2001;90(3):1192-200.
13. Balooch G, Marshall GW, Marshall SJ, Warren OL, Asif SAS, Balooch M. Evaluation of a new modulus mapping technique to investigate microstructural features of human teeth. *Journal of Biomechanics*. 2004;37(8):1223-32.
14. Lane NE, Yao W, Kinney JH, Modin G, Balooch M, Wronski TJ. Both hPTH(1-34) and bFGF increase trabecular bone mass in osteopenic rats but they have different effects on trabecular bone architecture. *Journal of Bone and Mineral Research*. 2003;18(12):2105-15.
15. Balooch G, Balooch M, Nalla RK, Schilling S, Filvaroff EH, Marshall GW, et al. TGF-beta regulates the mechanical properties and composition of bone matrix. *Proceedings of the National Academy of Sciences of the United States of America*. 2005;102(52):18813-8.
16. Lane NE, Yao W, Balooch M, Nalla RK, Balooch G, Habelitz S, et al. Glucocorticoid-treated mice have localized changes in trabecular bone material properties and osteocyte lacunar size that are not observed in placebo-treated or estrogen-deficient mice. *Journal of Bone and Mineral Research*. 2006;21(3):466-76.
17. Khanna R, Katti KS, Katti DR. Bone nodules on chitosan-polygalacturonic acid-hydroxyapatite nanocomposite films mimic hierarchy of natural bone. *Acta Biomaterialia*. 2011;7(3):1173-83.
18. Jirousek O, Kytýr D, Zlamal P, Doktor T, Sepitka J, Lukes J. Use of modulus mapping technique to investigate cross-sectional material properties of extracted single human trabeculae. *Chemicke Listy*. 2012;106:S442-S5.

19. Rzepiejewska-Malyska KA, Buerki G, Michler J, Major RC, Cyrankowski E, Asif SAS, et al. In situ mechanical observations during nanoindentation inside a high-resolution scanning electron microscope. *Journal of Materials Research*. 2008;23(7):1973-9.
20. Ghisleni R, Rzepiejewska-Malyska K, Philippe L, Schwaller P, Michler J. In Situ SEM Indentation Experiments: Instruments, Methodology, and Applications. *Microscopy Research and Technique*. 2009;72(3):242-9.
21. Mook WM, Niederberger C, Bechelany M, Philippe L, Michler J. Compression of freestanding gold nanostructures: from stochastic yield to predictable flow. *Nanotechnology*. 2010;21(5).
22. Gianola DS, Sedlmayr A, Monig R, Volkert CA, Major RC, Cyrankowski E, et al. In situ nanomechanical testing in focused ion beam and scanning electron microscopes. *Review of Scientific Instruments*. 2011;82(6).
23. Wheeler JM, Raghavan R, Michler J. In situ SEM indentation of a Zr-based bulk metallic glass at elevated temperatures. *Materials Science and Engineering a-Structural Materials Properties Microstructure and Processing*. 2011;528(29-30):8750-6.
24. Maschmann MR, Zhang Q, Wheeler R, Du F, Dai L, Baur J. In situ SEM Observation of Column-like and Foam-like CNT Array Nanoindentation. *Acs Applied Materials & Interfaces*. 2011;3(3):648-53.
25. Lee G, Choi M-j, Jeon S-w, Byun K-y, Kwon D, Ieee. Microstructure and Stress Characterization around TSV Using In-situ PIT-in-SEM. 2012 Ieee 62nd Electronic Components and Technology Conference (Ectc). 2012:781-6.

26. Huang H, Zhao H, Mi J, Yang J, Wan S, Xu L, et al. A novel and compact nanoindentation device for in situ nanoindentation tests inside the scanning electron microscope. *Aip Advances*. 2012;2(1).
27. Wasmer K, Pouvreau C, Breguet JM, Michler J, Schulz D, Giovanola JH. Nanoindentation cracking in gallium arsenide: Part I. In situ SEM nanoindentation. *Journal of Materials Research*. 2013;28(20):2785-98.
28. Williams JJ, Chapman NC, Chawla N. Mechanisms of Sn Hillock Growth in Vacuum by In Situ Nanoindentation in a Scanning Electron Microscope (SEM). *Journal of Electronic Materials*. 2013;42(2):224-9.
29. Heyer JK, Brinckmann S, Pfetzling-Micklich J, Eggeler G. Microshear deformation of gold single crystals. *Acta Materialia*. 2014;62:225-38.
30. Allison PG, Moser RD, Schirer JP, Martens RL, Jordon JB, Chandler MQ. In-situ nanomechanical studies of deformation and damage mechanisms in nanocomposites monitored using scanning electron microscopy. *Materials Letters*. 2014;131:313-6.
31. Fedarko N, Vetter U, Robey P. The bone cell biology of osteogenesis imperfecta. *Connective Tissue Research*. 1995;31(4):269-73.
32. Wallace JM, Orr BG, Marini JC, Holl MMB. Nanoscale morphology of Type I collagen is altered in the Brl mouse model of Osteogenesis Imperfecta. *Journal of Structural Biology*. 2011;173(1):146-52.
33. Kemp AD, Harding CC, Cabral WA, Marini JC, Wallace JM. Effects of tissue hydration on nanoscale structural morphology and mechanics of individual Type I collagen fibrils in the Brl mouse model of Osteogenesis Imperfecta. *Journal of Structural Biology*. 2012;180(3):428-38.

34. Fratzl P, Paris O, Klaushofer K, Landis WJ. Bone mineralization in an osteogenesis imperfecta mouse model studied by small-angle x-ray scattering. *Journal of Clinical Investigation*. 1996;97(2):396-402.
35. Camacho NP, Landis WJ, Boskey AL. Mineral changes in a mouse model of osteogenesis imperfecta detected by Fourier transform infrared microscopy. *Connective Tissue Research*. 1996;35(1-4):259-65.
36. Vanleene M, Porter A, Guillot PV, Boyde A, Oyen M, Shefelbine S. Ultra-structural defects cause low bone matrix stiffness despite high mineralization in osteogenesis imperfecta mice. *Bone*. 2012;50(6):1317-23.
37. Vetter U, Eanes ED, Kopp JB, Termine JD, Robey PG. Changes in apatite crystal size in bones of patients with osteogenesis imperfecta. *Calcified Tissue International*. 1991;49(4):248-50.
38. Vetter U, Weis MA, Morike M, Eanes ED, Eyre DR. Collagen cross-links and mineral crystallinity in bone of patients with osteogenesis imperfecta. *Journal of Bone and Mineral Research*. 1993;8(2):133-7.
39. Camacho NP, Hou L, Toledano TR, Ilg WA, Brayton CF, Raggio CL, et al. The material basis for reduced mechanical properties in oim mice bones. *Journal of Bone and Mineral Research*. 1999;14(2):264-72.
40. Coleman RM, Aguilera L, Quinones L, Lukashoya L, Poirier C, Boskey A. Comparison of bone tissue properties in mouse models with collagenous and non-collagenous genetic mutations using FTIRI. *Bone*. 2012;51(5):920-8.

41. Lindahl K, Barnes AM, Fratzl-Zelman N, Whyte MP, Hefferan TE, Makareeva E, et al. COL1 C-Propeptide Cleavage Site Mutations Cause High Bone Mass Osteogenesis Imperfecta. *Human Mutation*. 2011;32(6):598-609.
42. Roschger P, Fratzl-Zelman N, Misof BM, Glorieux FH, Klaushofer K, Rauch F. Evidence that abnormal high bone mineralization in growing children with osteogenesis imperfecta is not associated with specific collagen mutations. *Calcified Tissue International*. 2008;82(4):263-70.
43. Ji BH, Gao HJ. Mechanical properties of nanostructure of biological materials. *Journal of the Mechanics and Physics of Solids*. 2004;52(9):1963-90.
44. Katti DR, Pradhan SM, Katti KS. Directional dependence of hydroxyapatite-collagen interactions on mechanics of collagen. *Journal of Biomechanics*. 2010;43(9):1723-30.
45. Bhowmik R, Katti KS, Katti DR. Mechanics of molecular collagen is influenced by hydroxyapatite in natural bone. *Journal of Materials Science*. 2007;42(21):8795-803.
46. Landis WJ, Silver FH. Mineral Deposition in the Extracellular Matrices of Vertebrate Tissues: Identification of Possible Apatite Nucleation Sites on Type I Collagen. *Cells Tissues Organs*. 2009;189(1-4):20-4.
47. Fujisawa R, Kuboki Y. Affinity of bone sialoprotein and several other bone and dentin acidic proteins to collagen fibrils. *Calcified Tissue International*. 1992;51(6):438-42.
48. Bhowmik R, Katti KS, Katti DR. Mechanisms of Load-Deformation Behavior of Molecular Collagen in Hydroxyapatite-Tropocollagen Molecular System: Steered Molecular Dynamics Study. *Journal of Engineering Mechanics-Asce*. 2009;135(5):413-21.
49. Pradhan SM, Katti KS, Katti DR. A multiscale model of collagen fibril in bone: elastic response. *Journal of engineering mechanics*. 2012.

50. Nyman JS, Roy A, Shen XM, Acuna RL, Tyler JH, Wang XD. The influence of water removal on the strength and toughness of cortical bone. *Journal of Biomechanics*. 2006;39(5):931-8.
51. Zhu PZ, Xu JD, Sahar N, Morris MD, Kohn DH, Ramamoorthy A. Time-Resolved Dehydration-induced Structural Changes in an Intact Bovine Cortical Bone Revealed by Solid-State NMR Spectroscopy. *Journal of the American Chemical Society*. 2009;131(47):17064.
52. Hengsberger S, Kulik A, Zysset P. Nanoindentation discriminates the elastic properties of individual human bone lamellae under dry and physiological conditions. *Bone*. 2002;30(1):178-84.
53. Bushby AJ, Ferguson VL, Boyde A. Nanoindentation of bone: Comparison of specimens tested in liquid and embedded in polymethylmethacrylate (vol 19, pg 249, 2004). *Journal of Materials Research*. 2004;19(5):1581-.
54. B. B. The problem of demineralisation in thin sections of fully calcified bone. *The journal of cell biology*. 1964(1):165-73.
55. Chai XS, Dong CX, Deng YL. In situ determination of bacterial growth by multiple headspace extraction gas chromatography. *Analytical Chemistry*. 2008;80(20):7820-5.
56. Oliver WC, Pharr GM. An improved technique for determining hardness and elastic-modulus using load and displacement sensing indentation experiments. *Journal of Materials Research*. 1992;7(6):1564-83.
57. Rupin F, Saied A, Dalmas D, Peyrin F, Hauptert S, Raum K, et al. Assessment of Microelastic Properties of Bone Using Scanning Acoustic Microscopy: A Face-to-Face Comparison with Nanoindentation. *Japanese Journal of Applied Physics*. 2009;48(7).

58. Tai KS, Qi HJ, Ortiz C. Effect of mineral content on the nanoindentation properties and nanoscale deformation mechanisms of bovine tibial cortical bone. *Journal of Materials Science-Materials in Medicine*. 2005;16(10):947-59.
59. Pradhan SM, Katti KS, Katti DR. Multiscale Model of Collagen Fibril in Bone: Elastic Response. *Journal of Engineering Mechanics*. 2014;140(3):454-61.
60. Pradhan SM, Katti KS, Katti DR. Structural Hierarchy Controls Deformation Behavior of Collagen. *Biomacromolecules*. 2012;13(8):2562-9.
61. Fratzl P, Gupta HS, Paschalis EP, Roschger P. Structure and mechanical quality of the collagen-mineral nano-composite in bone. *Journal of Materials Chemistry*. 2004;14(14):2115-23.
62. Saber-Samandari S, Gross KA. Micromechanical properties of single crystal hydroxyapatite by nanoindentation. *Acta Biomaterialia*. 2009;5(6):2206-12.
63. Zamiri A, De S. Mechanical properties of hydroxyapatite single crystals from nanoindentation data. *Journal of the Mechanical Behavior of Biomedical Materials*. 2011;4(2):146-52.
64. Khanna R, Katti KS, Katti DR. Nanomechanics of Surface Modified Nanohydroxyapatite Particulates Used in Biomaterials. *Journal of Engineering Mechanics-Asce*. 2009;135(5):468-78.
65. Grant MC, Russel WB. Volume-fraction dependence of elastic-moduli and transition-temperatures for colloidal silica-gels. *Physical Review E*. 1993;47(4):2606-14.
66. Marotti G, Lees, Reeve. A new theory of bone lamellation. *Calcified Tissue International*. 1993;53:S47-S56.
67. Boyde A, Travers R, Glorieux FH, Jones SJ. The mineralization density of iliac crest bone from children with osteogenesis imperfecta. *Calcified Tissue International*. 1999;64(3):185-90.

68. Katti KS, Mohanty B, Katti DR. Nanomechanical properties of nacre. *Journal of Materials Research*. 2006;21(5):1237-42.
69. Rho JY, Kuhn-Spearing L, Zioupos P. Mechanical properties and the hierarchical structure of bone. *Medical Engineering & Physics*. 1998;20(2):92-102.
70. Ziv V, Weiner S. Bone crystal sizes - a comparison of transmission electron-microscopic and X-ray diffraction line-width broadening techniques. *Connective Tissue Research*. 1994;30(3):165-75.
71. The biochemistry and physiology of bone volume 1: structure. 2 ed. New York and London: Academic press; 1972.
72. Lees S, Probst KS, Ingle VK, Kjoller K. The loci of mineral in turkey leg tendon as seen by atomic-force microscope and electron- microscopy. *Calcified Tissue International*. 1994;55(3):180-9.
73. Sasaki N, Tagami A, Goto T, Taniguchi M, Nakata M, Hikichi K. Atomic force microscopic studies on the structure of bovine femoral cortical bone at the collagen fibril-mineral level. *Journal of Materials Science-Materials in Medicine*. 2002;13(3):333-7.
74. Lees S, Probst KS, Ingle VK, Kjoller K. The loci of mineral in turkey leg tendon as seen by atomic-force microscopy and electron-microscopy. *Calcified Tissue International*. 1994;55(3):180-9.
75. Legros R, Balmain N, Bonel G. Structure and composition of the mineral phase of periosteal bone. *Journal of Chemical Research-S*. 1986(1):8-9.
76. Wu YT, Ackerman JL, Kim HM, Rey C, Barroug A, Glimcher MJ. Nuclear magnetic resonance spin-spin relaxation of the crystals of bone, dental enamel, and synthetic hydroxyapatites. *Journal of Bone and Mineral Research*. 2002;17(3):472-80.

77. Ziv V, Wagner HD, Weiner S. Microstructure-microhardness relations in parallel-fibered and lamellar bone. *Bone*. 1996;18(5):417-28.
78. Fan ZF, Smith PA, Eckstein EC, Harris GF. Mechanical properties of OI type III bone tissue measured by nanoindentation. *Journal of Biomedical Materials Research Part A*. 2006;79A(1):71-7.
79. Fan Z, Swadener JG, Rho JY, Roy ME, Pharr GM. Anisotropic properties of human tibial cortical bone as measured by nanoindentation. *Journal of Orthopaedic Research*. 2002;20(4):806-10.
80. Roy ME, Rho JY, Tsui TY, Evans ND, Pharr GM. Mechanical and morphological variation of the human lumbar vertebral cortical and trabecular bone. *Journal of Biomedical Materials Research*. 1999;44(2):191-7.
81. Cusack S, Miller A. Determination of the elastic-constants of collagen by brillouin light-scattering. *Journal of Molecular Biology*. 1979;135(1):39-51.
82. Gu C, Katti DR, Katti KS. Photoacoustic FTIR spectroscopic study of undisturbed human cortical bone. *Spectrochimica acta Part A*. under review.
83. Pradhan S, Katti K, Katti D. Structural Hierarchy Controls Deformation Behavior of Collagen. *Biomacromolecules*, accepted. 2012.
84. Gupta HS, Stachewicz U, Wagermaier W, Roschger P, Wagner HD, Fratzl P. Mechanical modulation at the lamellar level in osteonal bone. *Journal of Materials Research*. 2006;21(8):1913-21.
85. Sissons HA, Jowsey J, Stewart L, editors. The microradiographic appearance of normal bone tissue at various ages. *X-ray Microscopy and X-ray Microanalysis, Proceedings of the*

Second International Symposium held in Stockholm; 1960; Sweden: Amsterdam/London/New York: Elsevier Publishing Company.

86. Crofts RD, Boyce TM, Bloebaum RD. Aging changes in osteon mineralization in the human femoral-neck. *Bone*. 1994;15(2):147-52.
87. Amprino R, Engstrom A. Studies on X-ray absorption and diffraction on bone tissue. *Acta Anatomica*. 1952;15(1-2):1-22.
88. Weaver JK. The microscopic hardness of bone. *The journal of bone and joint surgery*. 1966;48:273-88.
89. Paschalis EP, DiCarlo E, Betts F, Sherman P, Mendelsohn R, Boskey AL. FTIR microspectroscopic analysis of human osteonal bone. *Calcified Tissue International*. 1996;59(6):480-7.
90. Mendelsohn R, Paschalis EP, Boskey AL. Infrared spectroscopy, microscopy, and microscopic imaging of mineralizing tissues: Spectra-structure correlations from human iliac crest biopsies. *Journal of Biomedical Optics*. 1999;4(1):14-21.
91. Gourion-Arsiquaud S, Burket JC, Havill LM, DiCarlo E, Doty SB, Mendelsohn R, et al. Spatial Variation in Osteonal Bone Properties Relative to Tissue and Animal Age. *Journal of Bone and Mineral Research*. 2009;24(7):1271-81.
92. Bao YW, Wang W, Zhou YC. Investigation of the relationship between elastic modulus and hardness based on depth-sensing indentation measurements. *Acta Materialia*. 2004;52(18):5397-404.

CHAPTER 5. DYNAMIC NANOMECHANICAL BEHAVIOR OF HEALTHY AND OI HUMAN CORTICAL BONES³

This chapter presents viscoelastic response of demineralized and intact healthy human cortical bone and OI human cortical bone. The content of this chapter has been published in Gu, C.; Katti, D. R.; Katti, K. S.; Dynamic mechanical behavior of undisturbed and demineralized human cortical bone measured by nanoindentation. *Bioinspired, Biomimetic and Nanobiomaterials*. 2014, 3, 1-11.

5.1. Introduction

A wide range of materials show some combination of linearly elastic and viscous behavior, such as linear polymer, rubber, pliable biomaterials and bone. Bone tissue is composed of hydroxyapatite (HAP) mineral, organic collagen, water, as well as a small amount of noncollageneous proteins (1). Due to its complex composition, as well as hierarchical structure, bone tissue exhibits viscoelastic behavior such as creep deformation and stress-relaxation, especially when it is in a hydrated state (2-5). Because the organic collagen is primarily the type I collagen, which is a long-chain triple helix, collagen has been shown to cause creep deformation (6) or stress relaxation process (7) of bone. The cross-links between collagen molecules also affect the creep behavior of tendon (8). However, results also show that collagen does not significantly affect the viscoelasticity of bone (9); instead, moisture content has a significant effect on this property (10). HAP has also been reported to affect the viscoelasticity,

³ This chapter was co-authored by Chunju Gu, Kalpana Katti, and Dinesh Katti. Chunju Gu had primary responsibility for preparing samples, conducting all tests, and drafting this chapter. Kalpana Katti and Dinesh Katti directed the research orientation and revised this chapter.

which may be due to the energy dissipation influenced by the interaction between the mineral and collagen (11), or by dislocations in the HAP mineral itself (12). Viscoelastic behavior has been attributed to trapped water in mineral platelets in other natural biocomposites such as nacre from sea shells (13, 14). At the microscopic scale, many interfaces such as cement lines and the boundaries between the lamellae within osteons also contribute to viscoelasticity (15, 16).

In addition to the contribution from the above mentioned components to the viscoelastic property, the role of orientation is also noteworthy. Bone has long been recognized as an orthotropic material, since it has a roughly parallel alignment of the primary components to the long axis of bone. The orientation of HAP has been reported to cause the anisotropic viscoelasticity of bone (17). Macroscale tension tests of bovine cortical bone showed that the energy loss was noticeably larger for specimens in the longitudinal direction than in transverse direction (18).

There are several methods for measuring viscoelasticity of bone. Firstly, creep deformation is usually measured by detecting the change of strain when applying a constant stress, whereas stress-relaxation is measured by detecting the change of stress maintaining a constant strain. At the macroscopic scale, the response of bone to stress was examined with a biaxial, driven torsion pendulum system (4), three-point bending combined with force sensor (17), or compressive loading to allow creep strains (19). Secondly, dynamic mechanical analysis (DMA) technique, which is widely used for characterization of polymeric materials, was used to characterize bone by several researchers (9-11, 18, 20, 21). In DMA, a sinusoidal force (stress σ) is applied to a material and the resulting displacement (strain ϵ) is measured. The measured strain lags behind the applied stress by a phase difference for viscoelastic materials. Storage modulus (E'), loss modulus (E'') as well as mechanical damping factor are thus acquired. Thirdly, at the

microscopic scale, quasi-static nanoindentation has been developed to study the creep behavior of bone by fitting the depth vs. time data at constant load to rheological models in recent years (22-26). Lastly, based on the principle of traditional DMA and the development of nanoindentation, nanoDMA technique has emerged for conducting the microscopic scale dynamic nanoindentation tests (27). Some researchers have considered the $\tan \delta$ values versus frequency for bone tissue (5, 28, 29). Other researchers have also used nanoDMA to investigate the dynamic properties of different dehydrated bone specimens without considering the change of frequency (23, 26).

The studies on viscoelastic properties of bone at nanoscale are few, and studies on dynamic mechanical behavior are even less understood. Almost all of the bone specimens studied are either wet or dry. The wet specimens are kept in saline solution before testing or immersed in phosphate buffered saline (PBS) in a fluid cell during test duration; at shallow indentation depth, the indenter tip oscillation is not avoided during wet sample testing. In addition, the dry specimens are usually dehydrated and embedded, which affect the interactions and mechanical properties of bone (30, 31). Therefore, we attempt to study the bone specimens in their intact state without any treatment other than polishing the surface and conduct dynamic indentation tests under inert helium environment to reduce bacterial growth on the bone specimens. In our previous modeling work, we have demonstrated that the mechanical behavior of collagen is significantly influenced by collagen-mineral interaction as well as collagen-water-mineral interactions (32, 33). The mechanical behavior of collagen is direction-dependent and also influenced by strain rate (34). Therefore, in the current study, we evaluate the anisotropic viscoelasticity of intact human cortical bone at nanoscale and the influence of different components of bone on this property. In order to obtain a better understanding of the viscoelastic

behavior, demineralized bone specimens and osteogenesis imperfecta (OI) bone specimens were also selected for dynamic nanoindentation tests. Bone samples with OI are typically brittle and this disease is associated with collagen abnormality (35). In OI bone, the collagen molecules are often altered due to gene defects. These gene defects may affect the primary structure of a procollagen by preventing the zipper-like folding of the triple helix and causing degradation of normal and abnormal pro α chains through procollagen suicide, or producing a kink in the triple helix and causing assembly of abnormally branched or dendritic collagen fibrils (36).

5.2. Materials and Methods

5.2.1. Materials

A healthy human femur (No apparent metabolic bone disease record, 22 years old, female) and a human OI tibia (No apparent metabolic bone disease record, 27 years old, female, OI type was not identified; yet suspected to be type I since she had height of 67 inches, and weight of 180lb with pregnancy experience) were obtained (Figure 5.1) from National Disease Research Interchange, PA and stored in a freezer at -70°C . Bone specimens were cut from the mid-diaphysis of these two samples. A low-speed diamond saw was used for the initial rough cut and then a low-speed diamond-wafering blade (Buehler, Isomet, Lake Bluff, IL) was used to trim the sample down and subsequently the pieces were stored in a freezer at -70°C . Anterior sections were selected as the specimens from both femur and tibia. The specimens were about 1 mm thick in both transverse and longitudinal directions (Figure 5.2). Marrow and flesh were removed by scraping with a ceramic knife and then the bone samples was washed with deionized (DI) water at room temperature in approximately 10 minutes since longer time may begin to influence material behavior.

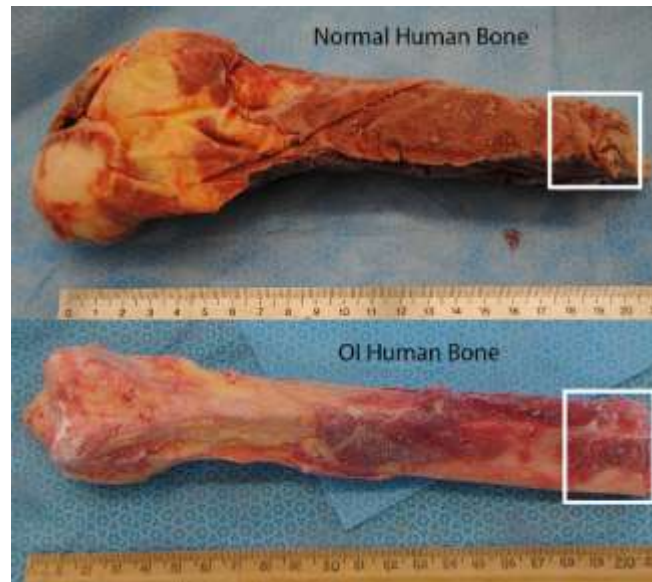


Figure 5.1. Bone samples (Specimens for testing are from the mid-diaphysis part as shown in squares).

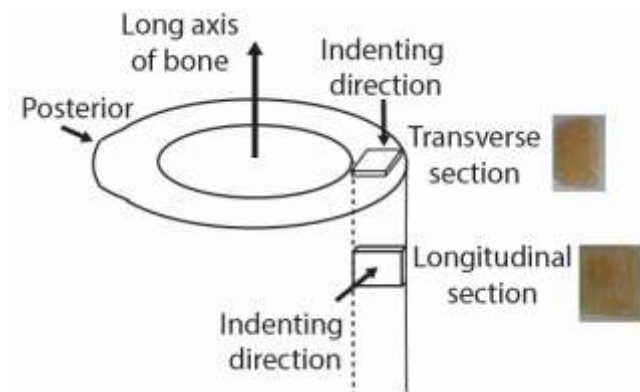


Figure 5.2. Schematic of bone specimen positions and indentation directions.

In order to perform the dynamic indentation tests, the specimens were polished with silicon carbide paper (Buehler, 600, 800 and 1200 grit), further polished using a series of diamond compound pastes (Buehler, 3 μ m, 1 μ m, 0.25 μ m) on a cloth and finished by polishing with a 0.02 μ m non-crystallizing colloidal silica polishing suspension. After each polishing step,

the specimens were ultrasonically cleaned in DI water for 30 seconds (the total rinsing time was limited about 3.5 minutes to avoid demineralization (37)).

After following the polishing steps and ultrasonically cleaning in DI water, one set of transverse sections of the normal bone were demineralized in 10% ethylenediamine tetraacetate (EDTA) (pH 7.5) for 5 minutes, 4, 24, and 72 hours at room temperature, washed exhaustively with DI water to remove all traces of EDTA. The same procedure was applied to another set of the longitudinal sections, but only demineralized for 5 minutes and 4 hours. The specimens demineralized for 5 minutes are denoted as Demi-5m, while the specimens demineralized for 4 hours are denoted as Demi-4h.

5.2.2. FTIR and AFM characterizations

Photoacoustic-Fourier transform infrared spectroscopy (PA-FTIR) experiments were performed on these demineralized bone specimens using Thermo Electron, Nexus 870 spectrometer equipped with MTEC Model 300 photoacoustic accessory. All spectra were collected in the range of 4000–400 cm^{-1} at a spectral resolution of 4 cm^{-1} . Root mean squared (RMS) roughness R_q of the normal and demineralized bone specimens was measured over the area of 1mm*1mm using Atomic Force Microscope (AFM, Veeco Metrology Group, Santa Barbara, CA), which is equipped with a Nanoscope IIIa controller and J-type piezo scanner. The mathematical definition of R_q are as follows

$$R_q = \sqrt{\left(\frac{1}{l} \int_0^l (y(x))^2 dx\right)} \quad (5.1)$$

The RMS mean line is the line that divides the profile so that the sum of the squares of the derivations of the profile height from it is equal to zero.

5.2.3. Dynamic nanoindentation tests

Dynamic nanoindentation tests were conducted on the polished bone specimens (intact and demineralized for 5 minutes and 4 hours) using nanoDMA® (Dynamic Mechanical Analysis) software in the Hysitron Triboscope nanomechanical instrument (Minneapolis, MN), equipped with a Nanoscope IIIa controller (Veeco Metrology, Santa Barbara, CA). The load and displacement resolutions of the instrument are 1 nN and less than 1 nm, respectively. A Berkovich (three sided pyramid, 100–200 nm tip radius) diamond indenter tip was used to perform the tests. During the performance of experiments, dry helium was kept flowing into the experimental chamber to prevent bacterial growth (38). Variable dynamic load tests were performed, in which the load and the load-amplitude were changed while a constant frequency was maintained. The static load was varied from 200 μN to a maximum of 1000 μN in 9 segment steps. The starting dynamic load was set at 20 μN . Tests were performed at three different frequencies, i.e. 25, 50, and 100 Hz, with 15 indents in each test. A schematic representation of the load function showing variation of load over time is shown in Figure 5.3. During the tests, the loss modulus (E''), storage modulus (E'), and the $\tan \delta$ ($\tan \delta$) were calculated by measuring the load amplitude, displacement amplitude, and the phase lag (δ). The dynamic model of indenter system in the instrument in contact with specimens was described in detail in literature (27, 39). Assuming linear viscoelasticity, dynamic mechanical behavior of the material can be obtained using the following equations:

$$E' = \frac{k_s \sqrt{\pi}}{2\sqrt{A_c}} \quad (5.2)$$

$$E'' = \frac{\omega C_s \sqrt{\pi}}{2\sqrt{A_c}} \quad (5.3)$$

$$\tan \delta = \frac{E''}{E'} = \frac{\omega C_s}{k_s} \quad (5.4)$$

where k_s , C_s denote the sample stiffness and damping coefficients, respectively, ω denotes the frequency of the applied force, and A_c is the projected contact area of the indent on the surface of the sample. Storage modulus measures the stored energy, representing the elastic portion, whereas the loss modulus measures the energy dissipated as heat, representing the viscous portion; and the $\tan \delta$, which describes the relative amount of energies stored/returned and lost by a specimen during mechanical deformation, has been considered as a measure of the degree of viscoelasticity of a material (5, 9, 40).

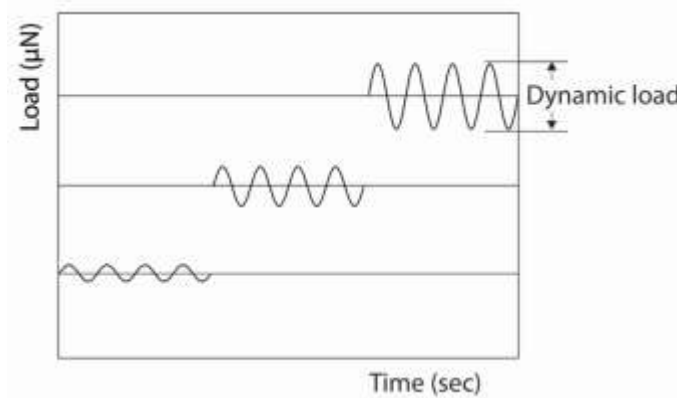


Figure 5.3. Schematic plot of load versus time for a variable dynamic load test.

5.3. Results and Discussion

5.3.1. Dynamic nanomechanical behaviour of intact normal human cortical bone

Figure 5.4(a) and (b) show the mean $\tan \delta$ with 95% confidence intervals for the intact bone specimens with variable static force (200-1000 μ N) at 25, 50 and 100Hz. As seen from

these figures, the $\tan \delta$ decreases with the increase of frequency for both longitudinal and transverse sections. This decrease of $\tan \delta$ is associated with the decrease of the internal friction, which can result from stiffening of the molecular configuration with increased frequency. Figure 5.4 (a) and (b) also show that the mean $\tan \delta$ and 95% confidence intervals of the transverse section are both greater than those of the longitudinal section for all three frequencies. It is observed that the mean $\tan \delta$ values are lower than 0.04 which indicates that the bone specimens exhibit low viscoelasticity. Figure 5.5 (a) and (b) show representative E' , E'' , and $\tan \delta$ values of the normal human bone during one dynamic nanoindentation with a maximum displacement of 246 nm. It is evident that, during this dynamic nanoindentation, E' is almost constant. However, both $\tan \delta$ and E'' vary significantly and are correlated.

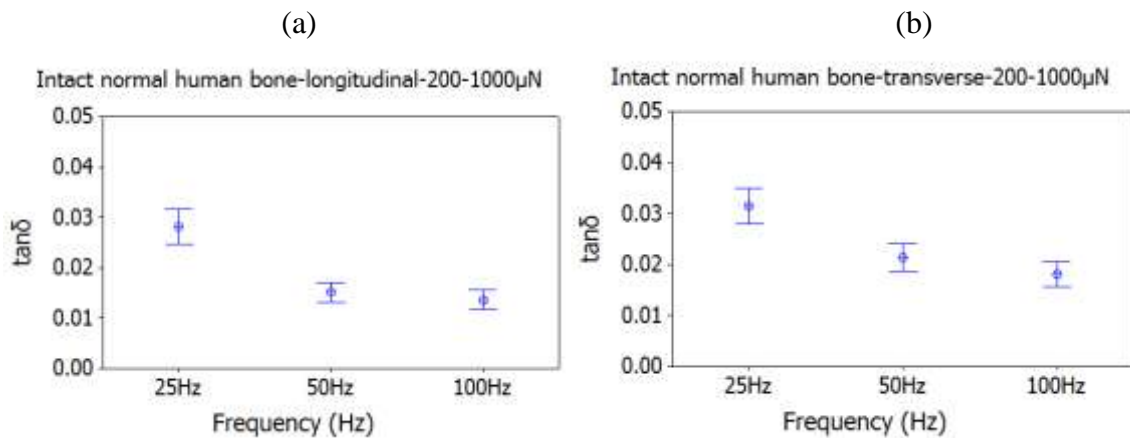


Figure 5.4. The mean loss tangent with 95% confidence intervals of normal bone specimens with variable static force (a) Longitudinal section; (b) Transverse section.

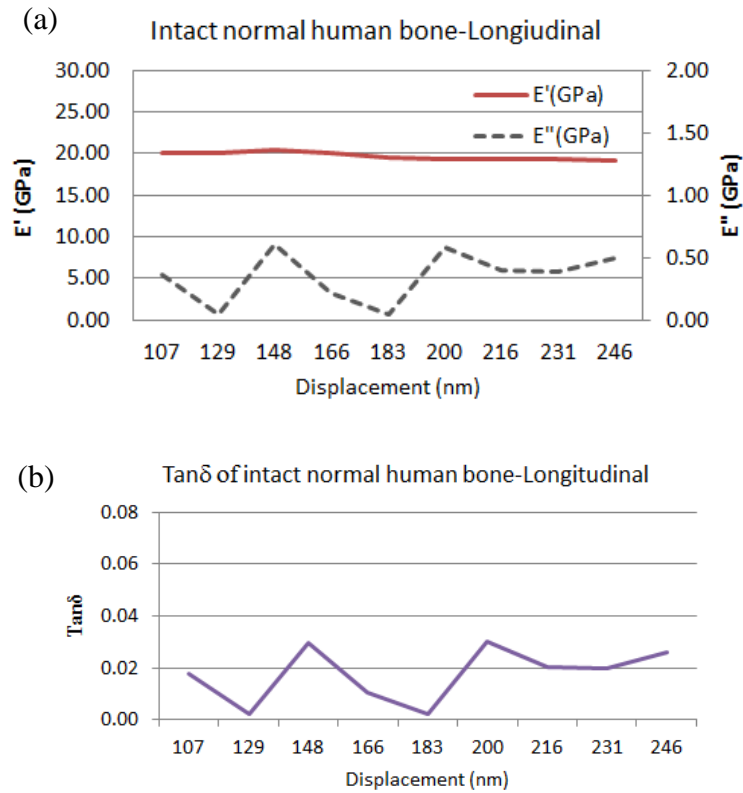


Figure 5.5. Representative storage modulus, loss modulus and loss tangent values of the human bone during one dynamic nanoindentation (Longitudinal section, frequency: 50Hz) (a) E' and E'' ; (b) $\text{Tan}\delta$.

5.3.2. Demineralization of normal human cortical bone

In order to better understand the dynamic nanoindentation results of bone, the transverse sections of the normal bone were demineralized to varying degrees with the demineralization times of 5 minutes, and 4, 8, 24, and 72 hours. The infrared spectra of demineralized transverse sections are shown in Figure 5.6a. It is seen that, after demineralization for 4 hours, the spectra appear to not vary much with additional time. The shape and position of the range of 1000-1300 cm^{-1} are also very similar as the spectra from pure type I collagen (41), which means that, after 4 hours of demineralization, the surfaces of the samples have been totally demineralized with the depth of about $30\mu\text{m}$ (calculated from the equation 2.2 in Chapter 2 (42)). When the sample is

demineralized after 5 minutes (Demi-5m), as shown in Figure 5.6a, the ν_1 and ν_3 PO_4^{3-} bands ($900\text{-}1180\text{cm}^{-1}$), $\nu_2\text{CO}_3^{2-}$ (at 874cm^{-1}), and ν_2 PO_4^{3-} bands (at $564\text{-}603\text{cm}^{-1}$) all remain in the same positions as those of intact bone specimen; however, their intensities decrease. Therefore, after 5 minutes, demineralization on the surface of the specimens has already occurred but still has not completed within the depth of about $30\mu\text{m}$ (the depth that infrared beam can penetrate). Since, after 4 hours (Demi-4h), the surface has been totally demineralized, the longitudinal sections were demineralized for 5 minutes and 4 hours to compare the dynamic nanomechanical properties. Figure 5. 6b shows the spectra from intact or demineralized specimens for 5 minutes and 4 hours in both transverse and longitudinal planes. The intact transverse and longitudinal sections have different ν_1 and ν_3 PO_4^{3-} bands ($900\text{-}1180\text{cm}^{-1}$) as also described in detail earlier (43); However, after demineralization, the PO_4^{3-} bands are almost the same in the two directions. Therefore, demineralization appears to damage the orientation of the mineral crystals. From Figure 5. 6b, it is also observed that all bands from the organic phase (C-H stretching, amide I, II, and III) remain in their positions regardless of the demineralization treatment. Therefore, it seems reasonable to assume that demineralization has a negligible effect on the collagen molecular structure and the three-dimensional network of the collagen fibers, as described in the literature (11).

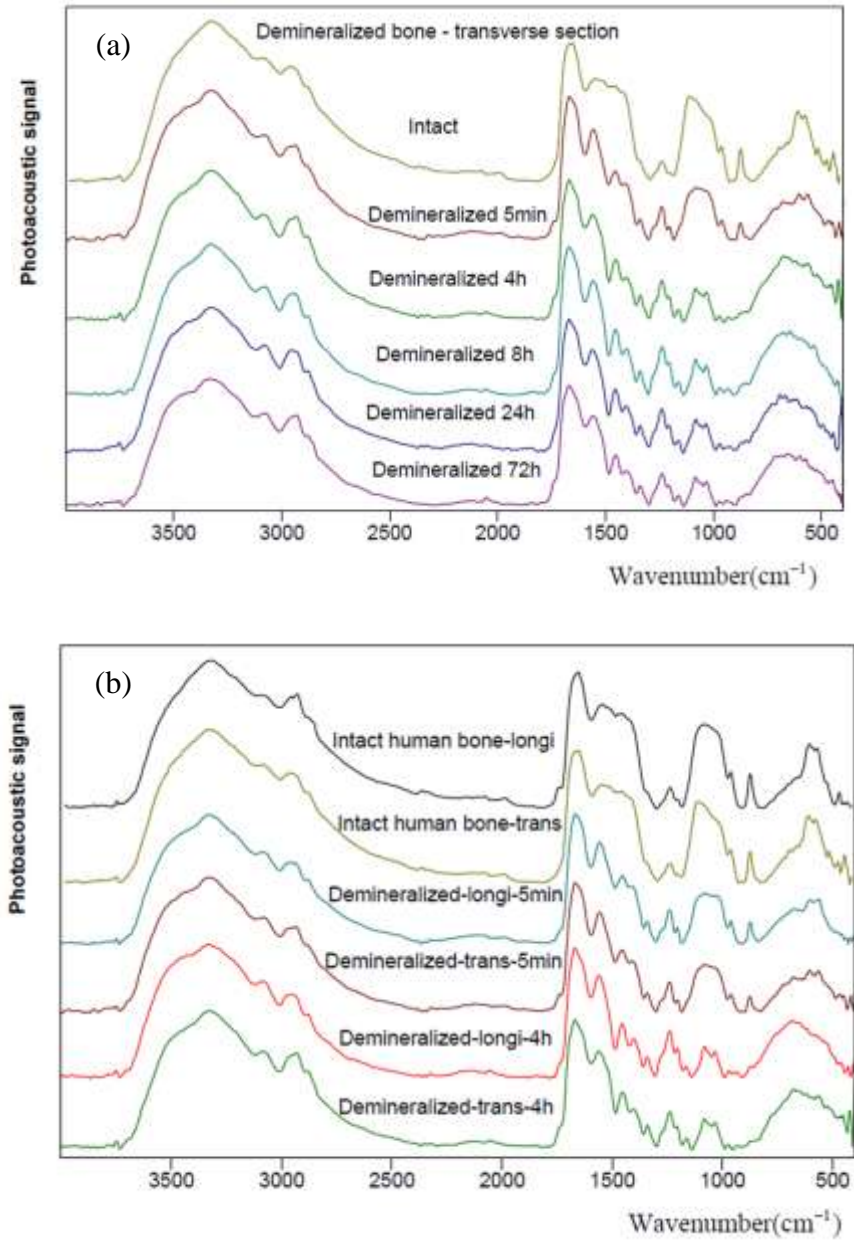


Figure 5.6. Photoacoustic infrared spectra of undisturbed and demineralized human bone in the energy range of 4000-400cm⁻¹ (a) Transverse section, time of demineralization: 5 minutes, 4, 8, 24, and 72hours; (b) Transverse and longitudinal sections, time of demineralization: 5 minutes, and 4hours.

5.3.3. Dynamic nanomechanical behaviour of demineralized normal human cortical bone

Roughness of the bone specimens of intact and demineralized bone samples are listed in Table 5.1, as assessed with AFM analysis of several $1\ \mu\text{m}\times 1\ \mu\text{m}$ regions. It is seen from Table 5.1 that the demineralized samples are much rougher than the intact samples. The viscoelastic response of the transverse and longitudinal sections after demineralization for 5 minutes and 4 hours are compared (Figure 5.7 (a-d)). The $\tan \delta$, E' , and maximum contact depths for intact and demineralized (5 minutes and 4 hour) samples are listed in Table 5.2. From Figure 5.7 (a-d) and Table 5.2, it is seen that for both longitudinal and transverse sections, $\tan \delta$ values of the Demi-4h specimens increase as compared with the intact bone specimens. In addition, this increase is exceptionally significant for the transverse section, whereas the increase is marginal for the longitudinal section. It is known that the collagen molecules are aligned roughly parallel to the c-axis of bone. After demineralization for 4 hours, only collagen molecules are left on the surface of these bone specimens ($<30\mu\text{m}$). Therefore, this difference of $\tan \delta$ between the longitudinal section and transverse section of Demi-4h reflects the viscoelastic response in the two directions of collagen molecules. In other words, along the long axis, the viscoelastic response of collagen molecules is greater than perpendicular to the c-axis of bone.

Table 5.1. Roughness R_q of the bone specimens of intact and demineralized bone samples (average \pm STDEV).

Sample	Longitudinal section			Transverse section		
	Intact	Demi. 5 minutes	Demi. 4 hours	Intact	Demi. 5 minutes	Demi. 4 hours
Roughness (nm)	18.52 ± 5.52	34.84 ± 7.28	39.63 ± 18.52	7.15 ± 1.62	47.21 ± 25.62	51.22 ± 31.75

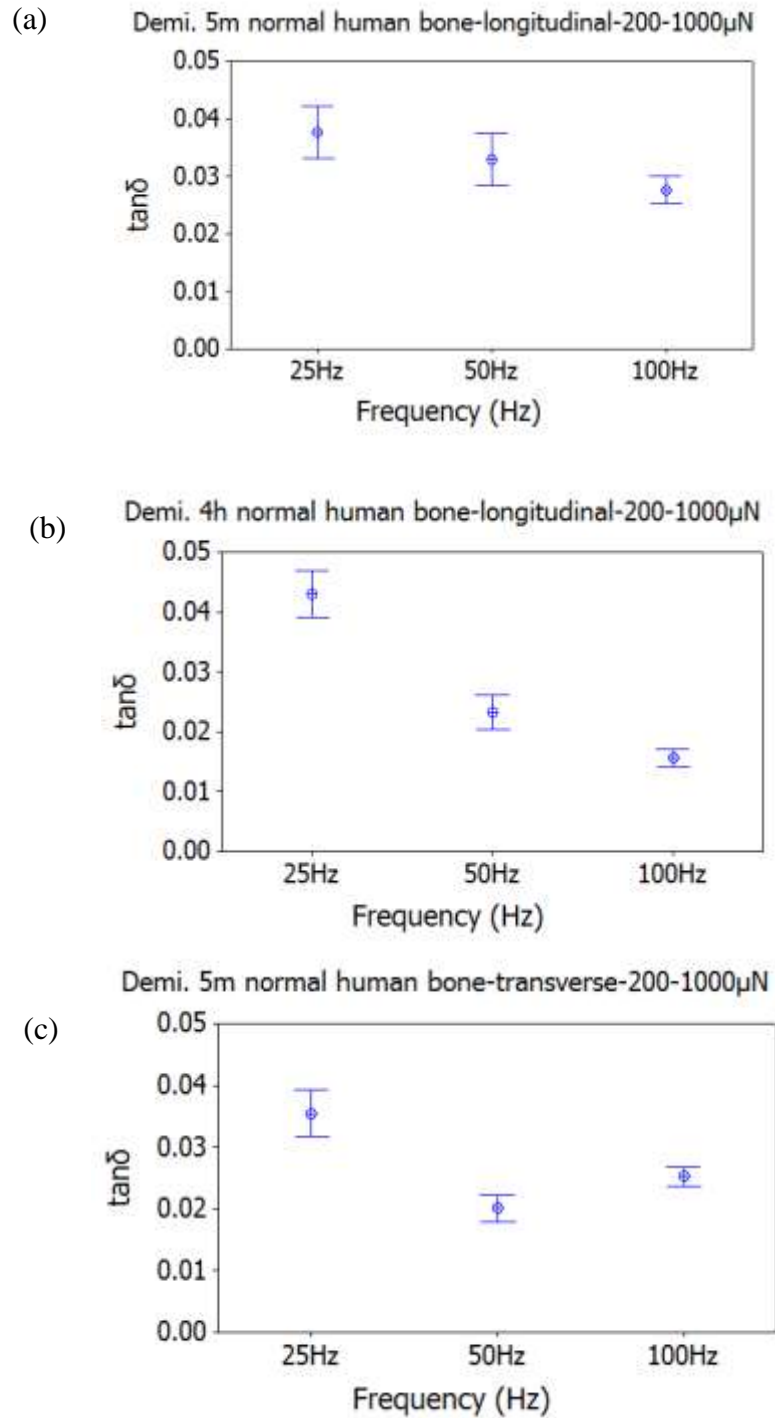


Figure 5.7. The mean loss tangent with 95% confidence intervals of demineralized normal bone specimens with variable static force (a) Longitudinal section, demineralized for 5 minutes; (b) Longitudinal section, demineralized for 4hours; (c) Transverse section, demineralized for 5 minutes; (d) Transverse section, demineralized for 4 hours.

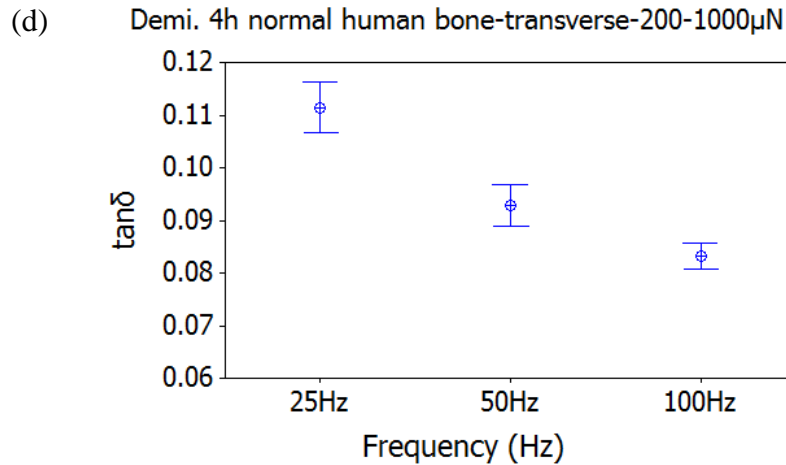


Figure 5.7. The mean loss tangent with 95% confidence intervals of demineralized normal bone specimens with variable static force (continued) (a) Longitudinal section, demineralized for 5 minutes; (b) Longitudinal section, demineralized for 4hours; (c) Transverse section, demineralized for 5 minutes; (d) Transverse section, demineralized for 4 hours.

From Figure 5.7 (a-d) and Table 5.2, it is also seen that most $\tan \delta$ values of Demi-5m bone specimens increase as compared to the intact bone specimens for both longitudinal and transverse sections. However, some of the $\tan \delta$ values of Demi-5m bone specimens are greater than the values of corresponding Demi-4h specimen. This phenomenon indicates that the surface properties of the Demi-5m specimens vary from site to site because of incomplete demineralization, which results in a combination of mineral and collagen proteins on the sample surface. Table 5.2 also shows that the $\tan \delta$ values of the transverse section of Demi-4h specimen are greater than corresponding $\tan \delta$ values of the longitudinal sections. In addition, the $\tan \delta$ values decrease with an increase of frequency for both longitudinal and transverse sections of Demi-4h specimens. These two trends for Demi-4h specimens as shown in Table 5.2 are the same as the intact bone specimens. However, the Demi-5m specimens do not exhibit these trends, indicating that these bone specimens have more heterogeneous state and properties. Table 5.2

shows the trend of E' after demineralization; E' decreases with the extent of demineralization as expected. Maximum displacement of bone specimens at frequencies of 25, 50 and 100Hz increases with the extent of demineralization, as listed in Table 5.2.

Table 5.2. $\text{Tan } \delta$, E' , and maximum displacement values of intact and demineralized normal bone specimens at frequencies of 25, 50 and 100Hz (average \pm STDEV).

Item	Specimen	Longitudinal section			Transverse section		
		25Hz	50Hz	100Hz	25Hz	50Hz	100Hz
$\text{Tan } \delta$	Intact	0.030 \pm	0.015 \pm	0.014 \pm	0.031 \pm	0.021 \pm	0.018 \pm
		0.014	0.006	0.003	0.009	0.010	0.005
	Demi. 5min.	0.038 \pm	0.032 \pm	0.028 \pm	0.035 \pm	0.020 \pm	0.025 \pm
		0.026	0.025	0.009	0.017	0.009	0.004
	Demi. 4hrs	0.043 \pm	0.023 \pm	0.016 \pm	0.111 \pm	0.093 \pm	0.083 \pm
		0.011	0.015	0.003	0.025	0.020	0.012
E' (GPa)	Intact	20.20 \pm	19.63 \pm	23.45 \pm	21.90 \pm	22.43 \pm	25.53 \pm
		3.76	4.42	2.96	8.77	6.85	6.98
	Demi. 5min.	8.00 \pm	11.37 \pm	11.31 \pm	9.49 \pm	8.67 \pm	9.87 \pm
		2.48	4.34	3.24	5.41	4.09	4.55
	Demi. 4hrs	3.70 \pm	5.94 \pm	7.41 \pm	7.43 \pm	5.91 \pm	5.77 \pm
		1.04	2.73	2.29	3.54	2.39	0.48
Max. displacement (nm)	Intact	247.36 \pm	246.89 \pm	220.01	265.16 \pm	248.89	251.03 \pm
		32.38	39.92	\pm 21.02	69.21	\pm 66.87	110.82
	Demi. 5min.	409.57 \pm	332.93 \pm	309.60	411.26 \pm	394.61	365.42 \pm
		87.99	72.10	\pm 33.33	164.36	\pm 93.11	88.97
	Demi. 4hrs	639.71 \pm	558.25 \pm	385.27	410.93 \pm	416.51	423.26 \pm
		156.67	361.76	\pm 87.45	192.74	\pm 80.49	71.68

5.3.4. Dynamic nanomechanical behaviour of OI human cortical bone

The mean $\tan \delta$ values with 95% confidence intervals of OI human bone specimens at variable static force are displayed in Figure 5.8 (a) and (b). The comparison of $\tan \delta$, E' , and maximum contact depths for normal and OI human cortical bone specimens are listed in Table 5.3. As shown in the table and figures, the same trends of $\tan \delta$ for OI bone as intact and Demi-4h normal bone specimens are observed: (1) $\tan \delta$ decreases with the increase of frequency; and (2) $\tan \delta$ of the transverse section is generally greater than that of the longitudinal section. As compared to the normal bone at different frequencies, OI bone has less $\tan \delta$ in most cases, indicating that viscoelastic response of OI bone is less than the normal bone. Table 5.3 shows that the average E' values of OI bone specimens are greater than those of normal bone. This is reasonable because OI bone has higher mineral/matrix ratio(44). It is also noticed that the maximum contact depth of OI bone specimens at each frequency is lower than that of normal bone. However, the overall difference of dynamic nanomechanical behavior between OI bone and intact normal bone is small.

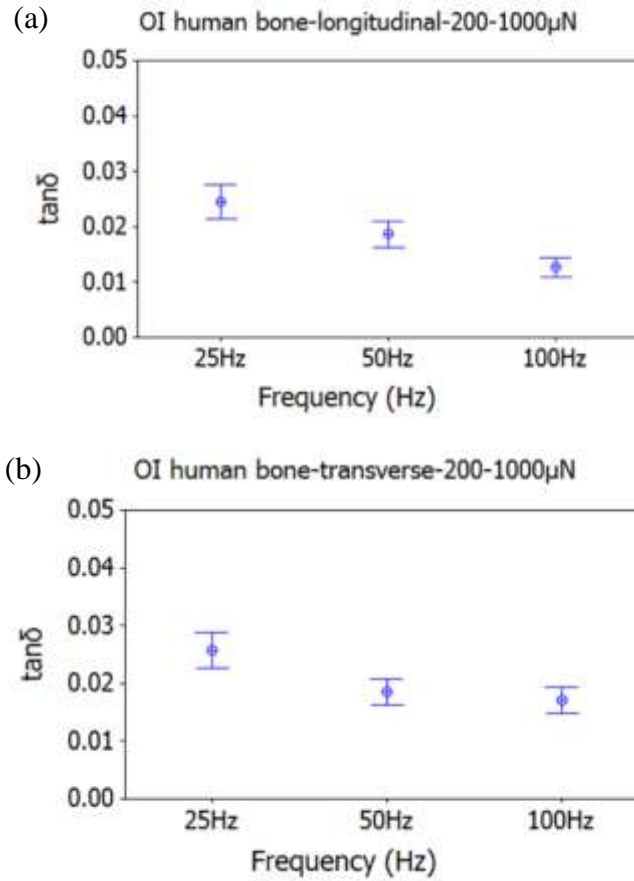


Figure 5.8. The mean loss tangent with 95% confidence intervals of OI bone specimens with variable static force (a) Longitudinal section (b) Transverse section.

Table 5.3. Tan δ , E', and maximum displacement values of normal and OI bone specimens at frequencies of 25, 50 and 100Hz (average \pm STDEV).

Item	Specimen	Longitudinal section			Transverse section		
		25Hz	50Hz	100Hz	25Hz	50Hz	100Hz
Tan δ	Normal	0.030 \pm 0.014	0.015 \pm 0.006	0.014 \pm 0.003	0.031 \pm 0.009	0.021 \pm 0.010	0.018 \pm 0.005
	OI	0.024 \pm 0.011	0.019 \pm 0.008	0.013 \pm 0.003	0.026 \pm 0.009	0.019 \pm 0.004	0.017 \pm 0.003
E' (GPa)	Normal	20.20 \pm 3.76	19.63 \pm 4.42	23.45 \pm 2.96	21.90 \pm 8.77	22.43 \pm 6.85	25.53 \pm 6.98
	OI	23.21 \pm 2.20	22.56 \pm 3.03	26.67 \pm 4.91	27.19 \pm 5.47	31.71 \pm 6.19	33.96 \pm 4.60
Max. displacement (nm)	Normal	247.36 \pm 32.38	246.89 \pm 39.92	220.01 \pm 21.02	265.16 \pm 69.21	248.89 \pm 66.87	251.03 \pm 110.82
	OI	211.76 \pm 13.88	218.87 \pm 20.55	198.36 \pm 22.96	211.20 \pm 59.98	185.85 \pm 19.96	174.70 \pm 15.11

5.3.5. Effects of frequency, orientation and composition on viscoelasticity of bone

Among other reasons, dynamic viscoelasticity arises due to molecular motions between collagen and also collagen-mineral structures. Collagen is highly constrained by crosslinks and close apposition with mineral crystallites; therefore, the molecular mobility of collagen is expected to result in a broad distribution of tan δ (45). In the Section 5.3.1, 5.3.3, and 5.3.4, we compared this viscoelastic behavior of bone specimens from three aspects: (1) tan δ changes with frequencies; (2) differences between the longitudinal sections and the transverse sections; and (3) different composition (e.g. intact, demineralized and abnormal OI bone specimens) leading to different viscoelastic behaviors.

In the literature, the examination of the $\tan \delta$ versus frequencies reveal that dehydrated human cancellous bone, saline solution soaked bovine bone, trabecular human bone, and hydrated mouse bone all have the same trend as discovered in the study: the $\tan \delta$ decreases with frequency (5, 18, 28, 29). This phenomenon is different in nacre from seashells, where we've seen $\tan \delta$ values positively correlated with frequencies (14). The relationship between $\tan \delta$ values and frequencies of viscoelastic materials are strongly related to their composition, internal structure and environmental condition. The specimens used in this study are in the same environmental conditions, therefore, the differences in viscoelastic behaviors are due to their composition (e.g. intact, demineralized and abnormal OI bone specimens) and internal structure.

By comparing the transverse sections with the longitudinal sections, it is found that the intact normal bone and OI bone have the same trend: the transverse sections have slightly higher $\tan \delta$ values than the longitudinal sections at almost all frequencies. In this work, the transverse section of bone is subjected to a vertical force while the longitudinal section is subjected to a perpendicular force as shown in Figure 5.2. The nanoindentation force for the transverse sections is along the long axis of bone, and therefore the indenter can penetrate in the long axis into collagen molecules which have the length of about 300 nm. However, after it is demineralized for 4 hours, when there is no mineral left within the indentation displacement, there is a significant difference between the transverse and longitudinal sections. The $\tan \delta$ values of transverse sections are markedly greater than the longitudinal sections. Therefore, (1) the anisotropic feature of collagen molecules is greater than bone, and (2) the viscoelastic response of collagen molecules is larger parallel to the long axis than perpendicular to the long axis of bone. It is also interesting to observe that after demineralization for 5 minutes, the $\tan \delta$ values of the transverse section are slightly smaller than those of the longitudinal sections at all

frequencies. This difference between Demi-5m and both the intact and Demi-4h specimens is attributable to the alteration of mineral because collagen molecules are regarded as intact in these specimens.

The comparison of dynamic nanomechanical properties of intact normal and OI bone specimens further accentuates the role of mineral to the viscoelasticity of bone. Although there is significant molecular defects in collagen molecules, the mineral crystal structure of OI bone is similar to that of normal bone and the dynamic nanomechanical behavior of OI bone is also similar to the intact normal bone. Therefore, the viscoelasticity of intact bone is primarily attributed to the mineral, although the collagen phase affects the viscoelasticity to some extent. This statement is in a good agreement with the study of Wang et al. (11). Differently, in the present study, the displacement in mechanical tests is hundreds of nanometer. The underlying mechanism is still required to be further explored.

5.4. Conclusion

Time-dependent characteristics of viscoelastic materials are strongly related to their composition, internal structure, and environmental condition. In this work, dynamic nanomechanical properties of normal human cortical bone (intact, demineralized) and OI human cortical bone were investigated using a nanoindentation instrument under the same environmental condition. Variable dynamic load tests showed that intact bone has low viscoelasticity. The viscoelastic response of all bone specimens (intact, demineralized, and OI) decreases with frequency, possibly arising from the stiffening of the molecular configuration when frequency increases. With demineralization, viscoelastic response of bone increases, so does the maximum displacement. Almost all transverse sections of intact normal and OI bone

specimens possess slightly higher viscoelastic response than the longitudinal sections except demineralized specimens. The transverse section of Demi-4h (totally demineralized) exhibits significantly greater viscoelastic response than the corresponding longitudinal section, indicating that the anisotropic feature of collagen molecules is greater than bone and the viscoelastic response of collagen molecules is greater along the long axis than perpendicular to the long axis of bone. On the contrary, the transverse section of Demi-5m (partially demineralized) exhibits lower viscoelastic response than the corresponding longitudinal section. This phenomenon is attributed to the alteration of the mineral phase. OI bone has slightly greater E' than normal bone due to its higher mineral/matrix ratio. Viscoelastic response of OI bone is slightly less than that of normal bone. Despite the significant altered collagen molecules, the overall similar dynamic nanomechanical behaviors of OI bone and normal bone indicates that the viscoelasticity of intact bone is mostly determined by the mineral. The collagen phase also contributes to the viscoelasticity to some extent.

5.5. Acknowledgement

I would like to acknowledge grants from National Science Foundation MRI grants for enabling experiments conducted in this work. I would also like to acknowledge financial support from ND EPSCoR and the support from Doctoral Dissertation Award of NDSU graduate school.

5.6. References

1. Murugan R, Ramakrishna S. Development of nanocomposites for bone grafting. *Composites Science and Technology*. 2005;65(15-16):2385-406.

2. Smith RW, Keiper DA. Dynamic measurement of viscoelastic properties of bone. *American Journal of Medical Electronics*. 1965;4(4):156-&.
3. Currey JD. Anelasticity in bone and echinoderm skeletons. *Journal of Experimental Biology*. 1965;43(2):279-&.
4. Lakes RS, Katz JL, Sternstein SS. Viscoelastic properties of wet cortical bone.1. Torsional and biaxial studies. *Journal of Biomechanics*. 1979;12(9):657-&.
5. Pathak S, Swadener JG, Kalidindi SR, Courtland HW, Jepsen KJ, Goldman HM. Measuring the dynamic mechanical response of hydrated mouse bone by nanoindentation. *Journal of the Mechanical Behavior of Biomedical Materials*. 2011;4(1):34-43.
6. Bowman SM, Gibson LJ, Hayes WC, McMahon TA. Results from demineralized bone creep tests suggest that collagen is responsible for the creep behavior of bone. *Journal of Biomechanical Engineering-Transactions of the Asme*. 1999;121(2):253-8.
7. Sasaki N, Nakayama Y, Yoshikawa M, Enyo A. Stress-relaxation function of bone and bone-collagen. *Journal of Biomechanics*. 1993;26(12):1369-76.
8. Puxkandl R, Zizak I, Paris O, Keckes J, Tesch W, Bernstorff S, et al. Viscoelastic properties of collagen: synchrotron radiation investigations and structural model. *Philosophical Transactions of the Royal Society of London Series B-Biological Sciences*. 2002;357(1418):191-7.
9. Yamashita J, Li XO, Furman BR, Rawls HR, Wang XD, Agrawal CM. Collagen and bone viscoelasticity: A dynamic mechanical analysis. *Journal of Biomedical Materials Research*. 2002;63(1):31-6.

10. Yamashita J, Furman BR, Rawls HR, Wang XD, Agrawal CM. The use of dynamic mechanical analysis to assess the viscoelastic properties of human cortical bone. *Journal of Biomedical Materials Research*. 2001;58(1):47-53.
11. Wang T, Feng Z. Dynamic mechanical properties of cortical bone: The effect of mineral content. *Materials Letters*. 2005;59(18):2277-80.
12. Rimnac CM, Petko AA, Santner TJ, Wright TM. The effect of temperature, stress and microstructure on the creep of compact bovine bone. *Journal of Biomechanics*. 1993;26(3):219-28.
13. Verma D, Katti K, Katti D. Nature of water in nacre: A 2D Fourier transform infrared spectroscopic study. *Spectrochimica Acta Part a-Molecular and Biomolecular Spectroscopy*. 2007;67(3-4):784-8.
14. Mohanty B, Katti KS, Katti DR, Verma D. Dynamic nanomechanical response of nacre. *Journal of Materials Research*. 2006;21(8):2045-51.
15. Lakes R, Saha S. Cement line motion in bone. *Science*. 1979;204(4392):501-3.
16. Katz JL. Anisotropy of Young's modulus of bone. *Nature*. 1980;283:106-7.
17. Iyo T, Maki Y, Sasaki N, Nakata M. Anisotropic viscoelastic properties of cortical bone. *Journal of Biomechanics*. 2004;37(9):1433-7.
18. Abdel-Wahab AA, Alam K, Silberschmidt VV. Analysis of anisotropic viscoelastoplastic properties of cortical bone tissues. *Journal of the Mechanical Behavior of Biomedical Materials*. 2011;4(5):807-20.
19. Deymier-Black AC, Yuan F, Singhal A, Almer JD, Brinson LC, Dunand DC. Evolution of load transfer between hydroxyapatite and collagen during creep deformation of bone. *Acta Biomaterialia*. 2012;8(1):253-61.

20. Les CM, Vance JL, Christopherson GT, Turner AS, Divine GW, Fyhrie DP. Long-term ovariectomy decreases ovine compact bone viscoelasticity. *Journal of Orthopaedic Research*. 2005;23(4):869-76.
21. Chang YT, Chen CM, Tu MY, Chen HL, Chang SY, Tsai TC, et al. Effects of osteoporosis and nutrition supplements on structures and nanomechanical properties of bone tissue. *Journal of the Mechanical Behavior of Biomedical Materials*. 2011;4(7):1412-20.
22. Bembey AK, Oyen ML, Bushby AJ, Boyde A. Viscoelastic properties of bone as a function of hydration state determined by nanoindentation. *Philosophical Magazine*. 2006;86(33-35):5691-703.
23. Huesa C, Yadav MC, Finnila MAJ, Goodyear SR, Robins SP, Tanner KE, et al. PHOSPHO1 is essential for mechanically competent mineralization and the avoidance of spontaneous fractures. *Bone*. 2011;48(5):1066-74.
24. Wu ZH, Baker TA, Ovaert TC, Niebur GL. The effect of holding time on nanoindentation measurements of creep in bone. *Journal of Biomechanics*. 2011;44(6):1066-72.
25. Wu ZH, Ovaert TC, Niebur GL. Viscoelastic properties of human cortical bone tissue depend on gender and elastic modulus. *Journal of Orthopaedic Research*. 2012;30(5):693-9.
26. Finnila MAJ, Zioupos P, Herlin M, Miettinen HM, Simanainen U, Hakansson H, et al. Effects of 2,3,7,8-tetrachlorodibenzo-p-dioxin exposure on bone material properties. *Journal of Biomechanics*. 2010;43(6):1097-103.
27. Asif SAS, Wahl KJ, Colton RJ. Nanoindentation and contact stiffness measurement using force modulation with a capacitive load-displacement transducer. *Review of Scientific Instruments*. 1999;70(5):2408-13.

28. Donnelly E, Williams RM, Downs SA, Dickinson ME, Baker SP, van der Meulen MCH. Quasistatic and dynamic nanomechanical properties of cancellous bone tissue relate to collagen content and organization. *Journal of Materials Research*. 2006;21(8):2106-17.
29. Polly BJ, Yuya PA, Akhter MP, Recker RR, Turner JA. Intrinsic Material Properties of Trabecular Bone by Nanoindentation Testing of Biopsies Taken from Healthy Women Before and After Menopause. *Calcified Tissue International*. 2012;90(4):286-93.
30. Nyman JS, Roy A, Shen XM, Acuna RL, Tyler JH, Wang XD. The influence of water removal on the strength and toughness of cortical bone. *Journal of Biomechanics*. 2006;39(5):931-8.
31. Zhu PZ, Xu JD, Sahar N, Morris MD, Kohn DH, Ramamoorthy A. Time-Resolved Dehydration-induced Structural Changes in an Intact Bovine Cortical Bone Revealed by Solid-State NMR Spectroscopy. *Journal of the American Chemical Society*. 2009;131(47):17064-+.
32. Bhowmik R, Katti KS, Katti DR. Mechanics of molecular collagen is influenced by hydroxyapatite in natural bone. *Journal of Materials Science*. 2007;42(21):8795-803.
33. Bhowmik R, Katti KS, Katti DR. Mechanisms of Load-Deformation Behavior of Molecular Collagen in Hydroxyapatite-Tropocollagen Molecular System: Steered Molecular Dynamics Study. *Journal of Engineering Mechanics-Asce*. 2009;135(5):413-21.
34. Katti DR, Pradhan SM, Katti KS. Directional dependence of hydroxyapatite-collagen interactions on mechanics of collagen. *Journal of Biomechanics*. 2010;43(9):1723-30.
35. Sykes B, Ogilvie D, Wordsworth P, Wallis G, Mathew C, Beighton P, et al. Consistent linkage of dominantly inherited osteogenesis imperfecta to the type-I collagen loci- COL1A1 and COL1A2. *American Journal of Human Genetics*. 1990;46(2):293-307.

36. Kuivaniemi H, Tromp G, Prockop DJ. Mutations in collagen genes - causes of rare and some common diseases in humans. *Faseb Journal*. 1991;5(7):2052-60.
37. B. B. The problem of demineralisation in thin sections of fully calcified bone. *The journal of cell biology*. 1964(1):165-73.
38. Chai XS, Dong CX, Deng YL. In situ determination of bacterial growth by multiple headspace extraction gas chromatography. *Analytical Chemistry*. 2008;80(20):7820-5.
39. Asif SAS, Wahl KJ, Colton RJ, Warren OL. Quantitative imaging of nanoscale mechanical properties using hybrid nanoindentation and force modulation. *Journal of Applied Physics*. 2001;90(3):1192-200.
40. Singh SP, Smith JF, Singh RP. Characterization of the damping behavior of a nanoindentation instrument for carrying out dynamic experiments. *Experimental Mechanics*. 2008;48(5):571-83.
41. Liu KZ, Dixon IMC, Mantsch HH. Distribution of collagen deposition in cardiomyopathic hamster hearts determined by infrared microscopy. *Cardiovascular Pathology*. 1999;8(1):41-7.
42. Michaelian KH. *Photoacoustic IR Spectroscopy: Instrumentation, Applications and Data Analysis*: Wiley-VCH; 2010.
43. Gu C, Katti DR, Katti KS. Photoacoustic FTIR spectroscopic study of undisturbed human cortical bone. *Spectrochimica acta Part A*. 2013;103:25-37.
44. Camacho NP, Landis WJ, Boskey AL. Mineral changes in a mouse model of osteogenesis imperfecta detected by Fourier transform infrared microscopy. *Connective Tissue Research*. 1996;35(1-4):259-65.

45. Garner E, Lakes R, Lee T, Swan C, Brand R. Viscoelastic dissipation in compact bone: Implications for stress-induced fluid flow in bone. *Journal of Biomechanical Engineering-Transactions of the Asme.* 2000;122(2):166-72.

CHAPTER 6. ANISOTROPIC PROPERTIES OF HUMAN CORTICAL BONE WITH OSTEOGENESIS IMPERFECTA

This chapter presents SEM images, FTIR studies of four sections (anterior, medial, posterior, and lateral) of OI human cortical bone and nanomechanical properties of anterior and posterior sections obtained using in situ FE-SEM nanoindentation technique.

6.1. Introduction

The heterogeneity of long bone (femur and tibia) diaphyseal shape and size variation are modulated by genetic, mechanical, nutritional, and hormonal patterning throughout its lifetime (1). According to Wolff's law, bone adapts itself to be stronger in positions subjected to higher loads (2). Non-uniform loading applied to different anatomical positions affect the formation of its microstructures, leading to various load-carrying capacities. A study of archaeological samples using high-resolution X-ray computed tomography reveals that the femoral and tibial midshaft shapes are relatively conserved throughout lifetime; yet, conversely, the proximal and distal femoral diaphysis and proximal tibial diaphysis appear more sensitive to developmentally induced changes in mechanical loading with high cross-sectional shape variability proximally and less change distally for tibia (3). The study also claims that the relative conservation of midshaft cortical geometry throughout development is due to the low strain that midshaft bears (3). The typical cross-sectional shape of tibia is divided into four areas: anterior, medial, posterior, and lateral sections (Figure 6.1). The cross-sectional shapes of the femoral and tibial midshaft are altered from a relatively circular shape in early childhood, to a less uniform structure in early puberty. The medio-lateral proximal femur and antero-posterior tibial expansions are due to hip breadth effects and locomotion loads (3). Meanwhile, another study on

human archaeological samples show that larger active remodeling areas are concentrated in the lateral and anterior portions of infant tibia, and the remodeling areas are more likely to spread throughout the entire cortex of adult tibia (4). This study also uses Geographical Information Systems (GIS) and observed that bone tissue reorganization seems to start in the lateral side during infancy and is concentrated in the anterior part of the tibia during youth and pre-adult stages. In adulthood, remodeling is mostly localized in the medial section and progressively reaches the medial-posterior region. Raman studies of these infant, juvenile, and adult samples further demonstrate that the lateral side in the infant and the posterior side in juveniles indicate the lower levels of crystallinity and thus active remodeling. It is worth mentioning that for adults, the crystallinity of the anterior section is markedly less than the other three sections (4). These studies demonstrate that the composition as well as modeling and remodeling processes in these four sections are different.

This phenomenon was also examined on animal bones. Abel-Wahab et al. (5) compared the mechanical properties of the four anatomical positions (anterior, medial, posterior, and lateral) in two directions (axial and transverse) of bone. They assessed microstructure-linked anisotropic mechanical properties of bovine femur using macroscale tension test and dynamic mechanical analysis (DMA). The study shows that the axial strength (longitudinal sections) for various anatomical positions is higher than the transversal strength (transverse sections) with significant differences in magnitude for those positions. For the longitudinal specimens, the anterior portion is the strongest while the lateral is the weakest. Differently, for the transverse specimens, the medial part is the stiffest and the posterior is the weakest. Authors linked these distinctions to the differences of their microstructures that the lateral and posterior sections contain more secondary osteons while the anterior and medial sections contain more primary

osteons (5). The anterior cortex and posterior cortex of equine bones are also extensively studied for examining the adaptation of bone histology to loading because in life the anterior cortex is loaded almost entirely in tension, while the posterior cortex in compression (6-14). Microscopic analysis reveals that primary lamellar bone is composed of predominantly longitudinal collagen fibers, irrespective of cortex; however, secondary osteons in the posterior cortex contained predominantly transverse collagen, while those formed elsewhere contain longitudinal collagen (8). Small-angle X-ray scattering (SAXS) experiments also reveals the differences of bone mineral crystals from the anterior and posterior zones: the average thickness of the mineral crystals are greater in the anterior section than in the posterior section; the orientation of the bone mineral crystals is predominantly in the longitudinal direction of bone, and the average tilt angle is about 30 degree for the anterior section and 45 degree for the posterior section (15). The anterior cortex shows a significantly higher ultimate tensile stress, a greater Young's modulus, and tensile and bending strength, as well as higher impact energy absorption than the posterior cortex and the trends are reversed in compression (7, 9). Currey et al. (6) utilized nanoindentation method and found that the anterior osteons are stiffer than the posterior osteons at 0° (parallel to the bone's long axis) and less stiffer at 90° (6).

Osteogenesis imperfect (OI) is a genetic disorder characterized by the fragility of bones and other tissues rich in type I collagen. The clinical manifestations include recurrent fractures with secondary deformities, muscle weakness, ligamentous laxity, bluish sclera, dentinogenesis imperfecta, and bone pain. Patients with OI, even the least severe type (type I), have major physical disabilities associated with the presence of deformities that directly affect mobility. However, the incentive of mobility in a safe environment helps to preserve bone resistance and

functional independence (16-18). It is beneficial to take a close look at the microstructure, molecular structure, and nanomechanical properties of tibia with OI disease.

Previous studies on the microstructure of OI bone specimens reveal five characteristics: thinner and more disrupted bone lamellation patterns; an increased number of vascular channels (19, 20); abnormal collagen aggregation and collagen fibrils (21); decreased mineral crystal size and crystallinity (22, 23); and altered D-periodic spacing (24, 25). The OI bone also has higher mineral:matrix ratio and lower carbonate: mineral ratio (26, 27), (34). Using nanoindentation, contradictory results are obtained. Both decreased elastic modulus and hardness of long bone were found in children with OI type III (28) and OI from mild to severe forms (29) as compared with normal data. *Oim* bone has lower stiffness (30). On the contrary, higher stiffness and hardness of the OI bone specimens than the controlled ones are also found (31). The nanoindentation method also reveals that bone from children with OI type III was more brittle than with OI type IV (32, 33) and that the use of sclerostin antibody does not alter the local tissue mineralization dynamics of OI bone (34). Studies also show that osteoblast in OI patients may interfere with multiple mechanisms that ensure adaptation of the skeleton to the increasing mechanical needs during growth because of three mechanisms leading to an increase in bone mass during childhood; that is, modeling of external bone size and shape, production of secondary trabeculae by endochondral ossification, and thickening of secondary trabeculae by remodeling (35).

In this study, we investigated the microstructural, molecular differences, and nanomechanical properties of OI bone specimens in transverse and longitudinal planes. The OI bone specimens are divided to anterior, medial, posterior, and lateral sections based on

anatomical positions. The goal of this study is not to merely compare the structure and mechanical properties of these sections, but to add to the understanding of OI disease.

6.2. Methods and Materials

6.2.1. Materials

One 20-mm-thick transverse section was cut from the mid-diaphysis of a human OI tibia which was obtained from National Disease Research Interchange, PA (No apparent metabolic bone disease record, 22 years old, female with pregnancy experience) and stored in a freezer at -70°C. The OI type was putative type I, the mild type, since the person had height of 67 inches and weight of 180lb with, which are typical of a healthy person. Marrow and flesh were removed by scraping with a ceramic knife and then the bone section was washed with deionized (DI) water at room temperature in approximately 10min to avoid deterioration of bone. Specimens with the size of about 5×5×1mm were cut from four anatomical positions parallel and transverse to the bone axis (Figure 6.1) using a low-speed diamond-wafering blade (Buehler, Isomet, Lake Bluff, IL). Three groups of these specimens were obtained for SEM, FTIR, and in situ FE-SEM nanoindentation experiments.

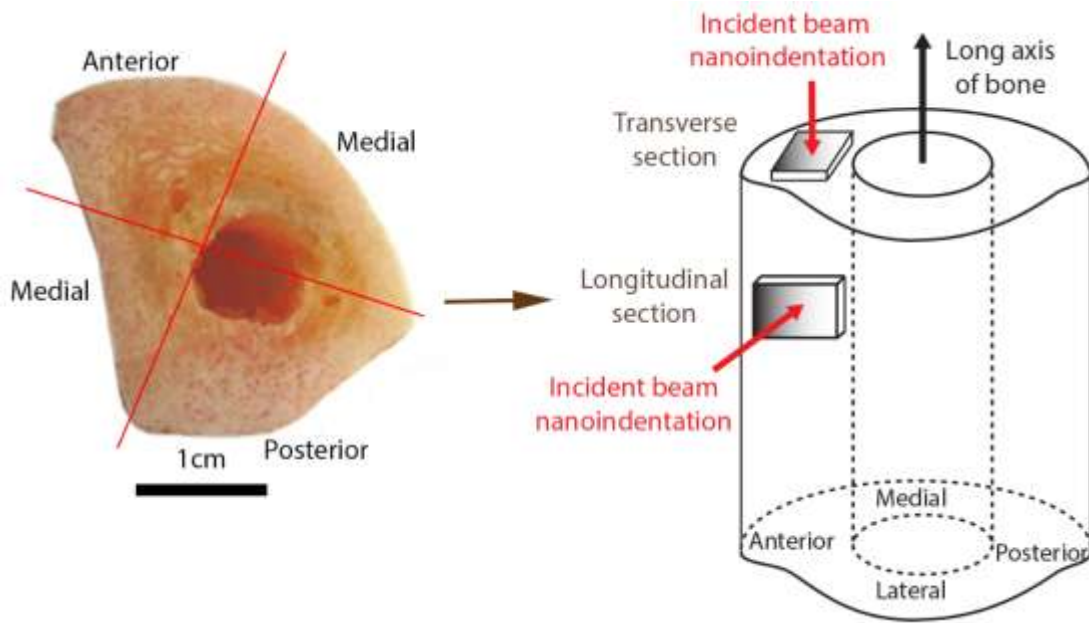


Figure 6.1. Schematic representation of bone showing from where the samples were cut, transverse section and longitudinal section are both from the anterior, medial, posterior, and lateral areas of OI bone specimen.

6.2.2. Experiment

6.2.2.1. Scanning electron microscopy studies

Microstructure of the bone specimens was studied using a JEOL JSM-6490LV scanning electron microscope (SEM) and a JEOL JSM-7600F analytical high resolution field-emission scanning electron microscope (FE-SEM). Sample preparation for the scanning electron microscope (SEM) imaging follows our previous work (36).

6.2.2.2. FTIR Spectroscopy studies

Photoacoustic (PA)-FTIR experiments were carried out using a Thermo Electron, Nexus 870 spectrometer which is equipped with MTEC Model 300 photoacoustic accessory. Before collecting data for each sample, the PA chamber was purged with dry helium for 15 minutes.

Linear photoacoustic spectra were collected after 1000 scans in the range of 4000-400 cm^{-1} at a mirror velocity of 0.15cm/s, with a spectral resolution of 4 cm^{-1} . GRAMS/32 software was used for spectra analysis.

6.2.2.3. In situ FE-SEM nanoindentation tests

Nanoindentation tests were performed with a Hysitron PI-85 nanomechanical instrument with a Berkovich tip made of boron-through-doped diamond (Minneapolis, MN), which was installed in a high-resolution Field Emission Scanning Electron Microscope (FE-SEM, mode: Jeol JSM-7600F). Detailed descriptions of the principle of this instrument can be found in the literature (37). The probe was also calibrated on fused quartz. Lower secondary electron images (LEI) were obtained by FE-SEM while nanoindentation was performed.

The elastic modulus and hardness of bone are determined by using the common method developed by Oliver and Pharr (38). With the assumption that bone tissue is elastically isotropic and homogeneous, the Young's modulus is calculated using the following equation (6.1):

$$\frac{1}{E_r} = \frac{(1 - \nu^2)}{E} + \frac{(1 - \nu_i^2)}{E_i} \quad (6.1)$$

where E is the elastic modulus, ν is Poisson's ratio, s and i refer to sample and indenter tip material, respectively. E_r is the reduced modulus which can be obtained from indentation curve; ν_s of bone is set to 0.3; E_i and ν_i are the same quantities for the diamond indenter: $E_i = 1141$ GPa, $\nu_i = 0.07$.

In situ FE-SEM nanoindentation was performed with static load control; 50 μN was applied as the load for the samples on the transverse section plane (Figure 6.2). An interlamellar cement band is obviously seen in the figure and separates the osteon and interstitial lamellae.

Sixty indents were performed inside the osteon, and thirty indents outside the osteon. For the samples on the longitudinal plane (Figure 6.2b), 15 μN , 50 μN , and 100 μN were applied with thirty indents for each load. To avoid pile-up effect, indent spacing was set about 1 μm . Some surface defects were observed (e.g., pitch, cracks, pop-outs) and excluded from the nanoindentation.

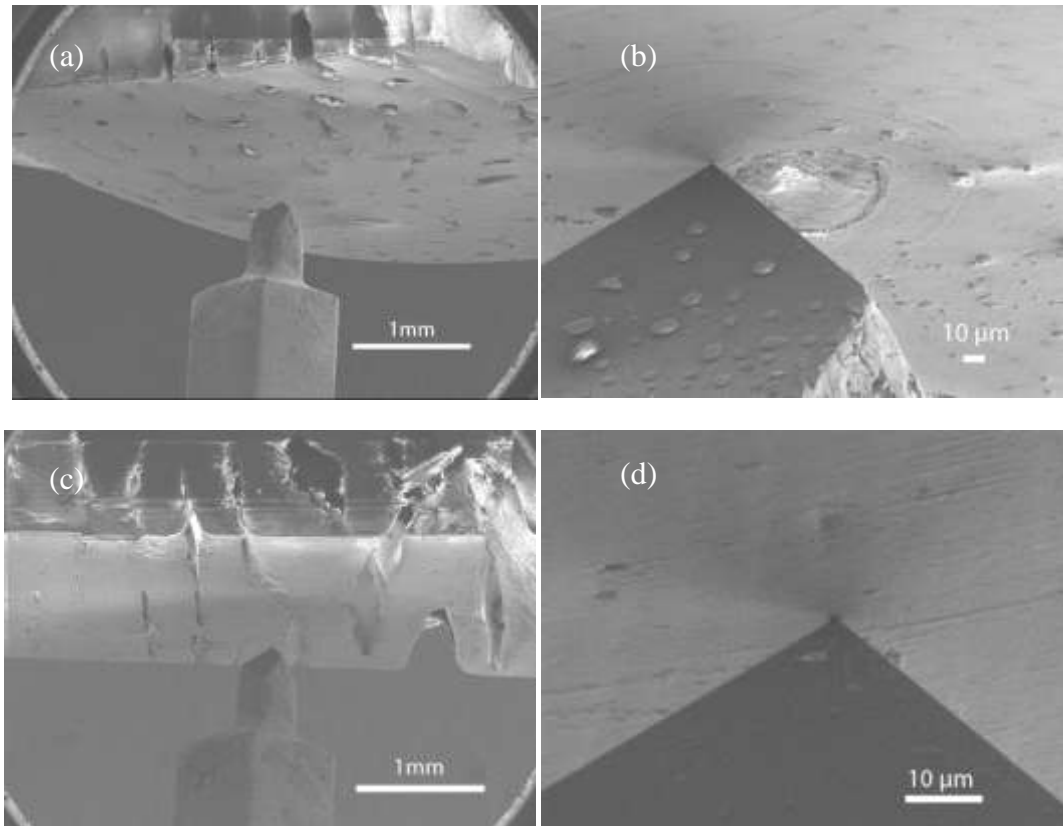


Figure 6.2. In situ FE-SEM nanoindentation performed on the surface of (a)(b) Trans-anterior section; (c)(d) Longi-anterior section.

6.3. Results

6.3.1. Microstructure of OI human cortical bone

Figure 6.3 (a-j) shows the SEM images of the surfaces of OI bone specimens fractured in liquid N_2 from different cortex positions (anterior, medial, posterior, and lateral) in the

longitudinal and transverse planes. The four sections all show trabecular structures near medullary cavity (Figure 6.3a, c), some of these structures are broken and lost after cutting and fracturing (Figure 6.3f, i). From these SEM images, it is hard to differentiate primary osteon and secondary osteon for some Harversian systems. However, some secondary osteons with cement lines as boundaries are still evidently seen in all of the four sections (Figure 6.3a, c, f, and i). Therefore, these four sections all have remodeling areas. It is also seen that the anterior, posterior, and lateral sections all contain big resorption cavities and more Harversian systems compared to the medial section. This reflects larger remodeling areas of the three sections than the medial section, which is different from the study on archaeological samples (4). As compared to the anterior section, the posterior section seems less porous and contains more bone mass.

The lateral section has parallel bundles of mineralized fibrils in alternating directions within adjacent lamellae (Figure 6.3j), which is the same as the normal bone microstructure (39). The anterior, posterior, and medial sections have fibril bundles in one direction with gaps between adjacent lamellae (Figure 6.3b, d, g). This structure is essentially similar to the normal bone. As the mutations of OI bone are heterozygous, some of the gene products should still be normal. There are always normal lamellar bone structures composed of normally mineralized fibrils even in severe OI bone (39). Figure 6.3e and 3h are areas from the medial and posterior sections, respectively. The fibril bundles in these two areas are aligned in many different directions and some cracks appear in some of the interfaces between fibril bundles.

Overall, each section has its own variation in microstructure including smooth, near-normal areas and messed up, cracked areas. Comparatively, the medial section is more mature than the other three, and the lateral section possesses normal areas.

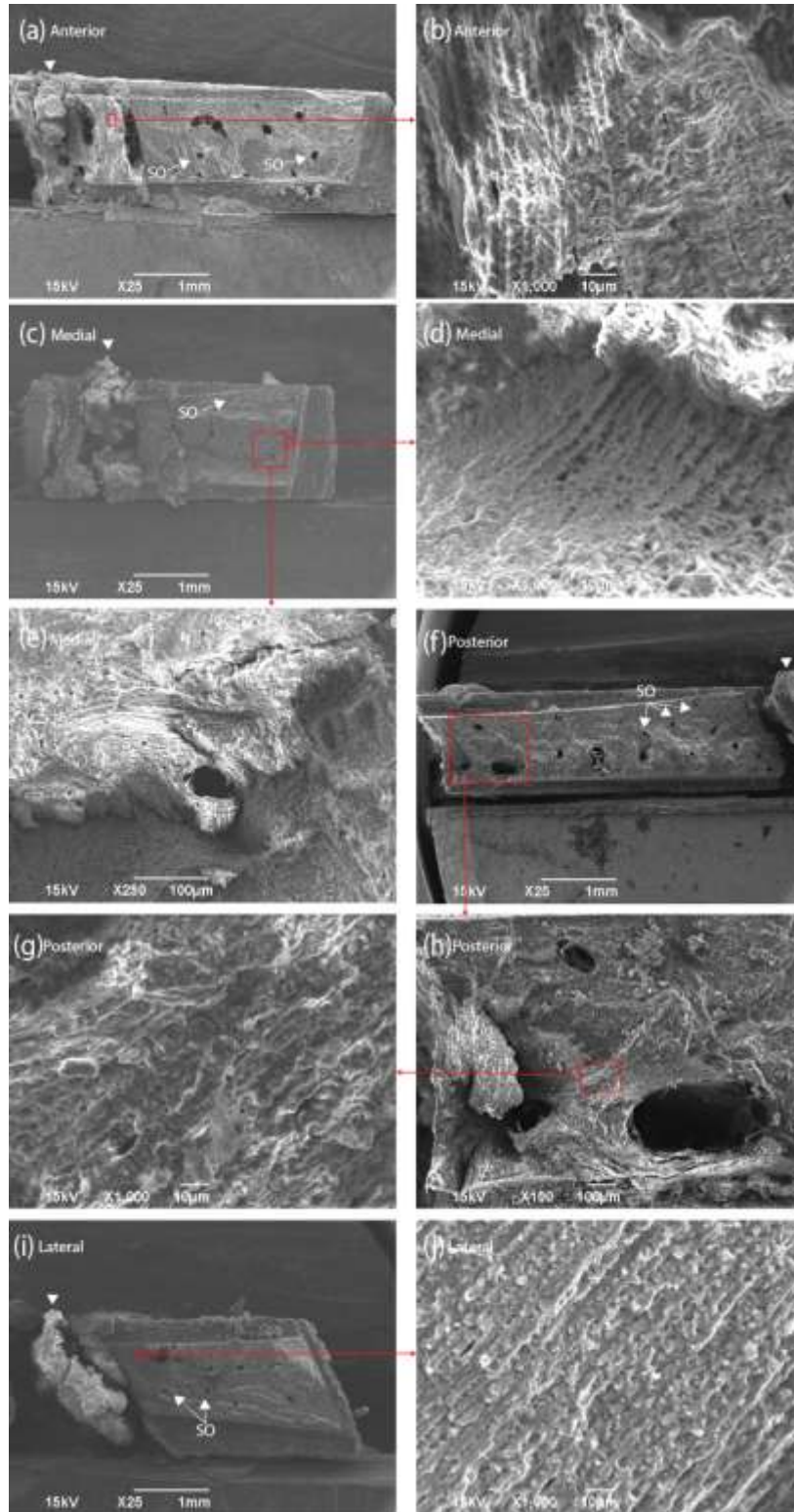


Figure 6.3. SEM images of human OI cortical bone (a, b) Anterior section; (c, d, e) Medial section; (f, g, h) Posterior section; (i, j) Lateral section (Thin arrows indicate secondary osteon (SO) regions and arrowheads bone powder probably created from cutting procedure).

6.3.2. Photoacoustic-FTIR (PA-FTIR) spectra

PA-FTIR was also conducted on the eight samples as mentioned in the microstructure study part. Figure 6.4 (a) and (b) show PA-FTIR spectra of these four sections (anterior, medial, posterior, and lateral) of OI bone in the longitudinal and transverse planes. The spectra were normalized with the OAH peak (3322 cm^{-1}). The assignments of the bands are shown in Table 6.1. Bone is primarily comprised of organic component (collagen molecules and other organic component such as non-collagenous proteins, lipid, etc.) and inorganic component (hydroxyapatite).

Figure 6.4 (a) shows that the intensities of C-H stretching (2926 cm^{-1}), C=O stretching (1745 cm^{-1}), and C-H bending (1455 cm^{-1}) bands are correlated. Therefore, it is reasonable to assume that these three bands are from the same source, which is mainly lipid, with a little contribution from proteins, carbohydrates, and nucleic acids (40). In addition, it is observed that there is a great variety of the intensities of these three band areas for the longitudinal sections. The order of their intensities of the longitudinal sections is: Medial>Anterior>Lateral>Posterior. For the transverse sections, the intensities are almost the same. The trend that the longitudinal section has higher C-H stretching and C=O stretching intensities than the transverse section (36) is also seen here for the medial, anterior, and lateral sections except the posterior section. This phenomenon indicates the composition differences in the four areas.

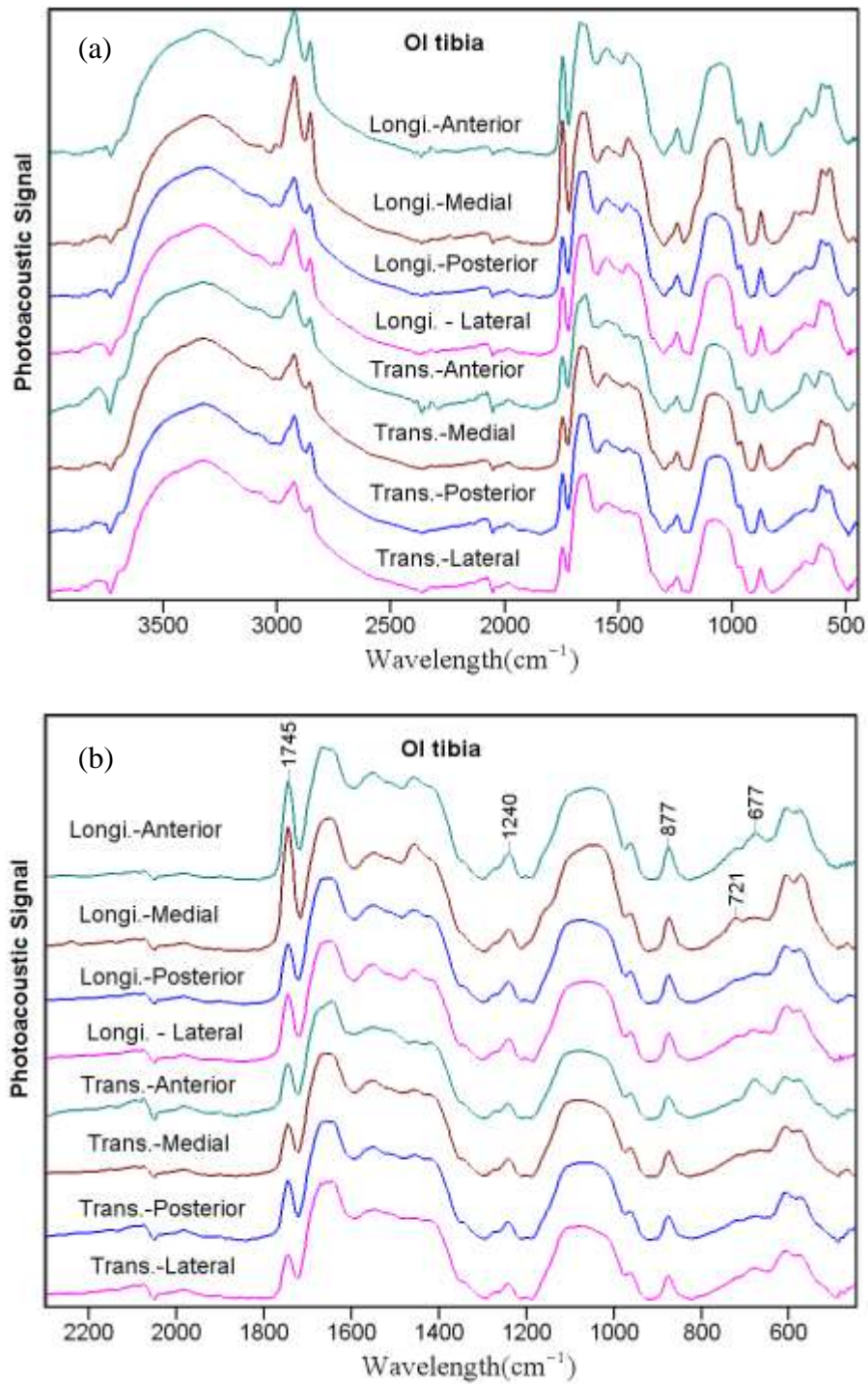


Figure 6.4. PA-FTIR spectra of human OI cortical bone (anterior, medial, posterior, and lateral sections for the longitudinal and transverse sections, respectively). Velocity of mirror: 0.158 cm/s . (a) 4000-450 cm^{-1} region; (b) 2300-450 cm^{-1} region.

Table 6.1. Band assignments of PA-FTIR spectra from OI bone.

Wavenumber (cm ⁻¹)	Band Assignment	Ref.
3322	OH stretching vibration from water and combination of Amide A with N-H stretching	(57)
2926	CH ₂ asymmetric stretch: mainly lipids, with the little contribution from proteins, carbohydrates, nucleic acids	(40)
2854	CH ₂ symmetric stretch: mainly lipids, with the little contribution from proteins, carbohydrates, nucleic acids	(40)
~2100	OH stretching vibrations from P-OH	(58-60)
1745	C=O stretch: lipids, cholesterol esters, triglycerides	(61)
~1652	Amide I (protein C=O stretch)	(61)
1550-1506	Amide II (Protein N-H bend, C-N stretch)	(61)
1455	CH ₃ and carbonate ν_3 vibration	(40)
~1240	Amide 3(C-N stretch, N-H bend, C-C stretch)	(57)
1180-927	$\nu_3 \nu_1 \text{PO}_4^{3-}$	(57)
877	$\nu_2 \text{CO}_3^{2-}$	(57)
721	C-H rocking	
677	C-S stretching vibration	(41)
572-610	$\nu_4 \text{PO}_4^{3-}$	(57)

The organic part from the collagen protein: Amide I band of C=O stretching at around 1652 cm⁻¹ band area varies from one another. Since this band is overlapped with O-H bending, it is not analyzed here. Amide II (Protein N-H bend, C-N stretch) at 1550-1506 cm⁻¹ and amide III (C-N stretch, N-H bend, C-C stretch) at around 1240 cm⁻¹ are not prominent and they have almost the same shapes at the same positions.

It is noticeable that a broad band at around 677 cm^{-1} , which is assigned to C-S stretching vibration (41), only appears strongly in the anterior section and less strongly in the lateral section, while it disappears in the other two sections. Instead, a small band exists at 721 cm^{-1} in the longitudinal section. This small band is assigned to C-H rocking vibration (41). These differences in spectra further prove that the four sections of tibia contain different compositions.

The spectra from the mineral component part, including OH stretching vibrations from P-OH around 2100 cm^{-1} , $\nu_4\text{ PO}_4^{3-}$ band at $572\text{-}610\text{ cm}^{-1}$, and ν_2 out-of-plane bending of CO_3^{2-} at 877 cm^{-1} almost all remains the same band position and shape. The broad profiles of $\nu_3\nu_1\text{ PO}_4^{3-}$ band at $1180\text{-}927\text{ cm}^{-1}$ all vary from one another due to orientation effect and the difference among bone species as well.

6.3.3. In situ FE-SEM nanoindentation

In situ FE-SEM nanoindentation was performed on the anterior and posterior sections of both normal and OI cortical bones in the two planes (Figure 6.1). The representative load-displacement curves are shown in Figure 6.5 (a) and (b) for both transverse sections. The curve for the trans-posterior section is less smooth than the normal bone, while the curve for the trans-anterior section is zigzag shaped with lots of small and short turns. These phenomena reflect a more heterogeneous nature of the anterior section of OI bone at nanoscale.

The resulting elastic moduli from the transverse sections are shown in Table 6.2 and Figure 6.6. For the convenience of comparison, the corresponding data from normal bone are also listed in the Table. Three items can be compared here. (1) Comparison of interstitial lamellae and osteonal lamellae. As seen from Table 6.2 and Figure 6.6, for both anterior and posterior sections of normal and OI bones, the median elastic modulus and hardness of interstitial lamellae are almost all higher than those of osteonal lamellae. The reason is that the

interstitial lamellae are more mature than the osteonal lamellae (42,43). This trend is consistent for both normal and OI bones. (2) Comparison of anterior and posterior section. Figure 6.6 and Table 6.2 show that almost all median elastic moduli and hardness of the posterior sections are greater than those of values of corresponding anterior sections except the harness of normal bone. However, the hardness of normal bone exhibits different trend that the posterior section of normal bone shows much lower hardness than its anterior section. For OI bone, the trend of hardness is the same as that of elastic modulus. (3) Comparison of normal and OI bones. The median elastic modulus of OI bone is greater than those of normal bone. The hardness of OI bone is lower in the anterior section but higher in the posterior section than normal bone.

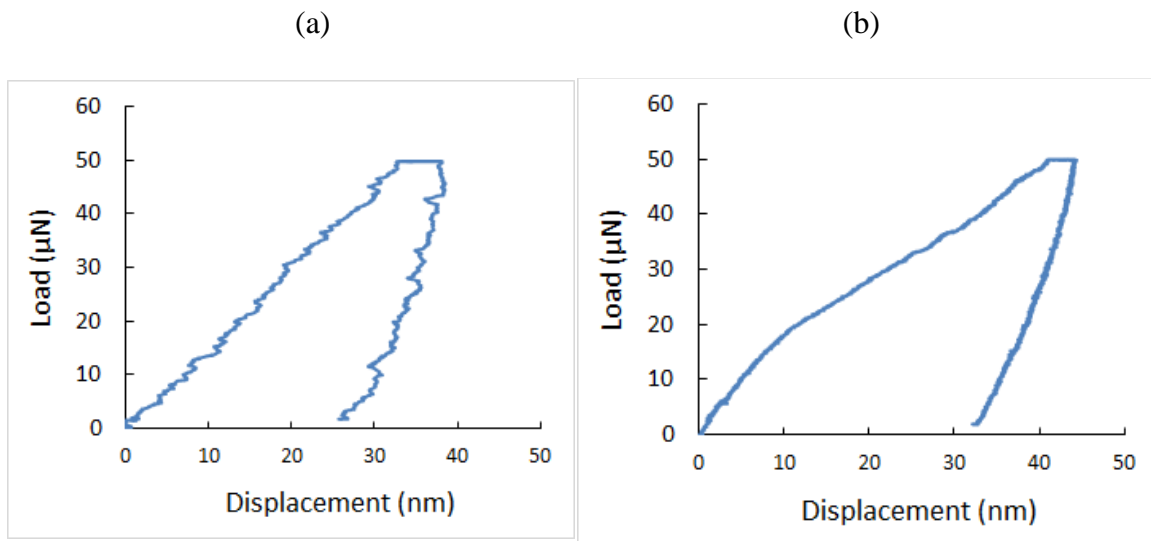


Figure 6.5. Representative load-displacement curve taken during a single nanoindentation test of the OI bone specimen with peak load of 50 μN : (a) Trans-anterior section; (b) Trans-posterior section.

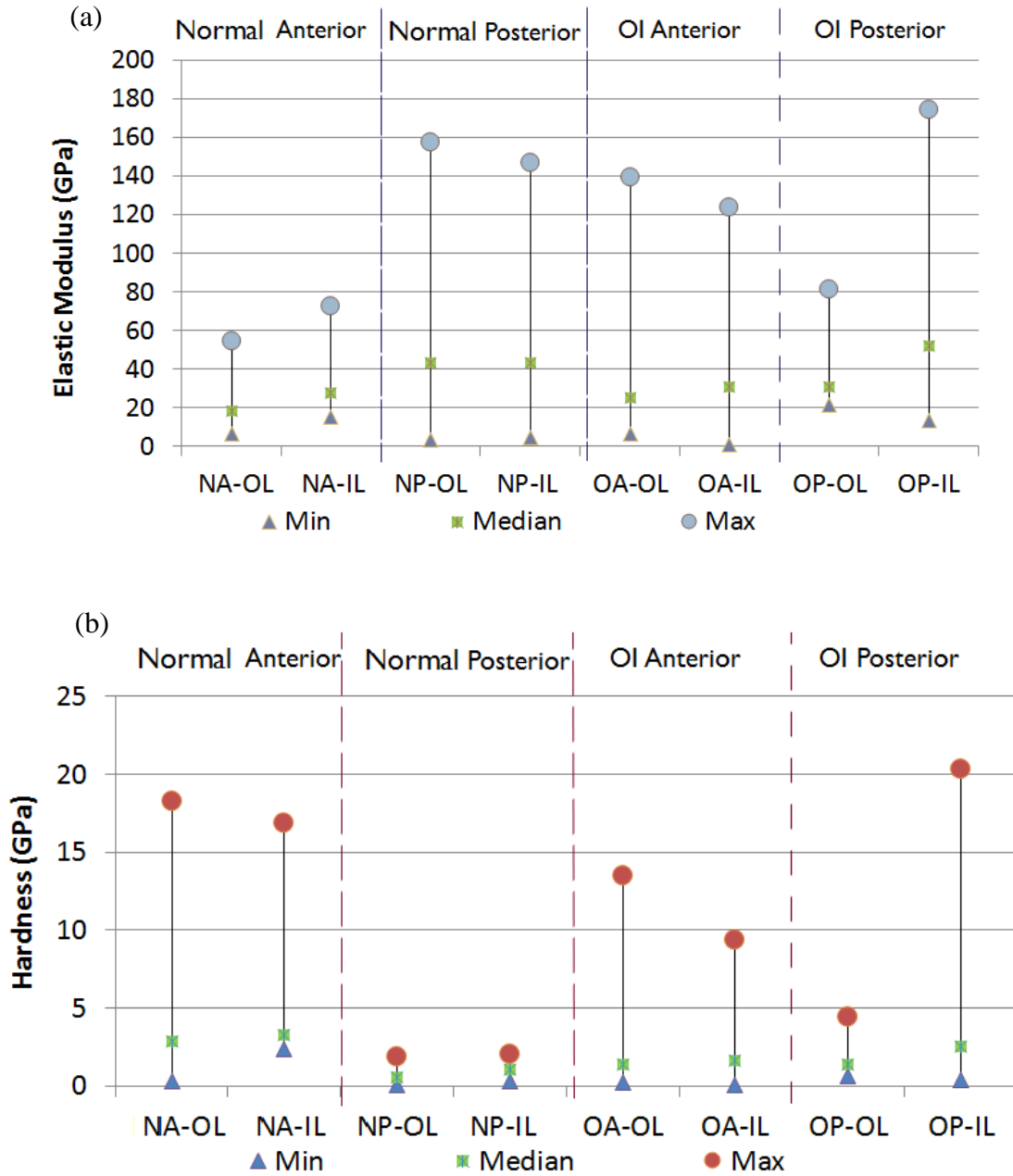


Figure 6.6. Nanomechanical properties of normal and OI bones (anterior and posterior sections) in the transverse plane. OL refers to osteonal lamellae, and IL refers to interstitial lamellae. (a) Elastic modulus; (b) Hardness.

Table 6.2. Elastic moduli and hardness of anterior and posterior sections of human OI cortical bone for the transverse sections.

Bone specimen			Elastic moduli(GPa)			Hardness(GPa)		
			Min	Median	Max	Min	Median	Max
OI bone	Anterior section	Osteonal lamellae	6.51	25.18	138.99	0.21	1.39	13.46
		Interstitial lamellae	1.13	30.77	123.51	0.04	1.65	9.40
	Posterior section	Osteonal lamellae	21.14	30.51	81.28	0.65	1.40	4.45
		Interstitial lamellae	13.61	52.12	174.05	0.39	2.58	20.31
Normal bone	Anterior section	Osteonal lamellae	6.78	18.35	54.28	0.34	2.86	18.26
		Interstitial lamellae	15.47	27.92	72.38	2.40	3.29	16.90
	Posterior section	Osteonal lamellae	3.54	43.41	157.22	0.09	0.57	1.89
		Interstitial lamellae	4.59	43.30	146.75	0.31	1.07	2.07

For the longitudinal sections, elastic modulus and hardness of anterior and posterior sections of normal and OI bones are shown in Table 6.3 and Figure 6.7. Similar three items are compared. (1) Comparison of different displacement. As seen from the Table 6.3 and Figure 6.7, the variation of elastic moduli with the lower load is greater than that with higher load in all bone sample types. This phenomenon has been observed previously (44). Lower load corresponds to shallow displacement which reflects more individual constituent properties rather than bulk properties with deep displacement. It is also noticed that the posterior section of OI bone has the same trend as the anterior section of normal bone: the median elastic modulus reduces with increased loading force. However, the trend of the anterior section of OI bone and the posterior section of normal is quite mixed. (2) Comparison of anterior and posterior sections. For normal bone, most median elastic moduli and hardness of posterior section are greater than those of anterior section. For OI bone, the median elastic moduli are hard to compare between anterior and posterior sections, while the hardness of posterior section is lower than that of anterior

section. (3) Comparison of normal and OI bones. Most median elastic moduli and hardness of normal bone are greater than those of OI bone.

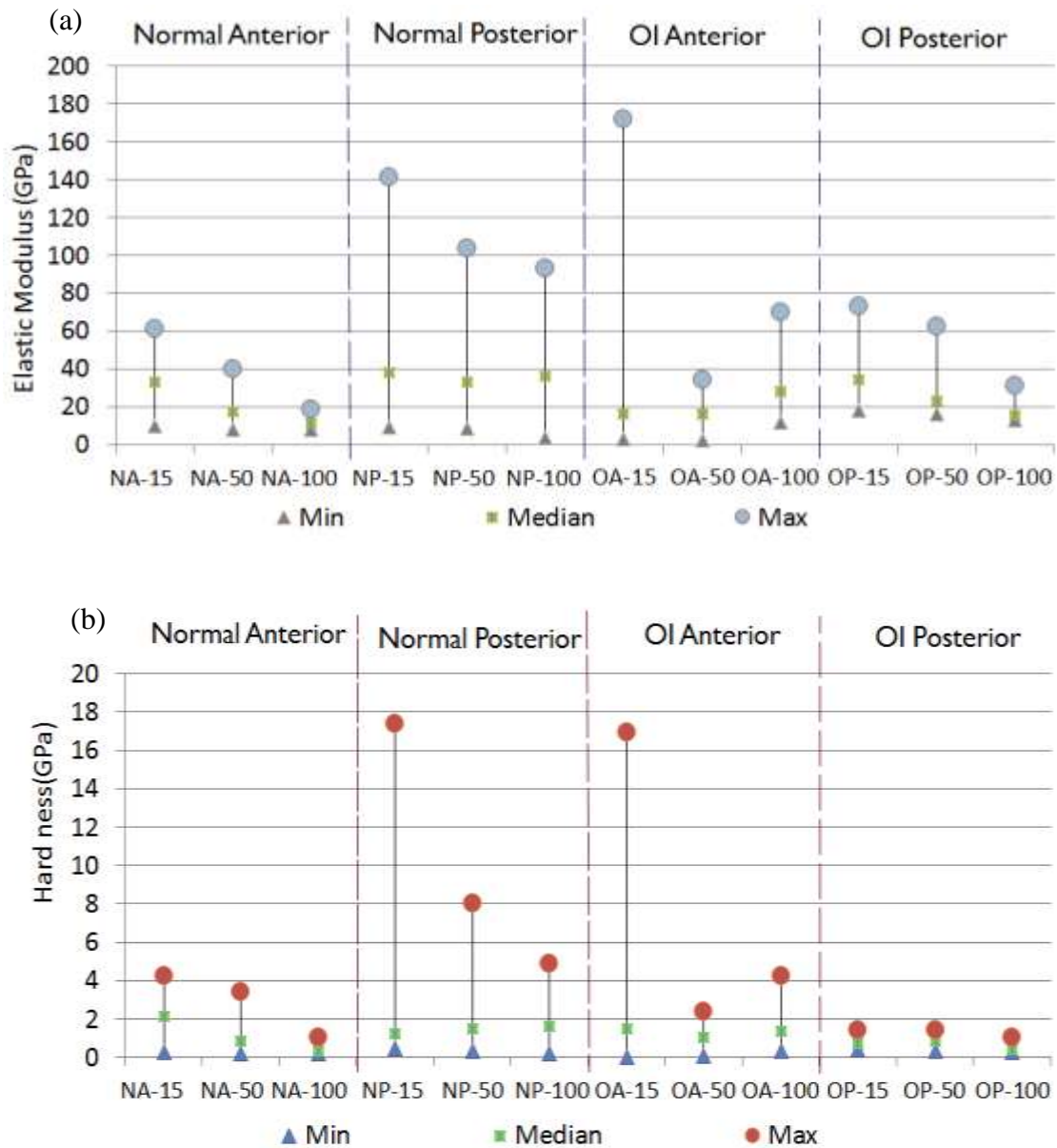


Figure 6.7. Nanomechanical properties of normal and OI bones (anterior and posterior sections) in the longitudinal plane. OL is osteonal lamellae, and IL is interstitial lamellae. (a) Elastic modulus; (b) Hardness.

Table 6.3. Elastic moduli and hardness of anterior and posterior sections of human OI cortical bone for the longitudinal sections.

Bone specimen		Load	Elastic modulus (GPa)			Hardness (GPa)		
			Min	Median	Max	Min	Median	Max
OI bone	Anterior section	15 μ N	2.96	15.86	172.17	0.02	1.47	16.92
		50 μ N	2.57	15.87	34.04	0.06	1.07	2.37
		100 μ N	11.55	27.92	69.72	0.33	1.36	4.27
	Posterior section	15 μ N	17.87	34.57	73.34	0.42	0.73	1.41
		50 μ N	16.21	23.15	62.30	0.35	0.83	1.41
		100 μ N	12.96	15.73	31.09	0.26	0.42	1.04
Normal bone	Anterior section	15 μ N	10.13	32.87	60.90	0.30	2.14	4.22
		50 μ N	8.00	17.57	40.20	0.21	0.88	3.42
		100 μ N	8.12	10.86	18.82	0.22	0.36	1.02
	Posterior section	15 μ N	9.54	38.26	141.24	0.46	1.23	17.41
		50 μ N	8.93	33.21	103.48	0.31	1.48	8.04
		100 μ N	3.92	36.47	92.96	0.20	1.61	4.86

6.4. Discussion

Bone constantly undergoes mechanical force induced modeling (reshaping) and remodeling processes to remove old, microdamaged bone and replace it with new bone to help preserve bone strength. Remodeling of bone involves resorption of old bone by osteoclasts and formation of new bone by osteoblasts. The round secondary osteons only appear in the existing bone tissue during remodeling process with a characteristic cement line seen at the junction between the outermost lamella of the new osteon and the preexisting older bone. In comparison, the primary osteons are created in the periosteum during the modeling process; therefore the primary osteons are usually surrounded by parallel circumferential lamellae (45). It is largely

accepted that remodeling exists from the perinatal and infant stages (46). Generally, the positions containing circumferential lamellae maintained higher elastic modulus and ultimate tensile strength than those with secondary osteons (47). In this study, SEM images show that remodeling occurs throughout all sections characterized by secondary osteons. The lateral section has some areas the same as the normal bone, while the other three sections have similar structures. However, from the SEM images, it is hard to identify the structural differences at the molecular scale or nanoscale among the four sections.

In another study, we find that the anterior section of OI bone is very porous and contains more non-collagenous proteins (48). SEM and FTIR studies of the four sections in the present study further confirm that OI bone is porous and contains more non-collagenous proteins. The medial section of OI bone has the largest amount of non-collagenous proteins based on the spectroscopic study. The intensity of C-S stretching vibration band at around $640-710\text{ cm}^{-1}$ is correlated for the longitudinal and transverse sections when it is from the same anatomical position of OI bone. The C-S band is probably from the replacement of cysteine for glycine in the collagen molecules or an increased amount of cysteine-rich osteonectin. The intensity of C-S band is the greatest in anterior, followed by lateral, and the least intense are posterior and medial, which have similar intensity. This order may reflect the extent of alteration in the collagen molecules or non-collagenous proteins in these four positions of OI bone. This phenomenon is in good agreement with the nanomechanical testing results. In situ FE-SEM nanoindentation shows that the anterior section of OI bone has unsmooth load-displacement curves and more site-specific nanomechanical properties than the posterior section, indicating that the anterior section is more heterogeneous than the posterior section. The nanomechanical properties of the posterior section are also seen to have similar trends as the anterior section of normal bone: (1) For the

transverse section, both of the median elastic moduli and hardness values of interstitial lamellae are greater than osteonal lamellae; (2) As the load increases, the elastic moduli and hardness values decrease; (3) The variation of nanomechanical properties of the posterior section decreases with increased load. On the other hand, the posterior section of normal bone has some similarities as the anterior section of OI bone: (1) Both of them have great variation of mechanical properties except the hardness of transverse section of normal bone; (2) Both of them show irregular trend for the longitudinal sections. Overall, the comparison of nanomechanical properties between OI and normal bones is mixed for the transverse and longitudinal sections because of the variation and site-specific nanomechanical properties of bone samples. Therefore, more nanoindentations and bone samples are required for a better statistical study.

As mentioned before, reduced nanomechanical properties are found in bones from OI type III children (3.2-12.4 years) and *oim* mice as compared with normal and controlled data (28, 30). The *oim* model mimics moderate to severe OI in humans, similar to OI type III (30). Therefore, one reason for those reduced nanomechanical properties of OI bone is that, as the second most severe type, OI type III bone contains structurally abnormal microstructure and abnormal cortical remodeling (39, 49), causing both reduced elastic modulus and reduced hardness. In the present study, the OI bone sample is putative type I OI, which is the mildest type with less abnormal microstructure than type III. The second possible reason for those reduced nanomechanical properties of bone from OI type III children (3.2-12.4 years) as compared with normal matured data is that, bone becomes stronger when it gets more mature (50). In other words, bone from an adult is more mature and, therefore, stronger than bone from a person before puberty. Bone constantly undergoes modeling and remodeling processes to help preserve bone strength. Holguin et al. find that the tibial structure and strength are both influenced by

compression. The cortical bone volume and strength of bone increase with the loading (51). Silva et al. find the same trend that with loading, there is an increase in cortical bone volume, and they also find that there is significant increases in osteoblast/matrix genes in older mice (52). Under microgravity conditions, there are changes in the bone tissue such as the decreasing of bone mass and the reduction of bone strength (53). These studies confirm that bone adapts itself to the bearing force. Even with genetic bone disease, bone still adapts itself to obtain a higher strength to adapt to the increased body weight. Therefore, in OI patients, after puberty bone usually becomes stronger and less fractures occur (50). Our study shows that for the transverse sections, all interstitial lamellae have greater elastic moduli and hardness values than osteonal lamellae (54). Interstitial lamellae are made up of the remnants of the remodeled old osteons or primary bone tissue. The interstitial lamellae are more mature than newly formed secondary osteons. Therefore, the stronger mechanical properties of bone after puberty are due to the replacement of microdamaged bone by new secondary osteons through the remodeling process.

6.5. Conclusion

In the present study, SEM and PA-FTIR are utilized to characterize the OI human cortical bone (putative type I). Microstructure and IR spectra from four anatomical positions (anterior, medial, posterior, and lateral) in two planes (longitudinal and transverse) are compared. In addition, nanomechanical properties of the anterior and posterior sections from both normal and OI bones are measured using in situ FE-SEM nanoindentation. SEM images show that remodeling process occurs throughout all of the OI sections. Comparatively, the medial section contains less secondary osteons and the lateral section contains normal microstructure while the other three sections contain microstructures similar to normal.

FTIR spectra showed that the medial section contains more non-collagenous proteins than the anterior section. The lateral and posterior sections have even less non-collagenous proteins. The abnormal C-S band, which is probably from the replacement of cysteine for glycine in the collagen molecules or an increased amount of cysteine-rich osteonectin, appears more prominently in the anterior section than the lateral section. Meanwhile, there is almost no C-S band from the posterior and medial sections. This FTIR spectra analysis is in a good agreement with nanomechanical testing results that the anterior section of OI bone seems more heterogeneous in its properties. As compared to the anterior section, the posterior section exhibits more similar nanomechanical properties to the anterior section of normal bone. The nanomechanical properties of interstitial lamellae in all these bone samples are consistently greater than those of osteonal lamellae due to more mature nature of interstitial lamellae. However, other nanomechanical properties of these sections do not accord with each other, indicating a heterogeneous and site-specific nature of bone samples. It also seems that the nanomechanical properties of bone depends on its anatomical section and its direction as well.

In order to better understand the molecular mechanism of OI, genomic identity of this bone material used in the present study is needed. Also, in situ FE-SEM nanoindentation on the medial and lateral sections are also required.

6.6. Acknowledgements

Instrumentation obtained from National Science Foundation MRI grants is acknowledged for enabling experiments conducted in this work. I would like to acknowledge assistance in electron microscopy laboratory from Mr. Scott Payne.

6.7. References

1. Bass SL, Saxon L, Daly RM, Turner CH, Robling AG, Seeman E, et al. The effect of mechanical loading on the size and shape of bone in pre-, peri-, and postpubertal girls: A study in tennis players. *Journal of Bone and Mineral Research*. 2002;17(12):2274-80.
2. Frost HM. Wolff law and bones structural adaptations to mechanical usage - an overview for clinician. *Angle Orthodontist*. 1994;64(3):175-88.
3. Gosman JH, Hubbell ZR, Shaw CN, Ryan TM. Development of Cortical Bone Geometry in the Human Femoral and Tibial Diaphysis. *The Anatomical Record*. 2013;296:774-87.
4. Cambra-Moo O, Nacarino Meneses C, Rodriguez Barbero MA, Garcia Gil O, Rascon Perez J, Rello-Varona S, et al. Mapping human long bone compartmentalisation during ontogeny: A new methodological approach. *Journal of Structural Biology*. 2012;178(3):338-49.
5. Abdel-Wahab AA, Alam K, Silberschmidt VV. Analysis of anisotropic viscoelastoplastic properties of cortical bone tissues. *Journal of the Mechanical Behavior of Biomedical Materials*. 2011;4(5):807-20.
6. Rho JY, Currey JD, Zioupos P, Pharr GM. The anisotropic Young's modulus of equine secondary osteons and interstitial bone determined by nanoindentation. *Journal of Experimental Biology*. 2001;204(10):1775-81.
7. Batson EL, Reilly GC, Currey JD, Balderson DS. Postexercise and positional variation in mechanical properties of the radius in young horses. *Equine Veterinary Journal*. 2000;32(2):95-100.
8. Riggs CM, Lanyon LE, Boyde A. Functional associations between collagen fiber orientation and locomotor strain direction in cortical bone of the equine radius. *Anatomy and Embryology*. 1993;187(3):231-8.

9. Riggs CM, Vaughan LC, Evans GP, Lanyon LE, Boyde A. Mechanical implications of collagen fiber orientation in cortical bone of the equine radius. *Anatomy and Embryology*. 1993;187(3):239-48.
10. Rubin CT, Lanyon LE. Limb mechanics as a function of speed and gait - a study of functional strains in the radius and tibia of horse and dog. *Journal of Experimental Biology*. 1982;101(DEC):187-211.
11. Biewener AA, Thomason J, Goodship A, Lanyon LE. Bone stress in the horse forelimb during locomotion at different gaits - a comparison of 2 experimental methods. *Journal of Biomechanics*. 1983;16(8):565-76.
12. Biewener AA, Thomason J, Lanyon LE. Mechanics of locomotion and jumping in the forelimb of the horse (equus) - invivo stress developed in the radius and metacarpus. *Journal of Zoology*. 1983;201(SEP):67-82.
13. Fratzl P, Paris O, Klaushofer K, Landis WJ. Bone mineralization in an osteogenesis imperfecta mouse model studied by small-angle x-ray scattering. *Journal of Clinical Investigation*. 1996;97(2):396-402.
14. Reilly GC, Currey JD. The development of microcracking and failure in bone depends on the loading mode to which it is adapted. *Journal of Experimental Biology*. 1999;202(5):543-52.
15. Fratzl P, Schreiber S, Boyde A. Characterization of bone mineral crystals in horse radius by small-angle X-ray scattering. *Calcified Tissue International*. 1996;58(5):341-6.
16. Martins Moreira CL, de Faria Domingues Lima MA, Cabral de Almeida Cardoso MH, dos Santos Gomes Junior SC, Lopes PB, Llerena Junior JC. Independent walk in osteogenesis imperfecta. *Acta Ortopedica Brasileira*. 2011;19(5):312-5.

17. Engelbert RHH, Uiterwaal C, Gulmans VAM, Pruijs H, Helders PJM. Osteogenesis imperfecta in childhood: Prognosis for walking. *Journal of Pediatrics*. 2000;137(3):397-402.
18. Van Brussel M, Takken T, Uiterwaal CSPM, Pruijs HJ, Van der Net J, Helders PJM, et al. Physical training in children with osteogenesis imperfecta. *Journal of Pediatrics*. 2008;152(1):111-6.
19. Rauch F, Glorieux FH. Osteogenesis imperfecta. *Lancet*. 2004;363(9418):1377-85.
20. Cassella JP, Stamp TCB, Ali SY. A morphological and ultrastructural study of bone in osteogenesis imperfecta. *Calcified Tissue International*. 1996;58(3):155-65.
21. Teitelbaum SL, Kraft WJ, Lang R, Avioli LV. Bone collagen aggregation abnormalities in osteogenesis imperfecta. *Calcified Tissue Research*. 1974;17(1):75-9.
22. Vetter U, Eanes ED, Kopp JB, Termine JD, Robey PG. Changes in apatite crystal size in bones of patients with osteogenesis imperfecta. *Calcified Tissue International*. 1991;49(4):248-50.
23. Vetter U, Weis MA, Morike M, Eanes ED, Eyre DR. Collage cross-links and mineral crystallinity in bone of patients with osteogenesis imperfecta. *Journal of Bone and Mineral Research*. 1993;8(2):133-7.
24. Wallace JM, Orr BG, Marini JC, Holl MMB. Nanoscale morphology of Type I collagen is altered in the Brl mouse model of Osteogenesis Imperfecta. *Journal of Structural Biology*. 2011;173(1):146-52.
25. Kemp AD, Harding CC, Cabral WA, Marini JC, Wallace JM. Effects of tissue hydration on nanoscale structural morphology and mechanics of individual Type I collagen fibrils in the Brl mouse model of Osteogenesis Imperfecta. *Journal of Structural Biology*. 2012;180(3):428-38.

26. Camacho NP, Landis WJ, Boskey AL. Mineral changes in a mouse model of osteogenesis imperfecta detected by Fourier transform infrared microscopy. *Connective Tissue Research*. 1996;35(1-4):259-65.
27. Camacho NP, Hou L, Toledano TR, Ilg WA, Brayton CF, Raggio CL, et al. The material basis for reduced mechanical properties in oim mice bones. *Journal of Bone and Mineral Research*. 1999;14(2):264-72.
28. Fan ZF, Smith PA, Eckstein EC, Harris GF. Mechanical properties of OI type III bone tissue measured by nanoindentation. *Journal of Biomedical Materials Research Part A*. 2006;79A(1):71-7.
29. Imbert L, Auregan J-C, Pernelle K, Hoc T. Mechanical and Mineral Properties of Osteogenesis Imperfecta Human Bones at the Tissue Level. *Bone*. 2014;65:18-24.
30. Vanleene M, Porter A, Guillot PV, Boyde A, Oyen M, Shefelbine S. Ultra-structural defects cause low bone matrix stiffness despite high mineralization in osteogenesis imperfecta mice. *Bone*. 2012;50(6):1317-23.
31. Weber M, Roschger P, Fratzl-Zelman N, Schoberl T, Rauch F, Glorieux FH, et al. Pamidronate does not adversely affect bone intrinsic material properties in children with osteogenesis imperfecta. *Bone*. 2006;39(3):616-22.
32. Fan ZF, Smith PA, Harris GF, Rauch F, Bajorunaite R. Comparison of nanoindentation measurements between osteogenesis imperfecta type III and type IV and between different anatomic locations (femur/tibia versus iliac crest). *Connective Tissue Research*. 2007;48(2):70-5.
33. Fan ZF, Smith P, Rauch F, Harris GF. Nanoindentation as a means for distinguishing clinical type of osteogenesis imperfecta. *Composites Part B-Engineering*. 2007;38(3):411-5.

34. Sinder BP, Eddy MM, Ominsky MS, Caird MS, Marini JC, Kozloff KM. Sclerostin Antibody Improves Skeletal Parameters in a *Brl/+* Mouse Model of Osteogenesis Imperfecta. *Journal of Bone and Mineral Research*. 2013;28(1):73-80.
35. Rauch F, Travers R, Parfitt AM, Glorieux FH. Static and dynamic bone histomorphometry in children with osteogenesis imperfecta. *Bone*. 2000;26(6):581-9.
36. Gu C, Katti DR, Katti KS. Photoacoustic FTIR spectroscopic study of undisturbed human cortical bone. *Spectrochimica acta Part A*. 2013;103:25-37.
37. Rzepiejewska-Malyska KA, Buerki G, Michler J, Major RC, Cyrankowski E, Asif SAS, et al. In situ mechanical observations during nanoindentation inside a high-resolution scanning electron microscope. *Journal of Materials Research*. 2008;23(7):1973-9.
38. Oliver WC, Pharr GM. An improved technique for determining hardness and elastic-modulus using load and displacement sensing indentation experiments. *Journal of Materials Research*. 1992;7(6):1564-83.
39. Traub W, Arad T, Vetter U, Weiner S. Ultrastructural studies of bones from patients with osteogenesis imperfecta. *Matrix Biology*. 1994;14(4):337-45.
40. Garip S, Severcan F. Determination of simvastatin-induced changes in bone composition and structure by Fourier transform infrared spectroscopy in rat animal model. *Journal of Pharmaceutical and Biomedical Analysis*. 2010;52(4):580-8.
41. Socrates G. *Infrared and Raman Characteristic group frequencies: tables and charts*. 3rd ed. Chichester: John Wiley & Sons; 2004.
42. Rho JY, Roy ME, Tsui TY, Pharr GM. Elastic properties of microstructural components of human bone tissue as measured by nanoindentation. *Journal of Biomedical Materials Research*. 1999;45(1):48-54.

43. Rho JY, Zioupos P, Currey JD, Pharr GM. Variations in the individual thick lamellar properties within osteons by nanoindentation. *Bone*. 1999;25(3):295-300.
44. Katti KS, Mohanty B, Katti DR. Nanomechanical properties of nacre. *Journal of Materials Research*. 2006;21(5):1237-42.
45. Skedros JG, Holmes JL, Vajda EG, Bloebaum RD. Cement lines of secondary osteons in human bone are not mineral-deficient: New data in a historical perspective. *Anatomical Record Part a-Discoveries in Molecular Cellular and Evolutionary Biology*. 2005;286A(1):781-803.
46. Burton P, Nyssenbehets C, Dhem A. Haversian bone remodeling in human-fetus. *Acta Anatomica*. 1989;135(2):171-5.
47. Currey JD. Differences in the tensile strength of bone of different histological types. *Journal of Anatomy*. 1959;93(1):87-&.
48. Gu C, Katti DR, Katti KS. Microstructural and Infrared Spectroscopic Studies of Human Cortical Bone in Osteogenesis Imperfecta. to be submitted ed.
49. Pazzaglia UE, Congiu T, Brunelli PC, Magnano L, Benetti A. The Long Bone Deformity of Osteogenesis Imperfecta III: Analysis of Structural Changes Carried Out with Scanning Electron Microscopic Morphometry. *Calcified Tissue International*. 2013;93(5):453-61.
50. <http://www.oif.org>.
51. Holguin N, Brodt MD, Sanchez ME, Kotiya AA, Silva MJ. Adaptation of Tibial Structure and Strength to Axial Compression Depends on Loading History in Both C57BL/6 and BALB/c Mice. *Calcified Tissue International*. 2013;93(3):211-21.
52. Silva MJ, Brodt MD, Lynch MA, Stephens AL, Wood DJ, Civitelli R. Tibial Loading Increases Osteogenic Gene Expression and Cortical Bone Volume in Mature and Middle-Aged Mice. *Plos One*. 2012;7(4).

53. Holick MF. Microgravity-induced bone loss - will it limit human space exploration?

Lancet. 2000;355(9215):1569-70.

54. Fan Z, Swadener JG, Rho JY, Roy ME, Pharr GM. Anisotropic properties of human tibial

cortical bone as measured by nanoindentation. Journal of Orthopaedic Research. 2002;20(4):806-

10.

CHAPTER 7. SUMMARY AND CONCLUSIONS

This chapter summarizes and concludes the research presented in this dissertation.

- Photoacoustic-Fourier transform infrared spectroscopy (PA-FTIR) experiments were conducted to investigate the orientational differences in molecular structure of human bone. PA-FTIR has the priority to investigate “undisturbed” bone samples with the protection of coupling inert gas which can inhibit bacterial growth of bone by replacing oxygen. It is found that the photoacoustic mode (linear-scan) can obtain basically similar spectra of bone as compared to the traditional transmission mode, but it seem more sensitive to amide III and ν_2 carbonate bands. As indicated by ν_1 phosphate band in the spectra, phosphate ion geometry appears less symmetric in its undisturbed state as detected by the photoacoustic mode as compared to higher symmetry observed using transmission mode on disturbed samples. Moreover, the PA-FTIR spectra indicate a band at 1747 cm^{-1} possibly resulting from C=O stretching of lipids, cholesterol esters, and triglycerides from the arteries. Comparison of the spectra in transverse and longitudinal cross-sections demonstrates that, the surface of the longitudinal section bone appears to have more organic matrix exposed and with higher mineral stoichiometry. The PA-FTIR depth profiling experiments on human cortical bone also indicate the influence of water on OH band and the cutting effects on amide I and mineral bands.
- PA-FTIR, scanning electron microscopy (SEM), and X-ray diffraction (XRD) are used to describe the structural and compositional differences between osteogenesis imperfecta (OI) and healthy bones at the molecular-, micro-, and macro- scale levels. OI bone exhibits more porous, fibrous features, abnormal collagen fibrils, and

abnormal mineral deposits, as revealed by SEM images. Likewise, photoacoustic-Fourier transform infrared spectroscopy (PA-FTIR) experiments indicate an aberrant collagen structure. The spectra also reveal a slightly altered mineral structure in OI. In contrast, there is neither significant difference in the non-collagenous proteins (NCPs) composition as shown in the spectra nor apparent change in the crystal structure between OI and healthy bone minerals as shown in x-ray diffraction (XRD) and Energy-dispersive X-ray spectroscopy (EDS) results. This phenomenon indicates that the biomineralization process is more controlled by the bone cells and non-collagenous phosphorylated proteins. PA-FTIR studies of OI bone also confirm that there is an orientational difference in the stoichiometry of the mineral in OI bone. In addition, a larger volume of the hydrated layer in the transverse plane than the longitudinal plane of the mineral crystal structure is proposed. The appearance of a new C-S band in FTIR spectra in OI bone suggests the substitution of glycine by cysteine in collagen molecules or/and an increased amount of cysteine-rich osteonectin which relates to mineral nucleation and mineral crystal formation.

- Modulus mapping technique and in situ field emission-scanning electron microscope (FE-SEM) nanoindentation are both applied for the first time on “undisturbed” normal and OI human cortical bones at the nanometer and sub-micro scale levels in this work. Modulus mapping test reveals the elastic moduli of near-pure hydroxyapatite and collagen to be 189.85 GPa and 2.42 GPa for normal bone, and 294.69 GPa and 2.85 GPa for OI bone, respectively. Modulus mapping also indicates spatial variation of elastic moduli consistent with the distribution of mineralized fibril and extrafibrillar mineral. From modulus maps, the diameter of collagen fiber and the

size of mineral crystals in OI are observed to be smaller and the mineral crystal in OI is also observed to be less heterogeneous than those from normal bone. The median elastic moduli of OI bone are greater than those of normal bone. In situ FE-SEM nanoindentation reveals the existence of a highly mineralized inner ring with higher elastic moduli adjacent to the Haversian canal, and that the elastic nanomechanical properties of interstitial lamellae are greater than osteonal lamellae. A periodic modulation in modulus corresponding to the width of a lamella is also observed in in situ FE-SEM nanoindentation. Varying median elastic moduli in the transverse and longitudinal orientations obtained from these two experiments indicate that at nanoscale, the interaction between mineral and collagen influences the mechanical properties; while at micro scale, the orientation and arrangement of mineral and collagen play more significant roles. OI bone in the transverse section (nanoindentation force is applied along the physiological loading direction) shows higher elastic moduli for both interstitial and osteonal lamellae, but lower hardness than normal bone.

- Time-dependent nanomechanical properties of human cortical bone were studied using dynamic nanoindentation (nanoDMA) at the sub-micro scale level. The samples include intact, demineralized, and OI human cortical bone specimens. Loss tangent, $\tan \delta$, was considered as a measure of the degree of the viscoelastic response. Variable dynamic load tests show that the viscoelastic responses of all bone specimens increase with frequency. With demineralization, bone specimens show greater viscoelastic response than intact specimens. OI bone shows similar viscoelastic response as normal bone. Results suggest that the viscoelasticity of bone

is mostly attributable to the mineral phase. The present study adds to the understanding of viscoelastic response of bone material. In addition, the dynamic mechanical properties of OI bone are firstly reported here.

- The microstructure and molecular composition of different anatomical positions (anterior, medial, posterior, and lateral regions) in the diaphysis of an OI human tibia are also examined for the first time. Study shows that although there is no significant microstructural difference seen in SEM images, FTIR results still reveals some differences in molecular composition of the four anatomical positions. This FTIR spectra analysis is in a good agreement with in situ FE-SEM nanoindentation testing that the anterior section of OI bone seems more heterogeneous in its properties. Nanomechanical properties of interstitial lamellae in all these bone samples are consistently greater than those of osteonal lamellae. The nanomechanical properties of bone depend on its anatomical section and its direction as well.

CHAPTER 8. MAJOR CONTRIBUTIONS

Our research makes four major contributions:

- The development of a novel methodology for conducting infrared spectroscopic study on “undisturbed” biological samples using photoacoustic-Fourier transform infrared spectroscopy (PA-FTIR). Comparison between photoacoustic and transmission modes were conducted. We find that orientational differences in stoichiometry of hydroxyapatite are influenced by the interactions between mineral and collagen molecules. Another finding is that FTIR spectra of OI (putative type I) bone show the appearance of a new C-S band which might be from either the substitution of glycine by cysteine in collagen molecules or/and an increased amount of cysteine-rich osteonectin which relates to mineral nucleation and mineral crystal formation.
- For the first time we performed in situ field emission-scanning electron microscopy (FE-SEM) nanoindentation on bone samples. In situ FE-SEM nanoindentation provides a new tool to investigate the mechanical properties of materials with high resolution image and precise positioning of the indenter. We find the existence of a highly mineralized inner ring with higher elastic moduli adjacent to the Haversian canal, and that the elastic nanomechanical properties of interstitial lamellae are greater than osteonal lamellae. A periodic modulation in modulus corresponding to the width of a lamella is also observed in in situ FE-SEM nanoindentation. The nanomechanical properties of bone depends on its anatomical section and its direction as well.
- The difference of elastic modulus values acquired from modulus mapping and nanoindentation tests indicates a scale issue, i.e. at different length scales, due to different

arrangement and different interactions among the constituents, materials exhibit different mechanical behaviors.

- We compared the microstructure, compositional differences, and nanomechanical properties of healthy and osteogenesis imperfect (OI) bones, helping to understand the molecular bases of OI disease and the mineralization condition in OI bone. We find that the defective collagen results in a distorted microstructure in bone and also that the mineralization of hydroxyapatite in OI bone is also altered.
- Several novel experimental findings: We find that modulus mapping reveals the elastic moduli of near-pure hydroxyapatite and collagen to be 189.85 GPa and 2.42 GPa for normal bone, and 294.69 GPa and 2.85 GPa for OI bone, respectively. Modulus mapping also shows the distribution of mineralized fibril and extrafibrillar mineral according to the spatial variation of elastic properties. From modulus maps, the diameter of collagen fiber and the size of mineral crystals in OI are observed to be smaller and the mineral crystal in OI is also observed to be less heterogeneous than those from normal bone. In addition, the viscoelastic response of all bone specimens (intact, demineralized, and OI) decreases with frequency. Despite the significant altered collagen molecules, the overall similar dynamic nanomechanical behaviors of OI (putative type I) bone and normal bone indicate that the viscoelasticity of intact bone is mostly determined by the mineral. The collagen phase also contributes to the viscoelasticity to some extent. Lastly, different anatomical positions (anterior, medial, posterior, and lateral regions) in the diaphysis of an OI human tibia show varying molecular compositions as revealed by FTIR spectra.


CHAPTER 9. FUTURE WORK

The following are possible future directions for investigating the multiscale behavior of both healthy and osteogenesis imperfecta (OI) bones:

- Acquiring an OI femur and then comparing healthy and OI femurs or acquiring a healthy tibia and then comparing healthy and OI tibias.
- Conducting nanomechanical testing on demineralized healthy and OI bones using atomic force microscope (AFM) to investigate the mechanical properties of their collagen fibrils.
- Conducting microindentation and/or larger scale mechanical testing of both healthy and OI bones.
- Obtaining more bone samples and conducting statistical study.
- Collagen analysis or Noncollagenous proteins (NCPs) analysis or genetic analysis of the OI bone is required to confirm the source of the C-S band at around $640\text{-}710\text{ cm}^{-1}$ on FTIR spectra.

APPENDIX A. INFORMATION SHEETS FOR HUMAN BONE SAMPLES

A.1. Healthy human femur



NDRI
National Disease Research Interchange Center
THE NATIONAL RESEARCH CENTER

National Disease Research Interchange (NDRI)
8 Penn Center, 8th Floor
1628 JFK Blvd
Philadelphia, PA 19103
800-222-6374
www.ndriresource.org

HTOR Donor Information Form

Researcher: Katti **NDRI #** 0058139

Procurement Date: 8/28/2006 **ID #** DTB 060349

Shipping Date: 8/5/2009

Qty	Size/Weight	Tissue	Normal/Diseased	Preservation Method	Hours Post	Recovery Time
1	whole	BONE/FEM/PART	NORMAL	FRZN	17.6	

Accepted by: Scott Payne Comments: proximal

Donor Information

A/R/S: 27 / C / F **Second To:** MVA

Cause of Death: Trauma

(Eastern Standard Time)

Date/Time of Death: 6/30/2006 17:24 **Date/Time Recovery Complete:** 7/1/2006 11:00

Medical History

Height: 61 " **Weight:** 115 LB's

Medications:
birth control

Diabetes: N

Chemo/Rad: N

Alcohol: Y vodka on weekends

Tobacco: N

Drugs: Y smoked marijuana


Sepsis: N

WBC

Vent: N

Figure A.1. Information sheet of healthy human femur from NDRI

A.2. Osteogenesis imperfecta human tibia



NDRI
National Disease Research Interchange
THE NATIONAL RESOURCE CENTER

(800) 332-NDRI (6374)
1A28 JFK Bldg. 8 Penn Center
Philadelphia, PA 19103
Fax: (215) 367-7194

Department: HTOR
Policy: QA-Donor - OBC

HTOR Donor Information Form

NDRI #: 0056817 Procurement Date: 2/6/2006 Shipping Date: 11/5/2012
Source Ref#: OTB050554 Tracking Info: FedEx -

Researcher: Katti Track -
Researcher Code: KAK4

<u>Qty</u>	<u>Size/Weight</u>	<u>Tissue</u>	<u>Normal/Diseased</u>	<u>Pres Meth</u>	<u>Media</u>	<u>Hours Post</u>	<u>Recovery Time</u>
1	distal	BONE/TIBIA/PART	OSTIMP	FRZN		24.0	

Accepted by: Scott Payne

A/R/S: 22 / C / F
(Eastern Standard Time)
Date/Time of Death: 12/30/1899

Medical History
Height: 67 " Weight: 180 LB's
Accidental overdose of methadone & diphenhydramine, broken bones (arms and ankles) second to osteogenesis imperfecta, asthma, c-section, portion of lung removed, second in congenital lobar emphysema (at time of birth)

Med Codes
Asthma; Emphysema; Osteogenesis imperfecta-

Meds
Antidepressives, vitamins, prenatal during pregnancy
Diabetes: N

Chemo/Rad: N
Alcohol: N
Tobacco: N
Drugs: Y History of methadone abuse; no IV drug use
Sepsis: N
WBC
Vent: N

Donor Information

Cause of Death: Accidental OD of Meth & Diphen
Second To:
Date/Time Recovery Complete: 12/30/1899

<u>Infectious Disease Testing Performed?</u>	Y	<u>Results Received?</u>	Y		
HIV 1 Ab Test Performed?	Y	Result: Nonreactive	HCV Ab Test Performed?	Y	Result: Nonreactive
HIV 2 Ab Test Performed?	Y	Result: Nonreactive	HBs Ab Test Performed?	Y	Result: Nonreactive
RPR Syphilis Test Performed?	Y	Result: Nonreactive	HBs Ag Test Performed?	Y	Result: Nonreactive

Figure A.2. Information sheet of OI human tibia from NDRI

APPENDIX B. SEM IMAGES OF HEALTHY HUMAN FEMUR

B.1. Anterior section

B.1.1. Transverse section

B.1.1.1. Transverse section of healthy human femur (anterior), fixed with a series of chemicals and fractured in liquid N₂

B.1.1.1.1. Acquired on 12/1/2010

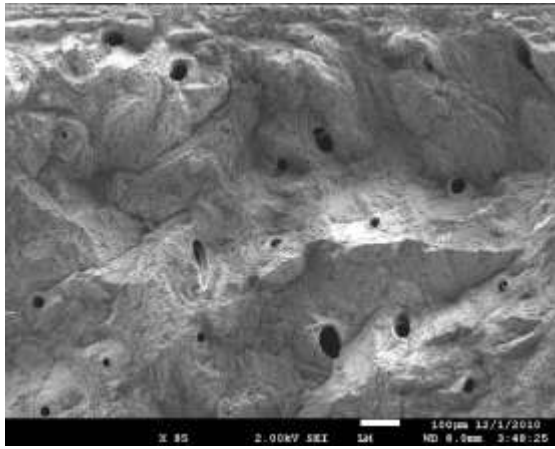


Figure B.1. SEM image of healthy human femur (transverse, anterior section) ×85

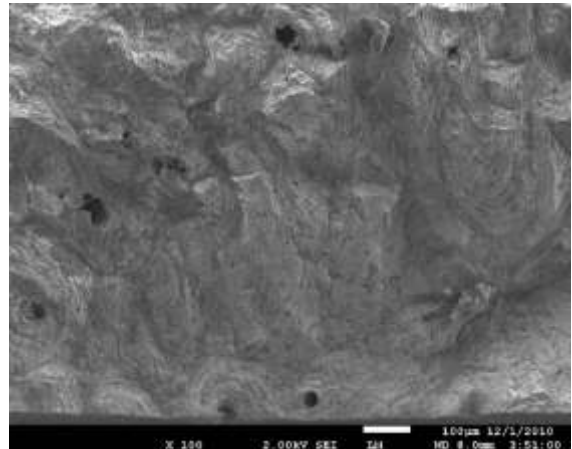


Figure B.2. SEM image of healthy human femur (transverse, anterior section) ×100

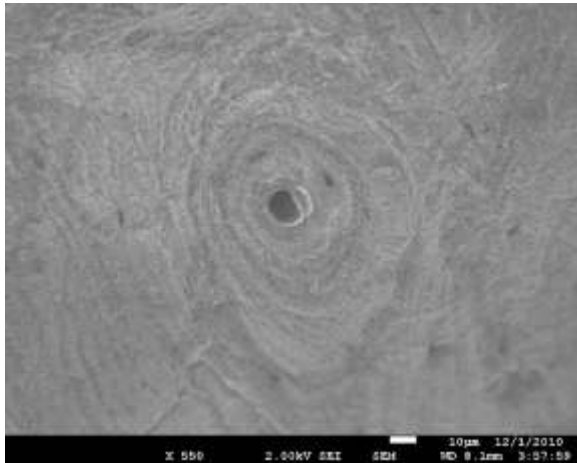


Figure B.3. SEM image of healthy human femur (transverse, anterior section) ×550

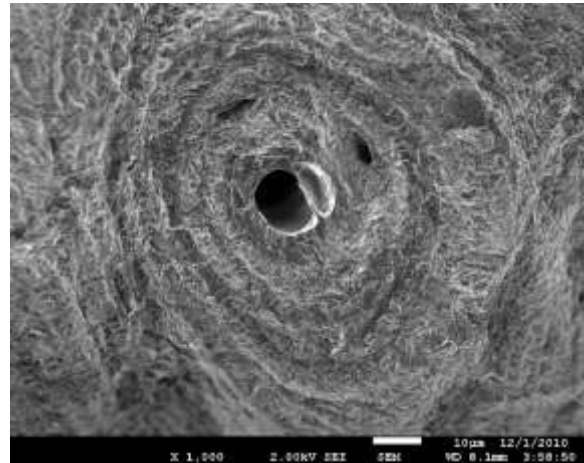


Figure B.4. SEM image of healthy human femur (transverse, anterior section) ×1,000

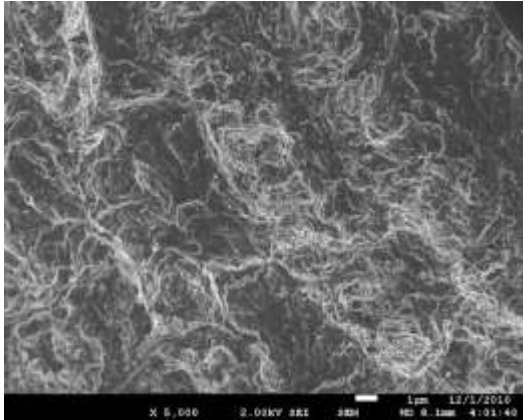


Figure B.5. SEM image of healthy human femur (transverse, anterior section) $\times 5,000$

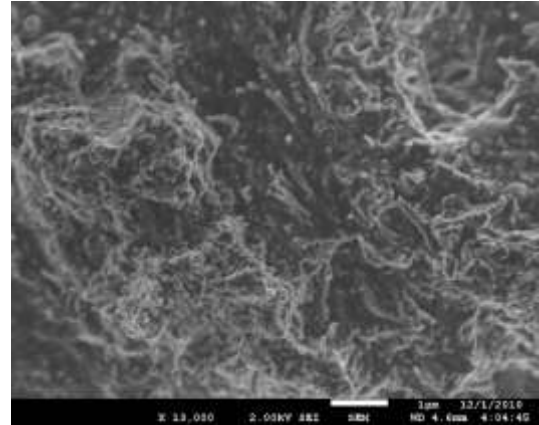


Figure B.6. SEM image of healthy human femur (transverse, anterior section) $\times 13,000$

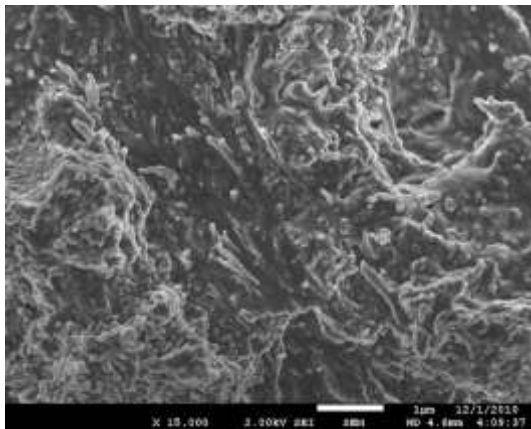


Figure B.7. SEM image of healthy human femur (transverse, anterior section) $\times 15,000$

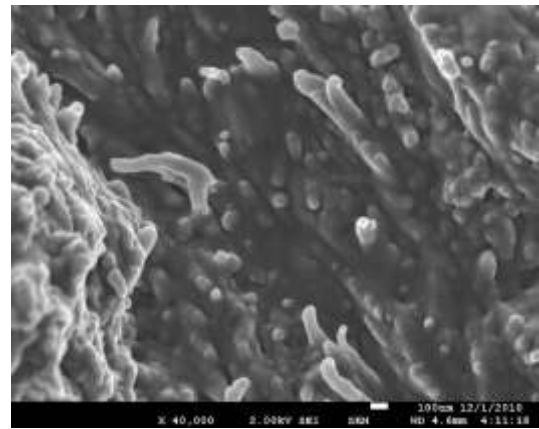


Figure B.8. SEM image of healthy human femur (transverse, anterior section) $\times 40,000$

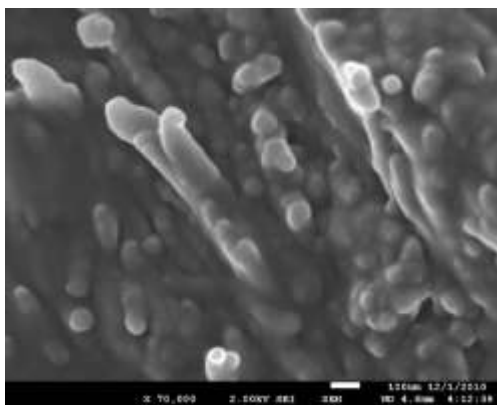


Figure B.9. SEM image of healthy human femur (transverse, anterior section) $\times 70,000$

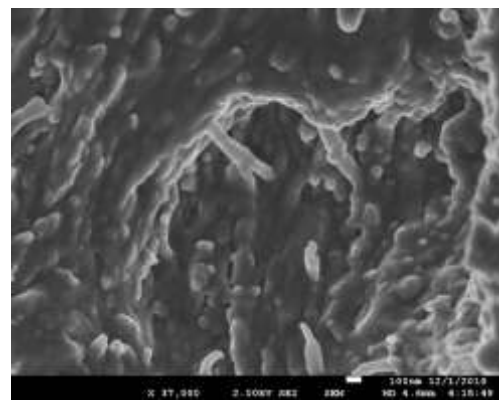


Figure B.10. SEM image of healthy human femur (transverse, anterior section) $\times 37,000$

B.1.1.1.2. Acquired on 3/2/2011

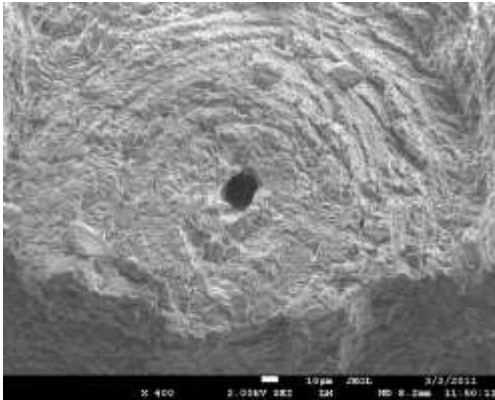


Figure B.11. SEM image of healthy human femur (transverse, anterior section) ×400

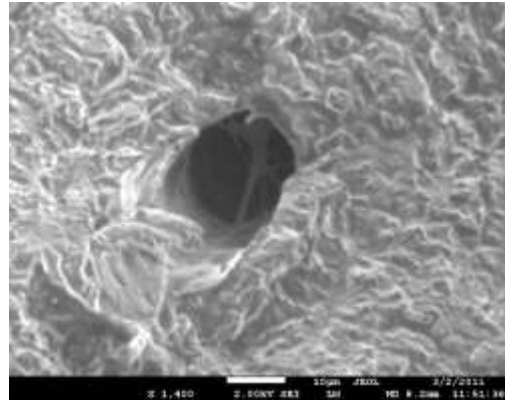


Figure B.12. SEM image of healthy human femur (transverse, anterior section) ×1,400

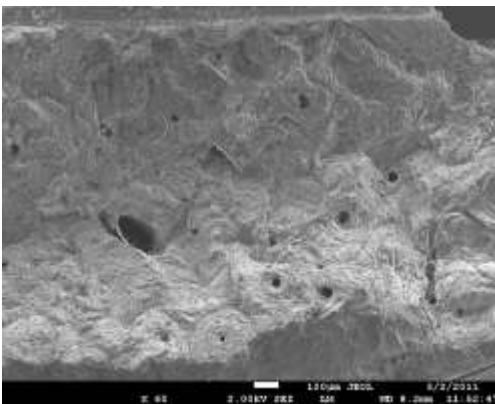


Figure B.13. SEM image of healthy human femur (transverse, anterior section) ×60

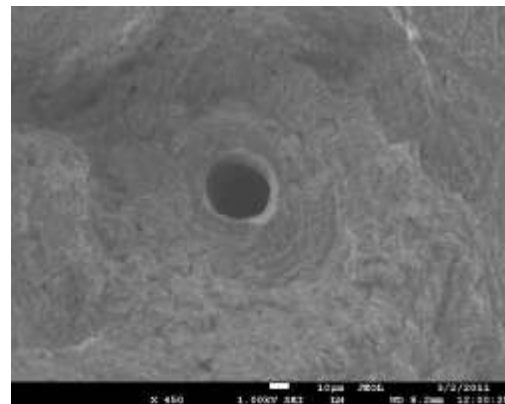


Figure B.14. SEM image of healthy human femur (transverse, anterior section) ×450

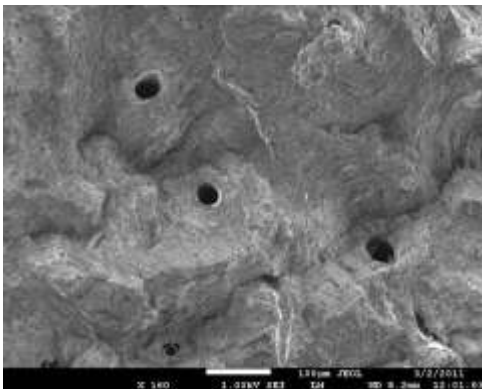


Figure B.15. SEM image of healthy human femur (transverse, anterior section) ×60

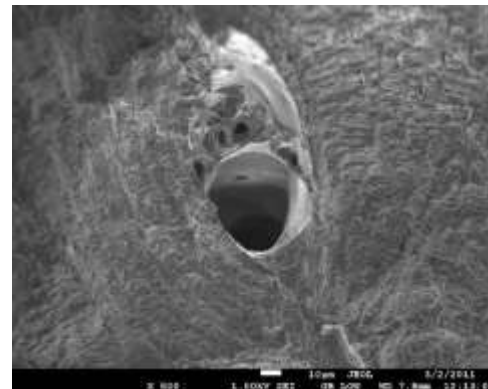


Figure B.16. SEM image of healthy human femur (transverse, anterior section) ×500

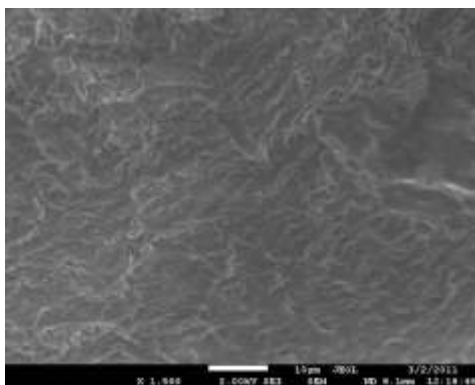


Figure B.17. SEM image of healthy human femur (transverse, anterior section) $\times 1,500$

B.1.1.2. Transverse section of healthy human femur (anterior), no chemical treatment, fractured in liquid N₂ (3/25/2011)

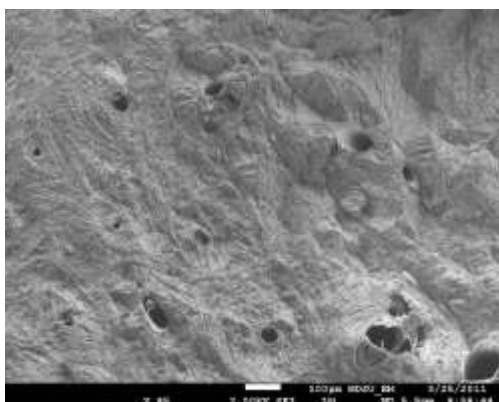


Figure B.18. SEM image of healthy human femur (transverse, anterior section) $\times 85$

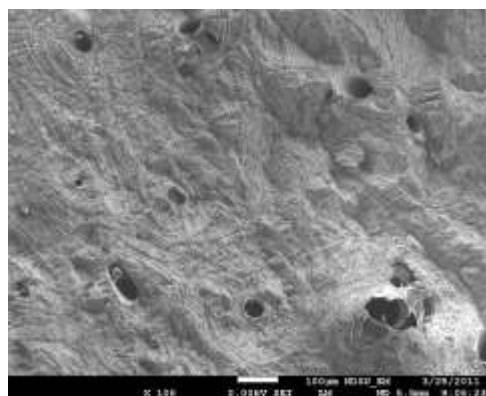


Figure B.19. SEM image of healthy human femur (transverse, anterior section) $\times 100$

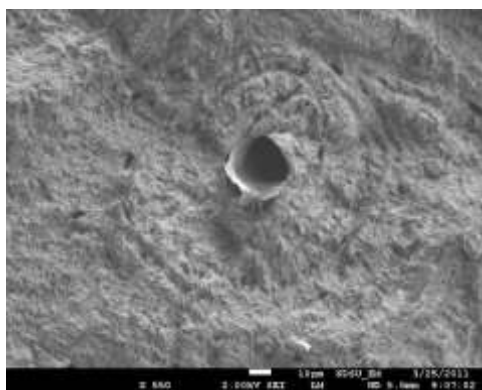


Figure B.20. SEM image of healthy human femur (transverse, anterior section) $\times 550$

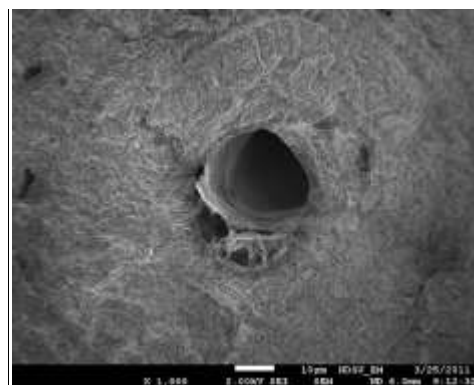


Figure B.21. SEM image of healthy human femur (transverse, anterior section) $\times 1,000$

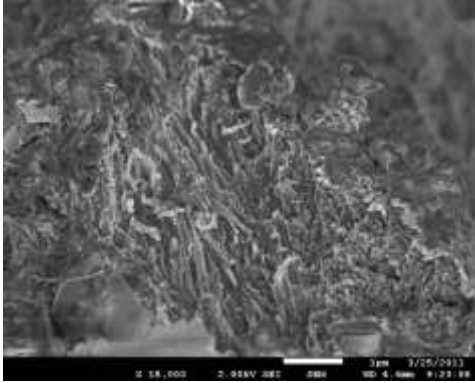


Figure B.22. SEM image of healthy human femur (transverse, anterior section) $\times 15,000$

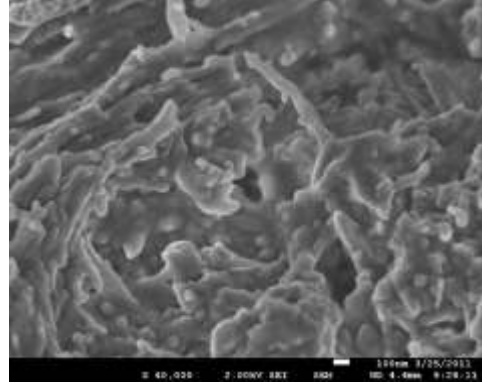


Figure B.23. SEM image of healthy human femur (transverse, anterior section) $\times 40,000$

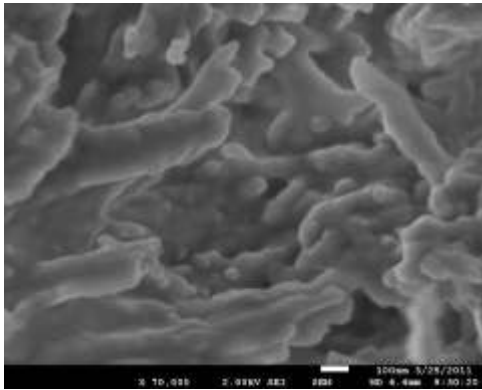


Figure B.24. SEM image of healthy human femur (transverse, anterior section) $\times 70,000$

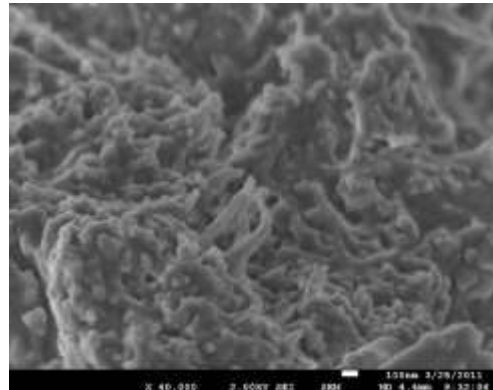


Figure B.25. SEM image of healthy human femur (transverse, anterior section) $\times 40,000$

B.1.1.3. Transverse section of healthy human femur (anterior), no chemical treatment, polished (3/2/2011)

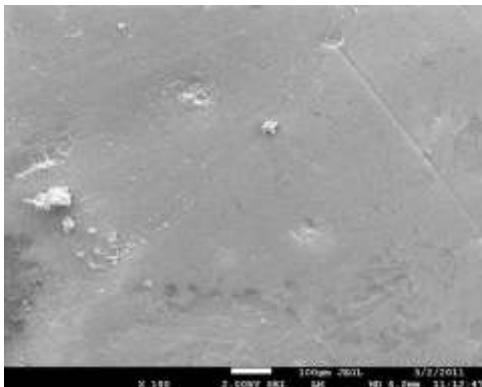


Figure B.26. SEM image of healthy human femur (transverse, anterior section) $\times 100$

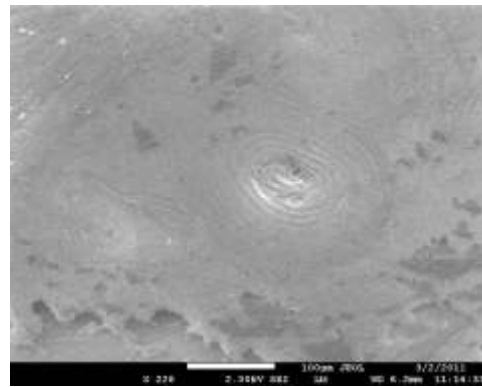


Figure B.27. SEM image of healthy human femur (transverse, anterior section) $\times 220$

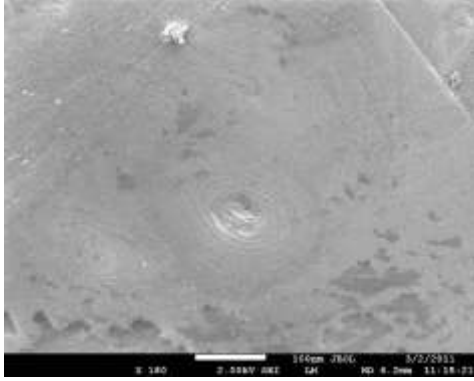


Figure B.28. SEM image of healthy human femur (transverse, anterior section) $\times 180$

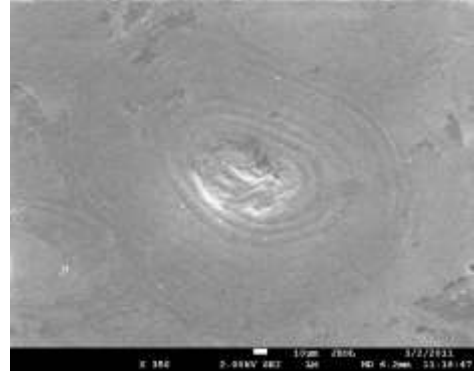


Figure B.29. SEM image of healthy human femur (transverse, anterior section) $\times 350$

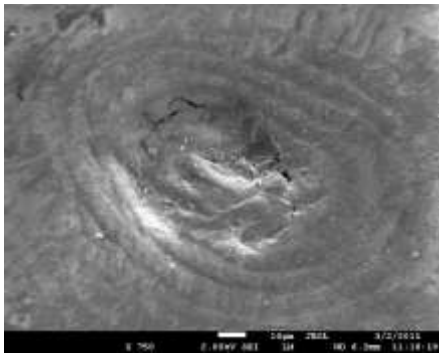


Figure B.30. SEM image of healthy human femur (transverse, anterior section) $\times 750$

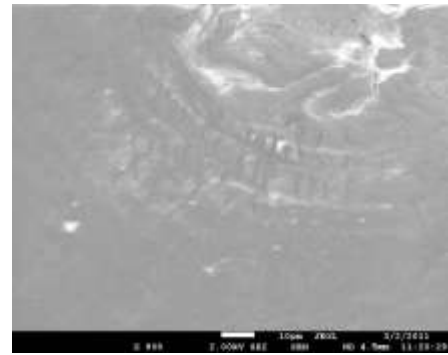


Figure B.31. SEM image of healthy human femur (transverse, anterior section) $\times 900$

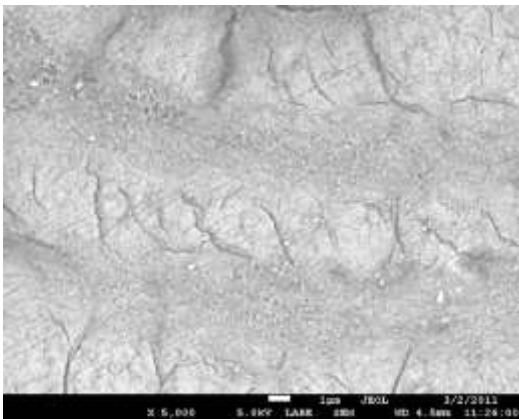


Figure B.32. SEM image of healthy human femur (transverse, anterior section) $\times 5,000$

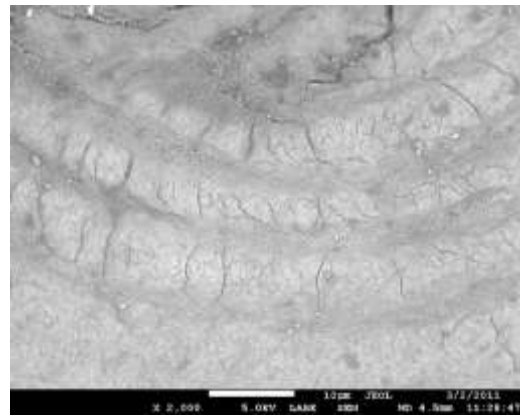


Figure B.33. SEM image of healthy human femur (transverse, anterior section) $\times 2,000$

B.1.2. Longitudinal section

B.1.2.1. Longitudinal section of healthy human femur (anterior), fixed with a series of chemical and fractured in liquid N₂ (12/1/2010)

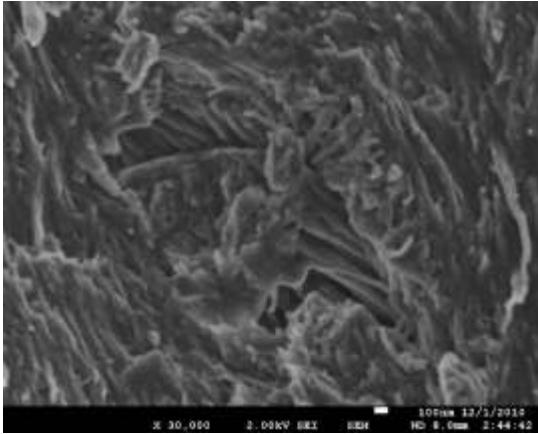


Figure B.34. SEM image of healthy human femur (longi., anterior section) ×30,000

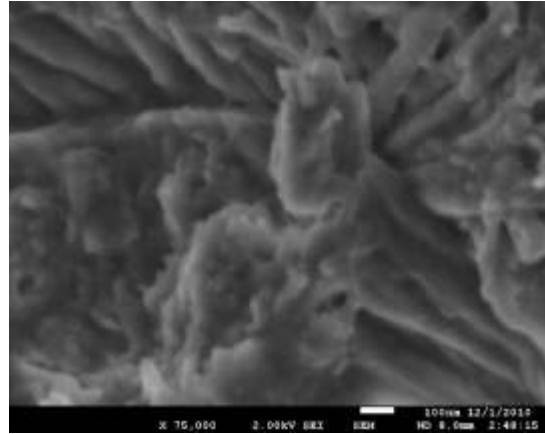


Figure B.35. SEM image of healthy human femur (longi., anterior section) ×75,000

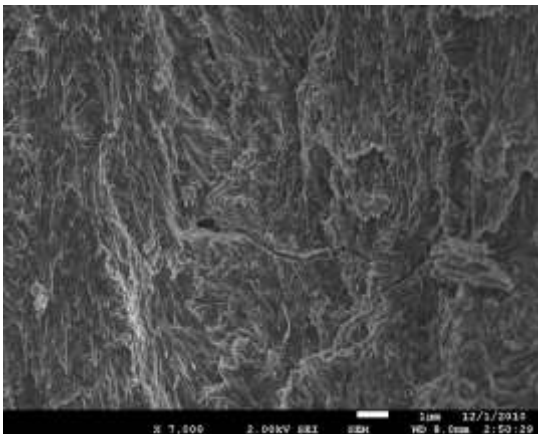


Figure B.36. SEM image of healthy human femur (longi., anterior section) ×7,000

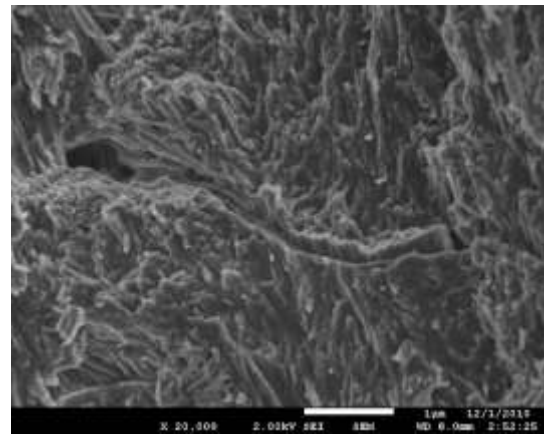


Figure B.37. SEM image of healthy human femur (longi., anterior section) ×20,000

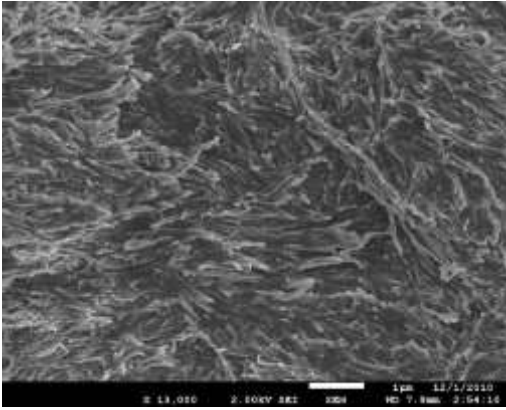


Figure B.38. SEM image of healthy human femur (longi., anterior section) $\times 13,000$

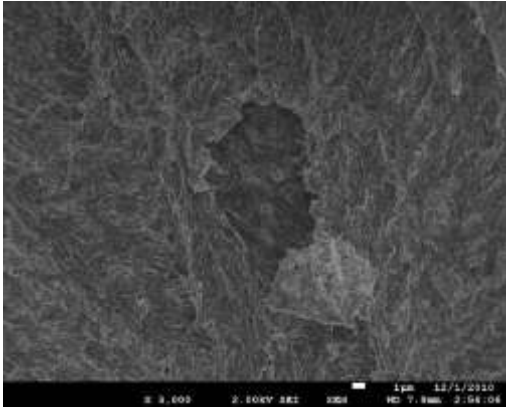


Figure B.39. SEM image of healthy human femur (longi., anterior section) $\times 3,000$

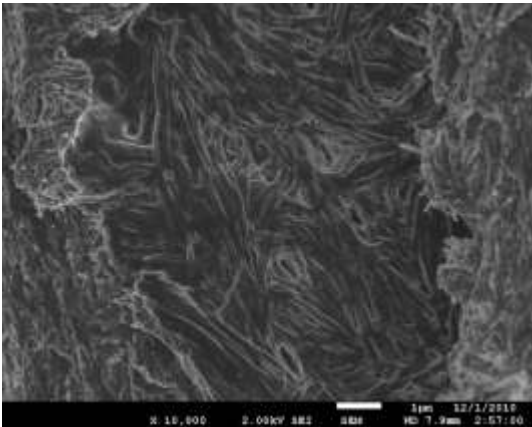


Figure B.40. SEM image of healthy human femur (longi., anterior section) $\times 10,000$

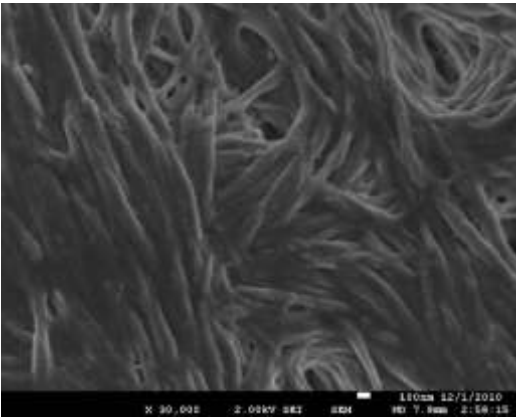


Figure B.41. SEM image of healthy human femur (longi., anterior section) $\times 30,000$

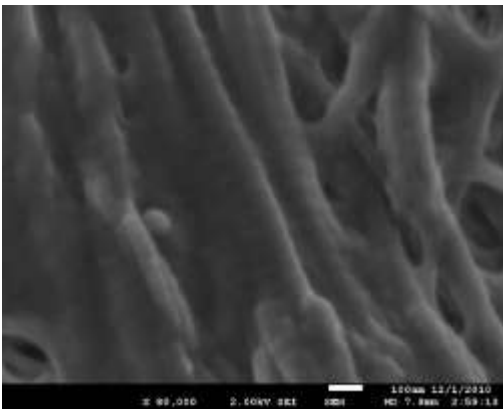


Figure B.42. SEM image of healthy human femur (longi., anterior section) $\times 80,000$

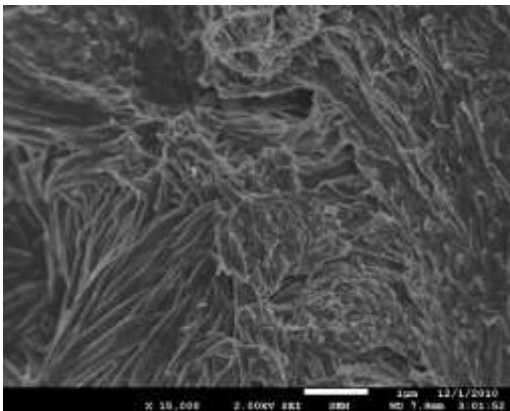


Figure B.43. SEM image of healthy human femur (longi., anterior section) $\times 15,000$

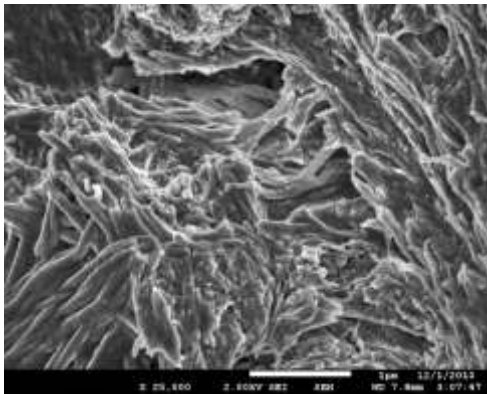


Figure B.44. SEM image of healthy human femur (longi., anterior section) $\times 25,000$
(2) Acquired on 3/2/2011

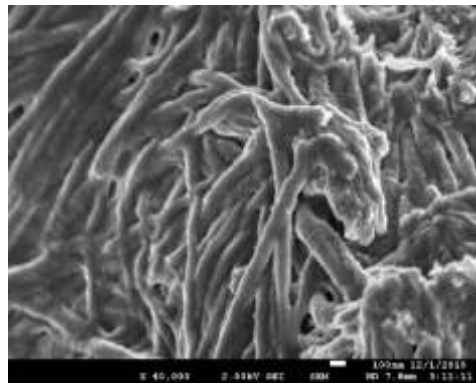


Figure B.45. SEM image of healthy human femur (longi., anterior section) $\times 40,000$

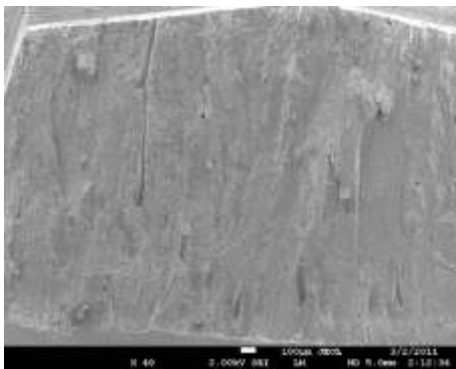


Figure B.46. SEM image of healthy human femur (longi., anterior section) $\times 40$

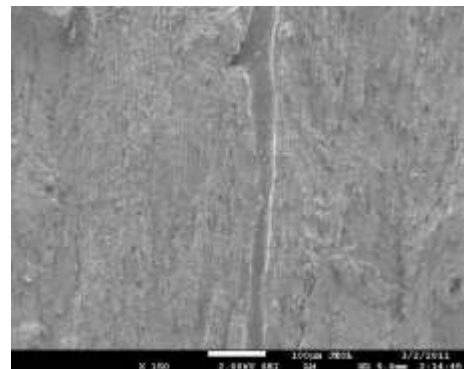


Figure B.47. SEM image of healthy human femur (longi., anterior section) $\times 150$

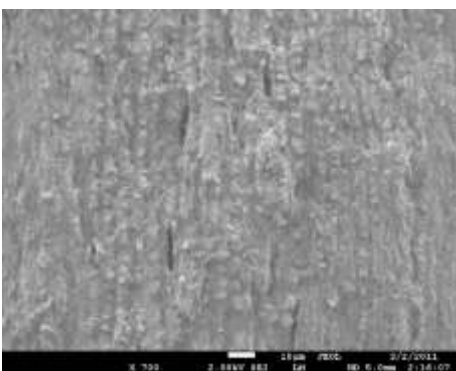


Figure B.48. SEM image of healthy human femur (longi., anterior section) $\times 700$

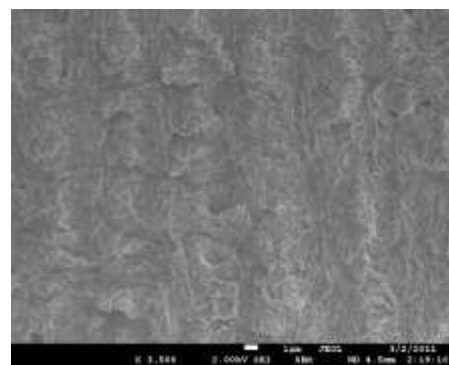


Figure B.49. SEM image of healthy human femur (longi., anterior section) $\times 3,500$

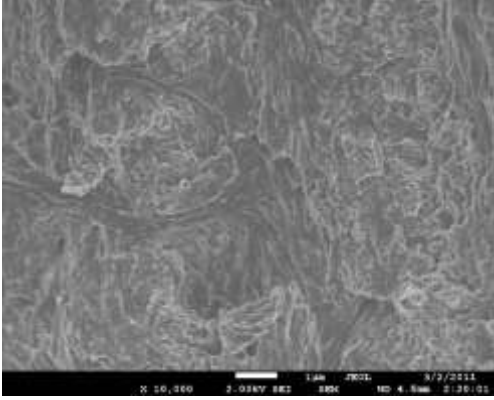


Figure B.50. SEM image of healthy human femur (longi., anterior section) $\times 10,000$

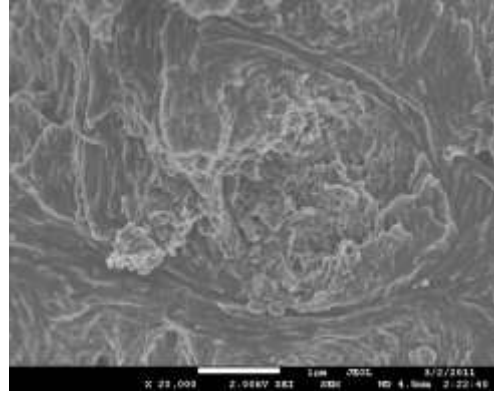


Figure B.51. SEM image of healthy human femur (longi., anterior section) $\times 20,000$

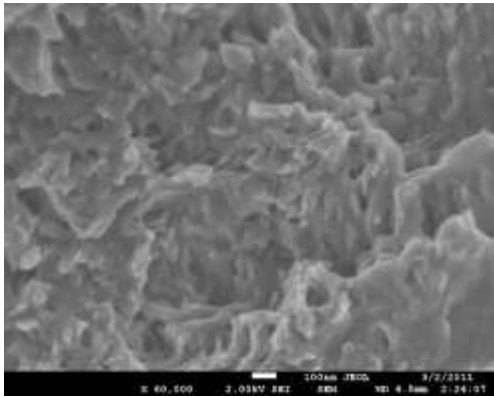


Figure B.52. SEM image of healthy human femur (longi., anterior section) $\times 60,000$

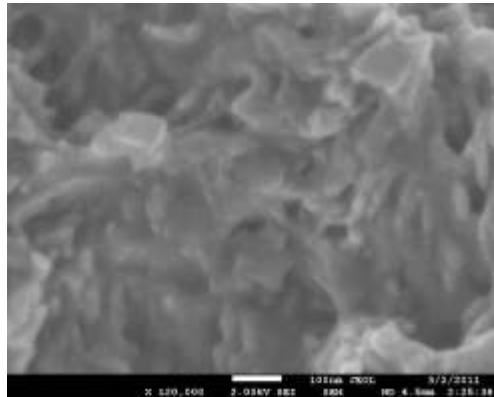


Figure B.53. SEM image of healthy human femur (longi., anterior section) $\times 120,000$

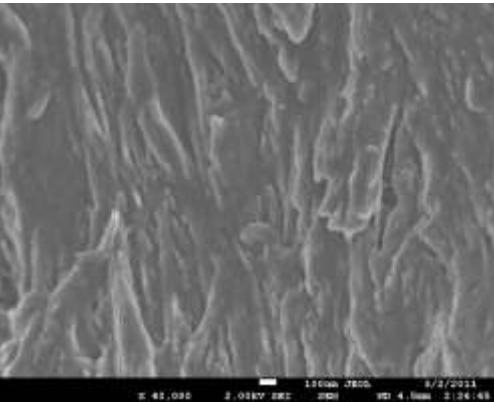


Figure B.54. SEM image of healthy human femur (longi., anterior section) $\times 40,000$

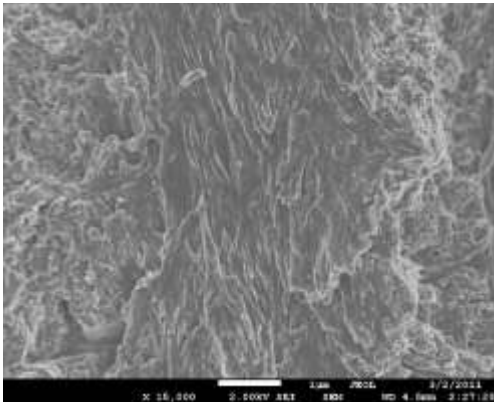


Figure B.55. SEM image of healthy human femur (longi., anterior section) $\times 15,000$

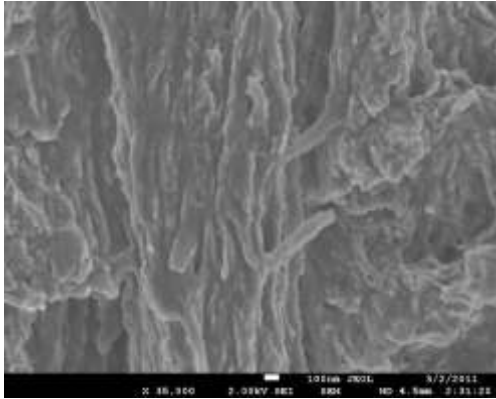


Figure B.56. SEM image of healthy human femur (longi., anterior section) $\times 35,000$

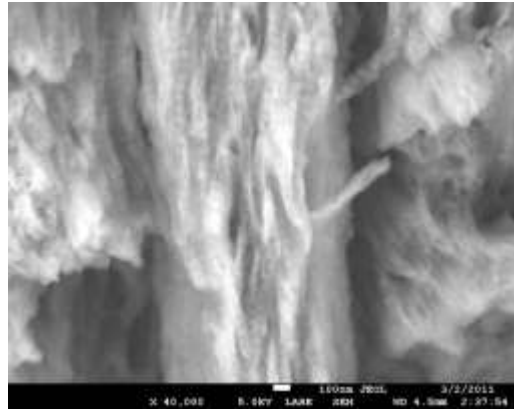


Figure B.57. SEM image of healthy human femur (longi., anterior section) $\times 40,000$

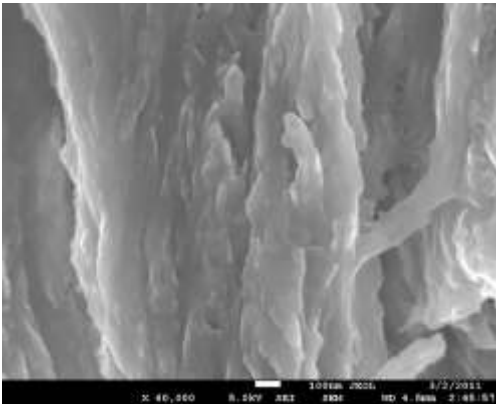


Figure B.58. SEM image of healthy human femur (longi., anterior section) $\times 60,000$

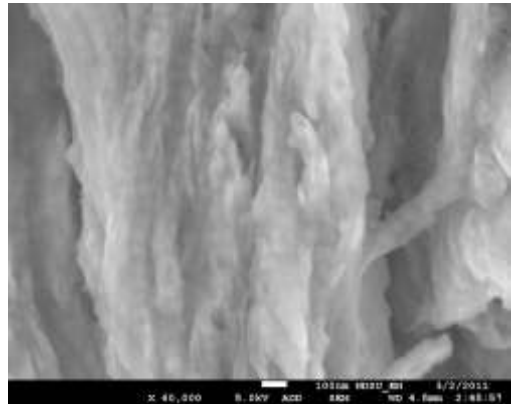


Figure B.59. SEM image of healthy human femur (longi., anterior section) $\times 60,000$

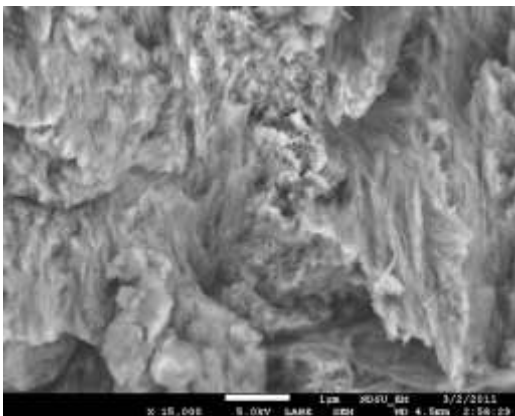


Figure B.60. SEM image of healthy human femur (longi., anterior section) $\times 15,000$

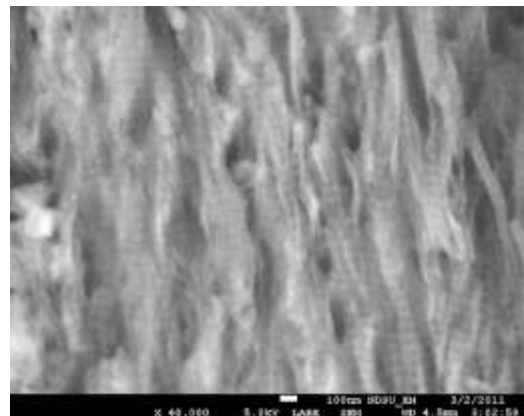


Figure B.61. SEM image of healthy human femur (longi., anterior section) $\times 40,000$

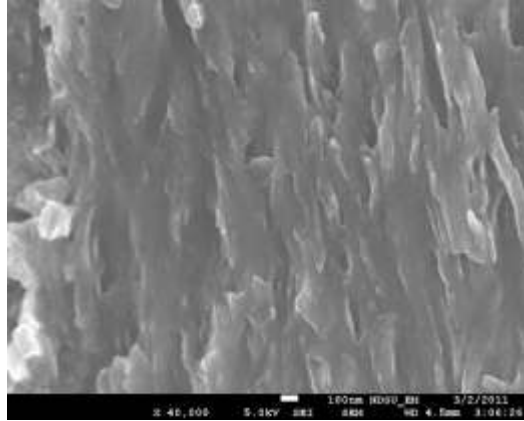


Figure B.62. SEM image of healthy human femur (longi., anterior section) $\times 40,000$

B.1.2.2. Longitudinal section of healthy human femur (anterior), polished (3/2/2011)

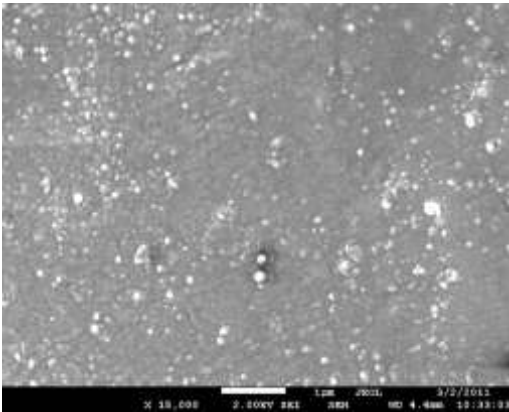


Figure B.63. SEM image of healthy human femur (longi., anterior section) $\times 15,000$

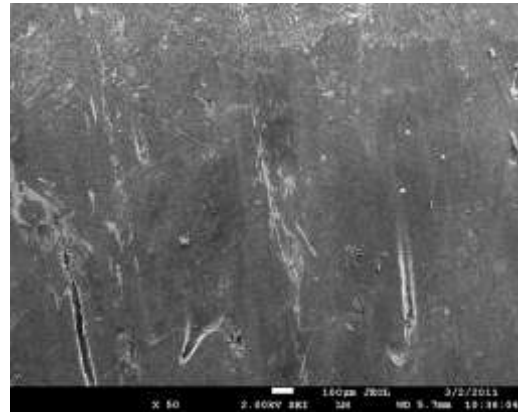


Figure B.64. SEM image of healthy human femur (longi., anterior section) $\times 50$

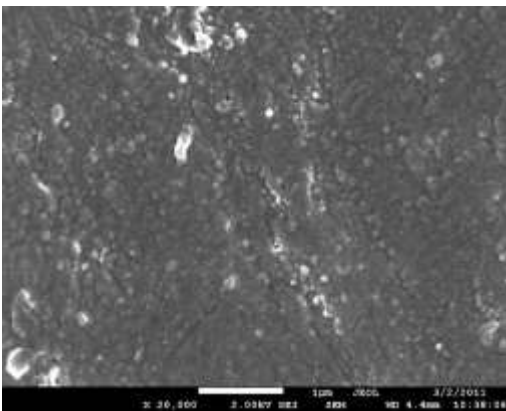


Figure B.65. SEM image of healthy human femur (longi., anterior section) $\times 20,000$

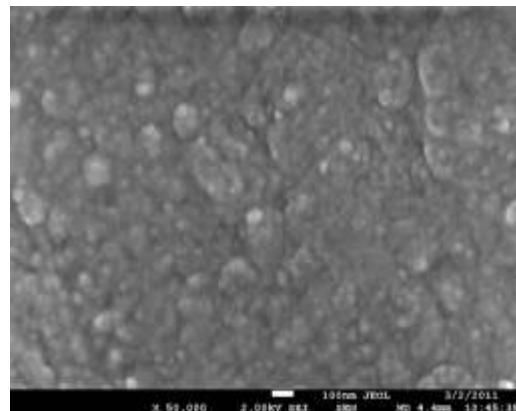


Figure B.66. SEM image of healthy human femur (longi., anterior section) $\times 50,000$

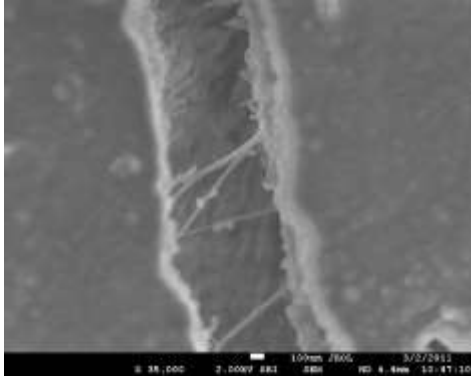


Figure B.67. SEM image of healthy human femur (longi., anterior section) $\times 35,000$

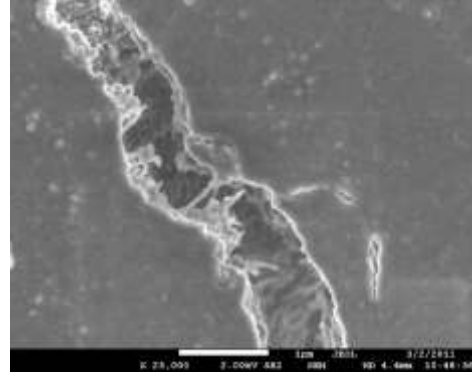


Figure B.68. SEM image of healthy human femur (longi., anterior section) $\times 23,000$

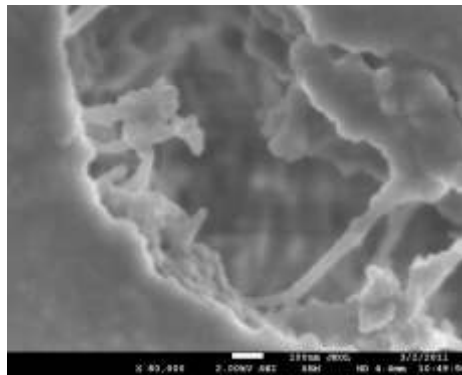


Figure B.69. SEM image of healthy human femur (longi., anterior section) $\times 80,000$

B.2. Medial section

B.2.1. Transverse section

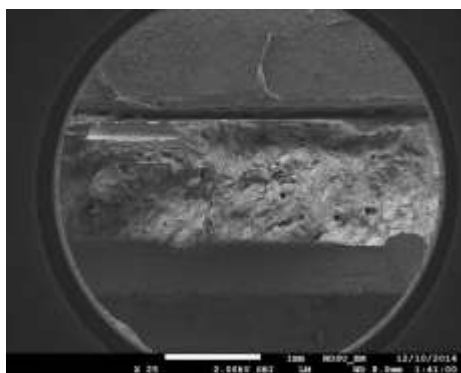


Figure B.70. SEM image of healthy human femur (transverse, medial section) $\times 25$

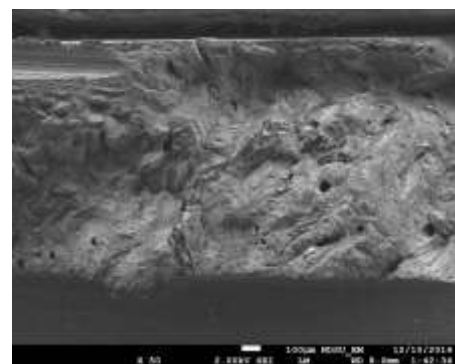


Figure B.71. SEM image of healthy human femur (transverse, medial section) $\times 50$

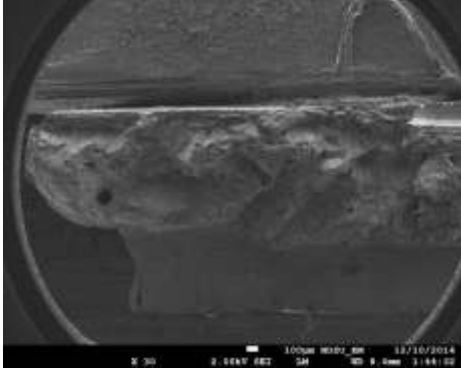


Figure B.72. SEM image of healthy human femur (transverse, medial section) $\times 30$

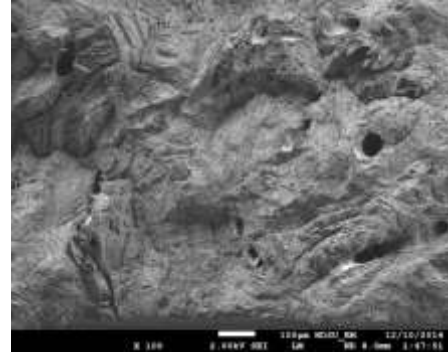


Figure B.73. SEM image of healthy human femur (transverse, medial section) $\times 100$

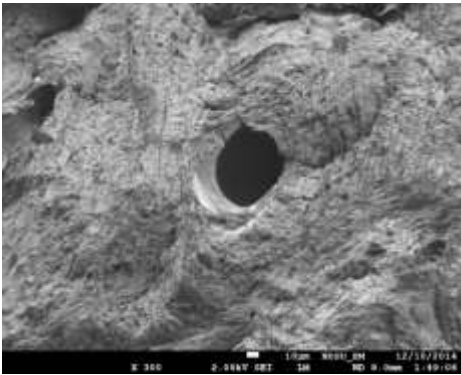


Figure B.74. SEM image of healthy human femur (transverse, medial section) $\times 300$

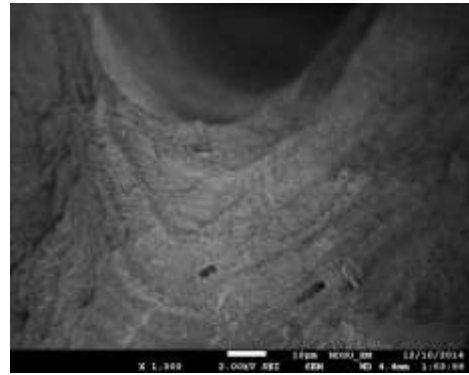


Figure B.75. SEM image of healthy human femur (transverse, medial section) $\times 1,000$

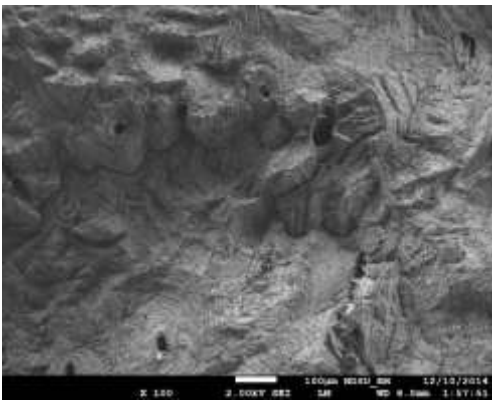


Figure B.76. SEM image of healthy human femur (transverse, medial section) $\times 1,000$

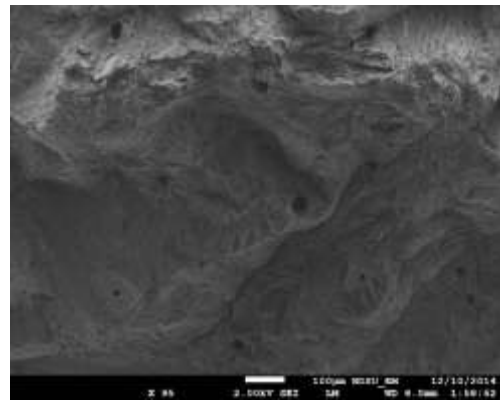


Figure B.77. SEM image of healthy human femur (transverse, medial section) $\times 95$

B.2.2. Longitudinal section

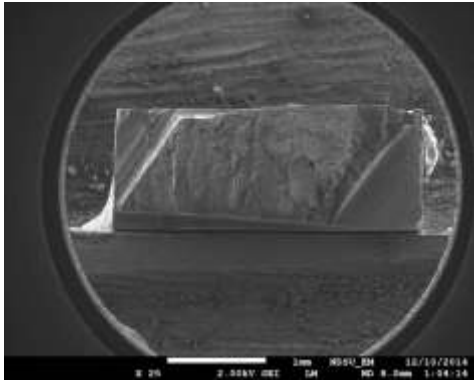


Figure B.78. SEM image of healthy human femur (longi., medial section) $\times 25$

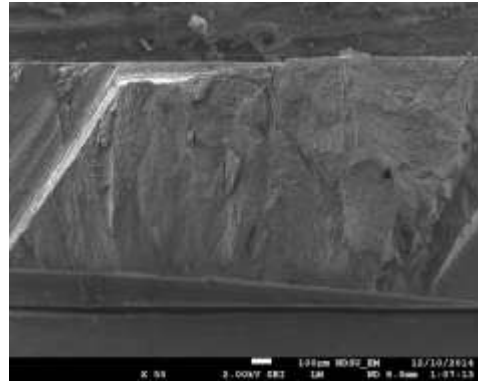


Figure B.79. SEM image of healthy human femur (longi., medial section) $\times 50$

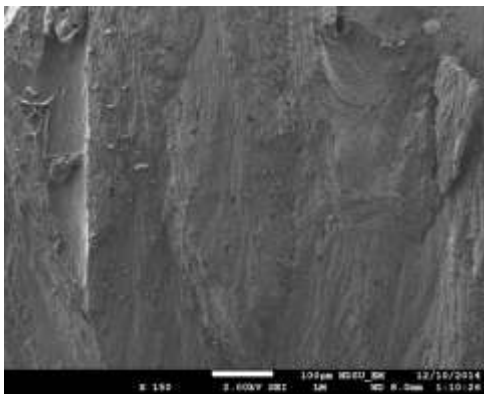


Figure B.80. SEM image of healthy human femur (longi., medial section) $\times 150$

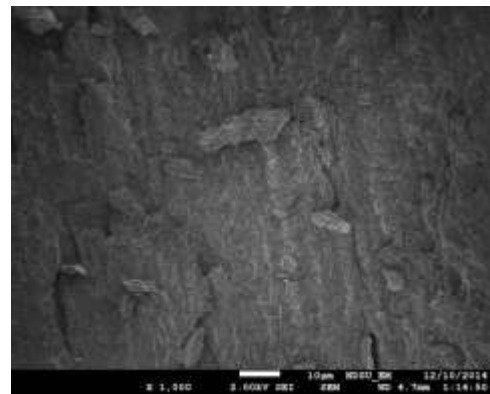


Figure B.81. SEM image of healthy human femur (longi., medial section) $\times 1,000$

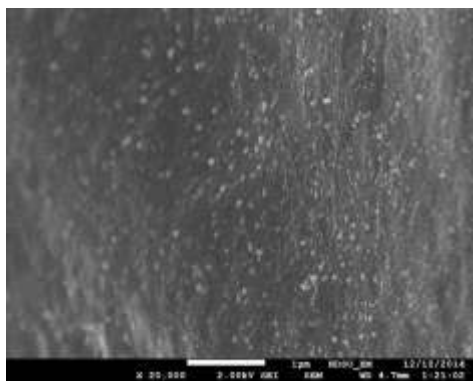


Figure B.82. SEM image of healthy human femur (longi., medial section) $\times 20,000$

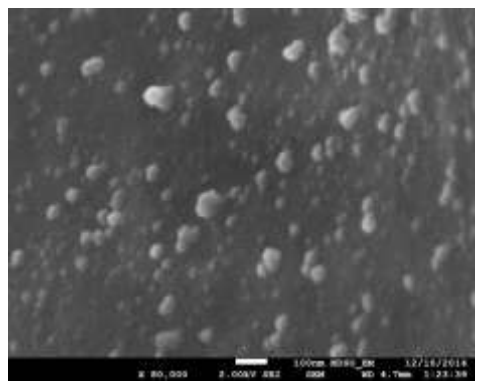


Figure B.83. SEM image of healthy human femur (longi., medial section) $\times 80,000$

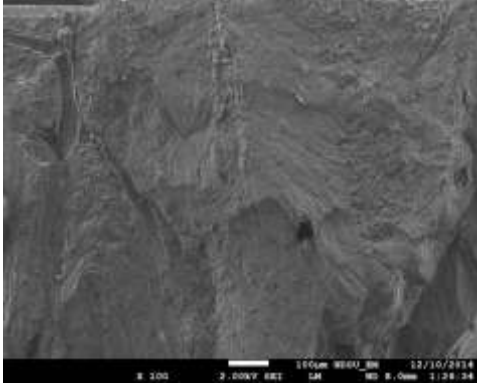


Figure B.84. SEM image of healthy human femur (longi., medial section) $\times 100$

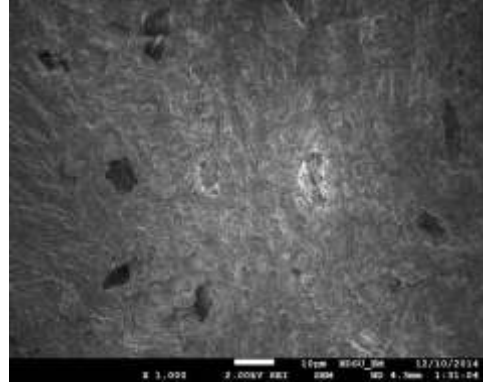


Figure B.85. SEM image of healthy human femur (longi., medial section) $\times 1,000$

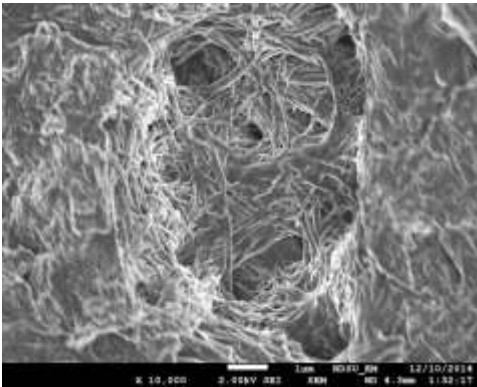


Figure B.86. SEM image of healthy human femur (longi., medial section) $\times 10,000$

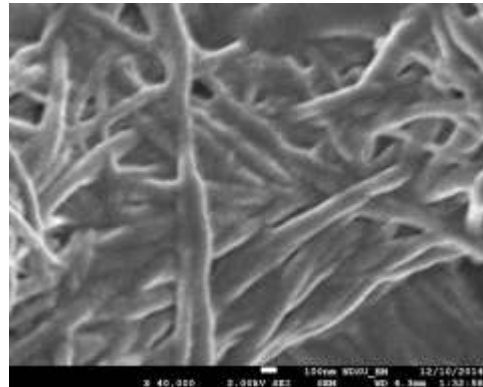


Figure B.87. SEM image of healthy human femur (longi., medial section) $\times 40,000$

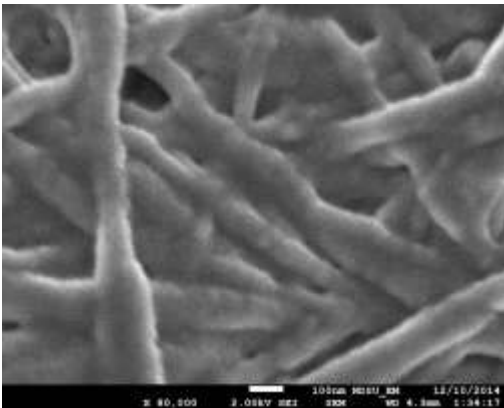


Figure B.88. SEM image of healthy human femur (longi., medial section) $\times 80,000$

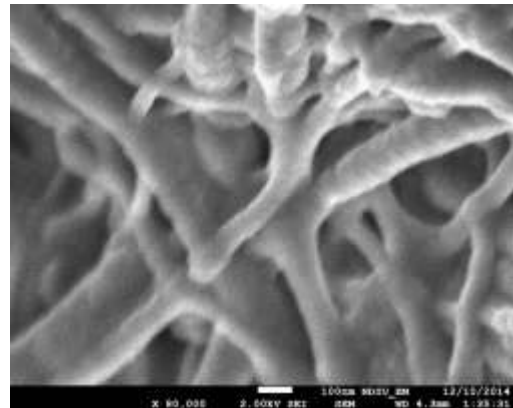


Figure B.89. SEM image of healthy human femur (longi., medial section) $\times 80,000$

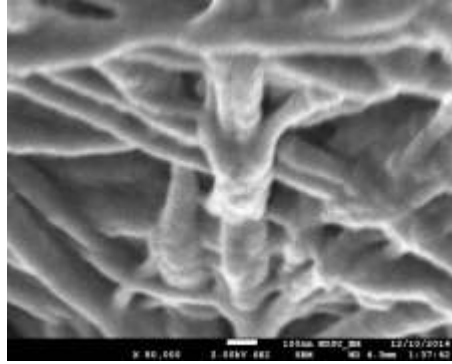


Figure B.90. SEM image of healthy human femur (longi., medial section) $\times 80,000$

B.3. Lateral section

B.3.1. Transverse section

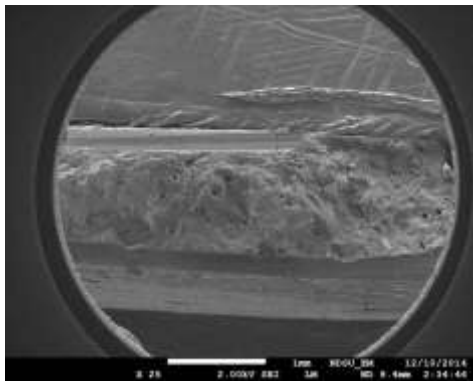


Figure B.91. SEM image of healthy human femur (transverse, lateral section) $\times 25$

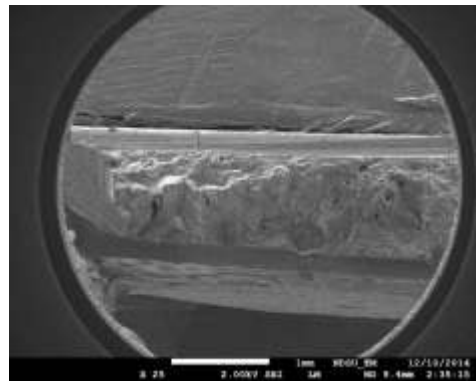


Figure B.92. SEM image of healthy human femur (longi., medial section) $\times 25$

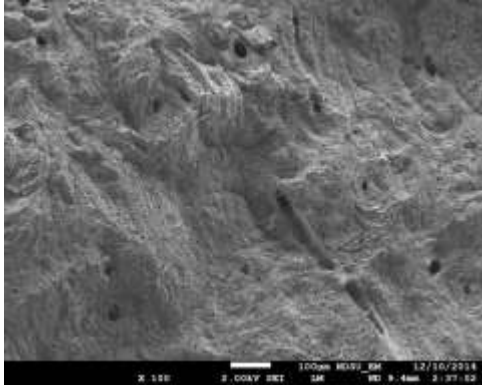


Figure B.93. SEM image of healthy human femur (transverse, lateral section) $\times 100$

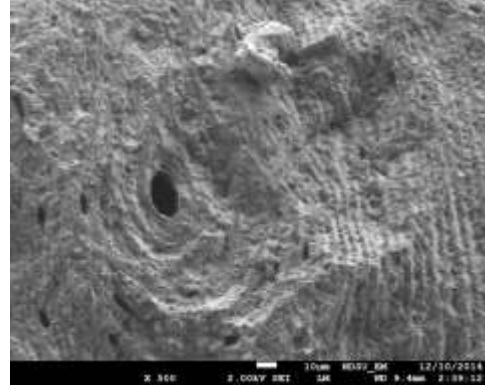


Figure B.94. SEM image of healthy human femur (transverse, lateral section) $\times 500$

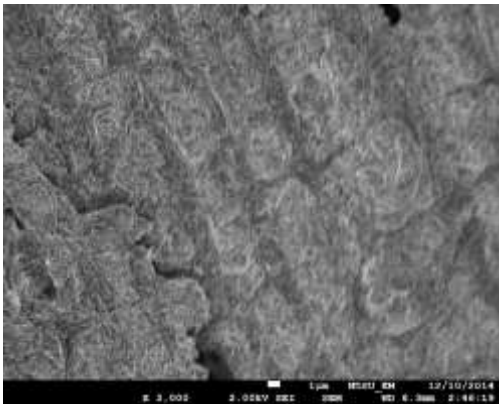


Figure B.95. SEM image of healthy human femur (transverse, lateral section) $\times 3,000$

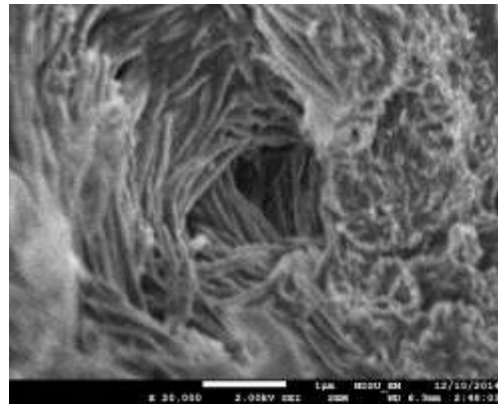


Figure B.96. SEM image of healthy human femur (transverse, lateral section) $\times 20,000$

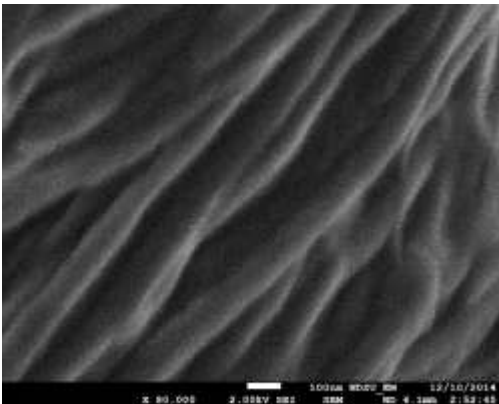


Figure B.97. SEM image of healthy human femur (transverse, lateral section) $\times 80,000$

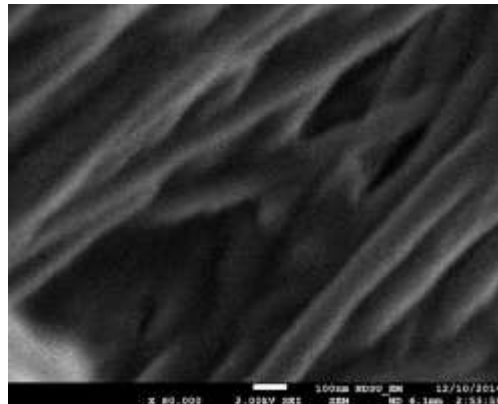


Figure B.98. SEM image of healthy human femur (transverse, lateral section) $\times 80,000$

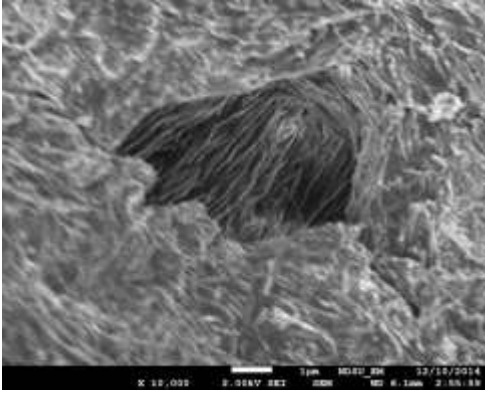


Figure B.99. SEM image of healthy human femur (transverse, lateral section) $\times 10,000$

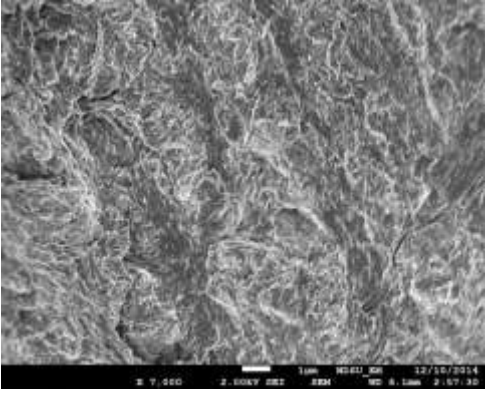


Figure B.100. SEM image of healthy human femur (transverse, lateral section) $\times 7,000$

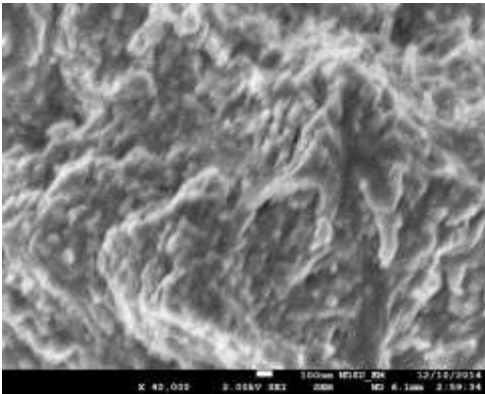


Figure B.101. SEM image of healthy human femur (transverse, lateral section) $\times 40,000$

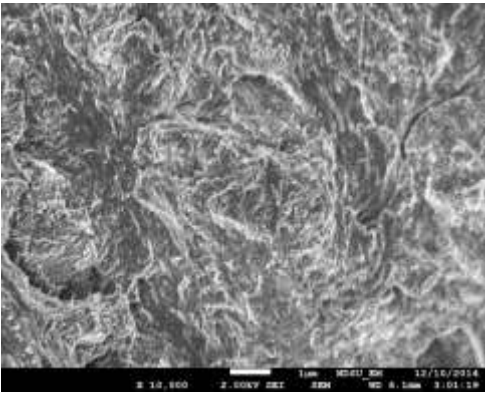


Figure B.102. SEM image of healthy human femur (transverse, lateral section) $\times 10,000$

B.3.2. Longitudinal section

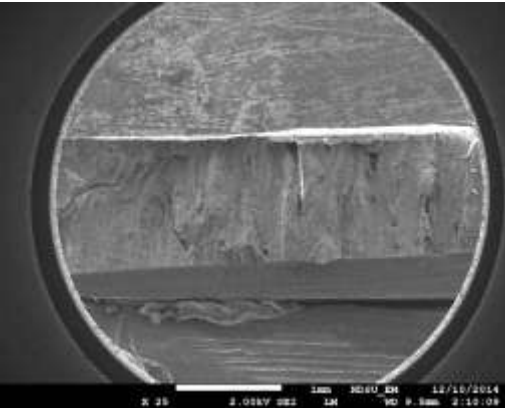


Figure B.103. SEM image of healthy human femur (longi., lateral section) $\times 25$

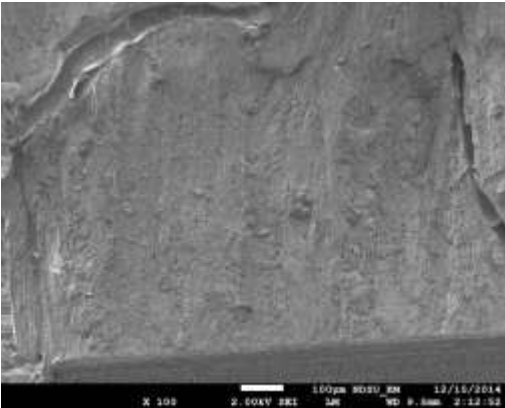


Figure B.104. SEM image of healthy human femur (longi., lateral section) $\times 100$

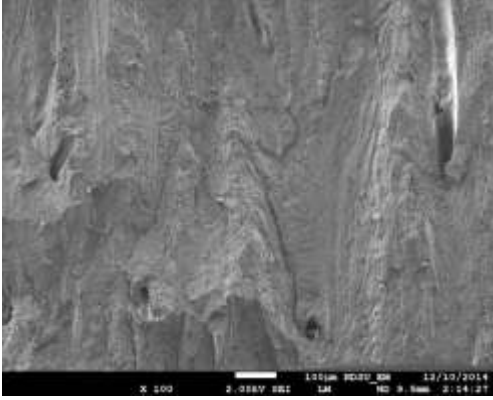


Figure B.105. SEM image of healthy human femur (longi., lateral section) $\times 100$

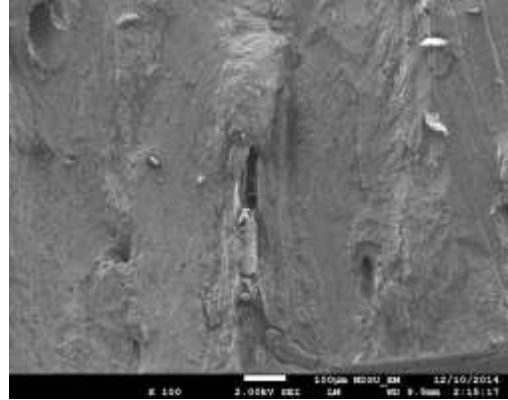


Figure B.106. SEM image of healthy human femur (longi., lateral section) $\times 100$

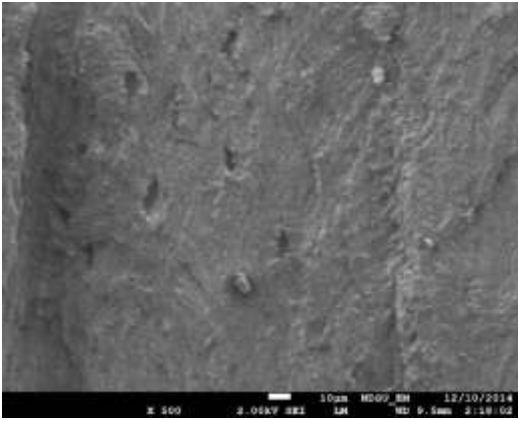


Figure B.107. SEM image of healthy human femur (longi., lateral section) $\times 500$

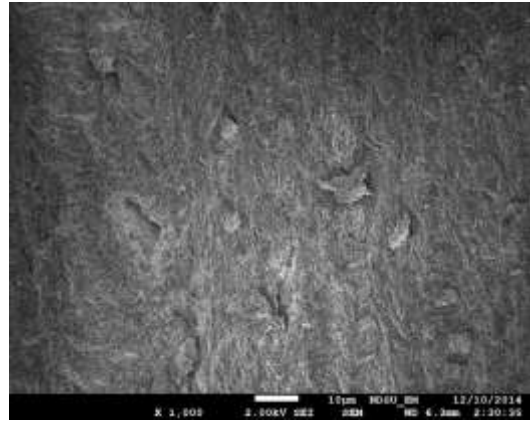


Figure B.108. SEM image of healthy human femur (longi., lateral section) $\times 1,000$

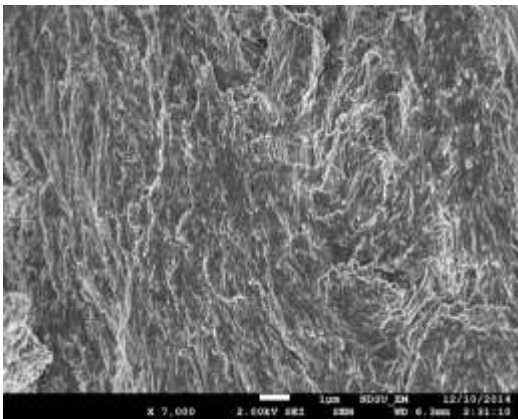


Figure B.109. SEM image of healthy human femur (longi., lateral section) $\times 7,000$

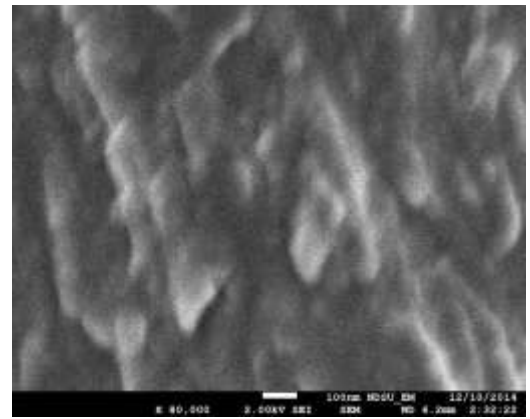


Figure B.110. SEM image of healthy human femur (longi., lateral section) $\times 80,000$

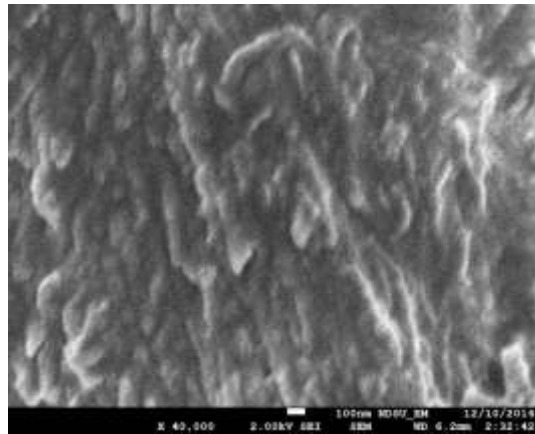


Figure B.111. SEM image of healthy human femur (longi., lateral section) $\times 40,000$

B.4. Posterior section

B.4.1. Transverse section

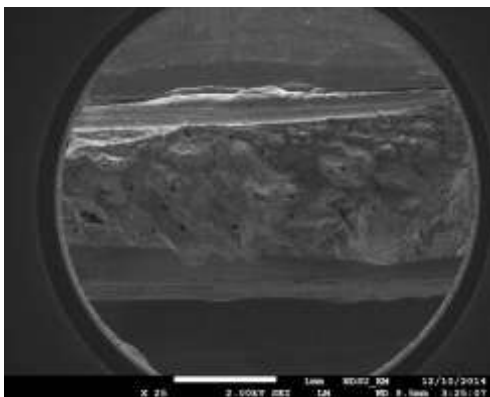


Figure B.112. SEM image of healthy human femur (transverse, posterior section) $\times 25$

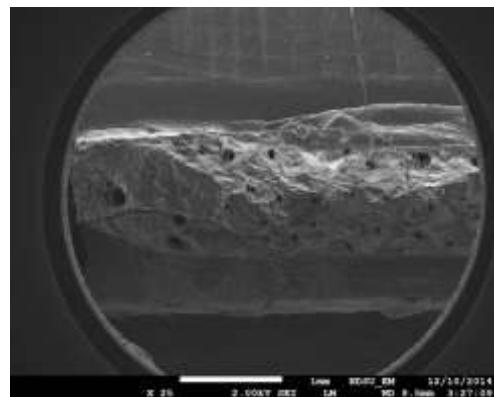


Figure B.113. SEM image of healthy human femur (transverse, posterior section) $\times 25$

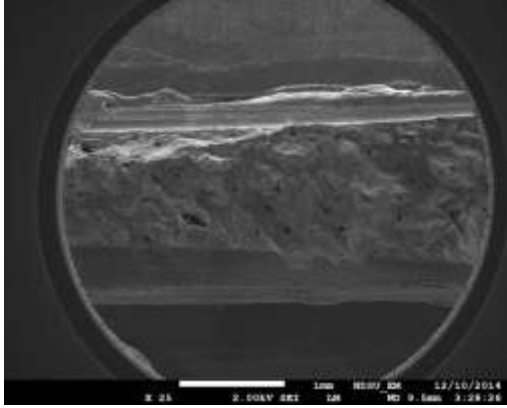


Figure B.114. SEM image of healthy human femur (transverse, posterior section) $\times 25$

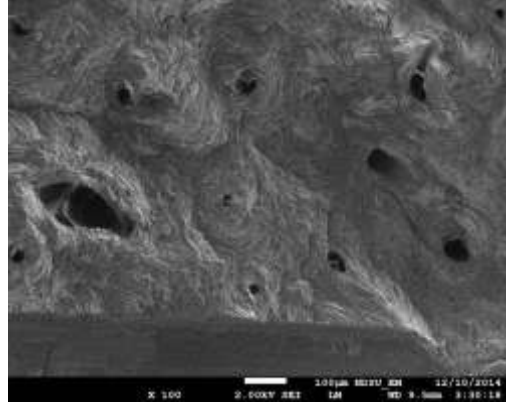


Figure B.115. SEM image of healthy human femur (transverse, posterior section) $\times 100$

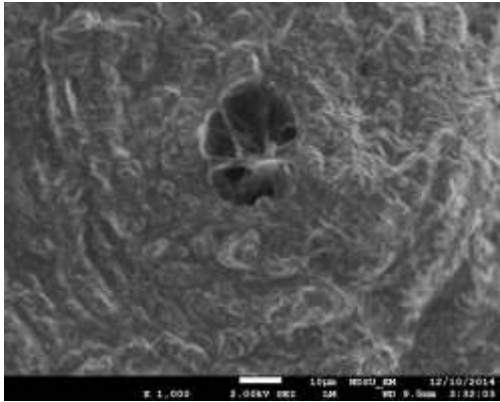


Figure B.116. SEM image of healthy human femur (transverse, posterior section) $\times 1,000$

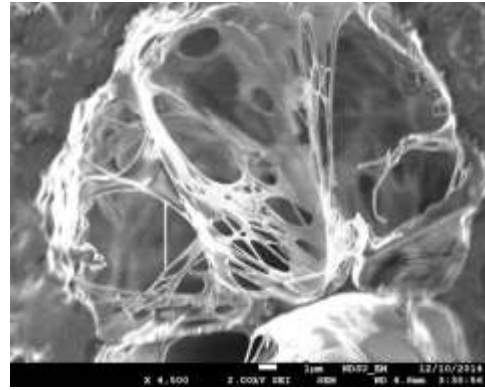


Figure B.117. SEM image of healthy human femur (transverse, posterior section) $\times 4,500$

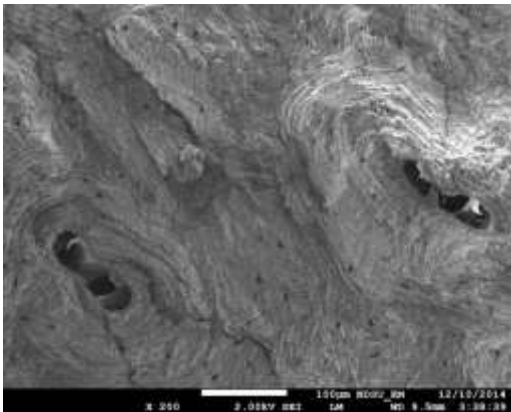


Figure B.118. SEM image of healthy human femur (transverse, posterior section) $\times 200$

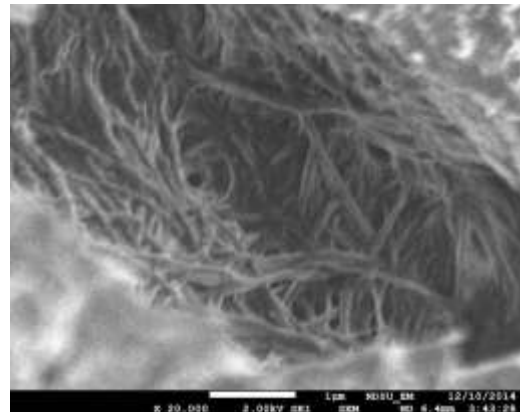


Figure B.119. SEM image of healthy human femur (transverse, posterior section) $\times 20,000$

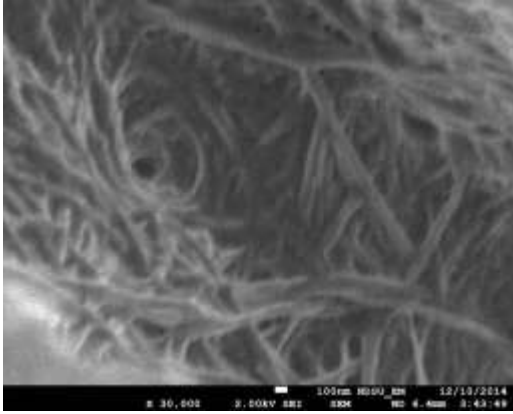


Figure B.120. SEM image of healthy human femur (transverse, posterior section) $\times 30,000$

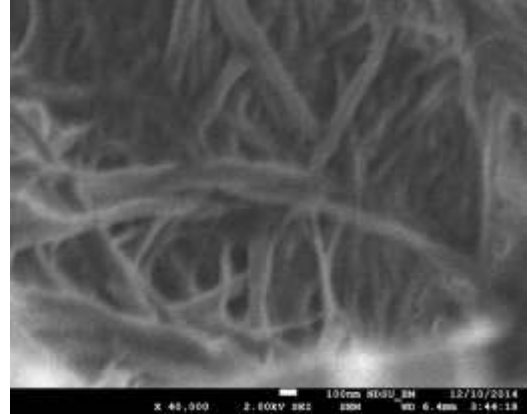


Figure B.121. SEM image of healthy human femur (transverse, posterior section) $\times 40,000$

B.4.2. Longitudinal section

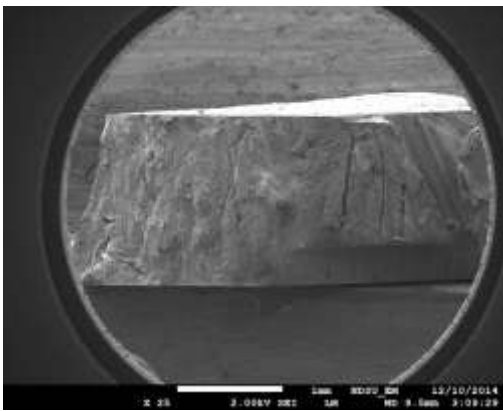


Figure B.122. SEM image of healthy human femur (longi., posterior section) $\times 25$

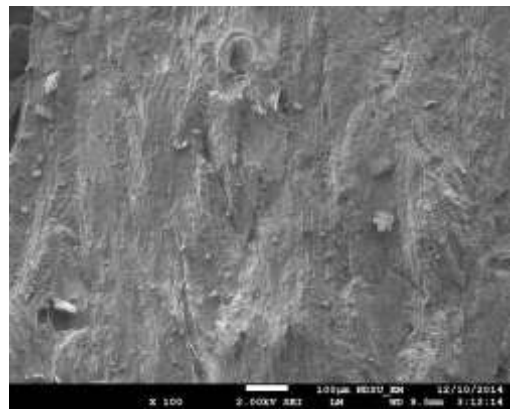


Figure B.123. SEM image of healthy human femur (longi., posterior section) $\times 100$

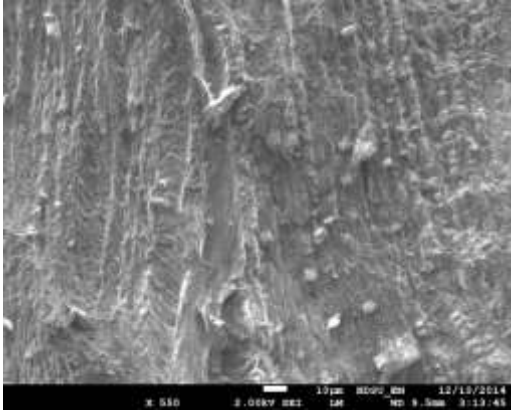


Figure B.124. SEM image of healthy human femur (longi., posterior section) ×550

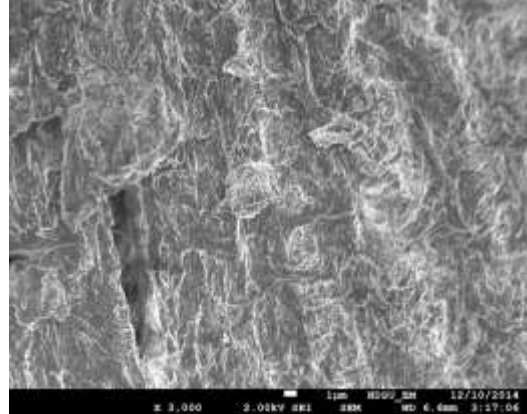


Figure B.125. SEM image of healthy human femur (longi., posterior section) ×3,000

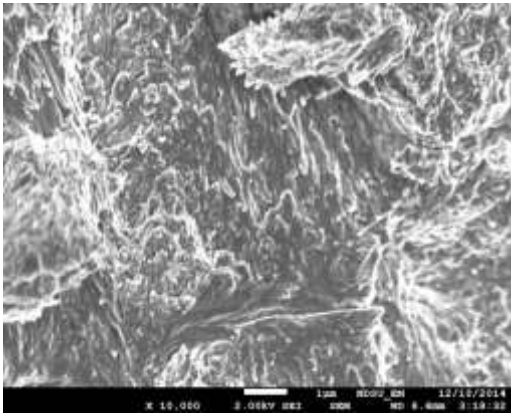


Figure B.126. SEM image of healthy human femur (longi., posterior section) ×10,000

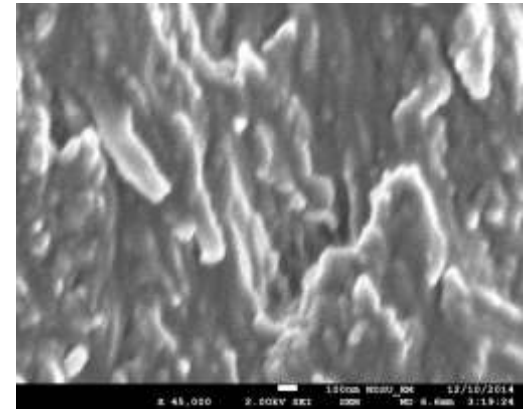


Figure B.127. SEM image of healthy human femur (longi., posterior section) ×45,000

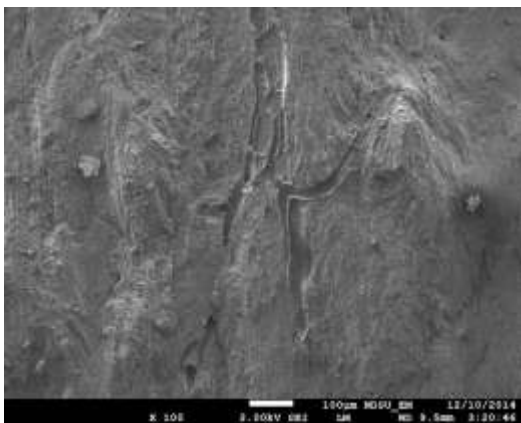


Figure B.128. SEM image of healthy human femur (longi., posterior section) ×100

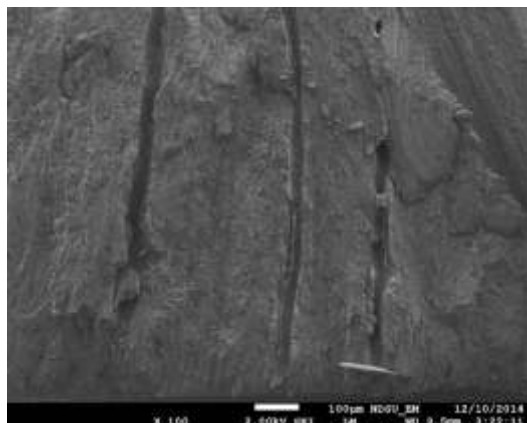


Figure B.129. SEM image of healthy human femur (longi., posterior section) ×100

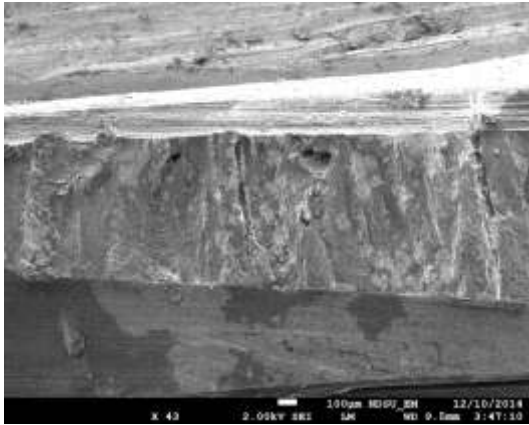


Figure B.130. SEM image of healthy human femur (longi., posterior section) ×43

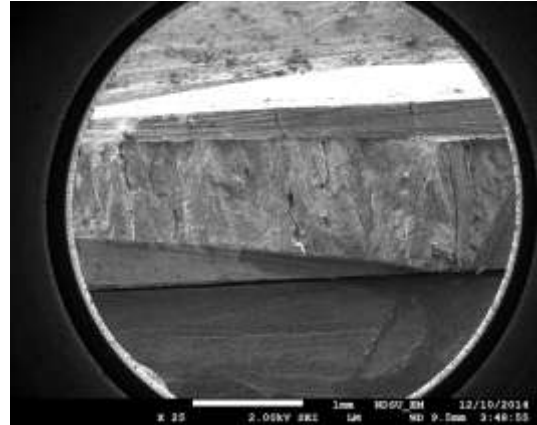


Figure B.131. SEM image of healthy human femur (longi., posterior section) ×25

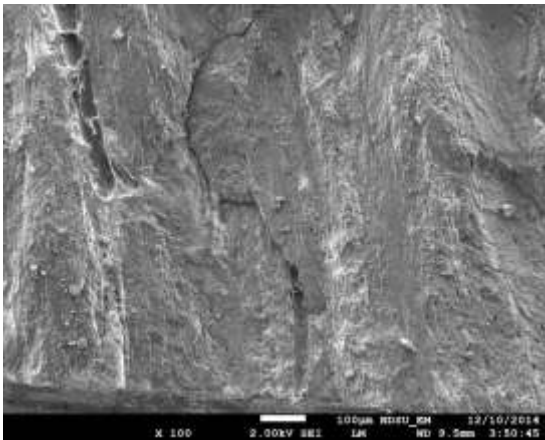


Figure B.132. SEM image of healthy human femur (longi., posterior section) ×100

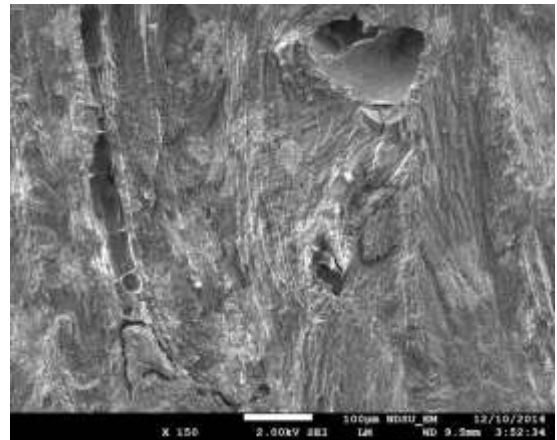


Figure B.133. SEM image of healthy human femur (longi., posterior section) ×150

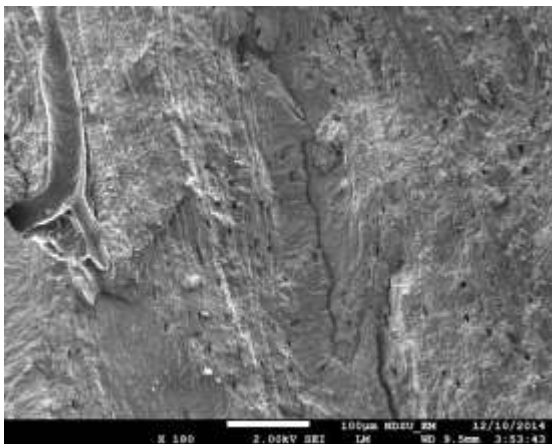


Figure B.134. SEM image of healthy human femur (longi., posterior section) ×180

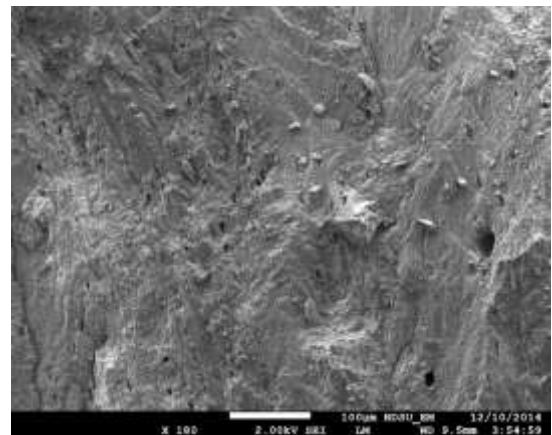


Figure B.135. SEM image of healthy human femur (longi., posterior section) ×180

APPENDIX C. SEM IMAGES OF OI HUMAN TIBIA

C.1. Anterior section, fixed with a series of chemicals and fractured in liquid N₂

C.1.1. Transverse section

C.1.1.1. Acquired on 12/10/2012 (JEOL JSM-7600F analytical high resolution field-emission scanning electron microscope (FE-SEM))

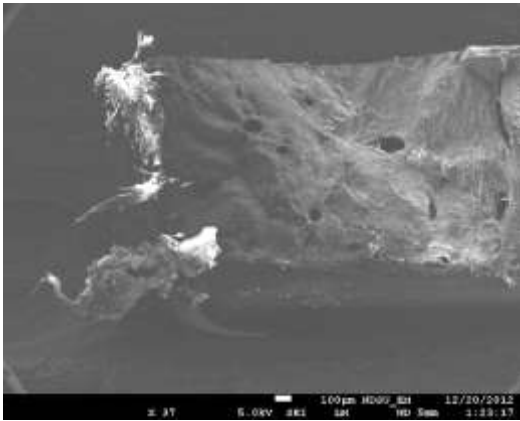


Figure C.1. SEM image of OI human tibia (transverse, anterior section) $\times 37$

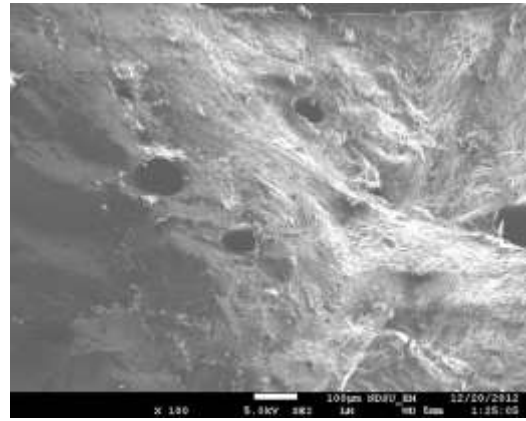


Figure C.2. SEM image of OI human tibia (transverse, anterior section) $\times 100$

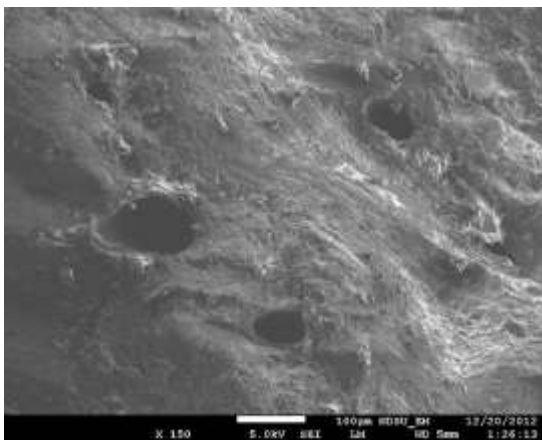


Figure C.3. SEM image of OI human tibia (transverse, anterior section) $\times 150$

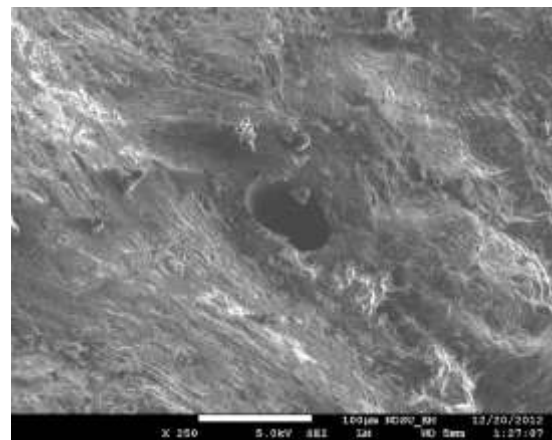


Figure C.4. SEM image of OI human tibia (transverse, anterior section) $\times 250$

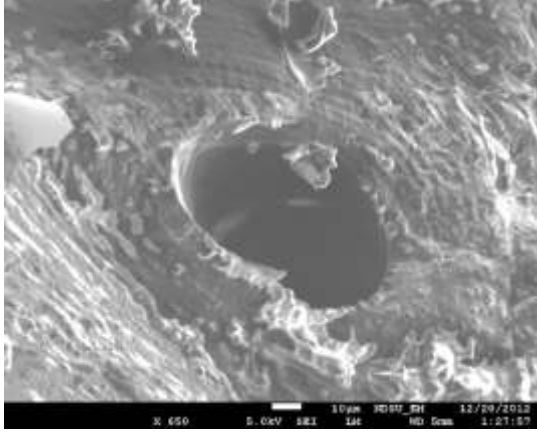


Figure C.5. SEM image of OI human tibia (transverse, anterior section) $\times 650$

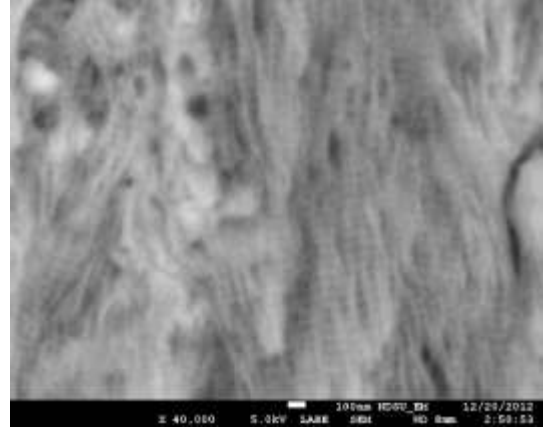


Figure C.6. SEM image of OI human tibia (transverse, anterior section) $\times 40,000$

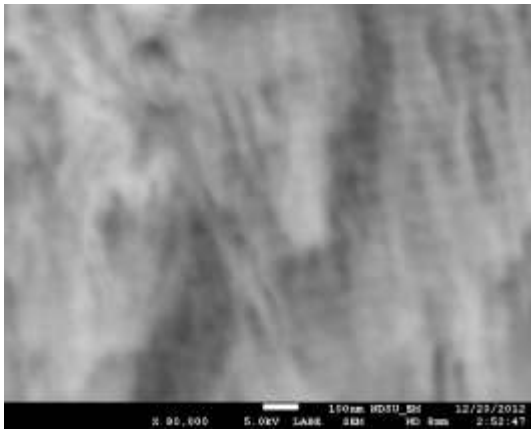


Figure C.7. SEM image of OI human tibia (transverse, anterior section) $\times 80,000$

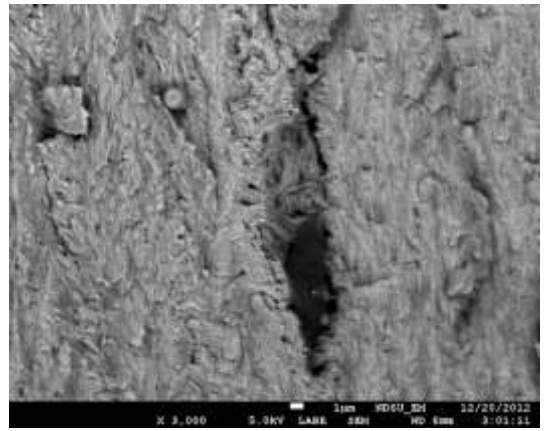


Figure C.8. SEM image of OI human tibia (transverse, anterior section) $\times 3,000$

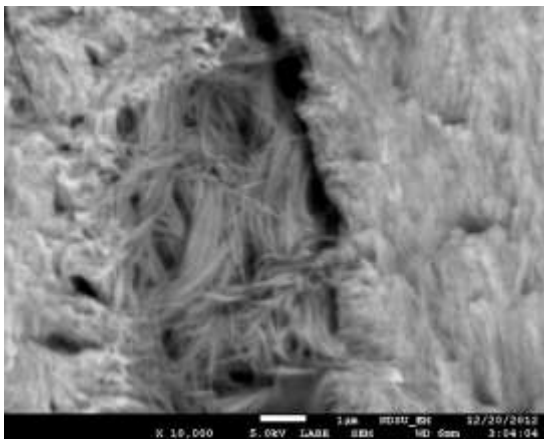


Figure C.9. SEM image of OI human tibia (transverse, anterior section) $\times 10,000$

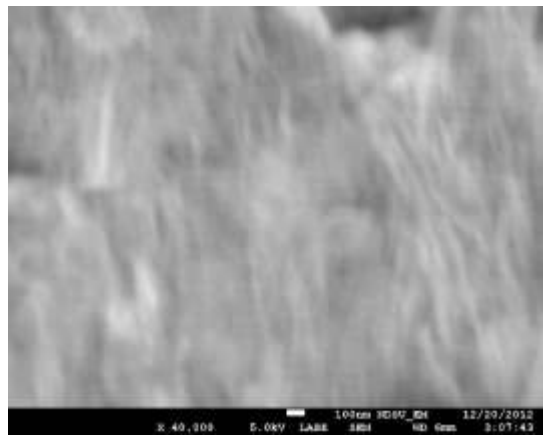


Figure C.10. SEM image of OI human tibia (transverse, anterior section) $\times 40,000$

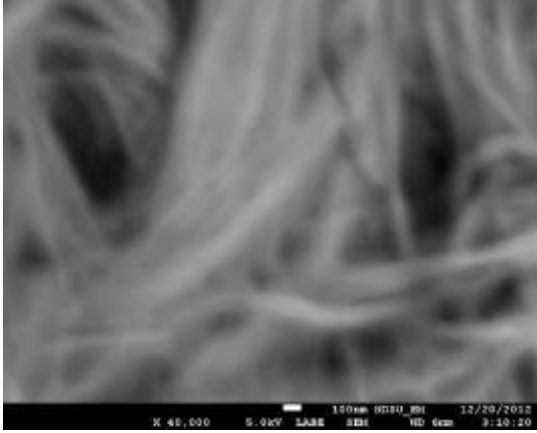


Figure C.11. SEM image of OI human tibia (transverse, anterior section) $\times 40,000$

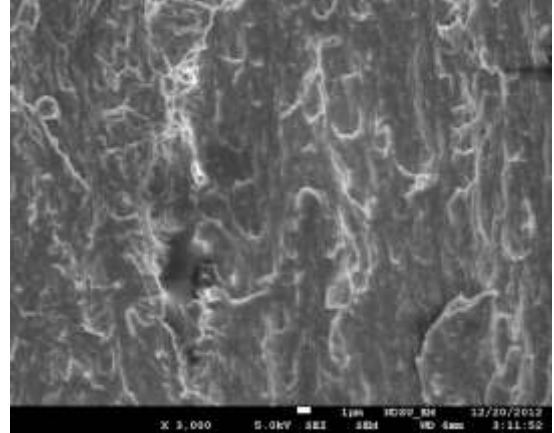


Figure C.12. SEM image of OI human tibia (transverse, anterior section) $\times 3,000$

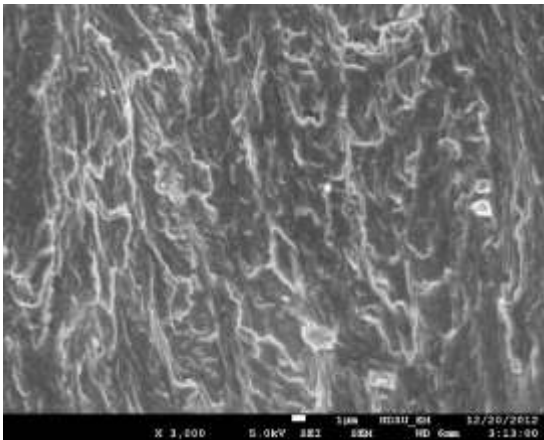


Figure C.13. SEM image of OI human tibia (transverse, anterior section) $\times 3,000$

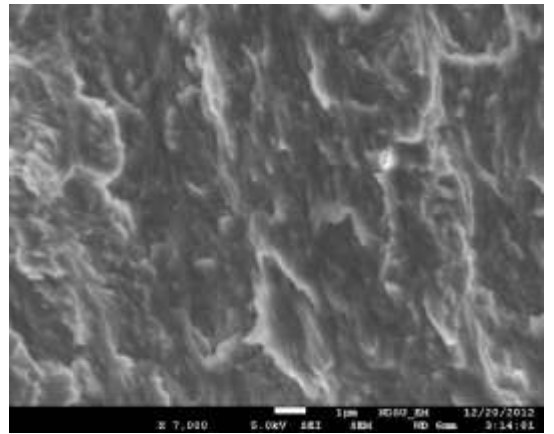


Figure C.14. SEM image of OI human tibia (transverse, anterior section) $\times 7,000$

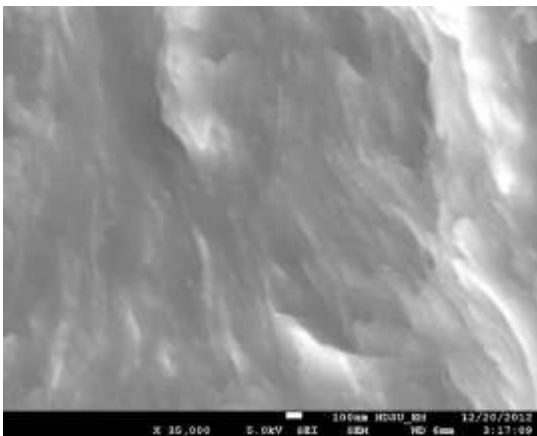


Figure C.15. SEM image of OI human tibia (transverse, anterior section) $\times 35,000$

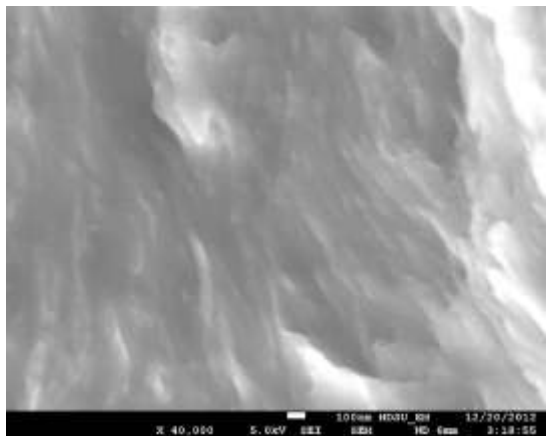


Figure C.16. SEM image of OI human tibia (transverse, anterior section) $\times 40,000$

C.1.1.2. Acquired on 2/6/2014 (JEOL JSM-6490LV scanning electron microscope (SEM))

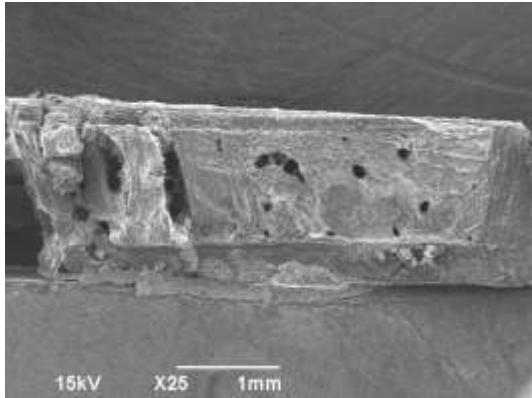


Figure C.17. SEM image of OI human tibia (transverse, anterior section) $\times 25$

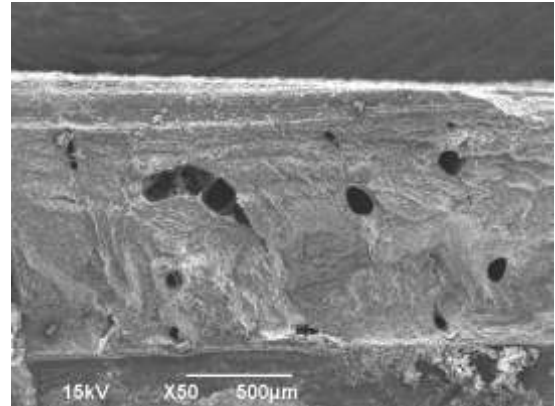


Figure C.18. SEM image of OI human tibia (transverse, anterior section) $\times 50$

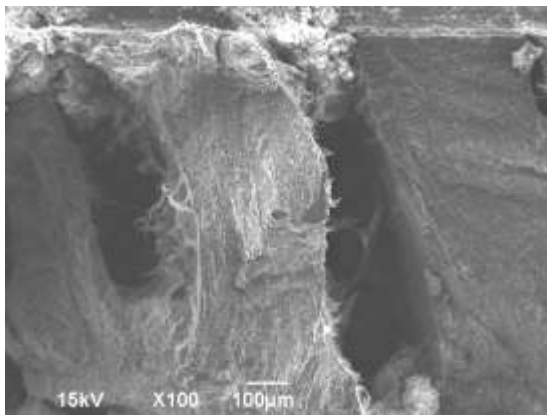


Figure C.19. SEM image of OI human tibia (transverse, anterior section) $\times 100$

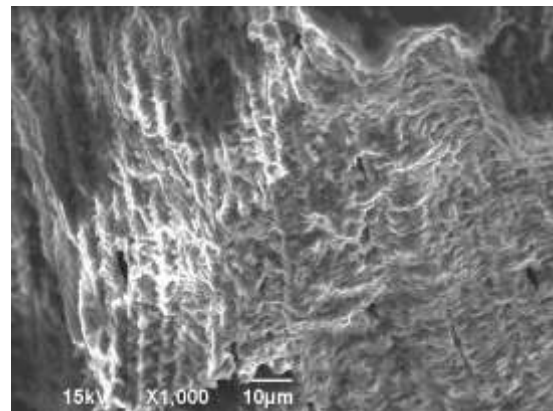


Figure C.20. SEM image of OI human tibia (transverse, anterior section) $\times 1,000$

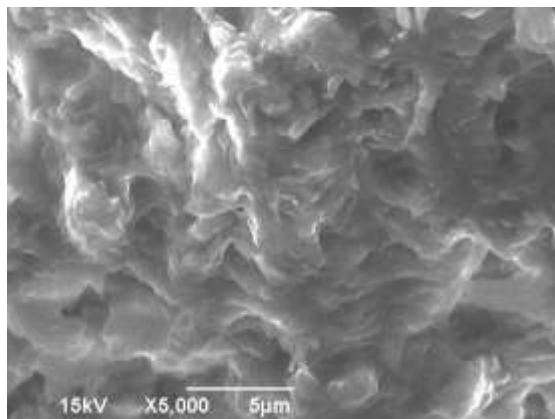


Figure C.21. SEM image of OI human tibia (transverse, anterior section) $\times 5,000$

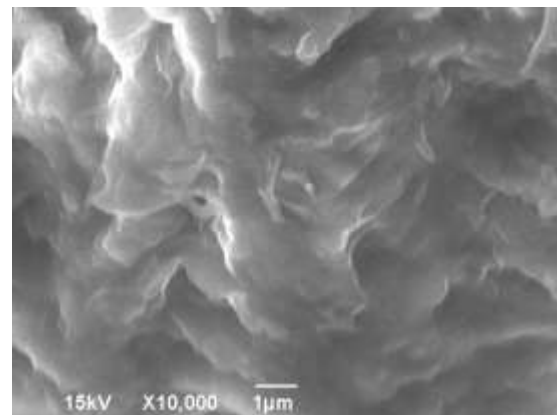


Figure C.22. SEM image of OI human tibia (transverse, anterior section) $\times 10,000$

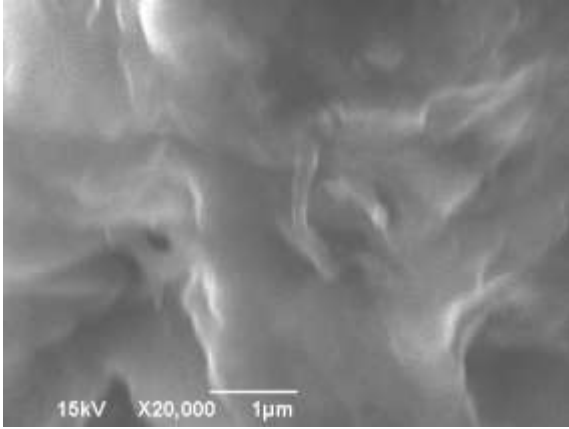


Figure C.23. SEM image of OI human tibia (transverse, anterior section) $\times 20,000$

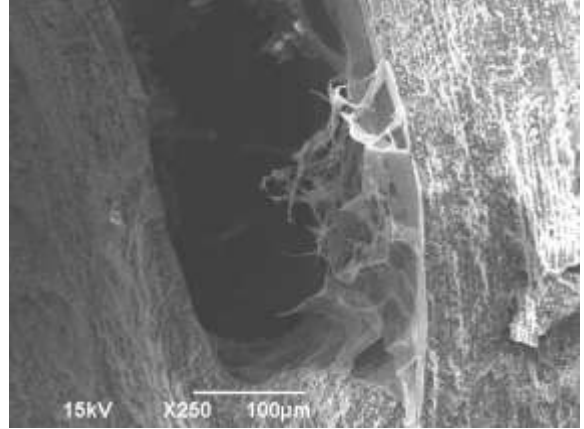


Figure C.24. SEM image of OI human tibia (transverse, anterior section) $\times 250$

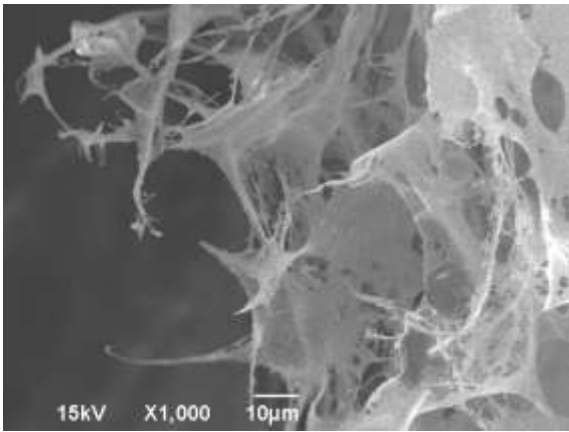


Figure C.25. SEM image of OI human tibia (transverse, anterior section) $\times 1,000$

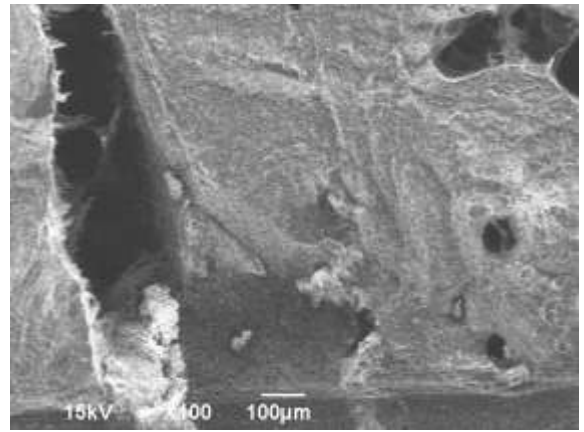


Figure C.26. SEM image of OI human tibia (transverse, anterior section) $\times 100$

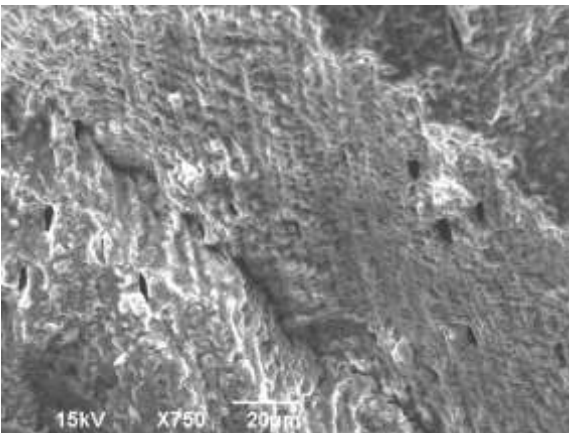


Figure C.27. SEM image of OI human tibia (transverse, anterior section) $\times 750$

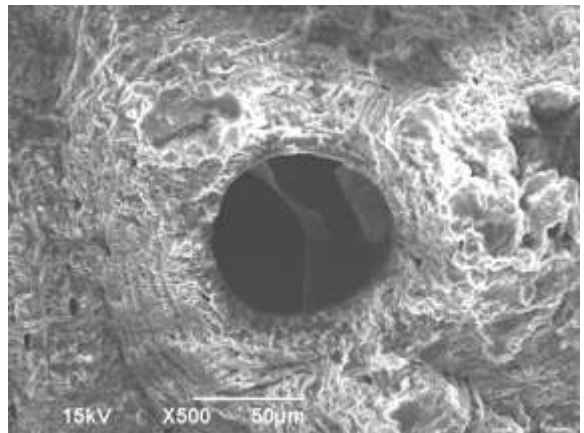


Figure C.28. SEM image of OI human tibia (transverse, anterior section) $\times 500$

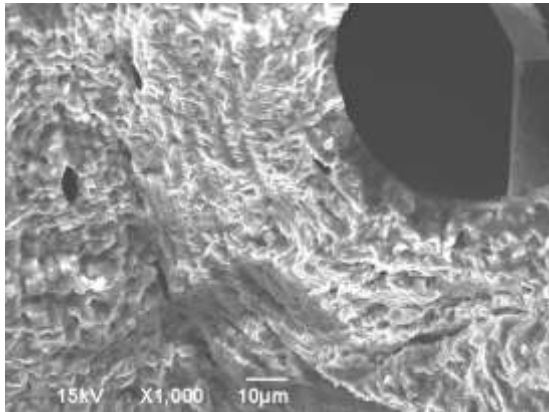


Figure C.29. SEM image of OI human tibia (transverse, anterior section) $\times 1,000$

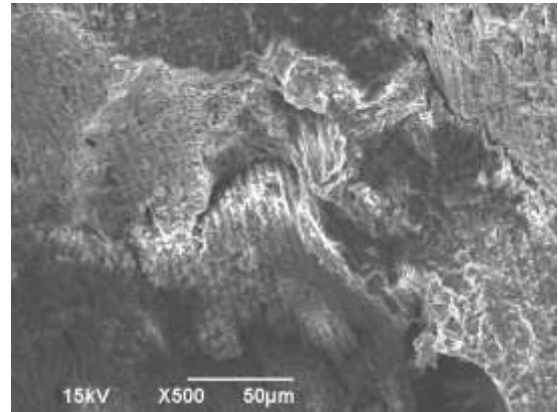


Figure C.30. SEM image of OI human tibia (transverse, anterior section) $\times 500$

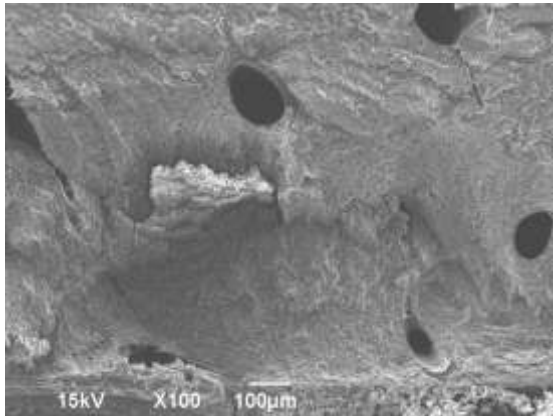


Figure C.31. SEM image of OI human tibia (transverse, anterior section) $\times 100$

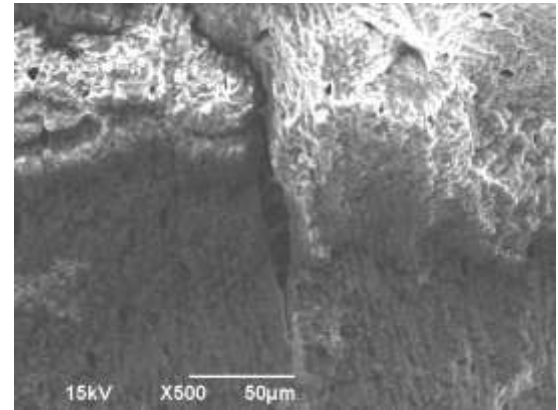


Figure C.32. SEM image of OI human tibia (transverse, anterior section) $\times 500$

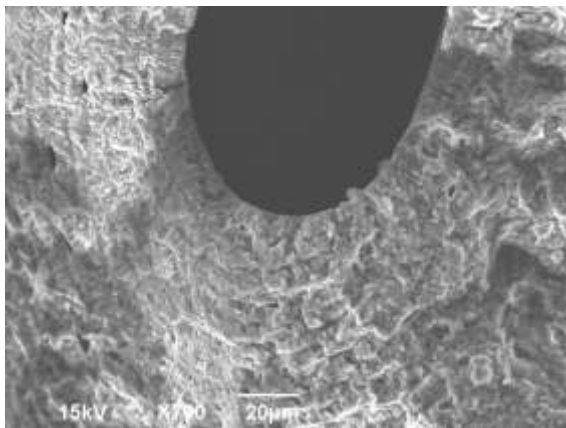


Figure C.33. SEM image of OI human tibia (transverse, anterior section) $\times 700$

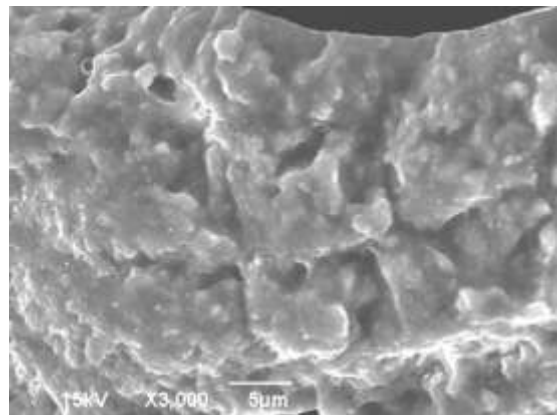


Figure C.34. SEM image of OI human tibia (transverse, anterior section) $\times 3,000$

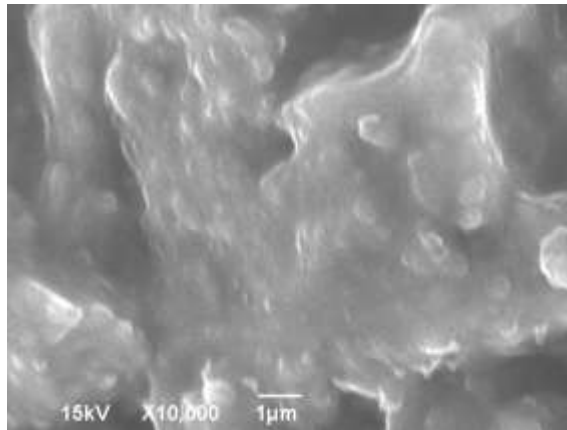


Figure C.35. SEM image of OI human tibia (transverse, anterior section) $\times 10,000$

C.1.2. Longitudinal section

C.1.2.1. Acquired on 1/30/201

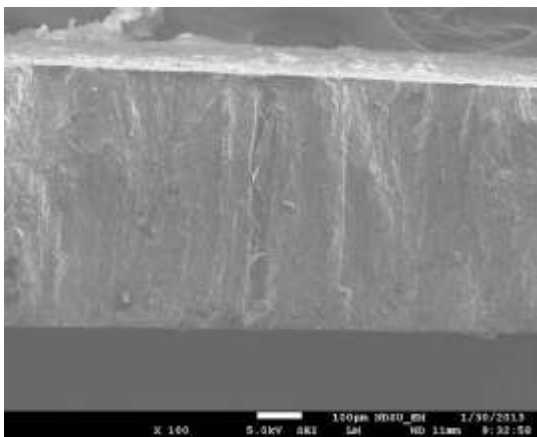


Figure C.36. SEM image of OI human tibia (longi., anterior section) $\times 100$

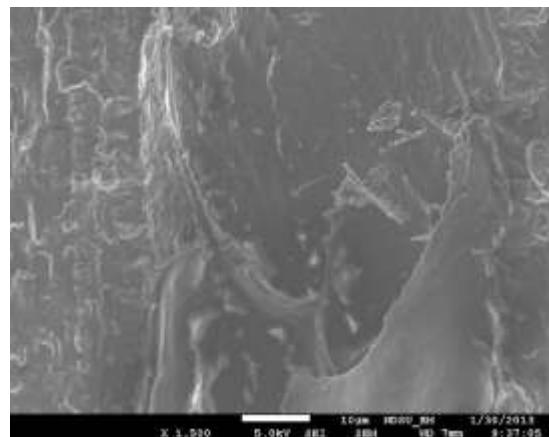


Figure C.37. SEM image of OI human tibia (longi., anterior section) $\times 1,500$



Figure C.38. SEM image of OI human tibia (longi., anterior section) $\times 6,000$

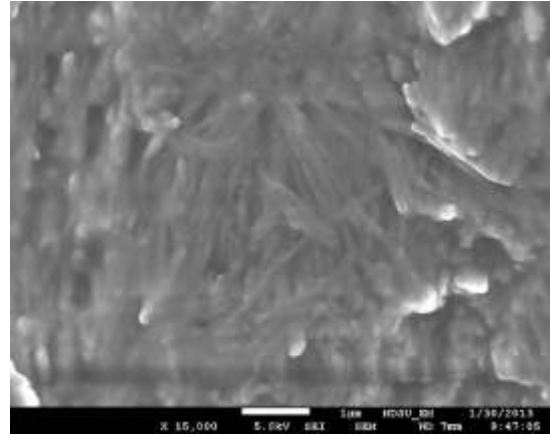


Figure C.39. SEM image of OI human tibia (longi., anterior section) $\times 15,000$

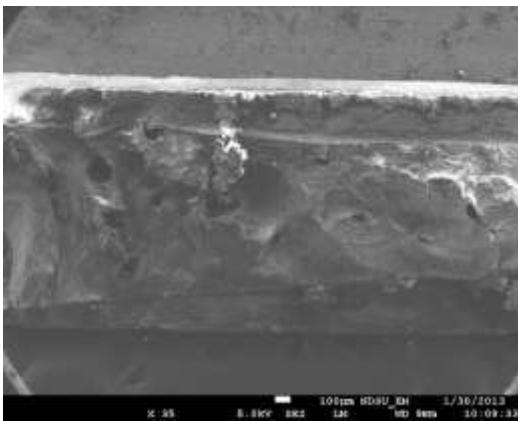


Figure C.40. SEM image of OI human tibia (longi., anterior section) $\times 35$

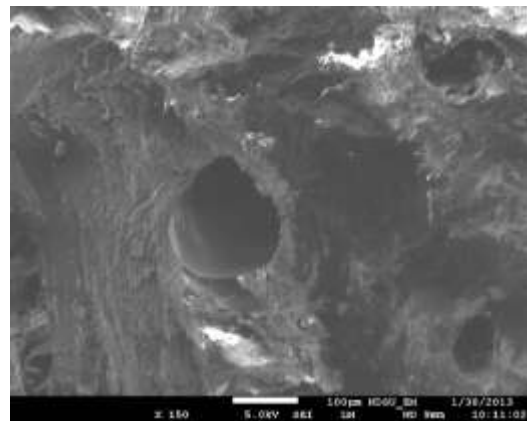


Figure C.41. SEM image of OI human tibia (longi., anterior section) $\times 150$

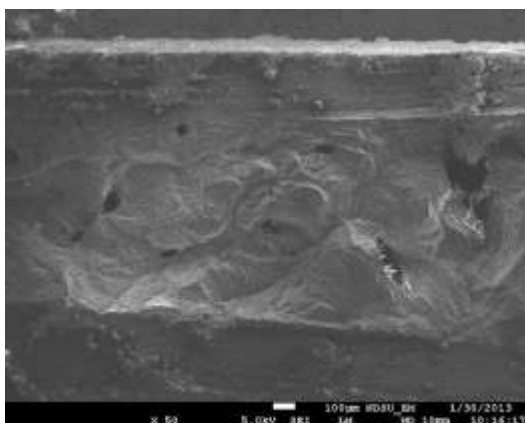


Figure C.42. SEM image of OI human tibia (longi., anterior section) $\times 50$

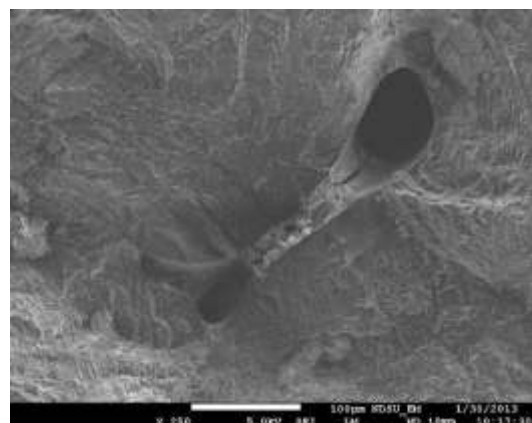


Figure C.43. SEM image of OI human tibia (longi., anterior section) $\times 250$

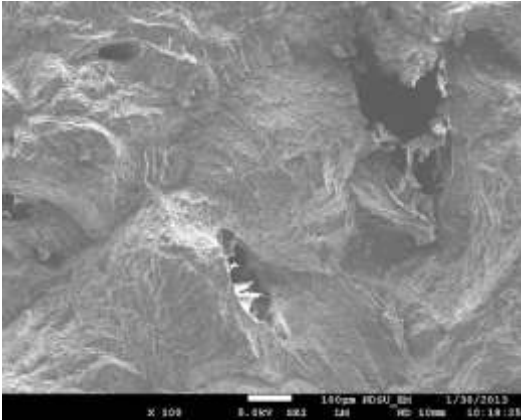


Figure C.44. SEM image of OI human tibia (longi., anterior section) $\times 100$

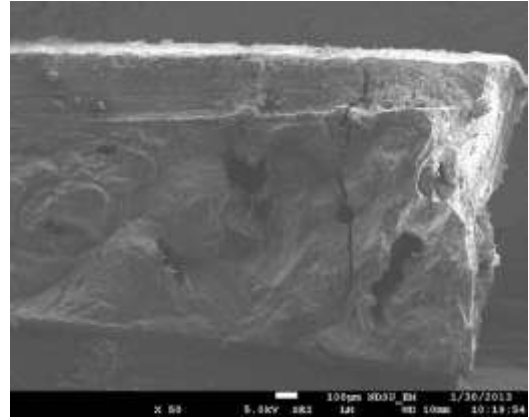


Figure C.45. SEM image of OI human tibia (longi., anterior section) $\times 50$

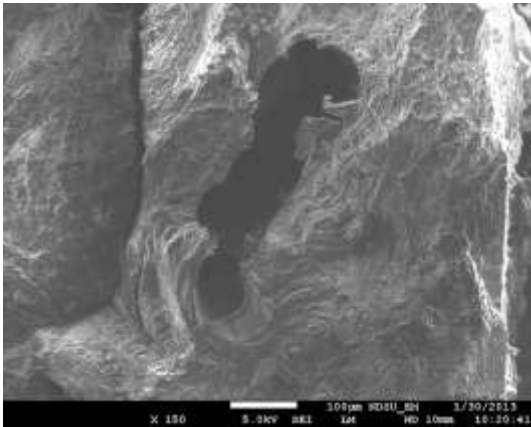


Figure C.46. SEM image of OI human tibia (longi., anterior section) $\times 150$

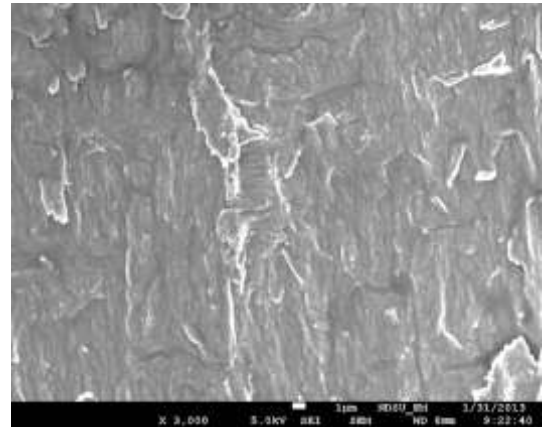


Figure C.47. SEM image of OI human tibia (longi., anterior section) $\times 3,000$

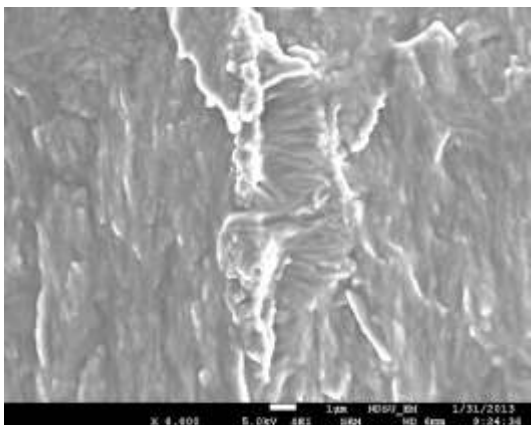


Figure C.48. SEM image of OI human tibia (longi., anterior section) $\times 6,000$

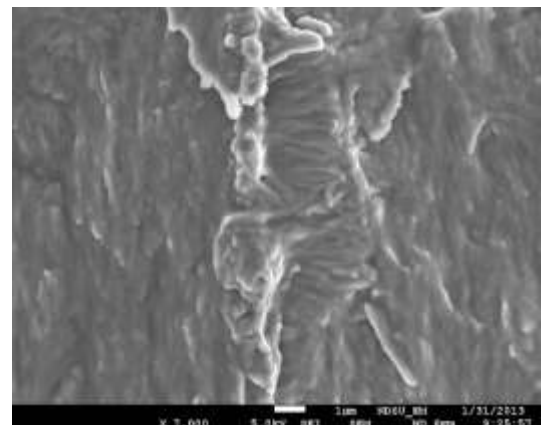


Figure C.49. SEM image of OI human tibia (longi., anterior section) $\times 7,000$

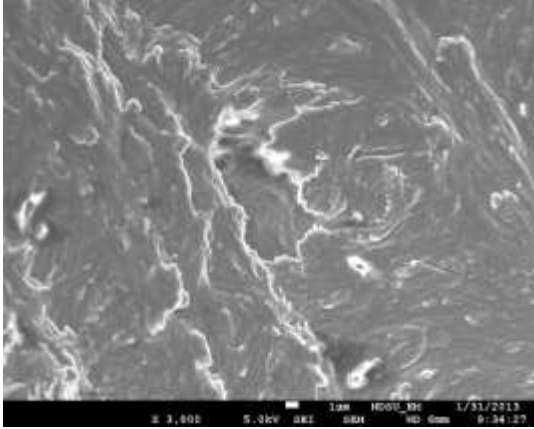


Figure C.50. SEM image of OI human tibia (longi., anterior section) $\times 3,000$

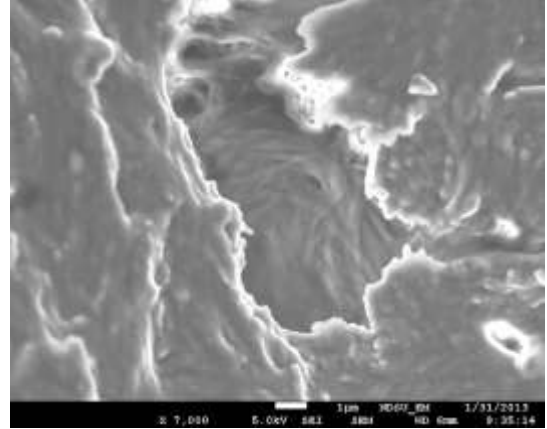


Figure C.51. SEM image of OI human tibia (longi., anterior section) $\times 7,000$

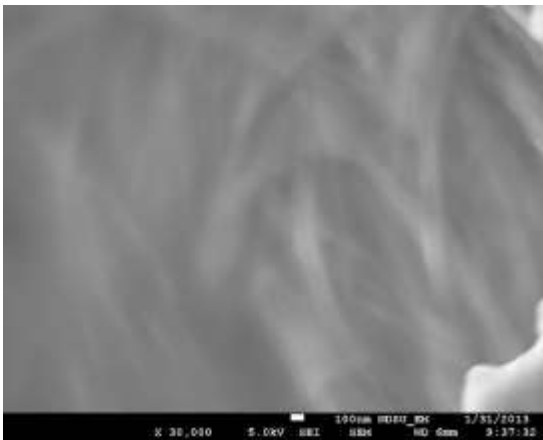


Figure C.52. SEM image of OI human tibia (longi., anterior section) $\times 30,000$

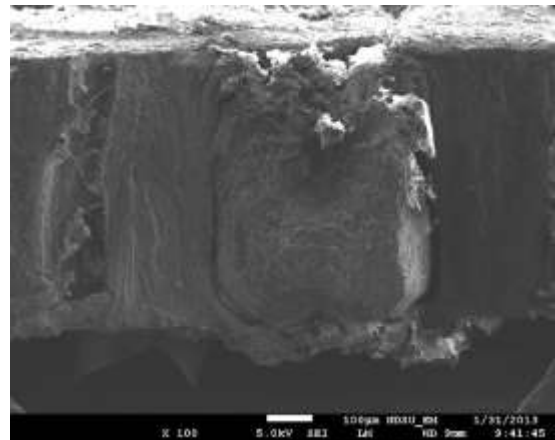


Figure C.53. SEM image of OI human tibia (longi., anterior section) $\times 100$

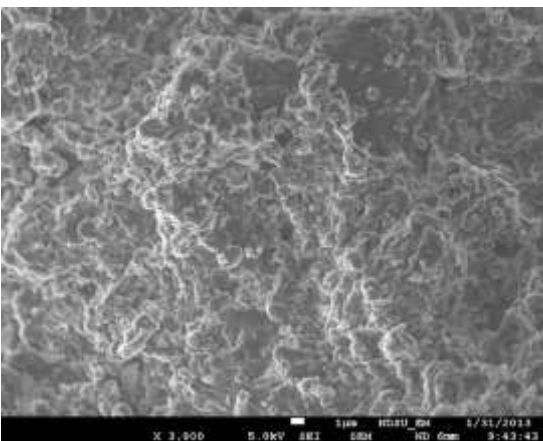


Figure C.54. SEM image of OI human tibia (longi., anterior section) $\times 3,000$

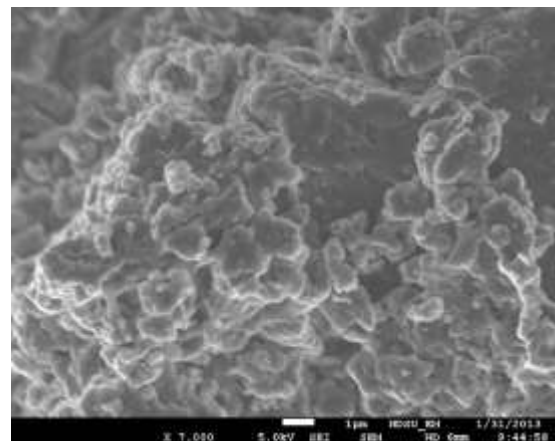


Figure C.55. SEM image of OI human tibia (longi., anterior section) $\times 7,000$

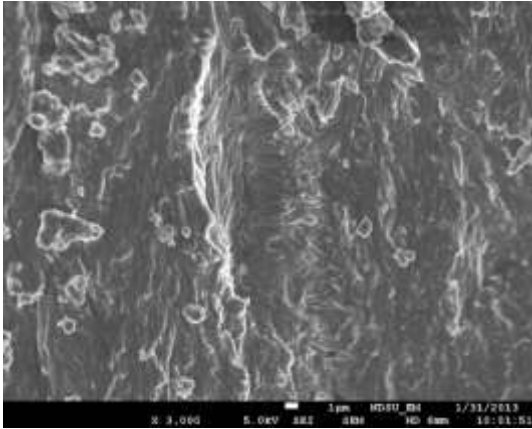


Figure C.56. SEM image of OI human tibia (longi., anterior section) $\times 3,000$

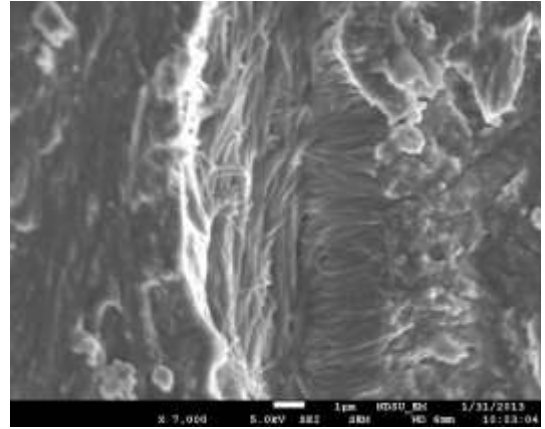


Figure C.57. SEM image of OI human tibia (longi., anterior section) $\times 7,000$

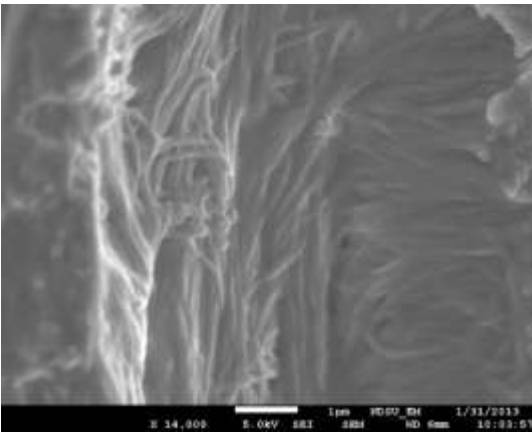


Figure C.58. SEM image of OI human tibia (longi., anterior section) $\times 14,000$

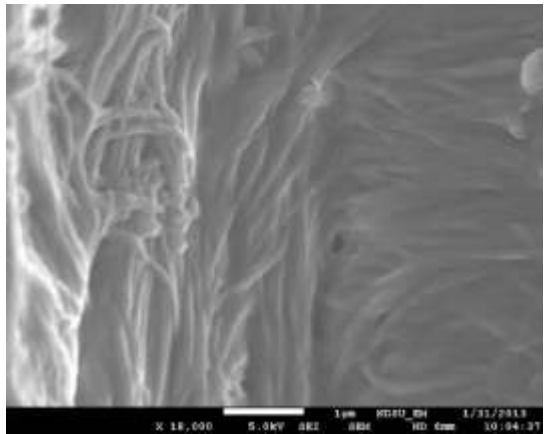


Figure C.59. SEM image of OI human tibia (longi., anterior section) $\times 18,000$

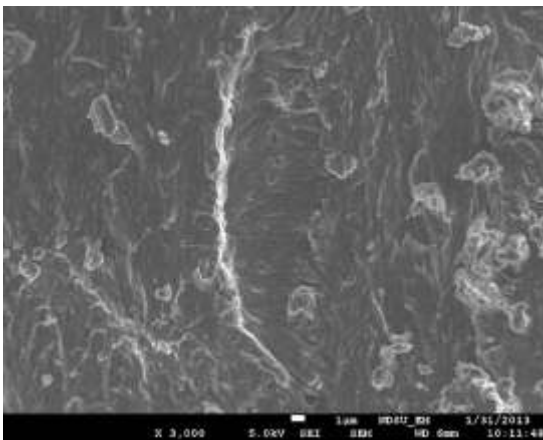


Figure C.60. SEM image of OI human tibia (longi., anterior section) $\times 3,000$

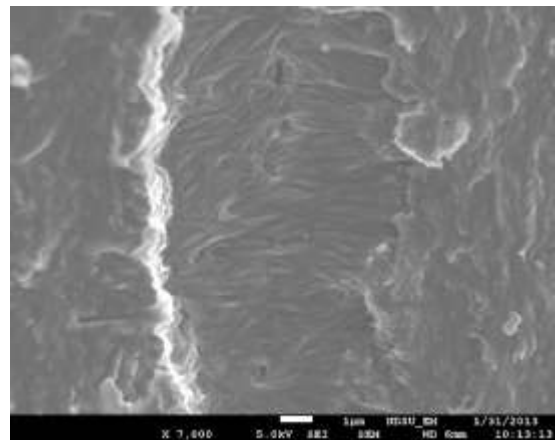


Figure C.61. SEM image of OI human tibia (longi., anterior section) $\times 7,000$

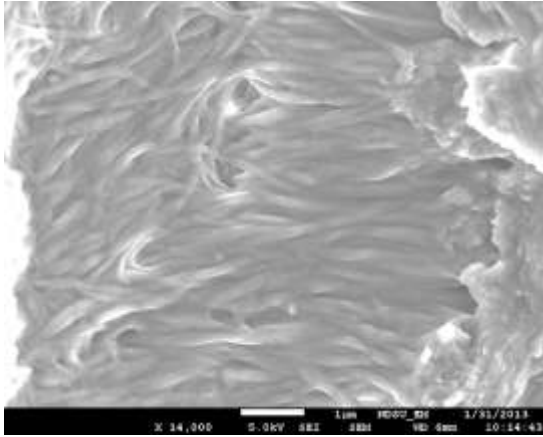


Figure C.62. SEM image of OI human tibia (longi., anterior section) $\times 14,000$

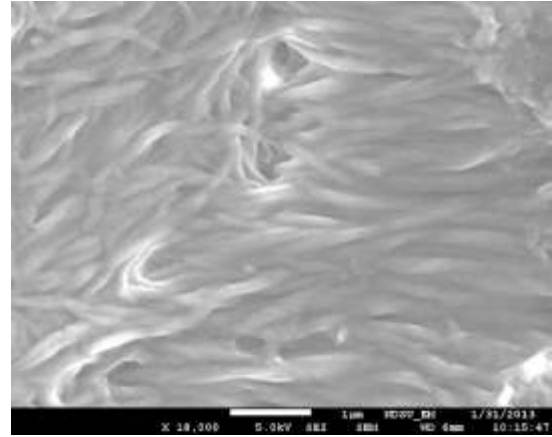


Figure C.63. SEM image of OI human tibia (longi., anterior section) $\times 18,000$

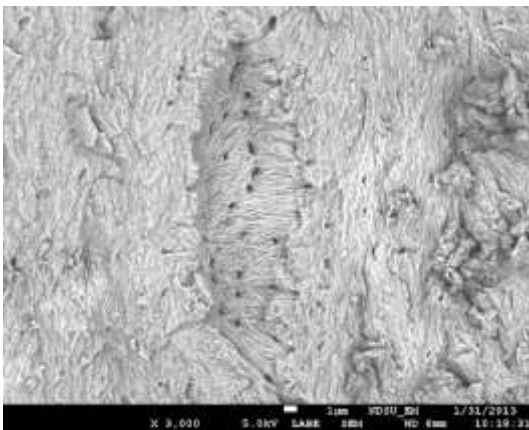


Figure C.64. SEM image of OI human tibia (longi., anterior section) $\times 3,000$

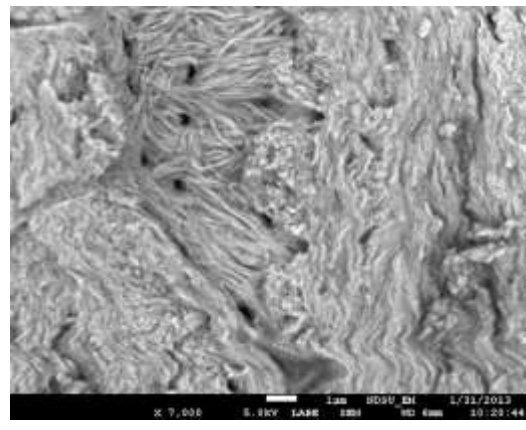


Figure C.65. SEM image of OI human tibia (longi., anterior section) $\times 7,000$

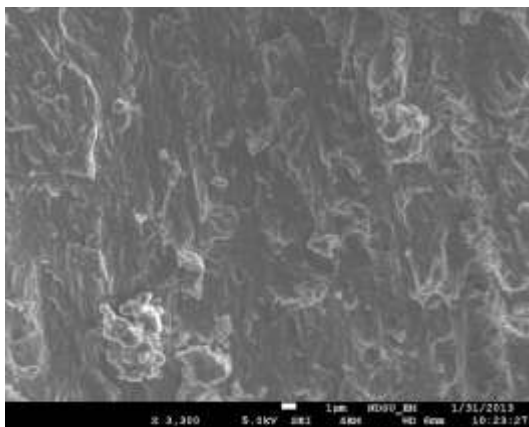


Figure C.66. SEM image of OI human tibia (longi., anterior section) $\times 3,300$

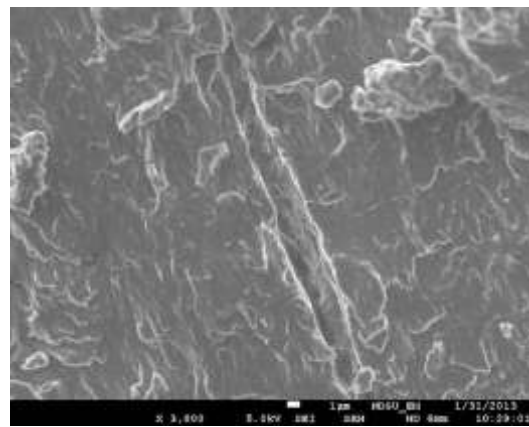


Figure C.67. SEM image of OI human tibia (longi., anterior section) $\times 3,000$

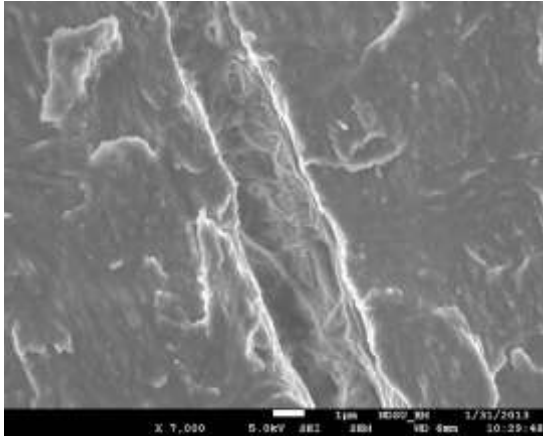


Figure C.68. SEM image of OI human tibia (longi., anterior section) $\times 7,000$

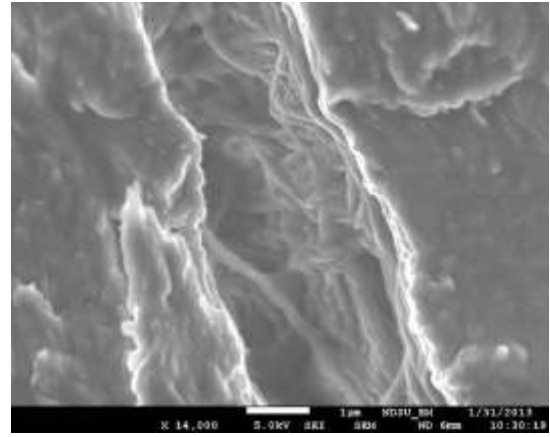


Figure C.69. SEM image of OI human tibia (longi., anterior section) $\times 14,000$

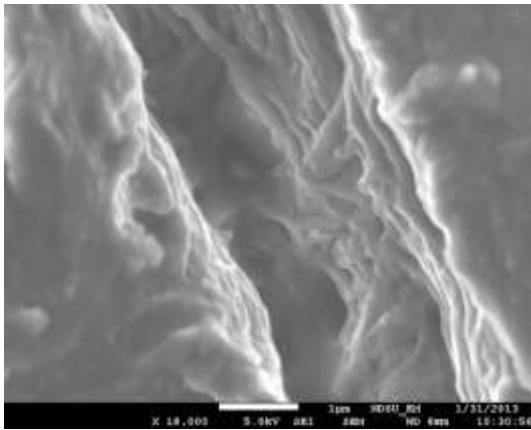


Figure C.70. SEM image of OI human tibia (longi., anterior section) $\times 18,000$

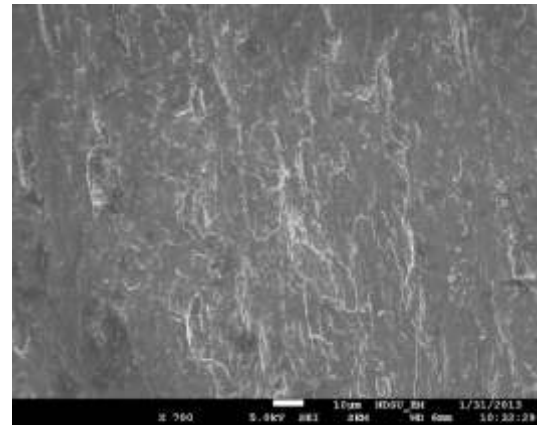


Figure C.71. SEM image of OI human tibia (longi., anterior section) $\times 700$

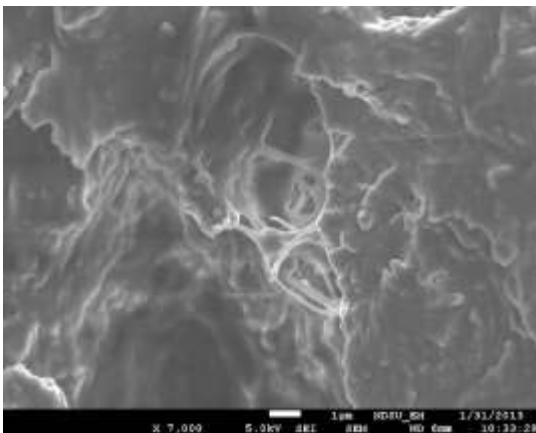


Figure C.72. SEM image of OI human tibia (longi., anterior section) $\times 7,000$

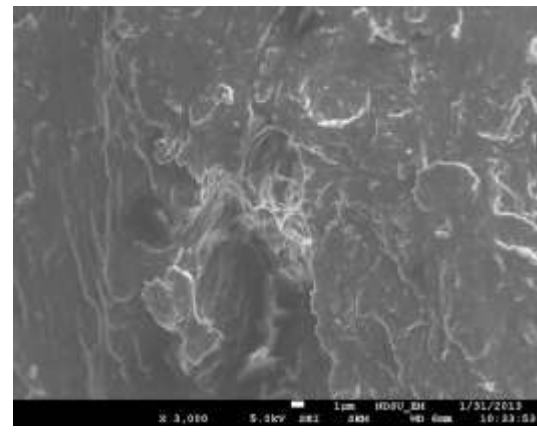


Figure C.73. SEM image of OI human tibia (longi., anterior section) $\times 3,000$

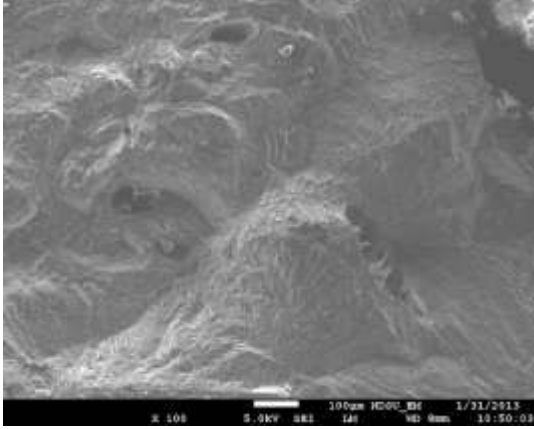


Figure C.74. SEM image of OI human tibia (longi., anterior section) $\times 100$

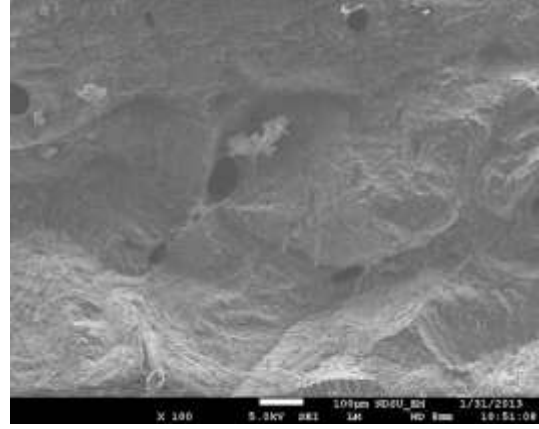


Figure C.75. SEM image of OI human tibia (longi., anterior section) $\times 100$

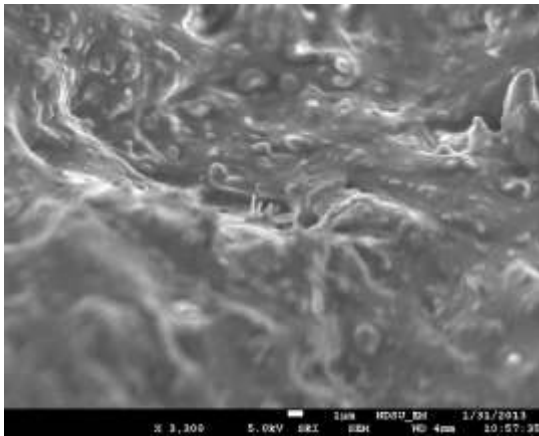


Figure C.76. SEM image of OI human tibia (longi., anterior section) $\times 3,300$

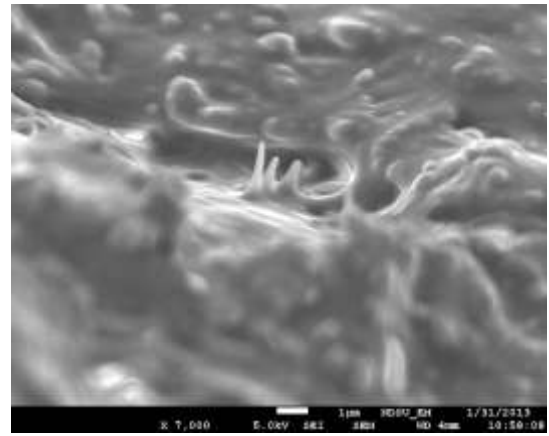


Figure C.77. SEM image of OI human tibia (longi., anterior section) $\times 7,000$

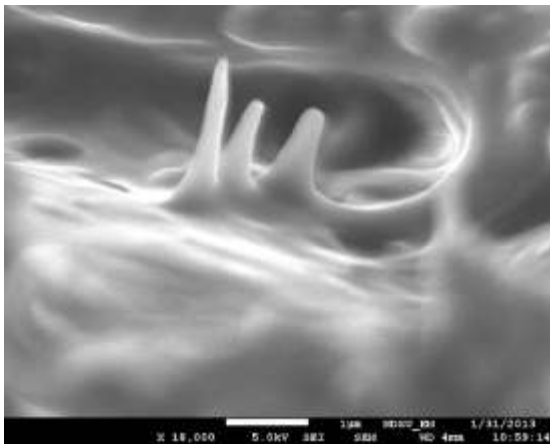


Figure C.78. SEM image of OI human tibia (longi., anterior section) $\times 18,000$

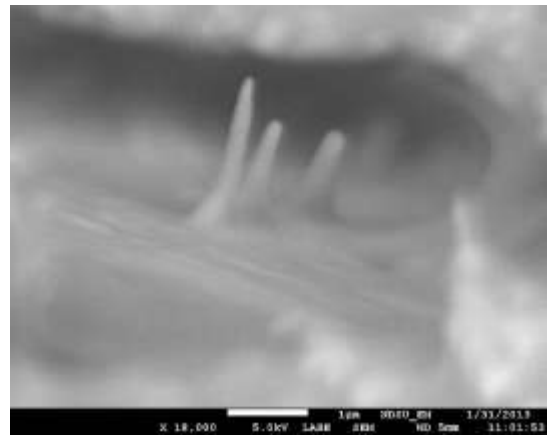


Figure C.79. SEM image of OI human tibia (longi., anterior section) $\times 18,000$

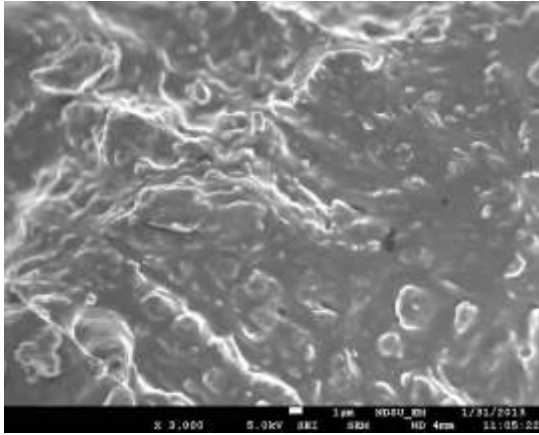


Figure C.80. SEM image of OI human tibia (longi., anterior section) $\times 3,000$

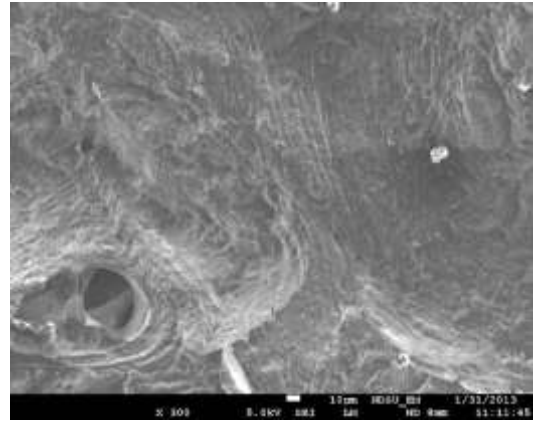


Figure C.81. SEM image of OI human tibia (longi., anterior section) $\times 300$

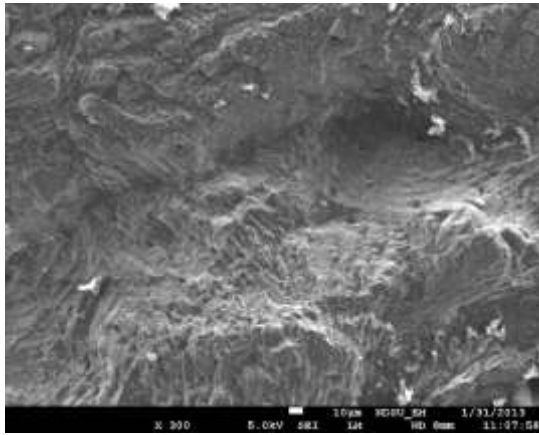


Figure C.82. SEM image of OI human tibia (longi., anterior section) $\times 300$

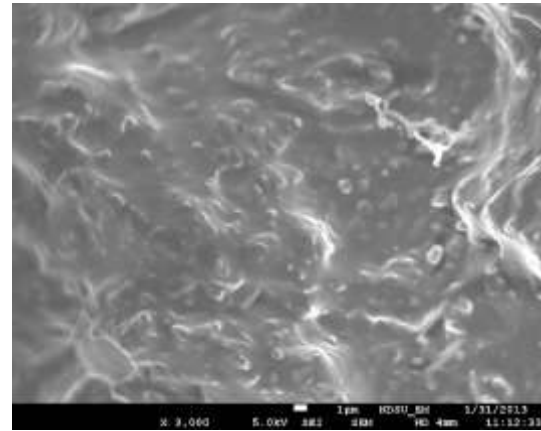


Figure C.83. SEM image of OI human tibia (longi., anterior section) $\times 3,000$

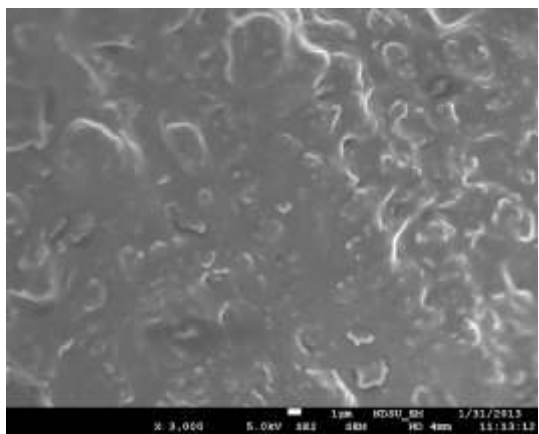


Figure C.84. SEM image of OI human tibia (longi., anterior section) $\times 3,000$

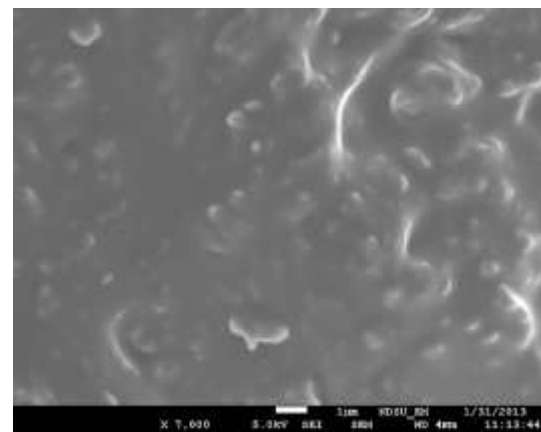


Figure C.85. SEM image of OI human tibia (longi., anterior section) $\times 7,000$

C.1.2.2. Acquired on 12/10/2012

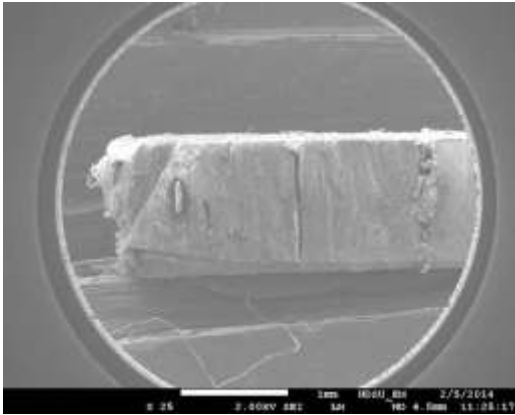


Figure C.86. SEM image of OI human tibia (longi., anterior section) ×25

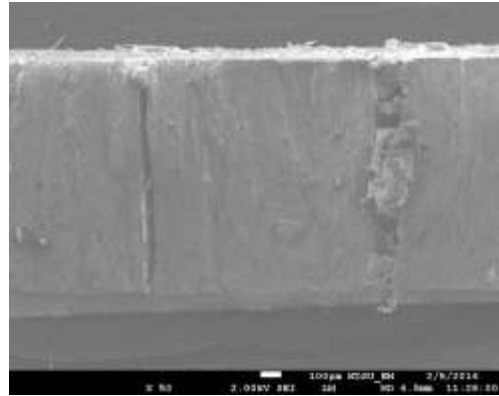


Figure C.87. SEM image of OI human tibia (longi., anterior section) ×50

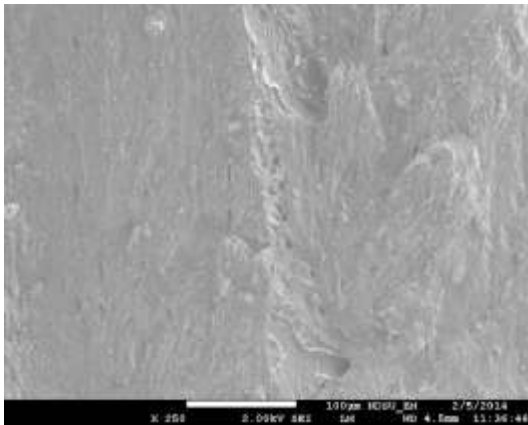


Figure C.88. SEM image of OI human tibia (longi., anterior section) ×250

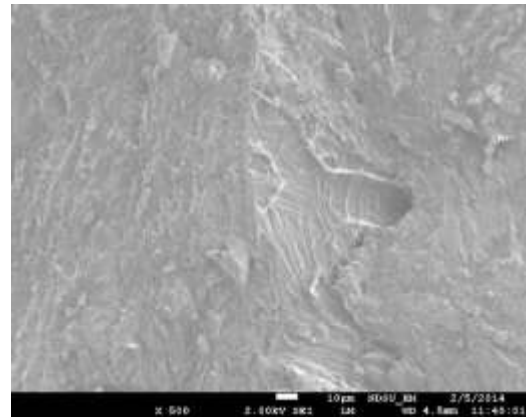


Figure C.89. SEM image of OI human tibia (longi., anterior section) ×500

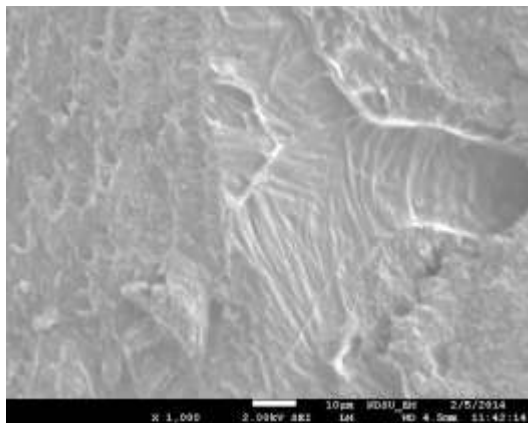


Figure C.90. SEM image of OI human tibia (longi., anterior section) ×1,000

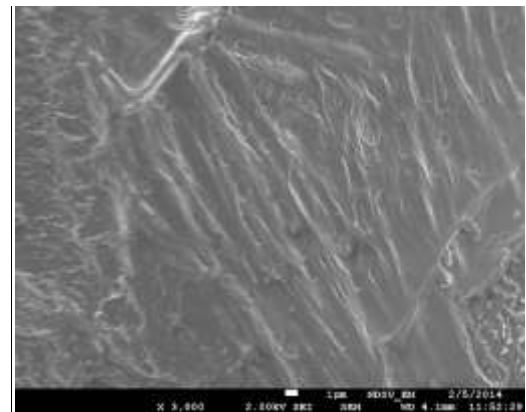


Figure C.91. SEM image of OI human tibia (longi., anterior section) ×3,000

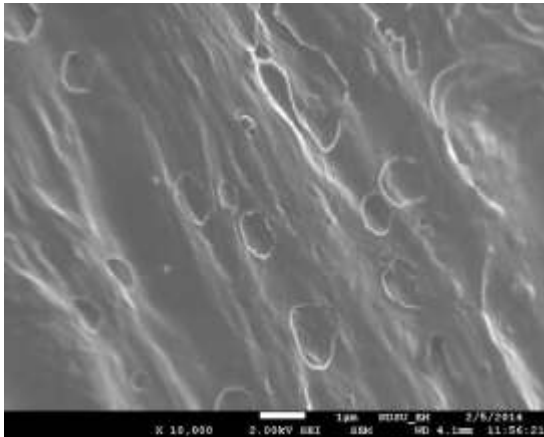


Figure C.92. SEM image of OI human tibia (longi., anterior section) $\times 10,000$

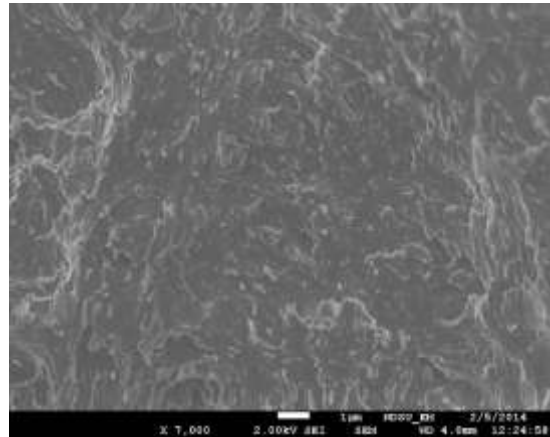


Figure C.93. SEM image of OI human tibia (longi., anterior section) $\times 7,000$

C.2. Medial section, fixed with a series of chemicals and fractured in liquid N₂

C.2.1. Transverse section (acquired on 2/6/2014)

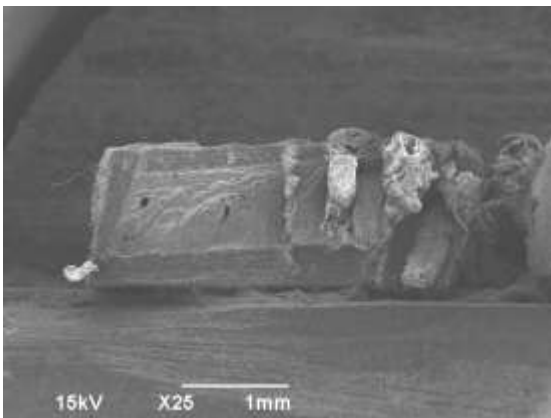


Figure C.94. SEM image of OI human tibia (transverse, medial section) $\times 25$

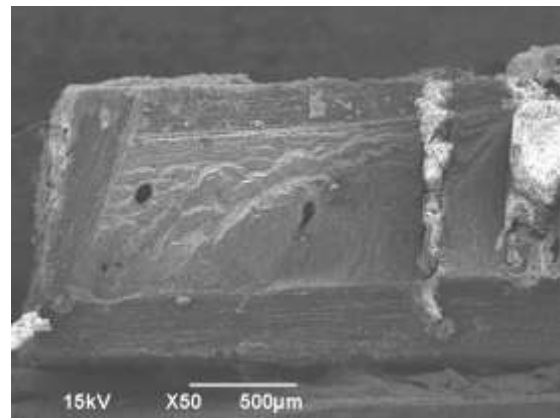


Figure C.95. SEM image of OI human tibia (transverse, medial section) $\times 50$

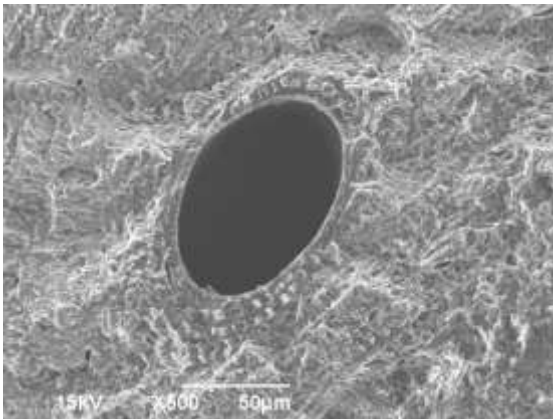


Figure C.96. SEM image of OI human tibia (transverse, medial section) $\times 500$

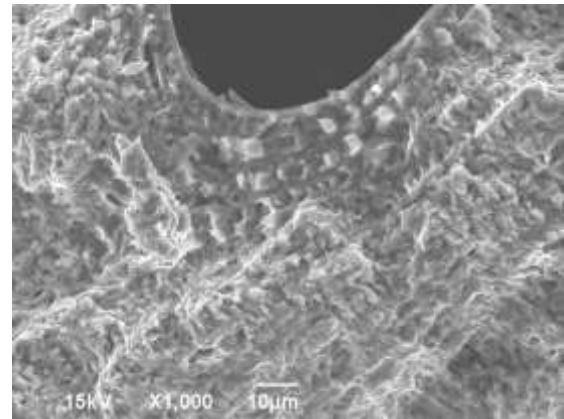


Figure C.97. SEM image of OI human tibia (transverse, medial section) $\times 1,000$

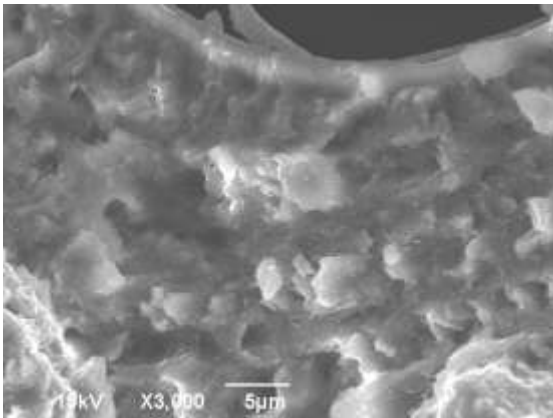


Figure C.98. SEM image of OI human tibia (transverse, medial section) $\times 3,000$

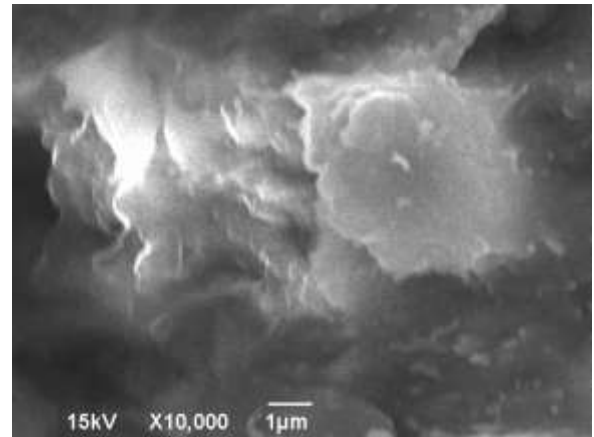


Figure C.99. SEM image of OI human tibia (transverse, medial section) $\times 10,000$

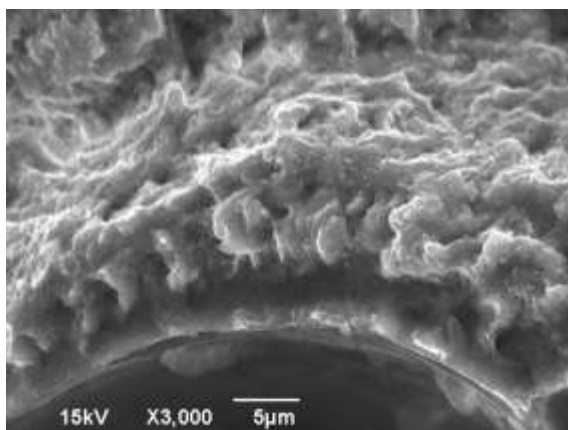


Figure C.100. SEM image of OI human tibia (transverse, medial section) $\times 3,000$

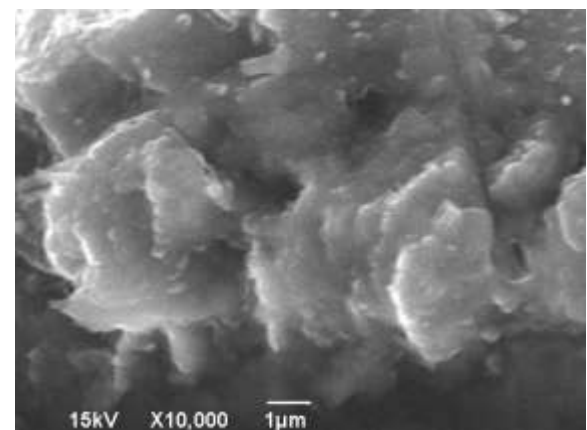


Figure C.101. SEM image of OI human tibia (transverse, medial section) $\times 10,000$

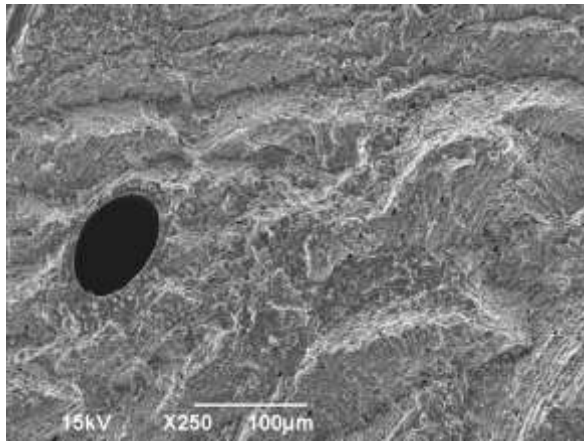


Figure C.102. SEM image of OI human tibia (transverse, medial section) $\times 250$

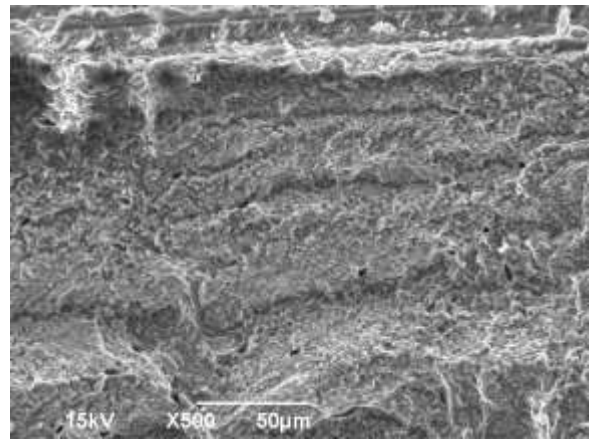


Figure C.103. SEM image of OI human tibia (transverse, medial section) $\times 500$

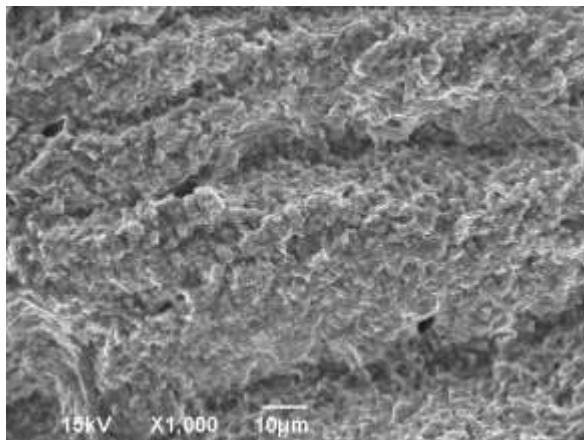


Figure C.104. SEM image of OI human tibia (transverse, medial section) $\times 1,000$

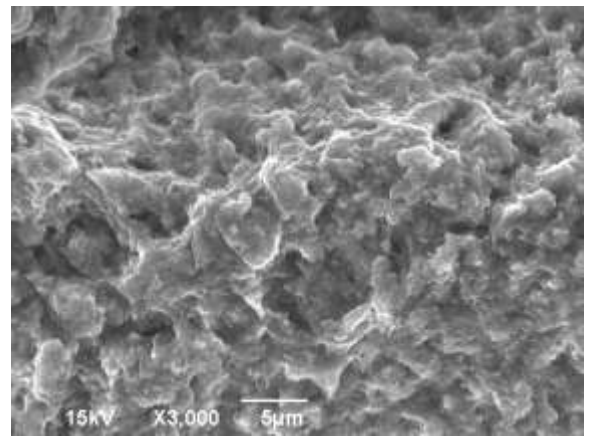


Figure C.105. SEM image of OI human tibia (transverse, medial section) $\times 3,000$

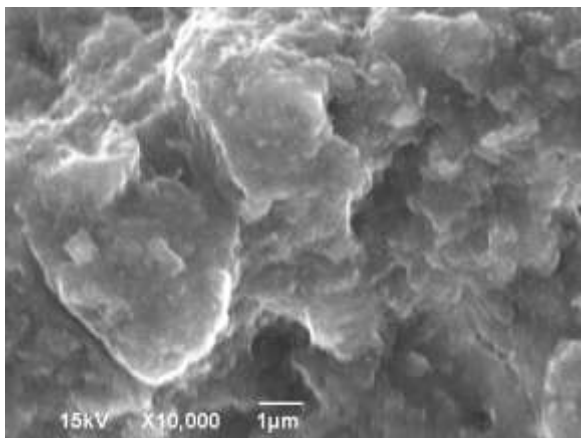


Figure C.106. SEM image of OI human tibia (transverse, medial section) $\times 10,000$

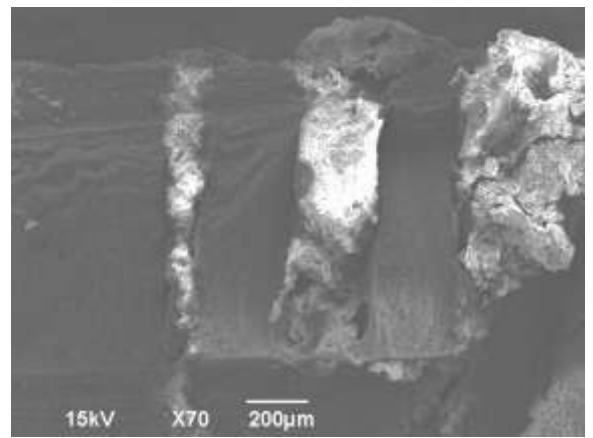


Figure C.107. SEM image of OI human tibia (transverse, medial section) $\times 70$

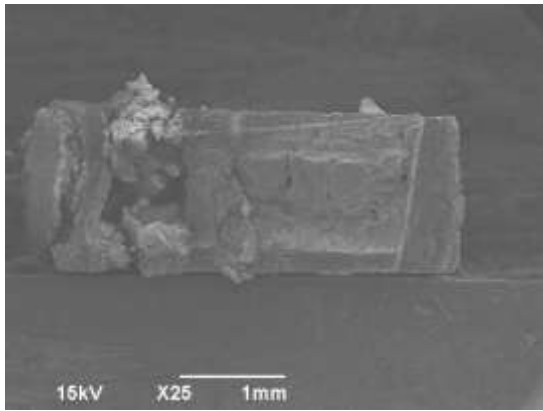


Figure C.108. SEM image of OI human tibia (transverse, medial section) $\times 25$

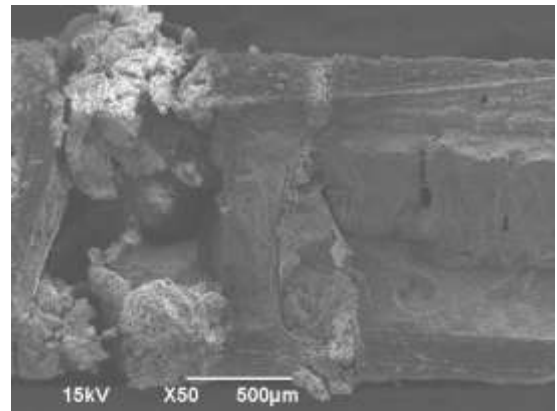


Figure C.109. SEM image of OI human tibia (transverse, medial section) $\times 50$

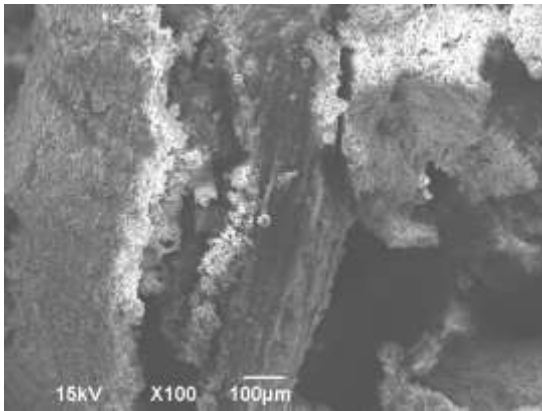


Figure C.110. SEM image of OI human tibia (transverse, medial section) $\times 100$

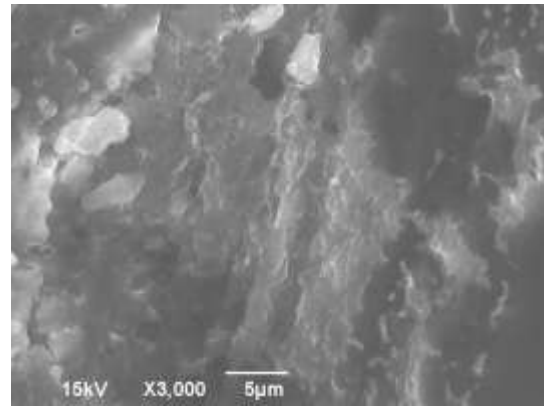


Figure C.111. SEM image of OI human tibia (transverse, medial section) $\times 3,000$

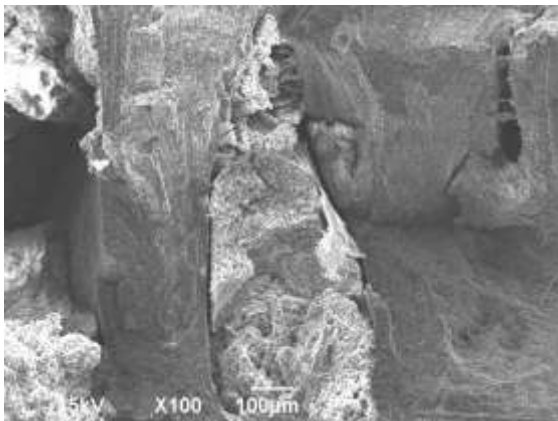


Figure C.112. SEM image of OI human tibia (transverse, medial section) $\times 100$

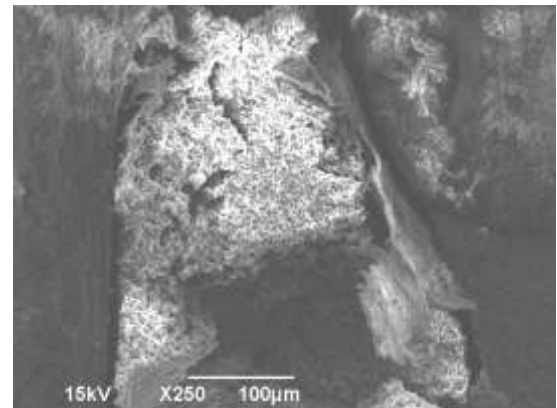


Figure C.113. SEM image of OI human tibia (transverse, medial section) $\times 250$

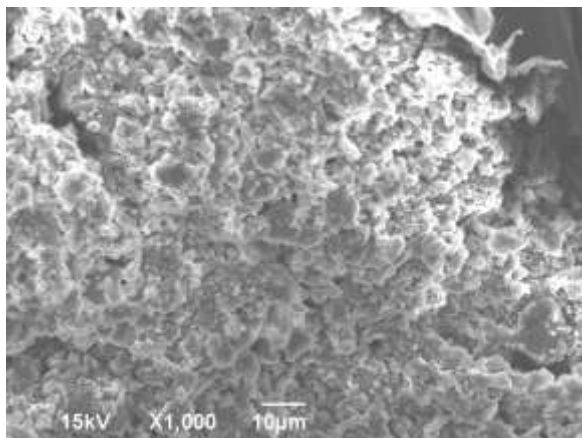


Figure C.114. SEM image of OI human tibia (transverse, medial section) $\times 1,000$

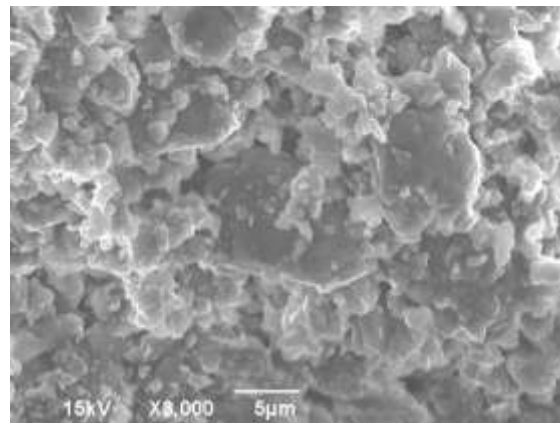


Figure C.115. SEM image of OI human tibia (transverse, medial section) $\times 3,000$

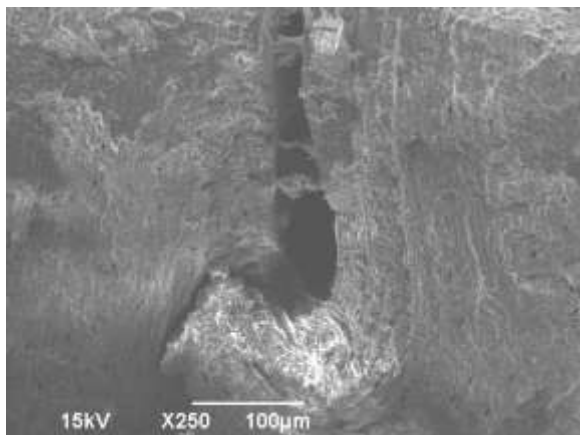


Figure C.116. SEM image of OI human tibia (transverse, medial section) $\times 250$

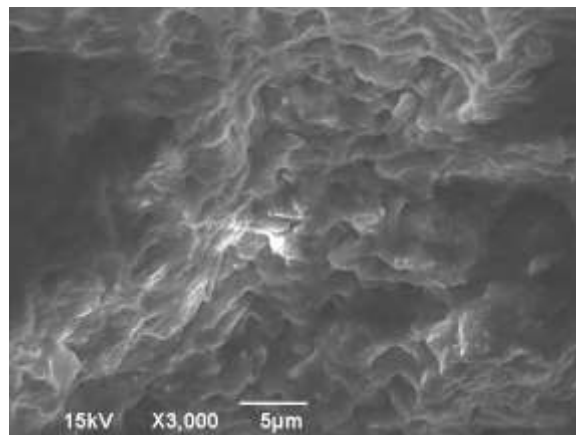


Figure C.117. SEM image of OI human tibia (transverse, medial section) $\times 3,000$

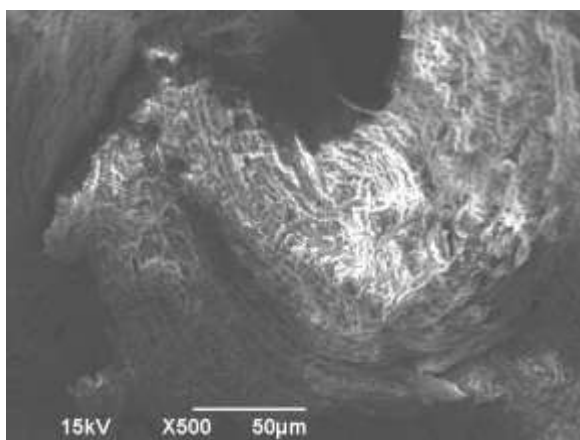


Figure C.118. SEM image of OI human tibia (transverse, medial section) $\times 500$

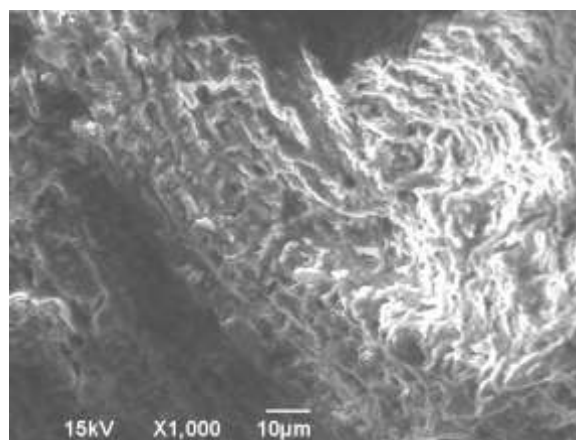


Figure C.119. SEM image of OI human tibia (transverse, medial section) $\times 1,000$

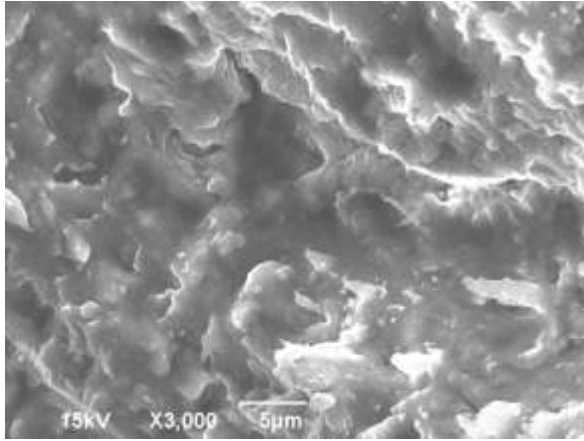


Figure C.120. SEM image of OI human tibia (transverse, medial section) $\times 3,000$

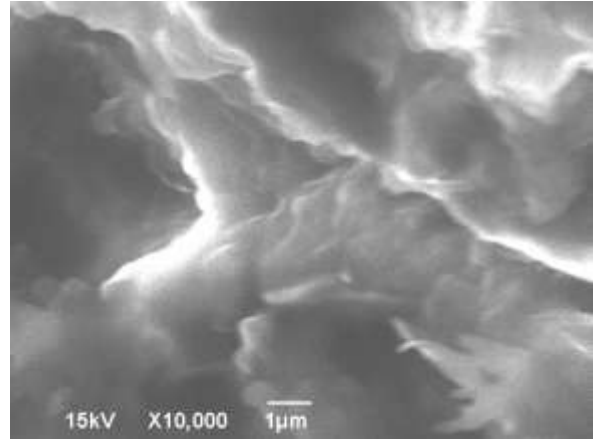


Figure C.121. SEM image of OI human tibia (transverse, medial section) $\times 10,000$

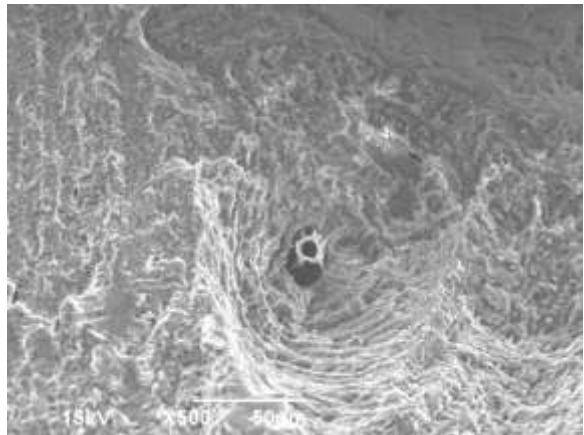


Figure C.122. SEM image of OI human tibia (transverse, medial section) $\times 500$

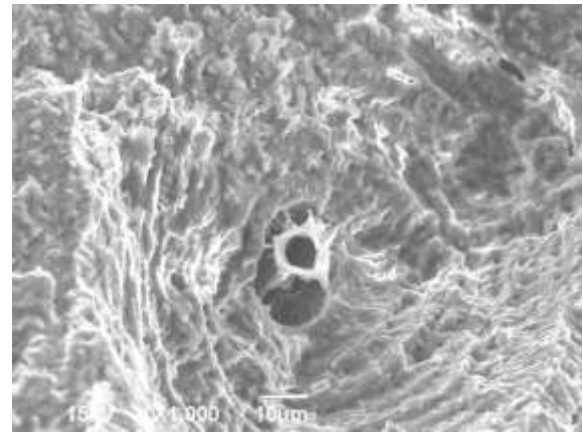


Figure C.123. SEM image of OI human tibia (transverse, medial section) $\times 1,000$

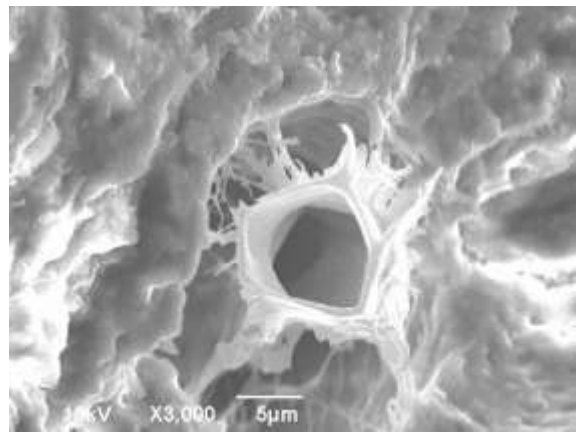


Figure C.124. SEM image of OI human tibia (transverse, medial section) $\times 3,000$

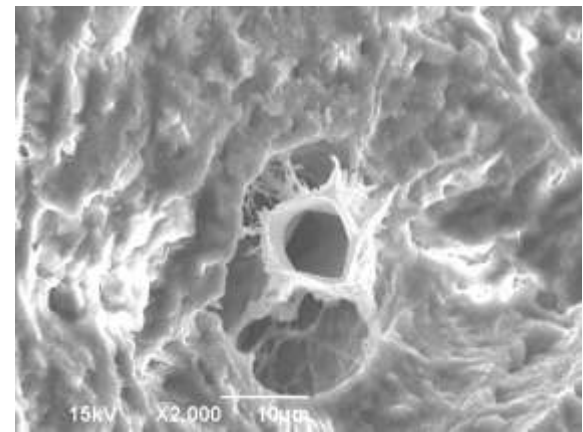


Figure C.125. SEM image of OI human tibia (transverse, medial section) $\times 2,000$

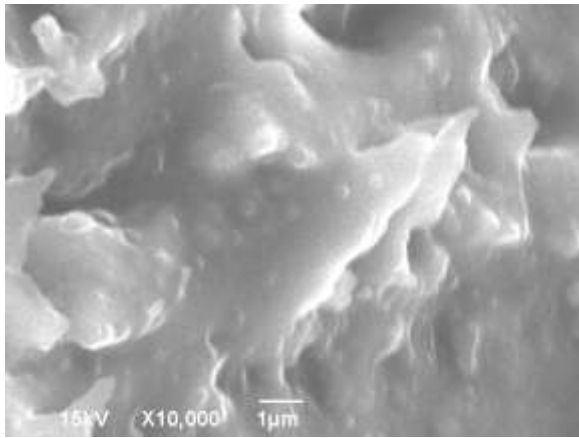


Figure C.126. SEM image of OI human tibia (transverse, medial section) $\times 10,000$

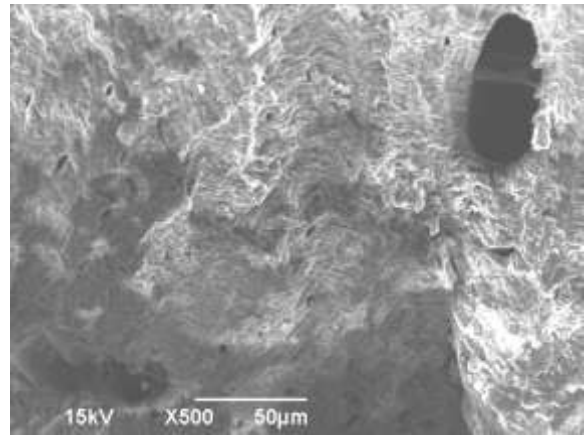


Figure C.127. SEM image of OI human tibia (transverse, medial section) $\times 500$

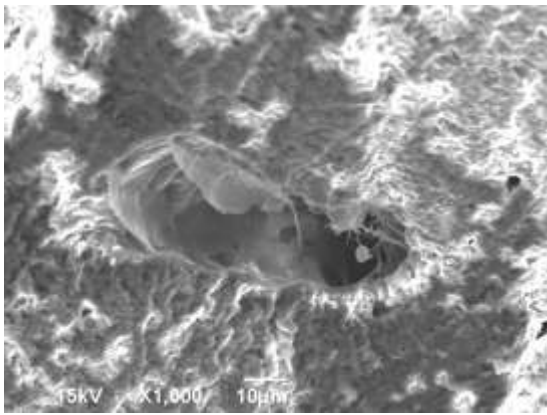


Figure C.128. SEM image of OI human tibia (transverse, medial section) $\times 1,000$

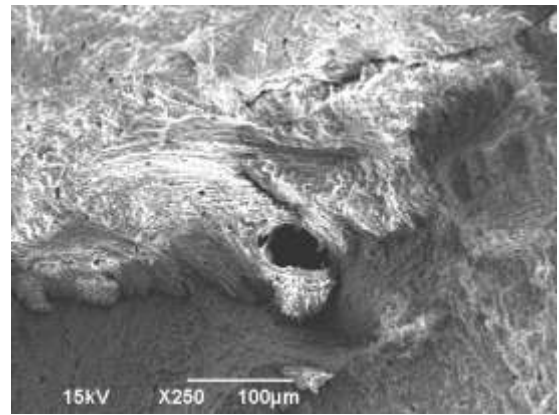


Figure C.129. SEM image of OI human tibia (transverse, medial section) $\times 250$

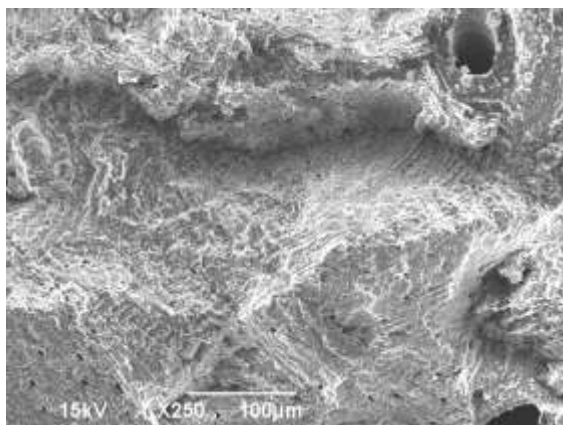


Figure C.130. SEM image of OI human tibia (transverse, medial section) $\times 250$

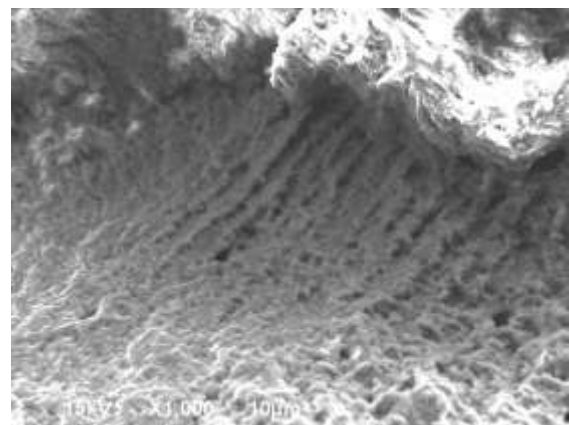


Figure C.131. SEM image of OI human tibia (transverse, medial section) $\times 1,000$

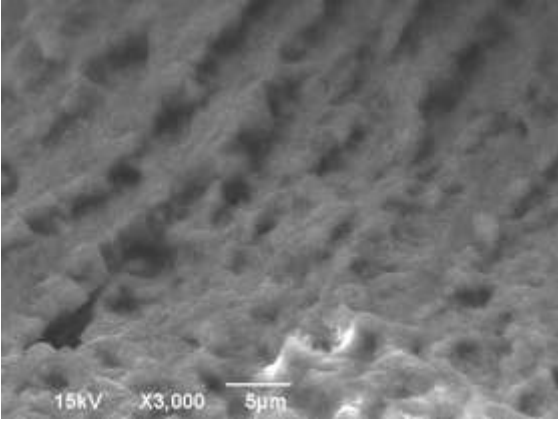


Figure C.132. SEM image of OI human tibia (transverse, medial section) $\times 3,000$

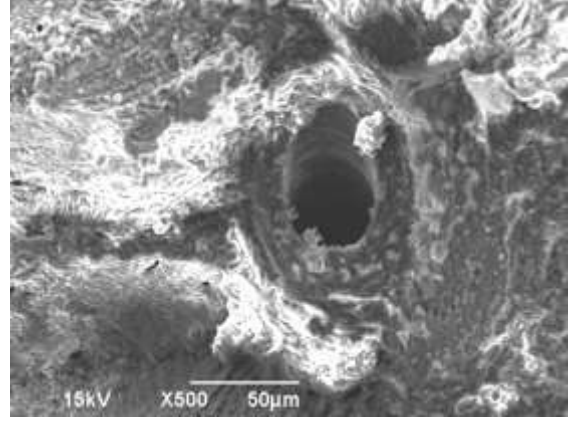


Figure C.133. SEM image of OI human tibia (transverse, medial section) $\times 500$

C.2.2. Longitudinal section (acquired on 2/5/2014)

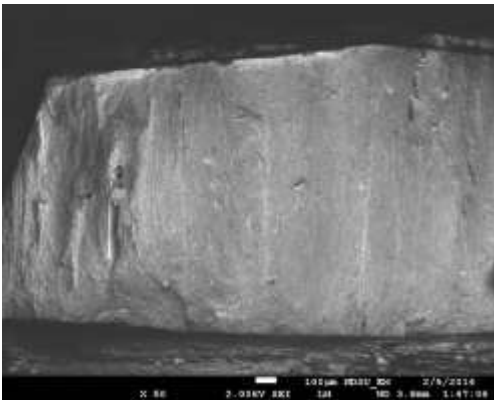


Figure C.134. SEM image of OI human tibia (longi., medial section) $\times 50$

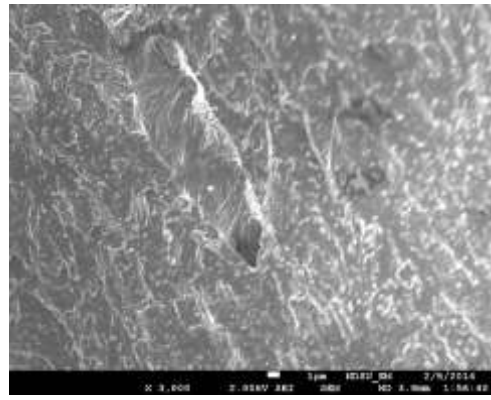


Figure C.135. SEM image of OI human tibia (longi., medial section) $\times 3,000$

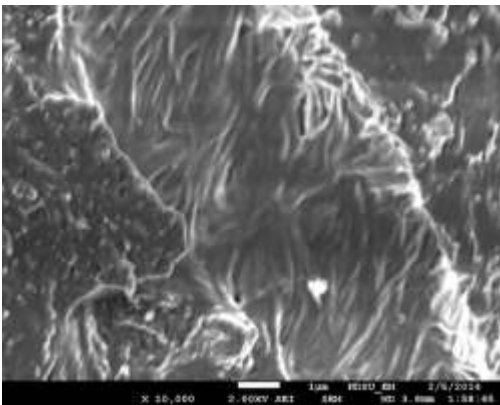


Figure C.136. SEM image of OI human tibia (longi., medial section) $\times 10,000$

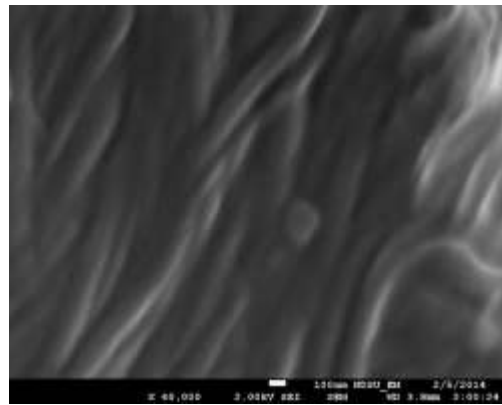


Figure C.137. SEM image of OI human tibia (longi., medial section) $\times 40,000$

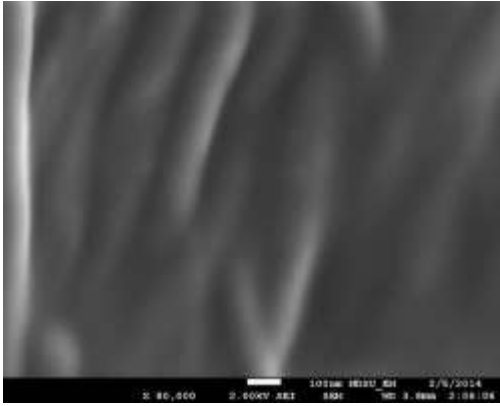


Figure C.138. SEM image of OI human tibia (longi., medial section) $\times 80,000$

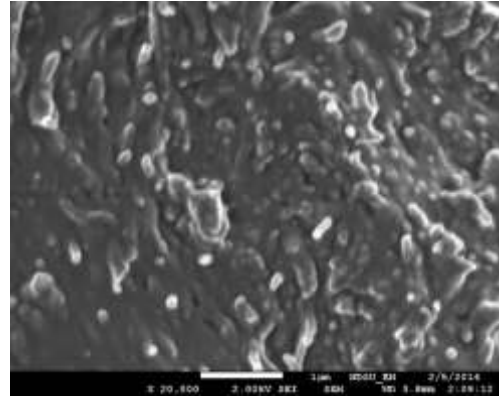


Figure C.139. SEM image of OI human tibia (longi., medial section) $\times 20,000$

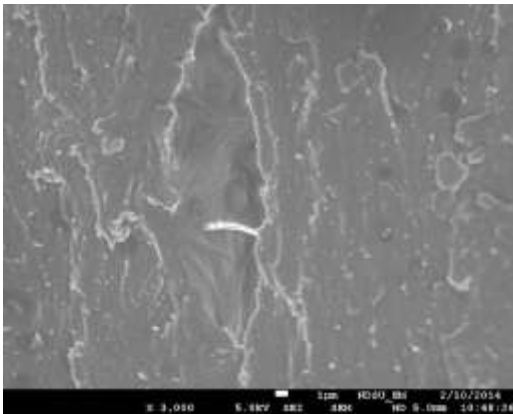


Figure C.140. SEM image of OI human tibia (longi., medial section) $\times 30,000$

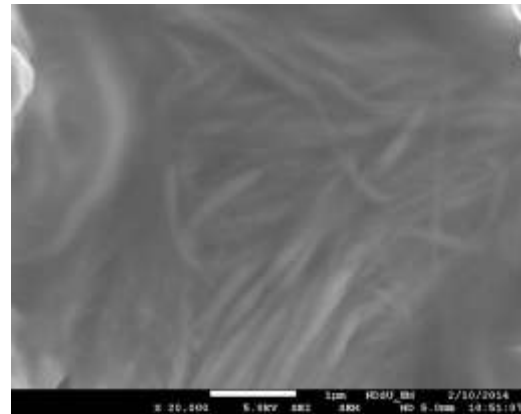


Figure C.141. SEM image of OI human tibia (longi., medial section) $\times 20,000$

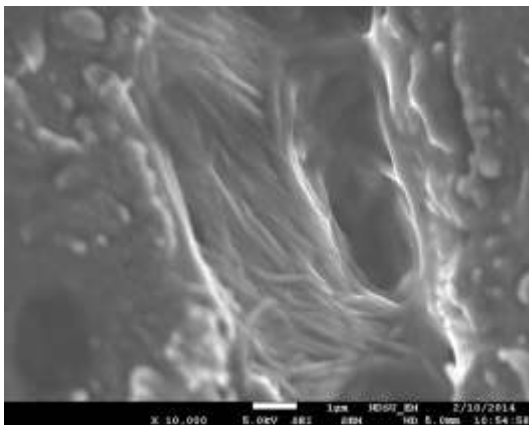


Figure C.142 SEM image of OI human tibia (longi., medial section) $\times 10,000$

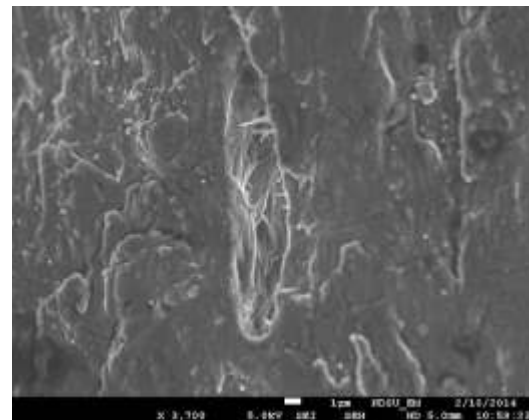


Figure C.143. SEM image of OI human tibia (longi., medial section) $\times 3,700$

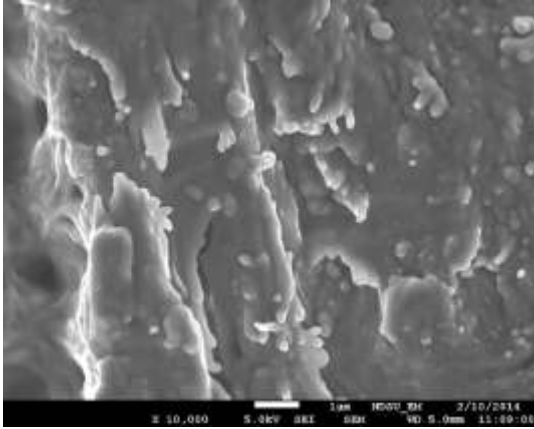


Figure C.144. SEM image of OI human tibia (longi., medial section) $\times 10,000$

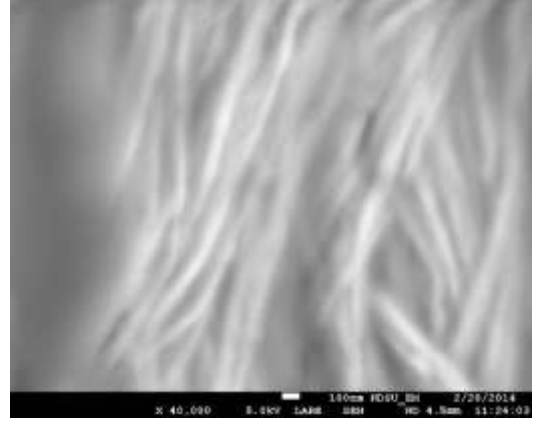


Figure C.145. SEM image of OI human tibia (longi., medial section) $\times 40,000$

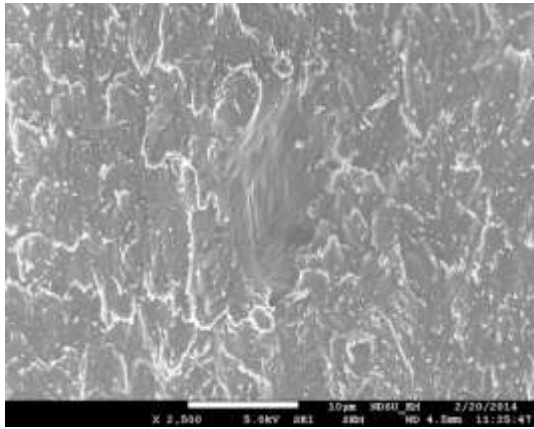


Figure C.146. SEM image of OI human tibia (longi., medial section) $\times 2,500$

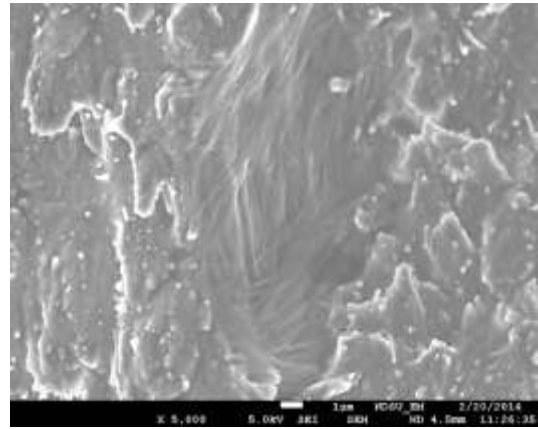


Figure C.147. SEM image of OI human tibia (longi., medial section) $\times 5,000$

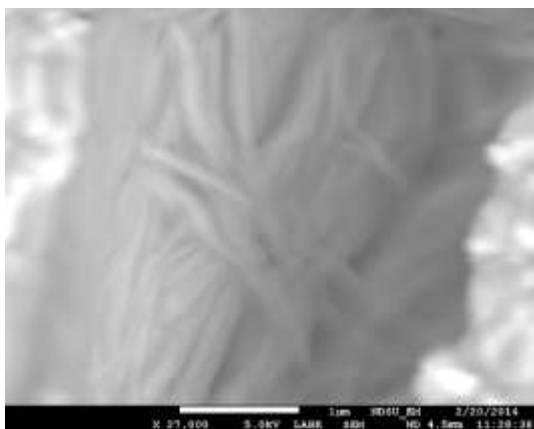


Figure C.148. SEM image of OI human tibia (longi., medial section) $\times 27,000$

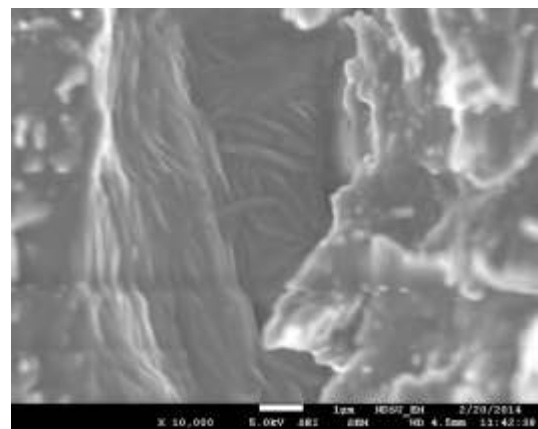


Figure C.149. SEM image of OI human tibia (longi., medial section) $\times 10,000$

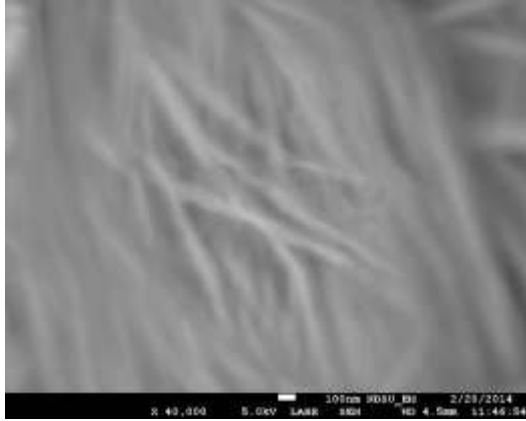


Figure C.150. SEM image of OI human tibia (longi., medial section) $\times 40,000$

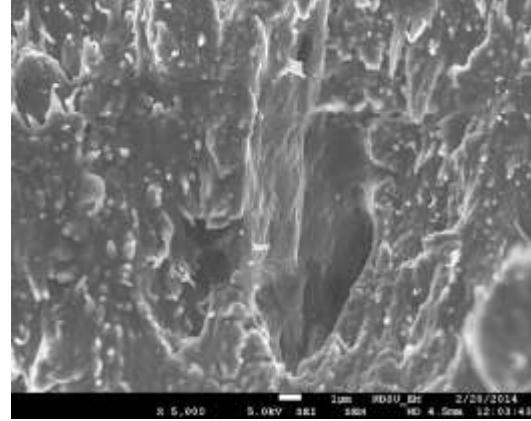


Figure C.151. SEM image of OI human tibia (longi., medial section) $\times 5,000$

C.3. Lateral section, fixed with a series of chemicals and fractured in liquid N₂

C.3.1. Transverse section (acquired on 2/6/2014)

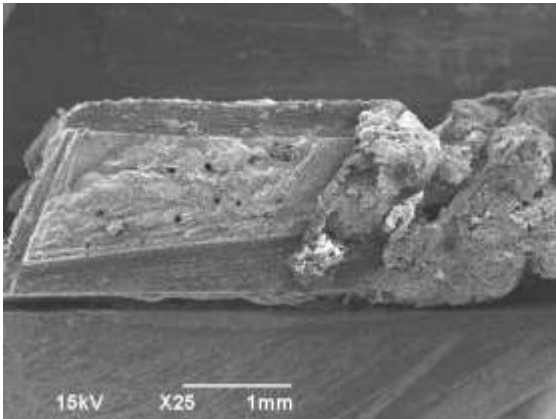


Figure C.152. SEM image of OI human tibia (transverse, lateral section) $\times 25$

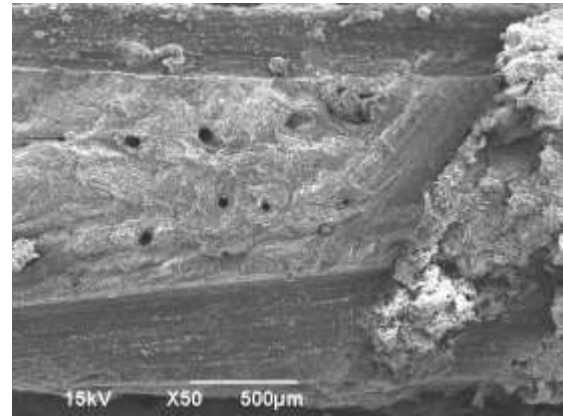


Figure C.153. SEM image of OI human tibia (transverse, lateral section) $\times 50$

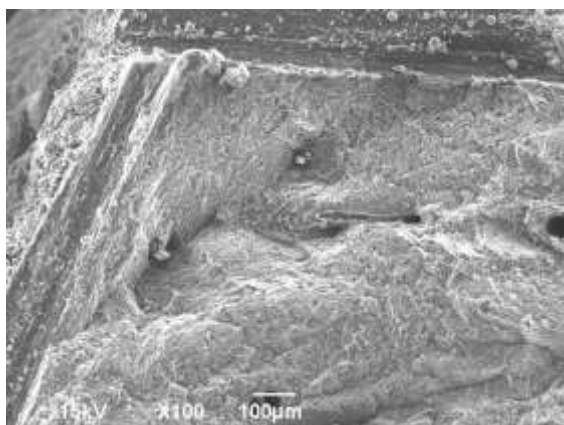


Figure C.154. SEM image of OI human tibia (transverse, lateral section) $\times 100$

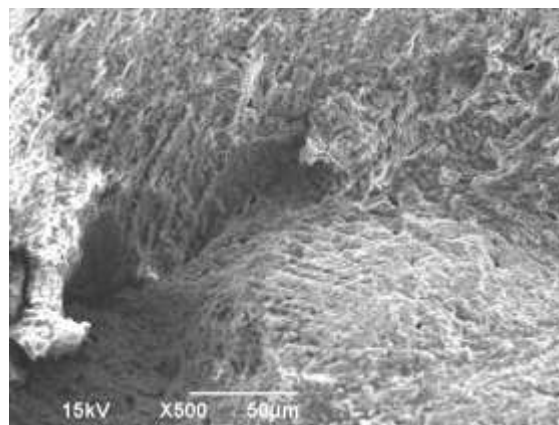


Figure C.155. SEM image of OI human tibia (transverse, lateral section) $\times 500$

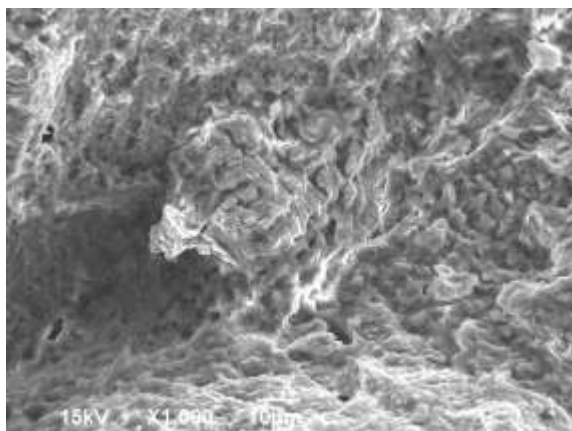


Figure C.156. SEM image of OI human tibia (transverse, lateral section) $\times 1,000$

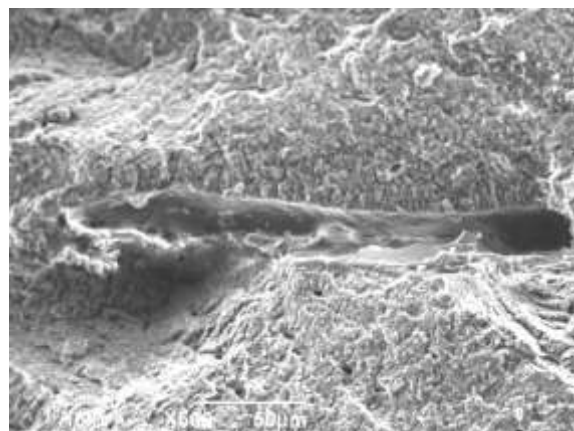


Figure C.157. SEM image of OI human tibia (transverse, lateral section) $\times 500$

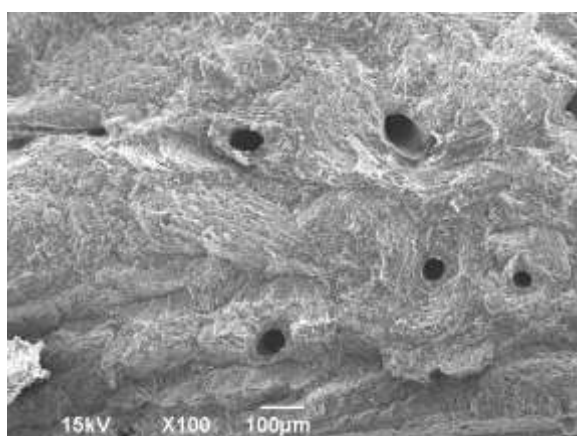


Figure C.158. SEM image of OI human tibia (transverse, lateral section) $\times 100$

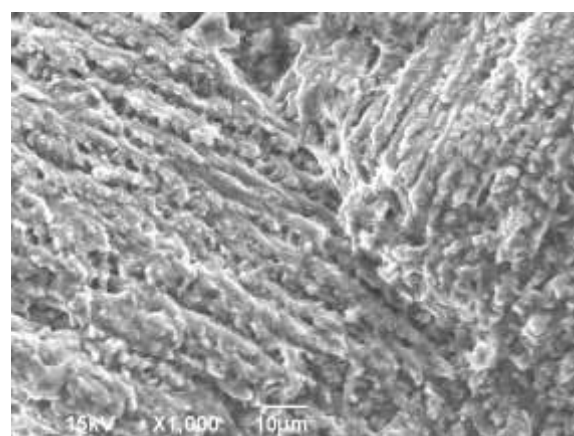


Figure C.159. SEM image of OI human tibia (transverse, lateral section) $\times 1,000$

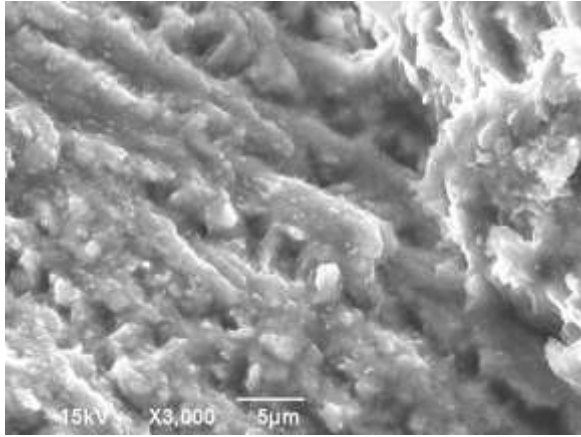


Figure C.160. SEM image of OI human tibia (transverse, lateral section) $\times 3,000$

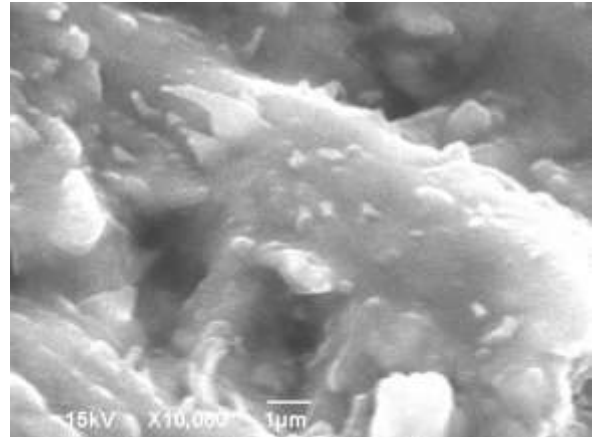


Figure C.161. SEM image of OI human tibia (transverse, lateral section) $\times 10,000$

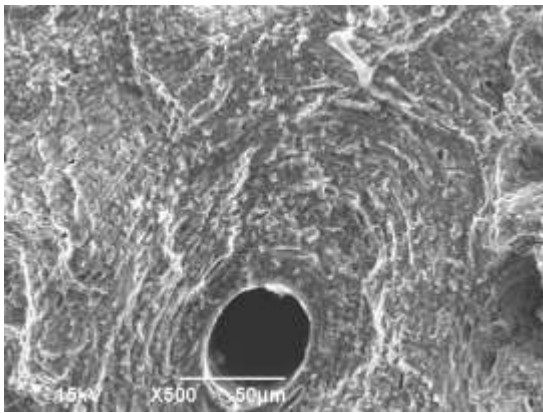


Figure C.162. SEM image of OI human tibia (transverse, lateral section) $\times 500$

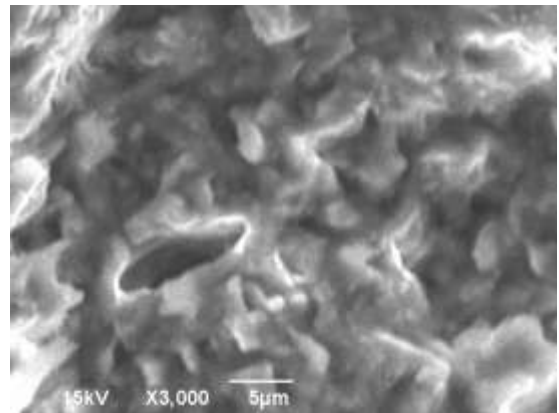


Figure C.163. SEM image of OI human tibia (transverse, lateral section) $\times 3,000$

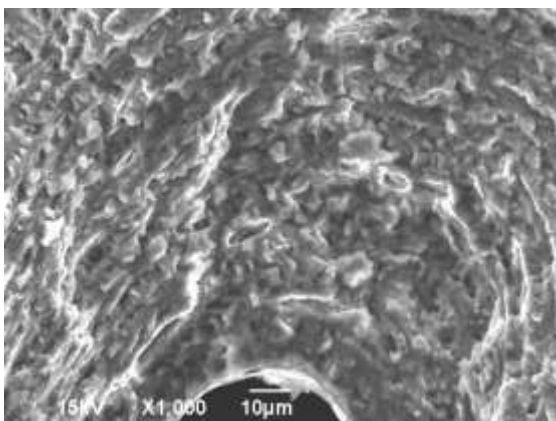


Figure C.164. SEM image of OI human tibia (transverse, lateral section) $\times 1,000$

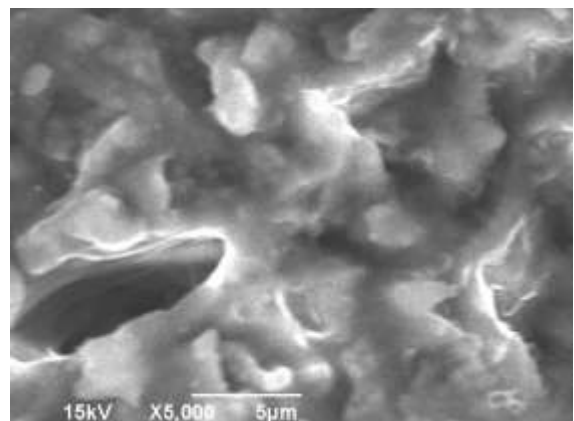


Figure C.165. SEM image of OI human tibia (transverse, lateral section) $\times 5,000$

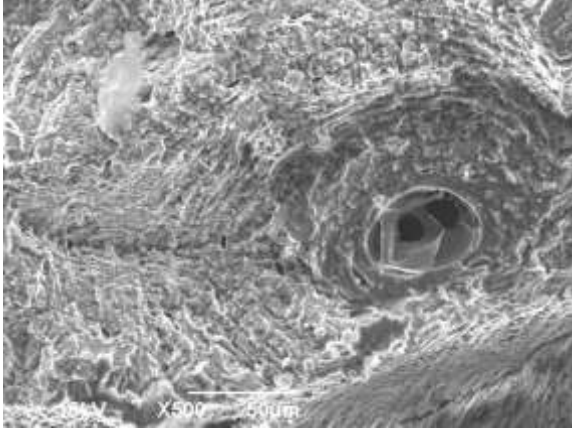


Figure C.166. SEM image of OI human tibia (transverse, lateral section) $\times 500$

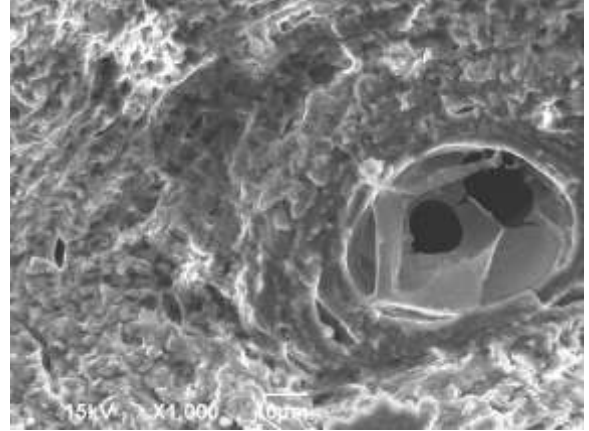


Figure C.167. SEM image of OI human tibia (transverse, lateral section) $\times 1,000$

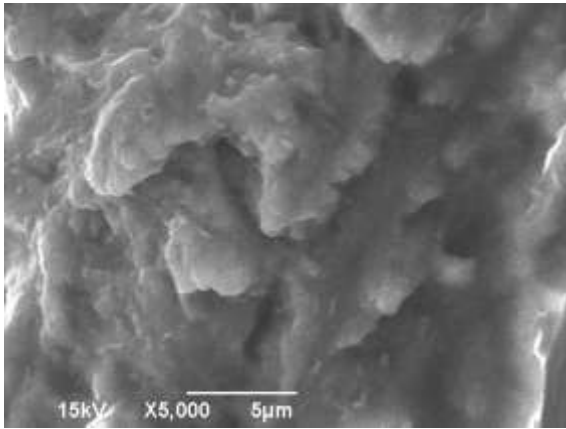


Figure C.168. SEM image of OI human tibia (transverse, lateral section) $\times 5,000$

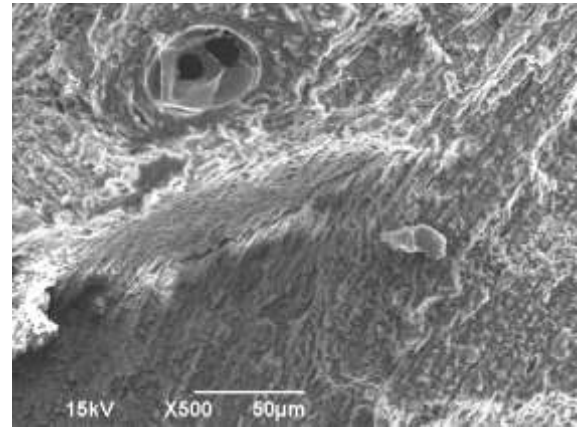


Figure C.169. SEM image of OI human tibia (transverse, lateral section) $\times 500$

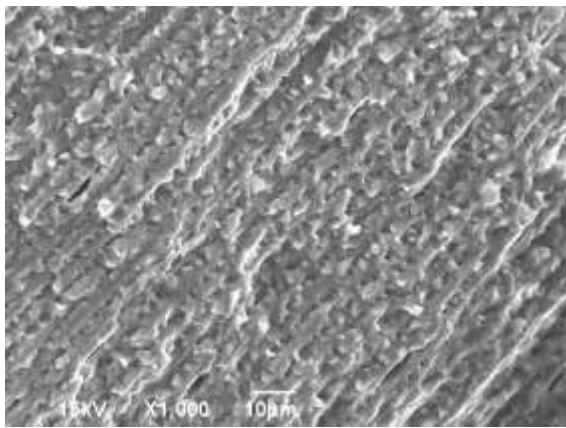


Figure C.170. SEM image of OI human tibia (transverse, lateral section) $\times 1,000$

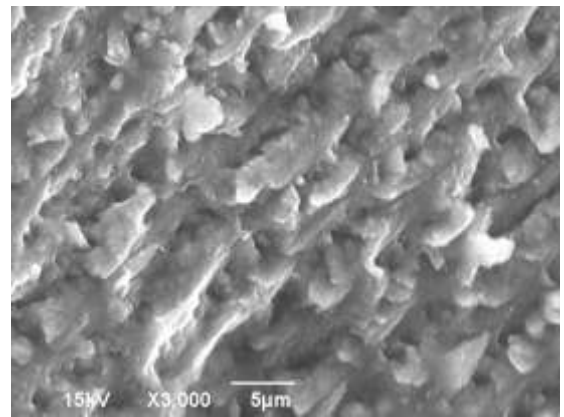


Figure C.171. SEM image of OI human tibia (transverse, lateral section) $\times 3,000$

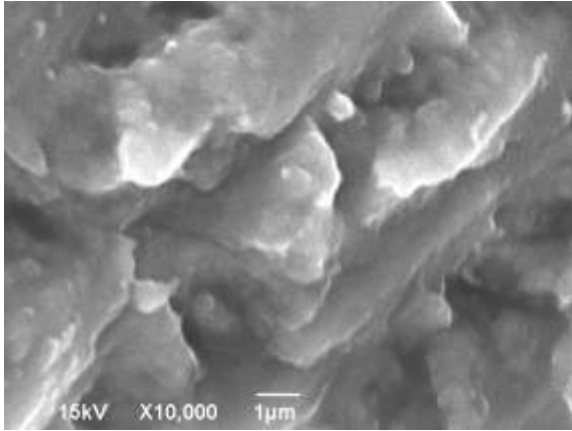


Figure C.172. SEM image of OI human tibia (transverse, lateral section) $\times 10,000$

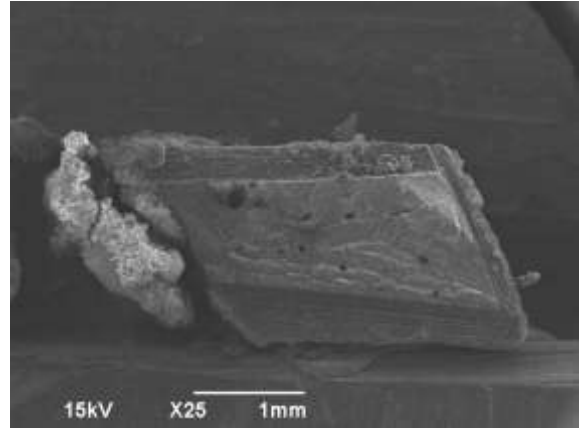


Figure C.173. SEM image of OI human tibia (transverse, lateral section) $\times 25$

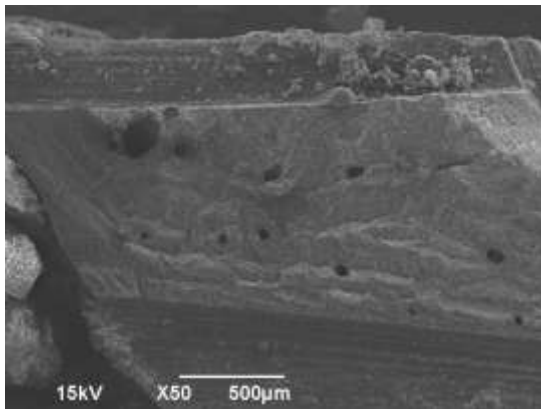


Figure C.174. SEM image of OI human tibia (transverse, lateral section) $\times 50$

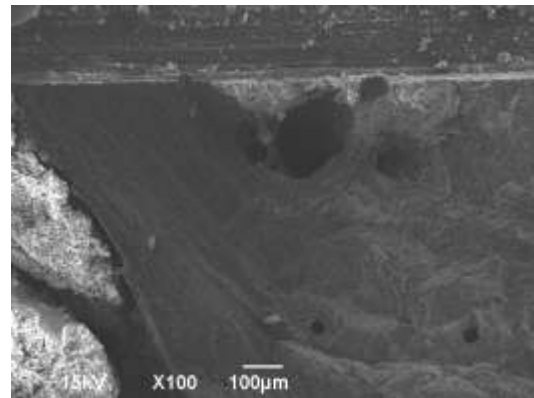


Figure C.175. SEM image of OI human tibia (transverse, lateral section) $\times 100$

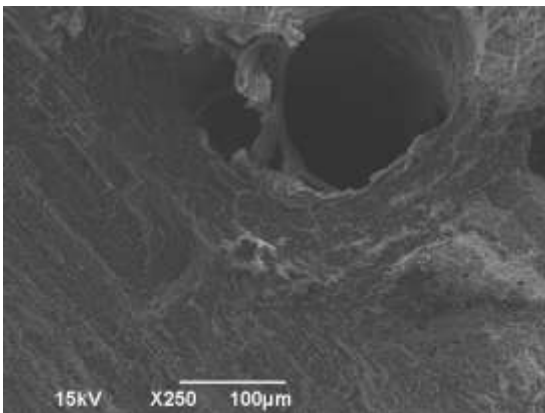


Figure C.176. SEM image of OI human tibia (transverse, lateral section) $\times 250$

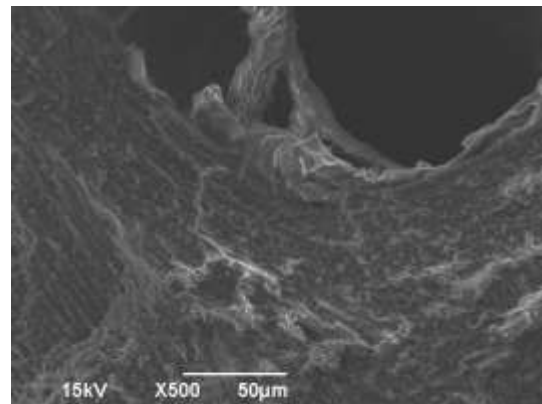


Figure C.177. SEM image of OI human tibia (transverse, lateral section) $\times 500$

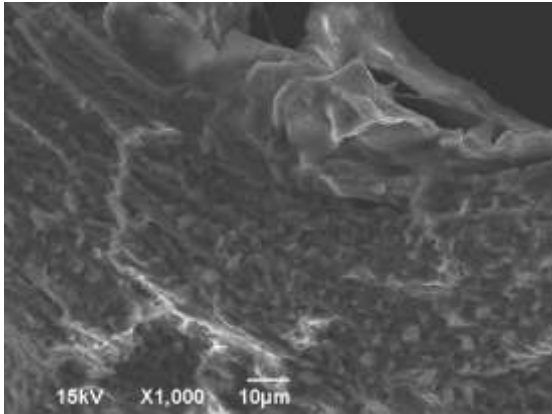


Figure C.178. SEM image of OI human tibia (transverse, lateral section) $\times 1,000$

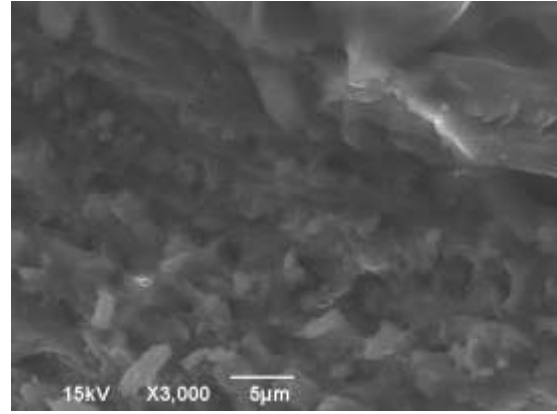


Figure C.179. SEM image of OI human tibia (transverse, lateral section) $\times 3,000$

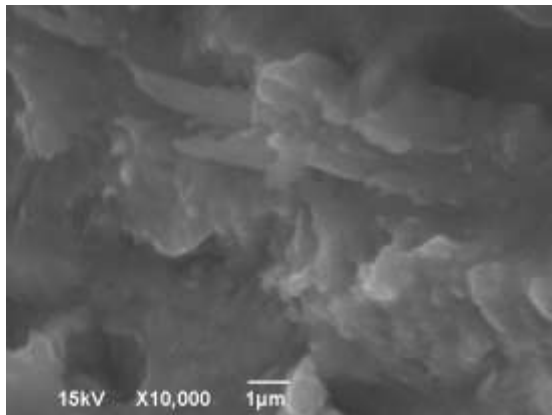


Figure C.180. SEM image of OI human tibia (transverse, lateral section) $\times 10,000$

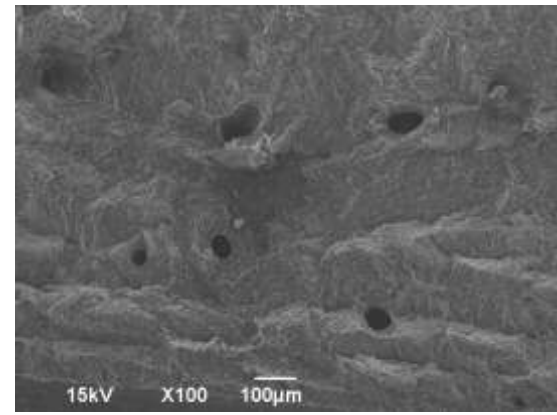


Figure C.181. SEM image of OI human tibia (transverse, lateral section) $\times 100$

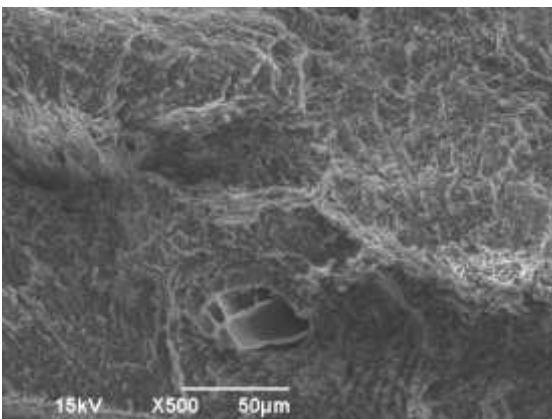


Figure C.182. SEM image of OI human tibia (transverse, lateral section) $\times 500$

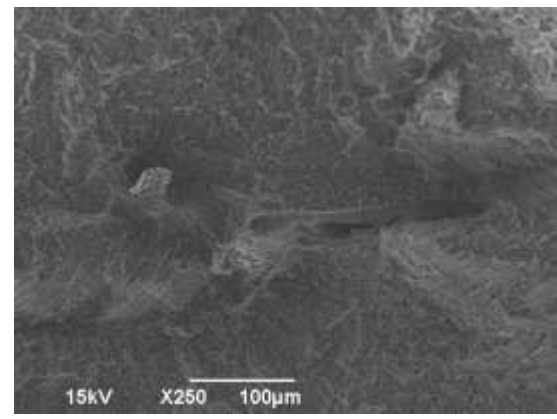


Figure C.183. SEM image of OI human tibia (transverse, lateral section) $\times 250$

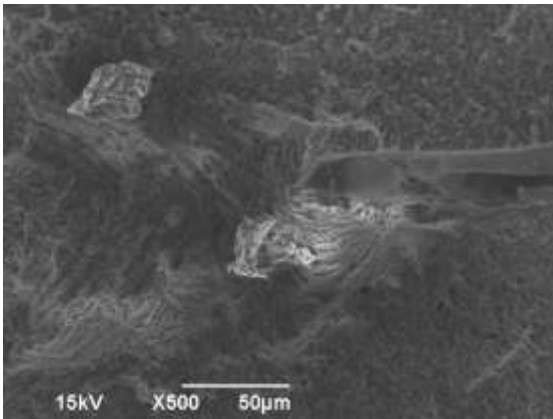


Figure C.184. SEM image of OI human tibia (transverse, lateral section) $\times 500$

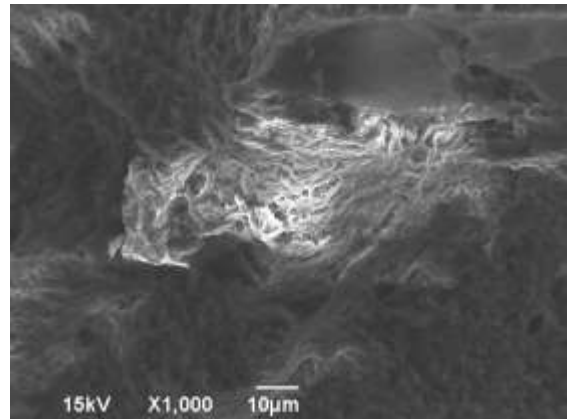


Figure C.185. SEM image of OI human tibia (transverse, lateral section) $\times 1,000$

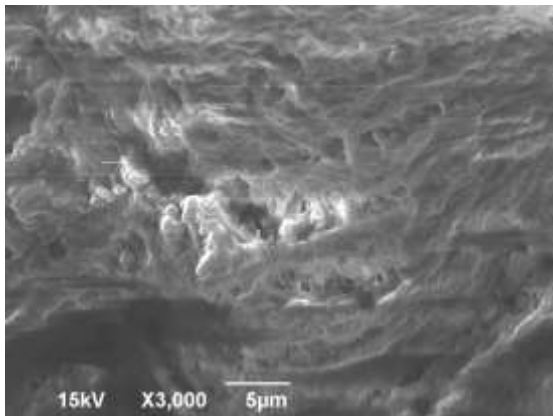


Figure C.186. SEM image of OI human tibia (transverse, lateral section) $\times 3,000$

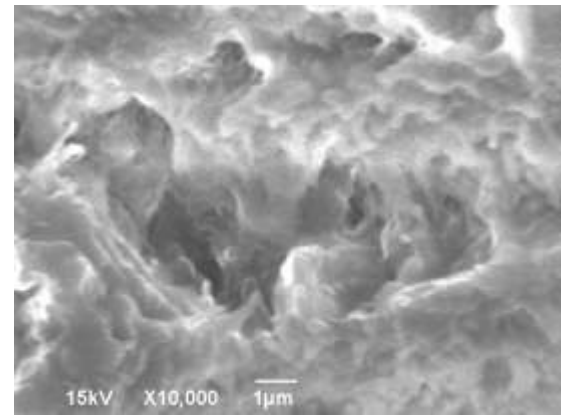


Figure C.187. SEM image of OI human tibia (transverse, lateral section) $\times 10,000$

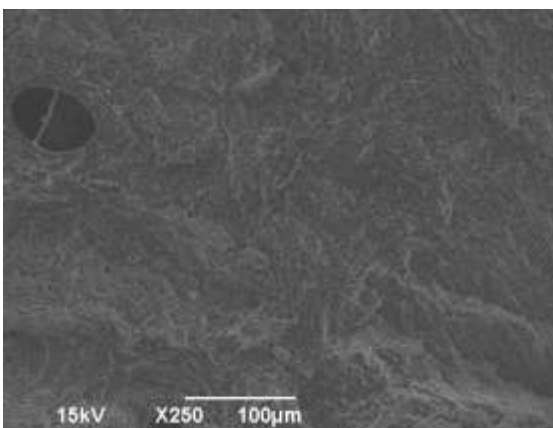


Figure C.188. SEM image of OI human tibia (transverse, lateral section) $\times 250$

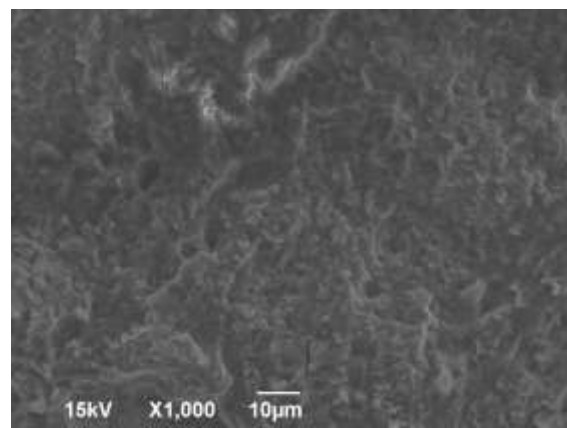


Figure C.189. SEM image of OI human tibia (transverse, lateral section) $\times 1,000$

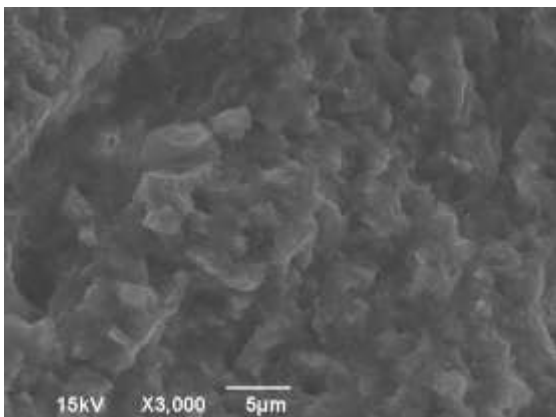


Figure C.190. SEM image of OI human tibia (transverse, lateral section) $\times 3,000$

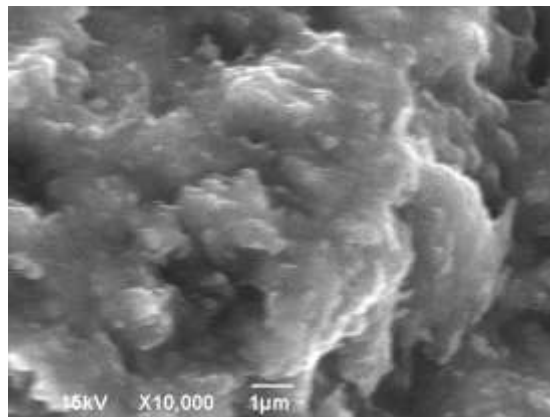


Figure C.191. SEM image of OI human tibia (transverse, lateral section) $\times 10,000$

C.3.2. Longitudinal section (acquired on 2/6/2014)

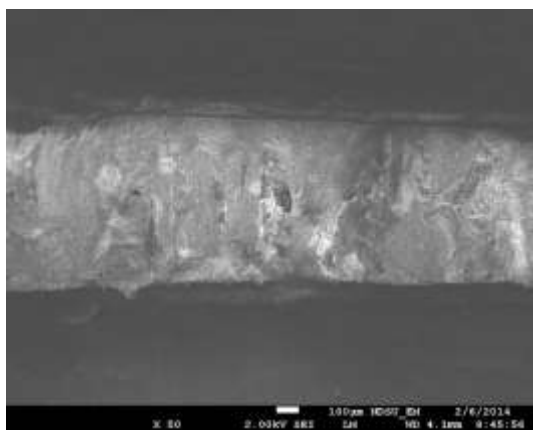


Figure C.192. SEM image of OI human tibia (longi., lateral section) $\times 50$

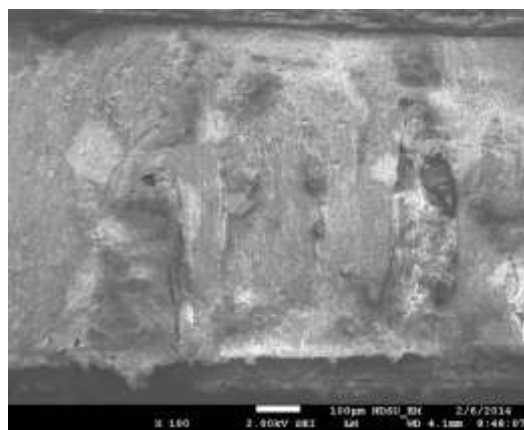


Figure C.193. SEM image of OI human tibia (longi., lateral section) $\times 100$

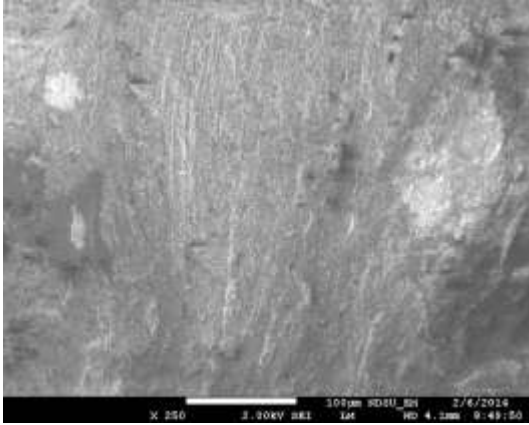


Figure C.194. SEM image of OI human tibia (longi., lateral section) ×250

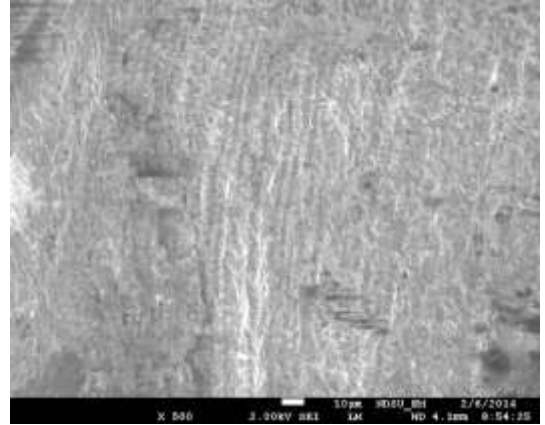


Figure C.195. SEM image of OI human tibia (longi., lateral section) ×500

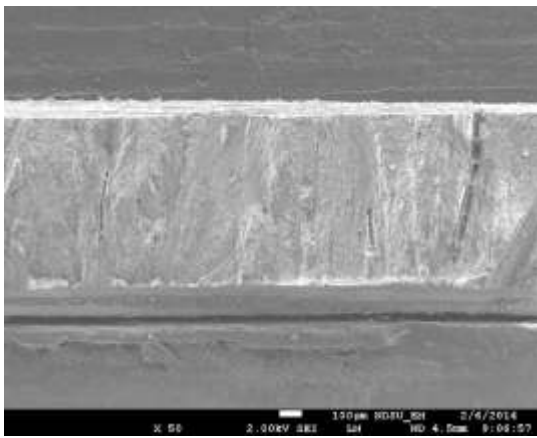


Figure C.196. SEM image of OI human tibia (longi., lateral section) ×50

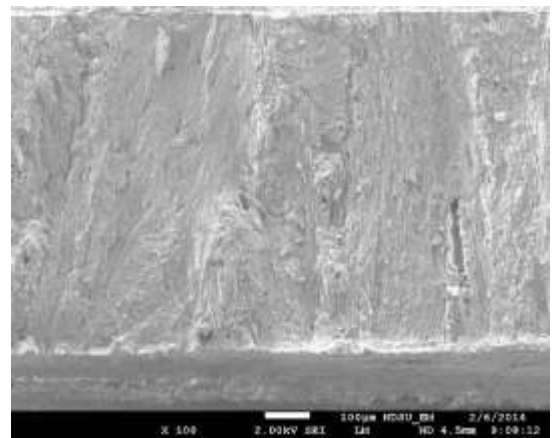


Figure C.197. SEM image of OI human tibia (longi., lateral section) ×100

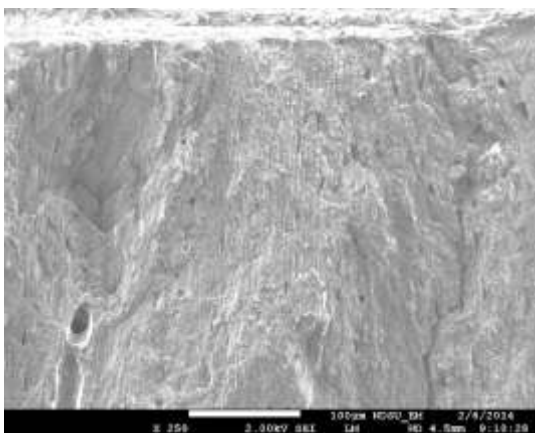


Figure C.198. SEM image of OI human tibia (longi., lateral section) ×250

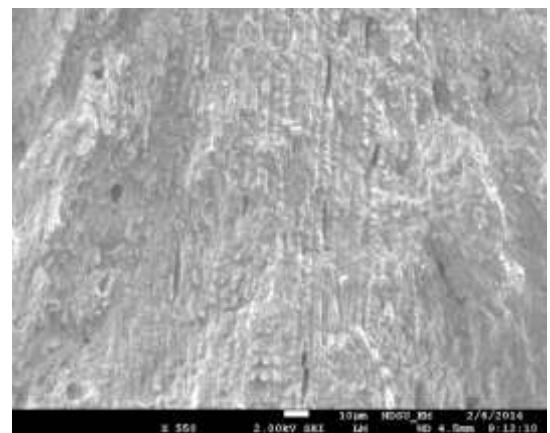


Figure C.199. SEM image of OI human tibia (longi., lateral section) ×550

C.4. Posterior section, fixed with a series of chemicals and fractured in liquid N₂

C.4.1. Transverse section (acquired on 2/6/2014)

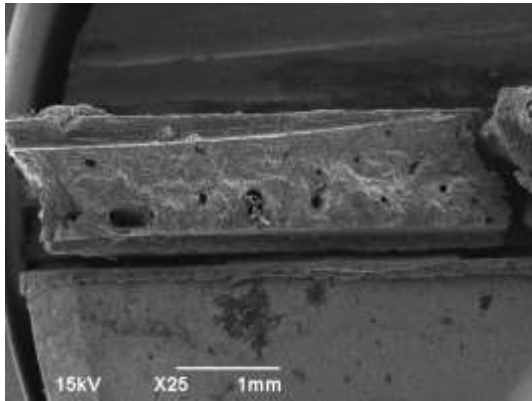


Figure C.200. SEM image of OI human tibia (transverse, posterior section) ×25

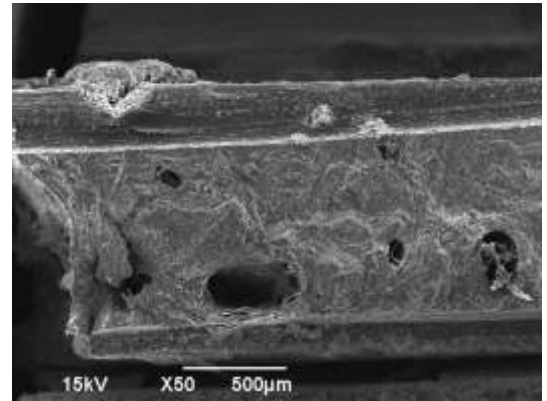


Figure C.201. SEM image of OI human tibia (transverse, posterior section) ×50

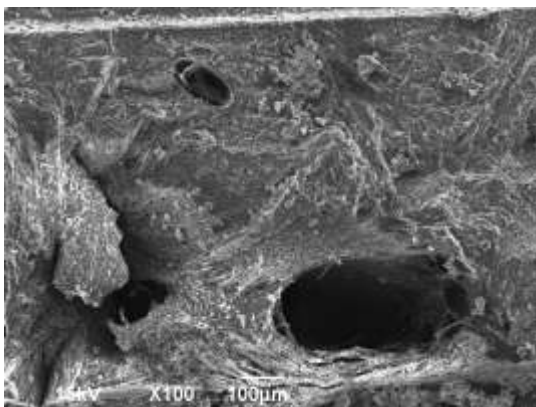


Figure C.202. SEM image of OI human tibia (transverse, posterior section) ×100

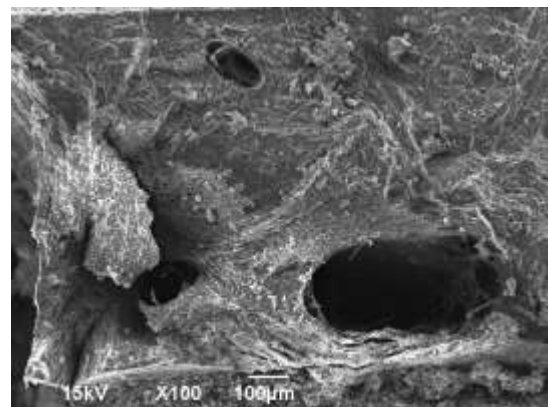


Figure C.203. SEM image of OI human tibia (transverse, posterior section) ×100

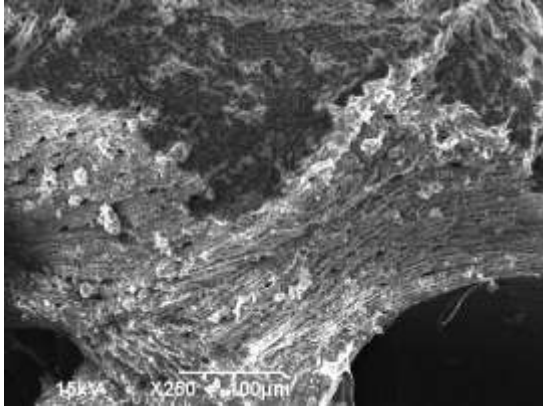


Figure C.204. SEM image of OI human tibia (transverse, posterior section) $\times 250$

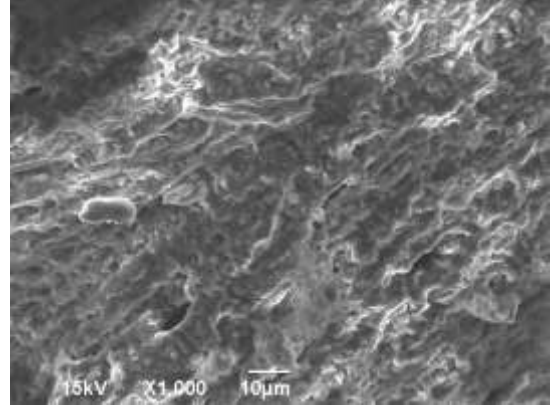


Figure C.205. SEM image of OI human tibia (transverse, posterior section) $\times 1,000$

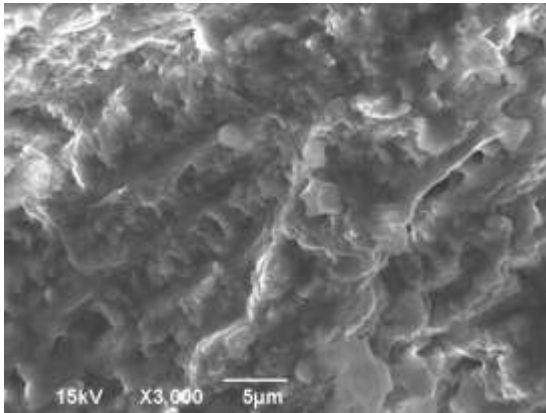


Figure C.206. SEM image of OI human tibia (transverse, posterior section) $\times 3,000$

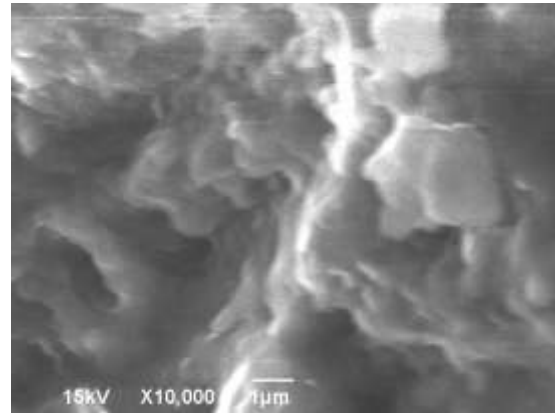


Figure C.207. SEM image of OI human tibia (transverse, posterior section) $\times 10,000$

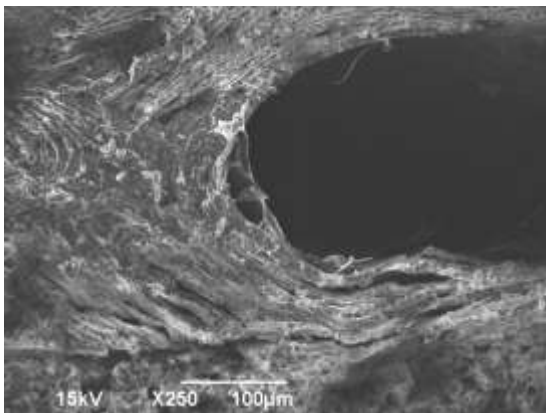


Figure C.208. SEM image of OI human tibia (transverse, posterior section) $\times 250$

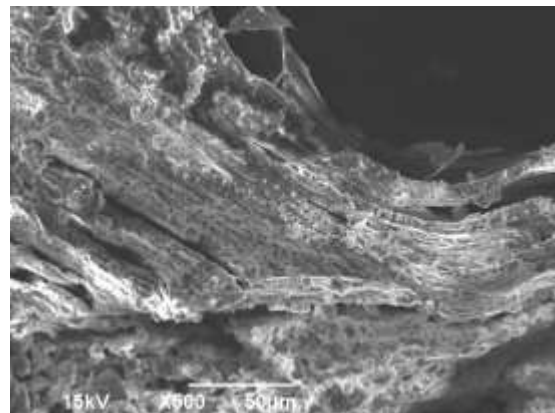


Figure C.209. SEM image of OI human tibia (transverse, posterior section) $\times 500$

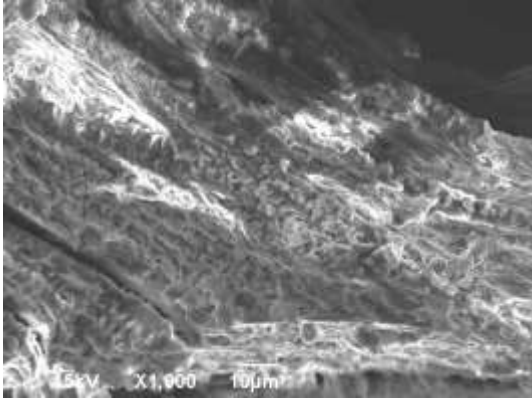


Figure C.210. SEM image of OI human tibia (transverse, posterior section) $\times 1,000$

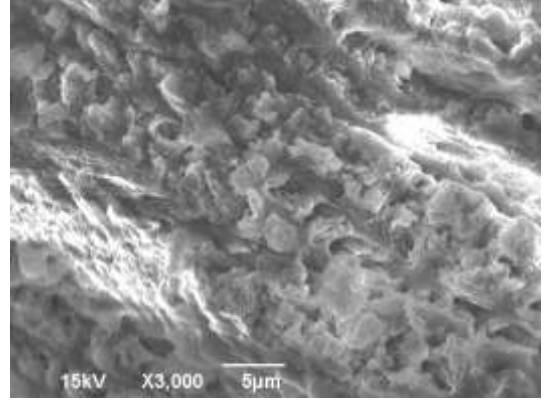


Figure C.211. SEM image of OI human tibia (transverse, posterior section) $\times 3,000$

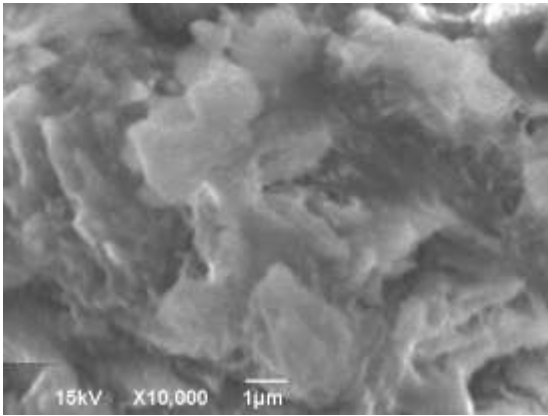


Figure C.212. SEM image of OI human tibia (transverse, posterior section) $\times 10,000$

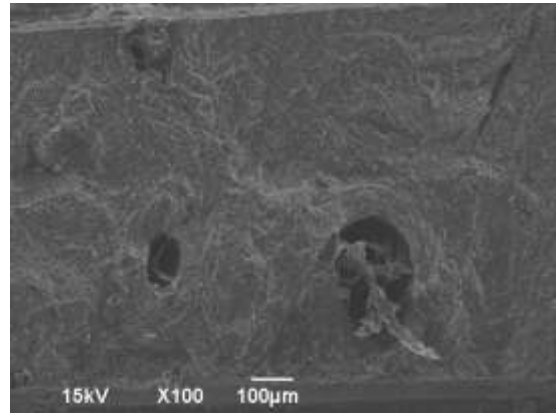


Figure C.213. SEM image of OI human tibia (transverse, posterior section) $\times 100$

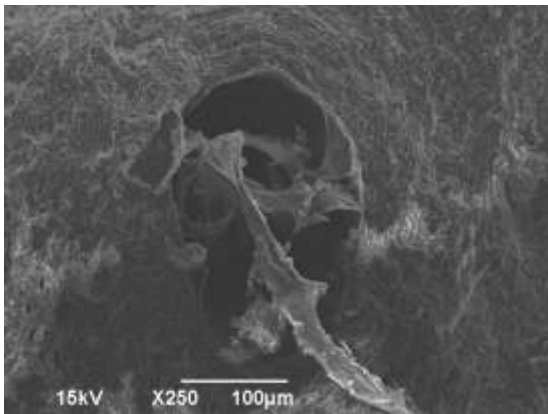


Figure C.214. SEM image of OI human tibia (transverse, posterior section) $\times 250$

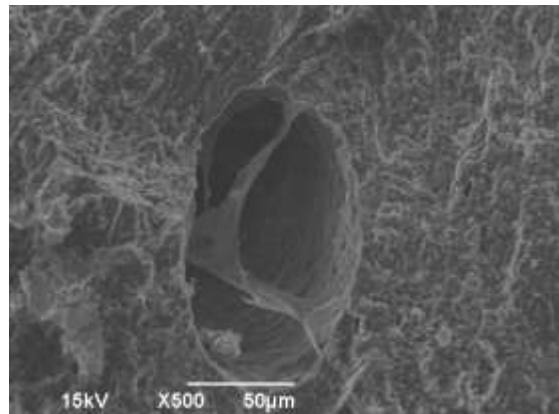


Figure C.215. SEM image of OI human tibia (transverse, posterior section) $\times 500$

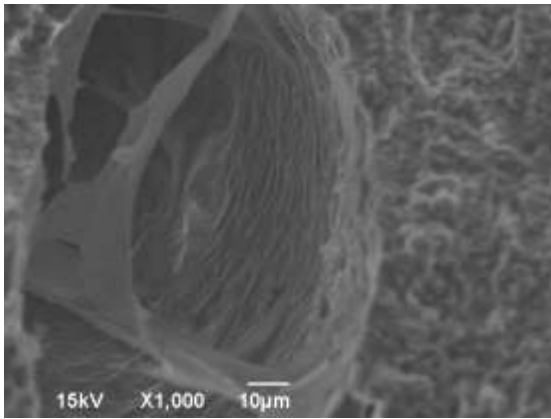


Figure C.216. SEM image of OI human tibia (transverse, posterior section) $\times 1,000$

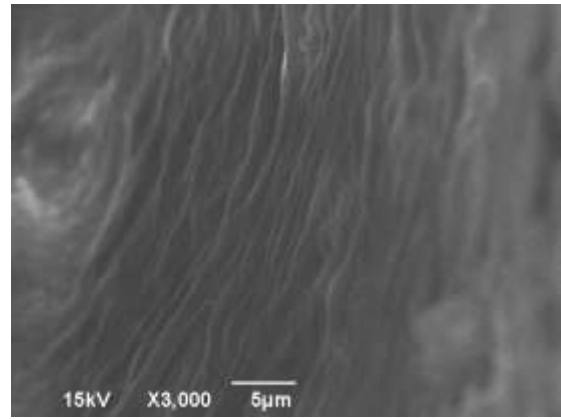


Figure C.217. SEM image of OI human tibia (transverse, posterior section) $\times 3,000$

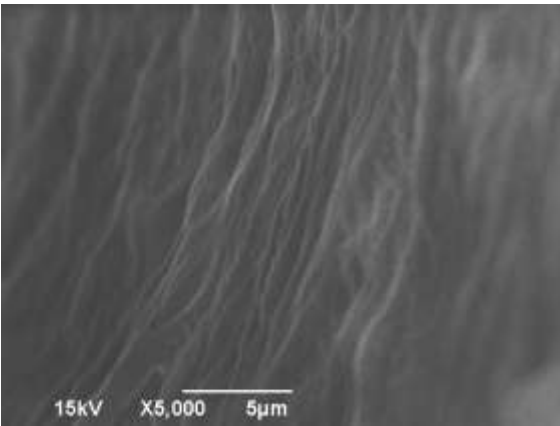


Figure C.218. SEM image of OI human tibia (transverse, posterior section) $\times 5,000$

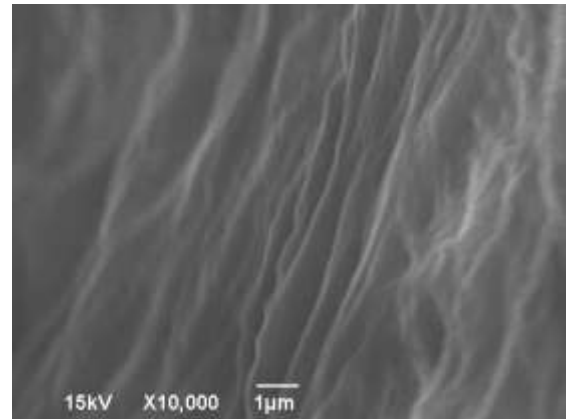


Figure C.219. SEM image of OI human tibia (transverse, posterior section) $\times 10,000$

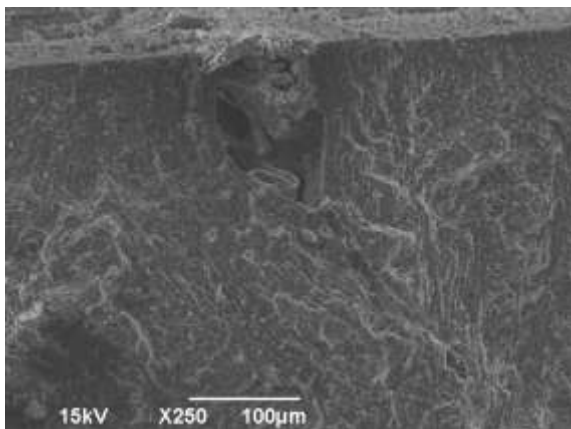


Figure C.220. SEM image of OI human tibia (transverse, posterior section) $\times 250$

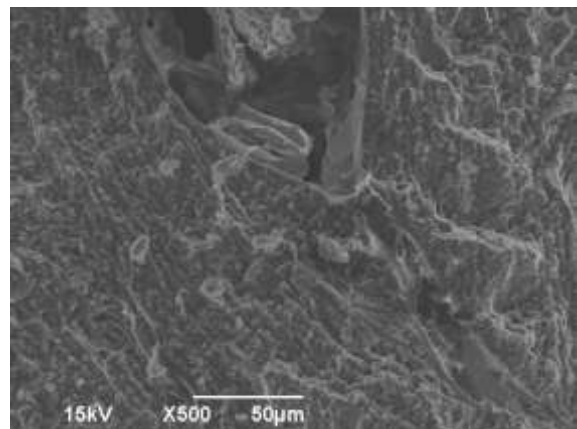


Figure C.221. SEM image of OI human tibia (transverse, posterior section) $\times 500$

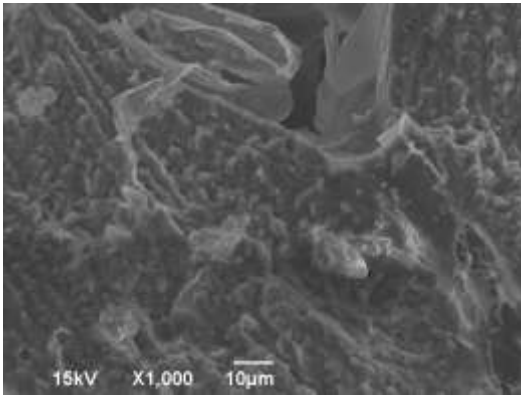


Figure C.222. SEM image of OI human tibia (transverse, posterior section) $\times 1,000$

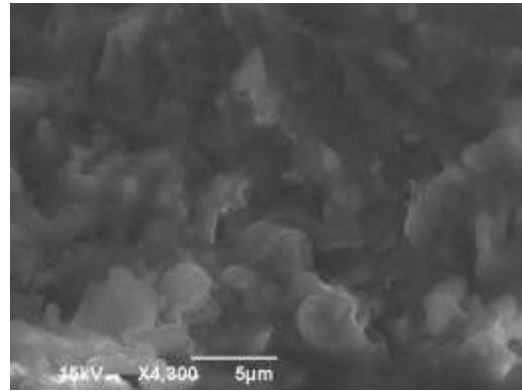


Figure C.223. SEM image of OI human tibia (transverse, posterior section) $\times 4,300$

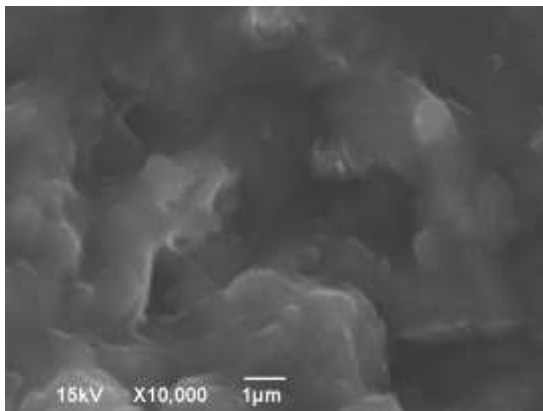


Figure C.224. SEM image of OI human tibia (transverse, posterior section) $\times 10,000$

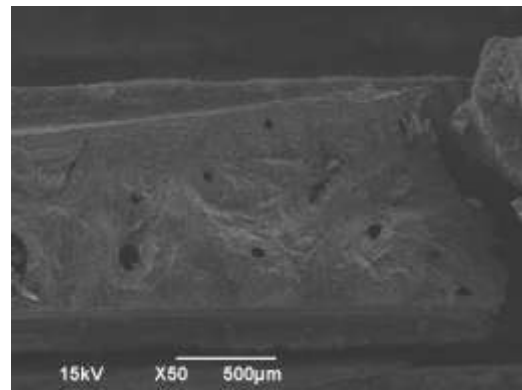


Figure C.225. SEM image of OI human tibia (transverse, posterior section) $\times 50$

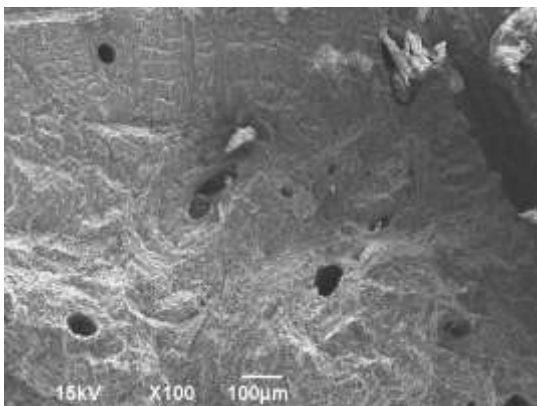


Figure C.226. SEM image of OI human tibia (transverse, posterior section) $\times 100$

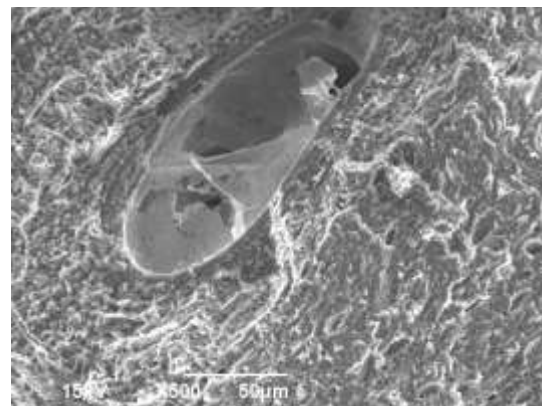


Figure C.227. SEM image of OI human tibia (transverse, posterior section) $\times 500$

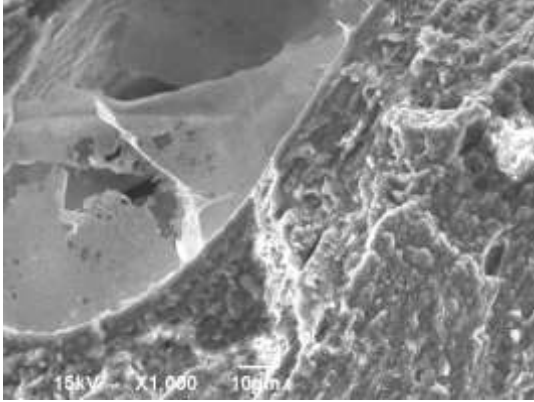


Figure C.228. SEM image of OI human tibia (transverse, posterior section) $\times 1,000$

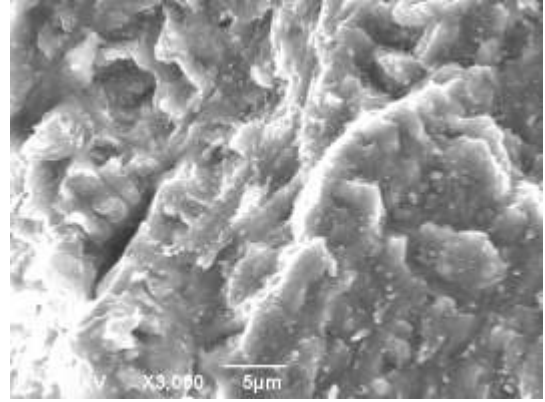


Figure C.229. SEM image of OI human tibia (transverse, posterior section) $\times 3,000$

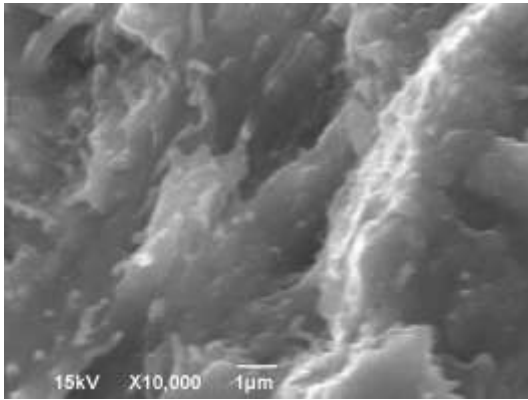


Figure C.230. SEM image of OI human tibia (transverse, posterior section) $\times 10,000$

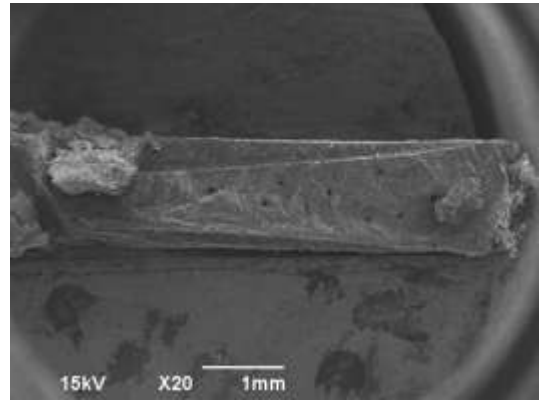


Figure C.231. SEM image of OI human tibia (transverse, posterior section) $\times 20$

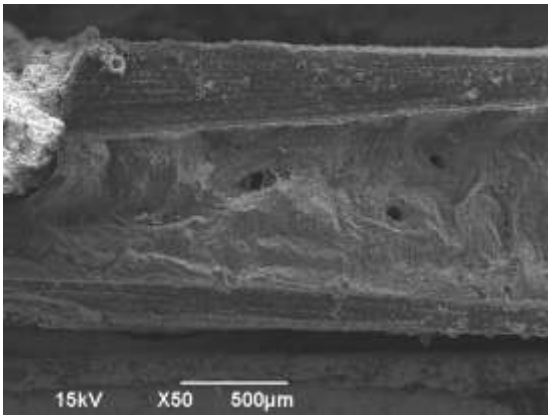


Figure C.232. SEM image of OI human tibia (transverse, posterior section) $\times 50$

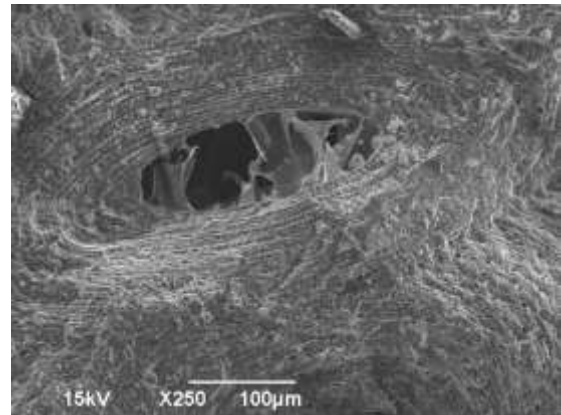


Figure C.233. SEM image of OI human tibia (transverse, posterior section) $\times 250$

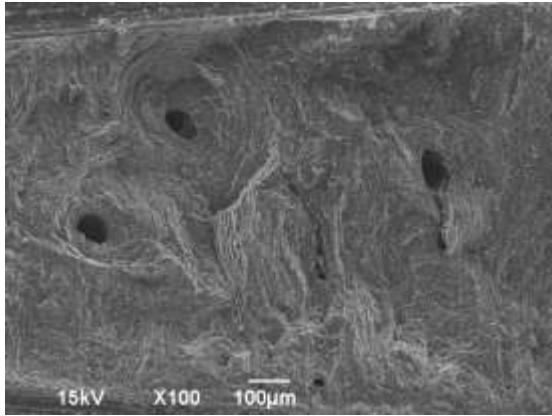


Figure C.234. SEM image of OI human tibia (transverse, posterior section) $\times 100$

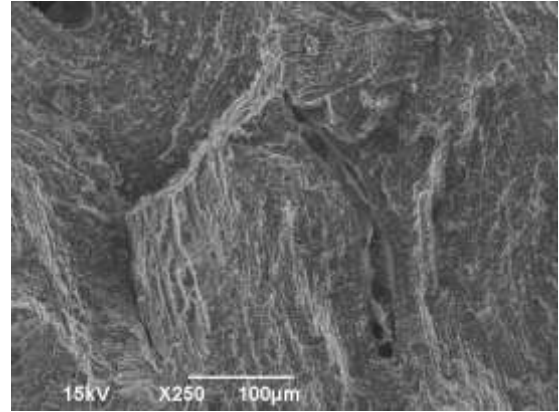


Figure C.235. SEM image of OI human tibia (transverse, posterior section) $\times 250$

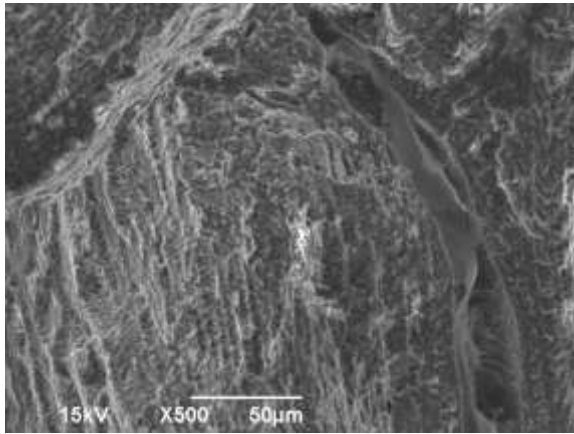


Figure C.236. SEM image of OI human tibia (transverse, posterior section) $\times 500$

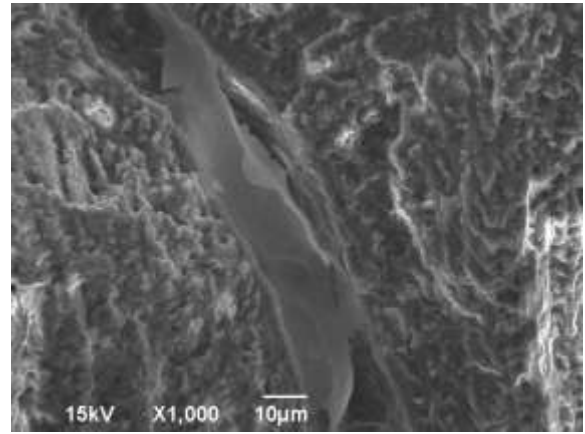


Figure C.237. SEM image of OI human tibia (transverse, posterior section) $\times 1,000$

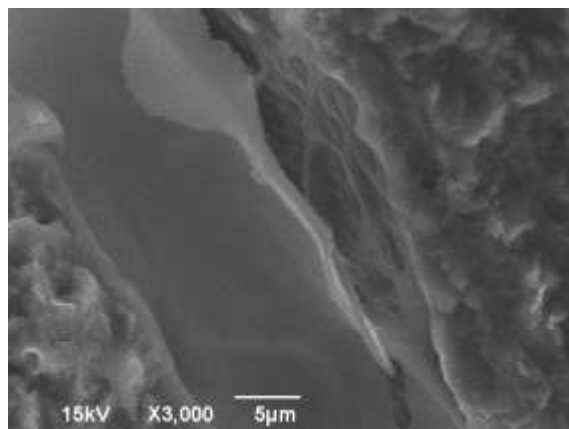


Figure C.238. SEM image of OI human tibia (transverse, posterior section) $\times 3,000$

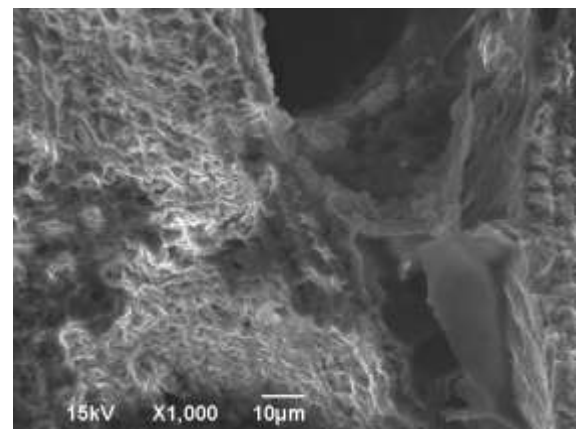


Figure C.239. SEM image of OI human tibia (transverse, posterior section) $\times 1,000$

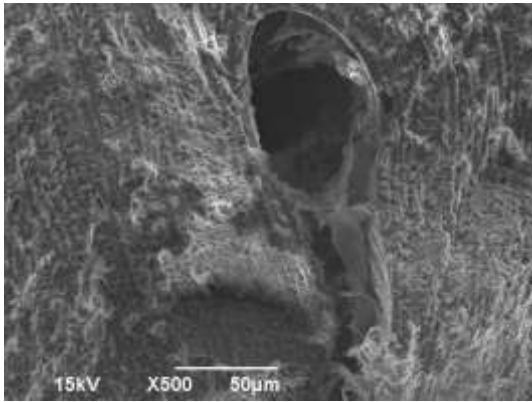


Figure C.240. SEM image of OI human tibia (transverse, posterior section) $\times 500$

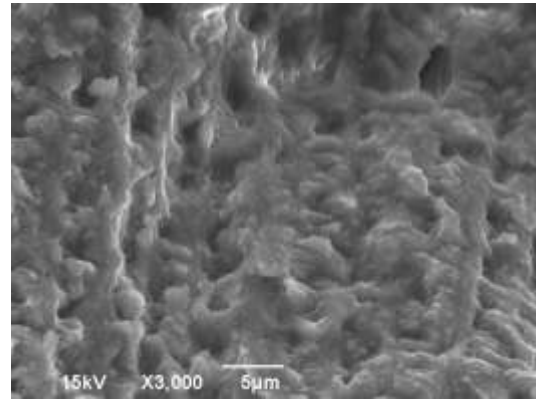


Figure C.241. SEM image of OI human tibia (transverse, posterior section) $\times 3,000$

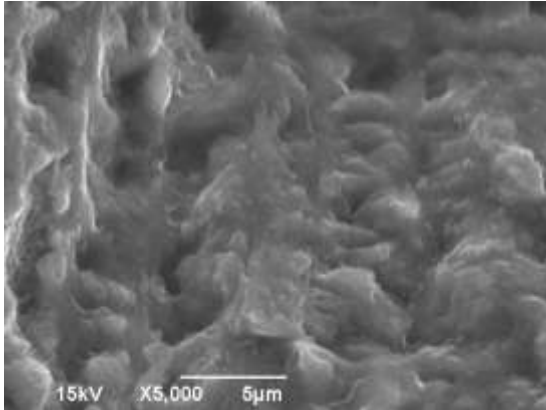


Figure C.242. SEM image of OI human tibia (transverse, posterior section) $\times 5,000$

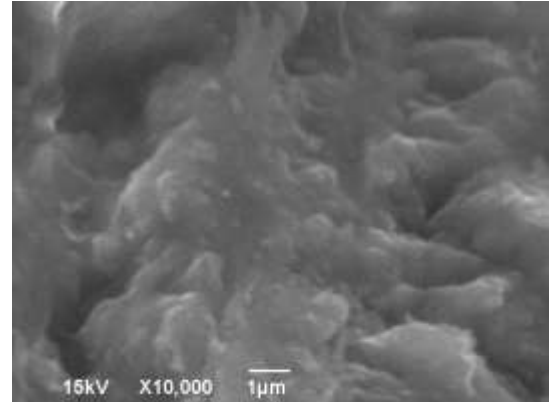


Figure C.243. SEM image of OI human tibia (transverse, posterior section) $\times 10,000$

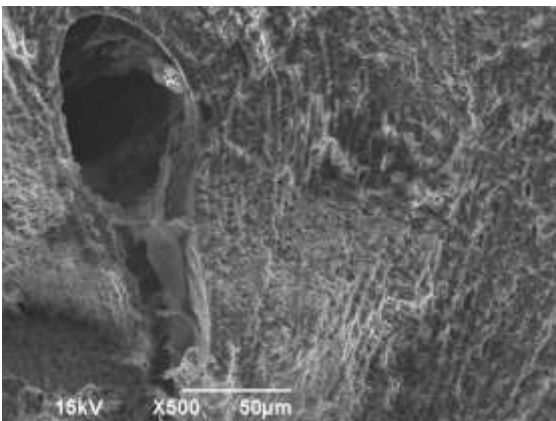


Figure C.244. SEM image of OI human tibia (transverse, posterior section) $\times 500$

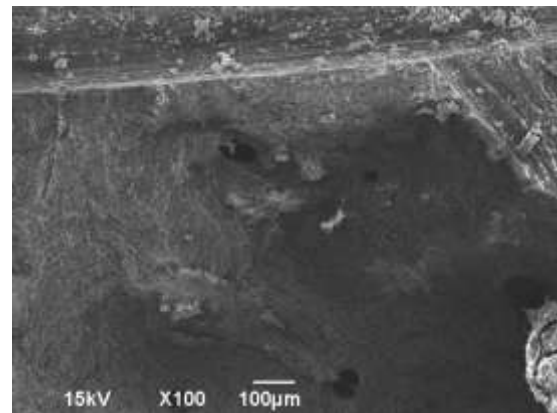


Figure C.245. SEM image of OI human tibia (transverse, posterior section) $\times 100$

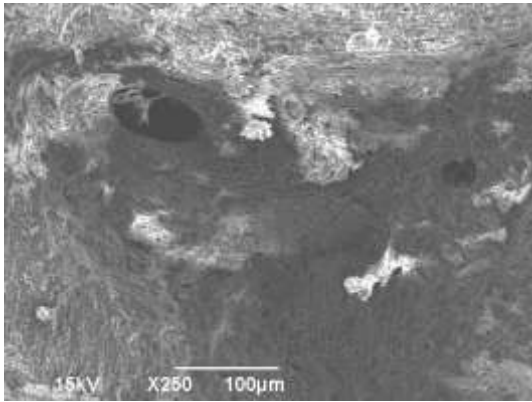


Figure C.246. SEM image of OI human tibia (transverse, posterior section) $\times 250$

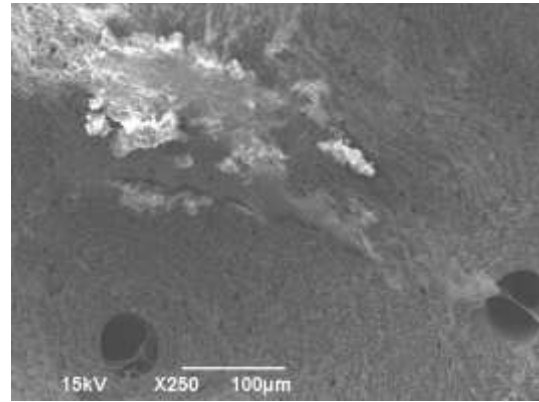


Figure C.247. SEM image of OI human tibia (transverse, posterior section) $\times 250$

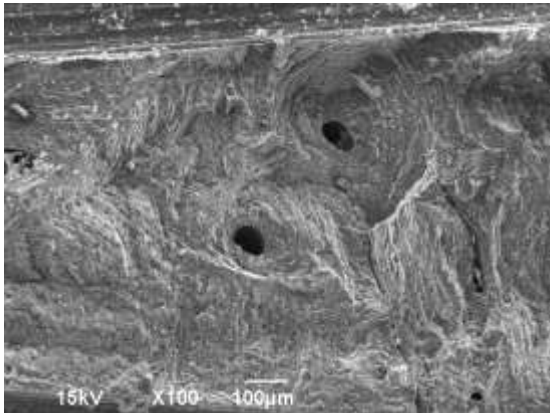


Figure C.248. SEM image of OI human tibia (transverse, posterior section) $\times 100$

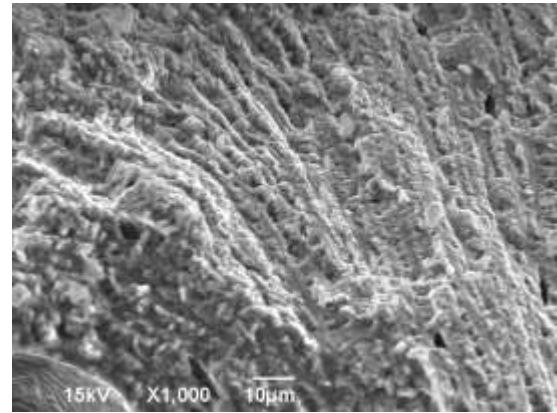


Figure C.249. SEM image of OI human tibia (transverse, posterior section) $\times 1,000$

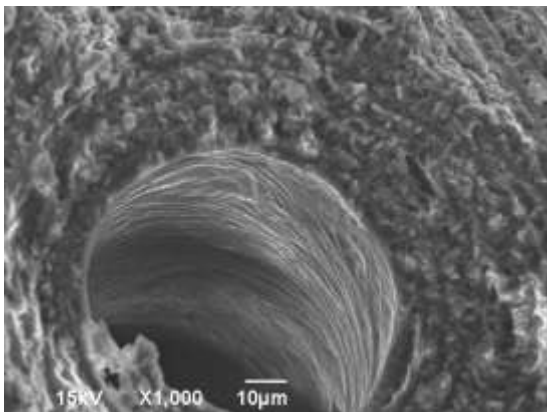


Figure C.250. SEM image of OI human tibia (transverse, posterior section) $\times 1,000$

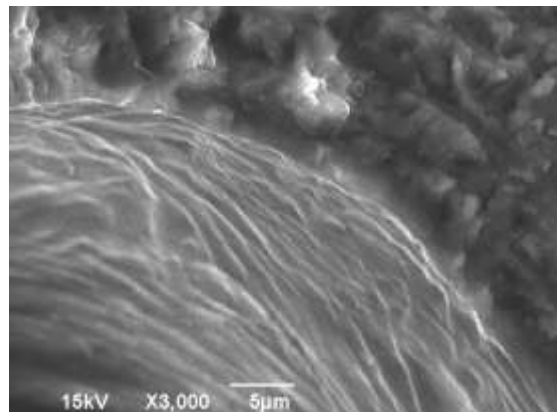


Figure C.251. SEM image of OI human tibia (transverse, posterior section) $\times 3,000$

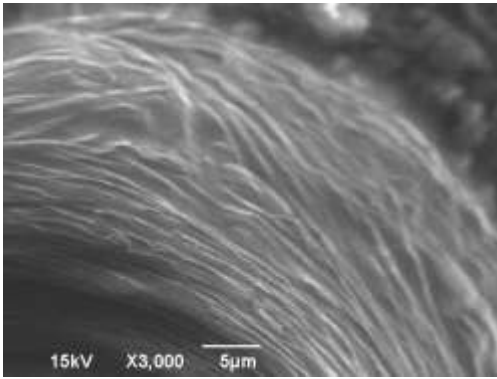


Figure C.252. SEM image of OI human tibia (transverse, posterior section) $\times 3,000$

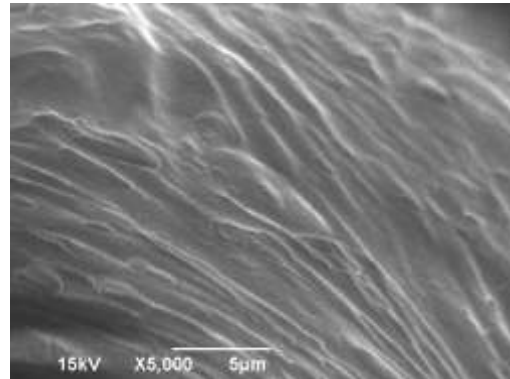


Figure C.253. SEM image of OI human tibia (transverse, posterior section) $\times 5,000$

C.4.2. Longitudinal section (acquired on 2/6/2014)

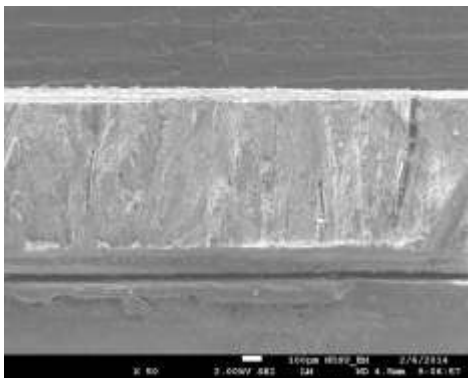


Figure C.254. SEM image of OI human tibia (longi., posterior section) $\times 50$

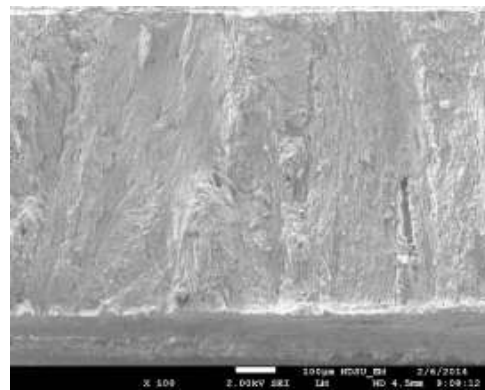


Figure C.255. SEM image of OI human tibia (longi., posterior section) $\times 100$

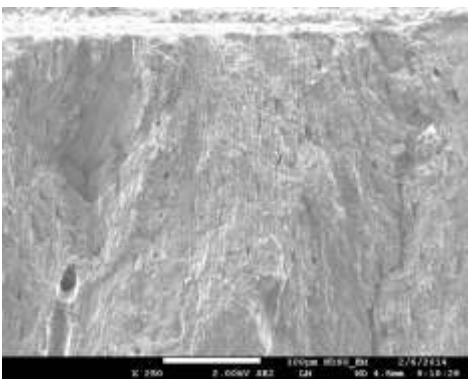


Figure C.256. SEM image of OI human tibia (longi., posterior section) $\times 250$

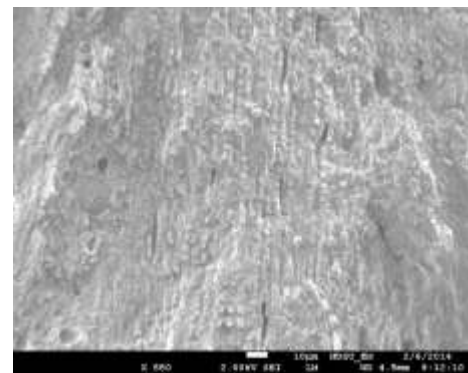


Figure C.257. SEM image of OI human tibia (longi., posterior section) $\times 550$

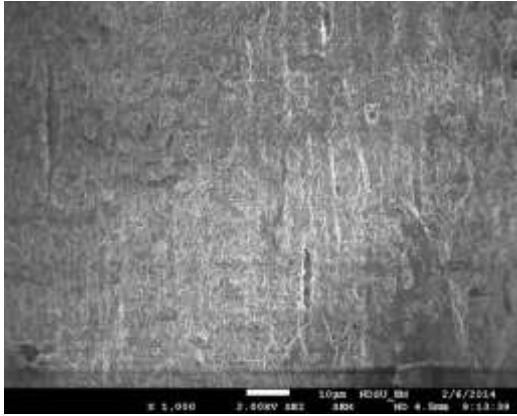


Figure C.258. SEM image of OI human tibia (longi., posterior section) $\times 1,000$

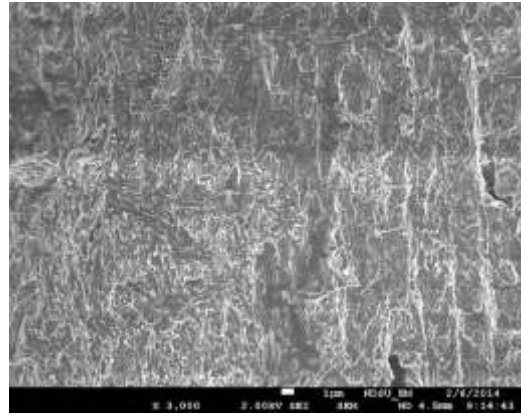


Figure C.259. SEM image of OI human tibia (longi., posterior section) $\times 3,000$

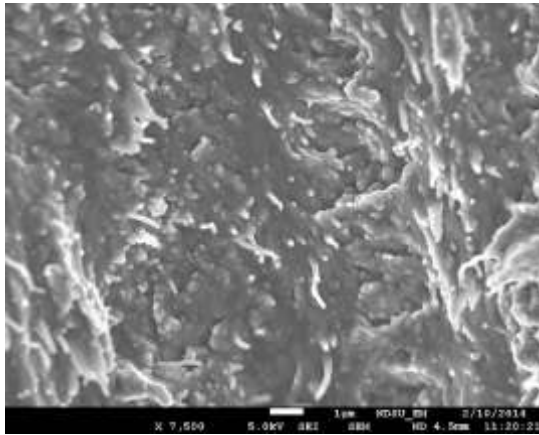


Figure C.260. SEM image of OI human tibia (longi., posterior section) $\times 7,500$

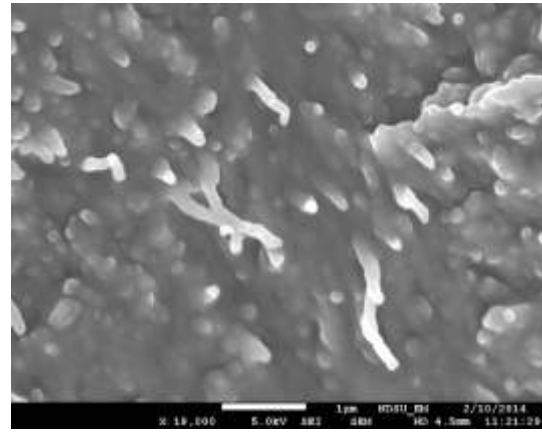


Figure C.261. SEM image of OI human tibia (longi., posterior section) $\times 19,000$

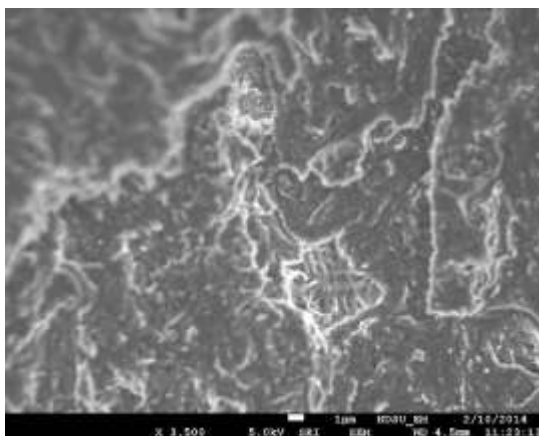


Figure C.262. SEM image of OI human tibia (longi., posterior section) $\times 3,500$

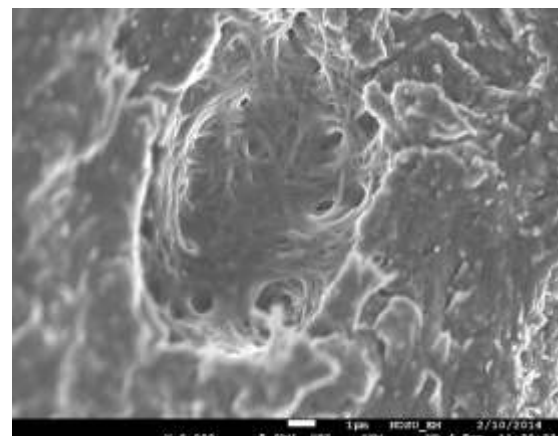


Figure C.263. SEM image of OI human tibia (longi., posterior section) $\times 6,000$

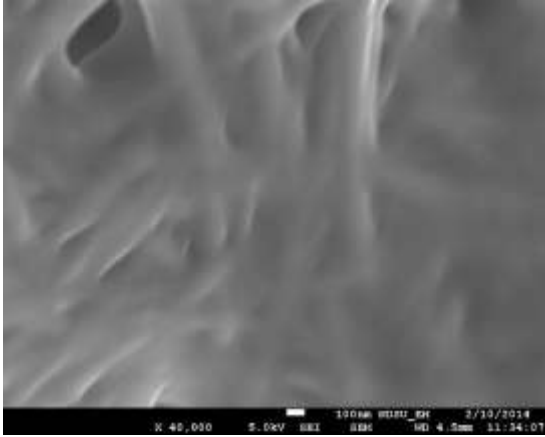


Figure C.264. SEM image of OI human tibia (longi., posterior section) $\times 40,000$

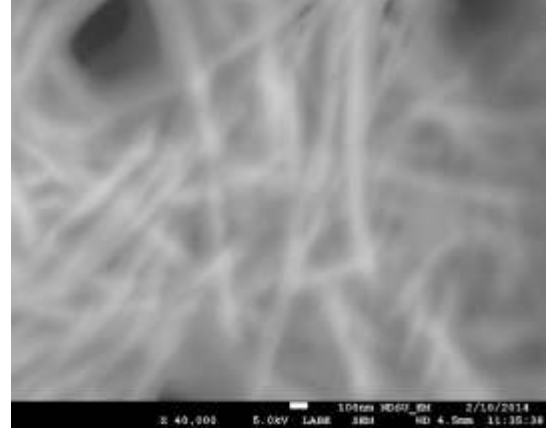


Figure C.265. SEM image of OI human tibia (longi., posterior section) $\times 40,000$

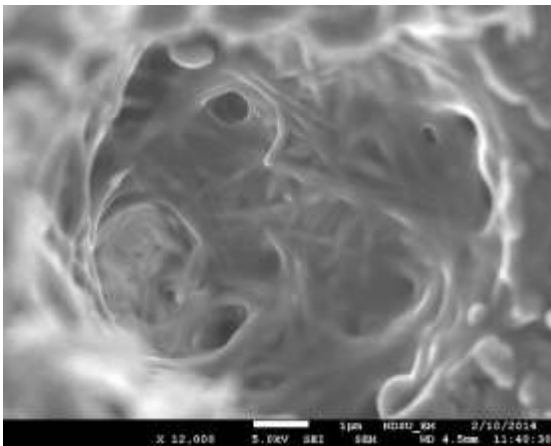


Figure C.266. SEM image of OI human tibia (longi., posterior section) $\times 12,000$

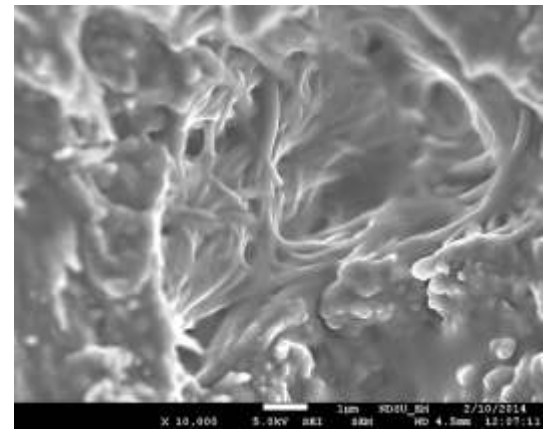


Figure C.267. SEM image of OI human tibia (longi., posterior section) $\times 10,000$

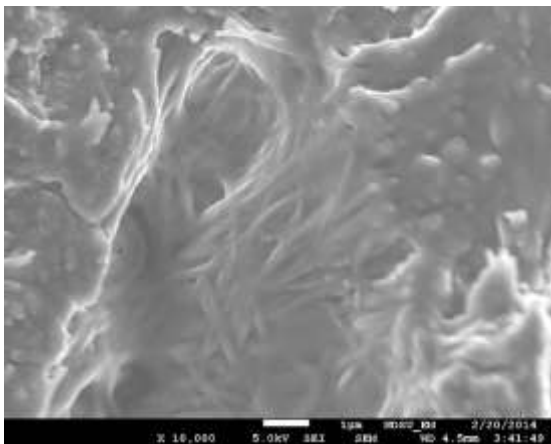


Figure C.268. SEM image of OI human tibia (longi., posterior section) $\times 10,000$

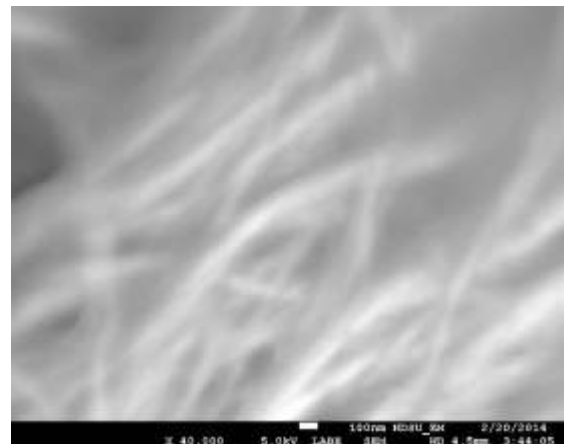


Figure C.269. SEM image of OI human tibia (longi., posterior section) $\times 40,000$

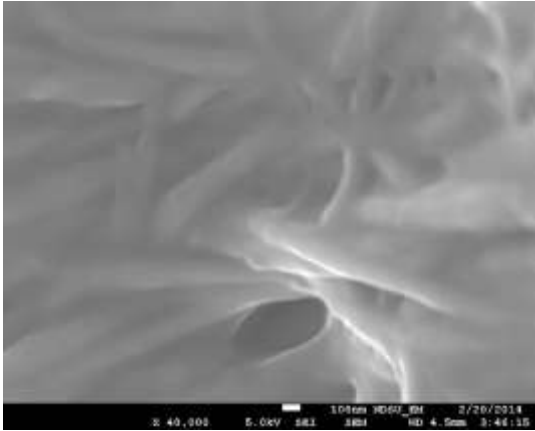


Figure C.270. SEM image of OI human tibia (longi., posterior section) $\times 40,000$

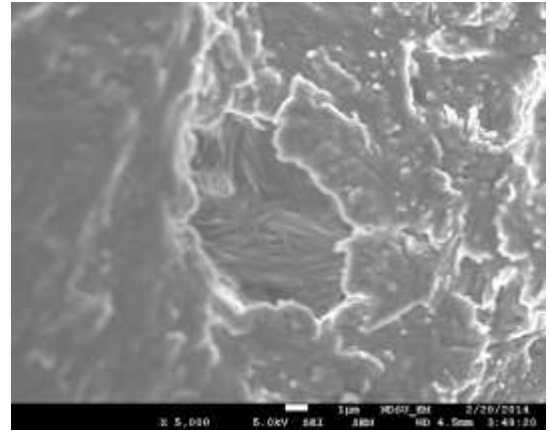


Figure C.271. SEM image of OI human tibia (longi., posterior section) $\times 5,000$

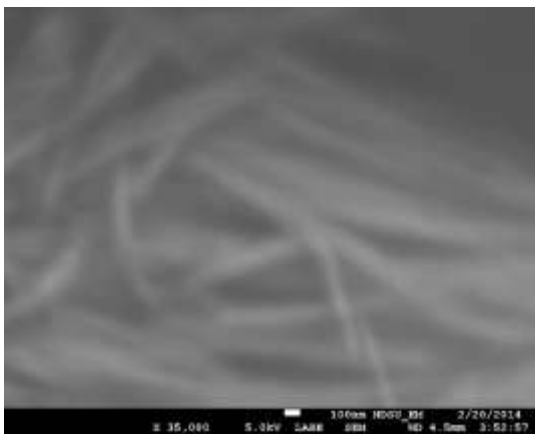


Figure C.272. SEM image of OI human tibia (longi., posterior section) $\times 35,000$

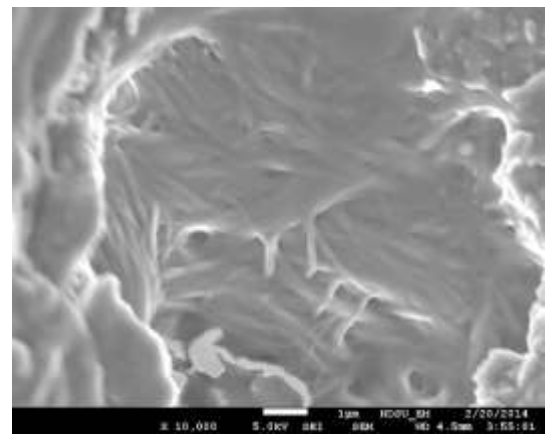


Figure C.273. SEM image of OI human tibia (longi., posterior section) $\times 10,000$

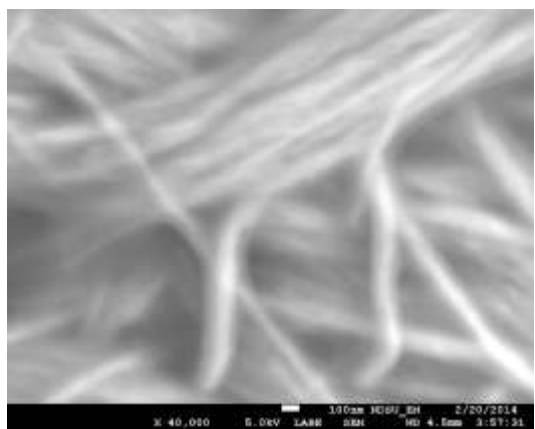


Figure C.274. SEM image of OI human tibia (longi., posterior section) $\times 40,000$

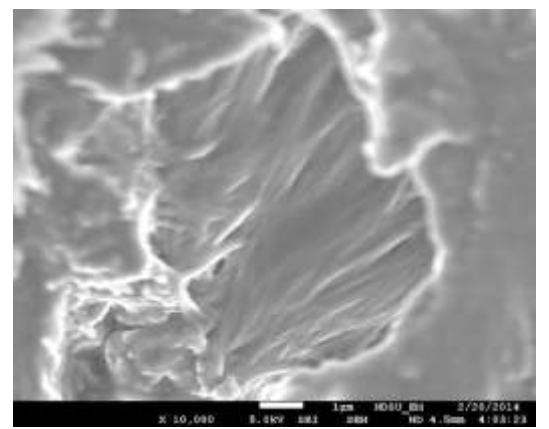


Figure C.275. SEM image of OI human tibia (longi., posterior section) $\times 10,000$

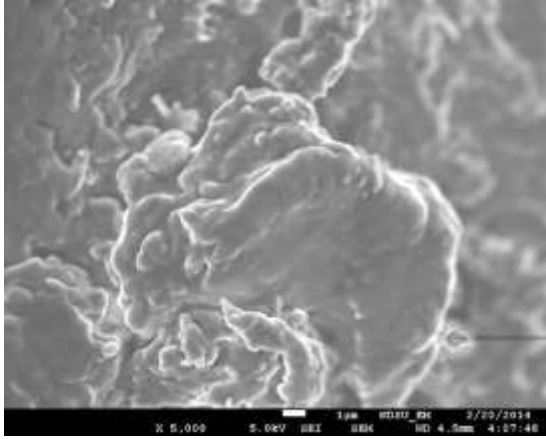


Figure C.276. SEM image of OI human tibia (longi., posterior section) $\times 5,000$

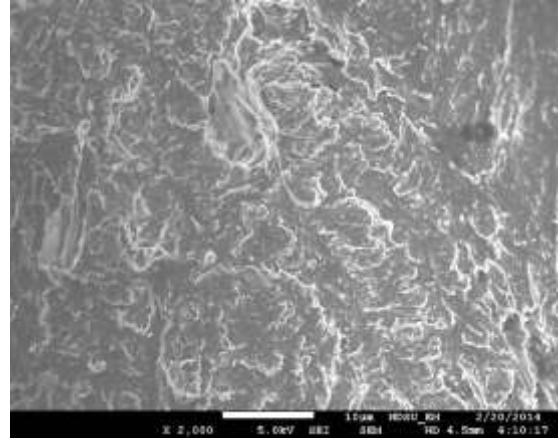


Figure C.277. SEM image of OI human tibia (longi., posterior section) $\times 2,000$

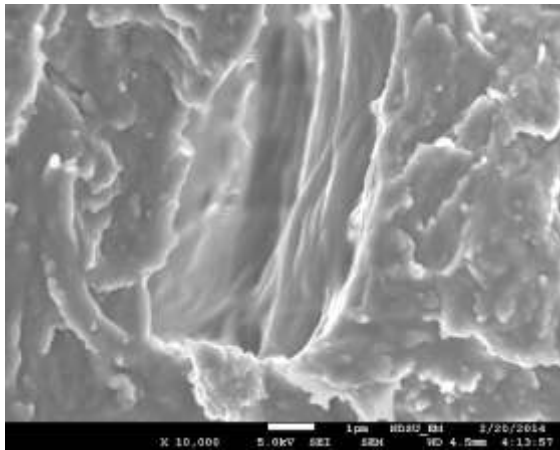


Figure C.278. SEM image of OI human tibia (longi., posterior section) $\times 10,000$

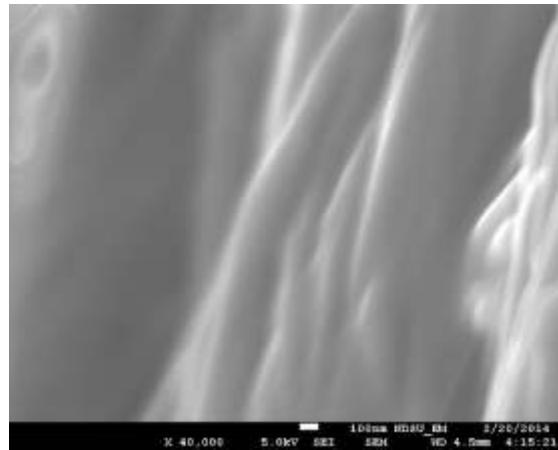


Figure C.279. SEM image of OI human tibia (longi., posterior section) $\times 40,000$

APPENDIX D. AFM IMAGES OF HEALTHY AND OI HUMAN BONES

D.1. Healthy human femur (left image: height, right image: phase)

D.1.1. No treatment, not polished

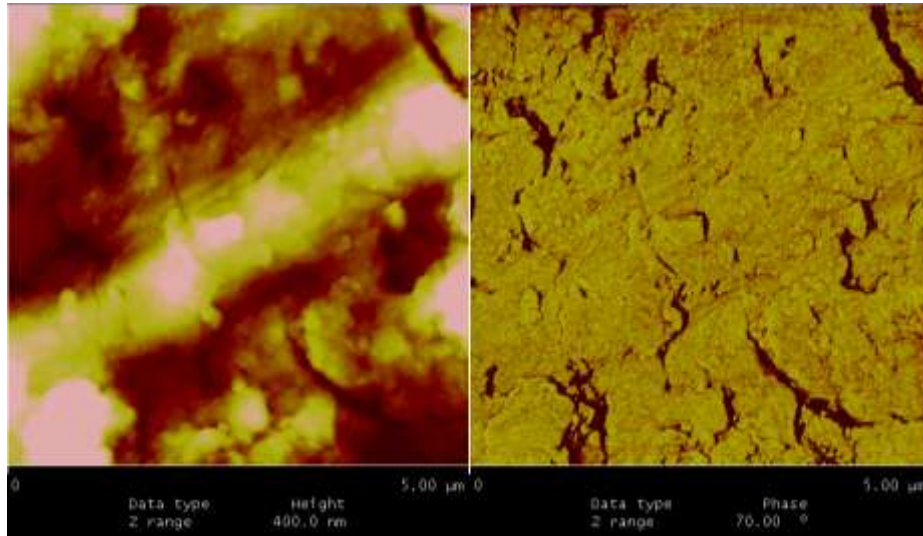


Figure D.1. AFM image of healthy human femur (longi., anterior section, no treatment, not polished), 5µm×5µm

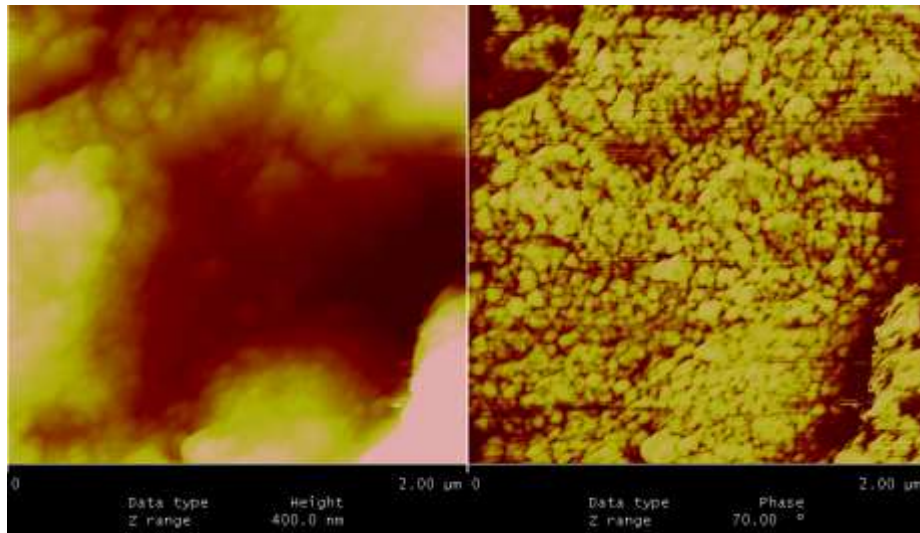


Figure D.2. AFM image of healthy human femur (longi., anterior section, no treatment, not polished), 2µm×2µm

D.1.2. No treatment, polished

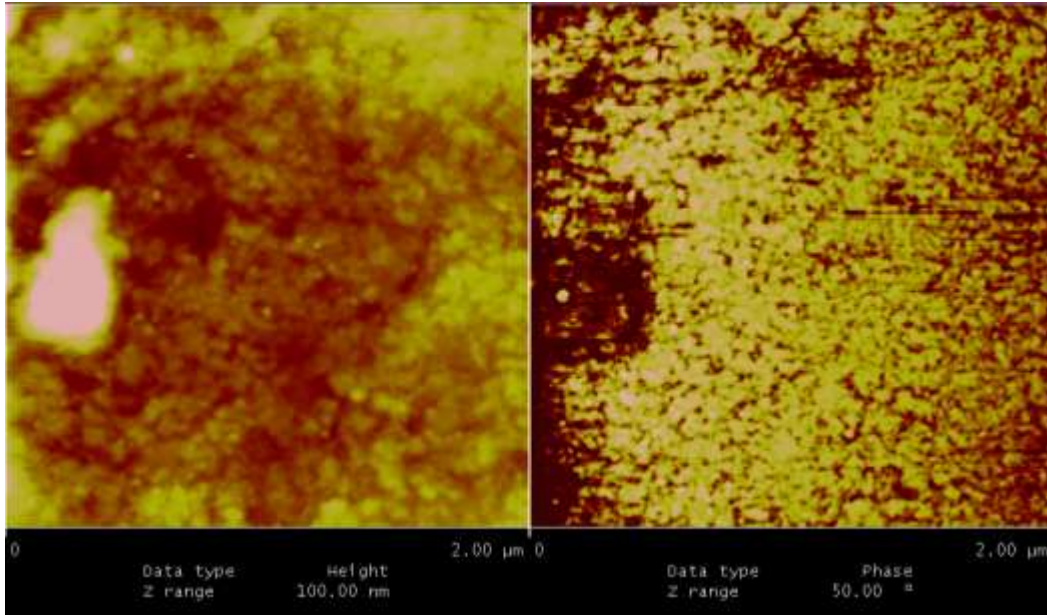


Figure D.3. AFM image of healthy human femur (longi., anterior section, no treatment, polished), $2\mu\text{m}\times 2\mu\text{m}$

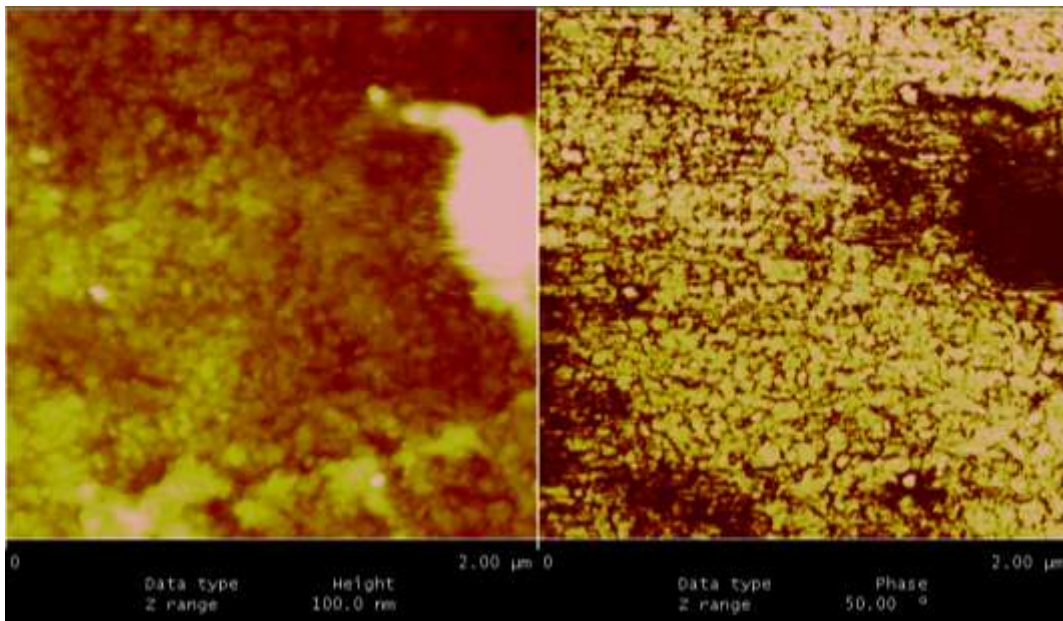


Figure D.4. AFM image of healthy human femur (longi., anterior section, no treatment, polished), $2\mu\text{m}\times 2\mu\text{m}$

D.1.3. Demineralized for 5 minutes in EDTA (left image: height, right image: phase)

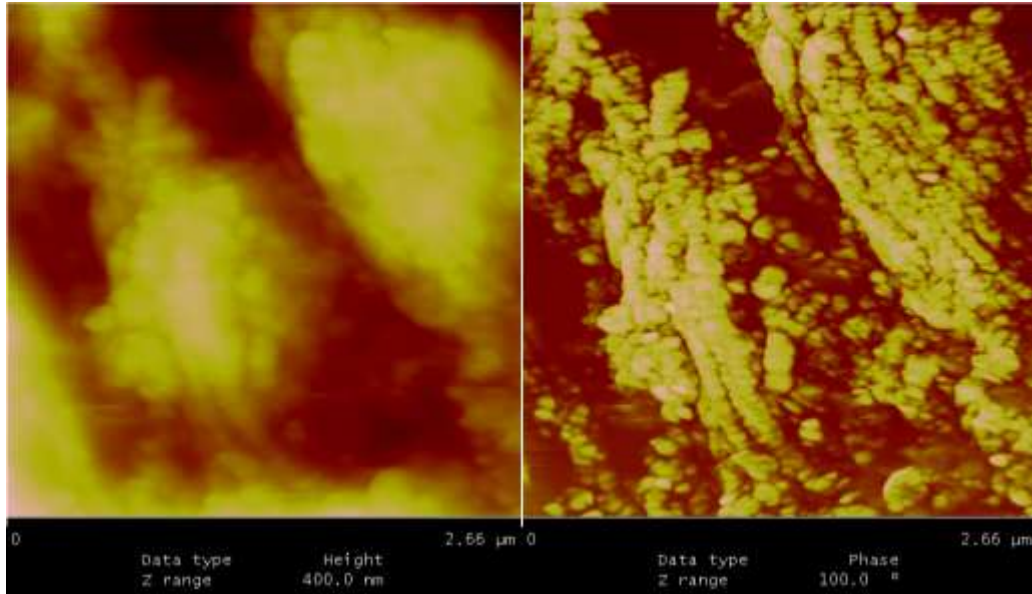


Figure D.5. AFM image of healthy human femur (longi., anterior section, demineralized for 5 minutes), $2.66\mu\text{m}\times 2.66\mu\text{m}$

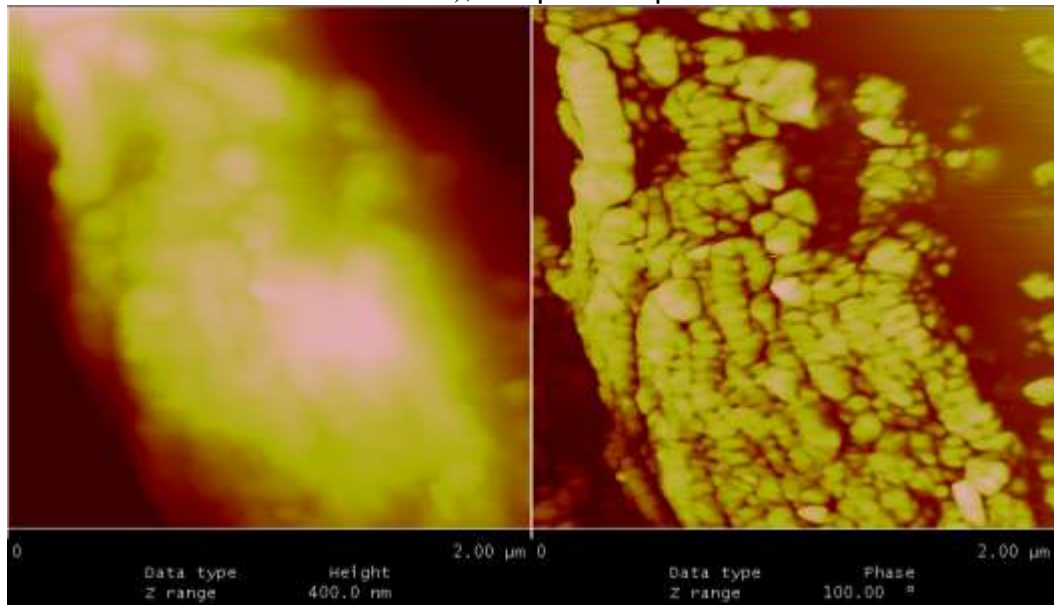


Figure D.6. AFM image of healthy human femur (longi., anterior section, demineralized for 5 minutes), $2\mu\text{m}\times 2\mu\text{m}$

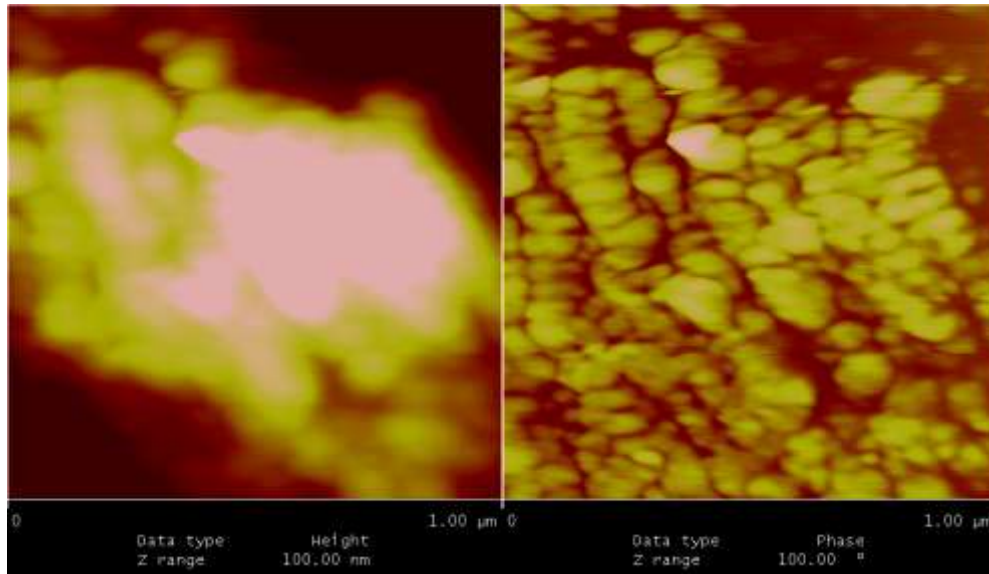


Figure D.7. AFM image of healthy human femur (longi., anterior section, demineralized for 5 minutes), $1\mu\text{m}\times 1\mu\text{m}$

D.1.4. Demineralized for 4 hours in EDTA

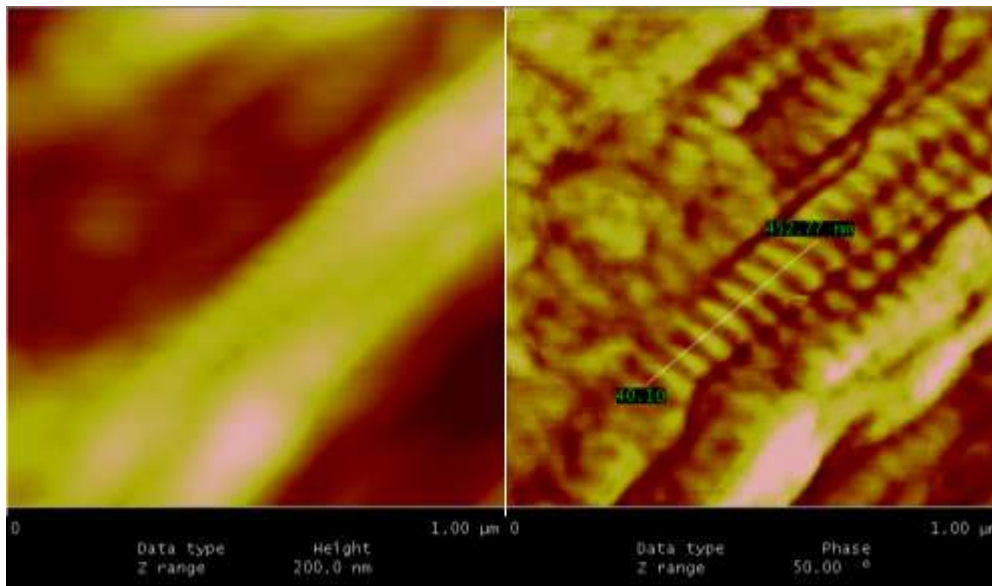


Figure D.8. AFM image of healthy human femur (longi., anterior section, demineralized for 4 hours), $1\mu\text{m}\times 1\mu\text{m}$

Period: $452.77/8=56.60$ nm (it should be 65.01nm after calibration adjustment)

After calibration (calibrated on 5/15/2013, 43.5nm becomes 50.0nm):

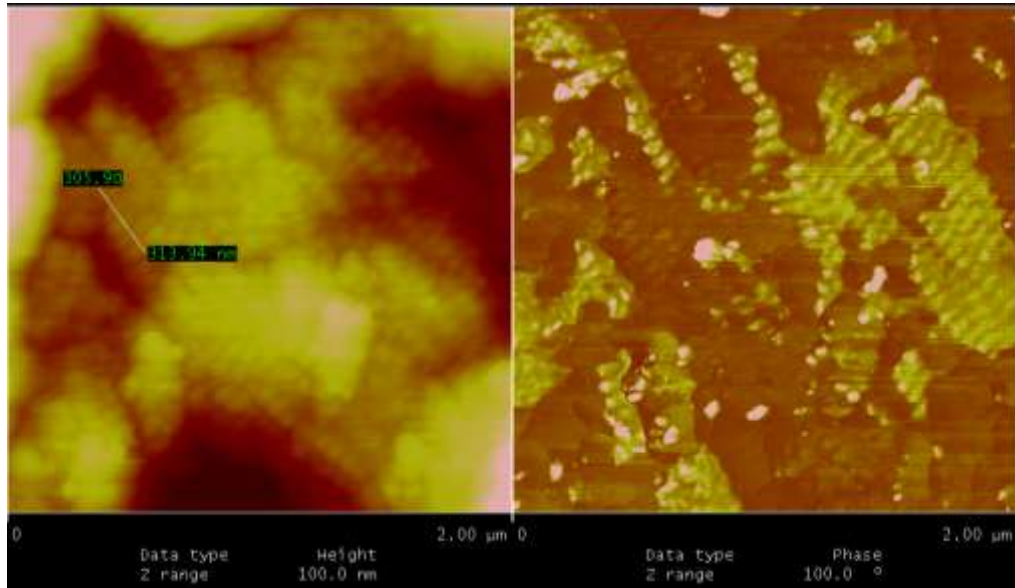


Figure D.9. AFM image of healthy human femur (longi., anterior section, demineralized for 4 hours), $2\mu\text{m}\times 2\mu\text{m}$

Period: $313.94/5=62.79$ nm

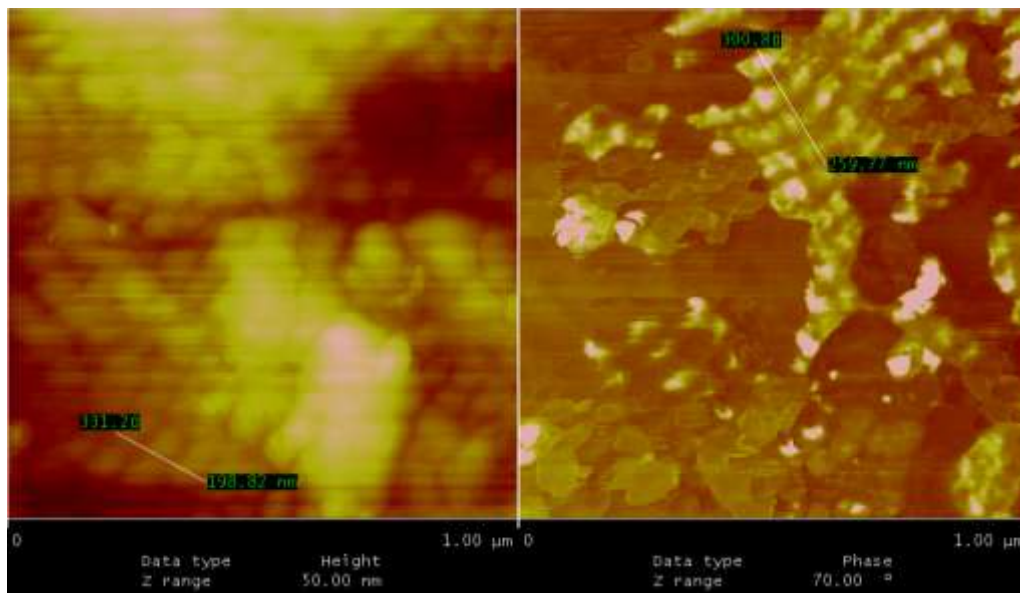


Figure D.10. AFM image of healthy human femur (longi., anterior section, demineralized for 4 hours), $1\mu\text{m}\times 1\mu\text{m}$

Period: $66.27/3=66.27$ nm; $259.77/4=64.94$ nm

D.2. OI human tibia

D.2.1. No treatment, not polished

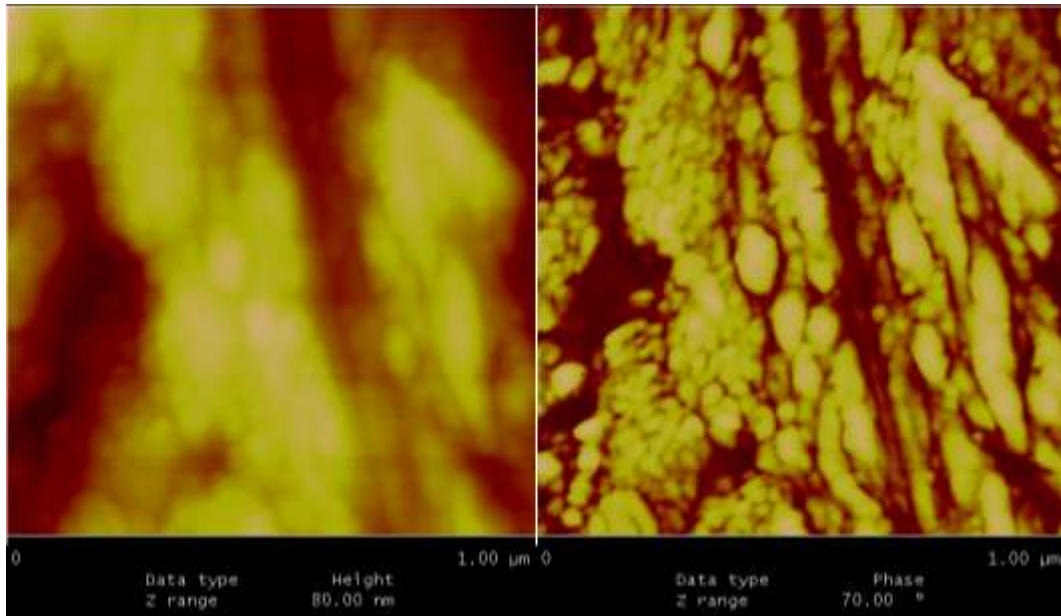


Figure D.11. AFM image of OI human femur (longi., anterior section, no treatment, not polished), $1\mu\text{m}\times 1\mu\text{m}$

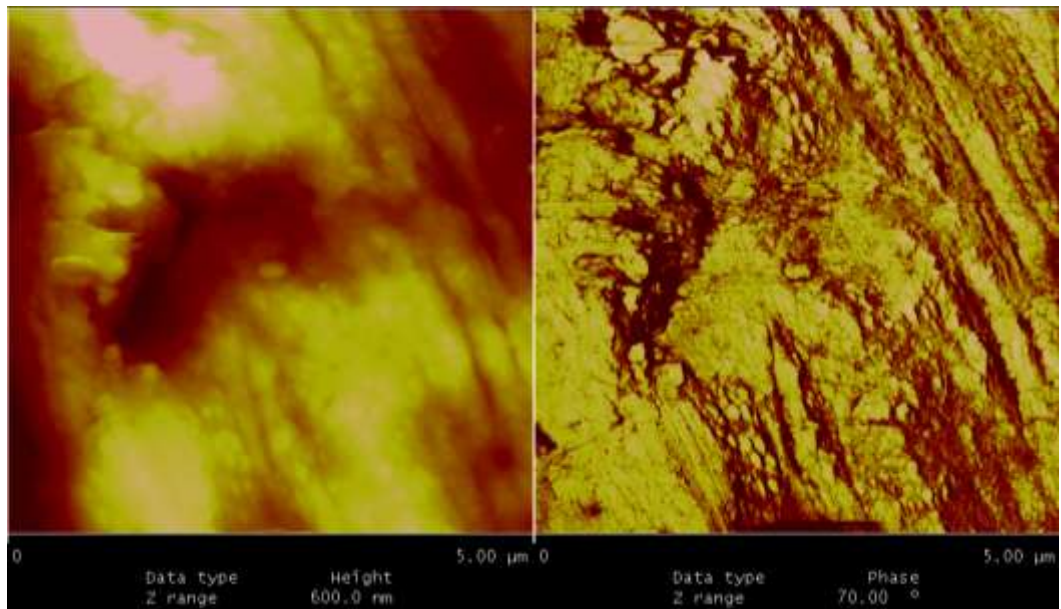


Figure D.12. AFM image of OI human femur (longi., anterior section, no treatment, not polished), $5\mu\text{m}\times 5\mu\text{m}$

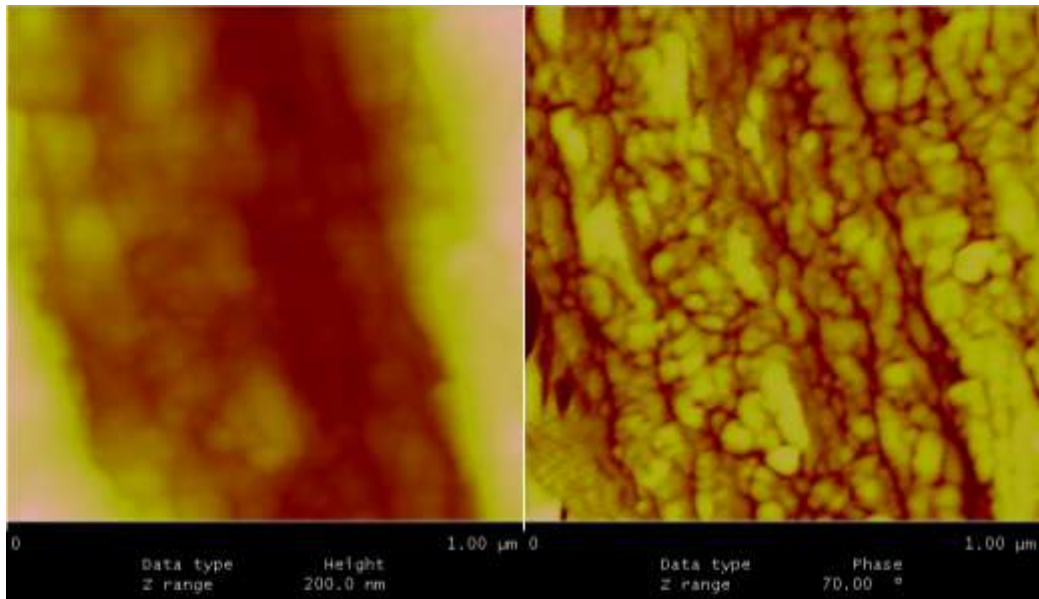


Figure D.13. AFM image of OI human femur (longi., anterior section, no treatment, not polished), $1\mu\text{m}\times 1\mu\text{m}$

D.2.2. No treatment, polished

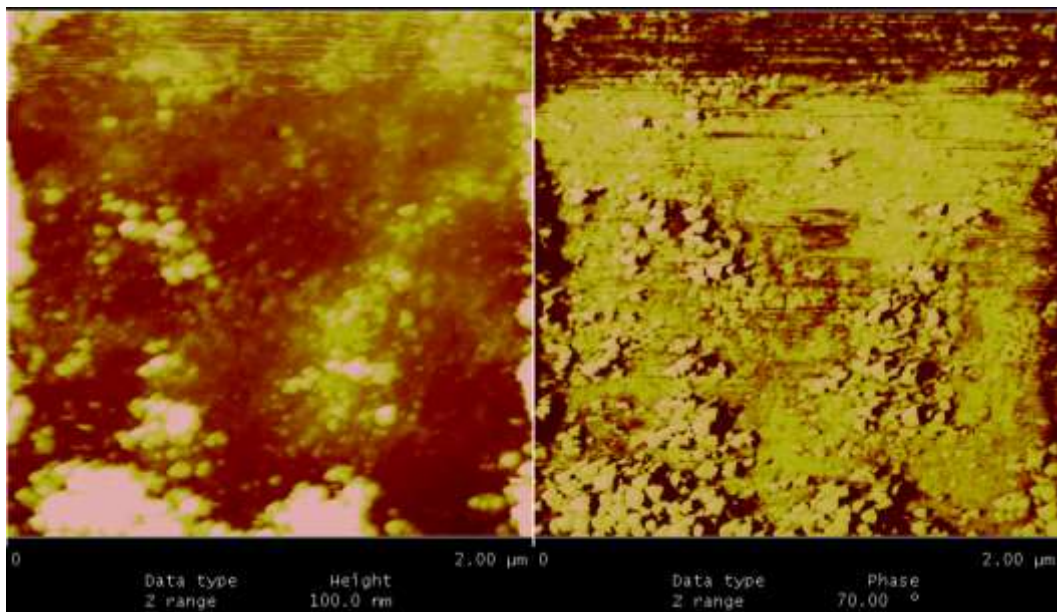


Figure D.14. AFM image of OI human femur (transverse, anterior section, no treatment, polished), $5\mu\text{m}\times 5\mu\text{m}$

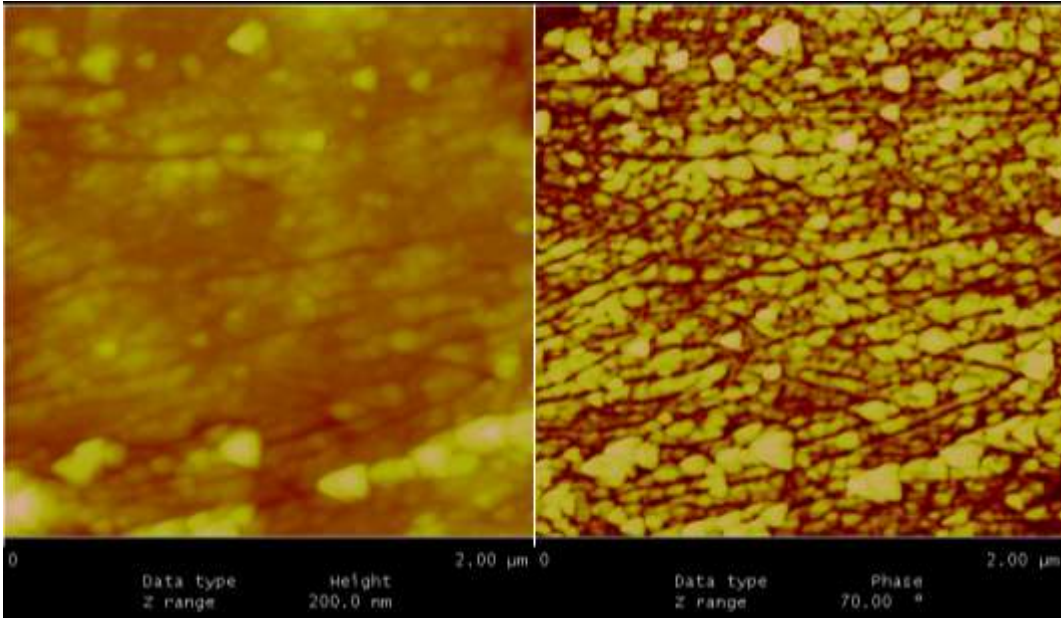


Figure D.15. AFM image of OI human femur (transverse, anterior section, no treatment, polished), 2µm×2µm

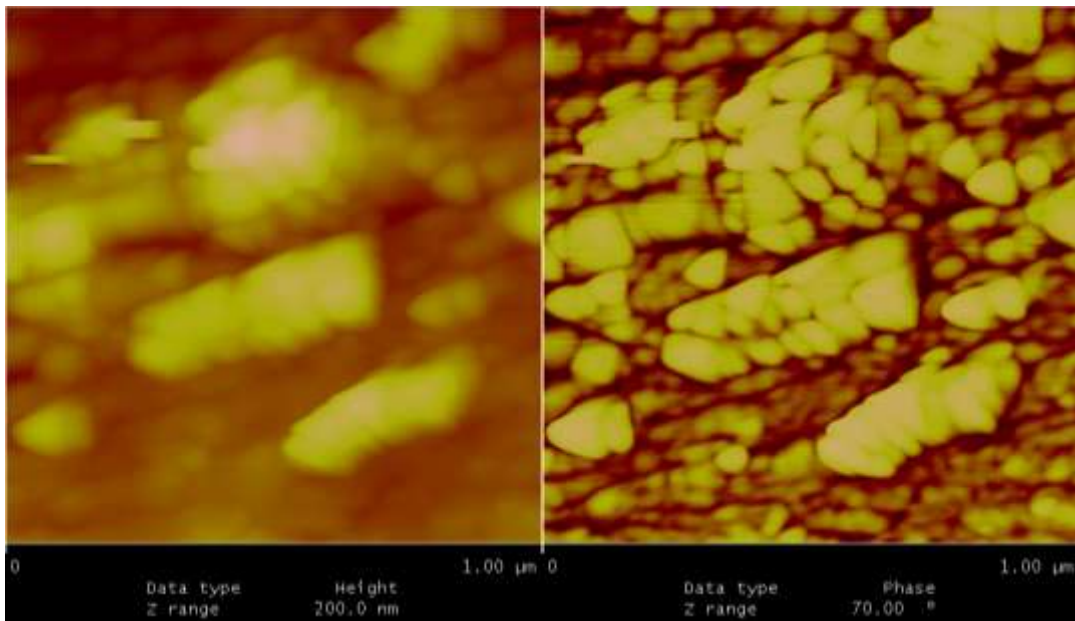


Figure D.16. AFM image of OI human femur (transverse, anterior section, no treatment, polished), 1µm×1µm

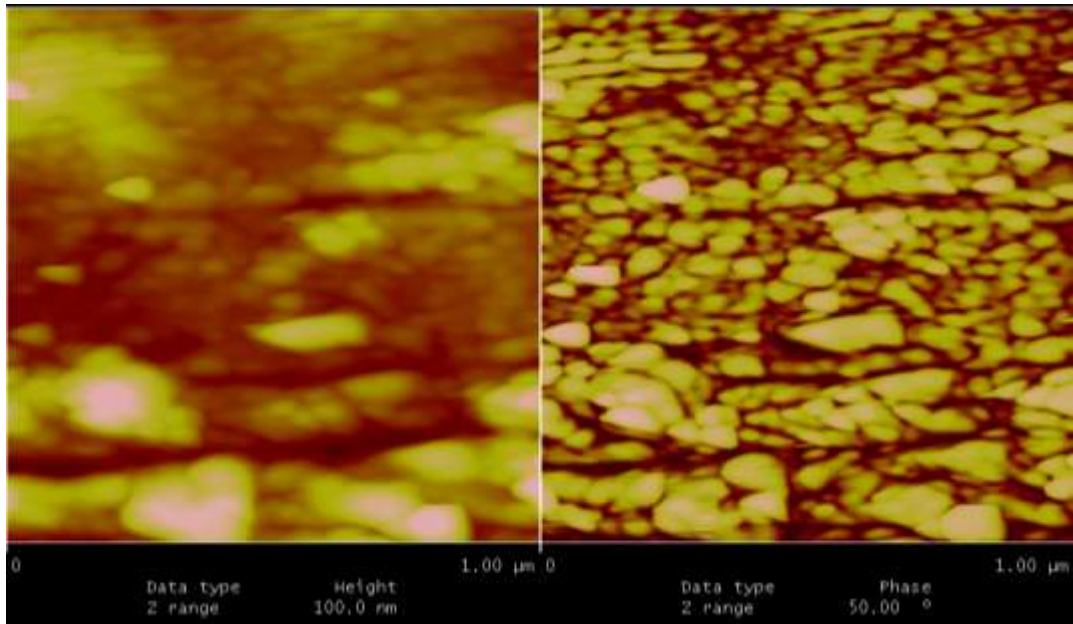


Figure D.17. AFM image of OI human femur (transverse, anterior section, no treatment, polished), $1\mu\text{m}\times 1\mu\text{m}$

Longitudinal section (acquired on 04/07/2013, 04/16/2013)

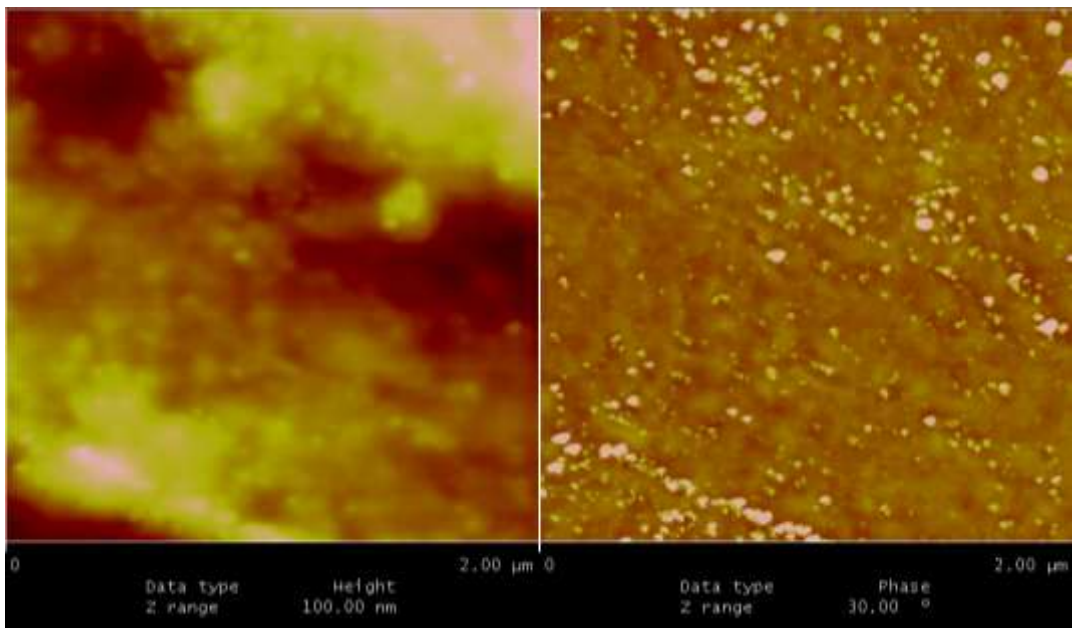


Figure D.18. AFM image of OI human femur (longi., anterior section, no treatment, polished), $2\mu\text{m}\times 2\mu\text{m}$

D.2.3. Demineralized for 5 minutes

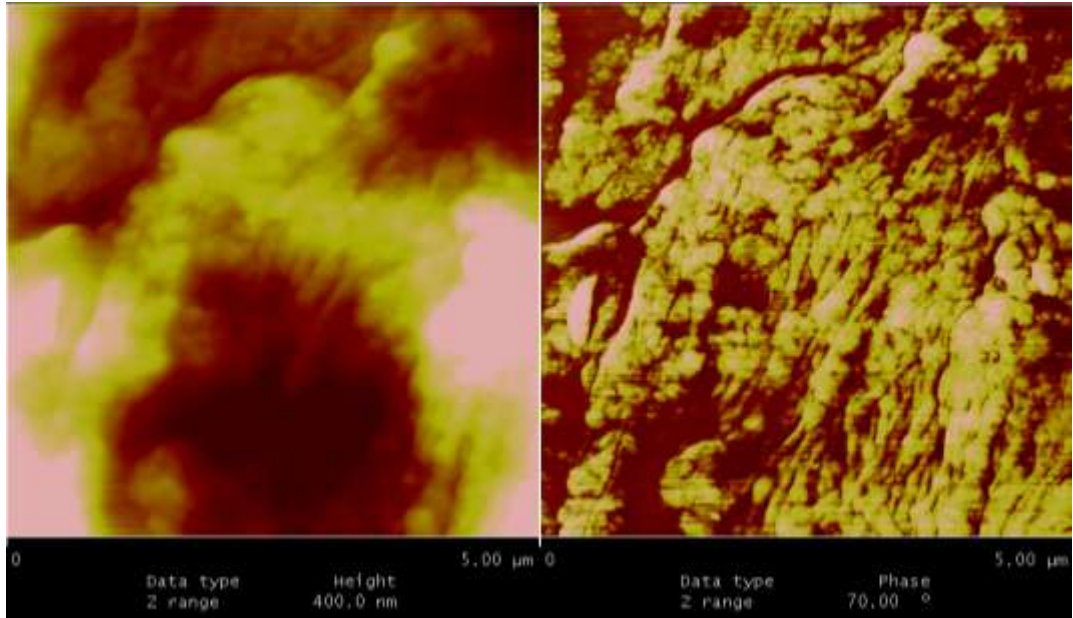


Figure D.19. AFM image of OI human femur (longi., anterior section, demineralized for 5 minutes), $5\mu\text{m}\times 5\mu\text{m}$

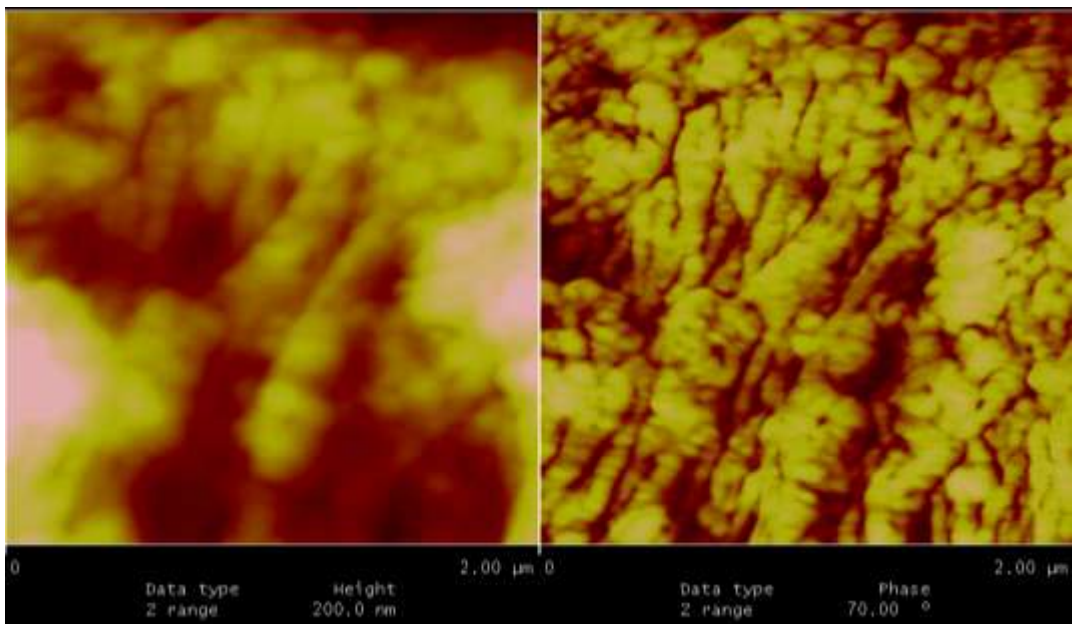


Figure D.20. AFM image of OI human femur (longi., anterior section, demineralized for 5 minutes), $2\mu\text{m}\times 2\mu\text{m}$

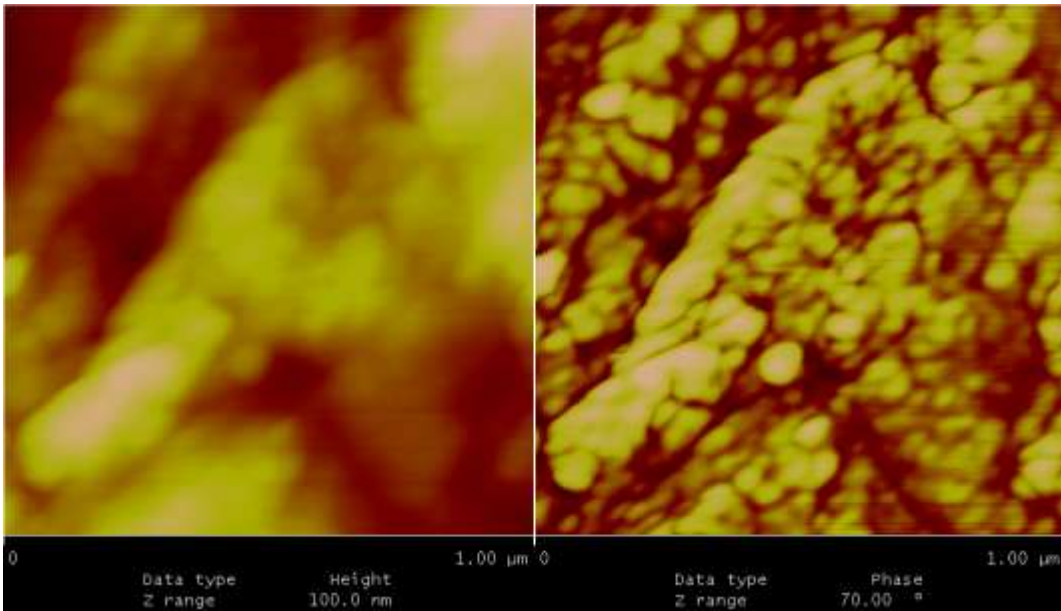


Figure D.21. AFM image of OI human femur (longi., anterior section, demineralized for 5 minutes), $1\mu\text{m}\times 1\mu\text{m}$

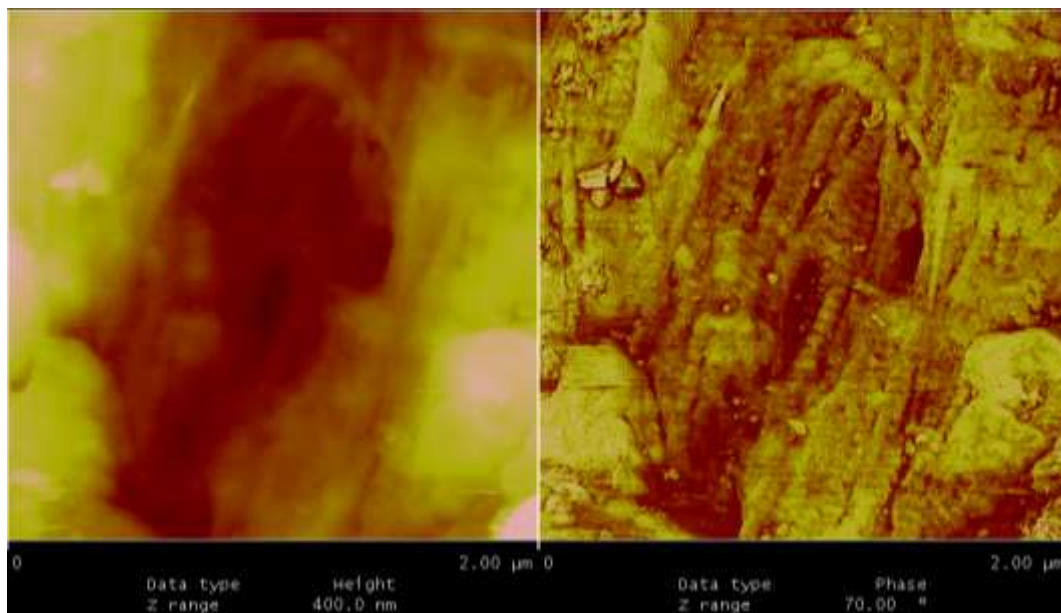


Figure D.22. AFM image of OI human femur (longi., anterior section, demineralized for 5 minutes), $2\mu\text{m}\times 2\mu\text{m}$

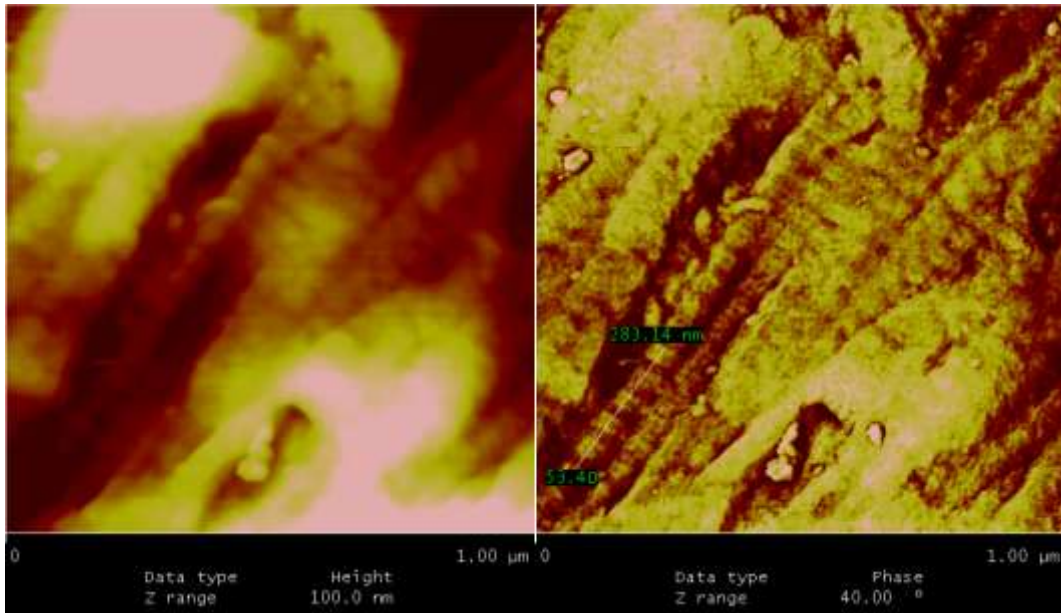


Figure D.23. AFM image of OI human femur (longi., anterior section, demineralized for 5 minutes), $1\mu\text{m}\times 1\mu\text{m}$

Period: $283.14/5=56.63$ nm (it should be 65.09 nm after calibration adjustment)